NASA CP-2001
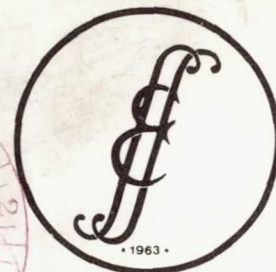
ADVANCES IN ENGINEERING SCIENCE

Volume 4

13th Annual Meeting
Society of Engineering Science
Sponsored by JIAFS
Hampton, VA, November 1—3, 1976

NASA

National
Aeronautics and
Space
Administration

Society of
Engineering Science

• 1963 •

NASA CP-2001

Advances In Engineering Science

Volume 4

13th Annual Meeting
Society of Engineering Science
Hampton, VA, November 1—3, 1976

Sponsored by Joint Institute for Advancement of Flight Sciences

NASA Langley Research Center

and

George Washington University

NASA
National
Aeronautics and
Space
Administration

Society of
Engineering Science

PREFACE

The technical program of the 13th Annual Meeting of the Society of Engineering Science, Inc., consisted of 159 invited and contributed papers covering a wide variety of research topics, a plenary session, and the Annual Society of Engineering Science Lecture. Thirty-three of the technical sessions contained invited and/or contributed papers while two of the sessions were conducted as panel discussions with audience participation.

These Proceedings, which contain the technical program of the meeting, are presented in four volumes arranged by subject material. Papers in materials science are contained in Volume I. Volume II contains the structures, dynamics, applied mathematics, and computer science papers. Volume III contains papers in the areas of acoustics, environmental modeling, and energy. Papers in the area of flight sciences are contained in Volume IV. A complete Table of Contents and an Author Index are included in each volume.

We would like to express particular appreciation to the members of the Steering Committee and the Technical Organizing Committee for arranging an excellent technical program. Our thanks are given to all faculty and staff of the Joint Institute for Advancement of Flight Sciences (both NASA Langley Research Center and The George Washington University) who contributed to the organization of the Meeting. The assistance in preparation for the meeting and this document of Sandra Jones, Virginia Lazenby, and Mary Torian is gratefully acknowledged. Our gratitude to the Scientific and Technical Information Prgrams Division of the NASA Langley Research Center for publishing these Proceedings is sincerely extended.

Hampton, Virginia 1976

J. E. Duberg

J. L. Whitesides

iii

Co-Chairmen

J. E. Duberg
NASA Langley Research Center

J. L. Whitesides
The George Washington University

Steering Committee

W. D. Erickson, NASA Langley Research Center
P. J. Bobbitt, NASA Langley Research Center
H. F. Hardrath, NASA Langley Research Center
D. J. Martin, NASA Langley Research Center
M. K. Myers, The George Washington University
A. K. Noor, The George Washington University
J. E. Duberg, NASA Langley Research Center, Ex-officio
J. L. Whitesides, The George Washington University, Ex-officio

Technical Organizing Committee

C. L. Bauer, Carnegie-Mellon University
L. B. Callis, NASA Langley Research Center
J. R. Elliott, NASA Langley Research Center
K. Karamcheti, Stanford University
P. Leehey, Massachusetts Institute of Technology
J. S. Levine, NASA Langley Research Center
R. E. Little, University of Michigan-Dearborn
J. M. Ortega, Institute for Computer Applications in Science
and Engineering
E. M. Pearce, Polytechnic Institute of New York
A. D. Pierce, Georgia Institute of Technology
E. Y. Rodin, Washington University
L. A. Schmit, University of California at Los Angeles
G. C. Sih, Lehigh University
E. M. Wu, Washington University

SOCIETY OF ENGINEERING SCIENCE, INC.

The purpose of the Society, as stated in its incorporation document, is "to foster and promote the interchange of ideas and information among the various fields of engineering science and between engineering science and the fields of theoretical and applied physics, chemistry, and mathematics, and, to that end, to provide forums and meetings for the presentation and dissemination of such ideas and information, and to publish such information and ideas among its members and other interested persons by way of periodicals and otherwise."

OFFICERS

L. V. Kline, President
  IBM Corporation

S. W. Yuan, First Vice President and Director
  The George Washington University

C.E. Taylor, Second Vice President and Director
  University of Illinois

E. Y. Rodin, Second Vice President and Director
  The George Washington University

R. P. McNitt, Secretary
  Virginia Polytechnic Institute and State University

J. Peddieson, Treasurer
  Tennessee Technological University

DIRECTORS

B. A. Boley, Northwestern University
G. Dvorak, Duke University
T. S. Chang, Massachusetts Institute of Technology
E. Montroll, University of Rochester
J. M. Richardson, North American Rockwell Corp.
E. Saibel, Army Research Office
J. W. Dunkin, Exxon Production Research Co.
J. T. Oden, University of Texas

CORPORATE MEMBERS

Chevron Oil Field Research Company
Exxon Production Research Company
IBM Corporation
OEA Incorporated

Page intentionally left blank

CONTENTS

MATERIALS SCIENCE III
Chairman: J. H. Crews, Jr.

COMPOSITE MATERIALS
Chairman: E. M. Wu

DYNAMIC FRACTURE MECHANICS
Chairman: G. C. Sih

FRACTURE MECHANICS
Chairman: H. F. Hardrath

IMPACT AND VIBRATION
Chairman: H. L. Runyan, Jr.

VOLUME II

STRUCTURAL SYNTHESIS
Chairman: F. Barton

NONLINEAR ANALYSIS OF STRUCTURES
Chairman: M. S. Anderson

BEAMS, PLATES, AND SHELLS
Chairman: M. Stern

COMPOSITE STRUCTURES
Chairman: J. Vinson

AEROACOUSTICS II
Chairman: A. Nayfeh

WAVE PROPAGATION
Chairman: E. Y. Rodin

ATMOSPHERIC SOUND PROPAGATION
Chairman: M. K. Myers

VOLUME IV

VISCOUS FLOW I
Chairman: S. Rubin

VISCOUS FLOW II
Chairman: D. M. Bushnell

PROSPECTS FOR COMPUTATIONAL

FLUID DYNAMICS IN THE NEXT DECADE

Percy J. Bobbitt
NASA Langley Research Center

With so many of our leading numerical fluid mechanicians participating in the 13th Annual Society of Engineering Science Meeting, and considering the phenomenal progress made in the area of computational fluid dynamics during the past few years, it was decided by the organizers that now was an appropriate time to consider where we are going in the next decade. Predictions are always hazardous and the farther we try to look ahead the more clouded our perception becomes. Still with all the uncertainties a look in the crystal ball can be very beneficial, particularly if it's done by a number of experts of diverse backgrounds and interests in an interactive mode.

The main benefits that I see from such an exercise are threefold: It enables those of us who depend on other disciplines (technologies), say as a computational fluid dynamicist depends on the capabilities of his computer, to anticipate future developments in those areas and set our long-range goals with greater accuracy, it requires us to think about where, and how fast, we are going collectively, and finally it gives us a clearer understanding of how truly interdependent we are.

New numerical techniques, some of which were exposed in earlier conference papers, show promise of decreasing our computation time from one to two orders of magnitude during the next few years. At the Langley and Ames Research Centers the STAR and ILLIAC computers are now being employed to provide additional reductions in computation time. For instance, a "Navier-Stokes" calculation made last spring on the STAR computer reduced CPU time by a factor of 65 over that required by the CDC 6600. These computers also have greatly expanded the size of problems that can be handled by virtue of their storage capacity. Nevertheless, if the past is any indication we will soon become impatient with the limitations of these machines and start looking for the next generation computer with hopefully one to two orders of magnitude greater speed and storage.

Numerical techniques and computing power are only two corners of the computational fluid dynamics triangle. What about transition prediction and turbulence modeling? Well, progress is being made but this technology remains the pacing one. It will be speeded, however, by the availability of increased computing power and more accurate/faster numerical methods. (One continues to hope for a more universal concept, a breakthrough, to codify all the diverse turbulent phenomena.) So all the important elements of computational fluid dynamics are moving ahead. What improvements do you foresee during the next decade in these elements? What will they lead to in terms of problem solving capabilities? Are we doing all we should to further the state of the art? Hopefully the panel members with an assist from the conferees can shed some light on these questions. Brief "position statements" of each of the panelists follow.

Page intentionally left blank

PROSPECTS FOR COMPUTATIONAL FLUID DYNAMICS

IN THE NEXT DECADE

J. P. Boris
U. S. Naval Research Laboratory

The prospects for computational fluid dynamics in the next decade couple closely to the steady improvement of computational power. Although the Texas Instruments Advanced Scientific Computer is fully operational now, the Cray I, which has the potential to be more powerful, will only be fully operational in a couple of years after at least a moderate spectrum of optimizing, user-oriented software has been developed. The predictions call for at most a factor of 2-3 in speed over the ASC in any case. Beyond these modest advances (roughly a factor of ten to twenty at most over the large IBM and CDC machines), very little hardware improvement is a certainty. Both Cray and T.I. speak hopefully about improvements of a factor of two to four in speed over their current top of the line products. Granting this advance during the next ten years suggests that the NRL ASC as it is currently configured (two arithmetic pipelines and 1,000,000 words of high speed bipolar memory) is nevertheless within a factor of ten of the fastest machine likely to be in use in the world by 1986.

The hardware technology for memory density is progressing faster than computation speed right now so I feel quite confident in predicting at least a ten-fold increase in useable high speed memory, say $1-5 \times 10^7$ words of primary direct access memory by 1986. This advance is timely because my view of the large IBM and CDC machines is that they are unbalanced in current configurations. An IBM 360/91 with half a million words is too small by a factor of three or four and the situation is worse still for the 195 and the 7600.

In computational fluid dynamics itself I expect the greatest advances to come from careful application of new but known techniques taking full advantage of the parallelism of the new vector architectures. These new machines are ideally suited to simple, brute-force calculations which lend themself to vectorization. Thus the balance point between explicit (iterative) techniques and more complicated implicit techniques will shift somewhat toward the simpler explicit methods from even the current position. To be more specific I would like to consider the four fields where I feel computational fluid dynamics can be expected to play the biggest role, weapons design, meteorology, aerodynamic (and reentry) design, and advanced fluid mechanics for plasma, reactive and turbulent flows.

The strong interest in laser fusion schemes is being augmented currently by new ideas for fusion breakeven using electron and ion beams. The nuclear weapons design codes are being revamped for the new computer systems now coming on line and are being applied to these "micro explosion" designs. By the end of the decade breakeven should be obtained using designs developed almost exclusively by computer simulation.

In meteorology the hardware advances in speed and memory are not likely to change current capabilities drastically. A doubling of resolution in all three dimensions is the most that can be expected and this isn't going to change our capability of understanding qualitatively. I look for the on-line, real time acquisition and integration of global satellite data into the numerical models to bring about the biggest qualitative changes in our numerical prediction ability during the decade. The patchy, often inaccurate or incomplete data used to drive existing models is the major source of error as often as not.

In aerodynamic and reentry design many adequate to excellent 3-dimensional calculations are already being performed on present day systems. The next decade will see a dissemination and solidification of this computer technology for steady state design calculations. It is in the realm of highly transient unsteady flow calculations that I expect the biggest gains to be made. Such calculations have been performed in three dimensions already but the resolution has invariably been low (40 x 40 x 30 grids for example). In plasma physics the NCTRCC machines at Livermore can be expected to significantly extend the frontiers of the fusion community and the recently procured CRAY machine at NCAR should have a corresponding role to play in turbulence calculations and important atmospheric flows. The ASC at NRL is already providing inroads into transient reactive flow problems such as arise in combustion research where the goals are increased efficiency, cleanliness, and safety. As one data point of the new capabilities the four conservation equations of ideal compressible hydrodynamics $(\rho, \rho V_x, \rho V_y \ \varepsilon)$ can be solved with strong shocks on a 200 x 200 finite-difference grid in about 2 sec per timestep (NRL ASC). This speed which is five to ten times what can be achieved on the 7600, should allow us to calibrate, by direct computation on finely resolved systems, the actual subgrid closure schemes which will be used in the large macroscopic reactive flow calculations.

SOME THOUGHTS ON NUMERICAL METHODS IN FLUID DYNAMICS

George J. Fix
Carnegie-Mellon University
and ICASE

Can the finite element methods be successfully used for problems in fluid dynamics? This question strikes me as being as inappropriate and misleading as the question of whether the finite difference method can be successfully used in fluid dynamics? The issue of course is which finite element or finite difference method and in which context? This point is crucial for I feel that the "general problem" of computational fluid dynamics, namely the integration of the full Navier-Stokes equations at physically realistic Reynolds numbers, eludes all existing methods and awaits major advances in computer hardware for its ultimate resolution. In the meantime significant advances can be made in "specialized models" where "specialized techniques" are both appropriate and significant.

For example, if the flow is incompressible and if the flow region has rectangular boundaries, then there are versions of the spectral and pseudo-spectral methods [1] which are very powerful. They are subject to cell Reynolds number restrictions [2], however the efficiency and speed of the F.F.T. permits a very large number of modes to be used in the approximation and hence very large Reynolds numbers. I remain quite skeptical of global mapping techniques and thus for curvilinear geometries feel that in this context specialized finite elements (as for example in [3]-[5])and the similar (if not computationally equivalent) finite volume methods are superior. These conclusions may be changed however by the emergence of finite differences which use local mappings of the computational domain.

The use of the velocity potential equation in transonic flow is another example where simplification of the full Navier-Stokes equation has led to advances. For years the Murman-Cole-Jameson difference scheme ([6]-[7]) has been a reliable workhorse. Finite elements also have a potential utility here in providing stable second order approximations (the Murman-Cole-Jameson scheme is only first order accurate) and in treating complicated geometries. Specialized variational principles have been recently developed and compare favorably with the difference approximation [8]. Special note should be made of finite element methods based on least square approximation of the associated first order system for transonics. These ideas seem to work out particularly well in the indefinite cases (i.e., where the time dependence in the potential equation has been removed by an e^{iwt} substitution) [9]. Some recent investigations have shown that least squares approximations may also be effective in treating the first order equations in gas dynamics.

REFERENCES

1. Orszag, S. A. and Israeli, M. (1974) Ann. Rev. Fluid Mech. 6, 281.

2. Roache, P. J. (1972) <u>Computational Fluid Dynamics</u>, Hermosa Publishers, Albuquerque, NM.

3. Fix, G. (1975) <u>Computational Methods in Nonlinear Mechanics</u>, T. Oden, ed., Springer-Verlag.

4. Fix, G. (1976) <u>SIAM Review</u>, Vol. 18, No. 3.

5. Baker, J. (1975) see 3.

6. Murman, E. M. and Cole, J. D., (1971) <u>AIAA J.</u> 9, 114.

7. Jameson, <u>Numerical Solution of Partial Differential Equations</u> III, (1976) B. Hubbard, ed., Academic Press.

8. Fix, G. (1976) "<u>A Mixed Finite Element Scheme for Transonic Flows</u>", NASA ICASE Report.

9. Fix, G. (1976) "<u>Least Squares Approximation of Indefinite Problems of the Mixed Type</u>", NASA ICASE Report.

PROSPECTS FOR COMPUTATIONAL FLUID DYNAMICS IN THE NEXT DECADE

R. W. MacCormack

The Navier-Stokes equations adequately describe aerodynamic flows at standard atmospheric temperatures and pressures. If we could efficiently solve these equations, there would be no need for experimental tests to design flight vehicles or other aerodynamic devices. Unfortunately, analytic or closed form solutions to these equations exist for only a few simple flow problems. During the past decade the computer has been used to generate many new solutions. However, even with the rapid progress in both numerical methods and computer resources, these solutions have been restricted to low Reynolds number or two-dimensional flows.

Recent progress in the development of efficient numerical methods has drastically reduced the computation time required to solve the Navier-Stokes equations at flight Reynolds numbers. Though flows past complete aircraft configurations are still beyond our reach, it is now possible and practical to calculate many important three-dimensional, high Reynolds number flow fields on today's computers.

During the next decade we must expect this progress in both numerical methods and computer hardware development to continue. Also we can expect a parallel development in the modeling of turbulent separated flows. By the end of the next decade we should be able to solve for the flow field about complete aircraft in sufficient detail for design purposes.

Page intentionally left blank

COMMENTS ON "PROSPECTS FOR COMPUTATIONAL

FLUID DYNAMICS IN THE NEXT DECADE"

Steven A. Orszag
Department of Mathematics
M.I.T.
Cambridge, Mass.   02139

The basic assumption for the following statements is that the speed and core storage of the computers available in 1986 will be about 100 times larger than those available on a CDC 7600 computer now.

1.   Calculations of transition and turbulence. Some problems that may be solved within the next decade are: (i) Back-transfer inertial range structure in two dimensions; (ii) Structure of three-dimensional turbulent shear flows at moderate Reynolds numbers; (iii) Study of three-dimensional homogeneous turbulence at Reynolds numbers $R \approx 500$; (iv) Solution of transition problems on simple bodies; (v) Calculations of transition on flat plates including accurate calculations of turbulent spot development.

2.   Numerical techniques and modelling. Accurate numerical tests of turbulence modelling hypotheses should be available. These will be based on comparisons of direct solutions of the Navier-Stokes equations with the modelling predictions. Further developments in the mathematics of spectral methods, finite element methods and difference techniques will influence computational fluid dynamics.

3.   Navier-Stokes computer. It may be possible and preferable to design a special purpose Navier-Stokes computer that is dedicated to problems of computational fluid dynamics. Recent developments in the minicomputer field suggest the utility of this approach.

Page intentionally left blank

Prospects for Computational Fluid Dynamics in the Next Decade:
    some thoughts by William C. Reynolds, Chairman, Department
    of Mechanical Engineering, Stanford University.

My interest is in the computation of turbulent flows of practical
concern. Great strides in phenomenological turbulence models have been
taken in the past decade, yet only for relatively simple flows can these
phenomenological models be used to accurately compute quantities of inter-
est, such as skin friction, heat transfer, and separation points. There
is a growing belief that the phenomenological models fail because the
large-scale turbulent motions, which provide the primary control over
these quantities, differ considerably from flow to flow, making a "uni-
versal" theory of turbulence unobtainable. An approach with which we
have been working may eventually do better. In this approach the large-
scale motions are computed as part of a three-dimensional time-dependent
computation, and one only need model the smaller scales, for which simple
phenomenological models appear to work quite adequately. Work on "large-
eddy simulations" is progressing, but it will be some time before flows
of significant technical interest can be handled. There are many ques-
tions which need to be resolved with simpler, laboratory-type flows, and
this is the direction of our current work.

At the conference I will present an update on large-eddy simulation
activities, which I believe may become the basis for practical turbulent
flow computations if computer technology advances by two orders of mag-
nitude in speed and storage beyond the most advanced machines now in ser-
vice.

Page intentionally left blank

FLUX-CORRECTED TRANSPORT TECHNIQUES FOR TRANSIENT

CALCULATIONS OF STRONGLY SHOCKED FLOWS

J. P. Boris
U. S. Naval Research Laboratory

SUMMARY

New flux-corrected transport algorithms are described for solving gener-
alized continuity equations. These techniques were developed by requiring
that the finite-difference formulae used ensure positivity for an initially
positive convected quantity. Thus FCT is particularly valuable for fluid-like
problems with strong gradients or shocks. Repeated application of the same
subroutine to mass, momentum, and energy conservation equations gives a simple
solution of the coupled time-dependent equations of ideal compressible fluid
dynamics without introducing an artificial viscosity. FCT algorithms span
Eulerian, sliding-rezone, and Lagrangian finite-difference grids in several
coordinate systems. The latest FCT techniques are fully vectorized for
parallel/pipeline processing and are being used on the Texas Instruments ASC
at NRL.

INTRODUCTION

This paper reviews the Flux-Correct Transport (FCT) techniques which have
been developed to solve the continuity equation

$$\frac{\partial \rho}{\partial t} = - \underline{\nabla} \cdot \rho \underline{V} \qquad \text{(conservation form)}. \qquad (1a)$$

In addition to (1a), there are two other ways to write the continuity equation
which get reflected in some of the numerical solution techniques:

$$\frac{\partial \rho}{\partial t} + \underline{V} \cdot \underline{\nabla} \rho = \frac{d\rho}{dt} = -\rho \nabla \cdot V, \qquad \text{and} \qquad (1b)$$

$$\underset{\text{convection}}{} \qquad \underset{\substack{\text{compression} \\ \text{(convection form)}}}{}$$

$$\frac{\partial}{\partial t} \int_{\text{region}} \rho d^3 r = - \oint_{\substack{\text{region boundary} \\ \text{(integral form)}}} \rho \underline{V} \, d\underline{A} \qquad . \qquad (1c)$$

The convective term $\underline{V} \cdot \underline{\nabla} \rho$ displayed explicity in Eq. (1b) gives (1a-c) its

intrinsically hyperbolic form and causes really severe problems numerically. The compression term $- \rho \underline{V} \cdot \underline{V}$ is sometimes absent, as in the Liouville Equation, in which case it is often called the convection or the advection equation.

Continuity equations underlay compressible and incompressible fluid dynamics, hydrodynamics, plasma physics (Vlasov Equation and MHD moment equations) and even quantum mechanics. They appear in most descriptions of dynamic physical systems simply because they express two of the more general principles in physics, conservation and causality. Continuity equations also display the positivity property: a quantity being transported will never turn negative anywhere in a reasonable flow field if that quantity was everywhere positive to start with. This positivity property expresses in a continuum way the intrinsic corpuscular nature of matter. Thus matter cannot be removed from a region which is devoid of matter to begin with. This duality, in which matter obeys both particle and fluid-like equations on microscopic and macroscopic scales respectively, has its ramifications for numerical solution techniques as well. The first three of the possible solution techniques listed below take advantage of the underlying discrete basis of the continuity equation while the last three aim more directly at solving the partial differential equation itself.

TABLE 1 - Possible Solution Techniques

- Quasiparticle Methods
    1. Collisionless particles, stars and plasmas
    2. Collisional particles for fluids

- Characteristic Methods

- Lagrangian Finite Difference Methods

- Eulerian Finite Difference Methods
    1. Explicit vs implicit
    2. Order vs accuracy

- The Finite Element Method

- The Spectral Method

Because of their speed and simplicity, finite-difference solutions of the continuity equation must always be considered carefully as the most likely of the six candidate methods (ref 1). Quoting three conclusions in a similar context from another source (ref 2):

- The spectral method has no stability problems but is much more complicated and slower than generalized difference methods.

- It is doubtful whether the finite-element method, based on piece-wise polynomials, can compete with the above methods.

- If difference methods are used, they should be at least fourth-order accurate.

While I agree basically with these remarks, they do not really encompass the quasiparticle schemes nor do they adequately reflect a very important piece of personal experience. Whenever a theory is to be tested, or an algorithm, or a new mathematical technique, attention rather quickly turns to the crucial yet simple conservation equations of ideal compressible flow.

Finite-difference methods have solved the transient Rankine-Hugoniot shock problem adequately. For that matter, various flavors of quasiparticle methods can do the same vital problem creditably if enough particles are used. I do not know of any calculation, even in one spatial dimension, using either a finite-element or a spectral method which has correctly solved for an ideal gas compressible shock. Until such calculations become common place and computationally attractive, finite-difference methods would seem to have the inside track.

IMPROVING FINITE-DIFFERENCE TECHNIQUES

There is undoubtedly some merit in trying to boost the performance of quasiparticle methods on the one hand and the basis-function expansion methods on the other toward the performance obtained from finite differences. But it is a low risk-high return investment to patch up the obvious failings of the front runners, finite differences. In the case of Lagrangian finite-difference methods, the major outstanding problems arise from secularly unattractive distortions of the grid which wreck calculations of interesting flows quite quickly (refs. 3,4,5). In the case of Eulerian methods, the major outstanding weakness in a hugh class of problems of real interest is the need for a large artificial damping (numerical diffusion) to fill in what would otherwise be pits of "negative density" in the calculated profiles. Since the "Eulerian" positivity problem is encountered even in Lagrangian calculations for many situations, it demands the greater share of attention.

The Flux-Corrected Transport techniques (FCT) which are the subject of this paper have been designed carefully to satisfy the following six requirements of an "ideal" algorithm for solving the continuity equation (ref. 6-9). An ideal algorithm should:

1. Be linearly stable for all cases of interest,

2. Mirror conservation properties of the physics,

3. Ensure the positivity property when appropriate,

4. Be reasonably accurate,

5. Be computationally efficient, and

6. Be independent of specific properties of one application.

FCT algorithms arise naturally (ref 6) as a result of trying to satisfy requirement 3. Most work in the past has centered on trying to increase the mathematical order of accuracy of a scheme while ignoring the physical positivity property which the fluids display prominently.

Consider the rather general three-point approximation to Eq. (1a)

$$\dot{\tilde{\rho}}_j = \rho^o_j - \frac{1}{2}\left(\rho^o_{j+1} + \rho^o_j\right)\ \epsilon_{j+1/2} + \frac{1}{2}\left(\rho^o_j + \rho^o_{j-1}\right)\ \epsilon_{j-1/2}$$

$$+ \nu_{j+1/2}\left(\rho^o_{j+1} - \rho^o_j\right) - \nu_{j-1/2}\left(\rho^o_j - \rho^o_{j-1}\right) ,$$

(2)

where $\epsilon_{j+1/2} \equiv V_{j+1/2}\delta t/\delta X_{j+1/2}$ and ρ_j is the density at mesh point j. Equation (2) is in finite-difference conservative form with whole indices representing cell centers and half indices indicating cell interfaces. The additional numerical diffusion terms with diffusion coefficients $\nu_{j+1/2}$

have to be added to ensure positivity. The <u>stability</u> of Eq. (2) is ensured, at least roughly, when

$$\frac{1}{2} > \nu_{j+1/2} > \frac{1}{2}\ \epsilon^2_{j+1/2} .$$

(3a)

The upper limit arises from the explicit diffusion time-step condition while the lower limit is the Lax-Wendroff damping. Unfortunately <u>positivity</u> is only ensured <u>linearly</u> when

$$\nu_{j+1/2} > \frac{1}{2}\left|\epsilon_{j+1/2}\right| , \quad \sigma$$

(3b)

the first-order upstream-centered scheme result.

We appear to be caught between a rock and a hard place here but the escape route is signaled in the preceding sentence by the word "linearly". By relaxing the linearity implied by Eq. (2) and letting the diffusion coefficients be nonlinear functionals of the flow velocities $\left\{\epsilon_{j+1/2}\right\}$, we can hope to reduce the integrated dissipation below the rather ghastly limit (3b) and yet retain sufficient dissipation near steep gradients to ensure positivity. A literature is beginning to form about these "monotonic" difference schemes (refs. 6-9, 10, 11) since the dilemma of accuracy versus positivity in Eulerian difference schemes can be resolved in no other way.

FLUX-CORRECTED TRANSPORT ALGORITHMS

The first, and so far the most developed and used, of the monotonic
schemes is Flux-Corrected Transport. The calculation in Fig. 1 was performed
by the first FCT Algorithm SHASTA (ref. 7) and had an error about four or
five times smaller than the simple linear methods also shown. The damping
was second order as were the relative phase errors. Figure 1 shows a
comparison of four common difference schemes solving the standard square wave
problem. The effects of excess numerical damping in the donor-cell treatment
(upstream-centered first-order), and of excess dispersion in the leap frog
and Lax-Wendroff treatments are clearly visible. Dispersion manifests itself
as a trail or projection of oscillations in the computed solution near dis-
continuities and sharp gradients of the "correct" solution.

The basic FCT technique shown in Figure 1 was quickly generalized to
cylindrical and spherical systems, to Lagrangian as well as fixed Eulerian
grids, and was applied to a number of one-, two-, and three-dimensional
problems. More recent work has been devoted toward extending the basic non-
linear flux-correction techniques to convection algorithms other than SHASTA
and toward discovering an "optimum" FCT algorithm.

Since the latest FCT algorithms have eliminated roughly 95% of the
removable error and the removable error that remains is barely half of the
irreducible error, it is natural to have turned next toward optimization
in speed, flexibility, and generality (ref. 12). In Flux-Corrected Transport
algorithms, the basic convective transport algorithm is augmented with a
strong enough linear diffusion to ensure positivity at the expense of excess
smoothing. Since the amount of diffusion which has been added is known, FCT
then performs a conservative antidiffusion step to remove the diffusion in
excess of the stability limit. However, the antidiffusive fluxes are
effectively multiplied by a coefficient which ranges from zero to unity to
preserve monotonicity. The criterion for choosing the reduction factors of
the antidiffusive fluxes is that the antidiffused solution will exhibit no new
maxima or minima where the diffused solution had none.

Although the limit (3b) represents the minimum amount of diffusion
needed for stability, FCT algorithms generally use a larger zero-order
diffusion because it has been found that the correct choice of the
$\left\{ \nu_{j+1/2} \right\}$ within the monotonic and stable range will reduce convective phase
errors from second to fourth order as suggested by Kreiss. Since the anti-
diffusion can also be chosen correspondingly larger, no real price is exacted
for this improvement in phase properties. The most recent efforts (ref. 12)
have taken advantage of this fact to generate minimum-operation-count FCT
algorithms for Cartesian, cylindrical, and spherical coordinate systems with
stationary (Eulerian) and moveable (Lagrangian) grid systems. Because these
algorithms, and in particular the nonlinear flux-correction formula, were
very carefully designed, they are fully "vectorizeable" for pipeline and
parallel processing and have been implemented in all generality in Fortran on
the Texas Instruments Advanced Scientific Computer at the Naval Research
Laboratory. The execution time per continuity equation per grid point is

roughly 1.3 μsec. A complete 2D calculation on a system of 200 grid points X200 grid points requires roughly 2 to 2.5 seconds per timestep depending on extra physics and boundary conditions incorporated in the problem.

Figure 2 shows a 1D calculation performed by the code FAST1D on the ASC. The problem chosen is the "Lapidus" problem (ref. 13) in cylindrical coordinates with $\gamma = 1.4$. The diaphragm is originally at r - 1.0 in Fig. 2 and bursts at t - 0.0 sec. The density solution is shown at 0.6 sec in Fig. 2 just after the shock has reached the axis and rebounded. Three different resolution calculations are overlapped to show the convergence. Even the calculation with 50 cells is at least as accurate as the original Payne and Lapidus solutions with 200 cells. The width of the contact discontinuity is about 3.5 cells while the shock is smeared over only 1.5 cells without noticeable overshooting or undershooting. The calculations are performed without any added artificial viscosity. The monotonicity control provided by FCT on each of the continuity equations separately is adequate to ensure stability and accuracy as shown.

Figures 3a, b show the evolution of Rayleigh-Taylor instability in the implosion of a laser pellet shell 30 microns thick. The calculation was performed using the FAST2D code on the ASC and the thermal conductivity was set to zero to show the full nonlinear evolution of the instability. An Eulerian "sliding-rezone" grid was used with 200 X 200 grid points. Strong deterioration of the shell is apparent by 3.85 nsec but breakthrough has not yet occurred. The jetting of material off the backside is severe enough by this time that grid distortion would obviate the usual Lagrangian solution techniques. Figure 3a shows the linear phase of the instability and 3b shows the onset of the nonlinear regime.

REFERENCES

1. Boris, J. P.: Numerical Solution of Continuity Equations. <u>Proceedings of the 2nd European Conference on Computational Physics</u>, Garching 27-30 April 1976.

2. Kreiss, H. O.: A Comparison of Numerical Methods Used in Atmospheric and Oceanographic Applications. in <u>Proc. of the Symposium on Numerical Models of Ocean Circulation</u>, National Academy of Sciences (U.S.G.P.O., Washington, D.C., 1972). See also in the same volume B. Wendroff, Problems of Accuracy with Conventional Finite-Difference Methods and G. Fix, A Survey of Numerical Methods for Selected Problems in Continuum Mechanics.

3. Boris, J. P., Fritts, M. J. and Hain, Klaus: Free Surface Hydrodynamics Using a Lagrangian Triangular Mesh. <u>Proc. First Int'l Conference on Numerical Ship Hydrodynamics</u>, NBS, Gaitherburg, Md. Oct 1975.

4. Fritts, M. J.: A Numerical Study of Free-Surface Waves. SAI Report SAI-76-528-WA, March 1976.

5. Chan, R.: A Generalized Arbitrary Lagrangian-Eulerian Method For Incompressible Flows with Sharp Interfaces. <u>J. Comput. Phys.</u> 17(3), pp. 311-331 (1974). See also Hirt, Amsden and Cook, <u>J. Comput. Phys.</u> 14, pp. 227-253 (1974).

6. Boris, J. P. and Book, D. L.: Solution of Continuity Equations by the Method of Flux Corrected Transport. Chap. 11 in <u>Methods in Computational Physics</u>, Vol. 16 (Academic Press, New York, 1976).

7. Boris, J. P. and Book, D. L.: Flux-Corrected Transport I: SHASTA-A Fluid Transport Algorithm that Works. <u>J. Comput. Phys.</u> 11, p. 38ff (1973).   [FCT I]

8. Book, D. L., Boris, J. P., Hain, K. H.: Flux-Corrected Transport II: Generalizations of the Method. <u>J. Comput. Phys.</u> 18(3), pp. 248-283 (1975).   [FCT II]

9. Boris, J. P. and Book, D. L.: Flux-Corrected Transport III: Minimal Error FCT Algorithms. <u>J. Comput. Phys.</u> 20, (1976).   [FCT III]

10. VanLeer, B.: Toward the Ultimate Conservative Difference Scheme. <u>J. Comput. Phys.</u> 14, 361-370 (1974).

11. Harten, A.: The Method of Artificial Compression. CIMS Report COO-3077-50, June 1974.

12. Boris, J. P.: Flux-Corrected Transport Modules for Generalized Continuity Equations. NRL Memorandum Report 3237, 1976 (to be published).

13. Lapidus, A.: Computation of Radially Symmetric Shocked Flows. J. Comput. Phys. 8, pp. 106-118 (1971).

t = 20   cycle = 100   t = 160   cycle = 800

ONE-SIDED

LAX-WEND.

LEAP-FROG

SHASTA (FCT)
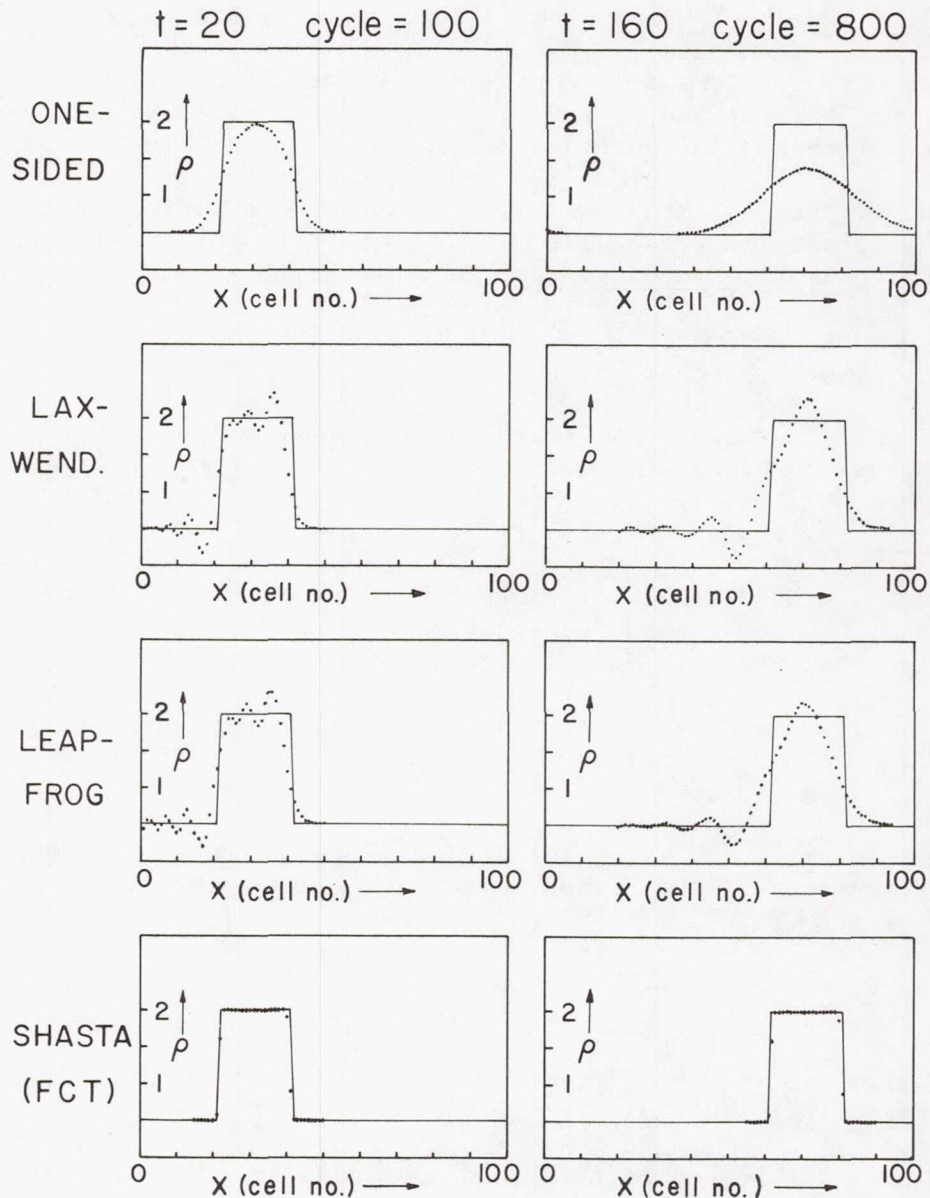
Figure 1.- Comparison of four difference schemes solving
the square wave problem. The merits of Flux-Corrected
Transport relative to the other methods are clear.
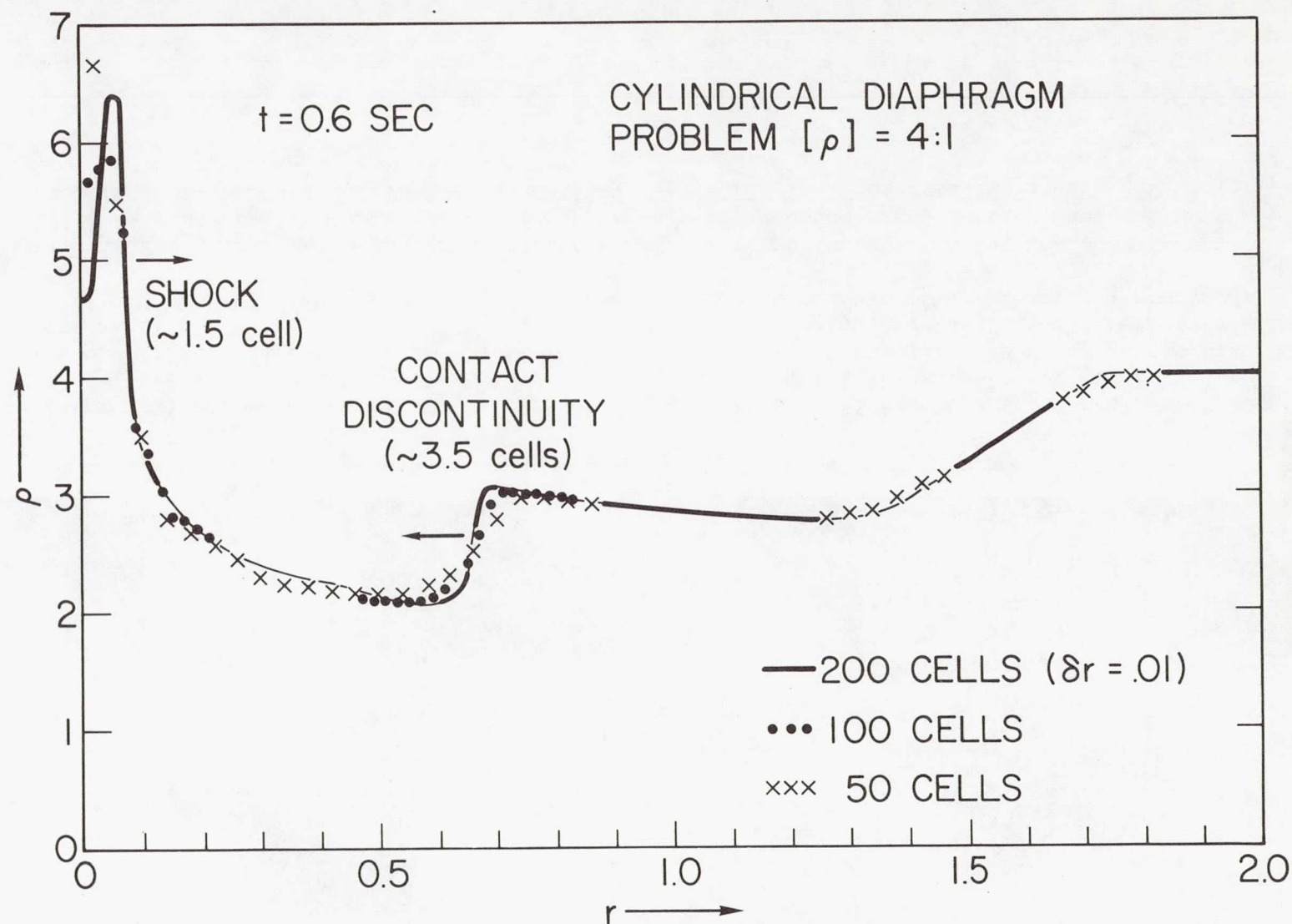
Figure 2.- A cylindrical diaphragm problem using FAST1D. Three different resolutions are shown to demonstrate convergence of the solution. FCT generally requires shock widths of about 1.5 cells.
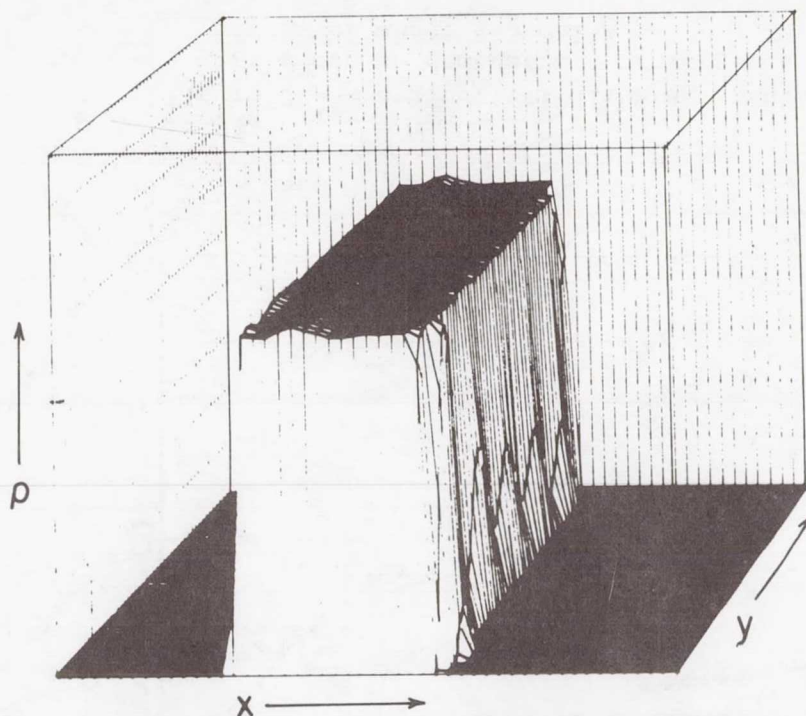
(a) After 1.05 nsec the beginnings of the Rayleigh-Taylor instability can be seen in the linear phase on the back side of the shell.
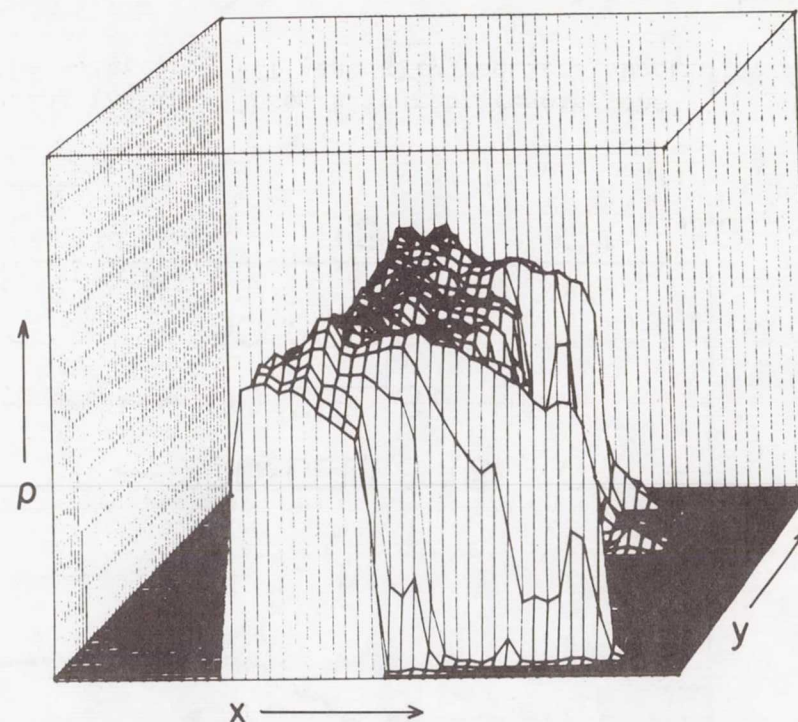
(b) After 3.85 nsec the shell has moved roughly two shell thicknesses and the Rayleigh-Taylor instability is fully developed. Usual Lagrangian treatments would be breaking down here because of severe grid distortion.

Figure 3.- Two plots from a FAST2D calculation of a laser pellet shell being imploded (toward the left) by a strong constant pressure (high temperature) on the right showing the nonlinear evolution of the Rayleigh-Taylor instability. The shell is 30 microns thick with an initial density of 3 gg/cc.

LIFTING SURFACE THEORY FOR

RECTANGULAR WINGS[*]

Fred R. DeJarnette
Department of Mechanical and Aerospace Engineering
North Carolina State University

SUMMARY

A new incompressible lifting-surface theory is developed for thin rectangular wings. The solution requires the downwash equation to be in the form of Cauchy-type integrals. Lan's method is employed for the chordwise integrals since it properly accounts for the leading-edge singularity, Cauchy singularity and Kutta condition. The Cauchy singularity in the spanwise integral is also accounted for by using the midpoint trapezoidal rule and theory of Chebychev polynomials. The resulting matrix equation, formed by satisfying the boundary condition at control points, is simpler and quicker to compute than other lifting surface theories. Solutions were found to converge with only a small number of control points and to compare favorably with results from other methods.

INTRODUCTION

Numerous subsonic lifting surface theories have been developed for thin wings over the past thirty years. A comparison of three of the more prominent numerical methods in 1968 is given in reference 1. Although all these methods give essentially the same results, they require tedious integration techniques and consume considerable computational time. Vortex lattice methods are simpler and can be applied to more complex configurations; however, they are generally less accurate than lifting surface methods. This author developed a lifting surface method for thin rectangular wings (ref. 2) which can also be interpreted as a vortex lattice method. The present paper examines the convergence of solutions and compares results with those of the NRL (National Aerospace Laboratory, Netherlands) method given in reference 1.

SYMBOLS

A   aspect ratio

b   wing span

c   wing chord

c_ℓ sectional lift coefficient

c_d sectional drag coefficient

C_{D_i} far-field induced-drag coefficient

$C_{D_{ii}}$ near-field induced-drag coefficient

C_L wing lift coefficient

C_M wing pitching-moment coefficient, about leading edge

C_S leading-edge suction parameter, see eq. (13)

G parameter defined by eq. (10)

$K_{ijk\ell}$ parameter defined by eq. (15)

$M-1$ number of spanwise control points over whole span

N number of chordwise control points

NLR   National Aerospace Laboratory, Netherlands

S wing planform area

V_∞ freestream velocity

w non-dimensional downwash velocity, referred to V_∞ and positive upwards

x chordwise coordinate measured from leading edge in direction of V_∞

x_{ac}, X_{ac} sectional and wing aerodynamic-center locations, respectively

y spanwise coordinate, positive to the right

α angle of attack

γ non-dimensional circulation per unit chord

Γ circulation

θ transformed chordwise coordinate, see eq. (7)

ϕ transformed spanwise coordinate, see eq. (8)

Subscripts:

i   chordwise control point, see eq. (5)

j   spanwise control point, see eq. (17)

k   chordwise integration point, see eq. (4)

ℓ spanwise integration point, see eq. (16)

p   evaluated at spanwise position $\phi_p = p\pi/M$

ANALYSIS

For simplicity, the present method is developed for rectangular wings. The downwash equation from lifting surface theory is usually given by one of the two following forms (ref. 3):

$$w(x,y) = \frac{1}{4\pi} \int \int_S \frac{\gamma(x_1, y_1)}{(y - y_1)^2} \left[1 + \frac{(x - x_1)}{\sqrt{(x - x_1)^2 + (y - y_1)^2}} \right] dx_1 \, dy_1 \tag{1}$$

or

$$w(x,y) = -\frac{1}{4\pi} \int \int_S \frac{\partial \gamma}{\partial y_1} \frac{1}{(y - y_1)} \left[1 + \frac{\sqrt{(x - x_1)^2 + (y - y_1)^2}}{(x - x_1)} \right] dx_1 \, dy_1 \tag{2}$$

Equation (1) is the form used by the three methods compared in reference 1. It contains the Mangler-type integral due to the term $(y - y_1)^2$ in the denominator. Equation (2), however, contains Cauchy-type integrals since the terms $(y - y_1)$ and $(x - x_1)$ in the denominator are linear. The present method requires the downwash to be in the form of equation (2).

In order to understand the development of the present method, consider the two-dimensional problem first. Lan (ref. 4) developed an ingenious method for thin airfoils by using the midpoint trapezoidal rule and the theory of Chebychev polynomials to reduce the two-dimensional downwash integral (Cauchy-type integral) to a finite sum. The remarkable accuracy of this technique is due to the following summational result:

$$\sum_{k=1}^{N} \frac{1}{\cos \theta_k - \cos \theta_i} = \begin{cases} -N^2 & (i = 0) \\ 0 & (i \neq 0, N) \\ N^2 & (i = N) \end{cases} \tag{3}$$

where

$$\theta_k = \frac{(2k - 1)\pi}{2N} \qquad \left(k = 1, \ldots, N \right) \tag{4}$$

are the integration points and

$$\theta_i = i\pi/N \qquad \left(i = 1, \ldots, N \right) \tag{5}$$

are the control points (positions where the boundary condition is applied). Note the similarity of equation (3) to the integral result

$$\int_0^\pi \frac{d\theta_1}{\cos \theta_1 - \cos \theta} = 0 \tag{6}$$

Lan used these equations to develop the two-dimensional downwash summation which properly accounts for the Cauchy singularity, the leading-edge square-root singularity, and the Kutta condition at the trailing edge.

Since equation (2) contains Cauchy-type integrals, Lan's approach will be applied to both the chordwise and spanwise integrals. First, transform the chordwise coordinate by

$$2x/c = 1 - \cos \theta \tag{7}$$

and the spanwise coordinate by

$$2y/b = - \cos \phi \tag{8}$$

Then, use Multhopp's interpolation formula to represent the circulation per unit chord by the trigonometric sum

$$\gamma(\theta,\phi) = \frac{2}{M} \sum_{p=1}^{M-1} \gamma_p(\theta) \sum_{n=1}^{M-1} \sin n\phi_p \sin n\phi \tag{9}$$

where the subscript "p" refers to the spanwise position $\phi_p = p\pi/M$ and $(M - 1)$ represents the number of spanwise control points. Substitute equations (7), (8), and (9) into equation (2) and consider the chordwise integral first. With

$$G(\theta,\theta_1,\phi,\phi_1) \equiv \sqrt{(\cos \theta_1 - \cos \theta)^2 + A^2(\sin \phi_1 - \sin \phi)^2} \tag{10}$$

the chordwise integrals are

$$\int_0^\pi \gamma_p(\theta_1) \sin \theta_1 \left[1 + \frac{G}{\cos \theta_1 - \cos \theta} \right] d\theta_1 = \frac{2\Gamma_p}{cV_\infty} + \int_0^\pi \frac{\gamma_p(\theta_1) \sin \theta_1 \ G \ d\theta_1}{\cos \theta_1 - \cos \theta} \tag{11}$$

1304

The integral on the right side can be reduced to a finite sum by the midpoint trapezoidal rule; and equations (3) and (6) can be used to account for the leading-edge singularity, Cauchy singularity, and Kutta condition ($\gamma_p(\pi) = 0$) as shown below:

$$\int_0^\pi \frac{\gamma_p(\theta_1) \sin \theta_1 \, G \, d\theta_1}{\cos \theta_1 - \cos \theta} = \int_0^\pi \frac{[\gamma_p(\theta_1) \sin \theta_1 \, G - \gamma_p(\theta) \sin \theta \, A|\cos \phi_1 - \cos \phi|]d\theta_1}{\cos \theta_1 - \cos \theta}$$

$$\approx \frac{\pi}{N} \sum_{k=1}^N \frac{\gamma_p(\theta_k) \sin \theta_k \, G_{ik}(\phi,\phi_1)}{\cos \theta_k - \cos \theta_i} + \begin{cases} 4\pi N C_{S_p} A|\cos \phi_1 - \cos \phi| & (i=0) \\ \\ 0 & (i \neq 0) \end{cases} \tag{12}$$

where θ_k are the chordwise integration points given by equation (4) and θ_i are the chordwise control points given by equation (5). The leading-edge suction parameter is defined as

$$4C_{S_p} = \lim_{\theta \to 0} \gamma_p(\theta) \sin \theta \tag{13}$$

Now substitute equation (12) into equation (2) and perform the spanwise integration in a somewhat similar manner, accounting for the Cauchy singularity, to obtain the final form of the downwash as

$$w_{i,j} = \frac{-\pi c}{2bM^2N} \sum_{\ell=1}^M \sum_{k=1}^N \sum_{p=1}^{M-1} \gamma_{p,k} \sum_{n=1}^{M-1} \frac{n \sin n\phi_p \cos n\phi_\ell \, K_{ijk\ell} \sin \theta_k}{(\cos \phi_\ell - \cos \phi_j)} + \begin{cases} -2NC_{S_j} & (i=0) \\ \\ 0 & (i \neq 0) \end{cases} \tag{14}$$

where

$$K_{ijk\ell} \equiv 1 + \frac{\sqrt{(\cos \theta_k - \cos \theta_i)^2 + A^2(\cos \phi_\ell - \cos \phi_j)^2}}{\cos \theta_k - \cos \theta_i} \tag{15}$$

The spanwise integration points are

$$\phi_\ell = \frac{(2\ell - 1)\pi}{2M} \qquad (\ell = 1, \ldots, M) \tag{16}$$

and the spanwise control points are

$$\phi_j = j\pi/M \qquad (j = 1, \ldots, M - 1) \tag{17}$$

The tangent-flow boundary condition for flat wings requires that $w_{i,j} = -\alpha$.

The $N(M - 1)$ values of $\gamma_{p,k}$ are calculated by solving the matrix equation formed by applying equation (14) for $i \neq 0$ at the chordwise and spanwise control points given by equations (5) and (17). Then after the $\gamma_{p,k}$ are calculated, the $(M-1)$ leading-edge suction parameters C_{S_j} can be computed by successively applying equation (14) with $i = 0$ (control point at the leading edge) at the spanwise positions $j = 1, \ldots, M - 1$. Regardless of the number (N) of chordwise control points used, there is always a control point at the trailing edge which accounts for the Kutta condition, and another control point at the leading edge which gives the leading-edge suction parameter, if desired.

The sectional and wing aerodynamic characteristics may now be calculated by using the midpoint trapezoidal rule to reduce the integrals to finite sums, as illustrated below:

$$(c_\ell)_p = \frac{2\Gamma_p}{cV_\infty} = \frac{2}{c} \int_0^c \gamma_p(x_1)\,dx_1 \simeq \frac{\pi}{N} \sum_{k=1}^{N} \gamma_{p,k}\,\sin\theta_k$$

$$C_L = \int_{-b/2}^{b/2} c_\ell\, c\, dy/S \simeq \frac{\pi}{2M} \sum_{p=1}^{M-1} (c_\ell)_p\,\sin\phi_p$$

$$C_{D_i} = \frac{C_L^2}{\pi A} \sum_{n=1}^{M-1} n\left[\sum_{p=1}^{M-1}\Gamma_p\,\sin n\phi_p\right]^2 \bigg/ \left[\sum_{p=1}^{M-1}\Gamma_p\,\sin\phi_p\right]^2$$

$$C_{D_{ii}} = C_L\,\alpha - \frac{\pi^2}{M} \sum_{j=1}^{M-1} C_{S_j}^2\,\sin\phi_j$$

The spanwise loading can be made continuous by equation (9), and the chordwise loading can also be made continuous by fitting C_{S_j} and $\gamma_{j,k}$ to the chordwise loading functions for thin airfoil theory.

RESULTS AND DISCUSSION

For one control point $(N = 1, M = 2)$ the present method yields

$$C_L/\alpha = \pi A/(1 + \sqrt{1 + A^2/2}) \quad \text{and} \quad C_{D_i} = C_L^2/\pi A$$

These results give the correct limit as $A \rightarrow 0$, but just as Lan found for airfoils, at least two chordwise control points are needed to get an accurate pitching moment. Reference 2 showed that the present spanwise integration method gives the exact classical solution to Prandtl's lifting line equation.

Table 1 gives a detailed comparison of the present method with the NLR method (ref. 1) for an A = 2 rectangular wing with N = 4 and M = 16. Although the NLR method used 15 spanwise loading functions, 127 spanwise integration points were employed. Excellent agreement is obtained between the two methods for the lift, pitching moment, aerodynamic center, far-field drag, and spanwise lift distribution. The spanwise variation of section drag and aerodynamic center compares well except near the wing tips, and the near-field drag values differ. As noted in reference 1, at least 8 chordwise control points are needed to get convergence of the section drag near the wing tips and the near-field drag. The computational time required for the results in Table 1 was 22 minutes for the NLR method on a CDC 3300 computer, whereas the present method required less than 10 seconds on an IBM 370/165 computer.

The effects of the number of control points on the convergence of lift and aerodynamic center are shown in figure 1 for rectangular wings with A = 2 and 7. These results indicate that good results are obtained for the A = 7 wing with N = 2 and M = 10, whereas more chordwise and less spanwise control points are needed for the A = 2 wing. Figure 2 illustrates the convergence of the near- and far-field induced drag for the same two wings. Note that the far-field induced drag is insensitive to both M and N for the A = 2 and A = 7 wings. On the other hand, the near-field induced drag depends on both M and N, particularly for the A = 2 wing.

CONCLUDING REMARKS

The present lifting-surface method for rectangular wings was found to compare favorably with other methods, but it is simpler and requires smaller computational times. The number of control points required for convergence of the aerodynamic characteristics is dependent on both the wing aspect ratio and the aerodynamic parameter. Convergence is fast for lift, pitching moment, aerodynamic center, far-field drag, and spanwise lift distribution. For the A = 7 wing two chordwise and about 10 spanwise control points gave good results, whereas at least 4 chordwise and 8 spanwise control points are needed for the A = 2 wing. The far-field induced drag is particularly insensitive to the number of control points, with good results for N = 2 and M = 4 on both wings. Convergence is slow for the section drag and aerodynamic center near the wing tips. The near-field drag converges more slowly than any of the other parameters. Other planforms are presently being investigated.

REFERENCES

1. Garner, H. C.; Hewitt, B. L.; and Labrujere, T. E.: Comparison of Three Methods for the Evaluation of Subsonic Lifting-Surface Theory. Reports and Memoranda 3597, Aeronautical Research Council, London, England, June 1968.

2. DeJarnette, Fred R.: Arrangement of Vortex Lattices on Subsonic Wings. Vortex-Lattice Utilization, NASA SP-405, 1976, pp. 301-323.

3. Ashley, Holt; and Landahl, M. T.: Aerodynamics of Wings and Bodies.
    Addison-Wesley Publishing Co., Inc., Mass., 1965.

4. Lan, C. E.: A Quasi-Vortex Lattice Method in Thin Wing Theory. J. Air-
    craft, vol. 11, no. 9, Sept. 1974, pp. 518-527.

TABLE 1.   RESULTS FOR RECTANGULAR PLANFORM, A = 2

Overall Values

	Present N=4, M=16	NLR (ref. 1) N=4, M=16
C_L/α	2.4732	2.4744
$-C_M/\alpha$	0.5187	0.5182
x_{ac}/c	0.2097	0.2094
$\pi A C_{D_i}/C_L^2$	1.0007	1.0007
$\pi A C_{D_{ii}}/C_L^2$	0.9951	1.0108

Values of c_d/C_L^2

$2y/b$	Present	NLR
0	0.1847	0.1848
0.1951	0.1832	0.1832
0.3827	0.1784	0.1781
0.5556	0.1693	0.1686
0.7071	0.1548	0.1541
0.8315	0.1331	0.1353
0.9239	0.0988	0.1131
0.9808	0.0394	0.0770

Values of c/C_L

$2y/b$	Present	NLR
0	1.2543	1.2543
0.1951	1.2331	1.2331
0.3827	1.1692	1.1692
0.5556	1.0625	1.0625
0.7071	0.9137	0.9137
0.8315	0.7257	0.7257
0.9239	0.5045	0.5044
0.9808	0.2588	0.2587

Values of x_{ac}/c

$2y/b$	Present	NLR
0	0.2200	0.2199
0.1951	0.2187	0.2187
0.3827	0.2150	0.2149
0.5556	0.2087	0.2085
0.7071	0.1999	0.1996
0.8315	0.1896	0.1886
0.9239	0.1798	0.1773
0.9808	0.1731	0.1685
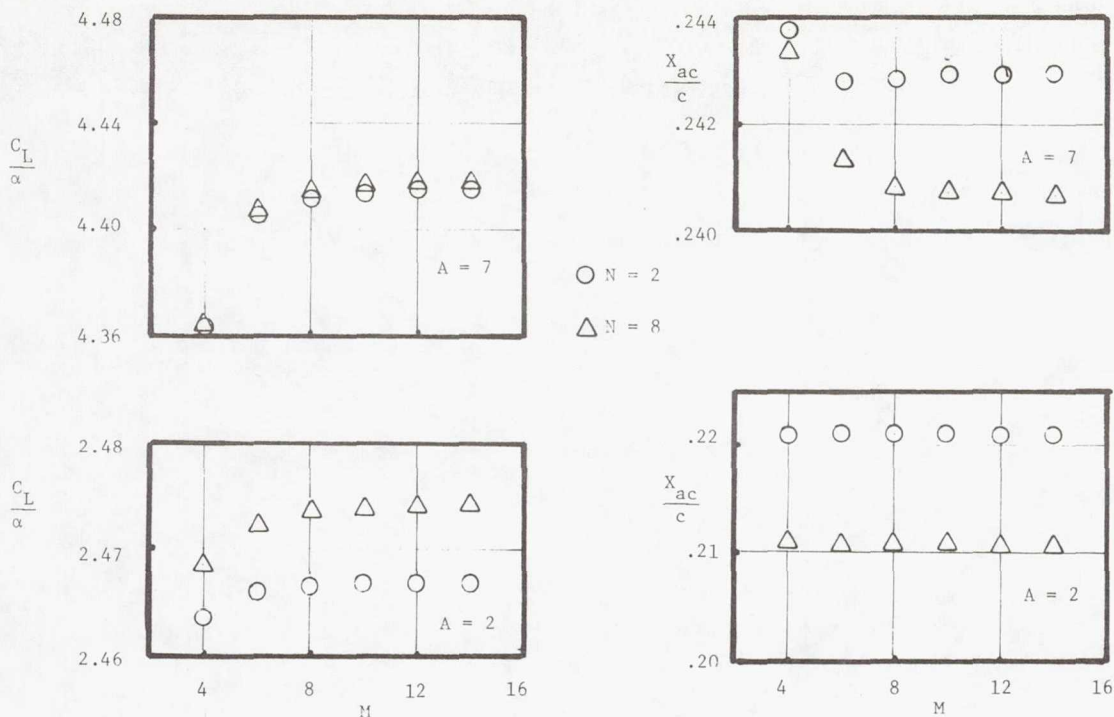
Figure 1.- Convergence of lift and aerodynamic center on rectangular wings. A = 2 and 7.
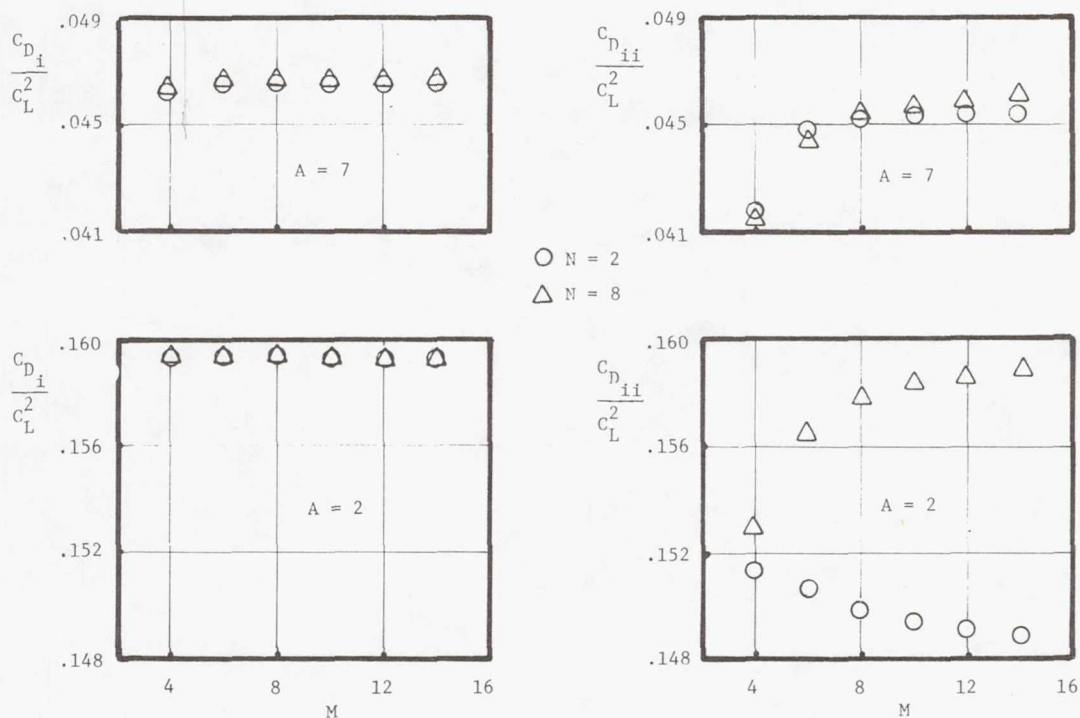
Figure 2.- Convergence of near- and far-field induced drag on rectangular wings. A = 2 and 7.

1309

Page intentionally left blank

IMPROVED COMPUTATIONAL TREATMENT OF TRANSONIC FLOW
ABOUT SWEPT WINGS

W. F. Ballhaus[*], F. R. Bailey[†], and J. Frick[‡]
NASA Ames Research Center

INTRODUCTION

Transonic small-disturbance theory is attractive in practical engineering design and analysis primarily because of the flexibility it offers in the treatment of boundary conditions. The theory can provide an understanding of the physics of complex, three-dimensional transonic flows, without the need of complicating features such as airfoil surface-oriented coordinate transformations, which are generally used in less approximate theories. However, as with any other asymptotic theory, problems can arise when the theory is applied to cases that differ from the assumptions under which it is derived.

Relaxation solutions to classical three-dimensional small-disturbance (CSD) theory for transonic flow about lifting swept wings were first reported in references 1 and 2. A deficiency in the treatment of wings with moderate-to-large sweep angles soon became apparent. For such wings, the CSD theory was found to be a poor approximation to the full potential equation in regions of the flow field that are essentially two-dimensional in a plane normal to the sweep direction. This was pointed out in reference 3, which emphasized determination of the effect of this deficiency on the capture of embedded shock waves in terms of (1) the conditions under which shock waves can exist and (2) the relations they must satisfy when they do exist. A modified small-disturbance (MSD) equation, derived by retaining two previously neglected terms, was proposed and shown to be a consistent approximation to the full potential equation over a wider range of sweep angles. The purpose of this paper is to demonstrate the important effect of these extra terms by comparing CSD, MSD, and experimental wing surface pressures.

THE EXISTENCE OF SHOCK WAVES ON AN INFINITE ASPECT
RATIO SWEPT WING

Consider an infinite aspect ratio wing with sweep angle λ. For a vertical shock wave to exist, the flow must be supercritical in a direction normal to the sweep. Since the derivatives of all flow quantities with respect to the span direction are zero, it can be shown that $\phi_y + \phi_x \tan \lambda = 0$, where

---

[*]Research Scientist, Computational Fluid Dynamics Branch, and U.S. Army AMRDL.

[†]Research Scientist, Computational Fluid Dynamics Branch.

[‡]Programmer/Analyst, Informatics, Inc., Palo Alto, Calif.

ϕ_y and ϕ_x are perturbation velocities parallel to the wing plane in the free-stream-normal and free-stream directions, respectively. The condition from the full potential formulation for sonic flow normal to the sweep direction is

$$\phi_x{}^*(\lambda) = -\cos^2 \lambda \left[1 - \sqrt{1 - \frac{2}{\gamma + 1} (1 - (M_\infty{}^2 \cos^2 \lambda)^{-1})} \right] \tag{1}$$

where the velocity in the free-stream direction is given by $U_\infty(1 + \phi_x)$, and the asterisk denotes critical (sonic) conditions in a direction normal to the shock. A shock with sweep λ can exist whenever $\phi_x{}^*(\lambda) < \phi_x < (\phi_x)_{MAX}$, where $(\phi_x)_{MAX}$ corresponds to zero sound speed.

For classical small-disturbance theory, the governing equation written in conservation form is

$$\left[(1 - M_\infty{}^2) \phi_x - \frac{(\gamma + 1)}{2} M_\infty{}^n \phi_x{}^2 \right]_x + (\phi_y)_y + (\phi_z)_z = 0 \tag{2}$$

and the equivalent expression for (1) is

$$\phi_x{}^*(\lambda) = \frac{\sec^2 \lambda - M_\infty{}^2}{(\gamma + 1) M_\infty{}^n} \tag{3}$$

The exponent n will be specified subsequently. Equations (1) and (3) are compared in figure 1. Note the increasing disparity as the sweep increases. At other than small sweep angles, the CSD equation does not permit the existence of shocks for values of ϕ_x for which they can exist according to the full potential equation.

This situation can be improved by the use of the MSD equation (ref. 3), written here in conservation form

$$\left[(1 - M_\infty{}^2)\phi_x - \left(\frac{\gamma + 1}{2} \right) M_\infty{}^n \phi_x{}^2 + \frac{1}{2}(\gamma - 3)M_\infty{}^p \phi_y{}^2 \right]_x \tag{4}$$
$$+ \left[\phi_y - (\gamma - 1)M_\infty^p \phi_x\phi_y \right]_y + (\phi_z)_z = 0$$

The corresponding sonic condition, also plotted in figure 1, is

$$\phi_x{}^*(\lambda) = \frac{\sec^2 \lambda - M_\infty{}^2}{(\gamma + 1)M_\infty{}^n + (\gamma + 1)M_\infty{}^p \tan^2 \lambda} \tag{5}$$

The MSD equation satisfies two-dimensional sweep theory; i.e., it is as consistent with the full potential equation as the two-dimensional transonic small disturbance theory taken in a plane normal to the sweep. The approximation improves as $M_n = M_\infty \cos \lambda$ approaches unity.

Values of n,p in equation (4) can be selected to improve the approximation for values of M_n that are not close to unity. For example, n,p, can be determined, *for a given* M_∞, to better approximate either the full potential $\phi_x{}^*(\lambda)$ (the shock *existence* condition) or its shock *jump* condition. This is illustrated in figure 1, where equation (5) is plotted for two sets of n and p: (1) n = 1.75, p = 2, used for the calculations presented in this paper, (2) n = 1.558, p = -0.162, for which the MSD and full potential $\phi_x{}^*(\lambda)$ agree

very well for $0° < \lambda < 50°$. We have not yet computed wing surface pressures for this set of values. Other MSD equations of the same form but with different coefficients have recently been proposed, such as the NLR equation (ref. 5); $\phi_x^*(\lambda)$ for this equation is also plotted in figure 1.

MODIFICATIONS TO THE CLASSICAL SMALL-DISTURBANCE PROCEDURE
AND DIFFERENCING TECHNIQUES FOR THE SUPERSONIC REGION

Use of an improved form of the governing equation does not, in itself, guarantee that shock waves will be properly captured by the computational method. The finite difference scheme used to solve the equation must: (1) enforce shock conditions consistent with the governing equation (this is guaranteed, in the limit of vanishing mesh spacing, by differencing the equation in conservation form), (2) be adaptable to a stable relaxation algorithm, and (3) avoid excessive dispersive or dissipative distortion of the shock profile.

In transonic flow relaxation methods, the mixed subsonic-supersonic character of the flow field is accounted for by the use of central differencing in subsonic regions and upwind differencing in supersonic regions. For the CSD equation the x-coordinate is the axis of the characteristic cone in supersonic regions. Thus, upwind differencing of the x derivatives and central differencing of the y and z derivatives leads to a numerical domain of dependence that always includes the mathematical domain of dependence; consequently, a necessary condition for stability is maintained. However, the characteristic cone axis for the MSD equation lies in a direction that corresponds to the local flow direction vector, which generally is not coincident with the x-direction. Differencing the MSD equation in supersonic regions in the same manner as the CSD equation can violate the domain of dependence restriction, thereby producing instabilities. We have investigated five supersonic difference schemes for modified equations in an attempt to find one with suitable stability and shock capturing properties. As in reference 3, only additional terms in the x and y directions are retained.

Scheme 1

In this scheme the CSD terms in the MSD equation are differenced in the same manner as for the CSD equation; the remaining terms are approximated by central differences. Thus, no account is taken of the local orientation of the stream direction vector. This procedure has the advantage that the equation can easily be differenced in conservation form. However, convergence properties of the relaxation process were found to be relatively poor. Furthermore, large overshoots at shock waves were observed in some cases.

Scheme 2

The principal part of equation (4) can be expressed in the canonical form

$$(a^2 - q^2)\phi_{ss} + a^2\phi_{nn} + a^2\phi_{zz} = 0 \tag{6}$$

where q and a are particle and sound speeds, and s and n are the local stream and stream-normal directions in the x-y plane. According to Jameson's (nonconservative) rotated differencing procedure (ref. 6), the ϕ_{xx}, ϕ_{xy}, ϕ_{yy} components of ϕ_{ss} and ϕ_{nn} should be upwind and central differenced, respectively, to maintain proper domains of dependence. An exact rotation of the MSD equation is unwieldy, so only an approximate rotation, such as the one in reference 5, is used for Scheme 2. Neglecting products of perturbation velocities gives for the terms in equation (6) (with n = p = 2)

$$(a^2 - q^2)/a_\infty^2 = 1 - M_\infty^2 - (\gamma + 1)M_\infty^2\phi_x \tag{7a}$$

$$\phi_{ss} = \phi_{xx} + 2\phi_y\phi_{xy} \tag{7b}$$

$$a^2/a_\infty^2 = 1 - (\gamma - 1)M_\infty^2\phi_x \tag{7c}$$

$$\phi_{nn} = -2\phi_y\phi_{xy} + \phi_{yy} \tag{7d}$$

Substituting equations (7) in equation (6) and again neglecting products of perturbation velocities gives the MSD equation in the split form

$$\left[1 - M_\infty^2 - (\gamma + 1)M_\infty^2\phi_x\right]\phi_{xx} + 2(1 - M_\infty^2)\phi_y\phi_{xy} - 2\phi_y\phi_{xy} + \left[1 - (\gamma - 1)M_\infty^2\phi_x\right]\phi_{yy} + \phi_{zz} = 0 \tag{8}$$

where the underlined terms are upwind differenced in supersonic regions, defined approximately by $\left[1 - M_\infty^2 - (\gamma + 1)M_\infty^2\phi_x\right] < 0$. The conservation form of equation (8) is

$$\left[(1 - M_\infty^2)\phi_x - \frac{(\gamma + 1)}{2}M_\infty^2\phi_x^2 + (1 - M_\infty^2)\phi_y^2\right]_x$$

$$- \left\{\left[1 - \frac{(\gamma - 1)}{2}M_\infty^2\right]\phi_y^2\right\}_x + \left[\phi_y - (\gamma - 1)M_\infty^2\phi_x\phi_y\right]_y + \phi_{zz} = 0 \tag{9}$$

Equation (9) is equivalent to the splitting given in reference 5. The convergence properties of this scheme were found to be even worse than those of Scheme 1, and no computed results from either of these schemes are presented in this report.

Scheme 3

This scheme is also an approximate rotation of the MSD equation. In this case, however, the term $-2(\gamma + 1)M_\infty^2\phi_x\phi_y\phi_{xy}$ is not neglected, since $1 - M_\infty^2$ and $(\gamma + 1)M_\infty^2\phi_x$ can be of the same order. Thus, the approximation

$$\frac{(a^2 - q^2)}{a_\infty^2}\phi_{ss} = \left[1 - M_\infty^2 - (\gamma + 1)M_\infty^2\phi_x\right]\left[\phi_{xx} + 2\phi_y\phi_{xy}\right] \tag{10}$$

is used. Note that this term, in conjunction with

$$(a^2/a_\infty^2)\phi_{nn} \doteq -2\phi_y\phi_{xy} + (1 - (\gamma - 1)M_\infty^2\phi_x)\phi_{yy}$$

is not consistent with the MSD equation. However, this new splitting can be applied as follows. By defining the central difference approximation for the MSD equation (4) as $L(\phi) = 0$, one can write the rotated equation

$$L(\phi) + \overline{J}(\phi) - J(\phi) = 0 \tag{11}$$

where $\overline{J}$ and J are upwind and central difference approximations to equation (10), respectively. Unfortunately, equation (11) cannot be expressed in conservation form, and, for the computations presented in the next section, J from equation (10) was expressed in the form

$$J(\phi) = \left[(1 - M_\infty^2)\phi_x - \frac{(\gamma + 1)}{2}M_\infty^2\phi_x + (1 - M_\infty^2)\phi_y^2\right]_x - \underline{2(\gamma + 1)M_\infty^2\phi_x\phi_y\phi_{xy}} \tag{12}$$

Hence, the complete equation is differenced conservatively except for the underlined term. The ϕ_{xy} part of this term in $\overline{J}(\phi)$ was upwind differenced in both x and y. The other term in equation (12) was upwind differenced only in x. Scheme 3 improved convergence and reduced shock overshoots relative to Scheme 1. Also, improved capture of weak swept shocks was observed, although overshoots occurred for stronger shocks in some cases.

Scheme 4

A less approximate and consistent (in the sense of Scheme 2) rotation can be accomplished by considering a second modified small-disturbance equation in the quasi-linear form

$$\left[1 - M_\infty^2 - (\gamma + 1)M_\infty^2\phi_x\right]\phi_{xx} - 2M_\infty^2\phi_y(1 + \phi_x)\phi_{xy} + \left[1 - (\gamma - 1)M_\infty^2\phi_x\right]\phi_{yy} + \phi_{zz} = 0 \tag{13}$$

Note that the coefficient of ϕ_{xy} is precisely that of the full potential equation and cannot be put into conservation form. In this scheme the rotation angle is approximated by

$$\sin^2\theta = \frac{\phi_y^2}{1 + 2\phi_x}$$

$$\cos^2\theta = 1 \tag{14}$$

$$\sin\theta\cos\theta = \frac{(1 + \phi_x)\phi_y}{1 + 2\phi_x}$$

resulting in the approximations

$$\phi_{ss} = \phi_{xx} + \frac{2(1 + \phi_x)}{1 + 2\phi_x} \phi_y \phi_{xy}$$

and

$$\phi_{nn} = \frac{-2(1 + \phi_x)}{1 + 2\phi_x} \phi_x \phi_{xy} + \phi_{yy}$$

Thus, the split equation becomes

$$\left[1 - M_\infty^2 - (\gamma + 1)M_\infty^2 \phi_x\right]\left[\phi_{xx} + 2\frac{(1 + \phi_x)}{(1 + 2\phi_x)} \phi_y \phi_{xy}\right]$$
$$+ \left[1 - (\gamma - 1)M_\infty^2 \phi_x\right]\left[\phi_{yy} - \frac{2(1 + \phi_x)}{(1 + 2\phi_x)}\phi_y \phi_{xy}\right] + \phi_{zz} = 0 \quad (15)$$

The less approximate trigonometric forms in equation (14) are necessary for equation (15) to be consistent with equation (13). Since the mathematics involved with equation (15) begins to approach that of the full potential equation in the x-y plane, this procedure was not tested but rather was abandoned in favor of Scheme 5.

Scheme 5

The MSD equation was modified to include all x-y derivitives in the full potential equation; the only z derivative retained was ϕ_{zz}. The equation was solved using Jameson's rotated differencing procedure, and Jameson's rules for constructing a stable relaxation algorithm were rigidly followed (see ref. 6 and appendices B and C of ref. 7). The relaxation process converged more rapidly than for the other schemes, and no shock overshoots were observed. However, the scheme is nonconservative and highly dissipative and tended to "smear" supersonic-to-supersonic shock waves.

The differencing in all schemes is complicated by the use of a transform-ation that maps the wing planform into a rectangle in the computational domain (refs. 1, 2, 4, 8). To "empirically correct" the (supersonic-to-subsonic) shock jumps for viscosity and thus improve the agreement in comparisons with experiment (refs. 3, 4, 8), the shock point operator was not used in any of the computations in this report.

CSD AND MSD COMPUTATIONS FOR THE ROCKWELL HiMAT RPRV

An example that demonstrates the usefulness of small-disturbance theory and illustrates the effect of the extra terms in the MSD equation is provided by computations for the HiMAT RPRV (highly maneuverable aircraft technology, remotely piloted research vehicle). A three view of the original HiMAT

configuration is shown in figure 2. At the maneuver design point for this configuration, the drag exceeded the design goal by several hundred counts. It was decided that the design goal could not be achieved, within the specified budget and calendar time constraints, by modifying the configuration using the traditional experimental "cut and file" approach. Rockwell therefore adopted and developed the following integrated design procedure: (1) establish base-line comparisons of experimental and computed surface pressures obtained using the Bailey-Ballhaus Transonic Wing Code (CSD), (2) "cut and file" computationally (rather than experimentally), and (3) verify experimentally.

A sample base-line comparison of CSD and experimental results is shown in figure 3. (The canard was omitted in both the experiment and the calculations.) The agreement at mid-semi-span is satisfactory. However, in the outboard region, where the flow is nearly two-dimensional in a plane normal to the sweep direction, the CSD code performed poorly. Consequently, the inboard 70 percent of the semi-span, where the flow was highly three-dimensional, was redesigned using the Bailey-Ballhaus code. The outboard 30 percent was analyzed and modified using the Garabedian-Korn two-dimensional program and sweep theory. The redesign weakened and swept embedded shock waves, reducing the extent of flow separation and reducing the drag to within a few counts of the design goal.

The HiMAT example pointed out the need for the extra terms in the governing equation for swept wing configurations. These terms were subsequently added; computed results using Schemes 3 and 5 are compared with the CSD and experimental results in figure 3. Results computed using Scheme 1 were very similar to those of Scheme 3 except the shock overshoot was greater. The more dissipative Scheme 5 shows no such overshoot.

THE DOUBLE SHOCK CONFIGURATION ON THE ONERA M-6 WING

Figure 4 shows a planform view of the ONERA M-6 wing along with the double shock configuration that occurs for $M_\infty = 0.84$, $\alpha = 3°$. Within the supersonic region there is a swept (35°), supersonic-to-supersonic shock wave, sometimes referred to as a "conical shock." Further downstream there is a less highly swept shock wave that terminates the supersonic region. The two shocks intersect to form a strong, unswept shock near the tip.

Computed CSD and experimental wing surface pressures for this condition were compared in reference 8. Satisfactory agreement was obtained except for the failure of the computations to resolve the relatively weak conical shock. It was mentioned that the use of the MSD equation should correct this deficiency. CSD and MSD solutions have been computed on a grid with points clustered in the vicinity of the conical shock. The results, compared with ONERA experimental data, are shown in figure 5. Section pressures for the MSD equation (Scheme 3) indicate the existence of a conical shock; those for the CSD equation do not. MSD results are also compared (fig. 6) with fine grid computations run by Mr. Ray Hicks of NASA Ames Research Center using the new full potential wing code written by Jameson (ref. 6). The Jameson code is based on the nonconservative rotated difference scheme; the conical shock is badly smeared at $\eta = 0.75$ and is totally smeared at $\eta = 0.8$. Scheme 5, which also uses the full potential

formulation with the nonconservative rotated difference scheme (for the x and y derivatives), produced the same smearing of the conical shock. Scheme 1 properly captured the conical shock but produced a large overshoot at the head of the downstream shock.

CONCLUDING REMARKS

Comparisons of computed and experimental surface pressures for the HiMAT wing (fig. 3b) and the ONERA M-6 wing (fig. 5) illustrate the importance of retaining additional terms in the governing equations, as suggested in reference 3. Inclusion of these terms permitted the capture of shock waves for both configurations that had been observed experimentally, but were not resolved by the CSD theory. Five schemes for differencing the small disturbance equation, modified with additional terms, have been discussed. It was determined from numerical tests that Scheme 3 performed best in treating cases with multiple embedded shock waves. Scheme 5 demonstrated the best convergence properties and produced results nearly indistinguishable (except at the leading edge) from those obtained from Jameson's code (ref. 6). However, because of its nonconservative and dissipative properties, this scheme gives relatively poor resolution of the conical shock wave on the ONERA M-6 wing.

REFERENCES

1. Ballhaus, W. F.; and Bailey, F. R.: Numerical Calculation of Transonic Flow About Swept Wings. AIAA Paper 72-677, June 1972.

2. Bailey, F. R.; and Ballhaus, W. F.: Relaxation Methods for Transonic Flow About Wing-Cylinder Combinations and Lifting Swept Wings. Lecture Notes in Physics, vol. 19, Springer-Verlag, 1972, pp. 2-9.

3. Lomax, H.; Bailey, F. R.; and Ballhaus, W. F.: On the Numerical Simulation of Three-Dimensional Transonic Flow with Application to the C-141 Wing. NASA TN D-6933, 1973.

4. Ballhaus, W. F.: Some Recent Progress in Transonic Flow Computations. VKI Lecture Series, "Computational Fluid Dynamics," Von Karman Institute for Fluid Dynamics, Rhode-St.-Genese, Belgium, March 15-19, 1976.

5. Van der Vooren, J.; Sloof, J. W.; Huizing, G. H.; and van Essen, A.: Remarks on the Suitability of Various Transonic Small-Perturbation Equations to Describe Three-Dimensional Flow; Examples of Computations Using a Fully-Conservative Rotated Difference Scheme. Presented at the Symposium Transsonicum II, September 1975.

6. Jameson, A.: Transonic Flow Calculations, VKI Lecture Series, "Computational Fluid Dynamics," Von Karman Institute for Fluid Dynamics, Rhode-St.-Genese, Belgium, March 15-19, 1976.

7. South, J. C.; and Keller, J. D.: Axisymmetric Transonic Flow Including Wind Tunnel Wall Effects. NASA SP-347, 1975, pp. 1233-1267.

8. Bailey, F. R.; and Ballhaus, W. F.: Comparisons of Computed and Experimental Pressures for Transonic Flows About Isolated Wings and Wing-Fuselage Configurations. NASA SP-347, 1975, pp. 1213-1231.

9. Monnerie, B.; and Charpin, F.: Essais de Buffeting d'une Aile en Fleche en Transsonique. 10e Colloque D'Aérodynamique Appliquée, November, 1973.
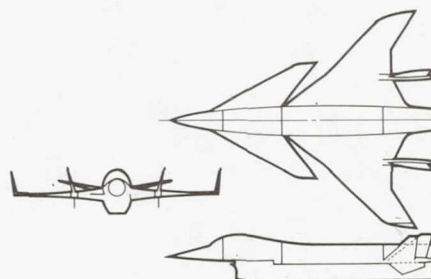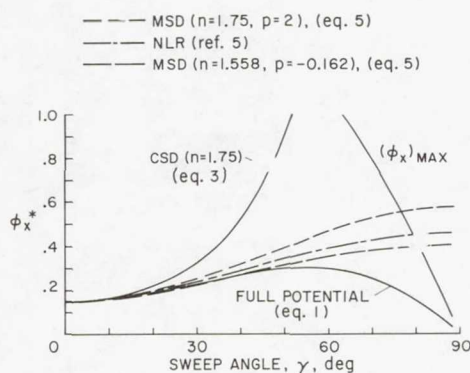
Figure 1.- Shock existence condition $\left[\phi_x^* < \phi_x < (\phi_x)_{MAX}\right]$ as a function of sweep angle.

Figure 2.- HiMAT RPRV three-view.
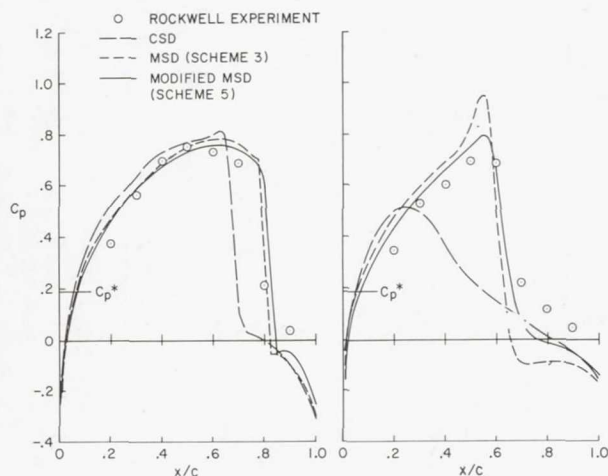
Figure 3.- Surface pressure coefficients on the HiMAT RPRV, $M_\infty = 0.9$, $\alpha = 5°$.

(a) 55 percent semi-span station.

(b) 85 percent semi-span station.
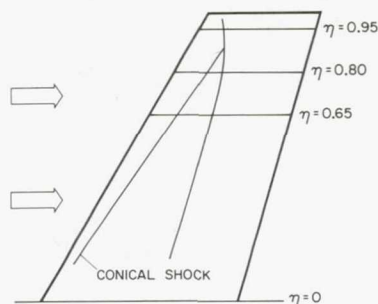
Figure 4.- Planform view of the ONERA M-6 wing showing double shock configuration for $M_\infty = 0.84$, $\alpha = 3°$.

1319
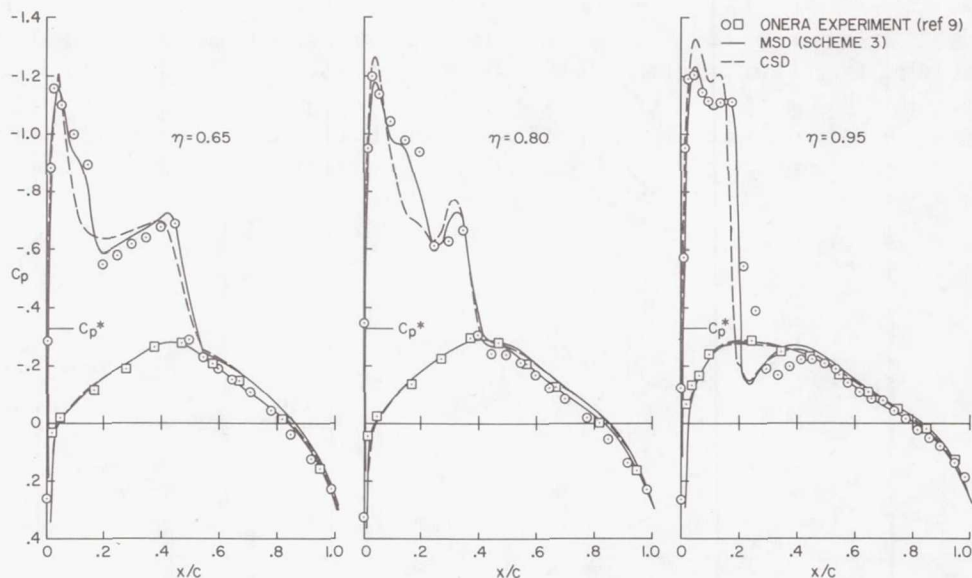
Figure 5.– Computed and experimental surface pressures for the
ONERA M-6 wing, $M_\infty = 0.84$, $\alpha = 3°$.
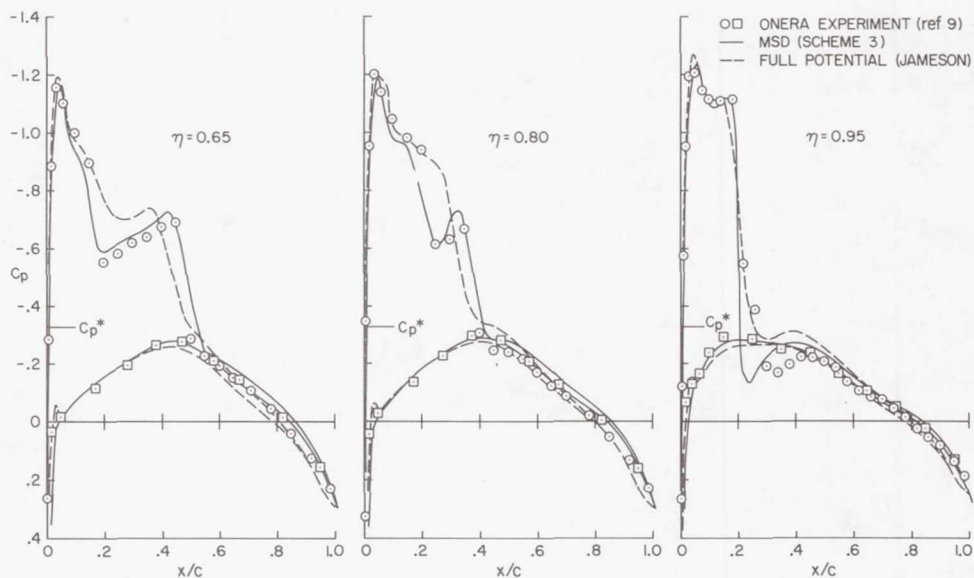
Figure 6.– Computed and experimental surface pressures for the
ONERA M-6 wing, $M_\infty = 0.84$, $\alpha = 3°$.

APPLICATION OF THE NONLINEAR VORTEX-LATTICE CONCEPT

TO AIRCRAFT-INTERFERENCE PROBLEMS

Osama A. Kandil, Dean T. Mook, and Ali H. Nayfeh
Virginia Polytechnic Institute and State University

SUMMARY

A discrete-vortex model is developed to account for the hazardous effects of the vortex trail issued from the edges of separation of a large leading wing on a small trailing wing. The model is divided into three main parts: the leading wing and its near wake, the near and far wakes of the leading wing, and the trailing wing and the portion of the far wake in its vicinity. The problem of the leading wing and its wake is solved by a nonlinear vortex-lattice technique which accounts for tip separation and the shape of the wake in the near and far fields. The trailing wing is represented by a conventional horseshoe-vortex lattice in which the tip separation and the shape of the wake are neglected. The solution is effected by iteration in a step-by-step approach. The normal-force, pitching-moment, and rolling-moment coefficients for the trailing wing are calculated. The circulation distribution in the vortex trail is calculated in the first part of the model where the leading wing is far upstream and hence is considered isolated. A numerical example is solved to demonstrate the feasibility of using this method to study interference between aircraft. The numerical results show the correct trends: The following wing experiences a loss in lift between the wing-tip vortex systems of the leading wing, a gain outside this region, and strong rolling moments which can change sign as the lateral relative position changes. All the results are strongly dependent on the vertical relative position.

INTRODUCTION

In recent years, there has been a significant increase in the use of wide-body and jumbo jets for civil air transports. The vortex trail associated with flying these heavy jets has high intensity and hence presents a serious hazard to small aircraft which enter this wake. Such a vortex encounter may produce high rolling moments on the trailing aircraft which could exceed the capability of the roll-control devices. In addition, the trailing aircraft could suffer a loss of altitude or climb rate and structural damage. The vortex trails may persist up to several miles and for long periods of time before they decay and dissipate by the action of atmospheric and viscous effects. Thus, they play a major factor in sequencing landing and take-off operations at airports where heavy and light aircraft are operating near each other (reference 1).

The vortices emanating from the wing tips of the leading aircraft roll up in the vicinity of the wing tips forming two helical-like cones of contra-rotating vortex cores. The strength of the vortex cores grows downstream from the leading edge up to the trailing edge. At the trailing edge, another wake emanates which has an increasing strength in the spanwise direction toward the wing tips (references 2-4). In the near wake beyond the trailing edge, the roll-up process continues and the strength of the trailing vortex grows due to the wake shed from the trailing edge. In the far wake, the core of the trailing vortex system increases and the vorticity decays with distance. When an aircraft originally with symmetric flow penetrates the wake, its freestream is no longer uniform; the flow may be asymmetric, depending on the aircraft position and orientation relative to this wake. In reference 5, three modes of penetration were reported. These modes, which are shown in figure 1, are called cross-track penetration, along-track penetration between vortices, and along-track penetration through the vortex center. Among these modes of penetration, it was shown that the third one is the most dangerous due to the rolling motion induced by the wake on the trailing airplane. This was calculated from an unsteady model of the trailing vortices in which vortex motion and decay were considered according to a two-dimensional model. Two equations based on a viscous vortex model were derived to calculate the change in lift and rolling-moment coefficients of the trailing aircraft wing from the undisturbed equilibrium flight condition (reference 6). In reference 7, a method was presented for predicting the geometry and the velocity field of a trailing vortex of an aircraft. The method is based on flight testing, model testing, and a solution of the Navier-Stokes equation for a two-dimensional axisymmetric flow. The results showed that the maximum tangential velocity in the core of the trailing vortex decreases with distance downstream of the generating aircraft. For large distances behind the aircraft, the decrease in this velocity was found to be inversely proportional to the square root of the distance. Moreover, the maximum tangential velocity and the corresponding core radius were found to be independent of the aircraft velocity.

DESCRIPTION OF THE PRESENT MODEL

In the present paper, we consider the three-dimensional flow to be steady, inviscid and irrotational everywhere except on the vortex lines which represent the wings and their wakes. This model was successfully applied to a short-coupled wing-wing configuration with delta planforms and leading-edge separations (reference 2). The full interaction between the wings and their wakes was considered, the shape of the wakes was determined, and the aerodynamic loads were calculated. It was found that when the trailing wing is at a distance equal to or larger than one-half the root chord of the leading wing, as measured from the trailing edge of the leading wing to the nose of the trailing wing, the aerodynamic loads of the leading wing are practically unaffected by the presence of the trailing wing. This leads to the conclusion that in the case of long-coupled wing-wing configurations or in the case of a trailing aircraft penetrating the wake of the leading aircraft, the model of the aerodynamic interaction can be simplified without any appreciable error in predicting the aerodynamic characteristics. This suggests modeling the flow field in the

1322

following three steps: In the first step, we consider the leading wing and its trailing vortex system as an isolated aerodynamic problem similar to the one in references 2 and 3. In this step, the shape of the wake is determined as part of the solution up to a distance of two chords beyond the trailing edge. The rest of the wake beyond this distance is considered to be parallel to the freestream velocity. The circulation distribution in the wake is also found from this step and kept the same through the next two steps. In the second step, we consider the interaction between the near wake represented by the two chords beyond the trailing edge and the rest of the far wake in a step-by-step technique, marching downstream in each step. In this way, the wake of the leading wing can be carried downstream to any distance until it encounters the trailing wing. In the third step, we let the trailing wing interact with the vortex trail of the leading wing over a certain distance determined by the ratio of the root chord of the leading wing to that of the trailing wing. Here, the trailing wing may encounter a symmetric or an asymmetric flow, depending on its position and orientation with respect to the vortex trail. In the present study, we considered the along-tract penetration mode, including penetrations between the vortices, through the vortex center,and outside the vortices.

Although the present model does not account for the growth of the vortex core and the vortex decay,it represents a realistic approach for the three-dimensional inviscid solution which may be considered for further modifications to account for the viscous effects and the flow unsteadiness as well.

THE METHOD OF SOLUTION

The present model consists of three main parts. The first part includes the leading wing and its near wake, the second part includes the near and far wakes, and the third part includes the trailing wing and the portion of the far wake in its vicinity.

In the first part, we imagine the leading wing and its wake to be a vortex sheet, and we use a series of discrete vortex lines to represent these sheets. For the lifting surface, these lines form a lattice; while for the wake, they are nonintersecting. The segments connecting the points of intersection in the lattice are straight. Each line representing the wake is composed of a series of short straight segments and one final, semi-infinite segment. The short straight segments are used in two chord lengths beyond the trailing edge. Altogether the finite segments are used for three chord lengths, because the lifting surface itself is included.

Associated with each element of area in the lattice and with each finite segment in the wake is a control point. For the elements of area, the control point is the average of the four corners; for the finite segments in the wake, the control point is the upstream end.

The disturbance velocity generated by the discrete vortex segments is calculated according to the Biot-Savart law. Thus, the total velocity field, which is composed of the freestream and the disturbance, satisfies the continuity

equation for incompressible flows. The circulations around each vortex segment and the positions of the finite segments in the wake must be determined so that simultaneously the normal component of the total velocity vanishes at each control point on the lattice, circulation is spatially conserved, and each finite segment in the wake is force-free (when the finite segments are aligned with the total velocity at their control points, they are practically force-free). To effect this, we use the iteration scheme given in references 2-4. The results of this step are the shape of the wakes emanating from the wing tips and trailing edge as well as the circulation distribution. In this part, the positions and strengths of the finite segments in only two chord lengths behind the trailing edge are of interest.

The fact that the disturbance dies out rapidly in the upstream direction is the basis for the scheme used to determine the position of the wake at large distances behind the leading wing in the second part of the model. It is essential that this position be determined before the trailing wing is considered in the third part of the model. To effect this, we move downstream in steps, considering three chord lengths of finite segments at a time, and iterating to align only the segments in the two downstream chord lengths with the total velocity. At each step, one chord length of finite segments is added downstream and one is removed upstream. The result is the positions of the finite segments in both the near and far wakes. The presence of the trailing wing disturbs the wake from the leading wing, but this disturbance dies out rapidly in the upstream direction (reference 2). Thus, for the third part of the model, only those finite segments in two chord lengths in the vicinity of the trailing wing are of interest.

In the third part of the model, the trailing wing is a conventional large-aspect wing, and hence one can predict its total loads quite accurately by simply taking the vortex lines in its wake to be straight and ignoring the wing-tip vortex system. A number of horseshoe-vortex methods have been based on these simplifications; e.g. references 8-9. Obviously, these simplifications cannot be used when one wants to determine the distributed loads or a model of the wake.

To determine the circulation on the trailing wing, we use the following procedure. First, we select anchor points on each vortex line trailing from the leading wing which are upstream from the trailing wing and out of its region of influence. Then, we use the undisturbed position of the vortex lines from the leading wing as a guess for their position near the trailing wing and determine the circulations on it. Second, we calculate the total velocity field and, starting at the anchor points, align each finite segment in the lines from the leading wing with the total velocity at its control point. Then this position of the wake is used as the new guess and the procedure is repeated until the position converges.

The loads on the trailing wing are then calculated by summing the forces acting on the vortex segments and their moments. In contrast with the conventional horseshoe-lattice model, here there are significant forces on the legs of the horseshoe elements between the spanwise segments and the trailing edge which are produced by the cross flow induced by the vorticity in the wake of

the leading wing; these forces have been included. Many more details of the
iterating scheme and many references related to the various models of the flow
field and to experimental investigations of single wings are given in references
2 and 3.

NUMERICAL EXAMPLE

The method of solution outlined in the preceding section is implemented
through three computer codes; each corresponds to one of the three parts of the
model. In figure 2, we show a typical solution for the first two parts of the
model. This includes the leading wing and the computed vortex lines represent-
ing its near and far wakes. The trailing wing is also shown. The drawing is
to scale. The portion of the far wake in the vicinity of the trailing wing is
the first guess for the solution of the third part. The aspect ratio of the
leading wing (AR_ℓ) is seven; it is tapered, the sweep-back angle of the leading
edge being twenty degrees and that of the trailing edge being ten degrees. The
trailing wing is rectangular; its aspect ratio (AR_t) is six. The root chord of
the leading wing $(c_r)_\ell$ is three times that of the trailing wing $(c_r)_t$. The
coordinates (X_0,Y_0,Z_0) give the relative position of the trailing wing. For
all the results presented below, the angle of attack is ten degrees for both
wings and $X_0/(c_r)_\ell$ is 9.25.

In figure 3, we show the influence of the normal separation $Y_0/(c_r)_\ell$ on
the normal-force coefficients (C_n) for four values of the lateral separation
$(Z_0/c_r)_\ell$. The corresponding curves of the pitching-moment (C_{mz}) and rolling-
moment (C_{mx}) coefficients are shown in figures 4 and 5, respectively. The re-
sults show that the load coefficients are very strongly dependent on the normal
and lateral separations between the trailing and leading wings. The maximum in-
crease and the minimum decrease in the load coefficients occur when the trailing
wing is one to two chord lengths above the leading wing. This range includes
the core of the vortex trail. In the lateral direction, the vortex core is lo-
cated between two and three chord lengths from the plane of symmetry of the
leading wing. When the trailing wing executes along-track penetration between
the vortex cores, it suffers a loss in lift due to the downwash generated by
the contra-rotating vortex cores. On increasing the lateral separation, the
wing gains lift as it passes outside the vortex cores. The same trend occurs
in the pitching-moment coefficients. But, the rolling-moment coefficient changes
from a positive value to a negative one (figure 6). These effects can cause a
serious hazard to the trailing aircraft.

The anomalies in the region near $Z_0 = 0$ are probably due to round-off
errors caused by some vortex segments getting very close to a control point.
These can be eliminated in a number of ways: e.g., one can multiply the velo-
city predicted by the Biot-Savart law by a pseudo-viscous term which renders
the velocity zero on the vortex line and nearly equal to that predicted by the

Biot-Savart law a short distance away (ref. 10), or one can put a "rigid-body" finite core along the vortex segment (ref. 11), or one can use small lengths for the vortex segments so that the ratio of the distance from the segment to the length of the segment is never small.

The present results apparently show the correct trends and are in qualitative agreement with the results of reference 6.

CONCLUDING REMARKS

We have demonstrated the feasibility of using a discrete-vortex method to model aerodynamic interference. Such a method has several desirable features. As a result of the way the wake from the leading wing is determined, one can predict the influence of the leading-wing planform on any trailing wing. Moreover, the method can be extended to include the tip-vortex system of the trailing wing. The growth of the vortex core and vortex decay can be accounted for by including a viscous core similar to that of reference 7. Finally, an unsteady model, which takes into account the relative motion between the two wings, can be developed by using the technique of reference 12.

REFERENCES

1. McGowan, W. A.: Trailing Vortex Hazard. SAE Transactions, Vol. 77, 1968, pp. 740-753.

2. Kandil, O. A.: Prediction of the Steady Aerodynamic Loads on Lifting Surfaces Having Sharp-Edge Separation. Ph. D. Dissertation, Virginia Polytechnic Institute and State University, December 1974.

3. Kandil, O. A., Mook, D. T. and Nayfeh, A. H.: Nonlinear Prediction of the Aerodynamic Loads on Lifting Surfaces. Journal of Aircraft, Vol. 13, No 1, January 1976, pp. 22-28.

4. Kandil, O. A., Mook, D. T. and Nayfeh, A. H.: New Convergence Criteria for the Vortex-Lattice Models of the Leading-Edge Separation. Presented at NASA-Langley Workshop on Vortex-Lattice Utilization, May 1976. (To appear in a forthcoming NASA SP).

5. Wetmore, J. W. and Reeder, J. P.: Aircraft Vortex Wakes in Relation to Terminal Operations. NASA TN D-1777.

6. Iversen, J. D. and Bernstein, S.: Trailing Vortex Effects on Following Aircraft. Journal of Aircraft, Vol. 11, No. 1, January 1974, pp. 60-61.

7. McCormick, B. W., Tangler, J. L. and Sherrieb, H. E.: Structure of Trailing Vortices. Journal of Aircraft, Vol. 5, No. 3, May-June 1968, pp. 260-267.

8. Rubbert, P. E.: Theoretical Characteristics of Arbitrary Wings by a Nonplanar Vortex Lattice Method. Boeing Company, Seattle, Washington, Rept. D6-9244, 1962.

9. Hedman, S. G.: Vortex Lattice Method for Calculation of Quasi-Steady-State Loadings on Thin Elastic Wings. Aeronautical Research Institute of Sweden, Stockholm, Rept. 105, 1966.

10. Yager, P. M., Holland, C. G., Jr. and Strand, T.: Modified Weissinger Lifting Surface Method for Calculating Aerodynamic Parameters of Arbitrary Wing-Canard Configurations. Air Vehicle Corporation, La Jolla, California, Report No. 354, 1967.

11. Scully, M. P.: A Method of Computing Helicopter Vortex Wake Distortion. Massachusetts Institute of Technology, Aeroelastic and Structure Research Laboratory, ASRL TR-138-1, 1967.

12. Atta, E. H., Kandil, O. A., Mook, D. T. and Nayfeh, A. H.: Unsteady Flow Past Wings Having Sharp-Edge Separation. Presented at NASA-Langley Workshop on Vortex-Lattice Utilization, May 1976. (To appear in a forthcoming NASA SP).
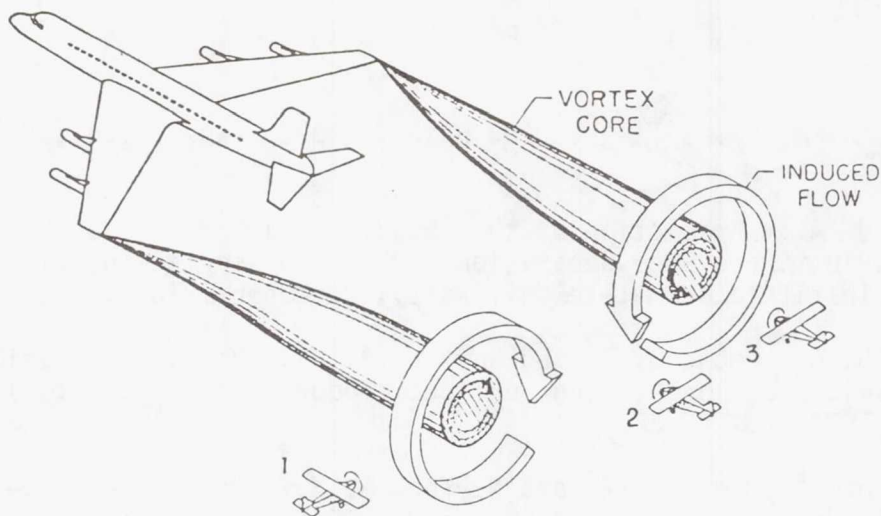
Figure 1.- Illustration of trailing vortex wake and types of encounter (from ref. 5): cross-track penetration (1), along-track penetration between vortices (2), and along-track penetration through vortex center (3).
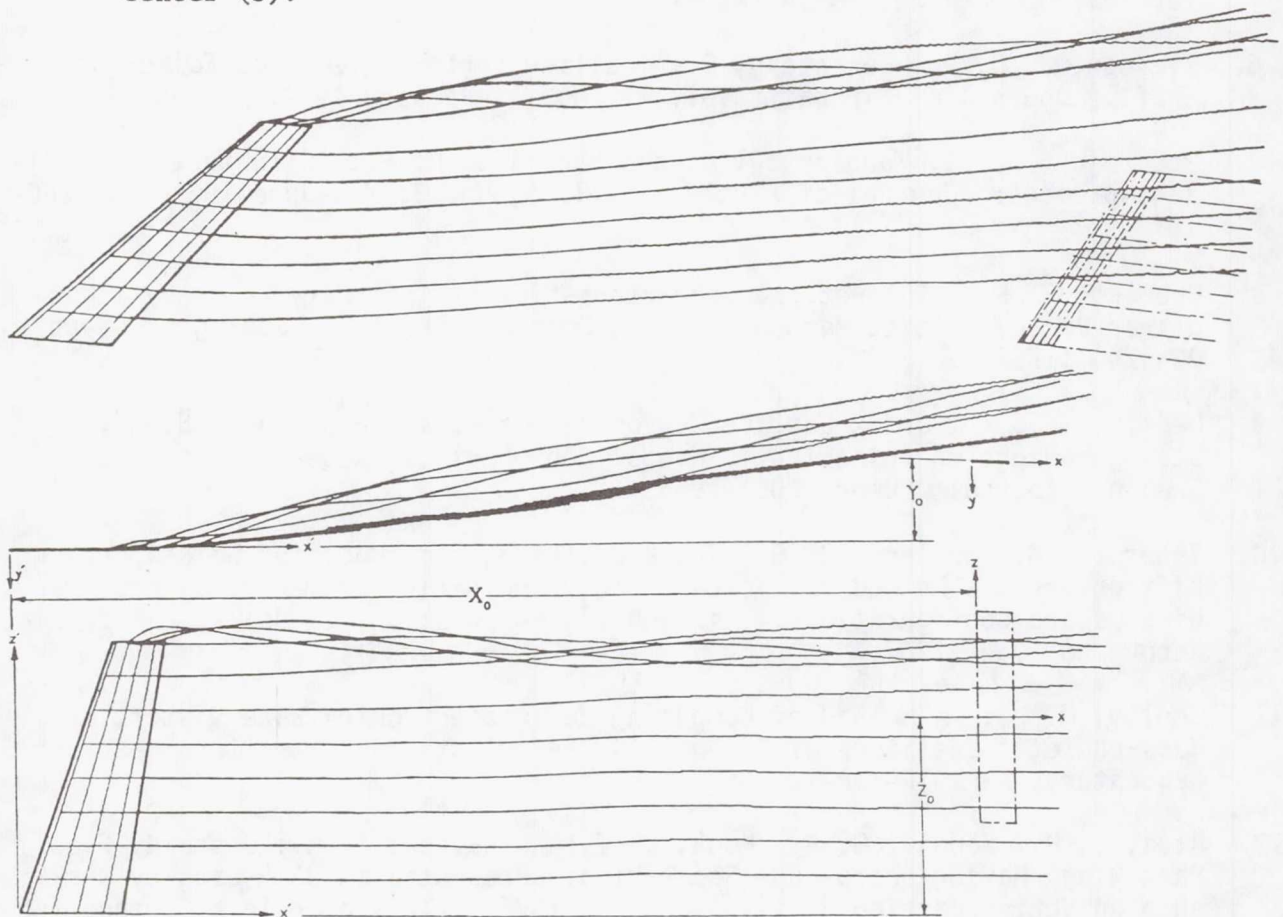
Figure 2.- Typical solution of the near and far wakes of the leading wing. Angle of attack = 10°; $AR_\ell = 7$; 4×8 lattice.
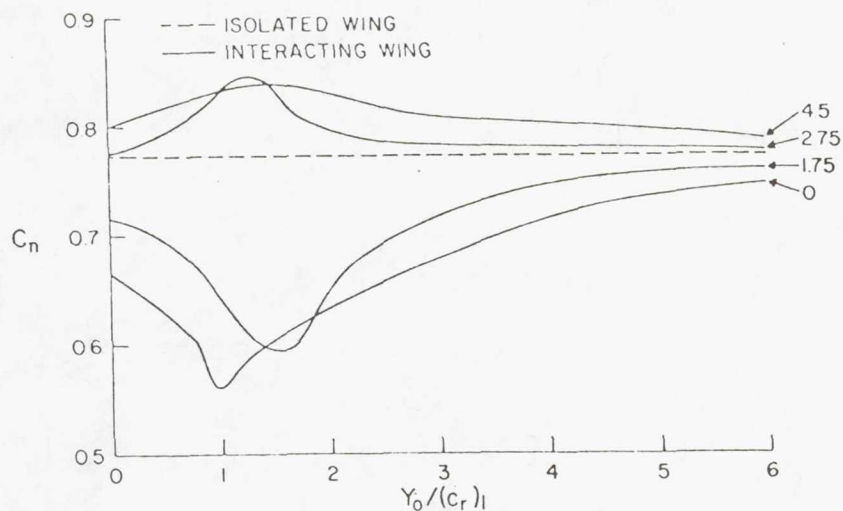
Figure 3. Normal-force coefficient vs. normal separation above the leading wing for various lateral separations $Z_0/(c_r)_\ell$. $X_0/(c_r)_\ell = 9.25$; $AR_\ell = 7$; $AR_t = 6$; $(c_r)_\ell/(c_r)_t = 3$.
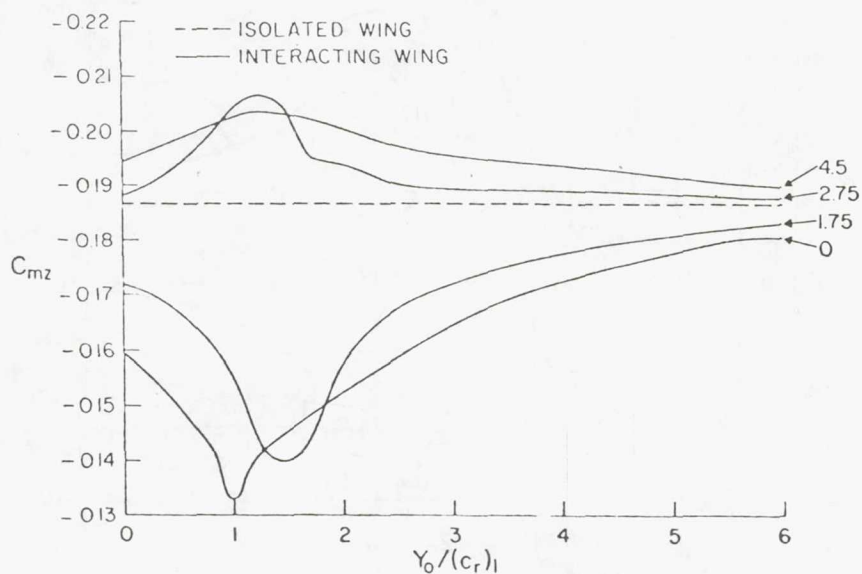
Figure 4. Pitching-moment coefficient vs. normal separation above the leading wing for various lateral separations $Z_0/(c_r)_\ell$. $X_0/(c_r)_\ell = 9.25$; $AR_\ell = 7$; $AR_t = 6$; $(c_r)_\ell/(c_r)_t = 3$.
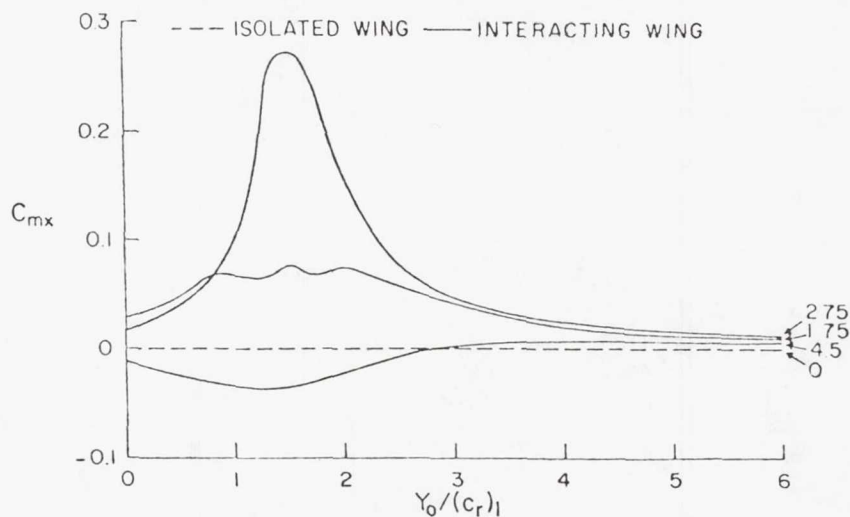
Figure 5.- Rolling-moment coefficient vs. normal separation above the leading wing for various lateral separations $Z_0/(c_r)_\ell$. $X_0/(c_r)_\ell = 9.25$; $AR_\ell = 7$; $AR_t = 6$; $(c_r)_\ell/(c_r)_t = 3$.
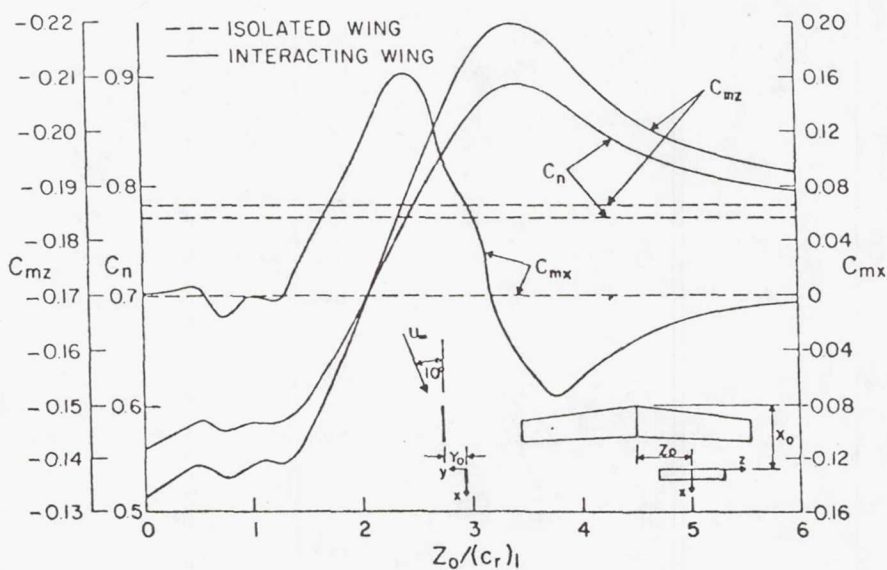
Figure 6.- Normal-force (C_n), pitching-moment (C_{mz}), and rolling-moment (C_{mx}) coefficients vs. lateral separation. $X_0/(c_r)_\ell = 9.25$; $Y_0/(c_r)_\ell = 1$; $AR_\ell = 7$; $AR_t = 6$; $(c_r)_\ell/(c_r)_t = 3$.

AN APPLICATION OF THE SUCTION ANALOGY FOR THE
ANALYSIS OF ASYMMETRIC FLOW SITUATIONS

James M. Luckring
NASA Langley Research Center

SUMMARY

This paper reviews a recent extension of the suction analogy for estimation of vortex loads on asymmetric configurations. This extension includes asymmetric augmented vortex lift and the forward sweep effect on side edge suction. Application of this extension to a series of skewed wings has resulted in an improved estimating capability for a wide range of asymmetric flow situations. Hence, the suction analogy concept now has more general applicability for subsonic lifting surface analysis.

INTRODUCTION

For lifting surfaces having relatively sharp leading and side edges, the commensurate separation associated with the vortex-lift phenomena can have considerable impact on the performance of high-speed maneuvering aircraft. A detailed knowledge of these flow phenomena, which are referred to as vortex flows, is necessary for proper design and analysis of such aircraft.

For estimating the lift associated with these vortex flows, Polhamus introduced the concept of the leading-edge suction analogy (ref. 1). The suction analogy states that for the separated flows situation, the potential-flow leading-edge suction force becomes reoriented from acting in the chord plane to acting normal to the chord plane (a rotation of 90°) by the local vortex action resulting in an additional normal force. (See insert on fig. 1.) The reasoning is that the force required to maintain the reattached flow is the same as that which had been required to maintain the potential flow around the leading edge.

An application of the suction analogy is shown in figure 1 for a 75° swept sharp-edge delta wing at a low subsonic Mach number taken from reference 2. Both lift as a function of angle of attack and drag due to lift are seen to be well estimated by the analogy. Since the original application, the suction analogy concept has not only been applied to more general planforms (refs. 3 and 4) but, also has been extended as shown in figure 2 to account for side-edge vortex flows (ref. 5).

Whereas the theories of references 1 to 5 have dealt with estimating the effects of separation-induced vortex flows on longitudinal aerodynamic characteristics for symmetrical configurations having symmetrical loads, it is desirable to have a method which allows for asymmetric configurations such as oblique or skewed wings, for example, and asymmetric flight conditions such as those associated with sideslip or lateral control.

Accordingly, this paper presents an overview of a recent extension of the suction analogy concept to include asymmetric flow situations (ref. 6). Although analysis may be performed on many different types of asymmetric flow situations, as shown in figure 3, this paper will focus on the analysis of wings with geometric asymmetries and, in particular, on untapered skewed wings having separated vortex flows along leading and side edges. The effect of forward sweep on side-edge suction is reviewed and the concept of augmented vortex lift as developed in reference 7 is applied to skewed wings.

SYMBOLS

A	aspect ratio
b	wing span
C_D	drag coefficient, $\dfrac{\text{Drag}}{q_\infty S_{ref}}$
$C_{D,o}$	experimental value of drag coefficient at $C_L = 0$
C_L	lift coefficient, $\dfrac{\text{Lift}}{q_\infty S_{ref}}$
$\Delta C_{L,v}$	C_L increment associated with augmented vortex lift
C_l	rolling-moment coefficient about reference point, $\dfrac{\text{Rolling moment}}{q_\infty S_{ref} b}$
$C_{l\beta}$	$= \dfrac{\partial C_l}{\partial \beta}$
C_{l_p}	$= \dfrac{\partial C_l}{\partial \left(\dfrac{pb}{2U}\right)}$
C_{l_r}	$= \dfrac{\partial C_l}{\partial \left(\dfrac{rb}{2U}\right)}$
C_m	pitching-moment coefficient about reference point which is located at $\dfrac{c_{ref}}{4}$ unless otherwise stated, $\dfrac{\text{Pitching moment}}{q_\infty S_{ref} c_{ref}}$
C_N	normal-force coefficient, $\dfrac{\text{Normal force}}{q_\infty S_{ref}}$

C_n yawing-moment coefficient about reference point, $\dfrac{\text{Yawing moment}}{q_\infty S_{ref} b}$

C_{n_β} $= \dfrac{\partial C_n}{\partial \beta}$

C_{n_p} $= \dfrac{\partial C_n}{\partial \left(\dfrac{pb}{2U}\right)}$

C_{n_r} $= \dfrac{\partial C_n}{\partial \left(\dfrac{rb}{2U}\right)}$

C_S leading-edge suction-force coefficient, $K_{v,le} |\sin \alpha| \sin \alpha$

C_T leading-edge thrust-force coefficient, $C_S \cos \Lambda$

C_Y leading-edge side-force coefficient, $C_S \sin \Lambda$

$C_{Y,se}$ side-edge side-force coefficient

c streamwise chord

$\tilde{c}$ characteristic length used in determination of $\bar{K}_{v,se}$

c_s section suction-force coefficient, $\dfrac{\text{Section suction force}}{q_\infty c}$

c_t section thrust-force coefficient, $\dfrac{\text{Section thrust force}}{q_\infty c}$

c_y section side-force coefficient, $\dfrac{\text{Section side force}}{q_\infty c}$

$f_{y,i}$ elemental side force

K_p potential-lift factor, $\dfrac{\partial \left(C_{N,p}\right)}{\partial (\sin \alpha \cos \alpha)}$

$K_{v,le}$ leading-edge-vortex lift factor,

$$\partial \left(\dfrac{\dfrac{\text{Leading-edge suction force from one edge}}{q_\infty S_{ref}}}{\partial \sin^2 \alpha}\right)$$

$K_{v,se}$ side-edge-vortex lift factor,

$$\partial \left(\frac{\frac{\text{Side-edge suction force from one edge}}{q_\infty S_{ref}}}{\partial \sin^2 \alpha} \right)$$

$\bar{K}_{v,se}$ augmented-vortex lift factor, $\dfrac{K_{v,le}}{(b) \sec \Lambda} \tilde{c}$

M free-stream Mach number

p roll rate, rad/sec

q_∞ free-stream dynamic pressure

r yaw rate, rad/sec

S surface area

U free-stream velocity

u induced velocity in x-direction at point (x,y)

v induced velocity in y-direction at point (x,y)

$\bar{x}$ centroid

α angle of attack

β angle of sideslip

γ distributed bound vorticity at point (x,y)

δ distributed trailing vorticity at point (x,y)

η spanwise location in percent semispan

Λ leading-edge sweep angle, positive for sweepback

Subscripts:

av   average

c   centroid

i   particular item of location

1334

le   leading edge

p   potential or attached flow

r   root

ref   reference; for S, true wing area; for c, mean geometric chord

se   side edge

tot   total

vle   vortex effect at leading edge

vse   vortex effect at side edge

RESULTS AND DISCUSSION

Modified Vortex-Lattice Method

In the analysis of separation-induced vortex flow effects for symmetric configurations by the method of references 8 and 9, the potential flow lift is computed from the symmetric vortex lattice and the vortex lift is computed from the symmetric potential flow solution by using the suction analogy. The application of this technique is not limited, however, to symmetric conditions and should be applicable to asymmetric conditions providing the appropriate values of K_p and K_v can be obtained.

Accordingly, the asymmetric vortex-lattice computer program was developed from its symmetric progenitors (refs. 8 and 9) to compute potential flow solutions about arbitrary thin asymmetric configurations. Once the asymmetric potential-flow solution (and, hence, K_p) is known, the suction analogy may be invoked to compute corresponding asymmetric vortex lift terms, $K_{v,le}$ and $K_{v,se}$. The method of references 8 and 9 may now be employed by using the K_p and K_v quantities as computed from the asymmetric potential flow.

In applying this analysis to a series of sharp-edged skewed wings, some additional aerodynamic effects associated with these wings had to be considered. The following sections describe these effects and present the analysis.

Additional Aerodynamic Considerations

The effect of forward sweep on side-edge suction was introduced in reference 6. On the swept forward portion of a skewed wing, shown in the upper portion of figure 4, the leading-edge and side-edge side forces are seen to act in opposition to one another and result in regions of positive and negative elemental side force. The change of sign of the elemental side force would tend to imply that the positive elemental side forces act on the side edge while the negative elemental side forces act on the leading edge. A comparison of the leading-edge side-force distribution computed by integrating the negative elemental side forces on the sweptforward semispan with the side-force component of the leading-edge thrust force on the swept-forward semispan is presented in the lower left part of figure 4. The agreement tends to substantiate the implication that the negative elemental side forces are in actuality the side-force component of the leading-edge thrust. In that this force has already been accounted for in the present method, only the positive elemental side forces inboard of the side edge are integrated to compute the side-edge force on the sweptforward semispan.

In reference 7, Lamar introduced the concept of augmented vortex lift for estimation of loads rising from a vortex persisting downstream and passing over lifting surfaces such as the aft part of a wing or a tail. This persistence results in an additional vortex lift term unaccounted for by the suction analogy which deals only with the forces generated along a particular edge.

Figure 5 illustrates the concept of augmented vortex lift applied to a skewed wing. In applying the method of reference 7, the leading-edge vortex lift factor developed along the leading-edge length persists over a portion of the wing aft of the leading edge taken to be the tip chord. This condition results in an additional vortex lift factor which has the same angle-of-attack dependence as the other vortex terms. Since the chordwise centroid of side-edge vortex lift distributions is generally near the midpoint of the tip chord, the chordwise centroid of the augmented vortex lift factor is taken to be the midpoint of the tip chord. It should be noted that the augmented vortex lift occurs only on the downwind side edge.

As long as the leading-edge vortex remains in the vicinity of the leading edge, it will pass over a region of the wing aft of the leading edge that has a length roughly equal to the tip chord. The choice of the tip chord for the characteristic length is consistent with the assumption employed in this analysis that the vortex loads act along the edge from which they originate. This assumption is valid as long as a substantial amount of vortex growth and subsequent inboard movement of the vortex core is not encountered.

Skewed Wing Analysis

Figure 6 presents a comparison between a swept and a skewed wing of the span load and section suction distributions. Although in each case the total loads remain essentially the same for both wings, the distribution of the load is seen to shift for the skewed wing to the sweptback semispan. A comparison between the separated flow theory and experiment for these two wings is shown in figure 7. Data for the swept wing was obtained from reference 10. Although the lift is well predicted in both cases, the augmented pitching moment for the skewed wing is seen to predict the data well up to an angle of attack of approximately 6°; above this angle it overpredicts the data. The discrepancy between theory and data for the skewed wing pitching moment may partly be attributed to excessive vortex growth and subsequent movement of the vortex core inboard as the angle of attack is increased. This behavior is illustrated in figure 8. In the application of the suction analogy, the vortex loads are assumed to be edge forces and no angle-of-attack dependence of the centroids is computed. Moreover, as the vortex moves inboard, the amount of the wing over which the vortex passes giving rise to the augmented term decreases and may even become negative. Hence, the present application of augmentation for moment calculation may only be applicable for low to moderate angles of attack depending on how much variance $\tilde{c}$ will experience as a function of α .

Figures 9 to 11 present lift, pitching-moment, and rolling-moment characteristics of several skewed wings having an aspect ratio of one and varying leading-edge sweep. A configuration having a cylindrical fuselage 0.24b in diameter and $1.85c_r$ in length with a midwing is also presented.

In all cases, the lift was well estimated by including the edge-vortex and augmented-vortex contributions. Similarly, the nonlinear pitching-moment trends were well predicted by the edge-vortex contribution, the augmentation enhancing the prediction at low to moderate angles of attack. The potential-flow pitching-moment curve is seen to have a sign opposite from that of the data. Rolling moments were well predicted by the edge-vortex terms up to approximately 8° where the inboard vortex movement became significant; this condition caused a sign reversal in the data except for the wing-fuselage configuration. The primary effect of the fuselage is to break the leading-edge vortex into two pieces, one emanating from the wing apex and bending downstream at the right-wing fuselage juncture and the other emanating from the left leading-edge fuselage juncture and bending downstream at the left wing tip. Regenerating the leading-edge vortex with the fuselage substantially decreases the extent of inboard movement of the vortex as exhibited by the agreement between theory and experiment for the pitching- and rolling-moment coefficients of figures 10 and 11.

Figures 12 to 14 present the lift, pitching-moment, and rolling-moment characteristics of several skewed wings of varying aspect ratio. As in the previous case, the lift was well predicted for the three wings. The experimental pitching moments are well predicted by including the augmented term, but the experimental rolling moments still depart from the theory at

approximately 6°. Hence, for these wings the chordwise distribution of the load is being well estimated whereas the spanwise distribution of the load can be estimated only as long as a substantial inboard movement of the vortex is not encountered.

CONCLUDING REMARKS

This paper has presented a recent extension of the suction analogy for the estimation of potential and vortex loads on asymmetric configurations. The analysis has been accomplished by the development and application of an asymmetric vortex-lattice computer program which may be used to compute the potential and vortex loads on asymmetric configurations. In applying this to a series of sharp-edge skewed wings, the effects of forward sweep on side-edge suction and of a skewed geometry on augmented vortex lift have been accounted for. Total loads have been well predicted whereas pitching and rolling moments have been well predicted only as long as the assumption that the vortex loads act along the edge from which the vortex has originated is not violated. Hence, the suction analogy concept may now be applied to a wider range of isolated planforms resulting in an improved estimating capability of separation-induced vortex flow.

REFERENCES

1. Polhamus, Edward C.: A Concept of the Vortex Lift of Sharp-Edge Delta Wings Based on a Leading-Edge-Suction Analogy. NASA TN D-3767, 1966.

2. Wentz, William H., Jr.; and Kohlman, David L.: Wind Tunnel Investigation of Vortex Breakdown on Slender Sharp-Edged Wings. Rep. FRL 68-013 (Grant NGR-17-002-043), University of Kansas Center for Research, Inc., November 27, 1969. (Available as NASA CR-98737.)

3. Polhamus, Edward C.: Charts for Predicting the Subsonic Vortex-Lift Characteristics of Arrow, Delta, and Diamond Wings. NASA TN D-6243, 1971.

4. Polhamus, Edward C.: Predictions of Vortex-Lift Characteristics by a Leading-Edge Suction Analogy. J. Aircraft, vol. 8, no. 4, April 1971, pp. 193-199.

5. Lamar, John E.: Extension of Leading-Edge-Suction Analogy to Wings With Separated Flow Around the Side Edges at Subsonic Speeds. NASA TR R-428, 1974.

6. Luckring, James M.: Some Recent Applications of the Suction Analogy to Asymmetric Flow Situations. Presented at the Vortex Lattice Utilization Workshop. NASA SP-405, 1976, pp. 219-236.

7. Lamar, John E.: Some Recent Applications of the Suction Analogy to Vortex-Lift Estimates. Aerodynamic Analyses Requiring Advanced Computers, Part II, NASA SP-347, 1975, pp. 985-1011.

8. Margason, Richard J.; and Lamar, John E.: Vortex-Lattice FORTRAN Program for Estimating Subsonic Aerodynamic Characteristics of Complex Planforms. NASA TN D-6142, 1971.

9. Lamar, John E.; and Gloss, Blair B.: Subsonic Aerodynamic Characteristics on Interacting Lifting Surfaces With Separated Flow Around Sharp Edges Predicted by a Vortex-Lattice Method. NASA TN D-7921, 1975.

10. Gersten, K.: Calculation of Non-Linear Aerodynamic Stability Derivatives of Aeroplanes. AGARD Rep. 342, April 1961.
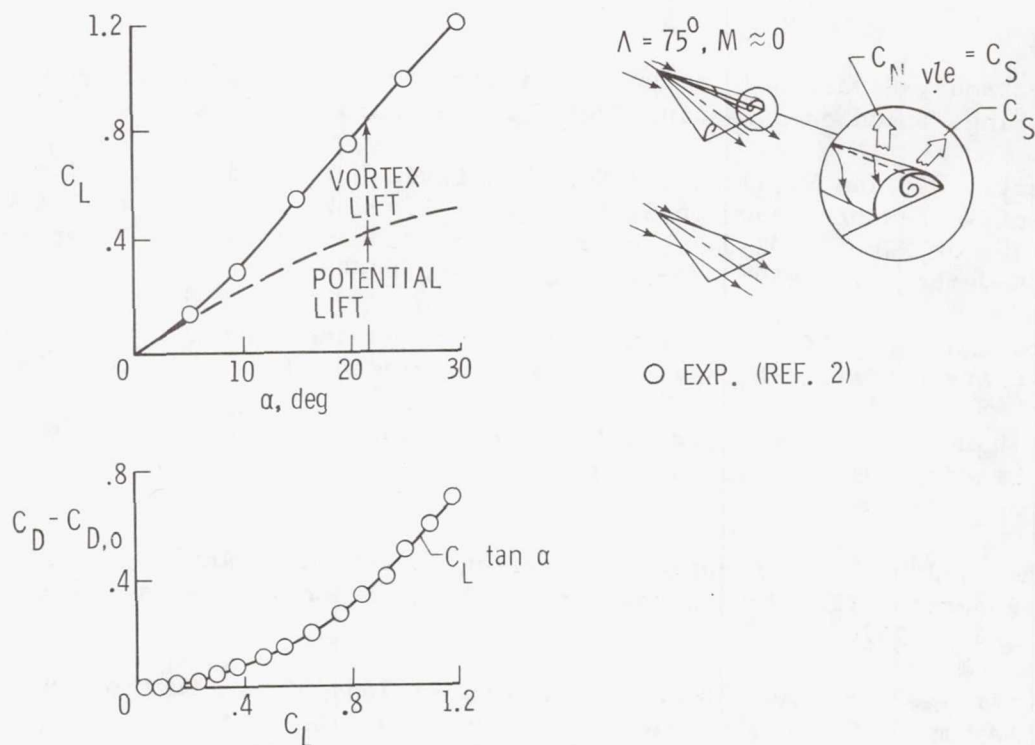
Figure 1.- Original application of leading-edge suction analogy.

$$C_L = K_p \sin \alpha \cos^2 \alpha + (K_{v,le} + K_{v,se}) |\sin \alpha| \sin \alpha \cos \alpha$$
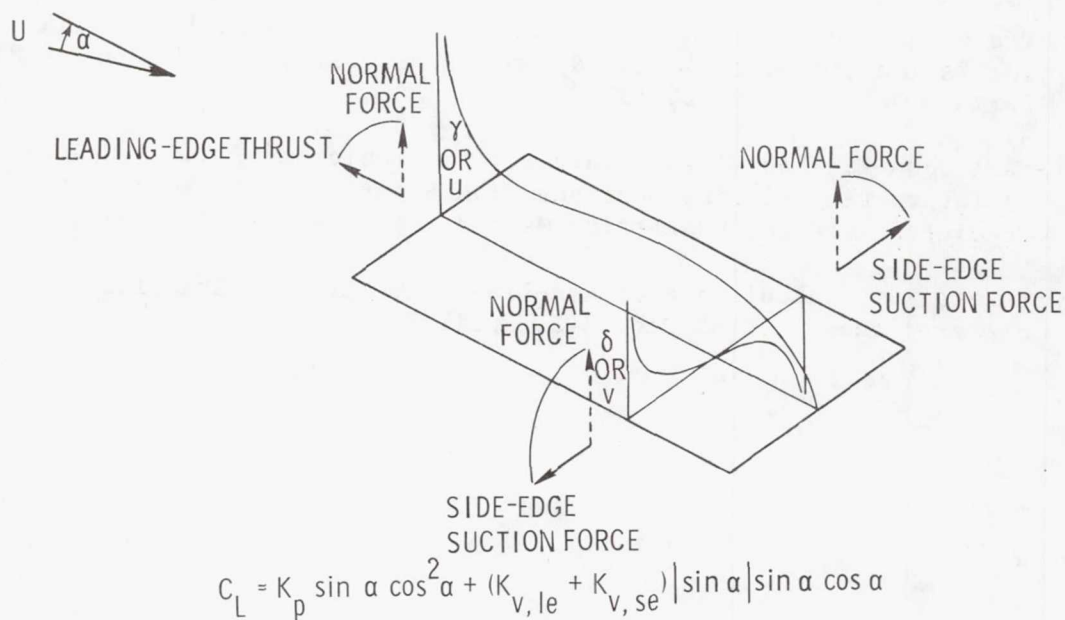
Figure 2.- Vortex-lift concept: suction analogy application
to leading edge and side edge.

GEOMETRIC ASYMMETRICS

- SINGLE PLANFORM
- SKEWED WINGS

- MULTIPLE PLANFORMS
- INTERACTION EFFECTS
- DIFFERENTIAL DEFLECTION

ONSETTING FLOW ASYMMETRICS

SIDESLIPPING
- C_{l_β}
- C_{n_β}

ROLLING
- C_{l_p}
- C_{n_p}

YAWING
- C_{l_r}
- C_{n_r}
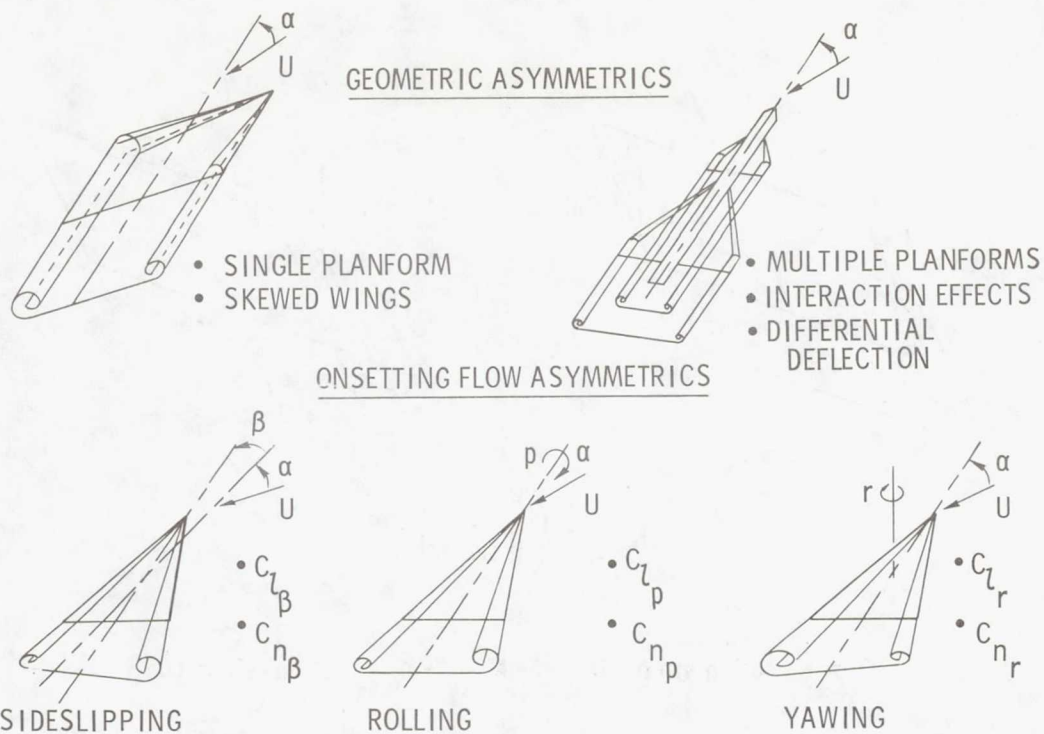
Figure 3.- Some recent applications of suction analogy to asymmetric vortex flow situations.

$M_\infty = 0$

○ L.E. THRUST * TAN Λ
— L.E. SIDE FORCE
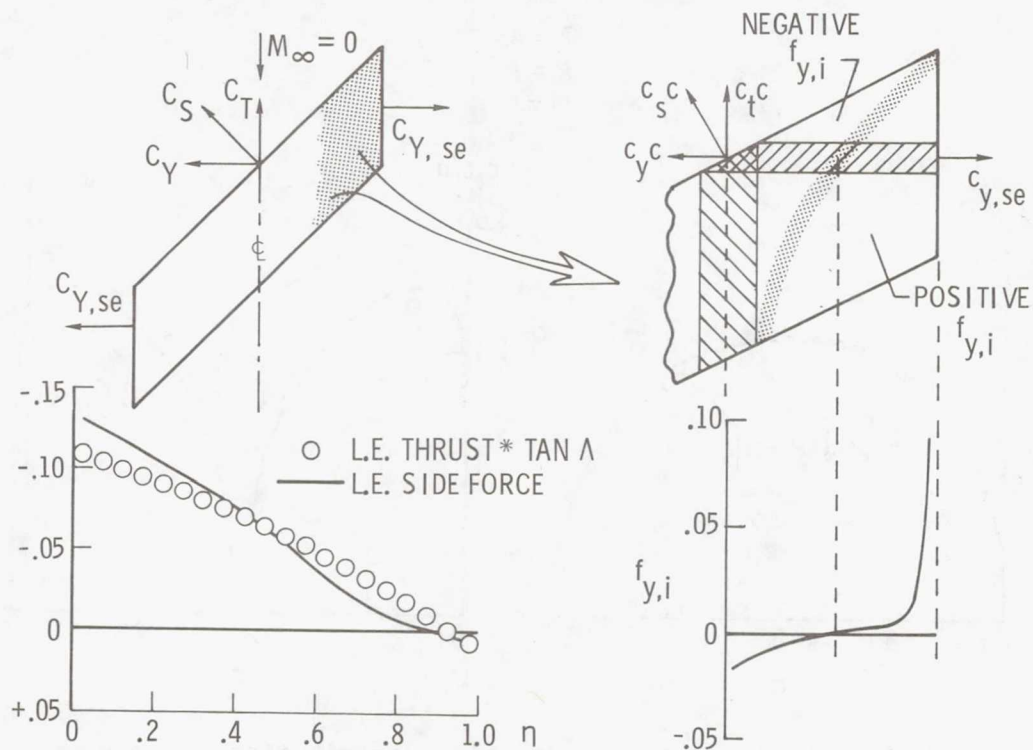
Figure 4.- Forward sweep effects on side-edge suction.

$$\overline{K}_{v,se} = \left(\frac{K_{v,\ell e}}{b \sec \Lambda} \right) \tilde{c}$$
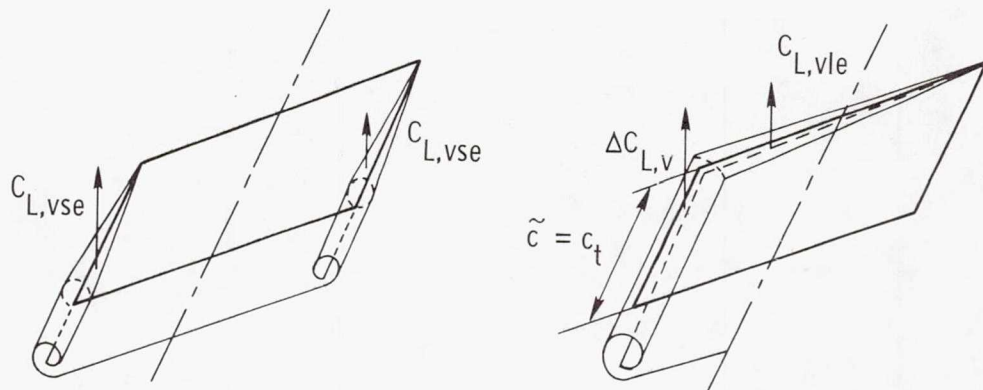
$$C_L = K_p \cos^2 \alpha \sin \alpha + (K_{v,\ell e} + K_{v,se} + \overline{K}_{v,se}) |\sin \alpha| \sin \alpha \cos \alpha$$

Figure 5.- Concept of augmented vortex lift applied to a skewed wing.
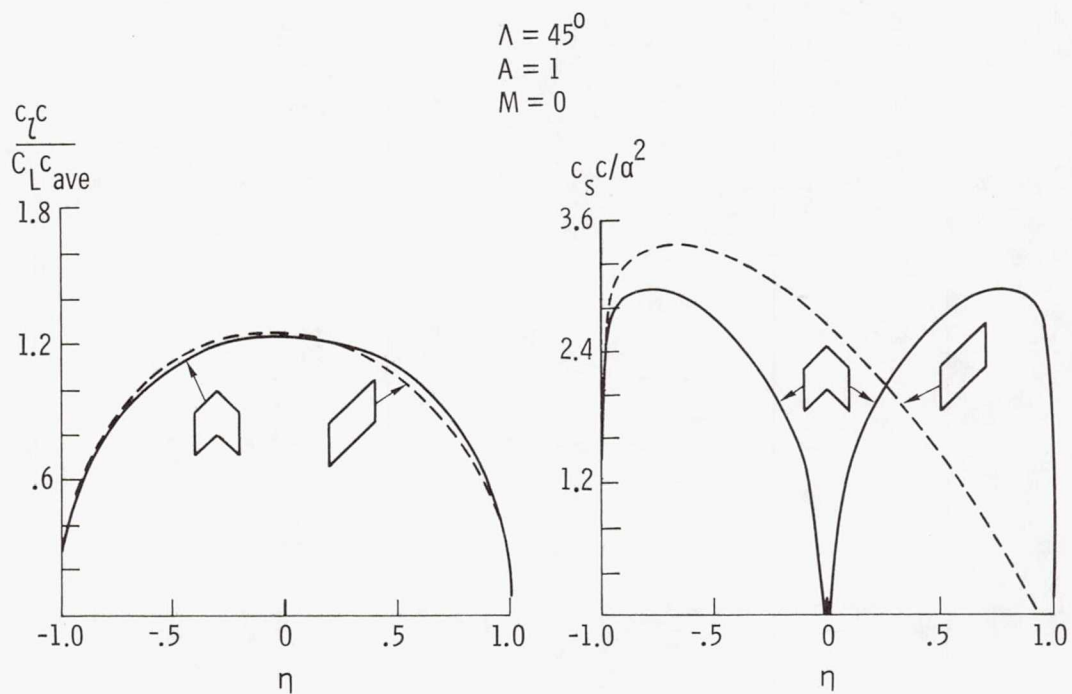
Figure 6.- Span load and section suction distributions on a swept and skewed wing. $\Lambda = 45°$; $A = 1$; $M = 0$.
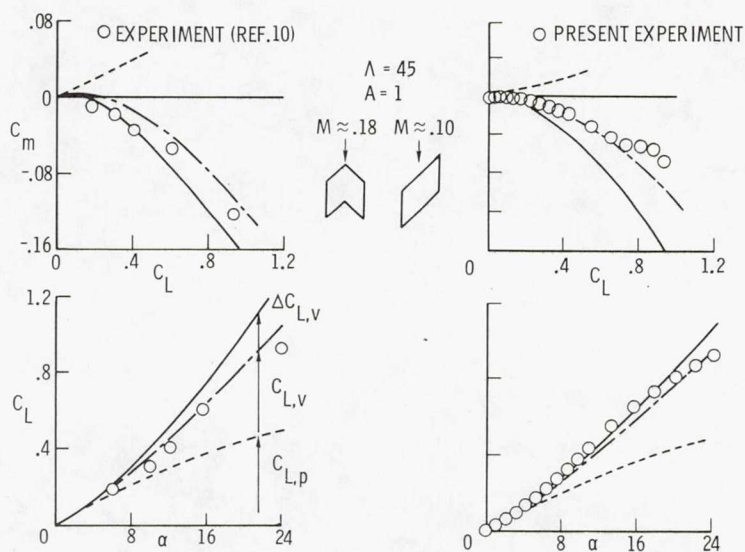
Figure 7.- Longitudinal characteristics of a swept and a skewed wing.
$\Lambda = 45$; $A = 1$.
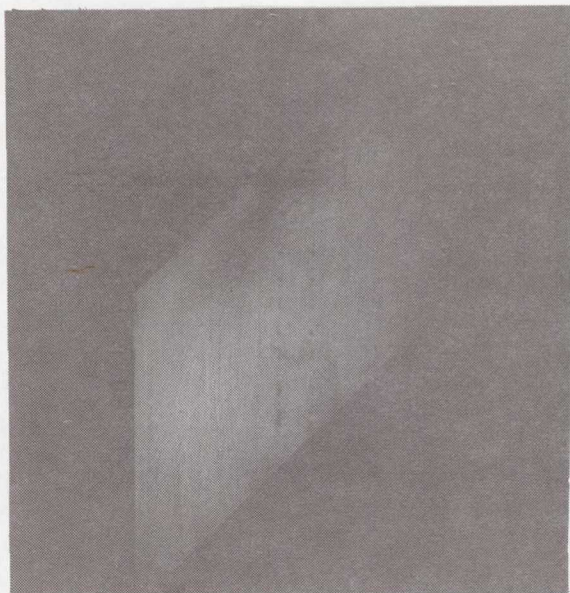
(a) $\Lambda = 45^{\circ}$; $A = 1$; $\alpha = 5^{\circ}$.
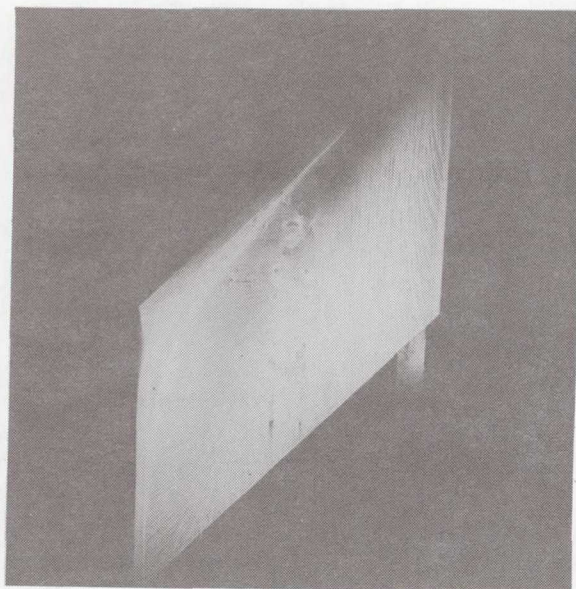
(b) $\Lambda = 45^{\circ}$; $A = 1$; $\alpha = 10^{\circ}$.
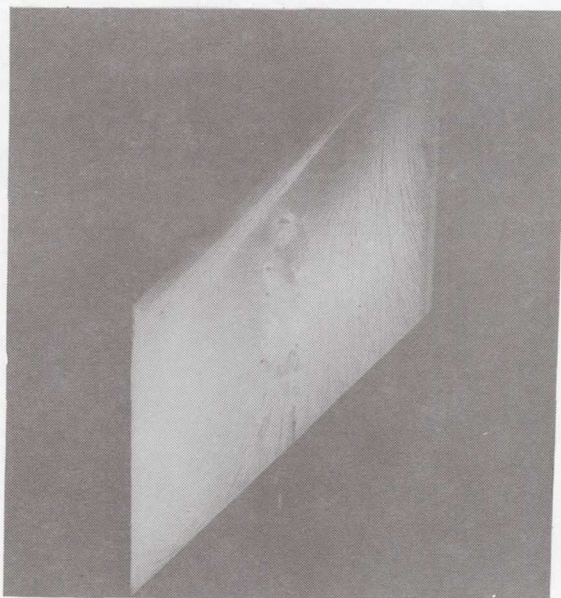
(c) $\Lambda = 45^{\circ}$; $A = 1$; $\alpha = 15^{\circ}$.

Figure 8.- Vortex flow on a skewed wing.
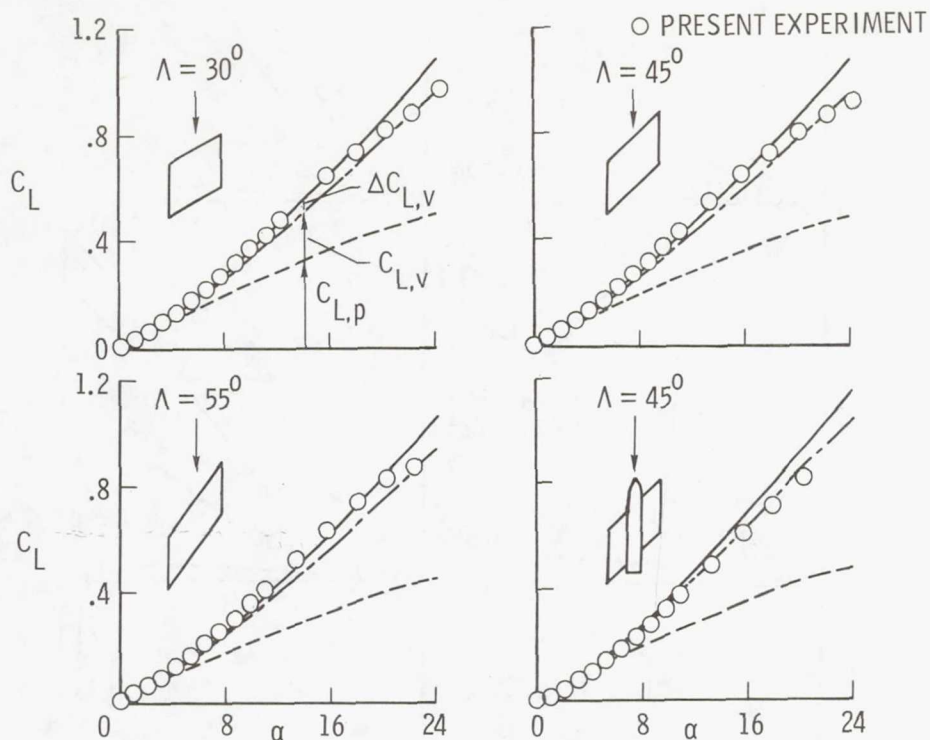
Figure 9.- Effect of leading-edge sweep on lift characteristics of several skewed wings. $A = 1$; $M \approx 0.10$.
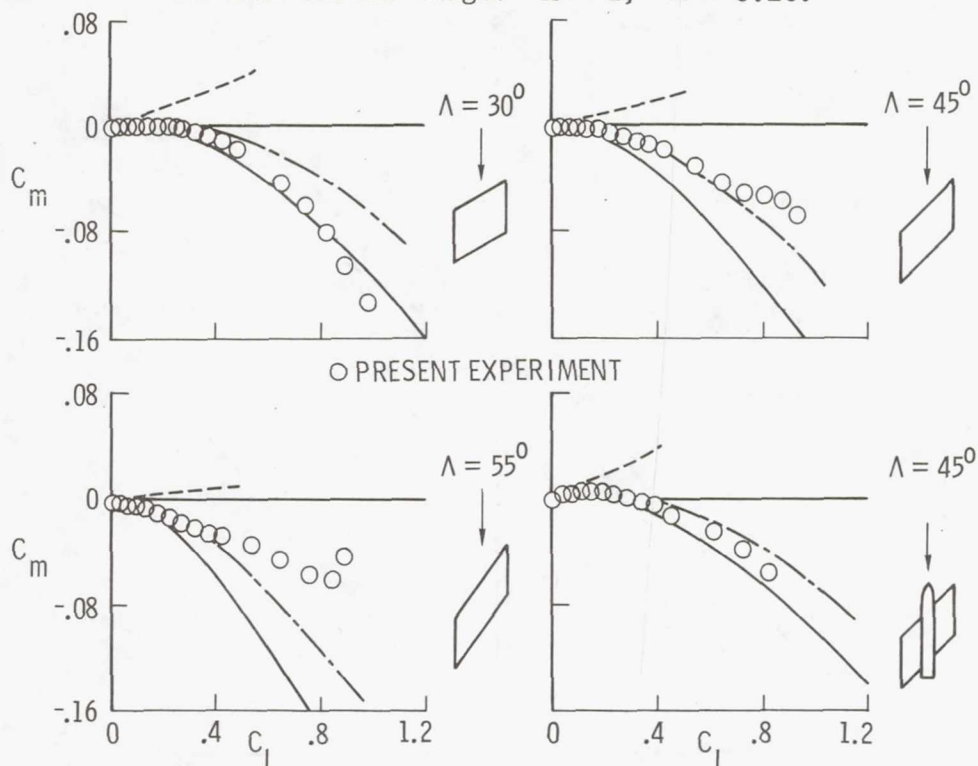
Figure 10.- Effect of leading-edge sweep on pitch characteristics of several skewed wings. $A = 1$; $M \approx 0.10$.
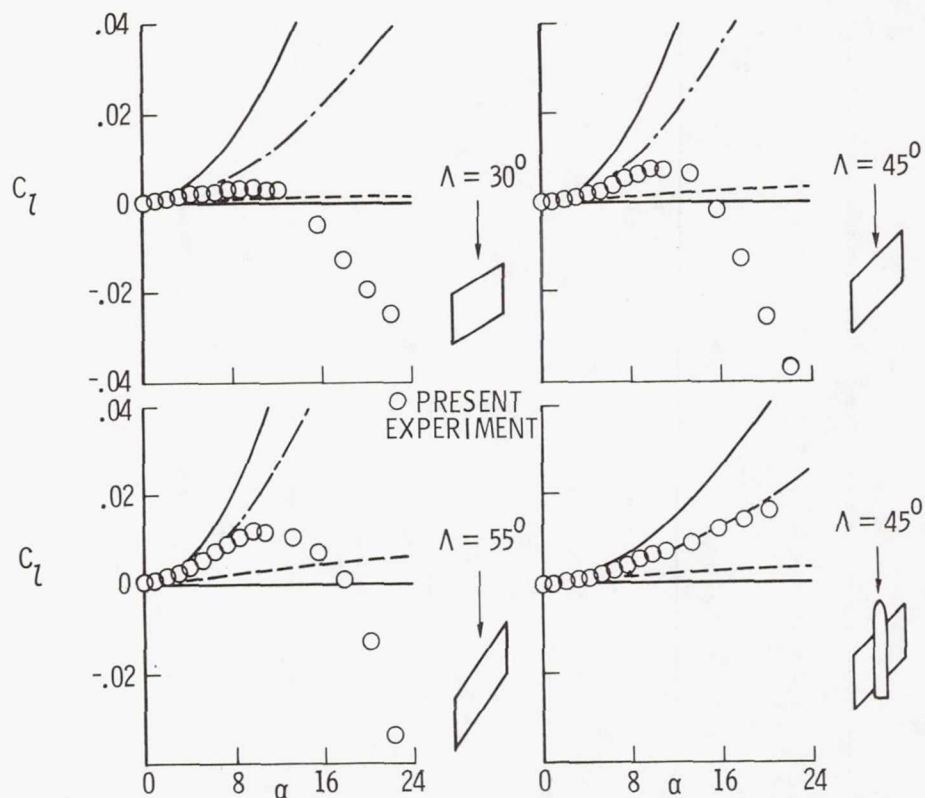
Figure 11.- Effect of leading-edge sweep on roll characteristics of several skewed wings. A = 1; M ≈ 0.10.
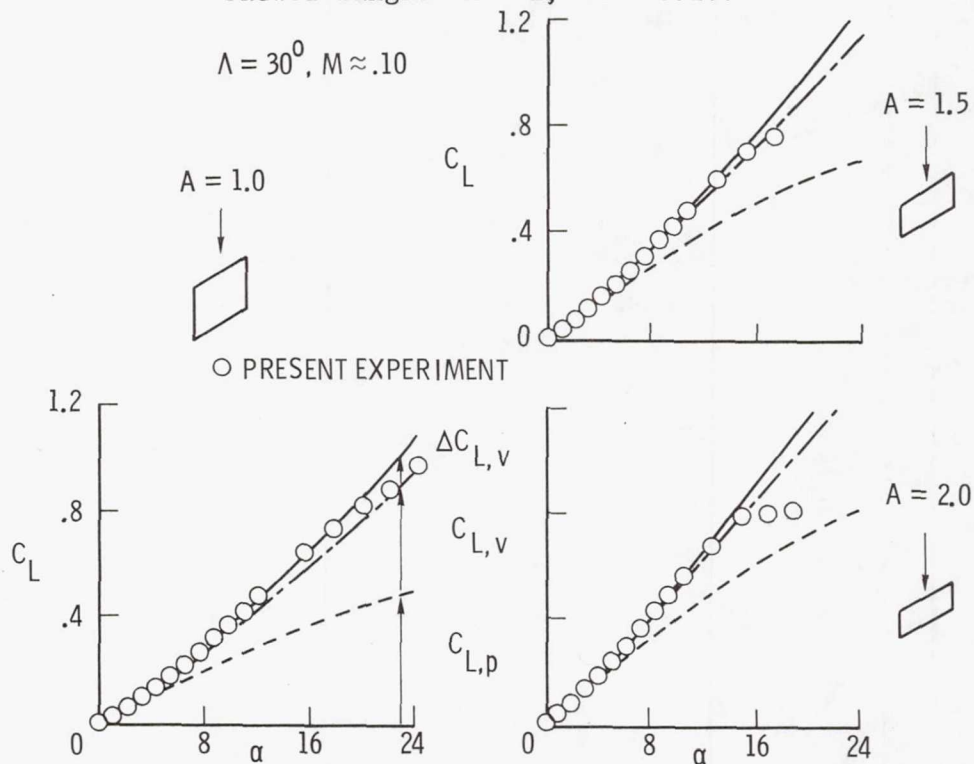
Figure 12.- Effect of aspect ratio on lift characteristics of several skewed wings. Λ = 30°; M ≈ 0.10.
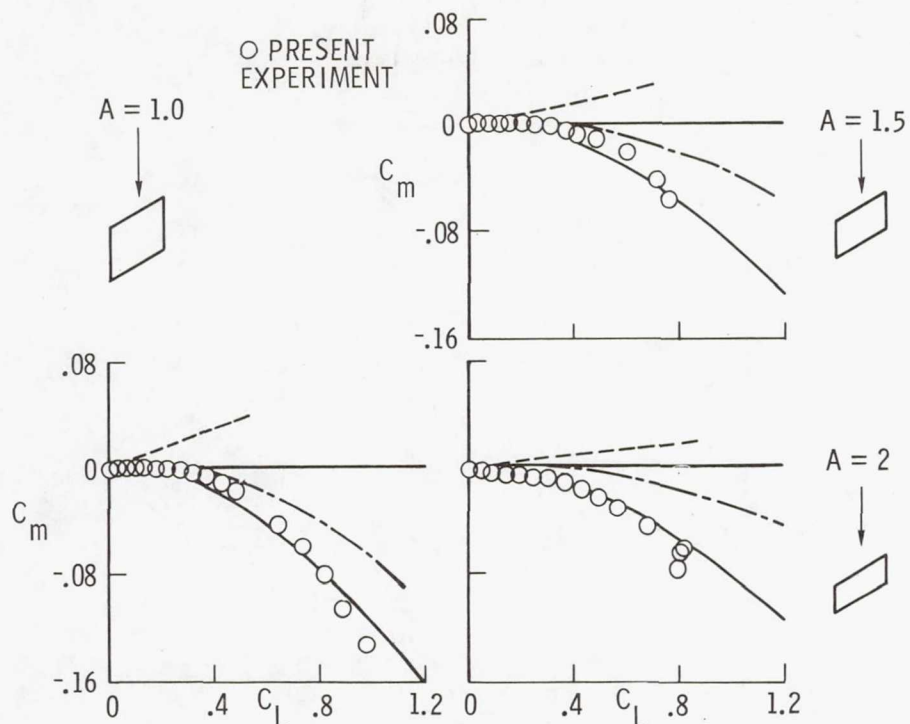
Figure 13.- Effect of aspect ratio on pitch characteristics of several skewed wings. $\Lambda = 30^{\circ}$; $M \approx 0.10$.
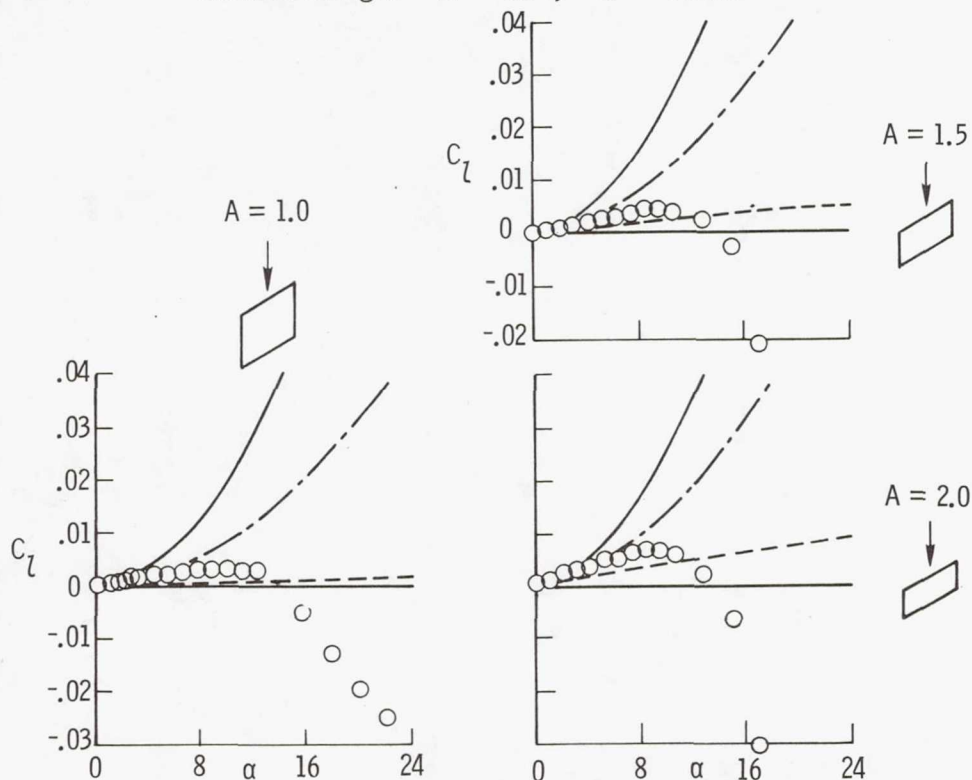
Figure 14.- Effect of aspect ratio on roll characteristics of several skewed wings. $\Lambda = 30^{\circ}$; $M \approx 0.10$.

Page intentionally left blank

TRANSONIC FLOW THEORY OF AIRFOILS AND WINGS[*]

P. R. Garabedian
Courant Institute of Mathematical Sciences

SUMMARY

Supercritical wing technology is expected to have a signifi-
cant influence on the next generation of commercial aircraft.
Computational fluid dynamics is playing a central role in the
development of new supercritical wing sections. One of the prin-
cipal tools is a fast and reliable code that simulates two-
dimensional wind tunnel data for transonic flow at high Reynolds
numbers. This is used widely by industry to assess drag creep and
drag rise. Codes for the design of shockless airfoils by the
hodograph method have not been so well received because they
usually require a lot of trial and error. However, a more advanc-
ed mathematical approach makes it possible to assign the pressure
as a function of the arc length and then obtain a shockless air-
foil that nearly achieves the given distribution of pressure.
This tool should enable engineers to design families of transonic
airfoils more easily both for airplane wings and for compressor
blades in cascade.

INTRODUCTION

There are plans to use the supercritical wing on the next
generation of commercial aircraft so as to economize on fuel
consumption by reducing drag. Computer codes have served well in
meeting the consequent demand for new wing sections. One of the
most widely adopted codes was developed at the Courant Institute
to simulate two-dimensional transonic flow over an airfoil at high
Reynolds numbers (ref. 1). This work is an example of the possibil-
ity of replacing wind tunnel tests by computational fluid
dynamics. Another approach to the supercritical wing is through
shockless airfoils. Here a novel boundary value problem in the
hodograph plane will be discussed that enables one to design a
shockless airfoil so that its pressure distribution very nearly
takes on data that have been prescribed. An advanced design code
of this kind has been written recently by David Korn and is turning
out to be so successful that it may ultimately gain the same
acceptance as the better established analysis code.

Physically realistic transonic flow computations can be based on a potential equation that presupposes conservation of entropy across shock waves, but permits a jump in the normal component of momentum. However, to treat either the problem of design or of analysis for transonic airfoils in a satisfactory way from the engineering point of view, it is necessary to take into account the effect of the turbulent boundary layer. The simplest procedure is to calculate the displacement thickness of the boundary layer from the inviscid pressure distribution by a momentum integral method of Nash and Macdonald (ref. 2). For analysis one adds the displacement thickness to the profile at each cycle of an iterative scheme determining the flow. In the case of design a corresponding quantity is subtracted from the airfoil coordinates, which therefore have to be provided with a slightly open trailing edge to begin with.

It is important to eliminate separation entirely in the problem of design if there is to be no loss of lift in practice. This can be accomplished by imposing a pressure distribution at the rear of the upper surface that just avoids separation according to a criterion of Stratford (ref. 3). The boundary layer correction has been found to give satisfactory results even when its implementation only involves a primitive model of the wake in which pressure forces balance across a parallel pair of trailing streamlines. Extensive wind tunnel tests from laboratories all over the world confirm that the analysis code agrees well with experimental data when the boundary layer correction is made. Preliminary test data on a cascade airfoil that was heavily aft-loaded also inspire confidence in the concept of using a Stratford pressure distribution to avoid loss of lift in design by the hodograph method.

The transonic flow codes developed at the Courant Institute have been distributed to industry by the Langley Research Center. In the future they will also become available through the Argonne Code Center of the Argonne National Laboratory.

THE METHOD OF COMPLEX CHARACTERISTICS

The partial differential equations for the velocity potential ϕ and stream function ψ of two-dimensional irrotational flow of a compressible fluid can be written in terms of characteristic coordinates ξ and η in the canonical form

$$\phi_\xi = i\sqrt{1-M^2}\,\psi_\xi/\rho \,, \qquad\qquad \phi_\eta = -i\sqrt{1-M^2}\,\phi_\eta/\rho \,,$$

where the local Mach number M and the density ρ are functions of the speed q defined by Bernoulli's law. A fast and flexible numerical scheme for the construction of smooth transonic flows in the hodograph plane has been developed by continuing these equa-

tions analytically into the domain of complex values of the two independent variables ξ and η (ref. 4). The coordinates ξ and η can be specified in terms of the speed q and the flow angle θ by the formulas

$$\log f(\xi) = \int \sqrt{1-M^2} \, \frac{dq}{q} - i\theta \ , \qquad \log \overline{f(\overline{\eta})} = \int \sqrt{1-M^2} \, \frac{dq}{q} + i\theta \ ,$$

where f is any complex analytic function. Prescription of a second arbitrary analytic function g serves to determine ϕ and ψ as solutions of the characteristic initial value problem

$$\psi(\xi,\eta_0) = g(\xi) \ , \qquad\qquad \psi(\xi_0,\eta) = \overline{g(\overline{\eta})} \ ,$$

where $\xi_0 = \overline{\eta}_0$ is a fixed point in the complex plane. With these conventions it turns out that $\psi(\xi,\eta) = \overline{\psi(\overline{\eta},\overline{\xi})}$, whence for subsonic flow the real hodograph plane corresponds to points in the complex domain where $\xi = \overline{\eta}$.

Consider the nonlinear boundary value problem of designing an airfoil on which the speed q has been assigned as a function of the arc length s. To construct a solution it is helpful to view f as a function mapping the region of flow onto the unit circle $|\xi| < 1$. There both log f and g have natural expansions as power series in ξ after appropriate singularities accounting for the flow at infinity have been subtracted off. The coefficients of truncations of these series can be determined by interpolating to meet boundary conditions on q and ψ at equally spaced points of the circumference $|\xi| = 1$. Such a numerical solution is easily calculated because the matrix of the system of linear equations for the coefficients is well conditioned. This analytical procedure has the advantage that its formulation can be extended to the case of transonic flow so as to yield a shockless airfoil nearly fitting the prescribed data even when an exact solution of the physical problem does not exist.

To calculate transonic flows by the method that has been proposed, it is necessary to circumvent the sonic locus M = 1, which becomes a singularity of the partial differential equations for ϕ and ψ in canonical form. In the plane $\xi = \overline{\eta}$ this locus separates the region of subsonic flow from a domain where $\psi(\xi,\overline{\xi})$ is no longer real. In the latter domain it is necessary to extend in some empirical fashion the relationship between ϕ and s that is imposed by assigning q as a function of s. A formulation of the boundary conditions that applies to both the subsonic and the supersonic flow regimes is given by the formulas

$$\text{Re} \ \{\log f(\xi)\} = h \ , \qquad \text{Re} \ \{\psi(\xi,\overline{\xi})\} + k \ \text{Im} \ \{\psi(\xi,\overline{\xi})\} = 0$$

on $|\xi| = 1$, where k is a real constant and h is a function of

1351

Re $\{\phi(\xi,\bar{\xi})\}$ obtained from the known relationships among s, q and ϕ. The nonlinearity of the problem makes it necessary to iterate on this relationship in finding a numerical solution.

Empirical data on the condition number of the matrix for the linear equations determining the power series coefficients of the analytic function g indicate that the boundary value problem for ψ that has been formulated is well posed even in the transonic case. In contrast with the Tricomi problem, boundary values are assigned around the whole circumference of the unit circle. The success of the procedure can be attributed to the fact that data are assigned in a suitable complex extension of the real plane.

In general limiting lines may appear in the physical plane, but it has been found that these can be suppressed by appropriate selection of the rules defining the function h and the real parameter k that occur in the specification of the boundary conditions. Thus a tool becomes available for the construction of supercritical wing sections from their pressure distributions. Figure 1 shows an example of a shockless airfoil that was obtained this way, together with its Mach lines. Observe that the input pressure coefficient C_p differs somewhat from the values calculated as output of the flow in the supersonic zone, which is rather large. The data that were assigned are based on a modification of the experimental pressure distribution on Whitcomb's original supercritical wing (ref. 5) shown in Figure 2.

The design code has been written to include the case of transonic airfoils in cascade. This model seems to offer considerable promise for improvement in the efficiency of certain stages of high speed compressors. However, to handle cascades of high solidity with adequate resolution it is desirable to replace a conformal mapping onto the unit circle $|\xi| < 1$ by the mapping onto an ellipse, where the Tchebycheff polynomials become preferable to powers of ξ for expansion of the analytic functions log f and g. Likewise, to achieve adequate resolution at the trailing edge in cases of heavy aft-loading it is helpful to insert a special term at the tail in the representation of the map function f.

The new code represents a major advance over what was achieved in earlier versions, whose use required excessive trial and error (ref. 4). A typical run takes about six minutes on the CDC 6600 computer. Closure of the airfoil is readily attained by adjusting the pressure at the trailing edge and the relative lengths of arc over the upper and lower surfaces between the stagnation point and the trailing edge. A general principle to be observed when using shockless airfoils to design supercritical wing sections is that drag creep can be reduced by diminishing the size of the supersonic zone of flow, especially toward the rear of the profile. In practice the best way to assess the performance of a new design is to run it through the analysis code, which will be discussed next.

Analysis of the transonic flow past an airfoil can be based on a partial differential equation for the velocity potential ϕ. Weak solutions modelling shock waves are calculated by adding artificial viscosity. This can be accomplished with a full conservation form (FCF) of the equation, but a simpler version not in conservation form (NCF) is sometimes more useful (ref. 1). To handle the boundary conditions it is convenient to map the region of flow conformally onto the exterior of the unit circle. If r and θ stand for polar coordinates there, the quasilinear equation for ϕ can be written as

$$a\ \phi_{\theta\theta} + 2b\ \phi_{\theta r} + c\ \phi_{rr} + d = 0$$

when artificial viscosity is omitted. The simplest way of introducing artificial viscosity numerically, suggested first by Murman and Cole in a fundamental paper (ref. 6), is to use finite difference approximations that are retarded in the direction of the flow, which for practical purposes can be taken as the direction of θ. This does not perturb the Neumann boundary condition on ϕ.

The finite difference equations for transonic flow can be solved iteratively by a variety of relaxation schemes, all of which take the form of marching processes with respect to an artificial time parameter. Antony Jameson has found that the rate of convergence can be accelerated by substituting a fast solver over the subsonic flow region between every few cycles of relaxation (ref. 7). Such a procedure has been programmed by Frances Bauer using fast Fourier transform with respect to the periodic variable θ. This reduces the calculation time by a factor of three even when a boundary layer correction is included in the computation. A standard run of her airfoil code now takes less than three minutes on the CDC 6600 computer.

Detailed comparisons with experimental data show that the NCF transonic equation gives significantly better simulation of shock wave-boundary layer interaction than does the FCF equation, especially in cases with a shock at the rear of the profile where the turbulent boundary layer is relatively thick. It would appear that the NCF method leads to less radical gradients in the pressure behind the shock, which is consistent with the observations. The NCF and experimental speeds both tend to jump down barely below the speed of sound behind a shock. Figure 2 shows the kind of agreement between theoretical and test data that is usually seen. Wall effect is accounted for by running the computer code at the same lift coefficient C_L that occurs in the experiment.

Because of erroneous positive terms in the artificial viscosity, the shock jumps defined by the NCF method create mass instead

of conserving it. However, the amount of mass produced is only of the order of magnitude of the square of the shock strength for nearly sonic flow. The resulting errors are therefore negligible except for their effect on the calculation of the wave drag, which has the order of magnitude of the cube of the shock strength. A correct estimate of the drag can be obtained from NCF computations by working with the path-independent momentum integral

$$D = \int [p \; dy + (\phi_x - c_*) d\psi] \; ,$$

where p and c_* stand for the pressure and the critical speed, respectively. The integrand has been arranged so that across a normal shock wave parallel to the y-axis it jumps by an amount of the third order in the shock strength. Therefore integration around the shocks gives a reasonable measure of the wave drag even when mass is not conserved.

The path of integration can be deformed onto the profile to define a standard integral of the pressure there, but a correction term evaluated over a large circle should be added because of a sink at infinity accounting for the mass generated by the NCF method. Let ℓ, ρ_∞ and q_∞ denote the chord length of the airfoil, the density at infinity and the speed at infinity, respectively. The corrected formula for the wave drag coefficient C_{DW} becomes

$$C_{DW} = \frac{2}{\ell \; \rho_\infty q_\infty^2} \int p \; dy - 2 \; \frac{c_* - q_\infty}{\ell \; \rho_\infty q_\infty^2} \int d\psi \; ,$$

where the first integral is extended over the profile and the second integral is extended over a large circle separating the profile from infinity. In Figure 3 a comparison is presented between experimental, corrected NCF, uncorrected NCF and FCF values of the total drag coefficient C_D for a shockless airfoil tested at Reynolds number $R = 20 \times 10^6$ by Jerzy Kacprzinski at the National Aeronautical Establishment in Ottawa. The corrected drag formula is seen to give a fairly reliable assessment of the performance of the airfoil.

There are examples where the results of the NCF code agree well with experimental data right up to the onset of buffet. Shock locations are predicted with remarkable accuracy over a wide range of conditions, although some improvement would be desirable at lower Reynolds numbers where transition becomes important. Thus the analysis code has been adequately validated for simulation of experimental data in two-dimensional flow. In particular, it models the trailing edge in a satisfactory way even for heavily aft-loaded airfoils. It is therefore of some interest that the code predicts no loss of lift for airfoils designed by the hodograph method when a Stratford distribution is used to eliminate separation completely over the whole profile. It would neverthe-less be desirable to confirm this result experimentally by further

testing of shockless airfoils such as the one shown in Figure 1.

There is need for more research on computational methods for transonic flow. The progress in supercritical wing technology should be extended to cascades of airfoils and flows in turbo-machinery. For the immediate future, the most challenging problem is analysis of the flow past wing-body combinations modelling an airplane in three dimensions. As a first step it would seem that the NCF equation for a velocity potential furnishes the most feasible mathematical formulation. Perhaps the Bateman variational principle asserting that the volume integral of the pressure is a stationary functional of the velocity potential, applied in the context of the finite element method, offers the best prospect of deriving convenient difference equations, provided artificial viscosity can be added successfully.

REFERENCES

1. Bauer, F.; Garabedian, P.; Korn, D.; and Jameson, A.: Supercritical Wing Section II. Lecture Notes in Economics and Mathematical Systems, vol. 108, Springer-Verlag, New York, 1975.

2. Nash, J. F.; and Macdonald, A. G. J.: The Calculation of Momentum Thickness in a Turbulent Boundary Layer at Mach Numbers up to Unity. Aeronautical Research Council C.P. No. 963, London, 1967.

3. Stratford, B. S.: The Prediction of Separation of the Turbulent Boundary Layer. J. Fluid Mech., vol. 5, 1959, pp. 1-16.

4. Bauer, F.; Garabedian, P.; and Korn, D.: Supercritical Wing Sections. Lecture Notes in Economics and Mathematical Systems, Vol. 66, Springer-Verlag, New York, 1972.

5. Whitcomb, R. T.: Review of NASA Supercritical Airfoils. Ninth International Congress on Aeronautical Sciences, Haifa, 1974.

6. Murman, E. M.; and Cole, J. D.: Calculation of Plane Steady Transonic Flows. A.I.A.A.J., vol. 9, 1971, pp. 114-121.

7. Jameson, A.: Accelerated Iteration Schemes for Transonic Flow Calculations Using Fast Poisson Solvers. ERDA Research and Development Report COO-3077-82, Courant Institute of Mathematical Sciences, N.Y.U., March 1975.
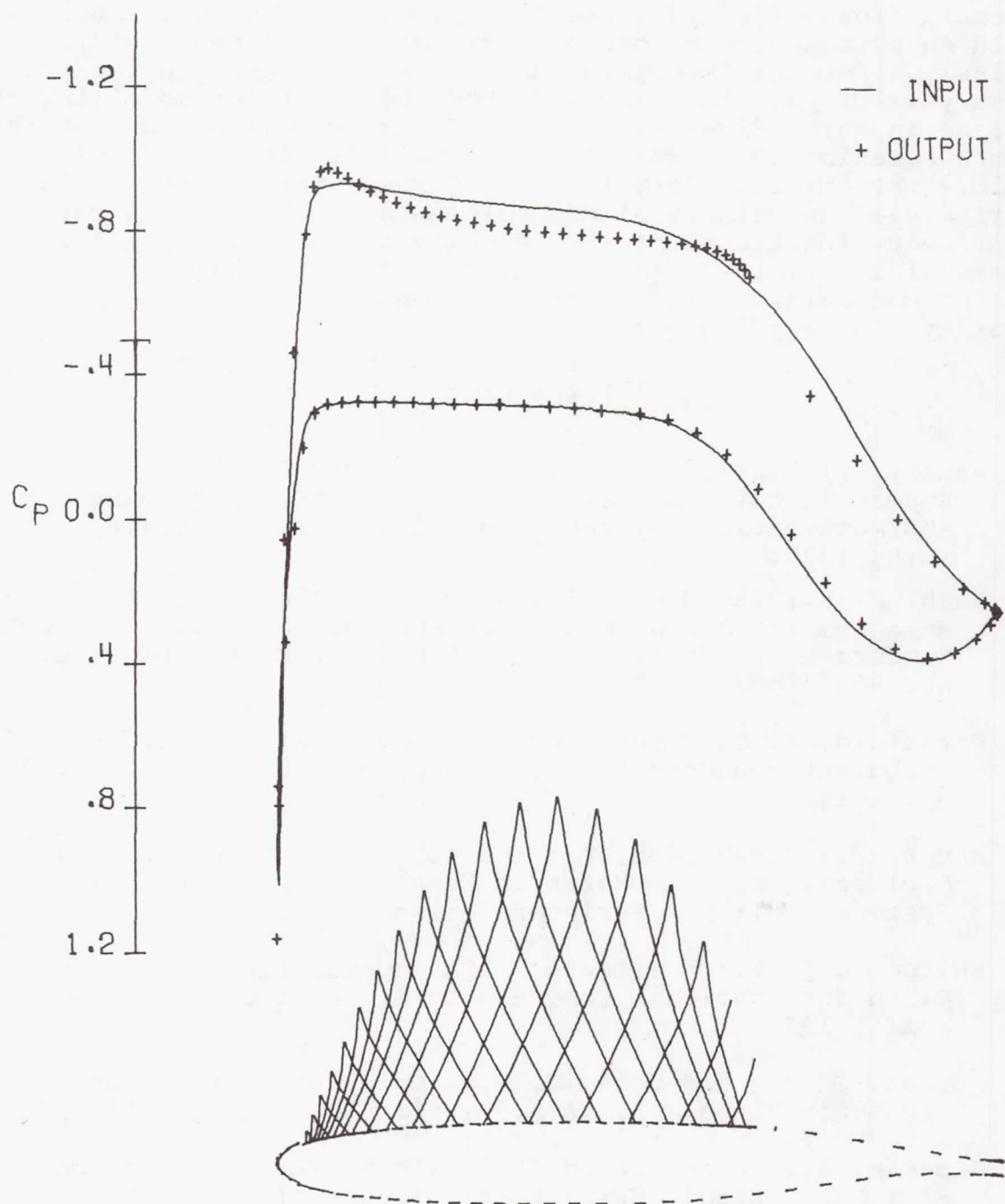
Figure 1.- Modification of Whitcomb wing at M = 0.78, C_L = 0.47.
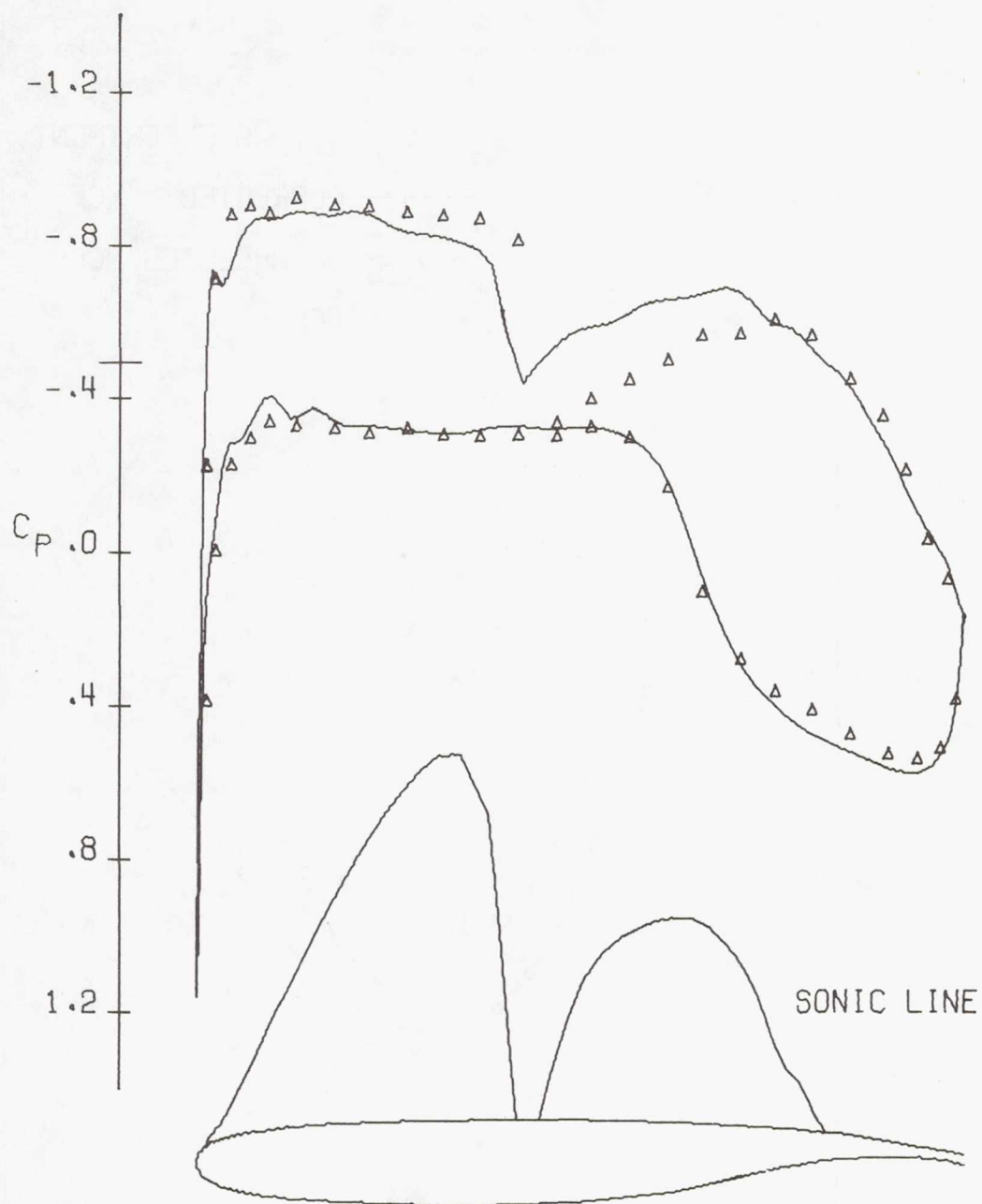
Figure 2.- Whitcomb wing at   M = 0.78, C_L = 0.58.
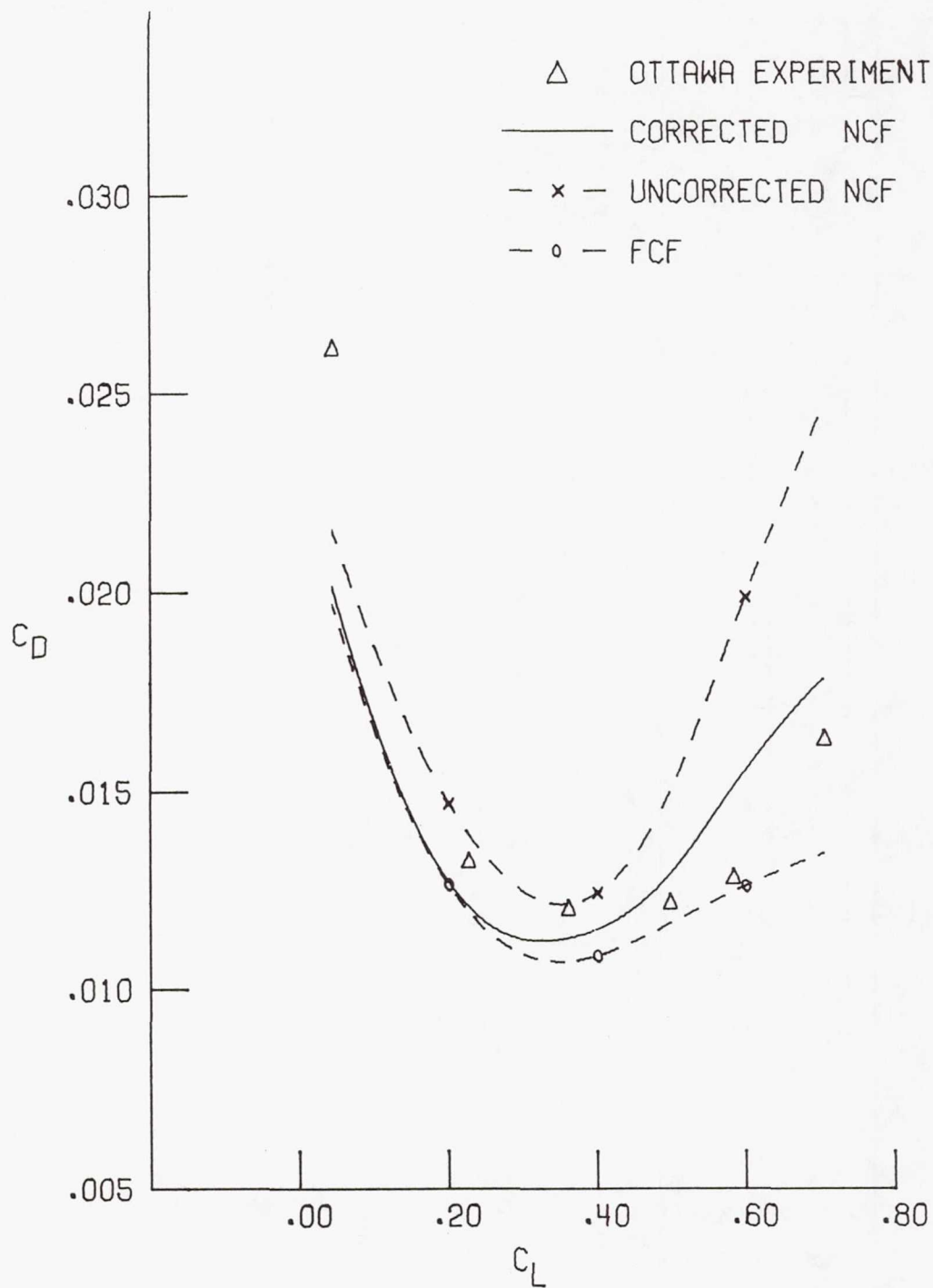
Figure 3.- Drag polar for transonic airfoil at M = 0.76.

THE MULTIGRID METHOD: FAST RELAXATION

FOR TRANSONIC FLOWS*

Jerry C. South, Jr.**
Langley Research Center

Achi Brandt***
Weizmann Institute of Science
Rehovot, Israel

SUMMARY

A multi-level grid method has been studied as a possible means of accelerating convergence in relaxation calculations for transonic flows. The method employs a hierarchy of grids, ranging from very coarse (e.g. 4×2 mesh cells) to fine (e.g. 64×32); the coarser grids are used to diminish the magnitude of the smooth part of the residuals, hopefully with far less total work than would be required with, say, optimal SLOR iterations on the finest grid. To date the method has been applied quite successfully to the solution of the transonic small-disturbance equation for the velocity potential in conservation form. Non-lifting transonic flow past a parabolic-arc airfoil is the example studied, with meshes of both constant and variable step size.

INTRODUCTION

The multi-level grid method, for accelerating convergence in relaxation calculations, has been shown to be very efficient for solving elliptic problems with Dirichlet boundary conditions. For background and historical material, see references 1 to 4. The idea of the method is based on the fact that in many typical elliptic boundary-value problems, the error is composed of a discrete spectrum of wave lengths, which range from the width of the region down to the width of a mesh cell. The short wave-length components of the error are usually diminished quite rapidly in a relaxation calculation, while the long wave-length components diminish very slowly. After only a few iterations the residual will be smooth, since the short wave-length error components have been eliminated; and thus the residual can be represented accurately on a coarser mesh. An equation called the "residual" equation is then solved on the coarser mesh, and the resulting correction is added to the last approximation on the fine mesh, yielding a significant improvement with very little work.

Since relaxation methods are currently the most attractive for obtaining numerical solutions to transonic aerodynamics problems, the question arises as to whether a multi-level, or multi-grid (MG), method can be used in a mixed flow with shock waves. In this paper we report some early results using the MG method to solve a simple transonic problem: we consider the transonic small-disturbance equation for the velocity potential, for nonlifting flow past a parabolic-arc airfoil.

PROBLEM DESCRIPTION

The transonic small-disturbance equation for the velocity potential can be written in conservation form as:

$$p_x + q_y = 0 \tag{1}$$

where

$$p = \left[K - \frac{(\gamma + 1)}{2} M_\infty^2 \phi_x \right] \phi_x \tag{2}$$

$$q = \phi_y \tag{3}$$

$$K = (1 - M_\infty^2)/\tau^{2/3} \tag{4}$$

Equation (1) is to be solved subject to the boundary conditions that the disturbance potential, ϕ, vanishes at infinity and the flow is tangent to the airfoil surface, in the interval $|x| \leq 1/2$; i.e.,

$$\text{at } y = 0, \quad \phi_y = F'(x) \quad \text{for } |x| \leq 1/2$$

$$= 0 \quad \text{for, } |x| > 1/2 \tag{5}$$

where $F(x)$ is the (upper surface) thickness distribution function, τ is the usual thickness ratio, and γ, M_∞, and K are the ratio of specific heats, free-stream Mach number, and transonic similarity parameter, respectively. The form of equations (1) to (5) is a correctly scaled transonic similarity form, in that all quantities are of order 1. Equation (1) is of hyperbolic or elliptic type depending on whether

$$U = K - (\gamma + 1)M_\infty^2 \phi_x \tag{6}$$

is negative or positive, respectively.

Finite-Difference Equations

Murman's conservative difference scheme (ref. 5) can be conveniently presented in terms of Jameson's "switching function" (ref. 6) as follows:

$$\left(1 - \mu_{ij}\right) P_{ij} + \mu_{i-1,j} P_{i-1,j} + Q_{ij} = 0 \tag{7}$$

where

$$P_{ij} = U_{ij}\left(\frac{\phi_{i+1,j} - 2\phi_{ij} + \phi_{i-1,j}}{\Delta x^2}\right) \tag{8}$$

$$U_{ij} = K - (\gamma+1)M_\infty^2\left(\frac{\phi_{i+1,j} - \phi_{i-1,j}}{2\Delta x}\right) \tag{9}$$

$$Q_{ij} = \frac{\phi_{i,j+1} - 2\phi_{ij} + \phi_{i,j-1}}{\Delta y^2} \tag{10}$$

and where

$$\mu_{ij} = 0 \quad \text{if} \quad U_{ij} > 0$$
$$= 1 \quad \text{if} \quad U_{ij} \leq 0 \tag{11}$$

It should be noted here that, in the interest of simplicity, we have presented only the constant-step-size (unstretched grid) form of the difference equations. The actual computer program is written for a stretched grid, with the identity transformation (constant step size) included as a special case.

Vertical Line Relaxation

A vertical line relaxation scheme for solving equation (7) by iteration can be written as:

$$AT_{i,j-1} + BT_{ij} + CT_{i,j+1} = R_{ij} + DT_{i-1,j} + ET_{i-2,j} \tag{12}$$

where

$$T_{ij} = \phi_{ij}^+ - \phi_{ij} \tag{13}$$

ϕ^+ denotes a "new" value of ϕ, obtained during the latest iteration sweep, while ϕ is the value from the previous sweep. R_{ij}, which is the left-hand side of equation (7), is evaluated with "old" values of ϕ_{ij}, as are the iteration coefficients A through E, which are given in the appendix.

Multi-Grid Approach

<u>Residual equation</u>.- Let us introduce a sequence of grids G_1, G_2, ..., G_m, where for simplicity, $h_k = 2h_{k+1}$, and h_k represents the step size of the G_k grid. We can represent the iteration operator (e.g., eq. (12)) on the finest grid G_M as:

$$L_M (\phi_M) = f_M \tag{14}$$

where ϕ_M is the exact discrete solution on the G_M grid. We can write

$$\phi_M = u_M + v_M \tag{15}$$

where u_M is the approximate solution and v_M is the error. Then we have the <u>residual</u> equation:

$$\overline{L}_M (v_M) = f_M - L_M (u_M)$$
$$= - R_M \tag{16}$$

where R_M is the residual of the approximation u_M on the G_M grid. $\overline{L}_M$ is in general different from L_M in the nonlinear case, which complicates matters. Nevertheless, if R_M is smooth, the error will be smooth, and the residual equation (16) can be solved on a coarser grid. Thus, for example, we can write

$$\overline{L}_{M-1} (w_{M-1}) = I_M^{M-1} (R_M) \tag{17}$$

where w_{M-1} is an approximation to the error v_M on the G_{M-1} grid, and I_k^ℓ denotes interpolation from the G_k to G_ℓ. After solving the problem (17) (usually with homogeneous boundary conditions), we interpolate the function w_{M-1} back onto the G_M mesh, and thus form an improved approximation:

$$(u_M)_{new} = (u_M)_{old} + I_{M-1}^M (w_{M-1}) \tag{18}$$

In the complete MG algorithm, the solution of equation (17) is also performed by relaxation; and if the convergence rate falls below a prescribed level, we can apply a similar procedure, backing up to the G_{M-2} grid level, and so on, until we arrive at G_1, if necessary. The G_1 grid is so coarse that a direct solution could be used economically, but we have used iteration here also.

Full approximation.- In the general nonlinear case, the form of the operation $\bar{L}$ can be quite complicated — more so than the original operator, L — and thus applications to, say, the full potential equation may be tedious to program. It turns out that for the transonic small-disturbance equation, the job is simple, and our first program did use the exact expression for $\bar{L}$ in an efficient way. However, there is an equivalent, easier method for solving the residual equation, which we call the full approximation method, as follows:

Suppose we add to both sides of equation (17) the function

$$L_{M-1}(u_M) - f_{M-1} = \tilde{R}_{M-1} \tag{19}$$

Then, since

$$\bar{L}_{M-1}(w_{M-1}) + L_{M-1}(u_M) \simeq L_{M-1}(\phi_M),$$

we have

$$L_{M-1}(\phi_M) \simeq \tilde{R}_{M-1} - I_M^{M-1}(R_M) \tag{20}$$

We can now use the original operator on all the grids, which greatly simplifies the programming. The right-hand side of equation (20) is the difference between the residuals of u_M calculated with the coarse- and fine-grid operators. Note that when the solution converges on the G_M grid, then

$$R_M \rightarrow 0 \tag{21a}$$

$$I_M^{M-1}(R_M) \rightarrow 0 \tag{21b}$$

but $\tilde{R}_{M-1}$ will remain finite, since ϕ_M is a solution on the G_M grid; $\tilde{R}_{M-1}$ is essentially the truncation error of the L_{M-1} operator.

After equation (20) is solved to sufficient accuracy, we determine the function

$$w_{M-1} = \phi_M - I_M^{M-1} (u_M) \tag{22}$$

by subtraction at all points of the grid G_{M-1}, and then interpolate w_{M-1} to the G_M grid as before in equation (18).

RESULTS AND DISCUSSION

In order to estimate the efficiency of the method, a <u>work unit</u> can be defined as the <u>amount of computational effort required for one relaxation sweep on the (finest) G_M grid</u>. Thus a relaxation sweep on the G_k grid costs $n_w = (1/4)^{M-k}$ work units, for example. Likewise, when we calculate the residuals for the G_k grid, we perform these calculations at the points of the G_{k-1} grid, i.e., 1/4 as few points; hence each residual calculation costs less than 1/4 the effort of a relaxation sweep on the G_k grid, or approximately $(1/4)^{M-k+1}$. Note that this is an overestimate, since the tridiagonal system (12) is not inverted, nor do we calculate the iteration coefficients during the residual calculations. On the other hand we did not count the work of interpolation in equation (18), for example, or any other "overhead" of that type.

An overall estimate of efficiency can be given by the effective spectral radius

$$a = \left\{ \left\| R_{M,n_w} \right\| \Big/ \left\| R_{M,1} \right\| \right\}^{1/n_w} \tag{23}$$

where

$$\left\| R_{M,1} \right\| = \text{norm of } R_M \text{ after first sweep on } G_M$$

$$\left\| R_{M,n_w} \right\| = \text{norm of } R_M \text{ after } n_w \text{ work units}$$

and

$$\left\| R_M \right\| = \left(\Delta x \, \Delta y \sum_{ij} R_M^2 \right)^{1/2} \tag{24}$$

Hence the norm we use is the root mean square of the residual on G_M. This number is typically about 5 to 10 times smaller than the maximum norm in transonic problems. We consider an <u>approximate solution to be converged</u> when

$$||R_M|| < C/(\text{no. of grid points}) \tag{25}$$

where the prescribed constant C is typically chosen as 1 so as to estimate the nominal truncation error.

Unstretched Grids

In the case of a grid with constant steps in both directions, the present MG method performed quite well. Some typical results are summarized in table I and discussed briefly in the following.

In all cases, the MG runs were made with a relaxation factor $\omega = 1.0$ on all grids.

<u>Laplace's equation with smooth boundary conditions</u>.- To illustrate just how fast the MG method works for a nice, smooth, elliptic problem, we present in table I results for the solution of Laplace's equation with the prescribed normal derivative equal to $\sin \pi x$ along $y = 0$. Because of the smoothness of the boundary data, it could be expected that interpolating a converged G_4 (32 × 16 grid) solution onto G_5 will give a very good starting approximation for G_5. This is true, for although the convergence rate on G_5 yielded $a = .583$, the efficiency of the two combined levels is more like $a = .46$! In contrast, successive line overrelaxation (SLOR) achieved $a = .924$ on G_5, starting from the zero solution, and using a relaxation factor $\omega = 1.85$.

<u>Nonlinear airfoil flows</u>.- The next three entries in table I show the results for the nonlinear problem of flow over a parabolic-arc airfoil. In these cases, the Neumann boundary condition is an "N-wave" — far from smooth — but the $M_\infty = 0.7$ subcritical case (i.e., no supersonic flow) converged as well as the previous smooth problem; hence, it can be concluded that discontinuous boundary conditions do not deteriorate MG performance. The "combined" mode of operation, where the converged solution for G_4 is used to start G_5, was not helpful, since the truncation errors around boundary singularities and shock waves were so large. That is, the G_4-solution gives a large residual when interpolated on the G_5-mesh. The $M_\infty = 0.85$ (moderately supercritical) case had 124 supersonic points out of a total of 2145 mesh points on G_5, or 6%. The relative efficiency between MG and SLOR is still unaffected. In both of the aforementioned nonlinear cases, the SLOR runs were carried out with $\omega = 1.85$, which was found to be near optimal by experiment.

The last of the unstretched grid cases is $M_\infty = 0.95$ (highly supercritical), with 355 supersonic points. The flow pattern exhibited a weak oblique shock at the trailing edge, followed by a triangular region of nearly constant supersonic flow, which was terminated by a normal shock in the wake. The final number of

supersonic points was established after 38 work units, and the solution converged after 67.6 work units, giving $a = 0.858$. The SLOR run was unstable with $\omega = 1.85$, and had to be "babied" by slowly increasing ω, using an interactive remote terminal. The best result achieved was $n_w = 228$, with $a = .957$.

Stretched Grids

An attractive way to satisfy the boundary condition at infinity is to transform the independent variables such that the infinite space is mapped onto a finite domain. However, it became quickly evident that vertical line relaxation alone is not the best way to relax the solution for a stretched grid, either in the MG mode or simple SLOR. Analysis of the difficulty shows that all the high-frequency error modes are <u>not</u> rapidly damped if the mesh aspect ratio differs significantly from 1.0; the success of the MG method, of course, hinges on this feature. The analysis, not given here, also indicates that a solution to this problem is to sweep in all directions alternately (forward, backward, up, and down).

The last entry in table I shows the results of a stretched-grid case, again for $M_\infty = 0.95$. The deterioration of the MG method is clear; some benefit over SLOR is achieved, however, by the MG method.

CONCLUDING REMARKS

The MG method for accelerating relaxation calculations has proved to be applicable to nonlifting transonic flows with embedded shock waves. The method appears to work from three to five times faster than optimal SLOR on unstretched grids of moderate size (64×32); the relative advantage of MG over SLOR increases as the grid gets finer, since the MG convergence rate is nearly independent of mesh size. It is probable that the gains in three-dimensional calculations would be even more impressive, since each coarser grid requires only 1/8 the work of the next finer grid.

On stretched grids, the present MG approach slows down, being only about twice as fast as SLOR. It is felt that a remedy is the use of alternating-direction relaxation sweeps.

In the future we hope to develop the MG method for flows with lift; for otherwise it will have limited usefulness in aerodynamics.

During the course of our work, Professor Antony Jameson of the Courant Institute of Mathematical Sciences, New York University, also carried out research on the multi-grid method. He showed independently that the "full approximation" approach would work, and some of his attempts at alternating-direction sweeps have been encouraging. Our many discussions have been beneficial.

APPENDIX

ITERATION COEFFICIENTS

We have used various choices for iteration coefficients in equation (12). The coefficients used to make the calculations presented in this paper are simply based on the Newton linearization of equations (7), (8), and (10). They are as follows:

First define: (dropping the j index, since all quantities are evaluated at the same j)

$$b_{i+\frac{1}{2}} = K - (\gamma+1)M_\infty^2 \frac{(\phi_{i+1} - \phi_i)}{\Delta x} \tag{A1}$$

Then we have

$$\bar{U}_i = \frac{1}{2}(b_{i+\frac{1}{2}} + b_{i-\frac{1}{2}}) = U_i \Delta x^{-2} \tag{A2}$$

$$A = C = -\Delta y^{-2} \tag{A3}$$

$$B = 2\Delta y^{-2} + 2(1-\mu_i)\bar{U}_i/\omega - \mu_{i-1} b_{i-\frac{1}{2}} \tag{A4}$$

$$D = (1-\mu_i) b_{i-\frac{1}{2}} - 2\mu_{i-1} \bar{U}_{i-1} \tag{A5}$$

$$E = \mu_{i-1} b_{i-\frac{3}{2}} \tag{A6}$$

where

$$\mu_i = 0 \quad \text{if} \quad U_i > 0$$
$$= 1 \quad \text{if} \quad U_i \leq 0 \tag{A7}$$

REFERENCES

1. Fedorenko, R. P.: A Relaxation Method for Solving Elliptic Difference Equations. USSR Computational Mathematics and Mathematical Physics, vol. 1, 1962, pp. 1092-1096.

2. Fedorenko, R. P.: The Speed of Convergence of One Iterative Process. USSR Computational Mathematics and Mathematical Physics, vol. 4, no. 3, 1964, pp. 227-235.

3. Bakhvalov, N. S.: On the Convergence of a Relaxation Method With Natural Constraints on the Elliptic Operator. USSR Computational Mathematics and Mathematical Physics, vol. 6, no. 5, 1966, pp. 101-135.

4. Brandt, Achi: Multi-Level Adaptive Technique (MLAT) For Fast Numerical Solution to Boundary Value Problems. Proceedings of the Third International Conference on Numerical Methods in Fluid Mechanics, vol. 1, 1972, pp. 82-89.

5. Murman, E. M.: Analysis of Embedded Shock Waves Calculated by Relaxation Methods. Proceedings of AIAA Computational Fluid Dynamics Conference, Palm Springs, California, July 19-20, 1973, pp. 27-40.

6. Jameson, Antony: Transonic Potential Flow Calculations Using Conservation Form. Proceedings AIAA 2nd Computational Fluid Dynamics Conference, Hartford, Connecticut, June 19-20, 1975, pp. 148-161.

TABLE I.- SUMMARY OF MULTI-GRID RESULTS, 64 × 32 CELLS

Problem description		Effective spectral radius[a] for —	
		MG	SLOR
Unstretched grid	Laplace's equation, smooth boundary conditions	0.583 (0.46 combined levels)	0.924
	Parabolic airfoil, $M_\infty = 0.70$	.549	.868
	Parabolic airfoil, $M_\infty = .85$	.593	.855
	Parabolic airfoil, $M_\infty = .95$	.858	.957
Stretched grid	Parabolic airfoil, $M_\infty = 0.95$	0.936	0.974

[a]See equation (23).

Page intentionally left blank

APPLICATION OF FINITE ELEMENT APPROACH TO TRANSONIC FLOW PROBLEMS*

Mohamed M. Hafez, Earll M. Murman, and London C. Wellford**
Flow Research, Inc.

SUMMARY

A variational finite element model for transonic small disturbance calculations is described. Different strategy is adopted in subsonic and supersonic regions, and blending elements are introduced between different regions. In the supersonic region, no upstream effect is allowed. If rectangular elements with linear shape functions are used, the model is similar to Murman's finite difference operators. Higher order shape functions, nonrectangular elements, and discontinuous approximation of shock waves are also discussed.

INTRODUCTION

The plane, steady, inviscid flow past a smooth configuration near sonic speed can be described by a perturbation velocity potential ϕ satisfying the transonic small disturbance equation (TSDE)

$$(K-\phi_x)\phi_{xx} + \phi_{yy} = 0 \tag{1}$$

where K is a similarity parameter. This equation is nonlinear and of mixed hyperbolic-elliptic type. Its weak solution admits discontinuity in the pressure,

$$<K-\phi_x> = -\left(\frac{dx^D}{dy}\right)^2 \tag{2}$$

and

$$\frac{dx^D}{dy} = -\frac{[\![\phi_y]\!]}{[\![\phi_x]\!]} \equiv [\![\phi]\!] = 0 \tag{3) \& (3'}$$

where $< >$ and $[\![\ ]\!]$ signify the average and the jump across the shock $x^D(y)$. The flow field solution is required to determine the pressure distribution on the airfoil (unlike the methods of singularities, or Kernel methods, used for incompressible flow calculations). Recently, finite difference solutions have been obtained with marked success (refs. 1 - 4).

In this paper, the feasibility of applying a finite element approach to transonic flow problems will be studied. A finite element method should handle

---

the same problems that finite differences did, namely, the change of the type of the equation in the domain of interest with a discontinuous solution satisfying prescribed jump conditions. In passing, the potential solution is completely reversible (no entropy changes), and an expansion shock must be excluded (using an artificial viscosity or a shock fitting procedure). Hopefully, complicated boundary conditions will be handled easily in the physical space, and the use of higher order shape functions will be efficient.

FINITE ELEMENTS - BACKGROUND

Elliptic Problems

Consider the classical boundary value problem,

$$L_e(\phi) = K\phi_{xx} + \phi_{yy} = f \text{ on a rectangular } \Omega \tag{4}$$

where ϕ is known on $\partial\Omega$; $K > 0$. The associated functional is

$$I(\phi) = \iint_{\Omega} K\phi_x{}^2 + \phi_y{}^2 + 2f\phi \ dxdy \tag{5}$$

The first variation is set equal to zero

$$\partial I(\phi) = \int_0^1 \int_0^1 (K\phi_{xx} + \phi_{yy} - f) \ \delta\phi \ dxdy = 0 \tag{6}$$

and the second variation is positive definite.

If linear shape functions on triangular elements are used, the algebraic equations for the nodal values are identical to those obtained by applying a centered difference scheme.

A gradient method for solving this problem is

$$\delta\phi = \phi^{n+1} - \phi^n = -\rho \delta I(\phi^n) \tag{7}$$

where n indicates the iteration and the optimum ρ may be obtained in terms of the Residual and the Hessian.

Many nonlinear elliptic problems are solved iteratively by casting them in Poisson's form, where nonlinearity acts as a driving force (incompressible sources) =

$$\delta\phi_{xx} + \delta\phi_{yy} = -\omega R(\phi^n) \tag{8}$$

and where R is the Residual and ω is a relaxation parameter.

Argyris (ref. 5) calculated compressible subsonic flows by the Galerkin method and obtained impressive results within a few iterations. Similar

1372

applications were reported by Gelder (ref. 6), Norrie and DeVries (ref. 7), Periaux (ref. 8), and Chan and Brashears (ref. 9).

Hyperbolic Problems

Finite element methods were also developed for approximate solutions of initial value problems. Both variational and weighted Residual methods were used (see refs. 10 - 16). Most of these investigators used either finite element in space with finite difference in time, a quasi-variational principle, or a convolution bilinear form. A variational formulation for initial value problems is not possible in the classical context of the calculus of variations. Consider the simple linear wave equation

$$L_h(\phi) = K\phi_{xx} + \phi_{yy} = f, \ K < 0 \qquad (9)$$

where $\phi(x = 0)$ and $\phi_x(x = 0)$ are given as initial conditions and x is the time-like coordinate. Application of Hamilton's principle requires knowledge of the conditions at the beginning and end of a time interval and does not apply here. This is difficult because we persist in employing boundary value techniques to solve an initial value problem.

Contrary to the conventional shooting method (an initial value technique), which employs a marching (step-by-step) scheme to solve a boundary value problem, here we will solve the initial value problem by a formal application of Hamilton's principle. The success of the shooting methods depends on the assumption that a variation in the initial slope has a one-to-one correspondence with a variation in the end position; hence, the problem can be solved iteratively. At each iteration, only an initial value problem is solved. For linear problems, iterations may not be needed. The reverse of this process is valid if the same assumption holds, namely, initial value problems can be solved iteratively, with each iteration consisting of a boundary value problem. Again, iterations may not be needed for linear problems.

So, if we assume that the end value $\phi(x = X)$ is known instead of the initial slope $\phi_x(x = 0)$, the associated functional (potential and kinetic energy) would be

$$I(\phi) = \int_0^X \int_0^1 K\phi_x^2 = \phi_y^2 + 2f\phi \ dxdy \qquad (10)$$

which can be discretized and expressed as a sum over finite elements. A basic requirement for application of Hamilton's principle is that we not vary the extreme positions of the physical system. The missing equation (the variation with respect to the end position) is replaced by an equation prescribing the variation with respect to the initial slope (see fig. 1).

Note that the second variation is not positive (stationary but not extremum), and there may be no advantage over weighted Residual methods with a sensible choice of suitable weighting functions. We note also that

arrangement of the elements is not completely arbitrary, and sometimes the element size is restricted by stability requirements. For example, if we use linear shape functions on triangular elements, the algebraic equations for the nodal values are identical to those obtained by explicit centered difference schemes. These requirements arise because a hyperbolic system has characteristics (or preferred directions of propagation) and by just minimizing the energy, we have not taken these features into account. Implicit (unconditionally stable) schemes will be discussed below.

For many nonlinear hyperbolic equations, the following iterative procedure can be used:

$$- \alpha \delta \phi_{xx} + \delta \phi_{yy} = - \omega R(\phi^n) \tag{11}$$

where α is determined to guarantee convergence of iterations (the approximate domain of dependence contains the exact one).

TRANSONIC FLOWS

Consider the functional

$$I(\phi) = \iint \frac{1}{2} (K\phi_x^2 + \phi_y^2) - \frac{1}{6} \phi_x^3 dxdy - \int_{s_1} g\phi \ ds \tag{12}$$

Perturbing ϕ in any direction η (η is an admissible function)

$$I(\phi + \varepsilon\eta) = I(\phi) + \varepsilon \iint (K\phi_x - \frac{1}{2} \phi_x^2)\eta_x + \phi_y \eta_y dxdy - \int_{s_1} g\eta \ ds$$

$$+ \frac{\varepsilon^2}{2} \iint (K - \phi_x)\eta_x^2 + \eta_y^2 \ dxdy + \frac{\varepsilon^3}{6} \iint \eta_x^3 \ dxdy \tag{13}$$

Vanishing of the first variation gives

$$\iint (K\phi_x - \frac{1}{2} \phi_x^2)\eta_x + \phi_y \eta_y dxdy - \int_{s_1} g\eta \ ds = 0 \tag{14}$$

Applying Green's theorem, equation (3) becomes

$$\iint \left[(K\phi_x - \frac{1}{2} \phi_x^2)_x + (\phi_y)_y \right] \eta dxdy - \int_{s_1} (\phi_n - g)\eta \ ds = 0 \tag{15}$$

Note that the second variation is not always positive.

Iterative Procedures

For a nonlinear problem, we need a linearization procedure and a discretization technique. In general, they do not commute.

If we start by discretizing the integral expression, minimization will lead to a nonlinear system of algebraic equations to be solved iteratively (e.g., Newton's method). On the other hand, consider the sequence of functionals

$$I_n(\phi) = \iint (K-\phi_x^{n-1})\phi_x^2 + \phi_y^2 - \int_{s_1} 2g\phi ds \qquad (16)$$

At each iteration, only a linear system of equations will be solved.

Discretization Procedures

The finite element method has been used to solve efficiently subsonic flow problems, with complex geometries employing nonrectangular elements, with a better approximation of the boundary conditions than finite differences. Although the matrix for the nodal values will not have the same regular structure as in finite differences, the number of unknowns is usually less (for higher order elements), and the matrix inversion procedure is different (banded Gaussian Elimination).

For transonic small disturbance theory, the streamlines are almost parallel to the x-axis, and the body boundary condition can be applied at y = 0. Moreover, in the supersonic bubble, x is the time-like coordinate, and the nodes may be located along x = constant lines. Finite differences suit the problem very well. The small disturbance simplifications eliminate the advantages of finite elements. The situation will be different, however, if the full potential equation is considered where the flow direction is unknown and if the exact boundary conditions are applied at the surface of the body.

Nevertheless, we will consider a simple example and use rectangular elements to study the feasibility of using a finite element approach to a mixed type equation. As a matter of fact, efficient finite difference schemes for elliptic and parabolic equations are constructed this way (see refs. 17 - 19).

Semi-Discretization

Let

$$\phi = \sum_{i=1}^{m} X_i(x)\, Y_i(y)$$

where m is the number of strips in the y — direction. The functional I_n becomes

$$I_n(\phi) = \sum_{i=1}^{m} \sum_{j=1}^{m} \left\{ K_{ij} \int_{x_1}^{x_2} X_i X_j \; dx + \int_{x_1}^{x_2} M_{i_j} \frac{dX_i}{dx} \frac{dX_j}{dx} \; dx \right\}$$

where

$$K_{ij} = \int_{0, y=y_F}^{y=y_F} \frac{dY_i}{dy} \frac{dY_j}{dy} \; dy$$

and

$$M_{ij} = \int_{y=0}^{y=y_F} (K - \phi_x^n) \; Y_i Y_j \, dy \equiv \int_{y=0}^{y=y_F} K_\ell Y_i Y_j \, dy \qquad (17)$$

The kinetic and potential energies are

$$T = \frac{1}{2} \sum \sum M_{ij} \frac{dX_i}{dx} \frac{dX_j}{dx} \qquad V = \frac{1}{2} \sum \sum K_{ij} X_i X_j$$

The Euler-Lagrange equation reads

$$\delta \int (T-V) dx = 0 \; \left(\text{i.e.,} \; - (M\dot{X})^{\boldsymbol{\cdot}} + KX = 0 \right) \qquad (18)$$

where M and K are the mass and the stiffness matrices. Or, in the canonical form,

$$M\dot{X} = P \qquad \dot{P} = + KX \qquad (18')$$

where $X_i(x)$ must satisfy the essential boundary conditions. For local hyperbolic regions, the end value $X_i(x = x_2)$ will be replaced by an initial condition, $\frac{dX_i}{dx} (x = x_1)$.

Full-Discretization

Instead of solving a system of ordinary differential equations along lines, we will consider different discretization procedures also in the x-direction.

Finite Element in Space, Finite Difference in Time. - If linear hat functions in y are used, M will be a triadiagonal matrix

$$-\frac{h}{6} K_\ell \begin{bmatrix} 1 & 4 & 1 \end{bmatrix} \quad \text{and} \quad K \; \text{will read} \quad \begin{bmatrix} -1 & 2 & -1 \end{bmatrix} \frac{1}{h}$$

These two matrices will be modified by introduction of the boundary conditions.

In the x-direction, centered differences in the subsonic segment will give star A, as shown in figure 2, while backward differences in the supersonic

1376

segment will give star B. At the parabolic point P, K_ℓ is set equal to zero.
At the shock point S the locally normal shock relation $<K-\phi_x> = 0$ provides
ϕ_x downstream of the shock and is used as a derivative boundary condition for
the rest of the unknowns on the line.

Finite Element in Space and Time. - If linear hat functions in both y
and x are used, both stars A and B will be the same as in figure 3.

Higher Order Shape Functions: Linear Hat Functions in y and Hermite
Cubics in x. - The cubic polynomial on $0 \leq x \leq \Delta x$, which takes on the four
prescribed values ϕ_0, ϕ_{x_0}, ϕ_1, and ϕ_{x_1} , is

$$\{X_i\} = H_{00}, \ H_{10}, \ H_{01}, \ H_{11} \begin{bmatrix} \{ \phi_0 \} \\ \{ \phi_{x_0} \} \\ \{ \phi_1 \} \\ \{ \phi_{x_1} \} \end{bmatrix}$$

with

$$H_{00} = 2\theta^3 - 3\theta^2 + 1$$

$$H_{01} = -2\theta^3 + 3\theta^2$$

$$H_{10} = (\theta^3 - 2\theta^2 = \theta)\Delta x$$

$$H_{11} = (\theta^3 - \theta^2)\Delta x$$

$$(\theta = \frac{x}{\Delta x}) \tag{19}$$

In the subsonic region, the contribution of the neighboring element will be
included through the assembly of the elemental expression into the global
system (see figure 4). In the supersonic region, the stationary value with
respect to $\phi_x(0)$ and $\phi_x(\Delta x)$, assuming $\phi(0)$ and $\phi(\Delta x)$ are known, will give
two algebraic equations that will be used to solve for $\phi(\Delta x)$ and $\phi_x(\Delta x)$
(according to the inverse shooting method described earlier), namely,

$$\int_0^{\Delta x} \begin{Bmatrix} H_{10} \\ H_{11} \end{Bmatrix} \left(\frac{\partial}{\partial x} \left(M \frac{\partial}{\partial x} \right) + K \right) \ \{X\} \ dx = 0 \tag{20}$$

or

$$\begin{bmatrix} A_{11} & A_{12} \\ A_{21} & A_{22} \end{bmatrix} \begin{Bmatrix} \{\phi_1\} \\ \{\phi x_1\} \end{Bmatrix} = - \begin{bmatrix} B_{11} & B_{12} \\ B_{21} & B_{22} \end{bmatrix} \begin{Bmatrix} \{\phi_0\} \\ \{\phi_{x_0}\} \end{Bmatrix} + \begin{Bmatrix} \{f_0\} \\ \{f_1\} \end{Bmatrix} \tag{20'}$$

Note, no upstream effect is allowed in the supersonic region.

Nonrectangular Elements. - All the previous approximates were special
cases of tensor products. To relax this restriction, consider

$$\phi = \sum_i \phi_i N_i(x,y) \tag{21}$$

where N_i are the global shape functions. (For example, the isoparametric element with four nodes, where ϕ, ϕ_x, and ϕ_y are given at each node, curved boundaries are allowed with the restriction that the nodes in the supersonic region lie on x = constant lines.)

Element Equations and Assembly Procedures

For simplicity, consider a bilinear element with four nodes:

$$\phi_e = a + bx + cy + dxy$$

The coefficients a, b, c, and d are given in terms of the four nodal values. (If the elements were rectangular, this case would reduce to the tensor product of linear hat functions in x and y .) If we consider the element equations rather than the nodal equations, the usual finite element assembly procedure in the supersonic region must be modified according to the inverse shooting method, as shown in figure 5.

The transition between the elliptic and hyperbolic parts of the flow is achieved by introducing blending elements between different regions. Two such elements are used: one for the sonic line; one for shock waves.

Sonic Elements

For sonic elements, the average of $(K-\phi_x^n)$ is set to zero. These elements act as a "buffer zone" between subsonic and supersonic elements. We can show that the system matrix will be positive definite if the above assembling strategy is adopted and if the sonic element is included.

Shock Elements

In transonic small disturbance calculations by finite differences, shocks are either captured (using artificial viscosity) or fitted (as a discontinuity). The artificial viscosity term required to smooth out the discontinuity is usually of the same order as the mesh size (because of large, but finite, gradients of the solution in the shock region, even if higher order schemes are used). The same comment holds for finite elements. On the other hand, the discontinuous finite element approximation of shock waves proved to be efficient in nonlinear elasticity (see ref. 20). Here we will describe a finite element analogue for the shock fitting procedure used by Hafez and Cheng (ref. 21).

Consider a shock element, as shown in figure 6. The Rankine-Hugoniot relations under the transonic small disturbance assumptions are given in equations (13) and (14).

The first relation can be derived actually from the weak solution admitted by TSDE, while the second is consistent with the irrotationality condition, which is equivalent to $[\![\phi]\!] = 0$. The equation for the nodal value at i - 1 will not be affected. The equation at i , however, will be different since only the contribution of segment II downstream of the shock will be considered. To the first order of accuracy, knowing ϕ_{i-1} and ϕ_{i-2} ,

we know the condition upstream of the shock. X_D can be determined according to relation (2) and in terms of ϕ_i . The righthand side $(dx/dy)^2$ may be evaluated from a previous iteration as the average of the slope of the shock in the adjacent elements. If this term is neglected, the scheme will reduce to the shock point operator, as discussed earlier. The compatibility relation (3') is satisfied by using linear shape functions in upstream and downstream segments. Thus, (in finite difference calculations) the introduction of shock relations will not make the system matrix singular or disturb the convergence of iterations.

As an alternative approach, instead of altering the nodal equation at the shock point to admit the jump in ϕ_x between i and i-1, according to equation (1), we may use the divergence theorem to obtain an integral relation as a conservation of mass over the element. The element equation will read

$$\iint \nabla \cdot \vec{g} dA = \oint \vec{g} \cdot n ds = 0 \tag{22}$$

$$\vec{g} = \begin{bmatrix} K\phi_x - 1/2 \ \phi_x^2 \\ \\ \phi_y \end{bmatrix}$$

Bilinear shape functions in I thru IV (fig. 6) may be used with a jump in ϕ_x across the shock. Similarly, the irrotationality condition (existence of potential) implies zero vorticity over each element and, by Stokes theorem, zero circulation, namely

$$\iint \nabla \times \vec{V} \cdot n dA = \oint \vec{V} \cdot d\vec{s} = 0 \tag{23}$$

where

$$\vec{V} = \begin{bmatrix} \phi_x \\ \phi_y \end{bmatrix}$$

So, as an alternative approach, relations (2) and (3) are replaced by relations (22) and (23).

REMARKS AND COMMENTS

Mixed Variational Principles

Note that higher order shape functions, namely, Hermite cubics, lead to equations (20) and (20') for ϕ and ϕ_x at the nodes. The resulting algebraic equations can be considered as finite difference approximations of two differential equations: the first is the TSDE (1), and the second is the x-derivative of the TSDE. Instead, the problem can be formulated in terms of two unknown functions ϕ and u , where ϕ is governed by the TSDE and u is governed by a compatability relation $u = \phi_x$. A mixed variational principle (in terms of ϕ and u), together with a dual iterative procedure for TSDE, is studied in a separate paper where the merits and the efficiency of the new

method is assessed.

Weighted Residual Methods

Chan and Brashears (ref. 9) used least squares to solve TSDE. Straight-forward application of the method fails (the solution diverges), so results can be obtained by changing the system matrix. The element matrices are constructed in the usual manner. Before assembling the element matrices into the system matrix, the rows corresponding to the nodes along the upstream side of any element in the supersonic zone are zeroed out; hence, no upstream effect is allowed there. Applying a similar procedure using the Galerkin method and cubic elements in the x-direction gives

$$\int_0^{\Delta x} \left\{ \begin{matrix} H_{01} \\ H_{11} \end{matrix} \right\} \left\{ \frac{\partial}{\partial x} \left(M \frac{\partial}{\partial x} \right) + K \right\} \quad \left\{ X \right\} \ dx = 0 \qquad (24)$$

or

$$\begin{bmatrix} \alpha_{11} & \alpha_{12} \\ \alpha_{21} & \alpha_{22} \end{bmatrix} \begin{bmatrix} \{ \phi_1 \} \\ \{ \phi_{x1} \} \end{bmatrix} = - \begin{bmatrix} \beta_{11} & \beta_{12} \\ \beta_{21} & \beta_{22} \end{bmatrix} \begin{bmatrix} \{ \phi_0 \} \\ \{ \phi_{x0} \} \end{bmatrix} + \begin{bmatrix} \{ f_0 \} \\ \{ f_1 \} \end{bmatrix} \qquad (24')$$

Note that equations (24) and (24') differ from equations (20) and (20') since different weighting functions are used.

Type-Insensitive Methods

In our method, a different strategy is adopted in subsonic and supersonic regions. A unified, type-insensitve method may be simpler, but not efficient, since different requirements in each region must be satisified simultaneously.

To obtain such a procedure, the steady problem is embedded in a higher dimensional space, where the problem is more amenable for analysis. The extra dimension may have a physical meaning, as in the unsteady (time-dependent) method or may be just a mathematical trick, like the use of complex character-istics or any parameter as in the method of parametric differentiation. Also, extra dependent variables may be used, as in the mixed variational principle. The usefulness of these imbedding techniques depends on how fast the limit solution will be obtained. As an example of a unified procedure, consider the TSDE in the form of a system of first order equations,

$$K_\ell u_x = v_y = f \qquad K_\ell = K - u$$

$$u_y - v_x = g$$

or

$$\begin{pmatrix} K_\ell & 0 \\ 0 & -1 \end{pmatrix} \begin{pmatrix} u \\ v \end{pmatrix}_x + \begin{pmatrix} 0 & +1 \\ +1 & 0 \end{pmatrix} \begin{pmatrix} u \\ v \end{pmatrix}_y = \begin{pmatrix} f \\ g \end{pmatrix}$$

For cases where K_ℓ was a linear function of y, Friedrichs (ref. 22) and Chu (ref. 23) found a transformation that put this system into a positive symmetric form. As shown by Lesaint (ref. 24) and reported by Levanthal and Aziz (ref. 25), the finite element method can be applied successfully using this transformation. In general, however, such a transformation may not exist. Nevertheless, if the problem is considered as the asymptotic limit of an un-steady problem, where the vector $\begin{pmatrix} f \\ g \end{pmatrix}$ is replaced by $\begin{pmatrix} \alpha & 0 \\ 0 & \beta \end{pmatrix} \begin{pmatrix} u \\ v \end{pmatrix}_t$, the situation is different. The modified system is symmetric and hyperbolic. Unlike the equilibrium equations, for symmetric hyperbolic equations positivity could always be attained by a simple transformation, as shown by Friedrichs (ref. 22). For such a modified system, no special treatment for subsonic and supersonic regions is needed.

However, based on the finite difference calculations of the Euler equations, where centered differences are used everywhere in space, this "iterative" procedure may be slow. On the other hand, it seems that efficient applications of finite element methods to the full potential equation may require such imbedding techniques (artificial time-dependent and viscosity terms).

CONCLUSIONS

Applications of a finite element approach to transonic flow problems have been discussed. Only small disturbance equations with streamlines almost parallel to the x-axis (hence, the nodes are located along x = constant lines in the supersonic region) have been considered. Currently, computations of a simple numerical example are underway. Extension of this approach to the full potential equation is possible as long as the direction of the flow in the supersonic region is almost known a priori.

REFERENCES

1. Murman, E. M. and Cole, J. D.: AIAA J., vol. 9, 1971, p. 114.

2. Murman, E. M.: Proceedings of AIAA Computational Fluid Dynamics Conference, Palm Springs, July, 1973.

3. Martin, E. D. and Lomax, H.: AIAA Paper No. 74-11, 1974.

4. Jameson, A.: Proceedings of AIAA, Hartford, June, 1975.

5. Argyris, Y. H. and Mareczek, G.: Ingenieur-Archiv, Jan. 1973.

6. Gelder, D.: Int. J. Num. Methods Eng., vol. 3, 1971, p. 35.

7. Norrie, D. H. and DeVries, G.: The Finite Element Method, AP, 1973.

8. Periaux, J.: Int. J. Num. Methods Eng., vol. 9, 1975, p. 775.

9. Chan, S. T. K. and Brashears, M. R.: AFFDL-TR-74-11, Wright-Patterson Air Force Base, Ohio, March, 1974.

10. Zienkiewicz, O. C.: The Finite Element Method in Engineering Science, McGraw-Hill, 1971.

11. Oden, J. T.: Finite Elements of Nonlinear Continua, McGraw Hill, 1972.

12. Strang, G. and Fix, G. J.: An Analysis of the Finite Element Method, Prentice-Hall, 1973.

13. Noble, B.: Proceedings of the Brunel Univ. Conference of the Institute of Mathematics and Its Application, April, 1972.

14. Fried, J.: AIAA J., vol. 7, 1969, p. 1170.

15. Gurtin, M. E.: Archieve Ratl. Mech. Analy., vol. 16, 1964, p. 34.

16. Tonti, E.: Report, Instituts di Meccanica Razionale del Politechnico di Milano, Piazza da Vinci, Milano, Italy, 1971.

17. Swartz, B. and Wendroff, B.: Math. of Computations, vol. 23, no. 105, June, 1969.

18. Marchuk, G. I.: Methods of Numerical Mathematics, Springer-Verlag, 1975.

19. Greenspan, D. and Jain, P.: J. Math. Analysis Appl., vol. 18, 1967, p. 85.

20. Wellford, L. C. and Oden, J. T.: J. of Comp. Physics, vol. 19, no. 2, Oct. 1975, p. 179.

21. Hafez, M. M. and Cheng, H. K.: AIAA Paper No. 75-51, 1975.

22. Friedrichs, K. O.: Comm. Pure Appl. Math., vol. 11, 1958, p. 333.

23. Chu, C. K.: Ph.D. Thesis, New York University, 1959.

24. Lesaint, P.: Numer. Math., vol. 21, 1973, p. 244.

25. Leventhal, S. H. and Aziz, A. K.: Proceedings of Symposium on the Numerical Solution of Partial Differential Equations, Maryland, 1975.
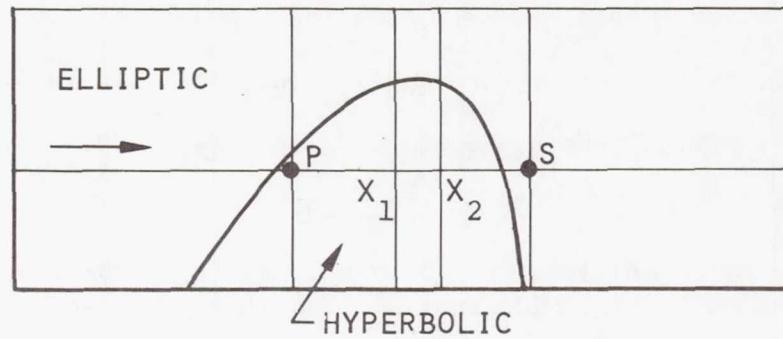
(a) Character of equations.
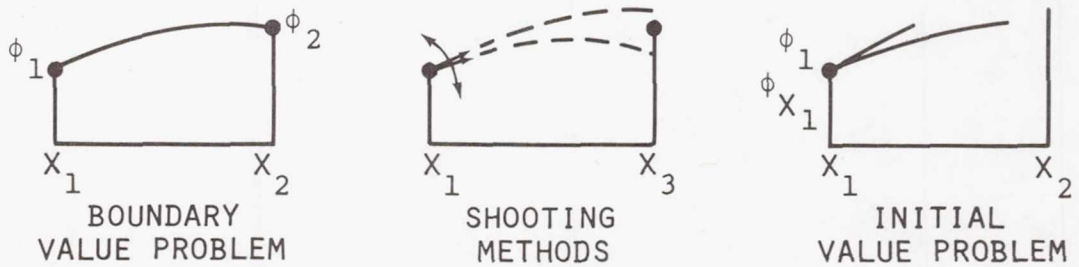
(b) Solution methods.

Figure 1.- Mixed flow problems.

$$\frac{-K_\ell}{6} \times \frac{-6+2K_\ell}{\bullet \ 6} \times \frac{-K_\ell}{6} \qquad\qquad \frac{-K_\ell}{6} \times \qquad \times \frac{2K_\ell}{6} \bullet \frac{-6-K_\ell}{6}$$

$$\frac{-4K_\ell}{6} \times \qquad \underset{\dfrac{12+8K_\ell}{6}}{\bullet} \times \frac{-4K_\ell}{6} \qquad\qquad \frac{-4K_\ell}{6} \times \qquad \times \frac{8K_\ell}{6} \bullet \frac{12-4K_\ell}{6}$$

$$\frac{-K_\ell}{6} \times \underset{\dfrac{-6+2K_\ell}{6}}{\overset{\bullet}{}} \times \frac{-K_\ell}{6} \qquad\qquad \frac{-K_\ell}{6} \times \qquad \times \frac{2K_\ell}{6} \bullet \frac{-6-K_\ell}{6}$$

A   B

SUBSONIC   SUPERSONIC

Figure 2.- Element for calculations using finite element
in space, finite difference in time.

A

$$\frac{-K_\ell -1}{6} \times \frac{2K_\ell -4}{\bullet\,6} \times \frac{-K_\ell -1}{6}$$

$$\frac{-4K_\ell +2}{6} \underset{i-1}{\times} \frac{8K_\ell +8}{\underset{i}{\bullet\,6}} \underset{i+1}{\times} \frac{-4K_\ell +2}{6}$$

$$\frac{-K_\ell -1}{6} \times \frac{-2K_\ell -4}{\bullet\,6} \times \frac{-K_\ell -1}{6}$$

B

$$\frac{-K_\ell -1}{6} \times \frac{2K_\ell -4}{\times\,6} \bullet \frac{-K_\ell -1}{6}$$

$$\frac{-4K_\ell +2}{6} \underset{i-2}{\times} \frac{8K_\ell +8}{\underset{i-1}{\times\,6}} \underset{i}{\bullet} \frac{-4K_\ell +2}{6}$$

$$\frac{-K_\ell -1}{6} \times \frac{-2K_\ell -4}{\times\,6} \bullet \frac{-K_\ell -1}{6}$$

SUBSONIC

SUPERSONIC

Figure 3.- Elements for calculations using finite element in space and time.

SUBSONIC

SUPERSONIC

I   II

$\phi(0)$ $\phi(\Delta x)$ $\phi(2\Delta x)$

$\phi_x(0)$ $\phi_x(\Delta x)$ $\phi_x(2\Delta x)$

I   II

$\phi(0)$ $\phi(\Delta x)$

$\phi_x(0)$ $\phi_x(\Delta x)$
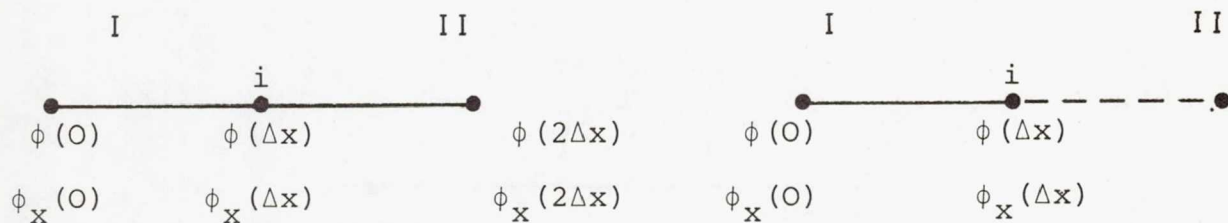
Figure 4.- Finite element calculations using higher order shape functions.

SUPERSONIC   SUBSONIC

$$\frac{K_\ell}{6} - \frac{2}{6}$$

$- \frac{K_\ell}{6} - \frac{1}{6}$

$\frac{2K_\ell + 2}{6}$

$- \frac{2K_\ell}{6} + \frac{1}{6}$
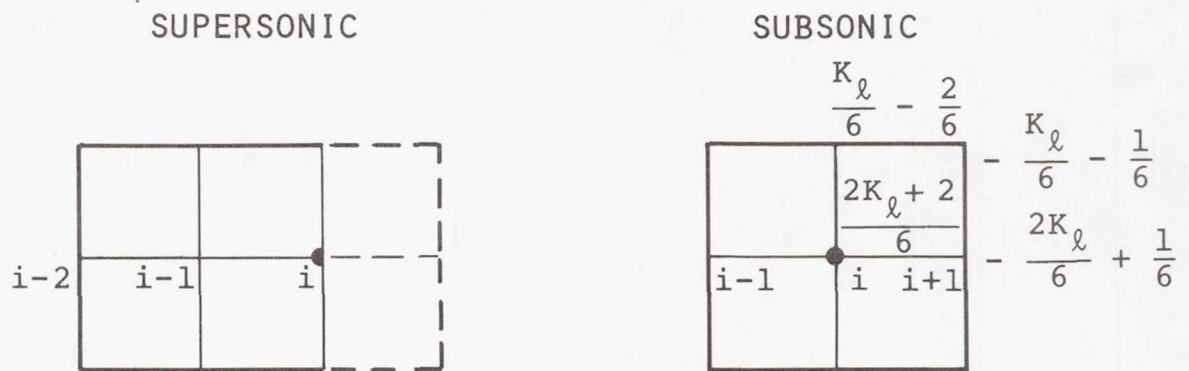
Figure 5.- Finite element assembly modified according to the inverse
shooting method.
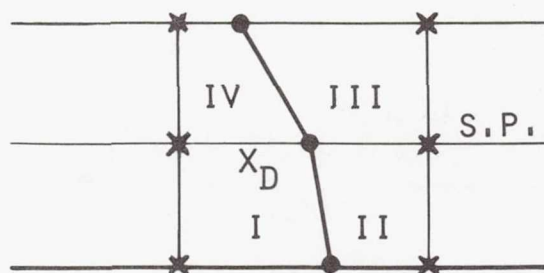
Figure 6.- Shock element in finite element scheme.

INVERSE TRANSONIC AIRFOIL DESIGN

INCLUDING VISCOUS INTERACTION*

Leland A. Carlson
Texas A&M University

SUMMARY

A numerical technique has been developed for the analysis of specified transonic airfoils or for the design of airfoils having a prescribed pressure distribution, including the effect of weak viscous interaction. The method uses the full potential equation, a stretched Cartesian coordinate system, and the Nash-Macdonald turbulent boundary layer method. Comparisons with experimental data for typical transonic airfoils show excellent agreement. An example shows the application of the method to design a thick aft-cambered airfoil, and the effects of viscous interaction on its performance are discussed.

INTRODUCTION

A numerical method for the design or analysis of transonic airfoils should not only be accurate but also should be as simple as possible in concept and approach. It should use coordinate systems, input variables, and boundary condition treatments that can be easily understood by the user. Finally, it should be able to handle both shocked and shockless flows and be suitable not only for complete design but also for airfoil modification.

One approach to this problem is the inverse method in which the airfoil surface pressure is specified and the airfoil shape subsequently determined. Admittedly, this approach requires knowledge of what would be a desirable pressure distribution, but this characteristic is probably understood by the designer as well as any other. Furthermore, the designer can select a pressure distribution that will approximate a desired lift and moment, have a reasonable supersonic zone, yield desirable boundary layer properties, and satisfy other transonic flow criteria.

The purpose of this paper is to present results obtained with a numerical method that is suitable for the analysis, design, or modification of subsonic and transonic airfoils. The method is similar to that of references 1-3, but it has been modified to include the effects of weak viscous interaction.

SYMBOLS

C_D drag coefficient

C_L lift coefficient

C_M pitching moment coefficient

C_p pressure coefficient

c   chord

M_∞ free stream Mach number

RN   Reynolds number

w   weighting factor

α angle of attack

δ^* boundary layer displacement thickness

PROBLEM FORMULATION

To solve the inviscid part of the flowfield, the method uses the exact equation for the perturbation potential in Cartesian coordinates. In order to avoid at supersonic points difficulties associated with nonalignment of the coordinates and the flowfield, a rotated finite difference scheme (ref. 4) is used in the solution; and in the actual program the infinite physical plane is mapped to a rectangular computational box. The resulting transformed finite difference equations are solved iteratively by column relaxation sweeping from upstream to downstream.

In the design mode, the shape of the nose region (typically 6-10% chord) is specified and a pressure distribution is prescribed over the remainder of the airfoil. Thus, the appropriate airfoil boundary condition in the direct region near the leading edge is the surface tangency requirement and in the inverse region, where the pressure is specified, it is essentially the specification of the derivative of the perturbation potential in the x-direction. In order to satisfy these at the airfoil boundary, which in general will not coincide with the Cartesian grid points, the derivatives in the boundary conditions are expanded as two term Taylor series about dummy points inside the airfoil. The derivatives in these series are then written in finite difference form using second order formulas for all first derivatives and at least first order ones for higher derivatives. In the direct region, central differences are used for x-derivatives and forward (on the upper surface) for the y-derivatives. However, to prevent numerical instability, the inverse region uses a second order backward difference formula for the first term of the Taylor series representing the x-derivative.

In the inverse case the airfoil must also be computed by integrating the surface tangency condition for the ordinates, y, as a function of x, with the initial conditions given by the slope and surface ordinate at the interface between the direct and inverse regions. In the present method, the latter are known because the nose region is solved directly, and the integration is accomplished using the Runge-Kutta method of order four.

It is believed, based on comparison with other results (ref. 3), that this method is an accurate and numerically consistent approach to the design and

1388

analysis of transonic airfoils in inviscid flow. For further details concerning
the finite difference, boundary condition, formulations, etc., see references
1 and 2.

BOUNDARY LAYER ANALYSIS

Experimental evidence (ref. 5-6) indicates that viscous boundary layer
effects are very important in transonic flow. For example, the difference be-
tween the actual airfoil surface and the effective surface, i.e. the displace-
ment surface, can cause an airfoil inviscidly designed to have a lift coef-
ficient of 0.6 to actually develop 25%-50% less lift. To prevent such discrep-
ancies, the effect of the boundary layer displacement thickness, δ^*, should be
included in both the analysis and design portions of any numerical method.

In the present approach, the basic idea in the design case is to treat the
airfoil determined by the inverse method as the displacement surface and to
subtract from it the displacement thickness determined by a boundary layer com-
putation. The result should be the actual airfoil ordinates. For the analysis
case, the approach is to calculate a boundary layer displacement thickness and
to use it to correct the location of the displacement surface (i.e. airfoil or-
dinate plus δ^*). The inviscid flowfield is then solved as before (ref. 1),
where at present the displacement surface is updated every ten relaxation cycles.

Obviously the boundary layer scheme must be efficient, reliable, and
accurate. Thus, three integral methods were considered for inclusion in the
present numerical method—Walz Method II (ref. 7), the Nash-Macdonald method
with smoothing (ref. 8-9), and Green's lag-entrainment method (ref. 10).
Figure 1 compares for a typical transonic case the upper surface displacement
thickness predictions from these methods with those obtained by Bavitz
(ref. 11), who used the Bradshaw scheme (ref. 12) modified with a trailing edge
correction. (The Walz results are not plotted but are between the Bradshaw and
Nash-Macdonald data.) Notice that the predictions are essentially identical
over most of the airfoil, and all but Green's method predict separation near
the trailing edge. Apparently Green's method needs some type of trailing edge
correction. Since the Walz and Green methods numerically fail at separation
due to their empirical equations and since the Nash-Macdonald approach is 3-6
times faster, it was selected for incorporation into the present transonic air-
foil design-analysis program.

ANALYSIS RESULTS

To start the direct problem the airfoil shape is inputed and a cubic
spline fit and used to determine the ordinates and slopes in the computational
plane. Next, to get some reasonable perturbation potentials, fifty relaxation
cycles are performed on a very coarse grid (typically 13 x 7). Then the grid
spacing is halved to a coarse grid (25 x 13) and fifty more cycles computed.
At that point δ^* is computed and the displacement surface ordinates updated
using under relaxation, i.e. $\delta^*_{new} = \delta^*_{old} + w(\delta^* - \delta^*_{old})$. The slopes are then
determined from cubic splines through the new ordinates. The ordinates are
updated every ten cycles thereafter. Typically, 400 cycles are performed on
the coarse grid before halving to the medium grid (49 x 25), where 200-250
cycles are carried out. While this grid yields 66 points on the airfoil, the

grid may be, if desired, halved again (to 97 x 49) to obtain 130 points on the airfoil. Compared to inviscid cases, convergence on the fine grid is slow, and 400 relaxation cycles may be required. Fortunately, in many cases accurate results can be obtained on the medium grid. However, if double shocks exist, the fine grid may be needed to resolve them accurately. Convergence is determined by monitoring the changes in perturbation potential and δ^*.

Typical total computation times on an Amdahl 470/V6 are one minute for medium grid results and less than 4 minutes for fine grid data (about 10 minutes on a CDC 6600). Convergence is usually faster on CDC type machines due to the increase in significant digits.

As shown on figure 2, the present method can be used to demonstrate the effects of viscous interaction on a Korn 75-06-12 airfoil (ref. 9) near its design point. While the primary effect of the boundary layer is a 25% decrease in lift from the inviscid design value due to the pressure change on the upper surface, the lower surface pressure distribution is also affected. In addition, notice the excellent agreement between the viscous theory predictions and NAE wind tunnel data (ref. 6).

Another comparison with experimental data is shown on figure 3, again for the Korn airfoil but at an off-design condition. Although the minimum peak pressure and shock jump are slightly in error, which is not surprising since the method uses nonconservative finite differences, the overall agreement is excellent. Other results are shown in Table I, which compares data obtained with the present theory with experimental values at about the same lift. Many of these were obtained using the medium grid results only, and it is believed that they indicate that the present viscous analysis method is adequate for engineering studies of lift, drag, and moment variation. This is particularly true when the large discrepencies between viscous and inviscid results and the small differences between viscous results and experiments are considered.

DESIGN RESULTS

The computational procedure used in the inverse case is the same as described in references 2 and 3 except that δ^* is subtracted from the displacement surface. The final design is usually obtained on the medium grid after 250 relaxation cycles, although strong aft-cambered cases may require 400. At present there are some minor difficulties, due to the use of backward differences on the pressure boundary condition, in obtaining a desired pressure distribution near the trailing edge; and thus, the possibility of using the fine grid in design is under study. At present, a typical inverse run takes about 70 seconds (Amdahl 470/V6). It should be noted that in obtaining the actual airfoil ordinates a transition point must be selected, and the final shape is somewhat sensitive to this choice.

The importance of including the boundary layer in the design process is shown on figure 4. The shockless pressure distribution (solid line) used for this typical inverse design yielded for this Mach 0.72 case a 16% thick, highly aft-loaded airfoil. If the displacement surface ordinates were to be used to fabricate the airfoil instead of the correct values (i.e. if the boundary layer were ignored), the actual pressure distribution would be as shown by the

symbols. This result, which was obtained using the present viscous analysis method, shows a lift and moment 20% less than the design values.

On the other hand, when δ^* is included in determining the ordinates and the resultant airfoil is analyzed with viscous effects included, the agreement is much better. The medium grid results for this case are shown on figure 5. Here, transition is assumed to occur just aft of the minimum peak pressure; and the δ^* computed for the design pressure distribution differs by less than 0.013% from the δ^* determined in the analysis calculation. Nevertheless, as can be seen on figure 5, there is still a slight difference in the pressure distributions. However, considering the accuracy of boundary layer computations, sensitivity to transition location, and the large difference between viscous and inviscid results, the agreement is quite good. In addition, it indicates acceptable numerical consistency between the present analysis and design techniques.

CONCLUSION

Based upon experimental comparisons, it is believed that the present viscous analysis method is suitable for obtaining engineering estimates of the characteristics of transonic airfoils. In addition, while the inverse design method has not been verified, it has been shown to be numerically consistent with the analysis results at the medium grid level. Efforts to extend the design procedure to a fine grid are in progress and will be reported later.

REFERENCES

1. Carlson, L.A.: Transonic Airfoil Flowfield Analysis Using Cartesian Coordinates. NASA CR-2577, August 1975.
2. Carlson, L.A.: Transonic Airfoil Design Using Cartesian Coordinates. NASA CR-2578, April 1976.
3. Carlson, L.A.: Transonic Airfoil Analysis and Design Using Cartesian Coordinates. Proc. AIAA 2nd Computational Fluid Dynamics Conference, June 19-20, 1975, pp. 175-183.
4. South, J.Jr.; and Jameson, A.: Relaxation Solutions for Inviscid Axi-symmetric Transonic Flow over Blunt or Pointed Bodies. Proc. AIAA Computational Fluid Dynamics Conference, July 1973, pp. 8-17.
5. Melnik, R.E.; and Ives, D.C.: On Viscous and Wind-Tunnel Wall Effects in Transonic Flows over Airfoils. AIAA Paper 73-660, July 1973.
6. Kacprzynski, J.J.: An Experimental Analysis and Buffet Investigation of the Shockless Lifting Airfoil No. 1. LR-569(NRC No. 13673), Nat. Res. Council Canada (Ottawa), August 1973.
7. Walz, A.: Boundary Layers of Flow and Temperature. MIT Press, Cambridge, Mass., 1969.
8. Nash, J.F.; and Macdonald, A.G.J.: The Calculation of Momentum Thickness in a Turbulent Boundary Layer at Mach Numbers up to Unity. Aero. Res. Council, C.P. No. 963, 1967.
9. Bauer, R., Garabedian, P., Korn, D.; and Jameson, A.: Supercritical Wing Sections II. Springer-Verlag, New York, 1975.
10. Green, J.E., Weeks, D.J.; and Brooman, J.W.F.: Prediction of Turbulent Boundary Layers and Wakes in Compressible Flow by a Lag-Entrainment Method. RAE Tech. Report TR-72231, January 1973.

11. Bavitz, P.C.: An Analysis Method for Two-Dimensional Transonic Viscous
        Flow. NASA TN D-7718, January 1975.
12. Bradshaw, P.; and Ferriss, D.H.: Calculation of Boundary Layer Develop-
        ment Using the Turbulent Energy Equation: Compressible Flow on
        Adiabatic Walls. Journal Fluid Mech., Vol. 46, pt. 1, March 1971.

Table I.- COMPARISON WITH EXPERIMENT

	M_∞	C_D Theory	Expt	C_D Theory	Expt	C_D Theory	Expt
1	.622	.48	.49	-.105	-.104	.0070	.0070
2	.699	.667	.667	-.107	-.106	.0108	.0107
3	.75	-.097	-.093	-.111	-.114	.0209	.0146
4	.75	.104	.100	-.118	-.126	.0086	.0092
5	.75	.454	.458	-.120	-.121	.0086	.0090
6	.75	.516	.515	-.122	-.121	.0089	.0086
7	.75	.523	.523	-.119	-.120	.0092	.0094
8	.75	.539	.535	-.122	-.120	.0095	.0088
9	.75	.601	.597	-.119	-.122	.0110	.0081
10	.75	.711	.712	-.130	-.125	.0151	.0125
11	.15	.475	.47	-.099	-.105	.0085	.009

Note: Cases 1-11, 75-06-12 at RN=21 x 10^6, Case 11 GA(W)-2 at 6 x 10^6
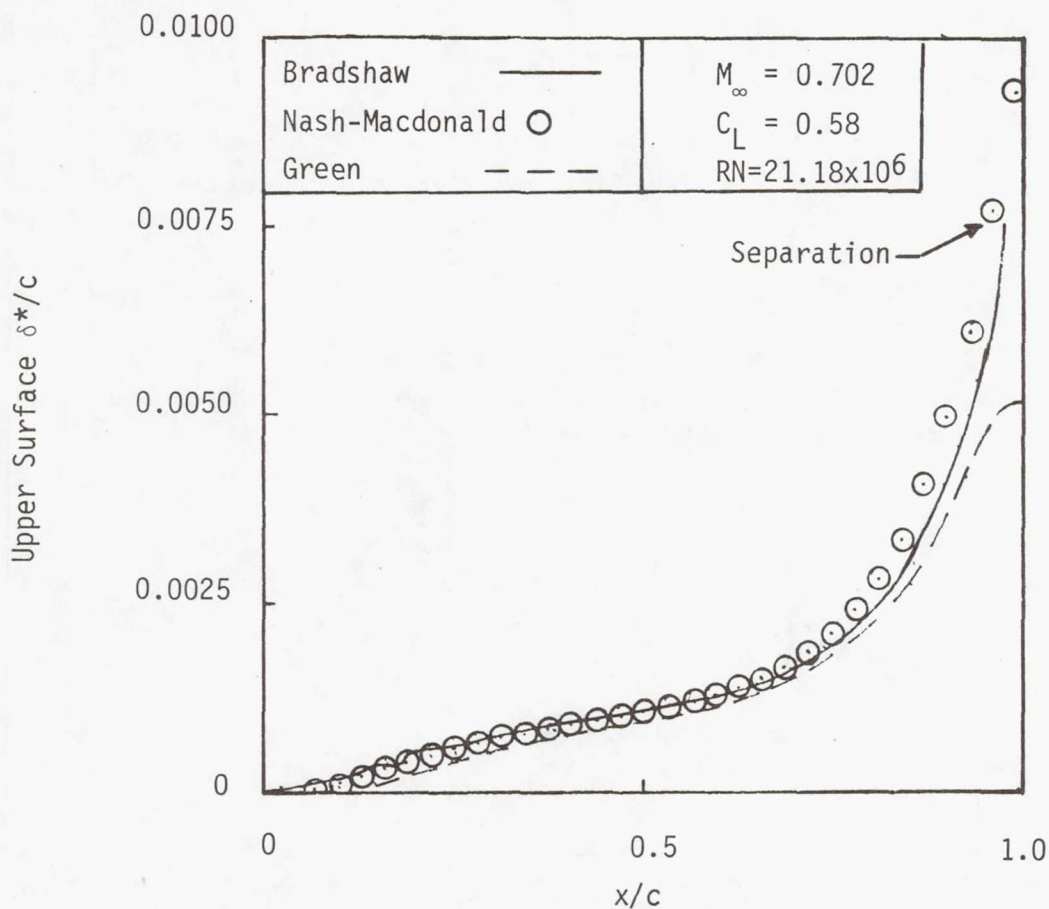
Figure 1.- Comparison of boundary layer results for
Korn airfoil 75-06-12.

	Inviscid	Viscous	Expt.	
C_L	0.609	0.454	0.458	$M_\infty=0.75$
C_D	0.0074	0.0086	0.0090	$\alpha=0^\circ$
C_M	-0.148	-0.120	-0.121	

INVISCID

$RN = 20.95 \times 10^6$

INVISCID

x/c
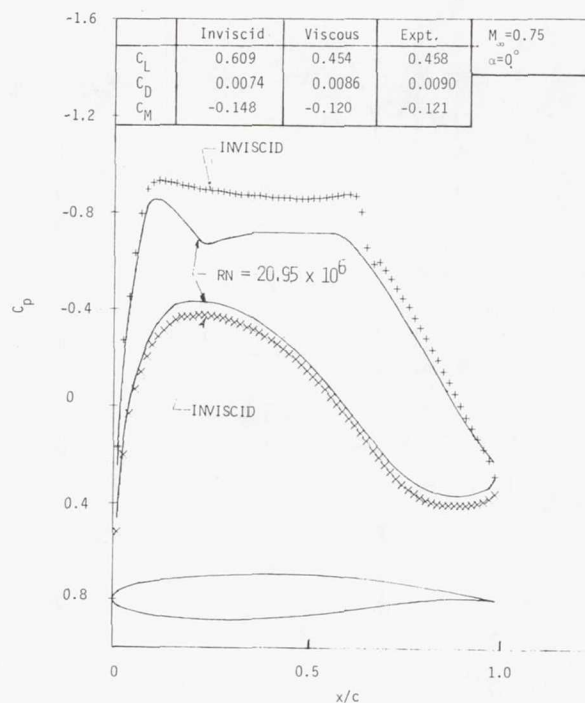
Figure 2.- The effect of viscous interaction
of the Korn airfoil 75-06-12.

$M_\infty=0.699$
$RN=21.14 \times 10^6$

	Symbol	C_L	C_D	C_M
Theory	——	0.667	0.0108	-0.107
NAE	□ ○	0.667	0.0107	-0.1056

x/c
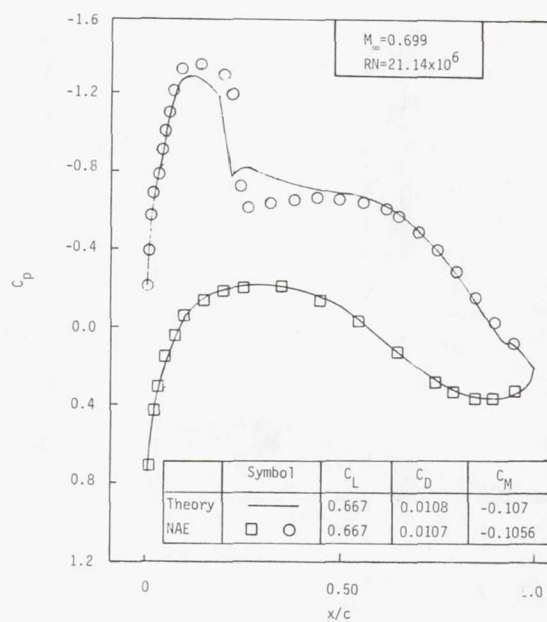
Figure 3.- Comparison of NAE data with
present results.
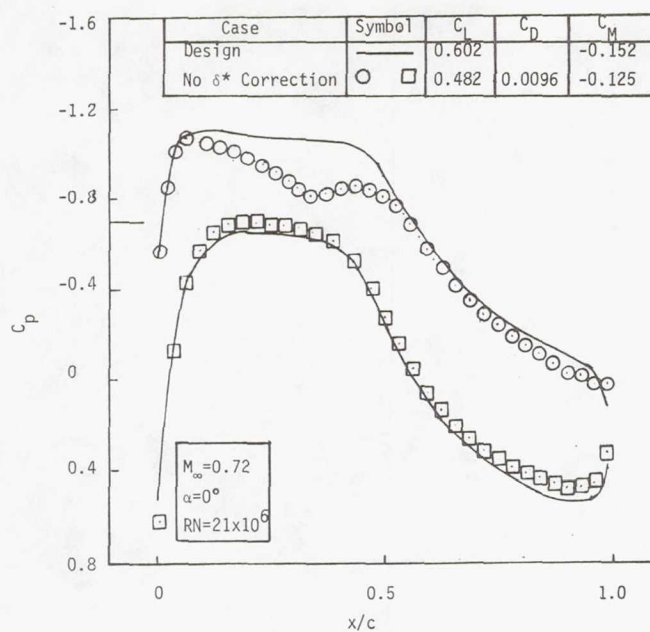
Figure 4.- Comparison of design predictions with results for airfoil
fabricated without boundary layer correction.
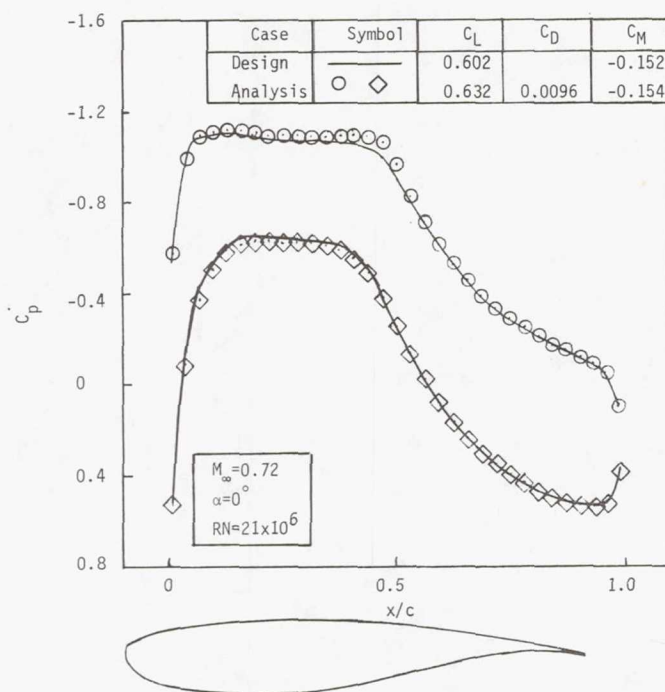
Figure 5.- Comparison of design predictions with
viscous analysis results.

Page intentionally left blank

NUMERICAL SOLUTIONS FOR LAMINAR AND TURBULENT VISCOUS FLOW OVER SINGLE AND MULTI-ELEMENT AIRFOILS USING BODY-FITTED COORDINATE SYSTEMS*

Joe F. Thompson, Z. U. A. Warsi, and B. B. Amlicke
Mississippi State University

SUMMARY

The technique of body-fitted coordinate systems, whereby curvilinear coordinate systems having coordinate lines coincident with all boundaries are generated numerically as solutions of an elliptic partial differential system, is applied in numerical solutions of the complete time-dependent compressible and incompressible Navier-Stokes equations for laminar flow and to the time-dependent mean turbulent equations closed by modified Kolmogorov hypotheses for turbulent flow. Coordinate lines are automatically concentrated near to the bodies at higher Reynolds number so that accurate resolution of the large gradients near the solid boundaries is achieved. Two-dimensional bodies of arbitrary shapes are treated, the body contour(s) being simply input to the program. The complication of the body shape is thus removed from the problem.

INTRODUCTION

The use of numerically generated boundary-fitted coordinate systems has made possible the development of numerical solutions of the Navier-Stokes equations that can treat bodies of arbitrary shapes as easily as simple bodies. Codes can be written that are independent of the body or boundary shape, which may even be changing with time.

These solutions are based on a method of automatic numerical generation of a general curvilinear coordinate system with coordinate lines coincident with all boundaries of a general multi-connected region containing any number of arbitrary shaped bodies (ref. 1). The curvilinear coordinates are generated as the solution of two elliptic partial differential equations with Dirichlet boundary conditions, one coordinate being specified to be constant on each of the boundaries, and a distribution of the other being specified along the boundaries. Regardless of the shape, number, or movement of the bodies and regardless of spacing of the curvilinear coordinate lines, all numerical computations, both to generate the coordinate system and to subsequently solve the Navier-Stokes equations or any other partial differential equations on the coordinate system, are done on a rectangular grid with a square mesh, (i.e., in the transformed plane). The physical coordinate system has been, in effect, eliminated from the problem, at the expense of adding two elliptic equations to

the original system. Since the curvilinear coordinate system has coordinate lines coincident with the surface contours of all bodies present, all boundary conditions may be expressed at grid points, and normal derivatives on the bodies may be represented using only finite differences between grid points on coordinate lines, without need of any interpolation even though the coordinate system is not orthogonal at the boundary. Numerical solutions for the lifting and non-lifting potential flow about Kármán-Trefftz airfoils using this coordinate system generation show excellent agreement with the analytic solutions (refs. 1 and 2).

This method of automatic body-fitted curvilinear coordinate generation has been used to construct finite-difference solutions of the full time-dependent Navier-Stokes solutions for unsteady viscous flow about arbitrary two-dimensional airfoils (refs. 2,3,4, and 5) and submerged and partially submerged hydrofoils (refs. 4 and 5).

A method of controlling the spacing of the coordinate lines encircling the body has been developed in order to treat higher Reynolds number flow, since the coordinate lines must concentrate near the surface to a greater degree as the Reynolds number increases. The solution shows excellent comparison with the Blasius boundary layer solution for the flow past a semi-infinite plate (refs. 6 and 7). Solutions are also being developed for compressible viscous transonic flow with both subsonic and supersonic free streams, and for compressible turbulent flow.

BOUNDARY-FITTED COORDINATE SYSTEMS

The basic approach of constructing body-fitted curvilinear coordinate systems in general multi-connected regions as the solution of an elliptic boundary value problem has been discussed in previous publications (refs. 1,3 and 8), and reference to related work by others has been made therein. A detailed report of the technique and code is now available (ref. 8), together with the code, a user's manual, and instructions with illustrations of its application to the numerical solution of partial differential equations.

Certain considerations must be taken into account in the choice of a suitable elliptic generating system for the coordinates as discussed in references 3 and 8. The system chosen in the present work allows considerable control of the coordinate line spacing as is illustrated in reference 8. Control of the spacing of the coordinate lines on the body is easily accomplished, since the points on the body are input to the program. The spacing of the coordinate lines in the field, however, must be controlled by varying the elliptic generating system for the coordinates. One method of variation is to add inhomogeneous terms to the right sides of the Laplace equation, so that the generating system becomes

$$\xi_{xx} + \xi_{yy} = P(\xi,\eta) \ , \ \eta_{xx} + \eta_{yy} = Q(\xi,\eta) \tag{1}$$

Since it is desired to perform all numerical computations in the uniform rectangular transformed plane, the dependent and independent variables must be interchanged in eq. (1). This results in the coupled system (see ref. 8 for

the transformation relations).

$$\alpha x_{\xi\xi} - 2\beta x_{\xi\eta} + \gamma x_{\eta\eta} = - J^2 [x_\xi P(\xi,\eta) + x_\eta Q(\xi,\eta)] \qquad (2a)$$

$$\alpha y_{\xi\xi} - 2\beta y_{\xi\eta} + \gamma y_{\eta\eta} = - J^2 [y_\xi P(\xi,\eta) + y_\eta Q(\xi,\eta)] \qquad (2b)$$

where

$$\alpha = x_\eta^2 + y_\eta^2 \qquad \beta = x_\xi x_\eta + y_\xi y_\eta \qquad \gamma = x_\xi^2 + y_\xi^2 \qquad J = x_\xi y_\eta - x_\eta y_\xi$$

The inhomogeneous functions $P(\xi,\eta)$ and $Q(\xi,\eta)$ allow coordinate lines to be attracted to specified lines and/or points in the field or on the boundaries as discussed in detail in reference 8. It is necessary to give some consideration to the rapidity with which the spacing varies else truncation error effects in the form of numerical diffusion, possibly negative, may be introduced. All derivatives in equation (2) are approximated by second-order central finite difference expressions. The resulting difference equations are given in reference 8. The set of nonlinear simultaneous difference equations is solved by point SOR iteration.

In the present application to the Navier-Stokes equations, all diffussive space derivatives in the transformed equations are represented by second-order, central difference expressions. Both second-order central and second-order upwind differences have been investigated for convective derivatives. Derivatives off a boundary are represented by backward difference expressions being solved simultaneously by point SOR iteration at each time step.

LAMINAR FLOW ABOUT MULTIPLE AIRFOILS

With the velocity and pressure as the dependent variables the transformed Navier-Stokes equations are (ref. 8)

$$u_t + [y_\eta (u^2)_\xi - y_\xi (u^2)_\eta]/J + [x_\xi (uv)_\eta - x_\eta (uv)_\xi]/J$$

$$+ (y_\eta p_\xi - y_\xi p_\eta)/J = (\alpha u_{\xi\xi} - 2\beta u_{\xi\eta} + \gamma u_{\eta\eta})/RJ_2$$

$$+ (Qu_\eta + Pu_\xi)/R \qquad (3)$$

$$v_t + [y_\eta (uv)_\xi - y_\xi (uv)_\eta]/J + [x_\xi (v^2)_\eta - x_\eta (v^2)_\xi]/J$$

$$+ (x_\xi p_\eta - x_\eta p_\xi)/J = (\alpha v_{\xi\xi} - 2\beta v_{\xi\eta} + \gamma v_{\eta\eta})/RJ_2$$

$$+ (Qv_\eta + Pv_\xi)/R \qquad (4)$$

$$\alpha p_{\xi\xi} - 2\beta p_{\xi\eta} + \gamma p_{\eta\eta} + (Qp_\eta + Pp_\xi)J_2 = - (y_\eta u_\xi - y_\xi u_\eta)^2$$

$$- 2(x_\xi u_\eta - x_\eta u_\xi)(y_\eta v_\xi - y_\xi v_\eta) - (x_\xi v_\eta - x_\eta v_\xi) - J^2 D_t \qquad (5)$$

1399

where R is the Reynolds number

and

$$D_t \equiv (y_\eta u_\xi - y_\xi u_\eta + x_\xi v_\eta - x_\eta v_\xi)/J \qquad (6)$$

Equation (5) is the transformed Poisson equation for the pressure, obtained by taking the divergence of the Navier-Stokes equations.

The boundary conditions are

$$u = v = 0 \text{ on body surface} \qquad (7a)$$

$$u = \cos\theta, \ v = \sin\theta, \ p = 0 \text{ on remote boundary} \qquad (7b)$$

The pressure at each point on the body was adjusted at each iteration by an amount proportional to the velocity divergence evaluated using second-order one-sided differences for the η-derivative on the body.

The body force components are obtained from the integration of the pressure and shear forces around the body surface:

$$F_x = + \oint py_\xi \ d\xi - \frac{2}{R} \oint \omega x_\xi \ d\xi \qquad (8a)$$

$$F_y = - \oint px_\xi \ d\xi - \frac{2}{R} \oint \omega y_\xi \ d\xi \qquad (8b)$$

and the lift and drag coefficients are given by

$$C_L = F_y \cos\theta - F_x \sin\theta \qquad (9a)$$

$$C_D = F_y \sin\theta + F_x \cos\theta \qquad (9b)$$

where θ is the angle of attack.

In the velocity-pressure formulation it is necessary to calculate the body vorticity before applying equation (8) from

$$\omega = - \frac{1}{J}(y_\xi v_\eta + x_\xi u_\eta) \qquad (10)$$

Figure 1a shows the coordinate system for a multiple airfoil consisting of two Kármán-Trefftz airfoils, one simulating a separated flap. Coordinate system control was used to attract the coordinate lines strongly to the first ten lines around the bodies and to the intersections of the cut between the bodies with the trailing edge of the forebody and the leading edge of the aftbody. Velocity vectors for the viscous flow at R = 1000 are shown in figures 1b - e. Included in these plots are detail views of the slot between the airfoils, the trailing edge of the aft airfoil, and the separated region about the aft airfoil.

Results have recently been obtained by Hodge at Flight Dynamics Laboratory, Wright-Patterson Airforce Base, (ref. 5), for a single NACA 0018 airfoil at R = 41,400 which compare very well with experimental drag values.

TURBULENT SHEAR FLOW AROUND A CIRCULAR CYLINDER

The aim of the following analysis is to select a turbulence model for the computation of mean turbulent flow fields around two-dimensional bodies of arbi-

trary shapes in the body-fitted coordinate systems. As a test case the coordinate system for a circular cylinder was generated over which the model equations of mean turbulent flow were solved.

As is well known, the mean turbulent flow equations and the moment equations of the desired order can be obtained from the non-steady three-dimensional Navier-Stokes equations. The specification of the unknown correlations forms the closure problem. This line of approach for closing the system of equations was initiated by Chou (ref. 9) and Rotta (ref. 10). Since then much work has been done on the closure problem (see refs. 11 and 12).

A philosophically different approach was initiated by Kolmogorov (ref. 13) in which the turbulent transport equations were written down heuristically to model the physics rather than to model the unknown correlations resulting from the averaged Navier-Stokes equations. A set of equations similar to those of Kolmogorov were proposed by Saffman (refs. 14 and 15). The prediction capabilities of the Kolmogorov's equations have not been investigated at all, while Saffman himself has used his equations only in the cases of plane Couette flow, plane Poiseuille flow, and the two-dimensional jet and wake.

The turbulence model chosen in this paper to describe the two-dimensional mean turbulent flow around finite bodies is comprised of the energy transport equation of Kolmogorov's model and the vorticity-density transport equation of the Saffman model. Both models have been described by Saffman (ref. 15).

Using Cartesian tensor rotation and the summation convention the equations of continuity and momentum for an incompressible flow are

$$\frac{\partial U_j}{\partial x_j} = 0 \tag{11}$$

$$\frac{\partial U_i}{\partial t_1} + U_j \frac{\partial U_i}{\partial x_j} = -\frac{1}{\rho} \frac{\partial p}{\partial x_i} + \nu \nabla_1^2 U_i - \frac{\partial}{\partial x_j} (\overline{u_i u_j}) \tag{12}$$

where t_1 is the physical time, ρ the density, ν the kinematic viscosity, U_i the Cartesian components of the mean velocity vector and u_i the fluctuating components. An overbar denotes the average.

To close the system of equations (11) and (12), the eddy viscosity formulation due to Boussinesq is used

$$\overline{u_i u_j} = \frac{2}{3} \overline{e} \delta_{ij} - 2\nu_T S_{ij} \tag{13}$$

where

δ_{ij} is the Kronecker delta

$$S_{ij} = \frac{1}{2}(\frac{\partial U_i}{\partial x_j} + \frac{\partial U_j}{\partial x_i})$$

$$\overline{e} = \frac{1}{2} \overline{u_i u_i} , \text{ the mean turbulence energy}$$

$$\nu_T = \text{kinematic eddy viscosity}$$

The Kolmogorov-Saffman model now depends in specifying ν_T as

$$\nu_T = \frac{\alpha_o^2 \overline{e}}{\theta} \tag{14}$$

where α_o is a constant and θ is the square root of the turbulence vorticity-density defined as

$$\theta = (\overline{\phi})^{1/2} = (\frac{1}{2}\overline{\omega_i \omega_i})^{1/2}$$

ω_i being the vorticity fluctuations. The quantities $\overline{e}$ and $\overline{\phi}$ are to be determined from their own transport equations which are

$$\frac{\partial \overline{e}}{\partial t_1} + U_j \frac{\partial \overline{e}}{\partial x_j} = \nu \nabla_1^2 \overline{e} + \nu_T \overline{Q} - \overline{e}\theta + \frac{\partial}{\partial x_j}(\frac{\nu_T}{2}\frac{\partial \overline{e}}{\partial x_j}) \tag{15}$$

$$\frac{\partial \overline{\phi}}{\partial t_1} + U_j \frac{\partial \overline{\phi}}{\partial x_j} = \nu \nabla_1^2 \overline{\phi} + \overline{P}\,\overline{\phi} - b(\overline{\phi})^{3/2} + \frac{\partial}{\partial x_j}(\frac{\nu_T}{2}\frac{\partial \overline{\phi}}{\partial x_j}) \tag{16}$$

where

$$\overline{P} = \frac{\alpha_o}{2}[(\frac{\partial U_i}{\partial x_j})^2]^{1/2}, \quad \alpha_o, \text{ b constants}$$

$$\overline{Q} = 2(S_{ij})^2$$

$$\nabla_1^2 = \frac{\partial^2}{\partial x_j \partial x_j}$$

The boundary conditions for equations (11), (12), (15), and (16) are
at the wall:

$$U_i = 0, \quad \overline{e} = 0, \quad \overline{\phi} = \frac{\alpha_o^2 \, S^2 u_*^4}{\nu^2} \tag{17}$$

at infinity:

$$U_i = U_{\infty i}, \quad \overline{e} = o \text{ or } \overline{e}_\infty, \quad \overline{\phi} = 0$$

where u_* is the friction velocity and S a non-dimensional constant having the value of about 8000 and $\alpha_o = 0.3$, b=5/3.

The required equations to predict the mean turbulent flow in two dimensions are equations (11)-(16). For the numerical computation the vorticity-stream function formulation is adopted in which

$$U_1 = \frac{\partial \overline{\psi}}{\partial x_2}, \quad U_2 = -\frac{\partial \overline{\psi}}{\partial x_1},$$

so that in place of (11) and (12) the equations are

$$\nabla_1^2 \overline{\psi} = -\overline{\omega} \tag{18}$$

and

$$\frac{\partial \overline{\omega}}{\partial t_1} + U_j \frac{\partial \overline{\omega}}{\partial x_j} = \nu \nabla_1^2 \overline{\omega} + \frac{\partial^2}{\partial x_1 \partial x_2}\overline{(u_1^2 - u_2^2)} + (\frac{\partial^2}{\partial x_2^2} - \frac{\partial^2}{\partial x_1^2})\overline{(u_1 u_2)} \tag{19}$$

The pertinent equations are now non-dimensionalized as follows

$$E = \bar{e}/V^2, \quad \omega = L\bar{\omega}/V, \quad \chi = L^2\bar{\phi}/V^2K^2,$$

$$T = \nu_T/2VL, \quad \psi = \bar{\psi}/VL, \quad t = Vt_1/L, \quad P = L\bar{P}/V,$$

$$Q = L^2\bar{Q}/V^2, \quad R = VL/\nu, \quad x = x_1/L, \quad y = x_2/L;$$

$$u = U_1/V, \quad v = U_2/V, \quad \nabla^2 = \frac{\partial^2}{\partial x^2} + \frac{\partial^2}{\partial y^2} \tag{20}$$

where V and L are the characteristic velocity and length respectively.

In the expression for χ the function K is assumed to be a non-dimensional function of the friction velocity $u_{\text{❋}}$. This function has been introduced to absorb the variation of $\bar{\phi}$ at the surface as indicated in equation (17) so as to make χ = a constant at the wall. Now at the wall

$$\chi = \alpha_o^2 S^2 R^2 U_{\text{❋}}^4/K^2$$

where $U_{\text{❋}} = \frac{u_{\text{❋}}}{V}$, so that the choice $\chi = 1$ at the wall gives

$$K = \alpha_o SR\, U_{\text{❋}}^2 \tag{21}$$

From the analysis of Saffman (ref. 15) the value of S for smooth walls is about 8000. Since R is the free stream Reynolds number the numerical values of K are quite large. Neglecting the gradients of K in the χ equation, the non-dimensional equations for numerical computation are

$$\nabla^2\psi = -\omega \tag{22}$$

$$\lambda_t + \psi_y\lambda_x - \psi_x\lambda_y = \frac{1}{H}\nabla^2\lambda + M(T_x\lambda_x + T_y\lambda_y) + A\lambda + B \tag{23}$$

where

$$H = \frac{R}{1+CR\,T}$$

$$T = \frac{\alpha_o^2\, E}{2K\chi^{1/2}} \tag{24}$$

and the variable subscripts denote partial differentiations. The values of A, B, M and C depend on the choice of the surrogate variable λ which are described below.

$$\lambda = \omega: \quad A = 2\nabla^2 T, \quad B = 4(T_{xx}u_y - T_{yy}v_x + 2T_{xy}v_y),$$

$$M = 4, \quad C = 2. \tag{25}$$

$$\lambda = E: \quad A = -K\chi^{1/2} \quad B = 2TQ, \quad M = 1, \quad C = 1 \tag{26}$$

$$\lambda = \chi: \quad A = P - bK\chi^{1/2}, \quad B = 0, \quad M = 1, \quad C = 1 \tag{27}$$

The boundary conditions are

at the body surface: $\psi=0$, $\psi_y=0$, $\chi=1$, $E=0$,

at infinity: $\omega \to 0$, $\chi \to 0$, $E \to 0$. \hfill (28)

Equations (22) and (23) have been transformed to the body-fitted coordinates and subjected to the finite difference approximations similar to that used in the laminar calculation. Velocity vector plots and the energy distribution for a circular cylinder at $R = 5\times10^5$ are shown in figures 2a and 2b. In figure 2b

$$\ell nr = .0576\eta(1.2)^{\eta-40}, \quad r = \text{non-dimensional radial distance}.$$

REFERENCES

1. Thompson, J.F.; Thames, F.C.; and Mastin, C.W.: Automatic Numerical Genera-
    tion of Body-Fitted Curvilinear Coordinate System for Field Containing
    Any Number of Arbitrary Two-Dimensional Bodies. J. Comp. Phy., Vol. 15,
    1974, pp. 299-319.

2. Thames, F.C.; Thompson, J.F.; and Mastin, C.W.: Numerical Solution of the
    Navier-Stokes Equations for Arbitrary Two-Dimensional Airfoils. Proc. of
    NASA Conf. on Aerodynamic Analyses Requiring Advanced Computers, Langley
    Research Center. NASA SP-347, 1975.

3. Thames, F.C.: Numerical Solution of the Incompressible Navier-Stokes Equa-
    tions About Arbitrary Two-Dimensional Bodies. Ph.D. Dissertation, Missis-
    sippi State Univ., 1974.

4. Thompson, J.F.; Thames, F.C.; Mastin, C.W.; and Shanks, S.P.: Use of Numer-
    ically Generated Body-Fitted Coordinate Systems for Solution of the
    Navier-Stokes Equations. Proc. AIAA 2nd Computational Fluid Dynamics Conf.,
    Hartford, Connecticut, 1974.

5. Thompson, J.F.; Thames, F.C.; Hodge, J.K.; Shanks, S.P.; Reddy, R.N.; and
    Mastin, C.W.: Solutions of the Navier-Stokes Equations in Various Flow
    Regimes or Fields Containing Any Number of Arbitrary Bodies Using Bound-
    ary-Fitted Coordinate Systems. Vth International Conference on Numerical
    Methods in Fluid Dynamics, 1976. (To be published in Lecture Notes In
    Physics, Springer-Verlag.)

6. Walker, R.L.: Numerical Solution of the Navier-Stokes Equations for Incom-
    pressible Viscous Laminar Flow Past a Semi-Infinite Flat Plate. M.S.
    Thesis, Mississippi State Univ., 1974.

7. Thompson, J.F.; Thames, F.C.; Walker, R.L.; and Shanks, S.P.: Numerical
    Solutions of the Unsteady Navier-Stokes Equations for Arbitrary Bodies
    Using Boundary-Fitted Curvilinear Coordinates. Proc. of Arizona/AFOSR
    Symposium on Unsteady Aerodynamics, Univ. of Arizona, 1975.

8. Thompson, J.F.; Thames, F.C.; and Mastin, C.W.: Boundary-Fitted Curvilinear
    Coordinate Systems for Solution of Partial Differential Equations on
    Fields Containing Any Number of Arbitrary Two-Dimensional Bodies. NASA
    CR-2729, 1976.

9. Chou, P.Y.: On Velocity Correlation and the Solution of the Equations of
    Turbulent Fluctuations. Quart. Appl. Math., Vol. 3, 1945, pp. 198-209.

10. Rotta, J.C.: Statistische Theorie Nichthomogener Turbulenz. Z. Physik,
    Vol. 129, 1951, pp. 547-572.

11. Mellor, G.L.; and Herring, H.J.: A Survey of the Mean Turbulent Field Closure Models. AIAA J., Vol. 11, No. 5, 1973, pp. 590-599.

12. Launder, B.E.; Reece, G.J.; and Rodi, W.: Progress in the Development of a Reynolds-Stress Turbulence Closure. J. Fluid Mech., Vol. 68, Part 3, 1975, pp. 537-566.

13. Kolmogorov, A.N.: Equations of Turbulent Motion of an Incompressible Liquid. IZV. Akad. Nauk SSR, Seria Fizichiska, Vol. 6, 1942, p. 56.

14. Saffman, P.G.: A Model for Inhomogeneous Turbulent Flow. Proc. Roy. Soc. A, Vol. 317, 1970, pp. 417-433.

15. Saffman, P.G.: Model Equations for Turbulent Shear Flow. Studies in Appl. Math., Vol. 53, 1974, pp. 17-34.
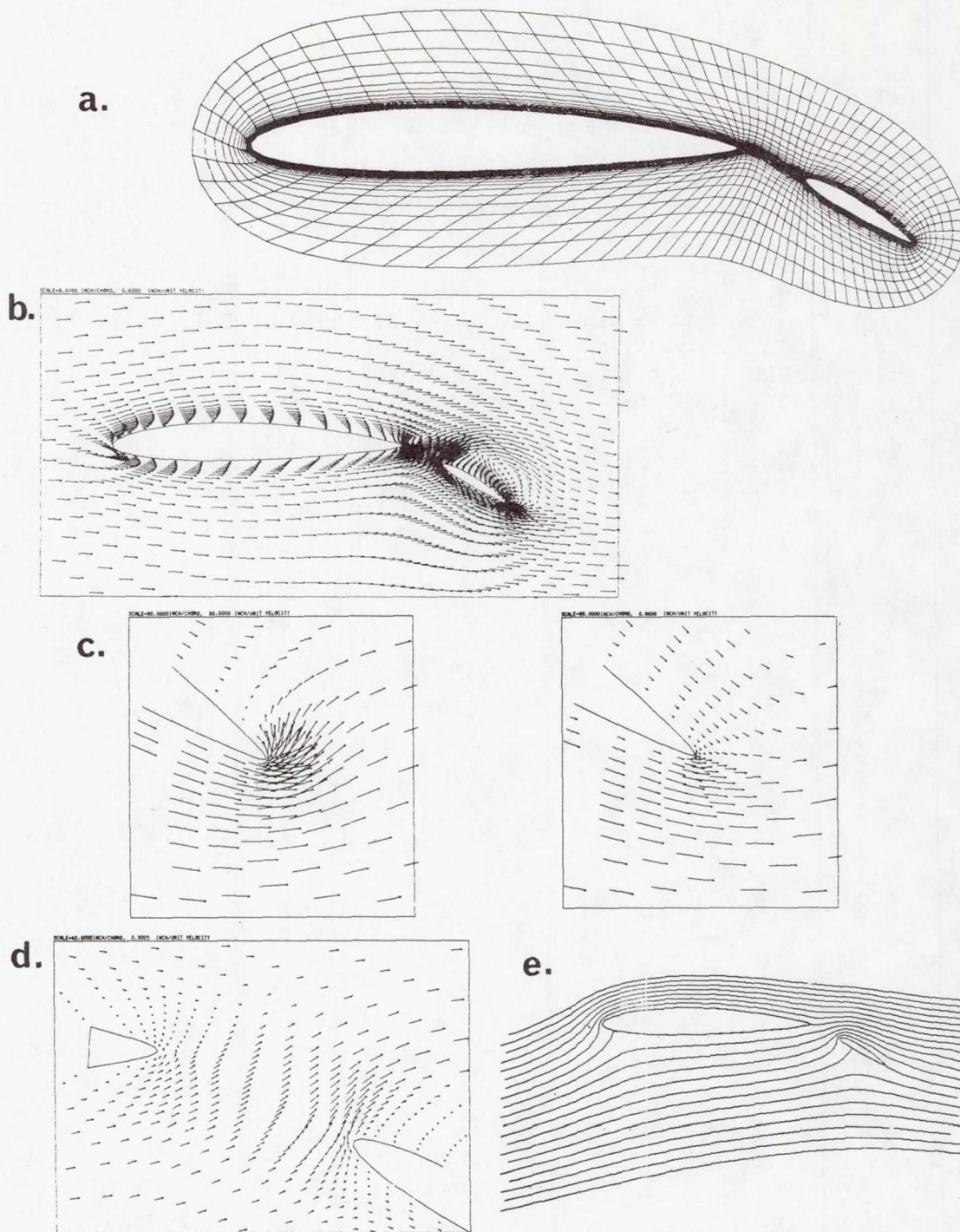
Figure 1. Multiple Airfoil (R = 1000, t = 1.2): (a) coordinate system, (b) velocity vectors (c) aft trailing edge, (d) slot detail, (e) potential
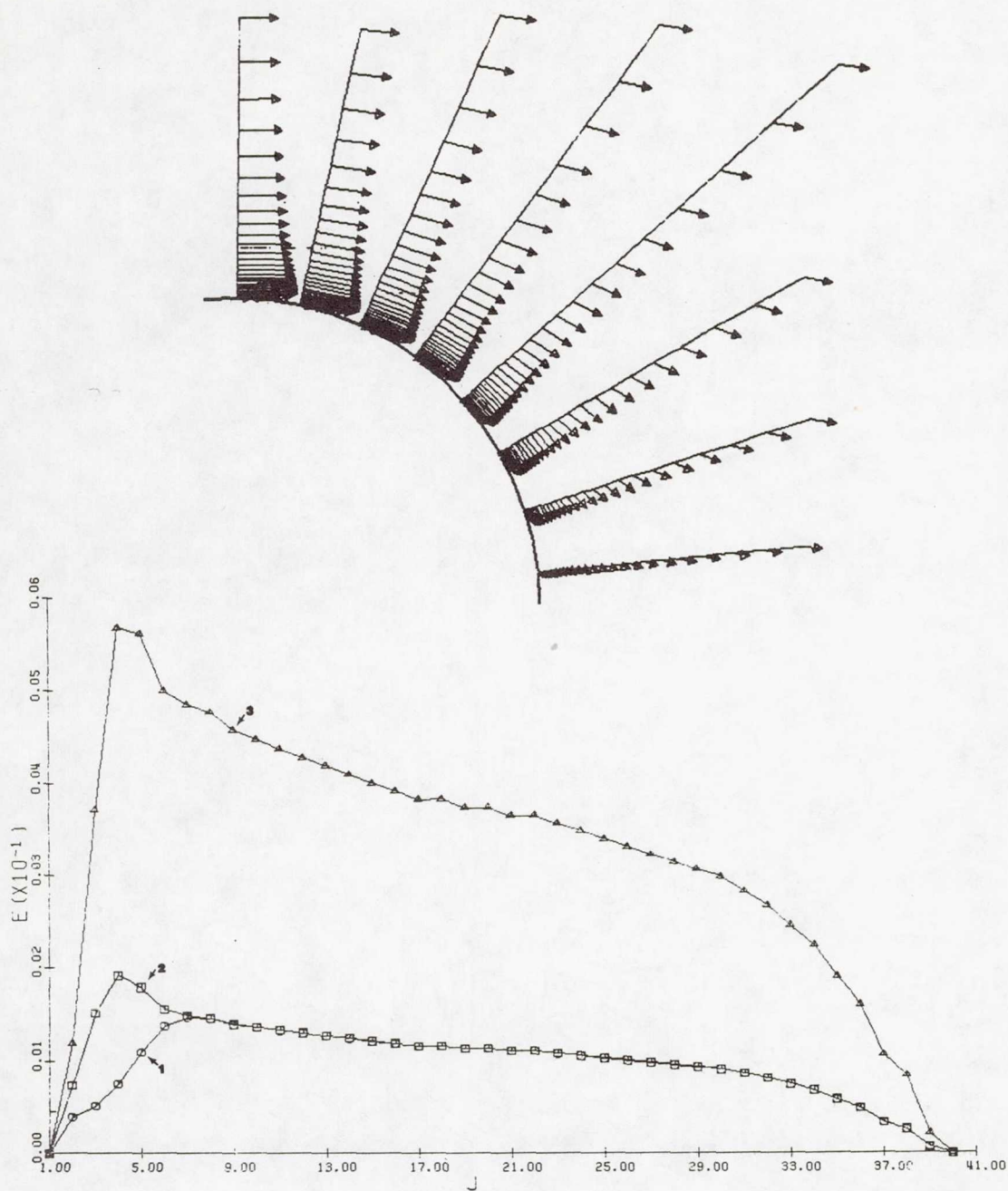
Figure 2.   Turbulent flow past a circular cylinder (R = 500,000,
t = 0.29; transition introduced at t = 0.12):(a)velocity vectors
from 90° to the aft stagnation point, (b) turbulence energy
distribution (1. front stagnation, 2. aft stagnation, 3. 90°)

Page intentionally left blank

THREE-DIMENSIONAL BOUNDARY LAYERS

APPROACHING SEPARATION

James C. Williams, III
Department of Mechanical and Aerospace Engineering
North Carolina State University

SUMMARY

The theory of semi-similar solutions of the laminar boundary layer equations is applied to several flows in which the boundary layer approaches a three-dimensional separation line. The solutions obtained are used to deduce the nature of three-dimensional separation. It is shown that in these cases separation is of the "ordinary" type. A solution is also presented for a case in which a vortex is embedded within the three-dimensional boundary layer.

INTRODUCTION

The determination of the aerodynamic forces and moments on many practical bodies requires the prediction of the location of boundary layer separation on the body. When the boundary layer is both laminar and two-dimensional this is not a very difficult problem. The phenomenon of two-dimensional separation is well understood and there are methods available which can be used to predict the flow up to separation and the location of separation with reasonable accuracy. When the boundary layer is three-dimensional the problem of predicting separation is considerably more difficult. In this case the usual methods of calculation, which involve such assumptions as similarity, small perturbations or yawed infinite cylinders, offer little aid. Furthermore, there are still pressing questions as to the nature of three-dimensional separation.

The criterion for three-dimensional laminar boundary layer separation is not necessarily the same as that for two-dimensional separation (i.e., the vanishing of the wall shear at the point of separation). In fact, both Maskell (ref. 1) and Lighthill (ref. 2) have pointed out that there are two possible modes of separation for the three-dimensional boundary layer. In one case the total wall shear may vanish at separation. This type of separation has been named by Maskell "singular" separation. In the second case the limiting streamlines, or streamlines closest to the solid wall, run close together and become tangent to the line of separation at separation. This type of separation has been named by Maskell "ordinary" separation.

The number of three-dimensional boundary layer calculations which have been carried out up to the vicinity of separation is quite limited. This is true, in part at least, because of the added mathematical difficulty arising from the addition of another independent variable (the third spatial coordinate) and the corresponding dependent variable (the third velocity component) in the

three-dimensional problem. Another difficulty which has served to limit solutions in the vicinity of separation is the fact that flow reversal of one velocity component parallel to the wall often occurs near separation.

The present work presents an investigation of several three-dimensional boundary layer flows, which approach separation, with the objective of studying, in some detail, the nature of the flow in the vicinity of separation. The method employed in the present analysis is that of semi-similar solutions. Mathematically the method of semi-similar solutions is a technique by which the three independent variables are reduced to two by an appropriate scaling. In cases where separation occurs, the technique has a more important physical interpretation. It may be viewed as a scaling of the two surface coordinates in such a way that separation occurs at a constant value of the new scaled surface coordinate (although the value of the new scaled coordinate corresponding to separation is not known *a priori*). This property is extremely helpful in determining, from the solutions, the physical characteristics of separation.

Solutions are presented for two cases which lead to three-dimensional separation of the ordinary type. In one of these cases one of the velocity components parallel to the wall becomes negative prior to separation. Finally, a case is presented in which a vortex is embedded within the three-dimensional boundary layer.

SYMBOLS

A, B, C, D, E, H, I, J	coefficients of ξ in the reduced momentum equation (eq. (7))
$F(\xi,\eta)$, $G(\xi,\eta)$	dimensionless stream functions
$g(x,y)$	scaling function for the z-coordinate
ℓ	characteristic length for the flow
p	pressure
U	characteristic velocity for the flow
u, v, w	the x, y and z components of velocity, respectively
x, y	coordinate directions on the body surface (fig. 1)
z	coordinate direction normal to body surface
η	scaled z-coordinate
ν	kinematic viscosity
ξ	scaled x and y coordinate

ρ density

τ_w wall shear

Subscripts

δ conditions at the "upper" edge of the boundary layer

w condition at the body surface (wall)

ANALYSIS

The boundary layer equations for steady, incompressible motion in three-dimensions over a surface with large radii of curvature are:

$$\frac{\partial u}{\partial x} + \frac{\partial v}{\partial y} + \frac{\partial w}{\partial z} = 0 \tag{1}$$

$$u \frac{\partial u}{\partial x} + v \frac{\partial u}{\partial y} + w \frac{\partial u}{\partial z} = - \frac{1}{\rho} \frac{\partial p}{\partial x} + \nu \frac{\partial^2 u}{\partial z^2} \tag{2}$$

$$u \frac{\partial v}{\partial x} + v \frac{\partial v}{\partial y} + w \frac{\partial v}{\partial z} = - \frac{1}{\rho} \frac{\partial p}{\partial y} + \nu \frac{\partial^2 v}{\partial z^2} . \tag{3}$$

The boundary conditions for this set of equations are:

$$u(x,y,0) = v(x,y,0) = w(x,y,0) = 0$$

$$\lim_{z \to \infty} u(x,y,z) = u_\delta(x,y) \qquad \lim_{z \to \infty} v(x,y,z) = v_\delta(x,y)$$

Here x and y are orthogonal Cartesian coordinates tangent to the body surface and z is the coordinate normal to this surface (Fig. 1). As noted earlier we wish to scale the physical coordinates x, y, and z into a new set of two scaled coordinates. The appropriate scaling is: $\eta = z/g(x,y)\sqrt{\nu}$, $\xi = \xi(x,y)$, where $g(x,y)$ and $\xi(x,y)$ are at this point unknown functions. In addition, we define two dimensionless stream functions $F(\xi,\eta)$ and $G(\xi,\eta)$ constructed so that the continuity equation is identically satisfied. The velocity components written in terms of these functions become:

$$u = u_\delta \frac{\partial F}{\partial \eta} \qquad v = v_\delta \frac{\partial G}{\partial \eta} \tag{4}$$

$$w = - \sqrt{\nu} \left\{ \frac{\partial u_\delta g}{\partial x} F + u_\delta g \frac{\partial \xi}{\partial x} \frac{\partial F}{\partial \xi} - u_\delta \frac{\partial g}{\partial x} \eta \frac{\partial F}{\partial \eta} + \frac{\partial v_\delta g}{\partial y} G + v_\delta g \frac{\partial \xi}{\partial y} \frac{\partial G}{\partial \xi} - v_\delta \frac{\partial g}{\partial y} \eta \frac{\partial G}{\partial \eta} \right\}$$

It is easily shown, by direct substitution, that this choice satisfies the

continuity equation. Now if the velocity components given by equations (4) and their derivatives are introduced into the x and y momentum equations (2) and (3), one obtains the following pair of partial differential equations in the two variables η and ξ:

$$F''' + (A + B)\, F\, F'' + (C + D)\, G\, F'' + A(1 - F'^2) +$$

$$E(1 - G'F') + H\left[F'' \frac{\partial F}{\partial \xi} - F' \frac{\partial F'}{\partial \xi}\right] + I\left[F'' \frac{\partial G}{\partial \xi} - G' \frac{\partial F'}{\partial \xi}\right] = 0 \qquad (5)$$

$$G''' + (C + D)\, G\, G'' + (A + B)\, F\, G'' + C(1 - G'^2) +$$

$$J(1 - F'G') + I\left[G'' \frac{\partial G}{\partial \xi} - G' \frac{\partial G'}{\partial \xi}\right] + H\left[G'' \frac{\partial F}{\partial \xi} - F' \frac{\partial G'}{\partial \xi}\right] = 0 \qquad (6)$$

In the transformed coordinate system the boundary conditions become:

$$F(\xi,0) = F'(\xi,0) = G(\xi,0) = G'(\xi,0) = 0 \qquad \lim_{\eta\to\infty} F'(\xi,\eta) = \lim_{\eta\to\infty} G'(\xi,\eta) = 1$$

Here the primes denote differentiation with respect to η and the coefficients A, B, C, D, E, H, I, J are functions of x and y given by:

$$A = g^{*2} \frac{\partial u_\delta^*}{\partial x^*} \qquad B = u_\delta^* \frac{\partial g^{*2}}{\partial x^*} \qquad C = g^{*2} \frac{\partial v_\delta^*}{\partial y^*} \qquad D = v_\delta^* \frac{\partial g^{*2}}{\partial y^*}$$

$$E = g^{*2} \frac{v_\delta^*}{u_\delta^*} \frac{\partial u_\delta^*}{\partial y^*} \qquad H = g^{*2}\, u_\delta^* \frac{\partial \xi}{\partial x^*} \qquad I = g^{*2}\, v_\delta^* \frac{\partial \xi}{\partial y^*} \qquad J = g^{*2} \frac{u_\delta^*}{v_\delta^*} \frac{\partial v_\delta^*}{\partial x^*}$$

$$(7)$$

In equations (7), we have normalized u_δ, v_δ, g, x, and y by introducing the dimensionless variables:

$$u_\delta^* = \frac{u_\delta}{U} \qquad v_\delta^* = \frac{v_\delta}{U} \qquad g^* = g\sqrt{\frac{U}{\ell}} \qquad x^* = \frac{x}{\ell} \qquad y^* = \frac{y}{\ell}$$

If semi-similar solutions are to exist, the coefficients A, B, C, D, E, H, I, and J must be functions of ξ alone. There are four relations between these eight coefficients, constructed using the fact that u_δ^*, v_δ^*, g^* and ξ must be continuous functions of x^* and y^* and thus, the second derivatives of each of these functions with respect to x^* and y^* must be independent of the order of differentiation. An additional relation between u_δ^* and v_δ^* is obtained if the component of vorticity normal to the surface vanishes outside the boundary layer. These auxillary equations together with a discussion of the method of solving the total problem is presented in reference 3. Once the eight coefficients in equations (5) and (6) are defined for a given problem, the solution of equations (5) and (6) is straight forward using an implicit finite difference technique similar to that of Blottner (ref. 4). In what follows we will be

interested in the angle of the streamlines relative to the x axis. In particular we will be interested in the two extremes of this angle, evaluated in the external flow and at the wall and given respectively by:

$$\tan \beta_\delta = \frac{v_\delta^*}{u_\delta^*} \qquad \tan \beta_w = \lim_{\eta \to 0} \frac{v}{u} = \frac{v_\delta^*}{u_\delta^*} \frac{G''(\xi,0)}{F''(\xi,0)}$$

In addition, we will consider the total wall shear, or more specifically, the normalized form of the total shear given respectively by:

$$\tau_w = \mu \left\{ \frac{\partial}{\partial z} \sqrt{u^2 + v^2} \right\}_{z=0}$$

$$\tau_w^* = \frac{\tau_w \, g \sqrt{\nu}}{\mu \, u_\delta} = \frac{F''(\xi,0) + \tan \beta_w \, \tan \beta_\delta \, G''(\xi,0)}{\sqrt{1 + \tan^2 \beta_w}}$$

Finally, we will wish to consider the effects of the pressure gradient in the x and y directions given respectively by:

$$\frac{1}{\rho U^2} \frac{\partial p}{\partial x} \frac{g^{*2}}{u_\delta^*} = -A(\xi) - E(\xi) \qquad \frac{1}{\rho U^2} \frac{\partial p}{\partial y} \frac{g^{*2}}{u_\delta^*} = -C(\xi) - J(\xi)$$

SOLUTIONS FOR TWO FLOWS LEADING TO SEPARATION

In the present analysis we will assume that $H(\xi) = \xi$ and that $A(\xi) + 2B(\xi) = 1$. These assumptions are made to simplify the analysis and because they correspond to the scaling usually used in the analysis of two-dimensional non-similar boundary layers. In addition, consideration will be limited to that family of flows in which the external velocity components may be written as explicit functions of ξ. As a result of these assumptions one obtains the results $g^{*2} u_\delta^* = x^*$ and $\xi = x^*/(1 - \alpha y^*)$. Specifically we will consider the velocity distributions:

$$u_\delta^* = \xi - \xi^2 = \frac{x^*}{1 - \alpha y^*} \left\{ 1 - \frac{x^*}{1 - \alpha y^*} \right\}$$

$$v_\delta^* = 1 + \frac{\alpha \, x^{*2}}{(1 - \alpha y^*)^2} \left\{ 1 - \frac{4}{3} \frac{x^*}{(1 - \alpha y^*)} \right\}$$

It may easily be shown that these velocity distributions correspond to an irrotational outer flow (i.e. the vertical component of vorticity vanishes). Clearly the nature of the external flow field depends on the sign of the parameter α. Solutions will be presented for typical cases in which α is negative or positive.

With these external velocity distributions given, all the coefficients $A(\xi)$, $B(\xi)$, $C(\xi)$, $D(\xi)$, $E(\xi)$, $H(\xi)$, $I(\xi)$ and $J(\xi)$, may be written explicitly in terms of ξ. Equations (5) and (6) then form a pair of coupled, third order, partial differential equations which are similar in form to the transformed, two-dimensional, non-similar boundary layer equation and may be solved, as mentioned earlier, using an implicit finite difference technique.

We consider first the case in which α is negative. Solutions for this family of flows have been obtained for several values of α. The results for $\alpha = -0.5$ are typical and are presented in Figure 2. In this particular case the pressure gradient in the x direction is negative for $0 \leq \xi < 0.5$, positive for $0.5 < \xi < 0.51$ and negative for $\xi > 0.51$ while the pressure gradient in the y direction is positive for $0 \leq \xi < 0.5$, negative for $0.5 < \xi < 0.51$ and positive for $\xi > 0.51$.

In this case, as in all others presented herein, the integration of equations (5) and (6) starts at $\xi = 0$, where similar solutions are obtained, and proceeds in the ξ direction with an iteration on the velocity profile at each ξ station. At some downstream station the number of iterations required to obtain convergence starts to grow with each succeeding station until, at one station, convergence cannot be obtained in a reasonable number of iterations. This behavior is taken, by analogy with finite difference calculation of the two-dimensional boundary layer, as an indication of approaching a point of singular behavior, in the boundary layer equations, associated with separation. With $\alpha = -0.50$ a solution is obtained at 0.510 with convergence at each point in the velocity profile in 10 iterations. At $\xi = 0.511$ convergence cannot be obtained in 120 iterations. Separation is assumed to occur, then, in the vicinity of $\xi = 0.511$.

Figure 2 presents the results obtained with $\alpha = -0.50$ for the angle of the streamlines in the free stream, β_δ, the angle of the limiting streamlines, β_w, and the normalized normal wall shear τ_w^*. The normalized wall shear is very large near $\xi = 0$ (in the limit as $\xi \to 0$, $\tau_w^* \to \infty$ because of the normalization) but decreases with increasing ξ. As ξ approaches 0.511, τ_w^* does not approach zero, in fact, at $\xi = 0.510$ $\tau_w^* = 0.878$. Clearly then, separation in this case is not a "singular" type separation as defined by Maskell. Now if separation occurs at a value of ξ denoted by ξ_{sep}, then the equation for the separation line is given by a rearrangement of the definition of ξ, i.e.

$$y^*_{sep} = \frac{1}{\alpha} \left(1 - \frac{x_{sep}}{\xi_{sep}} \right) \tag{8}$$

and the slope of the separation line is:

$$\beta_{sep} = \arctan \left(- \frac{1}{\alpha \xi_{sep}} \right) \tag{9}$$

Thus, if ordinary separation occurs, the angle of the limiting streamlines at the wall, β_w, should approach the angle of the separation line β_{sep}, as separation is approached. In the present case with ξ_{sep} taken to be 0.511, the value

1414

of β_w at $\xi = 0.510$ is 1.3184 which is very close to the value β_{sep} of 1.3206. This value of β_{sep} is also noted on Figure 2. Clearly β_w approaches β_{sep} as separation is approached verifying the concept of "ordinary" separation.

Next we consider a case in which α is positive. Again solutions for this family of flows have been obtained for several values of α; the results for $\alpha = 0.5$ are typical and are presented in Figure 3. In this case both the pressure gradient in the x direction and the pressure gradient in the y direction are negative for $0 \leq \xi < 0.5$ and positive for $\xi > 0.5$. The magnitude of the pressure gradient in the y direction is considerably smaller than the magnitude of the pressure gradient in the x direction.

With $\alpha = 0.5$ a solution is obtained at $\xi = 0.603$ in 39 iterations, at $\xi = 0.604$ in 43 iterations and at $\xi = 0.605$ in 68 iterations. Convergence cannot be obtained at $\xi = 0.606$ in 120 iterations. Separation is assumed to occur, then, in the vicinity of $\xi = 0.606$.

In this case the total wall shear τ_w^* decreases (from an infinite value at $\xi = 0$) with increasing ξ until it passes through zero at approximately $\xi = 0.596$. With further increase in ξ, τ_w^* becomes more negative and at $\xi = 0.605$ has the value $\tau_w^* = -0.0332$. The total wall shear is negative because the x component of velocity is reversed beyond $\xi = 0.596$. The x component of velocity is reversed because of the strong positive pressure gradient (adverse pressure gradient) which acts beyond $\xi = 0.5$. It should be noted that in this work, as in reference 3, solutions are obtained in regions where one or the other velocity components are reversed without any hint of an instability. This point will be discussed later.

The wall shear, although small, is not zero at separation. Thus, this case does not represent a "singular" type separation. As noted previously, if separation in this case is "ordinary" the angle of the limiting streamlines at the wall should approach the angle of the separation line as separation is approached. That this is the case, is shown in Figure 3. Both the angle of the limiting streamlines, β_w, and the angle of the streamlines in the freestream, β_δ, are $\pi/2$ at $\xi = 0$. As ξ increases β_δ decreases, fairly rapidly at first and then more slowly. The angle β_w decreases rapidly initially and then increases rapidly so that it approaches the value β_{sep} (noted on Figure 3) as separation is approached. Thus, the separation involved here is an "ordinary" separation.

INTEGRATION INTO REGIONS OF REVERSE FLOW

In the example just considered the x component of velocity near the wall changed directions near separation. Thus, it was necessary to integrate the boundary layer equations into a region of reverse flow to obtain the solution. Until quite recently the "conventional wisdom" was that integration of the boundary layer equations into regions of reverse flow lead to numerical instability problems since, in regions of reverse flow, the problem was ill posed. In the present case integration into regions of reverse flow apparently poses no problem. Since the next solution to be presented involves rather extensive

regions of reverse flow, it is necessary to determine under what circumstances integration into regions of reverse flow is permissible.

To investigate this problem we note that equations (5) and (6) may be rewritten in the form:

$$F''' + \alpha_{11} F'' + \alpha_{21} F' + \alpha_{31} = \alpha_{41} \frac{\partial F'}{\partial \xi} \tag{10}$$

$$G''' + \alpha_{21} F'' + \alpha_{22} G' + \alpha_{32} = \alpha_{42} \frac{\partial G'}{\partial \xi} \tag{11}$$

Here again primes denote differentiation with respect to η. The exact form of the α_{ij}'s in equations (10) and (11) may be determined by comparison with equations (5) and (6); it is only important to note that $\alpha_{41} = \alpha_{42} = HF' + IG'$. If F' and G' are treated as independent variables, equations (10) and (11) closely resemble the one-dimensional heat conduction equation. As in the mathematical solution of the heat conduction equation, the problem is well posed only if the coefficient α_{41} is positive. If α_{41} is positive, equations (10) and (11) are parabolic and solutions are possible if appropriate boundary and initial conditions are prescribed. If α_{41} becomes negative for any portion of the flow field, equations (10) and (11) are parabolic equations of the mixed type and additional information is needed in order to obtain a solution to these equations. Since $\alpha_{41} = \alpha_{42} = HF' + IG'$, it is clear that this coefficient may be positive even when one of the velocities is negative. For example, if the x component of velocity is negative near the wall then in this region $F' < 0$, but α_{41} will be positive provided the product IG' is positive and greater than the absolute value of the product HF'. For this reason, solutions to equations (5) and (6) may be obtained without any numerical instability problems even when one of the velocity components is reversed.

AN EMBEDDED VORTEX

We now consider a third case in which the solution represents physically a three-dimensional boundary layer with an embedded vortex. It is assumed, as before, that $A(\xi) + 2B(\xi) = 1$, $H(\xi) = \xi$ and that the velocity components are functions of the scaled variable ξ (i.e. $u_\delta = u_\delta(\xi)$, and $v_\delta = v_\delta(\xi)$). These assumptions lead to the relations $g*^2 u_\delta^* = x*$ and $\xi = x*/(1 - \alpha y*)$. In addition we assume $I(\xi) = \xi$. This assumption yields a relation between u_δ^* and v_δ^*, namely $u_\delta^*(\xi) = \alpha \xi v_\delta^*$. It should be noted that for this flow the component of vorticity normal to the wall does not vanish outside the boundary layer. Thus, this inviscid flow will represent some type of sheared flow (rotational flow). Finally, the y component of velocity at the upper edge of the boundary layer is taken to be:

$$v_\delta^* = 1 - \gamma(\xi - 5\xi^2/3 + 8\xi^3/9)$$

This form is chosen so that the normalized y component of velocity is unity at $\xi = 0$, has a minimum at $\xi = 0.5$ and a maximum at $\xi = 0.75$. This leads to a

pressure gradient in the x direction which is favorable for all ξ in the range $0 \leq \xi \leq 1$ but a pressure gradient in the y direction which is positive (adverse) for $0 \leq \xi \leq 0.5$, negative (favorable) for $0.5 < \xi < 0.75$ and positive (adverse) for $\xi > 0.75$.

Results are presented in Figures 4 and 5 for the case $\alpha = 0.5$ and for several values of γ. The variation of the limiting streamline angle, β_w, with ξ is shown in Figure 4 for $\gamma = 1.0$, 2.0 and 2.5. For $\gamma = 1.0$, β_w decreases with increasing ξ. For $\gamma = 2.0$, β_w decreases to a value of approximately zero at $\xi \cong 0.3$, increases beyond this point to a value of approximately 0.75 at $\xi \cong 0.75$ and then decreases slowly. For $\gamma = 2.5$, β_w decreases and reaches a minimum value of -0.96 and then increases again reaching a maximum at approximately $\xi = 0.8$. The variation of β_w with ξ for $\gamma = 3.0$ is similar to that for $\gamma = 2.5$ but is not shown. For $\gamma = 3.25$, 3.5 and 4 (also not shown) ordinary separation occurs. The velocity profiles for the v component of velocity are shown in Figure 5. These velocity profiles are presented for the case $\alpha = 0.5$, $\gamma = 3.0$. The y component of velocity is reversed between $\xi = 0.12$ and $\xi = 0.53$. This is also the region where the angle of the limiting streamlines is negative. Taken together, Figures 4 and 5 present a clear picture of a vortex embedded deep within the three-dimensional boundary layer. For $\xi < 0.12$ and $\xi > 0.53$ both the x and y components of velocity are positive everywhere and the flow proceeds down stream in a normal fashion. Between $\xi = 0.12$ and $\xi = 0.53$ both the x and y components of velocity are positive in the outer portion of the boundary layer but near the wall the x component of velocity is positive while the y component is reversed (negative). This results in a spiraling flow near the wall or an embedded vortex.

From the results presented for the wall shear, it is clear that for $\gamma \leq 2.0$ such a vortex does not exist (there is no flow reversal near the wall). As γ is increased beyond 2.0 a vortex is formed, a vortex which increases in size as the pressure gradient becomes more severe (γ is increased) until the pressure gradient becomes sufficiently severe that separation occurs.

Such a flow, with an embedded vortex, may at first appear strange. Such embedded vorticities do, however, occur in aerodynamics. The classical example occurs in the case of supersonic flow past a cone at moderate angle of attack. Moore (ref. 5) was apparently the first to recognize the nature of such an embedded vortex.

CONCLUDING REMARKS

The theory of semi-similar solutions has been used to investigate several three-dimensional laminar boundary layer flows which approach a separation line. The use of semi-similar solutions makes it possible to investigate the nature of the boundary layer as separation is approached. When separation occurred in the cases considered the three-dimensional separation was of the "ordinary" type in which the limiting or "wall" streamlines run close together and approach a tangent to the separation line. In one case considered, it is shown that as the pressure gradient becomes more severe, a vortex is formed within the boundary layer. If the pressure gradient becomes sufficiently large the boundary

layer separates.   The separation in this case is again an "ordinary" type separation.

REFERENCES

1. Maskell, E. C.: Flow Separation in Three-Dimensions. Royal Aircraft Establishment, RAE Report No. Aero. 2565, November, 1955.

2. Lighthill, M. J.: in Laminar Boundary Layers (L. Rosenhead, editor) Oxford Press, London, 1963.

3. Williams, J. C., III: Semi-Similar Solutions to the Three-Dimensional Laminar Boundary Layer. Appl. Sci. Res., Vol. 31, 1975, pp. 161-186.

4. Blottner, F. G.: Finite Difference Methods of Solution of the Boundary-Layer Equations. AIAA J., Vol. 8, No. 2, 1970, pp. 193-205.

5. Moore, F. K.: Laminar Boundary Layer on a Cone in Supersonic Flow at Large Angle of Attack. NACA TN 2844, November, 1952.
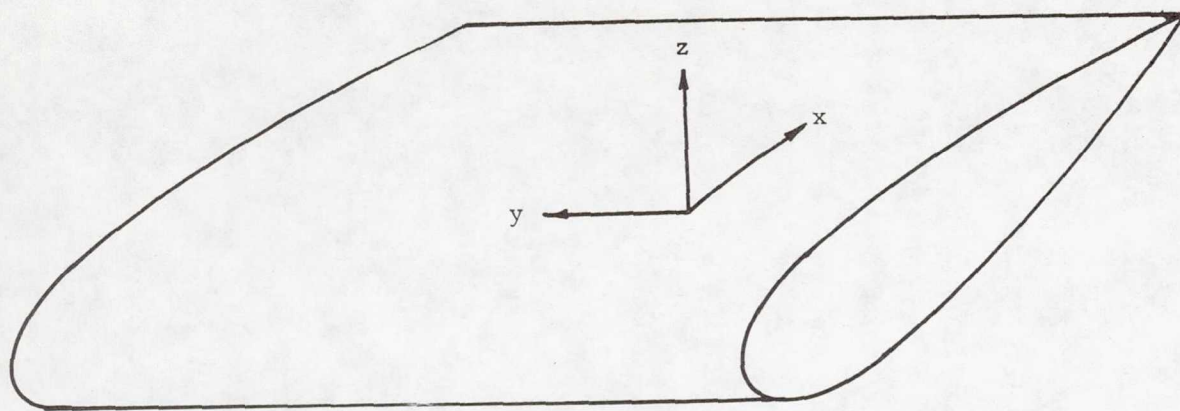
Figure 1.- Coordinate system for three-dimensional boundary layer analysis.
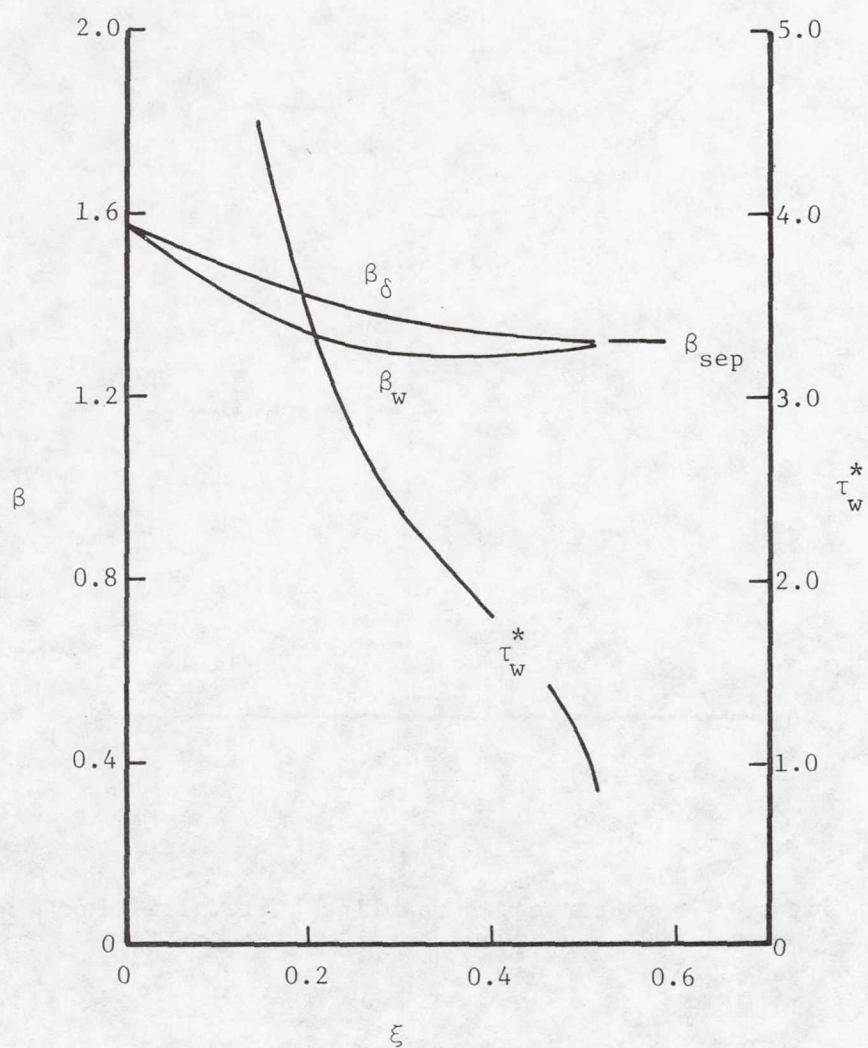
Figure 2.- Freestream streamline angle, limiting streamline angle, and total wall shear for $\alpha = -0.5$.
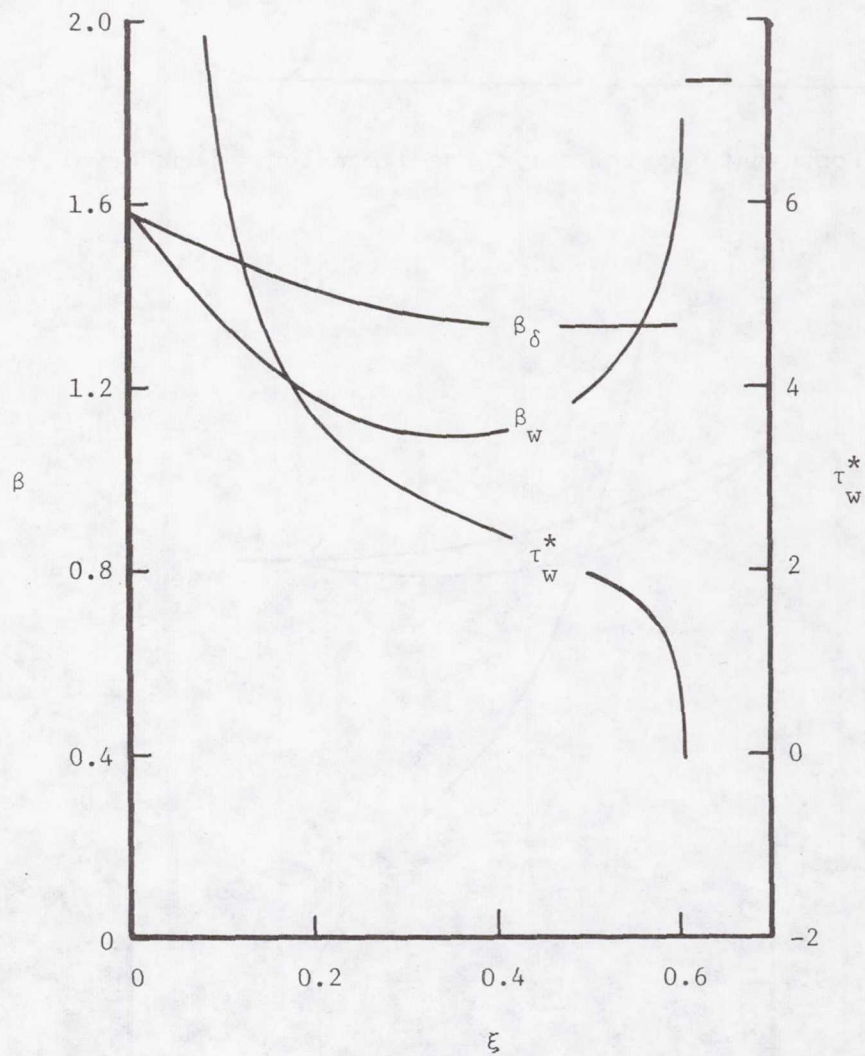
Figure 3.- Freestream streamline angle, limiting
  streamline angle, and total wall shear for
  $\alpha = 0.5$.
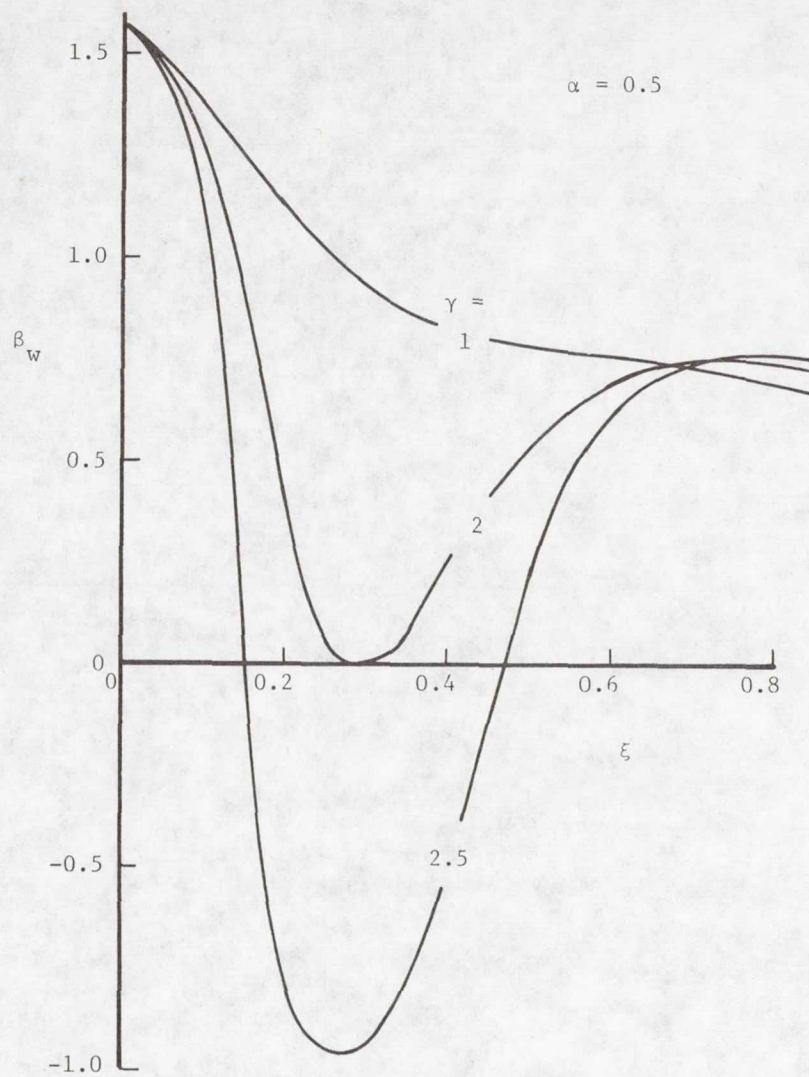
Figure 4.- Limiting streamline angles
for embedded vortex flow.
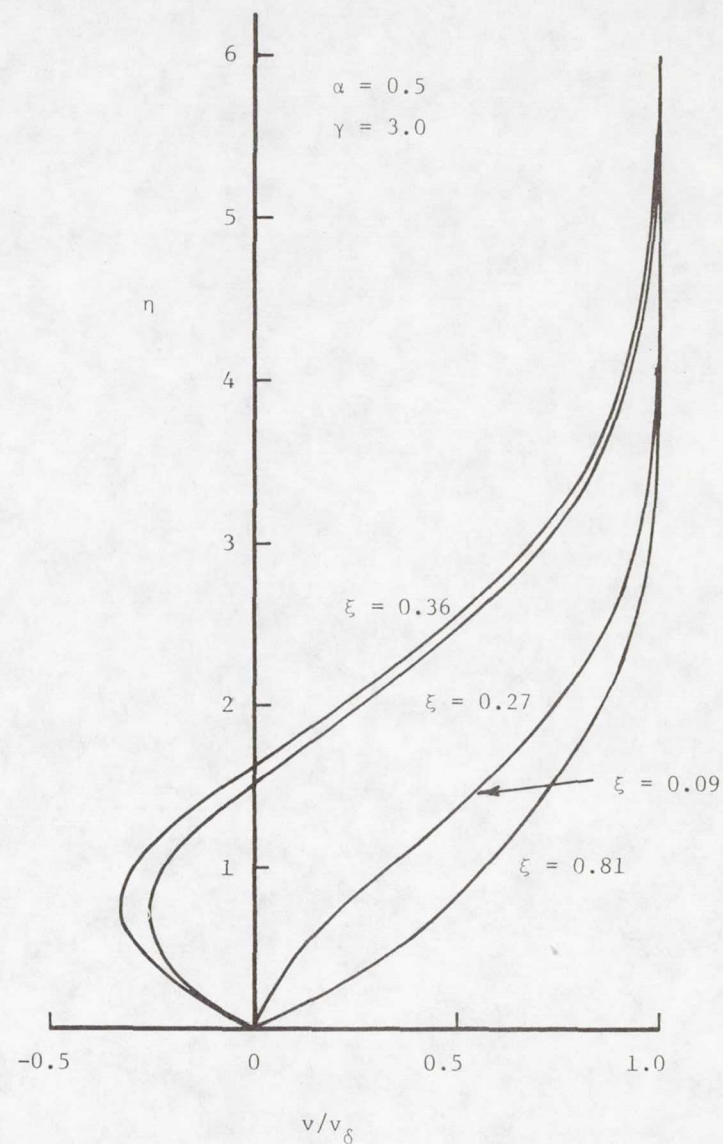
Figure 5.- y velocity profiles, embedded vortex.

Page intentionally left blank

TURBULENT INTERACTION AT TRAILING EDGES

R. E. Melnik and R. Chow
Research Department
Grumman Aerospace Corporation

SUMMARY

We are considering the effect of turbulent boundary layers on the lifting
characteristics of airfoils at high Reynolds numbers. The most important
effect arises from the local boundary-layer behavior near the trailing edge,
which directly affects the Kutta condition and leads to a significant reduction
in lift. Existing methods for predicting the boundary-layer effects on lift
are based on the displacement surface corrections of a second-order boundary-
layer theory. The displacement surface is assumed to be a streamline and the
corrections to the inviscid flow are determined by standard procedures.
Unfortunately, the displacement thickness distribution determined from the
solution of the boundary-layer equations develops singularities at trailing
edges. The singularities are caused by the discontinuous jump in the surface
boundary conditions across the trailing edge and by a singularity in the
pressure gradient of the inviscid solution at the trailing edge. Because of
these singularities a viscous Kutta condition cannot be imposed and the lift
coefficient cannot be determined by standard second-order theory.

To remedy this situation, we have developed an "inner solution" for the
strong interaction region at trailing edges.[1] In the present discussion, we
will outline the main features of the interaction theory and will describe
recent developments leading to a complete solution for the lift decrement due
to turbulent boundary layers.

The interaction theory of reference (1) is based on a large Reynolds
number, asymptotic expansion of the full (and unclosed) Reynolds equations
of turbulent flow. The theory leads to a three-layer description of the flow
near the trailing edge consisting of: (1) an outer, inviscid, rotational flow
region encompassing most of the boundary layer; (2) a thin, conventional,
constant stress, wall layer; and, (3) a blending layer of thickness
intermediate between that of the outer and wall layers. In this respect,
the theory is superficially similar to the "triple deck" structure arising in
the laminar interaction theory of Brown and Stewartson.[2]

---

[1]Melnik, R. E.; and Chow, R.: Asymptotic Theory of Two-Dimensional
Trailing Edge Flows. NASA SP 347 (also Grumman Research Department Report
RE510J), 1975.

[2]Brown, S. N.; and Stewartson, K.: Trailing Edge Stall, J. Fluid Mech.,
42, 1970.

Although they both involve a three-layer structure, the details of the laminar and turbulent solutions are vastly different. In the laminar problem the interaction distance is an order of magnitude larger than the boundary-layer, with boundary-layer approximations and the equivalent displacement body concept remaining valid in the trailing edge region. In turbulent flow, the interactions are compact with a streamwise extent of the order of a boundary-layer thickness, the boundary-layer approximation fails and the displacement surface is not a streamline in the trailing edge region. The reason for these differences will be discussed during the talk.

We will also discuss how the turbulent action equations for the outer solution are automatically closed to lowest order without the need for empirical closure assumptions. We will outline the procedures for obtaining a solution of the inviscid outer equations by analytic function theory. The effect of compressibility on the solution will be discussed, and the complete solution for the lift coefficient in a turbulent compressible flow will be given.

SHOCK WAVE-TURBULENT BOUNDARY LAYER
INTERACTIONS IN TRANSONIC FLOW[*]

T. C. Adamson, Jr. and A. F. Messiter
The University of Michigan

SUMMARY

The method of matched asymptotic expansions is used in analyzing the structure of the interaction region formed when a shock wave impinges on a turbulent flat plate boundary layer in transonic flow. Solutions in outer regions, governed by inviscid flow equations, lead to relations for the wall pressure distribution. Solutions in the inner regions, governed by equations in which Reynolds and/or viscous stresses are included, lead to a relation for the wall shear stress. Solutions for the wall pressure distribution are reviewed for both oblique and normal incoming shock waves. Solutions for the wall shear stress are discussed.

SYMBOLS

$\bar{a}^*$ critical velocity of sound, cm/sec (ft/sec)

$\bar{L}$ distance from leading edge of flat plate to shock impingement point, cm (in)

M   Mach number

P   pressure, dimensionless with critical pressure in external flow

R_e Reynolds number based on critical conditions in external flow and $\bar{L}$

U, V   dimensionless velocity components in the X, Y directions, equations (5a, 5b)

u, v   velocity perturbations

$u_{01}(y)$ variable part of dimensionless velocity in velocity defect layer in the undisturbed boundary layer.

u_τ dimensionless friction velocity, equation (1c)

X, Y   dimensionless coordinates; $Y = \bar{Y}/\bar{L}$, $X = (\bar{X} - \bar{L})/\bar{L}$

x, y   stretched coordinates

α inverse of Kármán constant $\alpha = (0.41)^{-1}$

β angle made by shock wave with the vertical

β_0 constant of order one

γ ratio of specific heats, C_p/C_v

δ order of thickness of undisturbed boundary layer at shock impingement point, dimensionless with $\overline{L}$

δ_* distance from wall to sonic line in undisturbed flow, dimensionless with $\overline{L}$; $\delta_* = \delta\, e^{-\beta_0/\alpha}\, e^{-\epsilon/\alpha u_\tau}$

Δ order of extent of outer inviscid flow region in X direction, dimensionless with $\overline{L}$; $\Delta = (\gamma+1)^{1/2}\, \epsilon^{1/2}\, \delta$

Δ_* order of extent of inner inviscid flow region in X direction, dimensionless with $\overline{L}$; $\Delta_* = \delta_*\, u_\tau^{1/2}$

ϵ parameter, $\epsilon = U_e - 1$

τ_w wall shear stress, dimensionless with undisturbed flow wall shear stress at shock impingement point

Subscripts

e   external

w   wall

u   upstream of interaction, in undisturbed flow

INTRODUCTION

Shock wave-boundary layer interaction is an important problem in both external and internal flows. At transonic speeds, asymptotic methods have proven successful in dealing with the problem when the boundary layer is laminar (refs. 1, 2) and are now being used in analyzing the interaction region in turbulent boundary layers. In general, these analyses are based on two parameters, ϵ and u_τ, where ϵ measures the difference between the flow velocity and the critical sonic velocity in the flow external to the boundary layer, and where u_τ is a dimensionless friction velocity which measures the change in velocity in the velocity defect region of the undisturbed boundary layer. Thus, if overbars denote dimensional quantities

$$U_e = \overline{U}_e / \overline{a}_e^* = 1 + \epsilon \qquad ; \qquad M_e = 1 + \frac{\gamma+1}{2}\,\epsilon + \cdots \qquad (1a,b)$$

$$u_\tau = \left(\frac{\overline{\tau}_{wu}}{\overline{\rho}_{wu}} \frac{T_e}{T_{wu}}\right)^{1/2} \bigg/ \overline{a}_e^* \quad ; \quad U_u = 1 + \epsilon + u_\tau u_{01}(y) + \cdots \qquad (1c,d)$$

For transonic flow, then $\epsilon \ll 1$, and u_τ is defined such that for $R_e \gg 1$, $u_\tau \ll 1$, and the various problems considered may be characterized by the relative orders of ϵ and u_τ. The first work done on the turbulent boundary layer problem was done by Adamson and Feo (ref. 3) who considered the case where the impinging shock is weak ($u_\tau^2 \ll \epsilon \ll u_\tau$) and oblique, and Melnik and Grossman (ref. 4) who considered the case where the shock is stronger ($\epsilon = O(u_\tau)$) and normal. In both papers, it was concluded that in order for the interaction to cause separation, it was necessary that $\epsilon = O(1)$. As a first step in this direction, the condition $\epsilon \gg u_\tau$ was discussed for the oblique wave case by Adamson (ref. 5) and for the normal wave case by Adamson and Messiter (ref. 6). In each of these papers it was pointed out, first, that the problem could be divided into two parts consisting of the flow structure in the outer inviscid flow regions and that in the inner near wall regions where Reynolds and viscous stresses had to be taken into consideration, and, second, that the wall pressure distribution could be derived from solutions in the inviscid flow regions, without having to find solutions in the near wall regions. In each case, attention was focused on the inviscid flow regions for near separation conditions.

The present paper is concerned with two objectives. First, it is desired to complete the picture of the shock structure in the oblique wave case, only the outer part of this structure having been given in reference 5, and to show the form of the pressure distribution inferred from such a structure. Second, it is desired to compare this structure and pressure distribution with their counterparts in the normal wave case, and discuss briefly the effects of the very different pressure distributions on the conditions for incipient separation. The presentation is aided by a brief review of the structure of the interaction region in the normal wave case, and this is given in the next section. It should be noted that in the following, parameters are defined such that $\delta = u_\tau$, and that the asymptotic relationship between u_τ and R_e is $u_\tau = b_0 (\alpha \ln R_e)^{-1} + \cdots$, where for $\gamma = 1.4$, $b_0 = 0.94$.

STRUCTURE OF THE INTERACTION REGION - NORMAL SHOCK

The structure of the interaction region for the impinging normal shock case is sketched in figure 1. It should be noted that the sketch is not to scale, and that there are two near wall regions, the so-called Reynolds stress sublayer region and the wall region (ref. 6).

As seen in figure 1, there are two inviscid flow regions. The outer region is scaled by the thickness of the boundary layer, δ, in the Y direction and

by the order of the extent of the overall interaction region, Δ, in the X direction. To this scale, one sees a normal shock penetrating the boundary layer, represented by the velocity defect region. In the inner inviscid flow region, scaled by δ_* and Δ_* in the Y and X directions, respectively, (δ_* is the order of the distance from the wall to the sonic line in the undisturbed flow) the upstream influence of the interaction, manifested by a deceleration of the fluid, causes compression waves emanating from the sonic line to coalesce and form a shock wave. This shock wave becomes more and more nearly normal, and as $Y/\delta_* = y^* \to \infty$, connects with the shock wave seen in the outer inviscid flow region.

The wall pressure distribution is found in the limit as the appropriate Y variable (i.e., in either the inner or outer inviscid region) goes to zero. The solution valid everywhere in the interaction region except at the inception of the interaction, where waves are coalescing and the wall pressure first begins to rise from its undisturbed value, is

$$P_w = 1 + \gamma \epsilon + u_\tau \frac{4 \gamma x}{\pi} \int_0^\infty \frac{u_{01}(\eta)}{(x^2 + \eta^2)} \, d\eta + \cdots \qquad (2a)$$

$$x = X/(\gamma + 1)^{1/2} \epsilon^{1/2} u_\tau \qquad (2b)$$

Since the asymptotic form for $u_{01}(y)$ as $y \to 0$ is $u_{01} \sim \alpha \ln y + \beta_0$, one can show that as $x \to 0$, P_w reduces to

$$P_w = 1 + \gamma \epsilon - u_\tau 2 \gamma \alpha \ln x + \cdots \qquad x \ll 1 \qquad (3)$$

A typical wall pressure distribution is shown in figure 2, for $\epsilon = 0.167$ ($M_e = 1.20$) and $u_\tau = 0.028$ ($R_e = 10^6$), using Coles' form (ref. 7) for u_{01},

$$u_{01} = \alpha \ln y - \frac{\alpha}{2} (1 + \cos \pi y) \qquad y < 1 \qquad (4a)$$

$$= 0 \qquad y > 1 \qquad (4b)$$

The important points to note are that there are two inviscid flow regions, with upstream influence existing only in the inner region which is exponentially small compared to the outer region (i.e., calculate δ_*/δ and Δ_*/Δ) and that the wall pressure increases monotonically. This point is borne out, for example, by the experimental measurements for flow in tubes described in reference 8.

STRUCTURE OF THE INTERACTION REGION - OBLIQUE SHOCK

The shock wave structure for the oblique shock wave case is sketched in figure 3. Again, it is important to note that this sketch is not to scale, and

that the shock occurs in regions in which the governing equations are those for inviscid, rotational flow. Viscous and Reynolds stresses must be taken into account in the Reynolds stress sublayer region and wall region which exist between the inviscid flow region and the wall.

As seen in figure 3, the oblique shock structure has many of the features of the normal shock structure deep in the boundary layer, with a more complicated outer structure. The analysis proceeds by considering first, the region far from the wall, and then proceeding toward the wall. In this regard, the upstream influence from the interaction region is confined to a very thin region, just as in the normal shock case. Thus, in analyzing the regions outside the inner inviscid region, one need not consider any waves arising from lower regions and affecting the incoming shock shape. Instead, as mentioned in reference 5, the incoming oblique wave shape may be found by considering a wave of known strength as it penetrates a shear layer represented by the boundary layer. Thus, if one writes the expansions for the velocity components as

$$U = \frac{\overline{U}}{a_e^*} = 1 + \epsilon + u_\tau u_{01} + \epsilon u_1 + \cdots = 1 + \epsilon u + \cdots \qquad (5a)$$

$$V = \frac{\overline{V}}{a_e^*} = \epsilon^{3/2} v + \cdots \qquad (5b)$$

where u_1 is the perturbation due to the shock, and if the local angle made by the shock with the vertical, β_s, is expanded as follows,

$$\beta_s = \epsilon^{1/2} \beta + \cdots \qquad (6)$$

Then, using the shock-wave relations, one can show that β and $u_u = 1 + u_\tau u_{01}/\epsilon$, the value of u upstream of the shock, are related as follows (ref. 5).

$$\left[\frac{3\beta}{\sqrt{\gamma+1}} + 2 \left(\frac{2\beta^2}{\gamma+1} - u_u \right)^{1/2} \right]^{3/5} \left[\frac{\beta}{\sqrt{\gamma+1}} - \left(\frac{2\beta^2}{\gamma+1} - u_u \right)^{1/2} \right]^{2/5} = c \qquad (7)$$

where c is a constant. The value of c in equation (7) is calculated by inserting the known value of β for the wave in the flow external to the boundary layer, where $u_u = 1$.

Unlike the normal shock wave case, it does not appear possible to consider one outer inviscid flow region in which the whole outer shock structure is contained; evidently the shock structure is too complicated for this. Instead, a series of regions is considered, each one being deeper in the boundary layer, and each one having smaller and smaller characteristic lengths in both the X and Y directions. In an asymptotic sense, each of these regions corresponds to a limit process such that $u_\tau \to 0$ with an intermediate variable $Y/\eta(u_\tau)$ held fixed where $\eta/u_\tau \to 0$, but $\eta/\delta_* \to \infty$ as $u_\tau \to 0$. To the scale of each of these regions the shock wave structure appears as shown in figure 4a,

that is, the solution is that for a regular reflection with the angles associated with each of the shock waves changing as the boundary layer is penetrated. If u_r denotes the value of u (eq. (5a)) downstream of the reflected shock for a given region, with given values of β and u_u, then

$$u_r = \frac{\beta^2}{\gamma + 1} - u_u + \frac{\beta}{\sqrt{\gamma + 1}} \sqrt{\frac{5\beta^2}{(\gamma + 1)} - 4u_u} \qquad (8)$$

and the corresponding pressure is,

$$P = 1 + \epsilon \, \gamma \, (-1 + u_u - u_r) + \cdots \qquad (9)$$

Now, in each region or limit process description the incoming velocity is uniform to order ϵ. Therefore, the velocity downstream of the reflected wave and thus the pressure there is uniform to order ϵ. Furthermore, for any regions between the one in question and the wall, with the same characteristic X dimension, $\partial P/\partial y = 0$ to order ϵ, so the pressure given in equation (9) is the wall pressure corresponding to the characteristic X dimension in question. Now from equations (7) through (9), one can show that $du_r/du_u < 0$ so that $dP/du_u > 0$. Thus, as one considers regions deeper and deeper in the boundary layer, i.e., as Y and in particular X decrease, the pressure downstream of the reflected shock increases. Hence, as one approaches the shock along the wall, from downstream of the shock, the wall pressure increases.

As successive regions, each deeper in the boundary layer, are considered, the structure shown in figure 4a is found until the limiting conditions for which a regular reflection is possible are reached. From equation (8), this is seen to occur when β has decreased such that

$$\beta^2 = 4 (\gamma + 1) u_u/5 \qquad (10)$$

As this condition is reached, the shock structure evidently takes on the Guderley Mach stem configuration (ref. 9). To the scale of the region in which this flow configuration is found, the shock structure, then, is that seen in figure 4b. That is, as the wall is approached, the incoming shock (Mach stem) becomes a normal shock.

Finally, beneath the Mach stem region is the inner inviscid region, the same region found in the normal shock wave case, in which compression waves emanating from the sonic line coalesce to form a shock which becomes more and more nearly normal as it moves away from the wall until it merges with the normal shock in the Mach stem region.

The wall pressures associated with the regular reflection and the normal shock problems have been calculated. Although the joining of these two parts of the solution (through the Guderley Mach stem region) is more difficult, the

general shape of the wall pressure distribution seems clear. Thus, just as in the normal shock wave case, as one moves downstream toward the Mach stem region and the shock becomes stronger, the wall pressure increases. On the other hand, from the outer inviscid regions discussed above, it was shown that as one moves upstream toward the Mach stem region, the wall pressure increases also. Therefore, the wall pressure distribution must, as shown in figure 5, go through a maximum in the Mach stem region, this maximum pressure being the pressure behind the normal part of the wave (Mach stem) shown in figure 4b. This form for the pressure distribution is also apparent in experimental results as shown, for example, in reference 10. In these experiments the external flow was supersonic but since the flow near the wall is transonic, the general features of the structure of the interaction region shown here must apply.

DISCUSSION

The structure of the shock wave in the interaction region is seen to be much more complicated in the oblique shock case (fig. 3) than in the normal shock case (fig. 1) and this is reflected in the fact that, in general, solutions are much more difficult to obtain in the oblique than in the normal shock case. The differences in the wall pressure distributions in the two cases are illustrated by comparing figures 2 and 5. In the normal shock wave case, the pressure increases monotonically, while in the oblique shock wave case, the pressure goes through a maximum and decreases then to its final value. Now, in the inviscid flow regions, the pressure perturbation is directly proportional to the negative of the perturbation in U, and as the wall is approached, the solution for U is matched with a corresponding solution from the Reynolds stress sublayer region which is in turn matched with a solution in the wall region. The result is that as the pressure increases, the velocity near the wall decreases, such that $\partial U/\partial Y$ near the wall decreases and hence the wall shear stress, τ_w, decreases. In fact, τ_w can be written directly in terms of the pressure perturbations (refs. 3 and 4). Therefore, in the normal-shock wave case, τ_w decreases monotonically to its lowest value, while in the oblique wave case, it goes through a minimum and rises to its final value. This situation is expected to hold up to separation, i.e., for the case of incipient separation. Hence, the point at which τ_w first goes to zero (incipient separation) will occur within the interaction region for the oblique shock case, and at the far downstream limit of the interaction region in the normal shock case. In the event that separation occurs, the results discussed above do not hold, of course; in that case, the displacement of the incoming flow by the separated bubble causes a change in the outer shock structure, and thus in the pressure distributions.

REFERENCES

(1) Messiter, A. F. ; Feo, A. ; Melnik, R. E. : Shock-Wave Strength for Separation of a Laminar Boundary Layer at Transonic Speeds. AIAA Journal, 9, 1971, pp. 1197-98.

(2) Brilliant, H. M. ; Adamson, T. C. , Jr. : Shock Wave Boundary-Layer Interactions in Laminar Transonic Flow. AIAA Journal, 12, 1974, pp. 323-329.

(3) Adamson, T. C. , Jr. ; Feo, A. : Interaction Between a Shock Wave and a Turbulent Boundary Layer in Transonic Flow. SIAM J. Appl. Math. , 29, 1975, pp. 121-145.

(4) Melnik, R. E. ; Grossman, B. : Analysis of the Interaction of a Weak Normal Shock Wave with a Turbulent Boundary Layer. AIAA Paper No. 74-598, 1974.

(5) Adamson, T. C. , Jr. : The Structure of Shock Wave-Boundary Layer Interactions in Transonic Flow. Symposium Transsonicum II, ed. Oswatitsch, K. ; Rues, D. , Springer Verlag, 1976, pp. 244-251.

(6) Adamson, T. C. , Jr. ; Messiter, A. F. : Normal Shock Wave-Turbulent Boundary Layer Interactions in Transonic Flow Near Separation. Proceedings of Workshop on Transonic Flow Problems in Turbomachinery, Monterey, California, Feb. , 1976.

(7) Coles, D. E. ; Hirst, E. A. (EDS): Proceedings of the AFOSR-1FP Stanford Conference, Vol. 2, 1968.

(8) Gadd, G. E. : Interactions Between Normal Shock Waves and Turbulent Boundary Layers. Aeronautical Research Council Rept. No. 22,559, F. M. 3051, 1961.

(9) Guderley, K. G. : The Theory of Transonic Flow. Pergamon Press, 1962, pp. 147-149.

(10) Sirieix, M: Decollement Turbulent en Écoulement Bidimensionnel. AGARD Conference Proceedings No. 168 on Flow Separation, 1975, pp. 12-1 to 12-27.
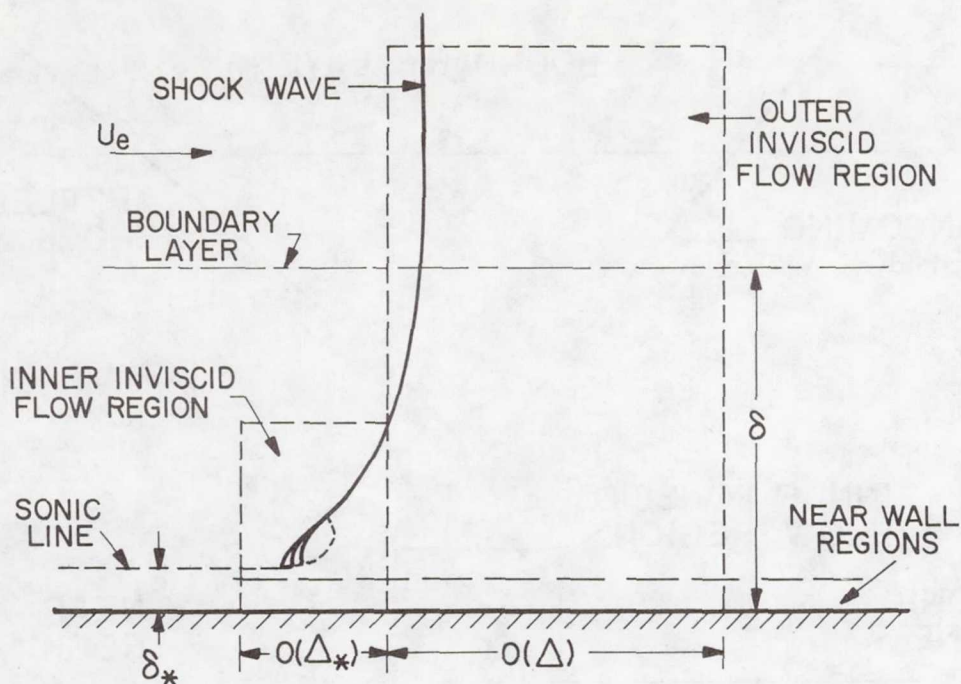
Figure 1.- Sketch of structure of interaction region for case where incoming wave is normal.
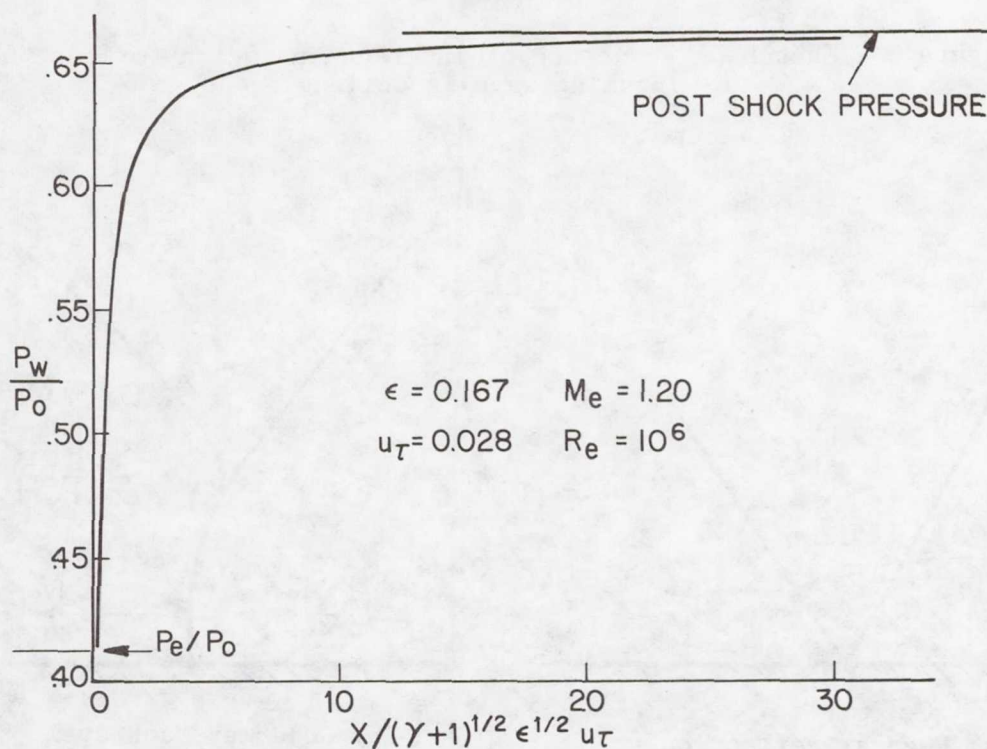
Figure 2.- Calculated wall pressure distribution for normal shock wave interacting with a turbulent flat plate boundary layer with $M_e = 1.20$ and $R_e = 10^6$.
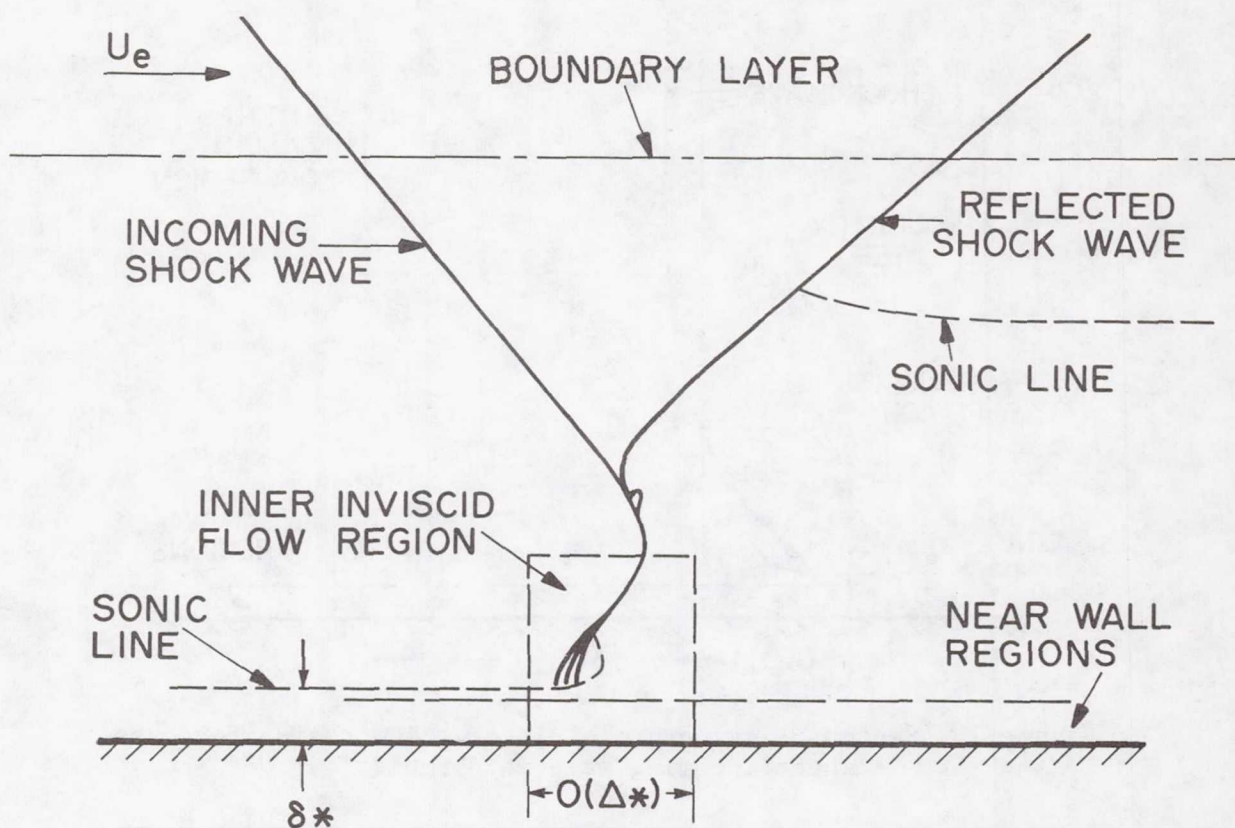
Figure 3.- Sketch of structure of interaction region for case where incoming wave is oblique.

(a) Regular reflection.

(b) Guderley Mach stem configuration.
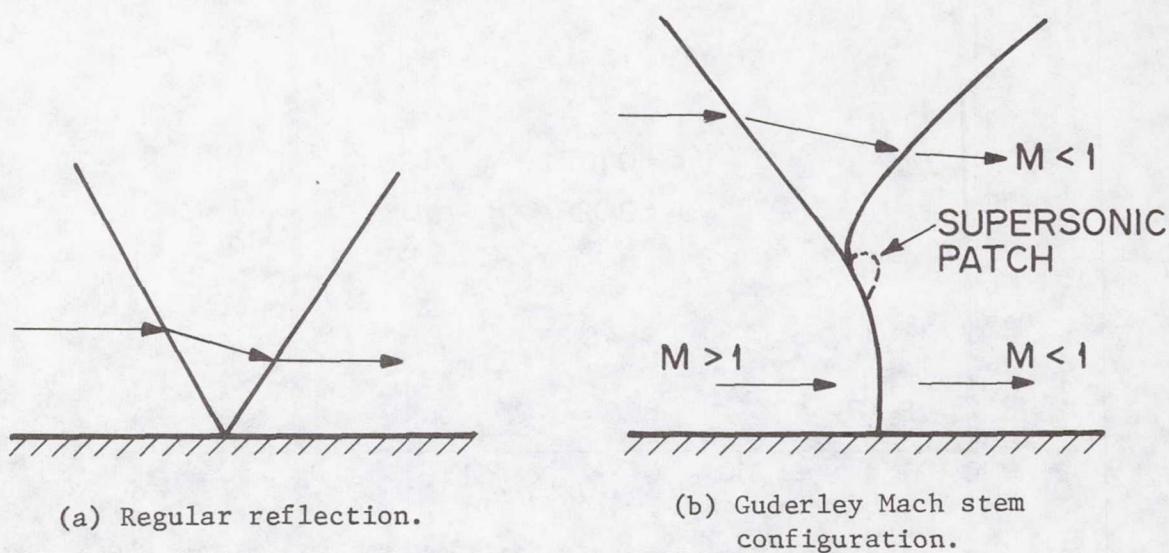
Figure 4.- Sketch of shock structure in intermediate inviscid flow regions for case where incoming wave is oblique.

BOUNDARY LAYER

SHOCK WAVE STRUCTURE
OBLIQUE SHOCK CASE

X

CORRESPONDING WALL
PRESSURE DISTRIBUTION

$\dfrac{P_W}{P_O}$

X
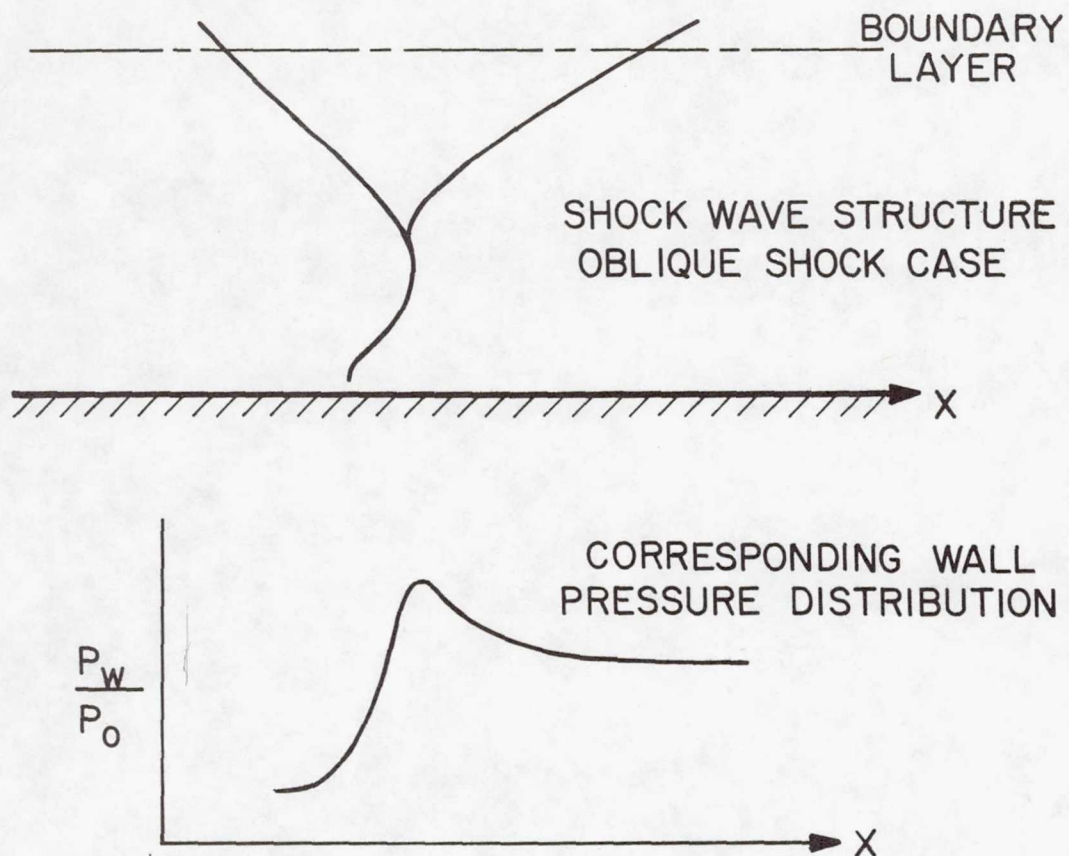
Figure 5.- Sketch of wall pressure distribution corresponding to indicated
shock wave structure for case where incoming wave is oblique.

Page intentionally left blank

SEPARATED LAMINAR BOUNDARY LAYERS

Odus R. Burggraf
The Ohio State University

SUMMARY

Classical boundary-layer theory is inadequate to deal with
the problem of flow separation owing to its underlying assumption
that the boundary layer has an insignificant effect on the exter-
nal stream. This difficulty is resolved by the modern theory
which includes interaction with the external flow. This newer
theory is described from the viewpoint of the asymptotic triple-
deck structure. Several triple-deck studies are reviewed with
emphasis on results of interest in aeronautical applications.

INTRODUCTION

Separated flow occurs when an attached boundary layer en-
counters a downstream compressive disturbance of sufficient magni-
tude. Observations show that the separation point lies at a
rather long distance upstream of the disturbance, contradicting
the inherent nature of Prandtl's boundary layer theory that no
upstream influence can occur. Crocco and Lees (ref. 1) have shown
that coupling the pressure of the external inviscid flow to the
displacement thickness of the boundary layer permits upstream in-
fluence to be consistent with the boundary-layer equations. This
concept led to the integral methods of Lees and Reeves (ref. 2),
and others, for viscous interacting flows. However, the correct
mathematical structure of such flows was not given until the
papers of Stewartson and Williams (ref. 3) and of Neiland (ref. 4)
on self-induced separation in supersonic flows at high Reynolds
number. Independently, the same asymptotic structure was shown to
hold for incompressible flow at the trailing edge of an airfoil by
Stewartson (ref. 5) and by Messiter (ref. 6). This flow structure,
which Stewartson has named "the triple deck", has been found to be
relevant in a wide variety of applications. The purpose of this
paper is to review several of these triple-deck studies that are
of interest in aeronautical applications.

THE TRIPLE DECK

A schematic of the triple-deck structure is shown in figure 1.

The parameter ε = Re$^{-1/8}$ (Re - Reynolds number) has been standard-
ized in the theory because of the occurrence of various integer
powers of ε. As indicated in the figure, the streamwise extent of
the triple deck is of order ε^3, while the thicknesses of the lower,
main, and upper decks are of order ε^5, ε^4, and ε^3, respectively.
The dominant physical processes for large Re in each of the decks
are as follows:

(1)   The main deck is the continuation of the upstream
      boundary layer. It is essentially inviscid because of
      the short length (ε^3) of the interaction region. A slip
      velocity is produced at the base of the main deck by the
      pressure interaction.

(2)   The lower deck is a viscous sublayer in which the slip
      velocity at the base of the main deck is reduced to zero
      at the wall. Because it is thin, the lower deck flow is
      governed by the boundary-layer equations. However, the
      condition of matching to the upper deck provides an un-
      conventional boundary condition on these equations.

(3)   The upper deck is a subregion of the outer potential
      flow where the pressure adjusts to the streamline dis-
      placement produced by the viscous flow below, thus com-
      pleting the interaction process. For supersonic flow,
      the upper deck equations of motion reduce to the classi-
      cal wave equation with simple-wave solutions. For sub-
      sonic flow, Laplace's equation results, with the usual
      Hilbert integrals governing the interaction between
      pressure and displacement thickness. In either subsonic
      or supersonic flow, upstream influence is permitted by
      the interaction process.

The mathematical details of triple-deck theory can be found in
references 3 through 6; we shall concentrate here on some results
of the theory.

COMPRESSION-RAMP STUDIES

Supersonic flow past a compression corner is a fundamental
problem in aerodynamics. The inviscid flow is especially simple,
with two uniform flow states divided by an oblique shock wave
originating at the corner. The classical boundary-layer problem,
however, has no solution since the upstream boundary layer is ter-
minated by the infinitely adverse pressure gradient associated
with the corner. Experimental observations show that the actual
pressure rise does not occur discontinuously as inviscid theory
predicts, but instead is smeared out over some interaction dis-
tance, with boundary-layer separation occurring ahead of the

corner. This problem is natural for triple-deck theory, and solutions taken from references 7 and 8 are shown in figure 2. Here P, X, and α are scaled variables representing the pressure p^*, distance from the corner x^*, and ramp angle α^*:

$$p^* = p^*_\infty + \rho^*_\infty u^{*2}_\infty Re^{-1/4} C^{1/4} \lambda^{1/2} (M^2_\infty - 1)^{-1/4} P(X)$$

$$x^*/L = Re^{-3/8} C^{3/8} \lambda^{-5/4} (M^2_\infty - 1)^{-3/8} (T_W/T_\infty)^{3/2} X$$

$$\alpha^* = Re^{-1/4} C^{1/4} \lambda^{1/2} (M^2_\infty 1)^{1/4} \alpha$$

The Reynolds number Re is based on conditions in the undisturbed inviscid flow ahead of the ramp (indicated by subscript ∞) and on the length L from leading edge to corner. C denotes the Chapman-Rubesin constant and λ is the Blasius constant (0.33206). ρ, u, T, and M are the usual symbols for density, velocity, temperature and Mach number.

The results of figure 2 show a smooth monotonically rising wall pressure for α below the value for incipient separation, $\alpha_i = 1.57$. (Note that classical theory would predict separation for any $\alpha^* > 0$). For α increasing above α_i, an inflection point appears and rapidly forms the pressure plateau observed in many experiments. The plateau pressure level is in close agreement with Williams value P = 1.8 for self-induced separation (ref. 9), corresponding to an obstacle far downstream of separation. In figure 2, the initial pressure distribution up to the plateau level is pushed upstream with invariant shape as α increases. This portion of the pressure distribution reproduces Williams' free-interaction solution, suggesting that as $\alpha \to \infty$ (α^* increasing beyond the $Re^{-1/4}$ scale) the separation point is pushed upstream to infinity (the interaction length exceeds the $Re^{-3/8}$ scale). In turn, this suggests that for large α (α^* beyond the $Re^{-1/4}$ scale), the separation region up to the plateau is still contained in the triple-deck structure, but that the constant pressure plateau and subsequent reattachment region develop on different scales.

An analysis of the flow structure based on these ideas is given in reference 10. The principal results are as follows. For ramp angle α^* of order one, the separation bubble is long, of the order of the distance L from leading edge to corner in length. The reattachment process is short, however, with length of the order of the boundary-layer thickness (i.e., of order $Re^{-1/2}$). Because of its small scale, reattachment is predominantly inviscid in nature, much as hypothesized by Chapman (ref. 11). Hence, the asymptotic analysis for large Reynolds number reveals the separating-reattaching flow to be three coupled but distinct regions: the separation region with length $O(L \ Re^{-3/8})$, in which the pressure rises to the plateau level (P = 1.8); the plateau region of constant pressure with length $O(L)$; and the reattachment region

with length $O(L\ Re^{-1/2})$, in which the pressure rises from the plateau level to its final value with mainstream parallel to the ramp.

Figure 3 illustrates results of computations based on the above asymptotic theory. The experimental data are taken from reference 12. The flow conditions were $M_\infty = 2.55$, $Re_\infty = 200{,}000$ based on the distance L from leading edge to corner. This comparison shows that the pressure levels predicted by the theory are very good, although the initiation of the pressure rise is predicted somewhat early. For comparison, it may be noted that momentum-integral interaction theories exhibit a similar uncertainty in the point of initiation of the pressure rise, which is usually chosen to best agree with experiment. A similar adjustment of the theory could be made in figure 3 by means of an arbitrary origin shift in the asymptotic formulas.

A composite theory for finite Reynolds number is provided by the compressible boundary-layer equations coupled with a pressure-displacement condition. This set of equations includes all the terms from the Navier-Stokes equations that are included in the governing equations for each of the three regions identified by the asymptotic theory. A finite-difference algorithm of these interacting boundary-layer equations has been programmed by Werle and Vatsa (ref. 13). Their experience has shown that at high Reynolds numbers, accurate solutions can be obtained only by choosing the mesh size smaller than the length scales given by triple-deck theory, and in that case, the interacting boundary-layer solutions asymptote the triple-deck results for very large Reynolds numbers (ref. 8). As indicated in figure 4, at lower Reynolds numbers of practical interest, the interacting boundary-layer solutions agree quite well with both experimental data (ref. 14) and with solutions of the Navier-Stokes equations (ref. 15). The flow conditions were adiabatic with $M_\infty = 4$, $Re_\infty = 68{,}000$ based on distance to the corner. The presence of the plateau "kink", present in both the experimental data and Navier-Stokes solutions, but not evident in the interacting boundary-layer results, is caused by the sharp corner which was slightly rounded in the modelling of Werle and Vatsa. Otherwise the agreement is excellent, and it can be concluded that the interacting boundary-layer theory models weakly separated flows with accuracy satisfactory for engineering purposes. It should be noted, however, that the asymptotic theory indicates that normal pressure gradients, not present in the boundary-layer model, become important near reattachment when the separation bubble is large.

TRAILING EDGE STUDIES

Another area of importance in aerodynamics is the problem of

viscous interaction at a trailing edge. The sudden change-over from the no-slip condition on the airfoil surface to the wake-continuity condition produces a significant viscous modification to the flow near the trailing edge, even for a flat plate at zero incidence. For the airfoil at incidence, lift is reduced due to viscous alteration of the Kutta condition. For unsteady motion, viscous phase effects may alter flutter boundaries. All these problems have been treated using triple-deck theory.

A schematic of the triple-deck structure is given in figure 5 for the case of an airfoil at zero incidence. The triple deck on the upper surface is reflected symmetrically below the airfoil. In classical boundary-layer theory, the viscous correction to the potential flow would produce a singularity in the pressure at the trailing edge, owing to the singular slope of the displacement thickness produced by the abrupt change of viscous boundary condition at the trailing edge. The coupling of pressure and displacement in the viscous-interaction theory eliminates this singularity. The fundamental trailing-edge problem of the flat plate at zero incidence has been solved independently by Jobe and Burggraf (ref. 16), by Veldman and van de Vooren (ref. 17), and by Melnik and Chow (ref. 18), all for incompressible flow. In addition, the same problem for supersonic flow has been treated by Daniels (ref. 19). A summary of the results is presented in figure 6, taken from reference 16. Here X is the triple-deck scaled-longitudinal coordinate, with X = 0 taken at the trailing edge, and P is the scaled pressure, both defined as before but with the Mach number factor, temperature ratio and Chapman-Rubesin constant deleted. A is a scaled (negative) displacement thickness, proportional to $Re^{-5/8}$.

The principal results indicated in figure 6 are the pressure fall as the flow is accelerated toward the trailing edge, and the accompanying rise of skin friction to a trailing-edge value nearly 35% greater than the Blasius value. Downstream of the trailing edge, the rapidly rising pressure overshoots the freestream value (P = 0) and then slowly decays for large X. The theoretical drag coefficient, also given in figure 6, compares amazingly well with both experimental data ($10 \leq Re \leq 10,000$), with RMS error of 3.5 percent over the range of the experimental data, and an error of 8 percent at Re = 1 and only 2 percent at Re = 15 when compared with the Navier-Stokes solutions.

The theoretical wake-velocity profile (ref. 18) is compared with experimental data (ref. 20) in figure 7. The centerline value predicted by Goldstein's non-interacting theory is shown for comparison. Transition to turbulence was observed to begin at a station coinciding with the maximum of the induced pressure, indicated in the figure, suggesting that viscous interaction may be important in predicting transition in wakes.

The case of an airfoil at angle of attack is more difficult to treat, as the upper and lower triple decks are no longer symmetrical. This problem has been solved for the supersonic case by Daniels (ref. 21), and very recently for the incompressible case by Chow and Melnick (ref. 22; see also ref. 18 for preliminary results). The flow structure is indicated in figure 8, which is now generalized to include the Stokes layers II_2 and III_2, which occur in the unsteady case only. For the steady case, regions II_1 and III_1 coincide and represent the conventional boundary layer; IV_1, IV_2, and IV_3 represent the triple deck, and regions V_1 and V_2 are the outer and inner layers of the wake as deduced by Goldstein. Viscous interaction occurs only in the triple deck, of course. Chow and Melnik carried out the flat-plate triple-deck solution for a range of angles-of-attack up to a value very near the stall limit α_s, which was estimated by extrapolating their solutions to zero shear stress on the upper surface. Below stall, the point of minimum shear stress occurs ahead of the trailing edge, but approaches the trailing edge in the stall limit. The reduction in lift coefficient due to viscous interaction is shown in figure 9. Chow and Melnik conclude that the stall is catastrophic, with $\Delta C_L \, Re^{-3/8} \to \infty$ in the double limit $Re \to \infty$, $\alpha \to \alpha_s$. However, this point is not yet definitely resolved.

The viscous flow about the trailing edge of a rapidly oscillating plate has been studied by Brown and Daniels (ref. 23). They find that to have an unsteady contribution of viscous interaction to the potential flow, the oscillation frequency, in either pitching or plunging motion, must satisfy $S = \omega^* L/u^*_\infty = 0(Re^{1/4})$ where L is the plate length. For S large, even on this scale, there results two contributions to the unsteady lift having phase leads of 45° and 90°, with similar results for the moment. Further details of the analysis may be found in reference 23.

CONCLUDING REMARKS

The examples of viscous interaction theory summarized above should give the reader some idea of the contributions being made by modern boundary-layer theory that were not possible in classical theory. Many other examples could be given, such as leading edge separation bubbles, mass injection effects, swept configurations, and more, but space does not permit further discussion here. It is hoped that the reader has gained some appreciation for the potential of this rapidly expanding field of study.

REFERENCES

1. Crocco, L., and Lees, L.: J. Aero. Sci., Vol. 19, 1952, p. 649.

2. Lees, L., and Reeves, B.: AIAA J., Vol. 2, 1964, p. 1907.

3. Stewartson, K., and Williams, P. G.: Proc. Roy. Soc. A, Vol. 312, 1969, pp. 181-206.

4. Neiland, V.: Izv. Akad. Nauk SSSR, Mekh. Zhidk. Gaza, No. 4, 1969, p. 40.

5. Stewartson, K.: Mathematika, Vol. 16, 1969, p. 106.

6. Messiter, A. F.: SIAM J. Appl. Math., Vol. 18, 1970, p. 241.

7. Jenson, R., Burggraf, O. R., and Rizzetta, D.: Proc. 4th Int. Conf. on Numerical Methods in Fluid Dynamics, Lecture Notes in Physics, Vol 35, Springer-Verlag, 1975, p. 218.

8. Rizzetta, D.: Asymptotic Solution for Two-Dimensional Viscous Supersonic and Hypersonic Flows past Compression and Expansion Corners, Ph.D. Dissertation, Ohio State Univ., June 1976.

9. Williams, P. G.: Proc. 4th Int. Conf. on Numerical Methods in Fluid Dynamics, Lecture Notes in Physics, Vol. 35, Springer-Verlag, 1975, p. 445.

10. Burggraf, O. R.: Proc. AGARD Symp. on Flow Separation, held in Göttingen, Germany, AGARD-CP-168, 1975.

11. Chapman, D. R., Kuehn, D., and Larsen, H.: NACA Rep. 1356, 1958.

12. Nielsen, J., Lynes, L., and Goodwin, F.: USAF FDL TR-65-107, 1965.

13. Werle, M. J., and Vatsa, V. N.: AIAA J., Vol. 12, 1974, pp. 1491-1497.

14. Lewis, J. E., Kubota, T., and Lees, L.: AIAA J. Vol. 6, 1968, pp. 7-14.

15. Carter, J. E.: NASA TR-R-385, 1972.

16. Jobe, C. E., and Burggraf, O. R.: Proc. Roy. Soc. A, Vol. 340, 1974, pp. 91-111.

17. Veldman, A.E.P., and van de Vooren, A. I.: Proc. 4th Int. Conf. on Numerical Methods in Fluid Dynamics, Lecture Notes in Physics, Vol. 35, Springer-Verlag, 1975, p. 423.

18. Melnik, R. E., and Chow, R.: NASA SP-347, 1975.

19. Daniels, P. G.: Quart, J. Mech. Appl. Math., Vol. 27, pt. 2, May 1974, pp. 175-191.

20. Sato, H., and Kuriki, K.: J. Fluid Mech., Vol. 11, pt. 3, 1961, pp. 321-352.

21. Daniels, P. G.: J. Fluid Mech., Vol. 63, pt. 4, 1974, pp. 641-656.

22. Chow, R., and Melnik, R. E.: Proc. 5th Int. Conf. on Numerical Methods in Fluid Dynamics, Lecture Notes in Physics, Springer-Verlag, 1977.

23. Brown, S. N., and Daniels, P. G.: J. Fluid Mech., Vol. 67, pt. 4, 1975, pp. 743-761.
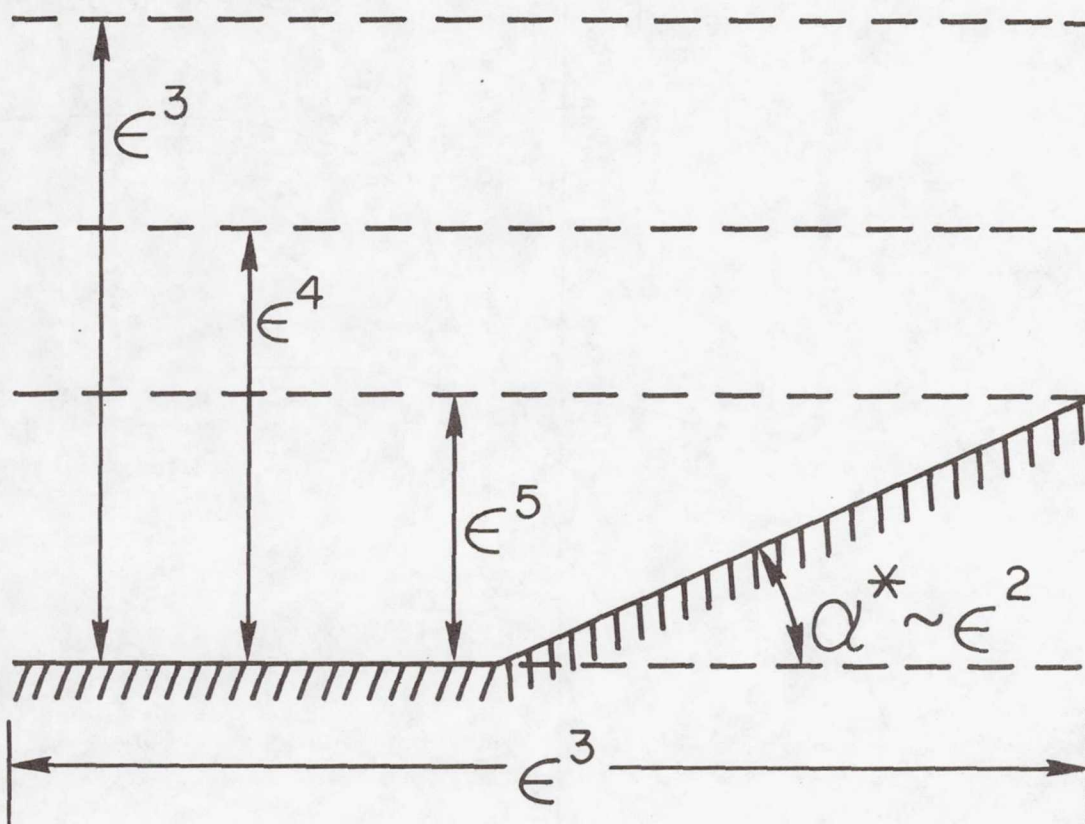
Figure 1.- Schematic of triple deck.
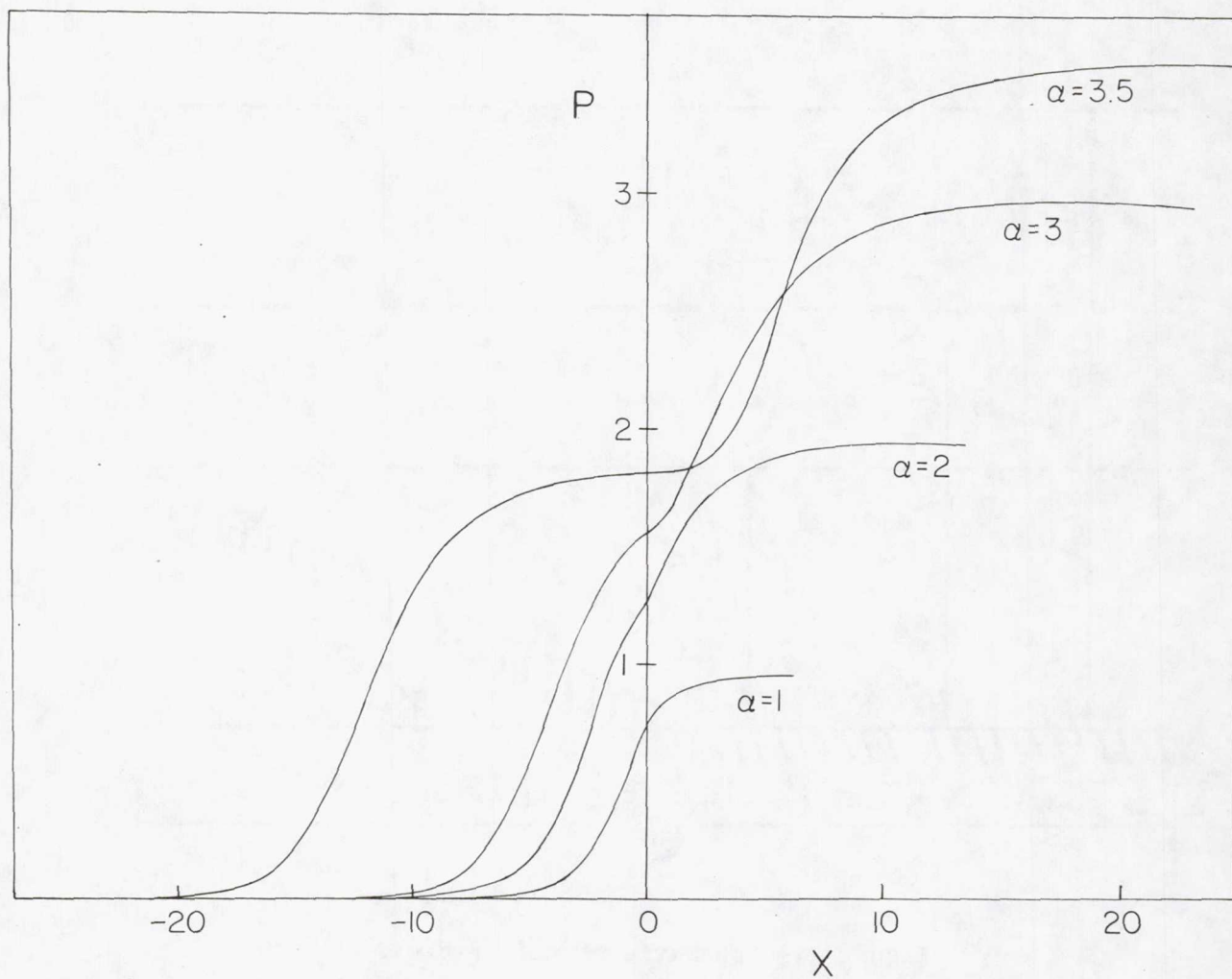
Figure 2.- Compression-ramp pressure distribution.
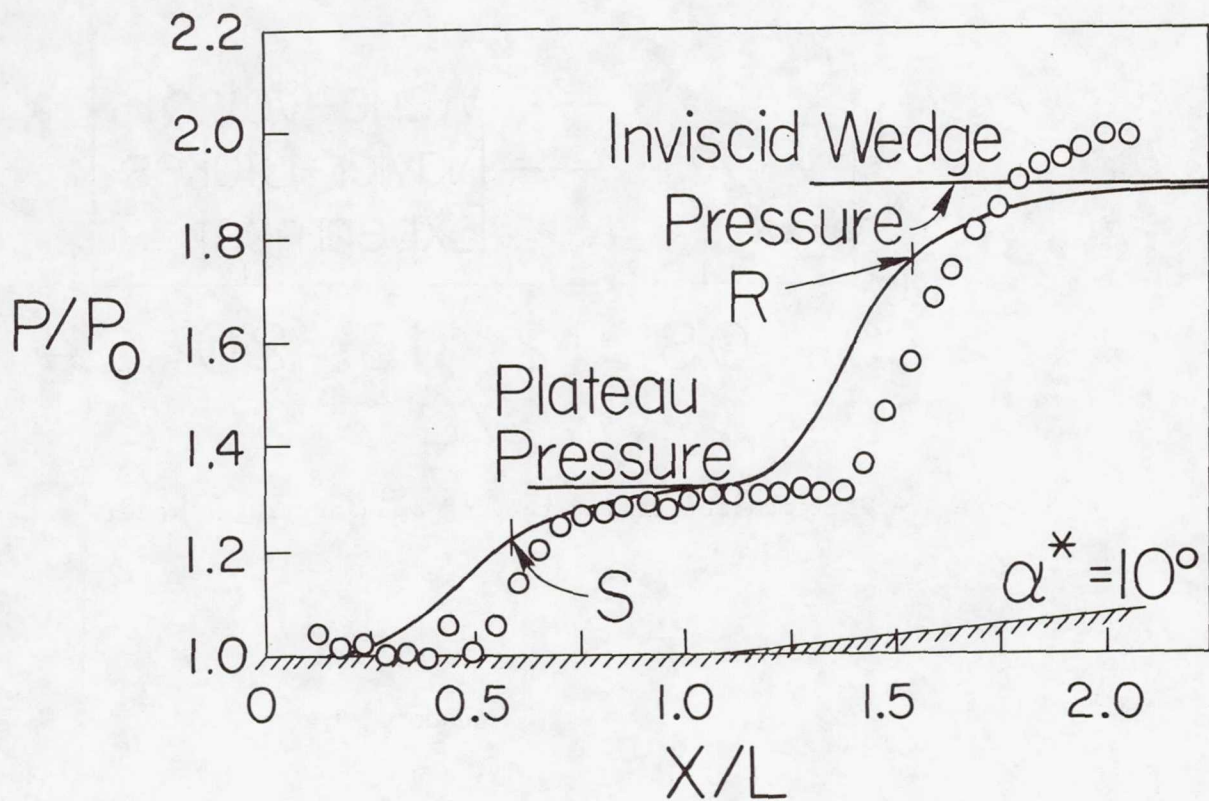
Figure 3.- Comparison of large α theory with experiment.
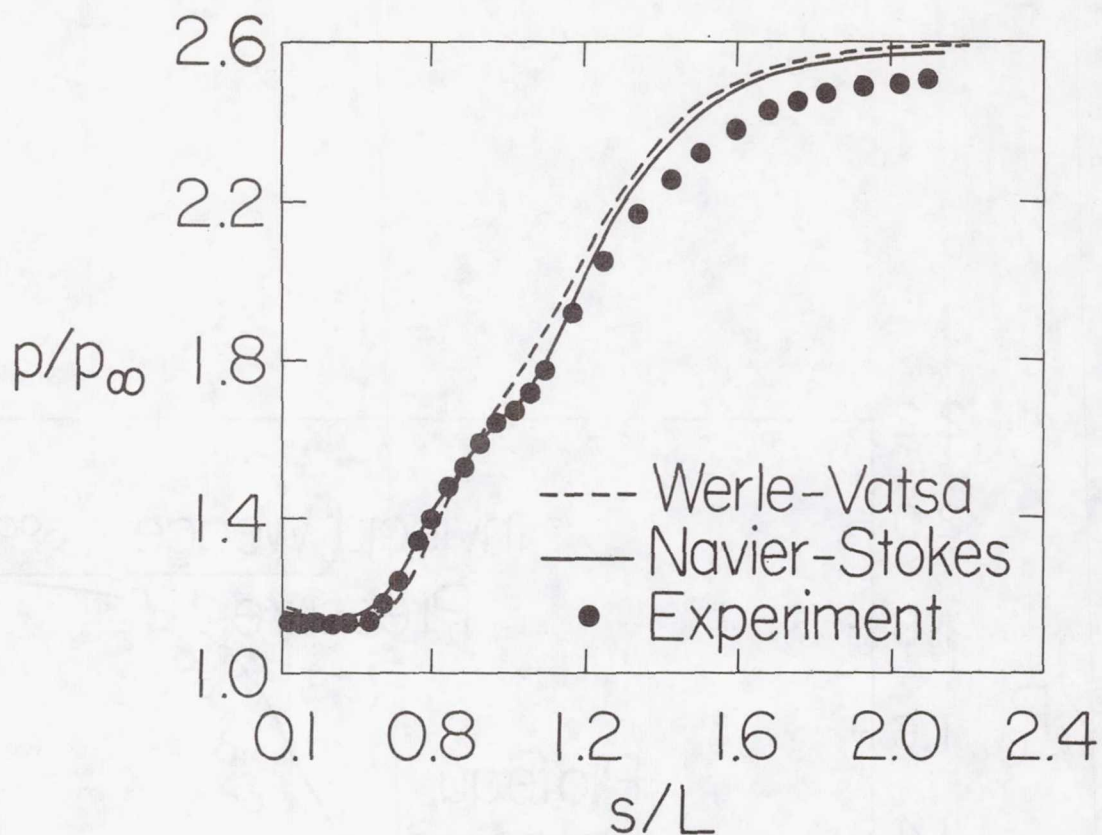
Figure 4.- Verification of interacting boundary layer model.

Notation : U – Upper Deck
            M – Middle Deck
            L – Lower Deck
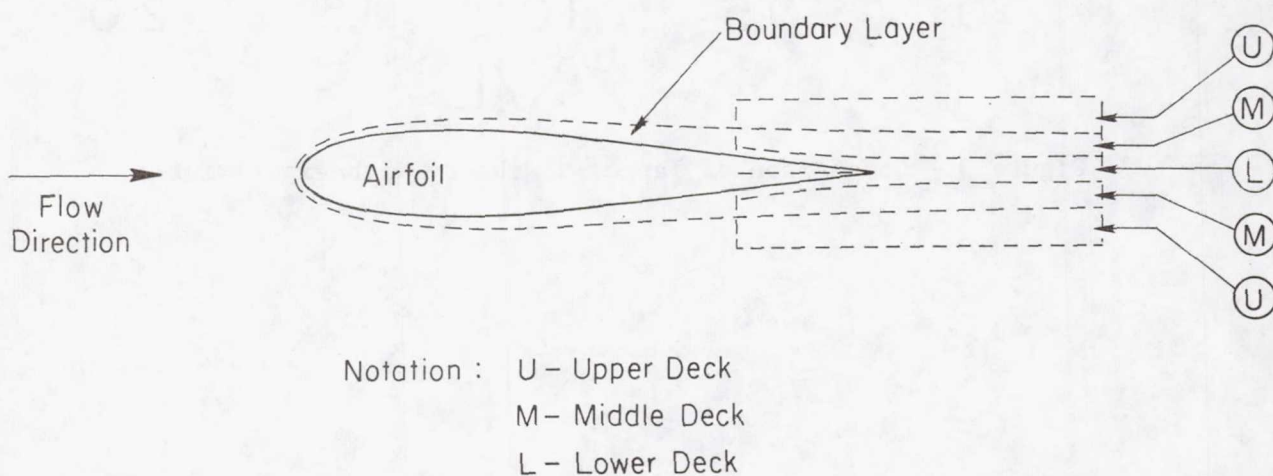
Figure 5.- Triple deck at trailing edge of airfoil.
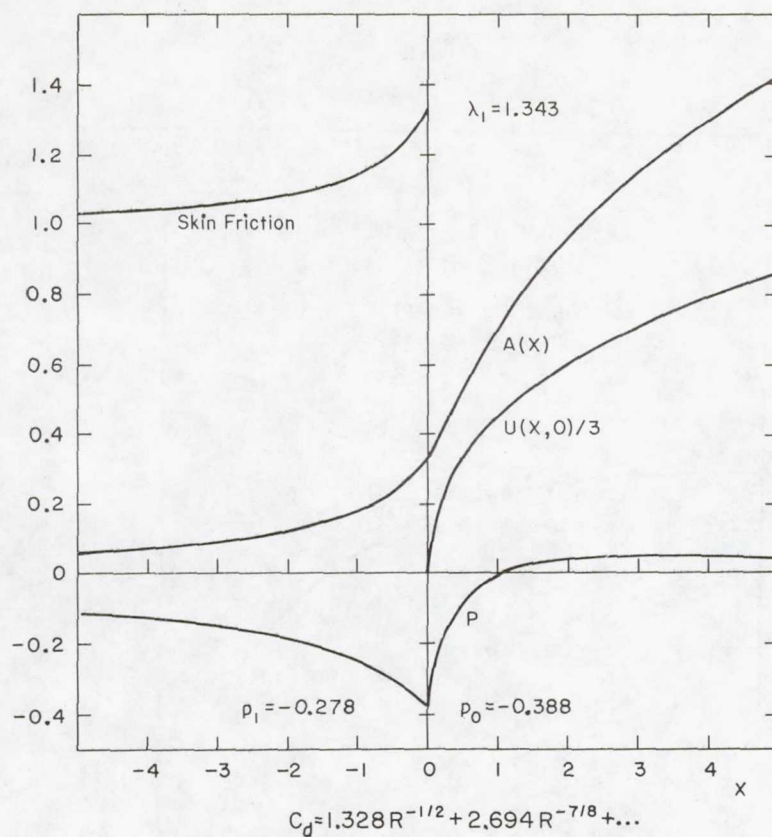
Figure 6.- Summary of trailing edge results.
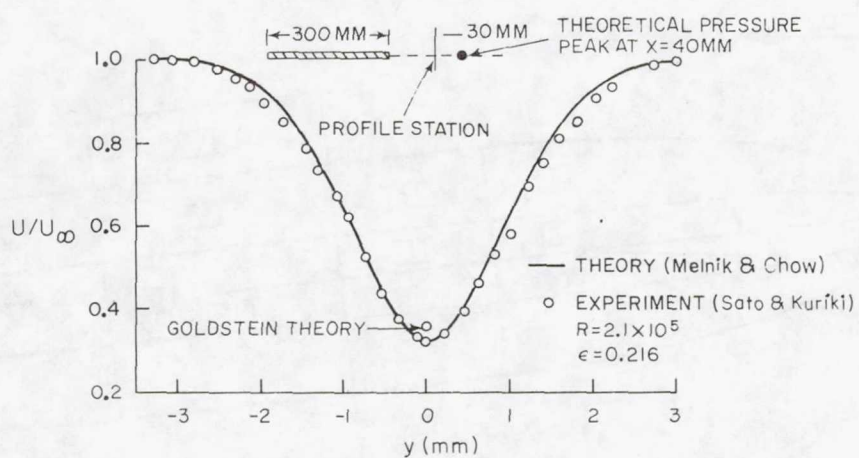
Figure 7.- Wake-velocity profile: theory vs. experiment.

1449
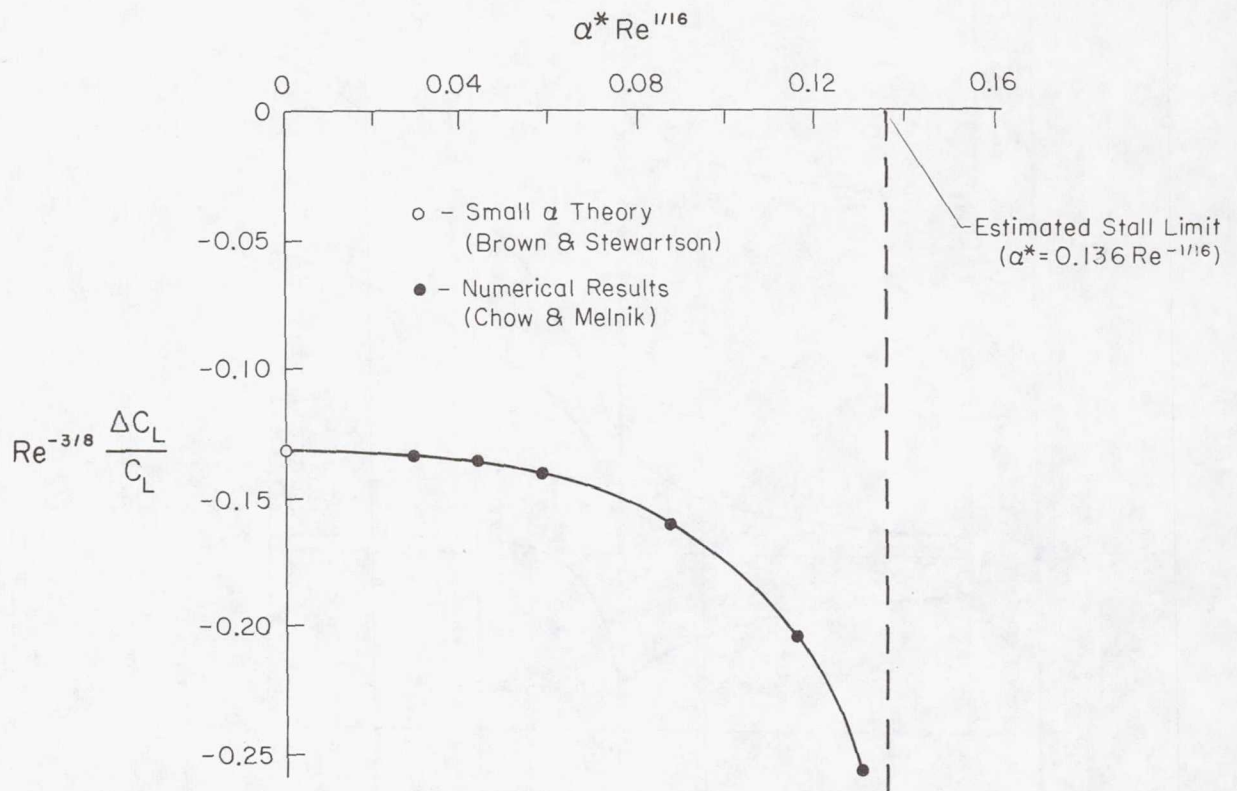
Figure 8.- Viscous correction to kutta condition for laminar flow.
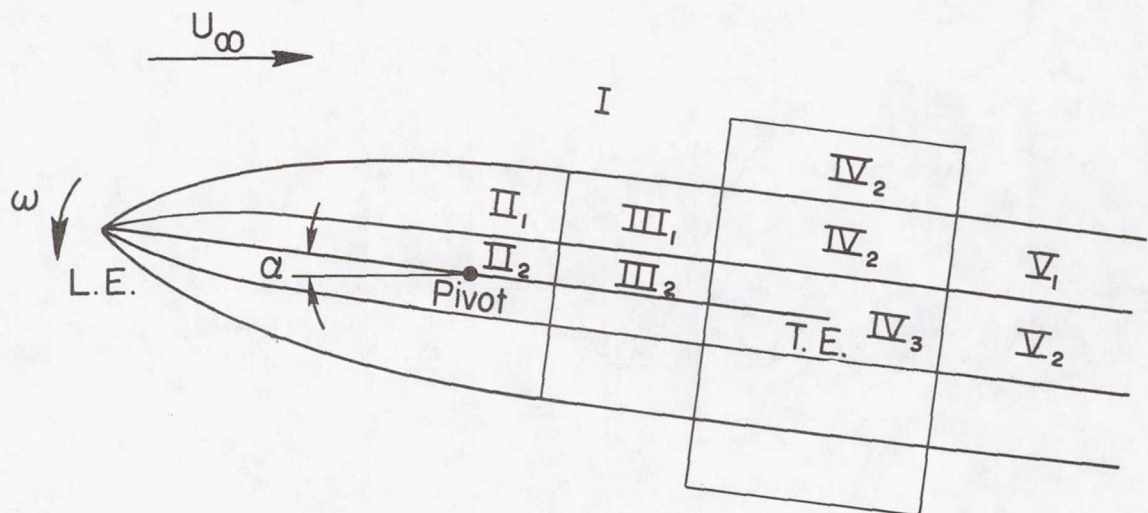
Figure 9.- Limit flow structure for oscillating plate.

NUMERICAL AND APPROXIMATE SOLUTION OF THE
HIGH REYNOLDS NUMBER SMALL SEPARATION PROBLEM[†]

R.T. Davis
University of Cincinnati

SUMMARY

The purpose of this paper is to explore several possible methods of solving the small separation problem at high Reynolds number. In addition to using analytical methods, there are several numerical approaches which can be used and in addition there is the possibility of using approximate integral methods. We will restrict ourselves to high Reynolds number laminar two-dimensional problems for simplicity. Presumably, the same techniques can be extended to more complicated flow fields. Only a brief discussion will be given of the finite difference methods since these methods are discussed in detail by Davis and Werle (ref. 1). Most of the emphasis will be placed on developing an approximate integral method. As a model problem we will choose the supersonic compression ramp problem since several numerical solutions along with experimental data are available for this case. The techniques discussed can be modified and applied to other similar type wall geometries.

INTRODUCTION

It has been recognized for many years that the problem of computing high Reynolds number separated flows is extremely difficult. The reason for the difficulty becomes clear if one examines the results of the asymptotic theory, see Stewartson (ref. 2). Davis and Werle (ref. 1) have discussed the implications of these results and suggested how one might use the results of the asymptotic analysis in order to do efficient numerical computations.

Briefly, the asymptotic theory reveals that at high Reynolds number severe scaling problems exist around and downstream of separation. In addition the asymptotic theory for the small separation problem reveals a mechanism for upstream propagation through boundary-layer interaction, even if the external flow is supersonic. These two features require that an efficient numerical scheme use properly scaled independent variables for resolution and in addition require that the boundary-layer interaction be handled in a manner appropriate to boundary value problems. These features should be accounted for even in the solution of the full Navier-Stokes equations.

The asymptotic theory is partially complete for some massive separation problems, see Messiter (ref. 3) for example, and the results indicate that numerical solutions will be extremely difficult to perform for this type of problem. On the other hand, the theory for the small separation problem is essentially complete, see Stewartson (ref. 2), and we can now begin to compute flows of this type with confidence. For the remainder of this paper we will therefore concentrate on the type of problem where separation is of limited extent and can be handled within the framework of boundary-layer theory.

According to the asymptotic theory, we may define a small separation problem to be one such that the scales of a bump or depression on a flat plate are the same as the length scales of the lower deck in the triple deck analysis, see Stewartson (ref. 2). This requires that the length of the bump or depression generating the separation scale as $Re^{-3/8}$ while the height must scale as $Re^{-5/8}$. If this is true, the separated region will be entirely confined to the lower (fundamental) deck and the high Reynolds number separation problem can be attacked entirely with the lower deck equations coupled with an interaction law for the outer inviscid flow. This is the approach taken by Jenson, Burggraf, and Rizzetta (ref. 4) and Rizzetta (ref. 5) in considering supersonic ramp type separations. Smith (ref. 6) has in addition solved the linear version of the small separation problem for flow over protuberances.

As an alternative, for the same type of separation problems, one may solve the ordinary Prandtl boundary-layer equations including interaction with the outer inviscid flow. It can be shown that these equations contain all of the terms in the triple deck equations plus some additional ones. The extra terms in fact provide some corrections which allow better agreement with experiment at moderately high Reynolds numbers. This is the approach taken by Werle and Vatsa (ref. 7) and Vatsa (ref. 8) in considering supersonic ramp type separations.

The supersonic ramp separation problem has also been solved by Carter (ref. 9) and others using the full Navier-Stokes equations. These calculations provide a basis for comparison with other less exact models of separation.

The high Reynolds number small separation problem may therefore be approached in a variety of ways. The most complicated method would involve the solution of the full Navier-Stokes equations. Next in complexity would be to solve interacting boundary-layer like equations or one of the sets of so-called parabolized Navier-Stokes equations. The simplest set of equations one could solve and retain all of the features of the flow would be the triple deck equations.

If one wishes to do for example a full Navier-Stokes calculation for flow over a complicated configuration one may not wish to provide the mesh refinements in small separated regions as is indicated as being necessary by the asymptotic theory. These regions can be excluded from the overall calculation and accounted for by a local calculation. This local calculation can then provide a slip type boundary condition on the edge of the small separated region. Thus by excluding the small separation bubble and replacing it with a slip type boundary condition, the overall calculation can be made accurately with a much larger mesh size than would be required if the separated bubble were included.

One important application of triple deck theory could thus be to provide local solutions in small separated regions to match into an overall calculation. It therefore seems important that we be able to solve the triple deck equations in as efficient a manner as possible.

The simplest and therefore fastest type of approximate solutions to the boundary-layer equations are obtained with integral methods. To test the applicability of the integral technique to triple deck theory, we will develop an integral method for solving the lower deck equations and compare solutions obtained from this method with more exact solutions. This is perhaps the fastest method for solving the small separation problem if one is willing to accept the inaccuracies associated with an approximate integral method. The method is attractive for doing local calculations, especially if one considers that the errors obtained from the integral method would probably be much smaller than those which would exist from a course mesh finite difference calculation which might be used as an alternative.

GOVERNING EQUATIONS FOR SMALL SEPARATIONS

The small separation problem is by definition a separation generated by a bump or depression on a flat plate such that the scaling of the bump or depression is the same as that given by the lower deck analysis of Stewartson (ref. 2). Thus such a bump or depression scales as ε^3 in the streamwise direction and ε^5 in the normal direction, as $\varepsilon \to 0$, where $\varepsilon = Re^{-1/8}$. Such a bump or depression generates an interaction which falls within the framework of triple deck analysis and the problem can thus be handled by solving the lower deck equations coupled with an interaction law.

In the lower deck variables defined by equations (4.4) in Stewartson (ref. 2), the small separation problem is governed by the following equations, see figure 1

$$\frac{\partial u}{\partial x} + \frac{\partial v}{\partial y} = 0 \quad , \tag{1}$$

and

$$u \frac{\partial u}{\partial x} + v \frac{\partial u}{\partial y} = -\frac{dP}{dx} + \frac{\partial^2 u}{\partial y^2} \quad , \tag{2}$$

with boundary and matching conditions

$$u = v = 0 \quad \text{at} \quad y = f(x) \quad , \tag{3}$$

$$u \sim y - f(x) - \delta(x) \quad \text{as} \quad y \to \infty \quad , \tag{4}$$

and

$$\delta(\pm \infty) = 0 \quad . \tag{5}$$

According to linear theory the interaction law is given by

$$P = f'(x) + \delta'(x) \qquad \qquad \text{for supersonic flow} \tag{6}$$

or

$$P = -\frac{1}{\pi} \int_{-\infty}^{\infty} \frac{f'(x_1) + \delta'(x_1)}{x - x_1} dx_1 \qquad \text{for subsonic flow.} \tag{7}$$

The quantity $f(x)$ denotes the dimensionless surface measured from the Cartesian coordinate system on the flat plate surface and δ is the dimensionless displacement thickness. Both of these quantities are nondimensionalized in the same manner as the y coordinate.

In order to solve the lower deck equations, it is convenient to shift the coordinate system such that the body surface lies along a constant coordinate curve. This can be accomplished with the use of Prandtl's transposition theorem, see Jenson, Burggraf, and Rizzetta (ref. 4) for example.

With the change of variables

$$z = y - f(x) \tag{8}$$

and

$$w = v - \frac{df}{dx} u \tag{9}$$

and all other variables remaining unchanged we obtain from equations (1)-(4)

$$\frac{\partial u}{\partial x} + \frac{\partial w}{\partial z} = 0 \quad , \tag{10}$$

$$u \frac{\partial u}{\partial x} + w \frac{\partial u}{\partial z} = -\frac{dP}{dx} + \frac{\partial^2 u}{\partial z^2} \quad , \tag{11}$$

$$u = w = 0 \quad \text{at} \quad z = 0 \quad , \tag{12}$$

and

$$u \sim z - \delta(x) \quad \text{as} \quad z \to \infty \quad . \tag{13}$$

The remaining equations (5)-(7) are unchanged by the transformations.

1454

INTEGRAL FORMULATION FOR THE LOWER DECK EQUATIONS

The lower deck equations (10)-(13) and (5)-(7) can be put into a form similar to the von Karman momentum integral equation for two-dimensional boundary layers. The advantage in doing this is that a simple approximate solution technique can be developed for the lower deck equations along the same lines as approximate solution methods for non-interacting boundary layers.

First let $z \to \infty$ in the momentum equation (11) and substitute the outer edge condition for u given by equation (13). This results in

$$v \sim (z - \delta)\delta' - P' \qquad \text{as} \qquad z \to \infty \quad . \tag{14}$$

Next integrate the continuity equation (10) with respect to z to find another expression for v as $z \to \infty$. Thus results in

$$v \sim \delta' z - \frac{d}{dx} \int_O^\infty (u-U_e)dz \qquad \text{as} \qquad z \to \infty \tag{15}$$

where we have defined U_e as

$$U_e = z - \delta \quad . \tag{16}$$

Equating the two expressions for v as $z \to \infty$ from equations (14) and (15) we find

$$\delta\delta' + P' = \frac{d}{dx} \int_O^\infty (u-U_e)dz \quad . \tag{17}$$

Integrating this expression with respect to x and using the condition that all quantities in the equation die out as $x \to -\infty$ we obtain

$$\frac{\delta^2}{2} + P = \int_O^\infty (u - U_e)dz \quad . \tag{18}$$

We next integrate the momentum equation (11) with respect to z from z equals zero to infinity. After some fairly straightforward algebra, this results in

$$\frac{d}{dx} \int_O^\infty (u^2 - U_e^2)dz + \delta \frac{dD}{dx} = 1 - u_z(x,0) \quad . \tag{19}$$

We therefore have three integral quantities which must be evaluated. The displacement thickness δ, from equation (13) can be written as

$$\delta = \int_O^\infty (1 - \frac{\partial u}{\partial z})dz \quad . \tag{20}$$

The remaining two integral quantities are defined as

$$D = \int_0^\infty (u - U_e)dz \tag{21}$$

and

$$M = \int_0^\infty (u^2 - U_e^2)dz \quad . \tag{22}$$

With these definitions the equations (18) and (19) become

$$\frac{\delta^2}{2} + P = D \tag{23}$$

and

$$\frac{dM}{dx} + \delta \frac{dD}{dx} = 1 - \tau_w \tag{24}$$

where

$$\tau_w = u_z(x,0) \quad . \tag{25}$$

The simplest possible approximate solution method to the integral equations (23) and (24) is to assume a linear shear profile of the following form

$$\frac{\partial u}{\partial z} = \tau_w + (1 - \tau_w) \frac{z}{\ell(x)} \qquad \text{for} \qquad z \leq \ell$$

and $\tag{26}$

$$\frac{\partial u}{\partial z} = 1 \qquad \text{for} \qquad z > \ell$$

where $\ell(x)$ is the boundary-layer thickness function. Substituting the above equations into equation (20) results in

$$\delta = (1 - \tau_w) \frac{\ell}{2} \quad . \tag{27}$$

Integrating equation (26) results in a parabolic velocity profile of the form

$$u = \tau_w z + (1 - \tau_w) \frac{z^2}{2\ell} + C(x) \qquad \text{for} \qquad z \leq \ell$$

and $\tag{28}$

$$u = U_e = z - \delta \qquad \text{for} \qquad z > \ell \quad .$$

We choose to satisfy the conditions that $u = 0$ and $z = 0$ and $u = U_e$ at $z = \ell$. The first condition results in $C(x) = 0$ and the second reproduces equation (27). Thus the velocity profile is given by

$$u = \tau_w z + (1 - \tau_w) \frac{z^2}{2\ell} \qquad \text{for} \qquad z \leq \ell$$

and   (29)

$$u = z - \delta \qquad \text{for} \qquad z > \ell \; .$$

This profile satisfies the no slip condition, is continuous and
has a continuous first derivative at $z = \ell$.

    Using the above velocity profile, the expression (21) for D
gives

$$D = \frac{\ell \delta}{3}$$ (30)

while the expression (22) for M gives

$$M = \frac{\ell^2 \delta}{6} - \frac{7}{15} \ell \delta^2 \; .$$ (31)

Substituting these expressions into the integral equations (18)
and (19) gives

$$P = \frac{\ell \delta}{3} - \frac{\delta^2}{2}$$ (32)

and

$$\frac{d}{dx} \left[\frac{\ell^2 \delta}{6} - \frac{7}{15} \ell \delta^2 \right] + \delta \frac{d}{dx} \left[\frac{\ell \delta}{3} \right] = \frac{2\delta}{\ell} \; .$$ (33)

    In order to close the problem, equation (6) or equation (7)
for P is used depending upon whether the flow is supersonic or
subsonic. Initial and downstream boundary conditions are pre-
scribed in the form of equation (5).

    The integral formulation therefore results in the solution of
two nonlinear first-order ordinary differential equations for ℓ
and δ for the supersonic case and the solution of one nonlinear
integral equation and one nonlinear first-order ordinary differ-
ential equation for the subsonic case.

    The present choice of profile shapes is the simplest possible.
However, more complicated profiles can easily be chosen. The pur-
pose of the present analysis is to show how an integral method
may be formulated without paying attention at this point in time
to accuracy of the method.

    We can easily find an approximate solution corresponding to
Lighthill's (ref. 10) analysis of the initiation of a free inter-
action process in supersonic flow. If we consider the possible
emergence of a sublayer at a point x_p^* on a flat plate, see Ste-
wartson (ref. 2), we can study the initiation of the sublayer
using the linearized version of equations (32) and (33). For
supersonic flow, if we consider δ to be small, these equations
result in

$$\frac{d\delta}{dx} = \frac{\ell \delta}{3}$$ (34)

and

$$\frac{d}{dx} \left(\frac{\ell^2 \delta}{6}\right) = \frac{2\delta}{\ell} \tag{35}$$

Dividing the first equation by the second and integrating, it is easy to show that the approximate solution corresponding to Lighthill's exact solution is

$$\ell = \sqrt{6} \tag{36}$$

and

$$\delta = \delta_o e^{kx} \tag{37}$$

where

$$k = \frac{\sqrt{6}}{3} = 0.8165 \quad . \tag{38}$$

The approximate value of k given by this analysis compares favorably with the exact value of 0.8272 given by Lighthill's analysis. From the expression (27) and the linear version of (32), assuming $\ell = \sqrt{6}$, δ can be eliminated to give

$$\tau_w = 1 - P \tag{39}$$

which also compares favorably with $\tau_w = 1 - 1.209P$ given by Lighthill's analysis.

Next we consider the case of compressive free interactions, see Stewartson and Williams (refs. 11 and 12), Stewartson (ref. 2) and Williams (ref. 13). The full approximate equations (32) and (33) for supersonic flow, i.e. $P = d\delta/dx$, were integrated numerically using a fourth-order Runge Kutta method.* The results were adjusted such that the zero shear point occurs at x = 0 in order to compare with Stewartson and William's results, see Stewartson (ref. 2) and Williams (ref. 13).

Figure 2 shows that the approximate results agree quite favorably up to and through the separation point. Far downstream of separation the approximate results produce a shear which asymptotically approaches -1/3 rather than zero from the exact results and a pressure which goes to zero rather than 1.800 [see Williams (ref. 13)] from the exact results. These deficiencies are due to the complicated nature of the lower deck free interaction solution as $x \to \infty$, see Williams (ref. 13). A more elaborate and physically meaningful assumption for a shear profile to handle the region for large x should overcome this deficiency. However, it is important to note that the present approximate integral method preserves the qualitative features of the exact results, except when the interaction region is too long.

---

* The author wishes to express thanks to Mr. S. Khullar for performing these and later calculations using the integral method.

1458

As a final example of the application of the approximate method, we consider flow past a compression ramp. Exact numerical solutions have been provided to the lower deck equations for this problem by Jenson, Burggraf and Rizzetta (ref. 4) and Rizzetta (ref. 5).

Consider supersonic flow along a flat plate which abruptly encounters a wedge type compression ramp. Jenson, Burggraf and Rizzetta (ref. 4) have considered the formulation and numerical solution of this problem within the framework of triple deck analysis. In terms of their formulation, the appropriate problem to be solved with the approximate set of equations is given by equations (32) and (33) with the supersonic interaction law (6) given by

$$P = \frac{d\delta}{dx} \qquad \text{for} \quad x < 0$$

and $\qquad\qquad\qquad\qquad\qquad\qquad\qquad\qquad\qquad\qquad\qquad\qquad\qquad$ (40)

$$P = \frac{d\delta}{dx} + \bar{\alpha} \qquad \text{for} \quad x \geq 0$$

where $\bar{\alpha}$ is related to the physical angle α through

$$\alpha = \lambda^{1/2} \left[\frac{C(M_\infty^2 - 1)}{Re} \right]^{1/4} \bar{\alpha} \quad . \qquad\qquad (41)$$

The governing equations were again integrated using a fourth-order Runge Kutta method. The initial conditions were applied at $x = -20$ with $\ell = \sqrt{6}$. A shooting method was used to find the correct initial condition on δ at $x = -20$ to produce a δ which goes to zero as $x \to \infty$. The solutions branch as downstream infinity is approached and therefore become very sensitive to initial guess. A more appropriate way to solve the problem is to recognize that it is boundary value in nature and therefore solve it as a time relaxation process using central differences on all of the space variables. This type of technique has been used by Werle and Vatsa (ref. 7) to solve the interacting boundary-layer equations.

Figures 3 and 4 show the results for pressure and wall shear as a function of the reduced angle $\bar{\alpha}$. Rizzetta (ref. 5) has presented exact numerical results for the same problem. For small $\bar{\alpha}$ there is good agreement between the present results and those of Rizzetta. A direct comparison is given for $\bar{\alpha} = 2.5$. The comparison between the present results and Rizzetta's becomes poorer as $\bar{\alpha}$ increases. This is at least partially due to the fact that the free interaction portion of the solution has extended far enough upstream for values of $\bar{\alpha}$ greater than 2.5 that the difficulties of the present approximate method with the free interaction plateau region are beginning to appear. However, overall this simple integral method gives the main features of the flowfield and with improvements would seem to be a reasonably accurate

and extremely fast method for finding lower deck solutions.

NUMERICAL FINITE DIFFERENCE SOLUTION OF
THE SMALL SEPARATION PROBLEM

Jenson, Burggraf, and Rizzetta (ref. 4) have developed a
finite difference numerical scheme for solving the lower deck
equations for the supersonic case. As was mentioned in the pre-
vious sections, they have applied their numerical method to the
problem of flow past a compression ramp. Rizzetta (ref. 5) gives
more extensive numerical results for the same problem using
essentially the same finite difference technique.

It can easily be shown that the ordinary Prandtl boundary-
layer equations contain all of the terms indicated as being im-
portant in the triple deck analysis as long as one takes into
account the interaction of the boundary layer with the outer in-
viscid flow. It is not a simple matter to solve the resulting
set of interacting boundary-layer equations since, like the lower
deck equations, they are boundary value in nature.

A very natural way to solve the interacting boundary-layer
equations is by the use of an alternating direction implicit (ADI)
method. This is the approach taken by Werle and Vatsa (ref. 7)
and Vatsa (ref. 8) in their solution of the same type of compres-
sion ramp problems as were considered by Jenson, Burggraf and
Rizzetta.

Figure 5 shows a comparison of the results for skin friction
obtained using Werle and Vatsa's method with those obtained from
the triple deck analysis by Rizzetta, see also Burggraf et al.
(ref. 14). The results show that the interacting boundary-layer
model slowly approaches the triple deck asymptotic solution as
Reynolds number goes to infinity.

Because of the slow approach to the infinite Reynolds number
limit indicated in the comparison, the triple deck results do not
tend to agree well with experimental data at high but finite
Reynolds numbers. On the other hand, interacting boundary-layer
results tend to agree well. Figure 6 shows a comparison of
Navier-Stokes and interacting boundary-layer results with the
experimental data of Lewis, Kubota and Lees (ref. 15).

Tu and Weinbaum (ref. 16) have suggested that the principle
cause of the poor agreement between triple deck results and
experimental data lies in the fact that triple deck analysis
neglects streamtube divergence in the middle deck region. Since
interacting boundary-layer results contain this effect, they tend
to show much better agreement with experiment.

CONCLUSION

The idea of solving separation problems using triple deck theory is still relatively new. It is anticipated that with time, the theory will be modified to incorporate the additional terms which will allow better agreement with experimental data. Even if this were not done, the insight gained from triple deck theory into the mechanism of high Reynolds number separation is in itself extremely valuable.

REFERENCES

1. Davis, R.T. and Werle, M.J., "Numerical Methods for Interacting Boundary Layers," in Proceedings of the 1976 Heat Transfer and Fluid Mechanics Institute, pp. 317-339, Stanford University Press, Stanford, California, 1976.

2. Stewartson, K., "Multistructured Boundary Layers on Flat Plates and Related Bodies," in Advances in Applied Mechanics, Vol. 14, pp. 145-239, Academic Press, Inc., 1974.

3. Messiter, A.F., "Laminar Separation - A Local Asymptotic Flow Description for Constant Pressure Downstream," in Flow Separation, AGARD CP 168, 1975.

4. Jenson, R., Burggraf, O. and Rizzetta, D., "Asymptotic Solution for Supersonic Viscous Flow Past a Compression Corner," in Proceedings of the 4th International Conference on Numerical Methods in Fluid Dynamics, in Lecture Notes in Physics, Vol. 35, Springer Verlag, Berlin, Heidelberg and New York, 1975.

5. Rizzetta, D., "Asymptotic Solution for Two Dimensional Viscous Supersonic and Hypersonic Flows Past Compression and Expansion Corners," Ph.D. Dissertation, Ohio State Univ., 1976.

6. Smith, F.T., "Laminar Flow Over a Small Hump on a Flat Plate," J. Fluid Mech., Vol. 57, Part 4, pp. 803-824, 1973.

7. Werle, M.J. and Vatsa, V.N., "A New Method for Supersonic Boundary Layer Separation," AIAA J., pp. 1491-1497, Nov. 1974.

8. Vatsa, V.N., "Quasi-Three-Dimensional Viscid/Inviscid Interactions Including Separation Effects," Ph.D. Dissertation, Univ. of Cincinnati, 1975.

9. Carter, J.E., "Numerical Solutions of the Navier-Stokes Equations for the Supersonic Laminar Flow Over a Two-Dimensional Compression Corner," NASA TR-R-385, July 1972.

10. Lighthill, M.J., "On Boundary Layers and Upstream Influence. Part II. Supersonic Flows Without Separation," Proc. Roy. Soc. London, A217, p. 478, 1953.

11. Stewartson, K. and Williams, P.G., "Self-Induced Separation," Proc. Roy. Soc. London, A312, pp. 181-206, 1969.

12. Stewartson, K. and Williams, P.G., "Self-Induced Separation II," Mathematika, 20, pp. 98-108, 1973.

13. Williams, P.G., "A Reverse Flow Computation in the Theory of Self-Induced Separation," in Proceedings of the 4th International Conference on Numerical Methods in Fluid Dynamics in Lecture Notes in Physics, Vol. 35, Springer Verlag, Berlin, Heidelberg and New York, 1975.

14. Burggraf, O.R., Werle, M.J., Rizzetta, D. and Vatsa, V.N. "Effect of Reynolds Number on Laminar Separation of a Supersonic Stream," paper in preparation, 1976.

15. Lewis, J.E., Kubota, T. and Lees, L., "Experimental Investigation of Supersonic Laminar Two Dimensional Boundary Layer Separation in a Compression Corner With and Without Cooling," AIAA J., Vol. 6, pp. 7-14, Jan. 1968.

16. Tu, K. and Weinbaum, S., "A Non-Asymptotic Triple Deck Model for Supersonic Boundary-Layer Interaction," accepted for publication, AIAA J., 1976.
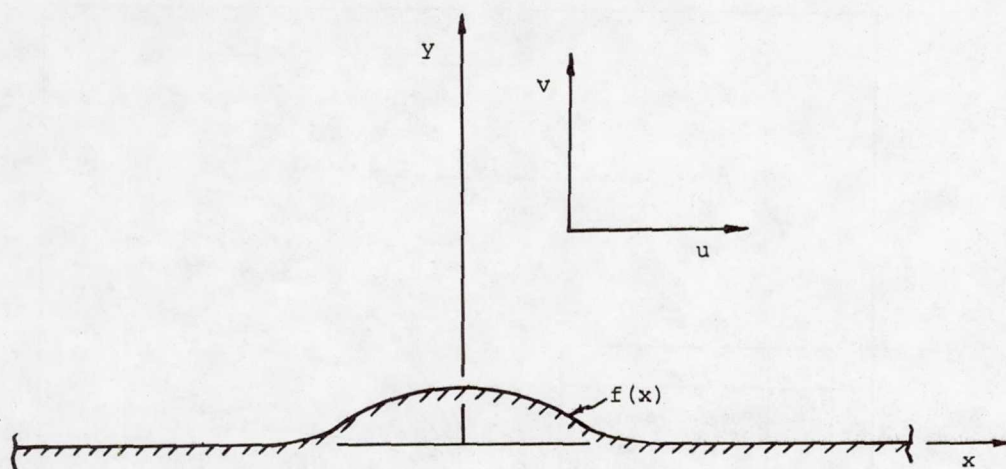
Figure 1.- Coordinate system and bump in lower deck variables.
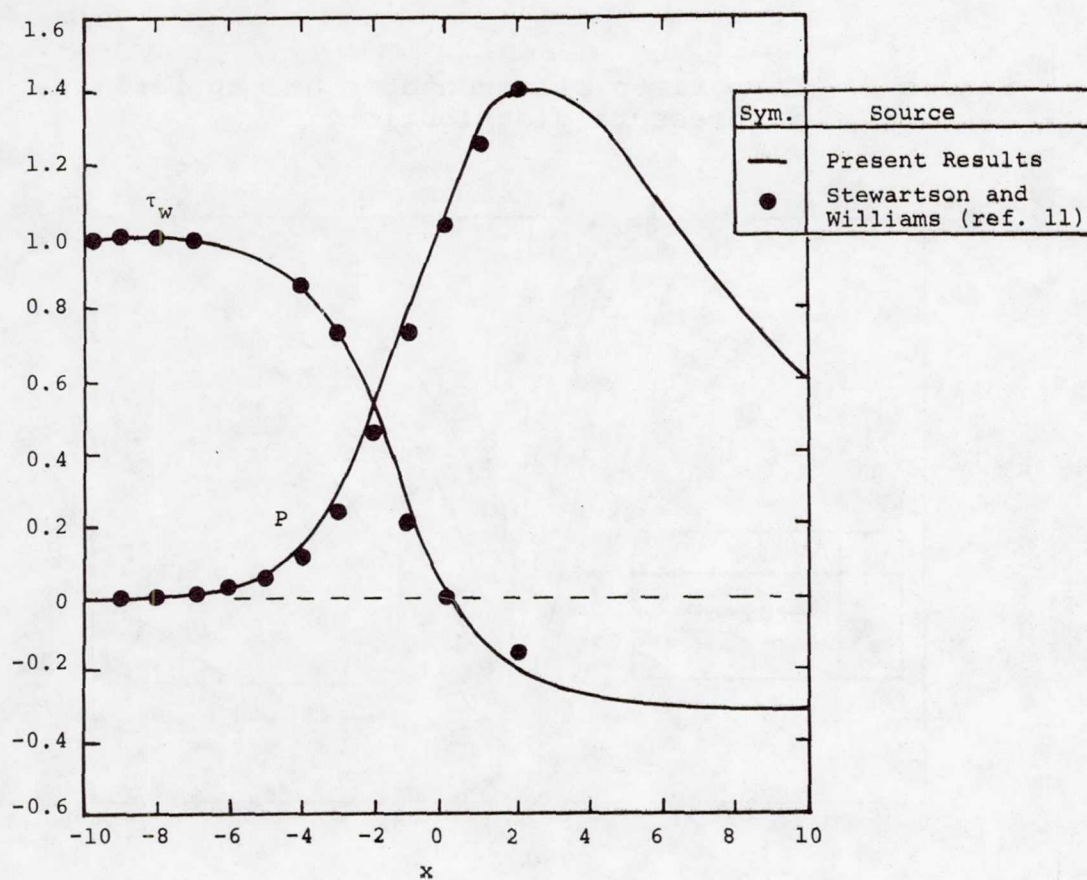
Figure 2.- Compressive free interaction results.
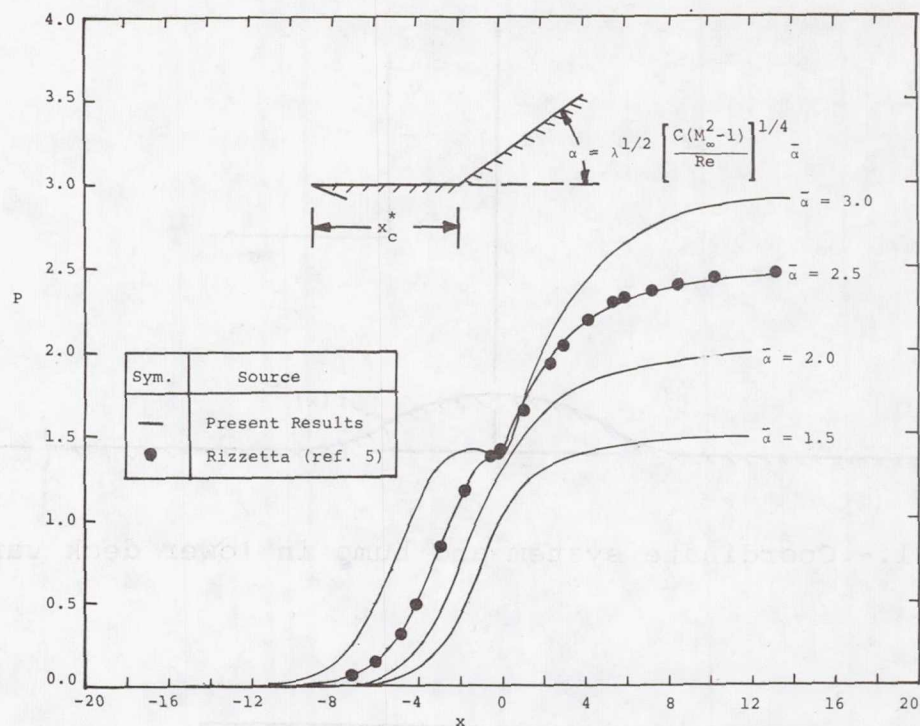
Figure 3.- Comparison of asymptotic and approximate pressure distribution.
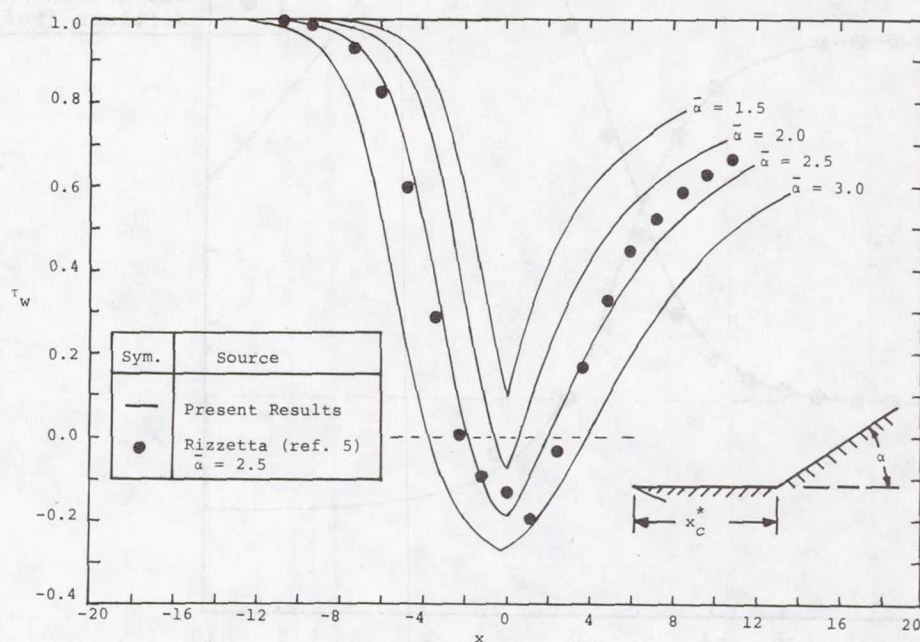
Figure 4.- Comparison of asymptotic and approximate shear distribution.
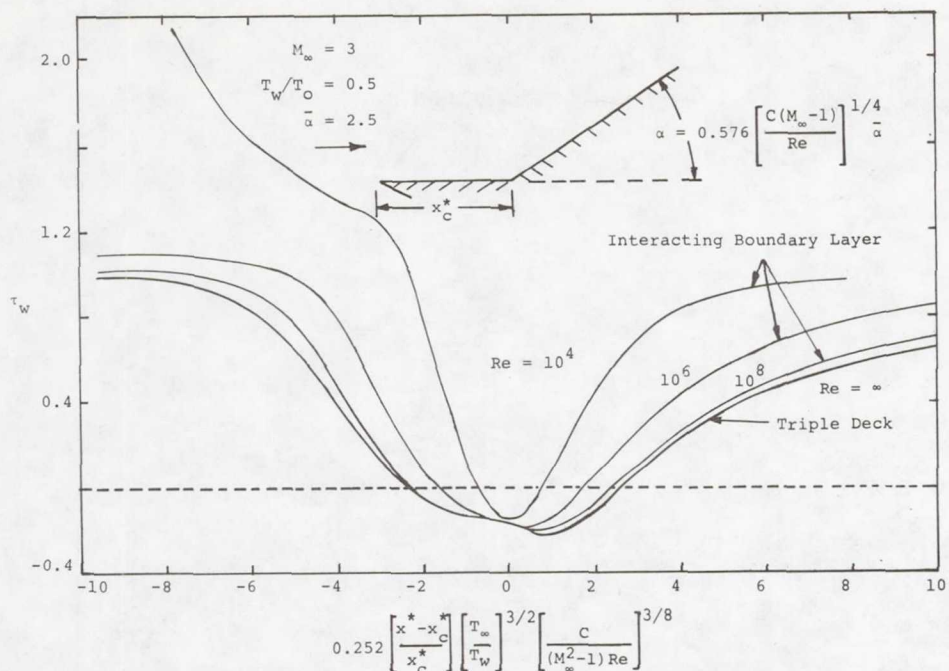
Figure 5.- Comparison of asymptotic and interacting boundary-
layer solutions, after Burggraf et al. (ref. 14).
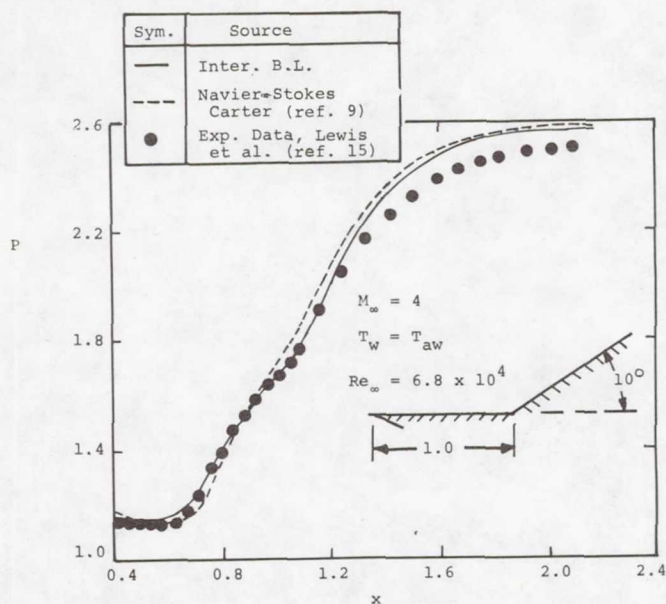
Figure 6.- Comparison of supersonic interacting
boundary-layer with Navier-Stokes solutions
for a compression ramp, after Vatsa (ref. 8).

Page intentionally left blank

THE RELATIVE MERITS OF SEVERAL NUMERICAL TECHNIQUES FOR

SOLVING THE COMPRESSIBLE NAVIER-STOKES EQUATIONS

Terry L. Holst
Langley Research Center

SUMMARY

Four explicit finite-difference techniques designed to solve the time-dependent, compressible Navier-Stokes equations have been compared. These techniques are (1) MacCormack, (2) modified Du Fort-Frankel, (3) modified hopscotch, and (4) Brailovskaya. The comparison was made numerically by solving the quasi-one-dimensional Navier-Stokes equations for the flow in a converging-diverging nozzle. Solutions with and without standing normal shock waves were computed for unit Reynolds numbers (based on total conditions) ranging from 45374 to 2269. The results indicate that all four techniques are comparable in accuracy; however, the modified hopscotch scheme is two to three times faster than the Brailovskaya and MacCormack schemes and three to six times faster than the modified Du Fort-Frankel scheme.

INTRODUCTION

Recently, considerable interest has surfaced in the numerical solution of the compressible Navier-Stokes equations (refs. 1-4). Explicit numerical techniques have been used in most of these studies, especially those involving shock waves. The limited use of implicit methods is due to (1) coding complexity associated with the Navier-Stokes equations, (2) limited success in obtaining the large time steps as predicted by linear stability analysis, and (3) limited success in capturing shock waves. Another factor involved is the apparent success of explicit methods over implicit methods for adapting to the new fourth generation computers (STAR 100 and ILLIAC IV).

The purpose of the present study is to investigate the relative merits of several explicit finite-difference techniques for solving the compressible, time-dependent Navier-Stokes equations. Some of the important aspects evaluated are (1) computational speed, (2) numerical accuracy, (3) computer storage requirements, (4) Reynolds number limitations, and (5) effects of artificial smoothing. The four numerical techniques investigated are (1) modified hopscotch, (2) MacCormack, (3) modified Du Fort-Frankel, and (4) Brailovskaya. Each of these methods has been used to solve a quasi-one-dimensional converging-diverging nozzle problem. Solutions with and without standing normal shock waves are presented for unit Reynolds numbers ranging from 45374 to 2269.

SYMBOLS

A   nozzle cross-sectional area, m^2

c   speed of sound, m/sec

E   total internal energy per unit volume, $N\text{-}m/m^3$

M   Mach number

p   pressure, N/m^2

R   Reynolds number per unit length, m^{-1}

S   smoothing term

t   time, sec

T   temperature, K

u   velocity, m/sec

x   distance along nozzle axis, m

Δt time increment, sec

Δx space increment, m

ρ density, kg/m^3

Subscripts:

i   space index

t   total conditions

Superscript:

n   time index

GOVERNING EQUATIONS AND TEST PROBLEM

The converging-diverging nozzle problem used in this study represents a rigorous test case for the numerical techniques. The steady-state flow field is initially subsonic, goes sonic at the throat, passes through a standing normal shock wave in the diverging portion of the nozzle, and exits the nozzle with subsonic flow. Cases which do not contain a standing normal shock wave are also computed. For these cases the flow field downstream of the throat is supersonic. Different exit boundary conditions are required for each of these cases and will be discussed in a subsequent section.

The time-dependent, quasi-one-dimensional flow of a compressible, viscous fluid is governed by a set of three partial differential equations expressing the conservation of mass, momentum, and energy. These equations in conservative form are as follows:

$$\frac{\partial U}{\partial t} + \frac{\partial F}{\partial x} - \frac{\partial}{\partial x}\left(B \frac{\partial C}{\partial x}\right) + H = 0 \tag{1}$$

where

$$U = A\begin{bmatrix} \rho \\ \rho u \\ E \end{bmatrix} ; F = A\begin{bmatrix} \rho u \\ \rho u^2 + p \\ (E+p)u \end{bmatrix} ; B = A\begin{bmatrix} 0 & 0 & 0 \\ 0 & \frac{4}{3}\mu & 0 \\ 0 & \frac{4}{3}\mu u & k \end{bmatrix} ; C = \begin{bmatrix} 0 \\ u \\ T \end{bmatrix} ; H = \begin{bmatrix} 0 \\ -p\frac{\partial A}{\partial x} \\ 0 \end{bmatrix} \tag{2}$$

The coefficients of viscosity (μ) and thermal conductivity (k) are given by Sutherland's viscosity law and a constant Prandtl number assumption.

Differencing Schemes

Several characteristics are common to each of the numerical schemes evaluated in this study. They are all second-order-accurate (for the steady-state solution) finite-difference techniques which solve the time-dependent form of the governing equations in search of a final steady-state solution. The methods are explicit, and hence, easily programmed. In particular, the methods evaluated here have been chosen especially with regard to programming simplicity for the Navier-Stokes equations.

Modified Hopscotch

The current version of hopscotch was first introduced in reference 5 where it was applied to the compressible Navier-Stokes equations for a shear layer mixing problem. This modified hopscotch technique (applied to eq. (1)) is expressed in two sweeps given by

first sweep (i+n even)

$$U_i^{n+1} = U_i^n - \frac{\Delta t}{2\Delta x}\left(F_{i+1}^n - F_{i-1}^n\right) - \frac{\Delta t}{2}\left(H_{i+1}^n + H_{i-1}^n\right)$$

$$+ \frac{\Delta t}{\Delta x}\left[\frac{B_{i+1}^n + B_i^n}{2}\left(\frac{C_{i+1}^n - C_i^n}{\Delta x}\right) - \frac{B_i^n + B_{i-1}^n}{2}\left(\frac{C_i^n - C_{i-1}^n}{\Delta x}\right)\right] \tag{3}$$

second sweep (i+n odd)

$$U_i^{n+1} = U_i^n - \frac{\Delta t}{2\Delta x} \left(F_{i+1}^{n+1} - F_{i-1}^{n+1} \right) - \frac{\Delta t}{2} \left(H_{i+1}^{n+1} + H_{i-1}^{n+1} \right)$$

$$+ \frac{\Delta t}{\Delta x} \left[\frac{B_{i+1}^{n+1} + B_i^n}{2} \left(\frac{C_{i+1}^{n+1} - C_i^n}{\Delta x} \right) - \frac{B_i^n + B_{i-1}^{n+1}}{2} \left(\frac{C_i^n - C_{i-1}^{n+1}}{\Delta x} \right) \right] \tag{4}$$

Gottlieb and Gustafsson (ref. 6) have investigated the stability of the current version of hopscotch and have found it to be governed by the following CFL condition:

$$\Delta t_{CFL} \leqq \frac{\Delta x}{|u| + c} \tag{5}$$

In addition reference 6 found the viscous stability condition for the modified hopscotch technique to be

$$\frac{\mu \; \Delta t}{\rho \; (\Delta x)^2} \leqq 1 \tag{6}$$

Gourlay (ref. 7) suggested a simplification to the standard two-sweep hopscotch scheme which almost entirely removed the first sweep where equation (3) is replaced by

$$U_i^{n+1} = 2U_i^n - U_i^{n-1} \qquad \text{(i+n even)} \tag{7}$$

Numerical tests were performed with and without the use of equation (7) yielding identical results. The use of equation (7) increases the speed of the modified hopscotch technique by a factor of two without requiring additional storage.

Modified Du Fort-Frankel

The current version of the Du Fort-Frankel scheme was introduced by Gottleib and Gustafsson (ref. 8) as follows:

$$U_i^{n+1} = U_i^{n-1} - \frac{\Delta t}{\Delta x} \left(F_{i+1}^n - F_{i-1}^n \right) - 2\Delta t \, H_i^n + \frac{2\Delta t}{\Delta x} \left[\frac{B_{i+1}^n + B_i^n}{2} \left(\frac{C_{i+1}^n - C_i^n}{\Delta x} \right) \right.$$

$$\left. - \frac{B_i^n + B_{i-1}^n}{2} \left(\frac{C_i^n - C_{i-1}^n}{\Delta x} \right) \right] - \frac{2\Delta t \, \omega}{(\Delta x)^2} \, B_i^n \left(U_i^{n+1} - 2U_i^n + U_i^{n-1} \right) \tag{8}$$

1470

where the last term is a stabilizing term. The value of ω (stabilizing coefficient) must be determined by numerical experiment. The stabilizer takes the place of the time averaging appearing in the viscous terms of the standard Du Fort-Frankel scheme. This simplifies the resulting numerical code, especially for the Navier-Stokes equations in multiple dimensions.

In addition to equation (8) an additional dissipative term must be added for stable operation

$$S_i^n = \frac{\varepsilon}{16} \left(U_{i+2}^n - 4U_{i+1}^n + 6U_i^n - 4U_{i-1}^n + U_{i-2}^n \right) \tag{9}$$

where the constant ε is determined numerically.

MacCormack

The version of the two-step Lax-Wendroff scheme used in this study was first introduced by MacCormack (ref. 9). Using the MacCormack technique to difference equation (1) yields

predictor step

$$\overline{U_i^{n+1}} = U_i^n - \frac{\Delta t}{\Delta x} \left(F_{i+1}^n - F_i^n \right) + \frac{\Delta t}{\Delta x} \left[B_{i+1}^n \frac{C_{i+1}^n - C_i^n}{\Delta x} - B_i^n \frac{C_i^n - C_{i-1}^n}{\Delta x} \right] - H_i^n \Delta t \tag{10}$$

corrector step $\quad U_i^{n+1} = \frac{1}{2} \left(\overline{U_i^{n+1}} + U_i^n \right) - \frac{\Delta t}{2\Delta x} \left(\overline{F_i^{n+1}} - \overline{F_{i-1}^{n+1}} \right) - \frac{\Delta t}{2} \overline{H_i^{n+1}}$

$$+ \frac{\Delta t}{2\Delta x} \left[\overline{B_i^{n+1}} \frac{\overline{C_{i+1}^{n+1}} - \overline{C_i^{n+1}}}{\Delta x} - \overline{B_{i-1}^{n+1}} \frac{\overline{C_i^{n+1}} - \overline{C_{i-1}^{n+1}}}{\Delta x} \right] \tag{11}$$

where the overbar on the n superscript indicates a predicted value. The stability requirement for this scheme is the CFL condition (eq. (5)). In addition, a stability condition due to viscous effects is also present:

$$\frac{\mu \Delta t}{\rho (\Delta x)^2} \leq \frac{1}{2} \tag{12}$$

To surpress pointwise oscillations an artificial smoothing term can be added to the right-hand side of equations (10) and (11) as follows:

predictor step

$$S_i^n = C_x \frac{|\rho_{i+1}^n - 2\rho_i^n + \rho_{i-1}^n|}{\rho_{i+1}^n + 2\rho_i^n + \rho_{i-1}^n} \left(U_{i+1}^n - 2U_i^n + U_{i-1}^n \right) \tag{13}$$

1471

<u>corrector step</u>

$$S_i^{\overline{n+1}} = C_x \ \frac{\left| \rho_{i+1}^{\overline{n+1}} - 2\rho_i^{\overline{n+1}} + \rho_{i-1}^{\overline{n+1}} \right|}{\rho_{i+1}^{\overline{n+1}} + 2\rho_i^{\overline{n+1}} + \rho_{i-1}^{\overline{n+1}}} \ \left(U_{i+1}^{\overline{n+1}} - 2U_i^{\overline{n+1}} + U_{i-1}^{\overline{n+1}} \right) \qquad (14)$$

where C_x is an adjustable constant. In regions of smooth flow these terms will be negligible and will not influence the solution. In regions of point-wise oscillations these terms will provide the effect of solution smoothing.

Brailovskaya

The two-step finite-difference scheme introduced by Brailovskaya in 1965 (ref. 10) is **second-order** accurate in space and **first-order** accurate in time. Using this technique to difference equation (1) yields

<u>predictor step</u>

$$U_i^{\overline{n+1}} = U_i^n - \frac{\Delta t}{\Delta x} \left(F_{i+1}^n - F_{i-1}^n \right) - \Delta t \ H_i^n$$
$$+ \frac{2\Delta t}{\Delta x} \left[\frac{B_{i+1}^n + B_i^n}{2} \left(\frac{C_{i+1}^n - C_i^n}{\Delta x} \right) - \frac{B_i^n + B_{i-1}^n}{2} \left(\frac{C_i^n - C_{i-1}^n}{\Delta x} \right) \right] \qquad (15)$$

<u>corrector step</u>

$$U_i^{n+1} = U_i^n - \frac{\Delta t}{\Delta x} \left(F_{i+1}^{\overline{n+1}} - F_{i-1}^{\overline{n+1}} \right) - \Delta t \ H_i^n$$
$$+ \frac{2\Delta t}{\Delta x} \left[\frac{B_{i+1}^n + B_i^n}{2} \left(\frac{C_{i+1}^n - C_i^n}{\Delta x} \right) - \frac{B_i^n + B_{i-1}^n}{2} \left(\frac{C_i^n - C_{i-1}^n}{\Delta x} \right) \right] \qquad (16)$$

The viscous terms in the predictor step are identical with the viscous terms in the corrector step and, therefore, need to be computed only once per time step. This feature reduces the required amount of computer time. The stability requirement for the Brailovskaya scheme is the usual CFL condition (eq. (5)). An additional viscous stability condition is required and is given by equation (12). The artificial smoothing applied to the MacCormack scheme (eqs. (13) and (14)) was also applied to the Brailovskaya scheme.

Boundary Conditions

The boundary conditions described in this section were used for each numerical method. Three boundary conditions at both the inflow and outflow boundaries must be specified. At the subsonic inflow total pressure and total temperature were specified and held fixed. The third inflow boundary condition was obtained by requiring a zero gradient on static pressure.

At the outflow boundary $(i = N)$ for the supersonic case the boundary conditions were

$$p_N^n = p_{N-1}^n \quad , \quad u_N^n = u_{N-1}^n \quad , \quad \rho_N^n = \rho_{N-1}^n \tag{17}$$

At the outflow boundary for the normal shock wave case the flow is subsonic; consequently, the boundary conditions are modified as follows

$$p_N^n = p_{exit}, \quad u_N^n = u_{N-1}^n \quad , \quad \rho_N^n = \rho_{N-1}^n \tag{18}$$

where p_{exit} is specified and held fixed. Obtaining accurate results with such simple boundary conditions is made possible by adding constant area duct segments at the inflow and outflow stations of the nozzle.

These boundary conditions when applied to the modified Du Fort-Frankel code resulted in unstable oscillations at the boundaries. These oscillations were eliminated by two different methods. The first method was to apply second-order damping given by

$$S_i^n = \frac{\varepsilon}{16} \left(U_{i+1}^n - 2U_i^n + U_{i-1}^n \right) \tag{19}$$

at $i = 2$ for the inflow and $i = N - 1$ for the outflow.

The second method of removing the oscillations consisted of replacing the original boundary conditions with a new set given by

$$p_t = \text{const}, \quad T_t = \text{const}, \quad p_1^n = p_2^{n-1} \tag{20}$$

$$p_N^n = p_{N-1}^{n-1} \quad , \quad u_N^n = u_{N-1}^{n-1} \quad , \quad \rho_N^n = \rho_{N-1}^{n-1} \tag{21}$$

$$p_N^n = p_{exit}, \quad u_N^n = u_{N-1}^{n-1} \quad , \quad \rho_N^n = \rho_{N-1}^{n-1} \tag{22}$$

where equations (20) and (21) were used for the no shock wave case and equations (20) and (22) for the normal shock wave case. For shock-free flow solutions the second method of removing the oscillations produced the best results and are presented in the next section. For the normal shock wave case, both methods produced similar results.

DISCUSSION OF RESULTS

Shock-Free Solution

The initial condition solution for the isentropic calculation was established by first computing the inflow and outflow endpoints from one-dimensional isentropic theory. Then linear distributions for all the flow variables were computed between the endpoints.

Table I summarizes the computing statistics of all the results presented. The results of the isentropic (shock free) calculation are presented in figure 1. Included are Mach number, pressure, and temperature distributions along the nozzle axis for all four numerical techniques. Overall the agreement is very good. In particular, all four numerically predicted values of pressure at the throat lie within 0.5 percent of the theoretical value. The largest disagreement occurs at the outflow where theory predicts an exit Mach number of 1.925. The numerically predicted exit Mach numbers are below this and lie between 1.907 and 1.920.

The maximum error (ERR) versus the central processor unit time (CPU time) is presented in figure 2 where

$$ERR = \max_{i} \frac{|\rho_i^{n+1} - \rho_i^n|}{\rho_i^n \quad \Delta t/\Delta t_{CFL}} \tag{23}$$

The CPU time required for computing initial conditions and solution input/output has been subtracted from the CPU time displayed in figure 2. The curves have been continued until the maximum error dropped below 0.001 although the actual calculations were carried to 0.0001 accuracy. For the test problem the modified hopscotch technique is clearly the fastest of the four techniques tested, being 2.2 times faster than Brailovskaya, 2.5 times faster than MacCormack, and 4.0 times faster than modified Du Fort-Frankel.

Normal Shock Wave Solution

The initial conditions for the cases with a standing normal shock wave were obtained from one-dimensional isentropic theory. The initial solution was entirely subsonic with the standard expansion in the converging portion in the nozzle, the sonic condition at the throat, and subsonic compression in the diverging portion of the nozzle. This condition was chosen because the use of initial conditions with supersonic outflows caused difficulties when the out-flow pressure was specified.

Mach number and pressure distributions are presented in figures 3 and 4. A standing normal shock wave with a pressure ratio of approximately 3.7 has been captured by all four methods at $i \simeq 38$. The shock wave is spread over two to three grid points with minimal overshoots and no undershoots. The

Reynolds number was not low enough for any significant viscous effects to appear. The grid Reynolds numbers $(\rho u \, \Delta x/\mu)$ were between 10 and 20. In general the agreement is quite good between the four techniques.

Both the MacCormack and Brailovskaya results were computed with artificial smoothing added; however, the smoothing was not required for a stable solution. Instead, it was used to improve the characteristics of the captured shock by reducing the overshoot and undershoot oscillations.

Again the modified hopscotch technique is the fastest of the four methods tested (see table I, case 2) being 1.7 times faster than Brailovskaya, 1.8 times faster than MacCormack, and 3.9 times faster than modified Du Fort-Frankel.

Reynolds Number Effects

Three of the techniques (modified hopscotch, MacCormack, and Brailovskaya) have viscous stability conditions and therefore, should exhibit smaller time steps and longer CPU times for lower Reynolds numbers. Two test cases were computed with lower Reynolds numbers by decreasing the total pressure (see table I, cases 3 and 4). Mach number distributions for these two cases are shown in figures 5 and 6. The effect of the reduced Reynolds number is clearly evident. In figure 5 ($R = 11345$ m^{-1}) the shock wave is spread across five to six grid points, and in figure 6 ($R = 2269$ m^{-1}) the solution is so smeared by the physical viscosity that a shock wave cannot be recognized. The grid Reynolds numbers are between 2 and 5 for case 3 and between 0.5 and 1.0 for case 4.

The shock position predicted by the modified Du Fort-Frankel technique for case 3 (see fig. 5) is in slight disagreement with the shock position predicted by the other three methods. This is due to the different outflow boundary conditions used by the modified Du Fort-Frankel technique (see eqs. (19) - (22)). The effect is to alter the value of exit pressure and thus, change the shock position. The modified Du Fort-Frankel scheme failed to converge for case 4.

As expected, the viscous stability condition was more restrictive and therefore dominated the low Reynolds number calculations, especially case 4. Modified hopscotch seemed to have a slightly more severe viscous stability condition than MacCormack or Brailovskaya, but, possibly due to the added physical viscosity, actually reached a converged solution sooner in physical time. For instance, in case 3, modified hopscotch was 2.8 times faster than Brailovskaya, 3.2 times faster than MacCormack, and 6.2 times faster than modified Du Fort-Frankel.

The lack of a viscous stability limit for modified Du Fort-Frankel could not be fully tested due to its failure to converge for case 4. The reduced time step ratio exhibited by modified Du Fort-Frankel for all cases is due to the artificial dissipation which must be added for stable operation. Hence, even if modified Du Fort-Frankel is not restricted by a viscous stability condition, it must pay the price of a reduced time step for another reason, regardless of Reynolds number.

Artificial Smoothing

Artificial smoothing has been used in this study on three of the four methods tested (MacCormack, Brailovskaya, and Du Fort-Frankel). To investigate the effect of smoothing, a series of Mach number distributions for three different values of C_x (smoothing constant) are presented in figure 7. The three curves correspond to no smoothing (C_x = 0.0), moderate smoothing (C_x = 0.2), and massive smoothing (C_x = 1.0). All three curves were computed by the same numerical technique (Brailovskaya) and at the same flow conditions (R = 45374 m^{-1} and p_{exit}/p_t = 0.7). Enlargements of the Mach number profiles around the standing normal shock wave are presented in figure 7. The no smoothing case spreads the shock wave across three grid points and exhibits pre-shock oscillations. The moderate smoothing case, likewise, spreads the shock over three grid points, almost identically matching the no smoothing shock, but without pre-shock oscillations. The massive smoothing case spreads the shock over four or five grid points and effectively causes a position shift in the shock wave. All three profiles away from the shock are in good agreement regardless of how much smoothing is applied. Therefore, it is clear that artificial smoothing in a limited amount has helped the quality of the solution.

CONCLUDING REMARKS

The modified hopscotch technique was superior in speed for all cases tested, being 1.7 to 2.8 times faster than the Brailovskaya technique, 1.8 to 3.2 times faster than the MacCormack technique, and 3.9 to 6.2 times faster than the modified Du Fort-Frankel technique.

All methods tested were comparable in accuracy for the cases tested, with or without shock waves.

The modified hopscotch scheme seemed to have a slightly more severe viscous stability condition than the MacCormack or Brailovskaya schemes. However, for the viscous stability restricted cases, solutions computed by the modified hopscotch technique actually reached steady state sooner in physical time than any of the other techniques tested.

REFERENCES

1. Baldwin, B. S.; and MacCormack, R. W.: Numerical Solution of the Inter-
    action of a Strong Shock Wave With a Hypersonic Turbulent Boundary Layer.
    AIAA Paper No. 74-588, 1974.

2. Carter, James E.: Numerical Solutions of the Navier-Stokes Equations for
    the Supersonic Laminar Flow Over a Two-Dimensional Compression Corner.
    NASA TR R-385, 1972.

3. Tannehill, J. C.; Holst, T. L.; and Rakich, J. V.: Numerical Computation
    of Two-Dimensional Viscous Blunt Body Flows With an Impinging Shock.
    AIAA J., Vol. 14, No. 2, 1976, pp. 204-211.

4. Peyret, R.; and Viviand, H.: Computation of Viscous Compressible Flows
    Based on the Navier-Stokes Equations. AGARDograph No. 212, Sept. 1975.

5. Rudy, D. H.; Morris, D. J.; Blanchard, D. K.; Cooke, C. H.; and
    Rubin, S. G.: An Investigation of Several Numerical Procedures for
    Time-Asymptotic Compressible Navier-Stokes Solutions. Aerodynamic
    Analyses Requiring Advanced Computers, Part I, NASA SP-347, 1975,
    pp. 437-468.

6. Gottlieb, D.; and Gustafsson, B.: On the Navier-Stokes Equations With
    Constant Total Temperature. NASA CR-132664, 1975.

7. Gourlay, A. R.: Hopscotch: A Fast Second-Order Partial Differential
    Equation Solver. J. Inst. Math. & Its Appl., Vol. 6, No. 4, 1970,
    pp. 357-390.

8. Gottlieb, D.; and Gustafsson, B.: Generalized Du Fort-Frankel Methods
    for Parabolic Initial-Boundary-Value Problems. NASA CR-132653, 1975.

9. MacCormack, R. W.: The Effect of Viscosity in Hypervelocity Impact
    Cratering. AIAA Paper No. 69-354, 1969.

10. Brailovskaya, I. Yu.: A Difference Scheme for Numerical Solution of the
    Two-Dimensional Nonstationary Navier-Stokes Equations for a Compressible
    Gas. Soviet Physics - Doklady, Vol. 10, No. 2, 1965, pp. 107-110.

Table I.- Summary of results.

	Case 1 Isentropic Supersonic R =45374				Case 2 Normal Shock R =45374 p_{exit}/p_t=.7				Case 3 Normal Shock R =11345 p_{exit}/p_t=.7				Case 4 Normal Shock R =2269 p_{exit}/p_t=.7			
	$\frac{\Delta t}{\Delta t_{CFL}}$	n	Physical Time (μsec)	CPU Time (sec)	$\frac{\Delta t}{\Delta t_{CFL}}$	n	Physical Time (μsec)	CPU Time (sec)	$\frac{\Delta t}{\Delta t_{CFL}}$	n	Physical Time (μsec)	CPU Time (sec)	$\frac{\Delta t}{\Delta t_{CFL}}$	n	Physical Time (μsec)	CPU Time (sec)
MacCormack	1.0	345	143	5.8	.9	338	140	5.3	.9	546	223	8.5	.5	896	217	14.0
Modified Hopscotch	.9	395	147	2.2	1.0	565	246	3.0	.8	514	188	2.7	.3	1193	175	6.2
Brailovskaya	1.1	334	152	5.2	1.1	323	161	5.2	1.0	485	222	7.5	.4	1110	221	17.6
Modified Du Fort-Frankel	.5	858	177	10.7	.5	990	216	11.8	.4	1350	243	16.9				

△ Modified Hopscotch
◇ Brailovskaya
▣ Modified Du Fort-Frankel (ω=10, ϵ=.6)
⊙ MacCormack
— Theory

R = 45374
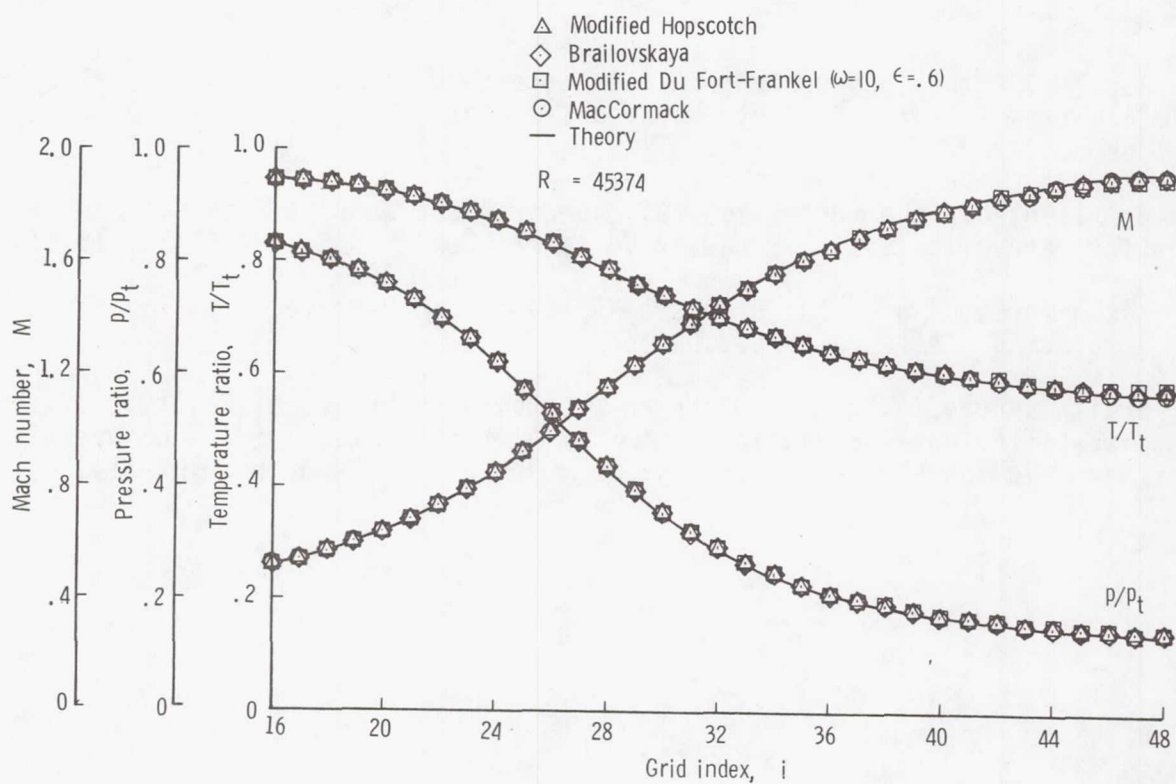
Figure 1.- Shock-free calculation.
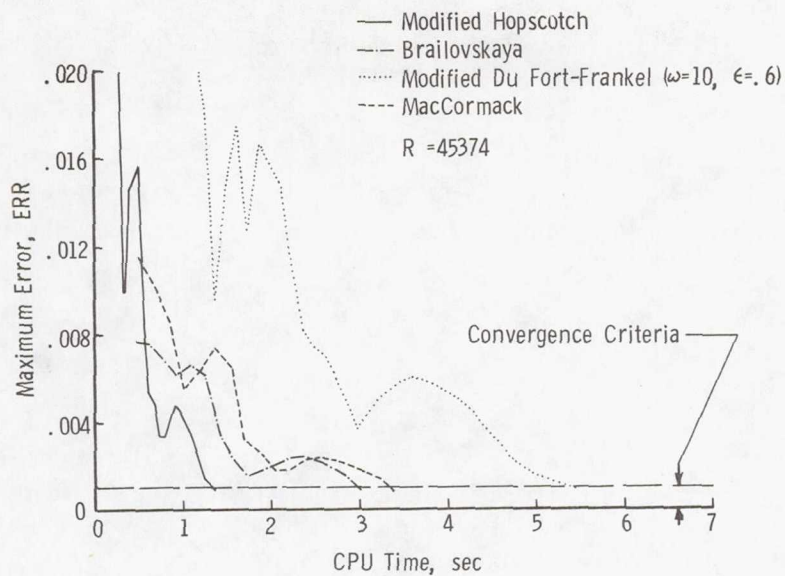
Figure 2.- Convergence rate comparison.
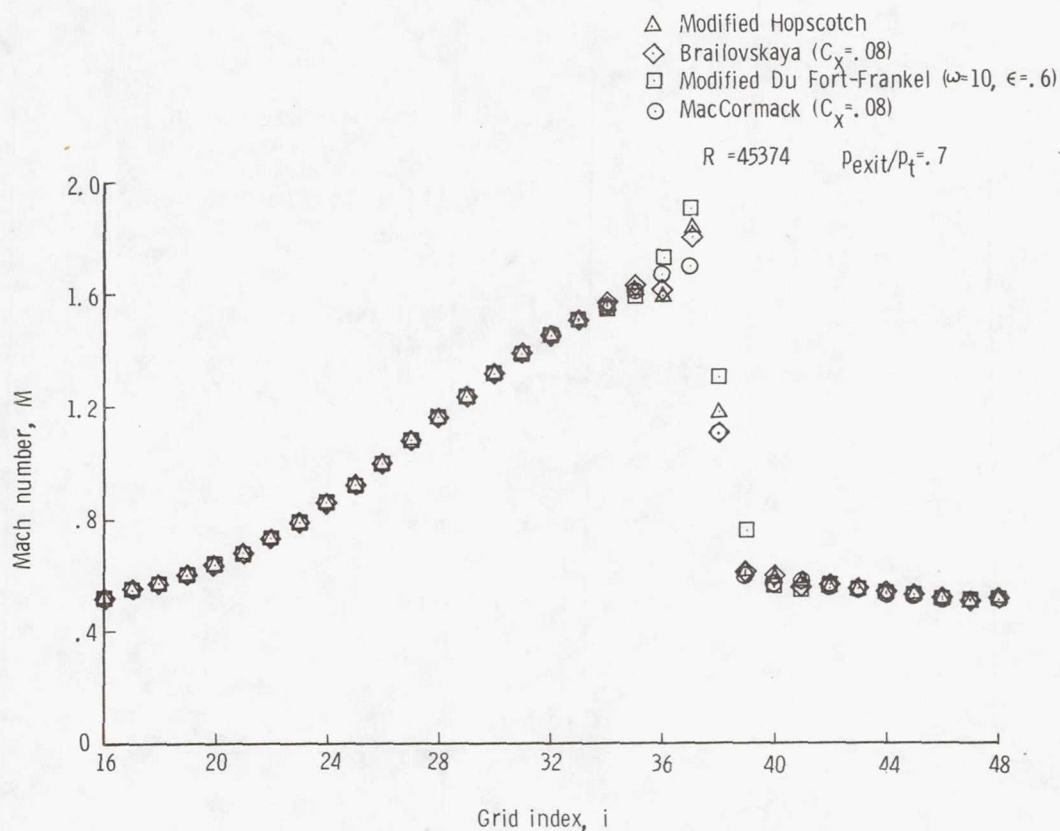
Figure 3.- Mach number distribution (case 2).
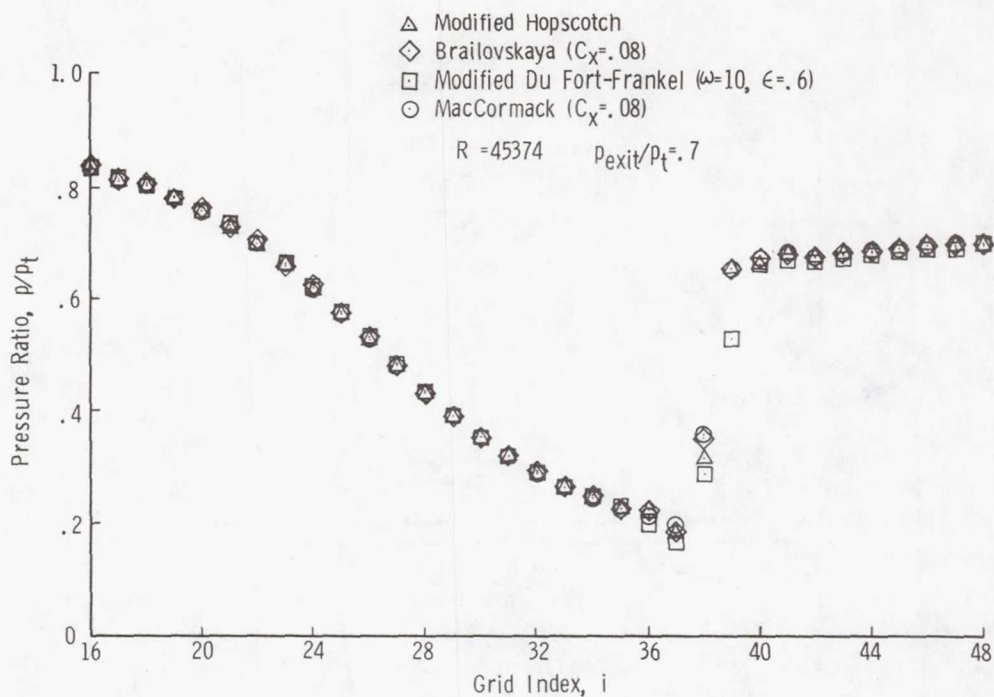
Figure 4.– Pressure ratio distribution (case 2).
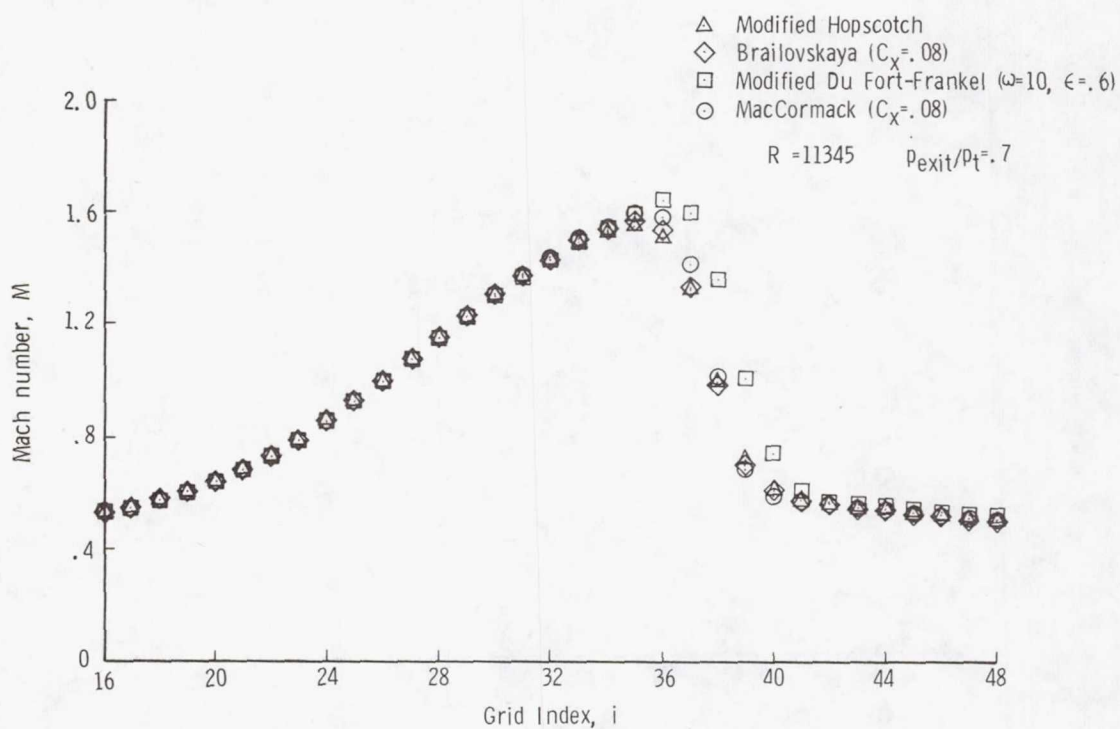
Figure 5.– Mach number distribution (case 3).
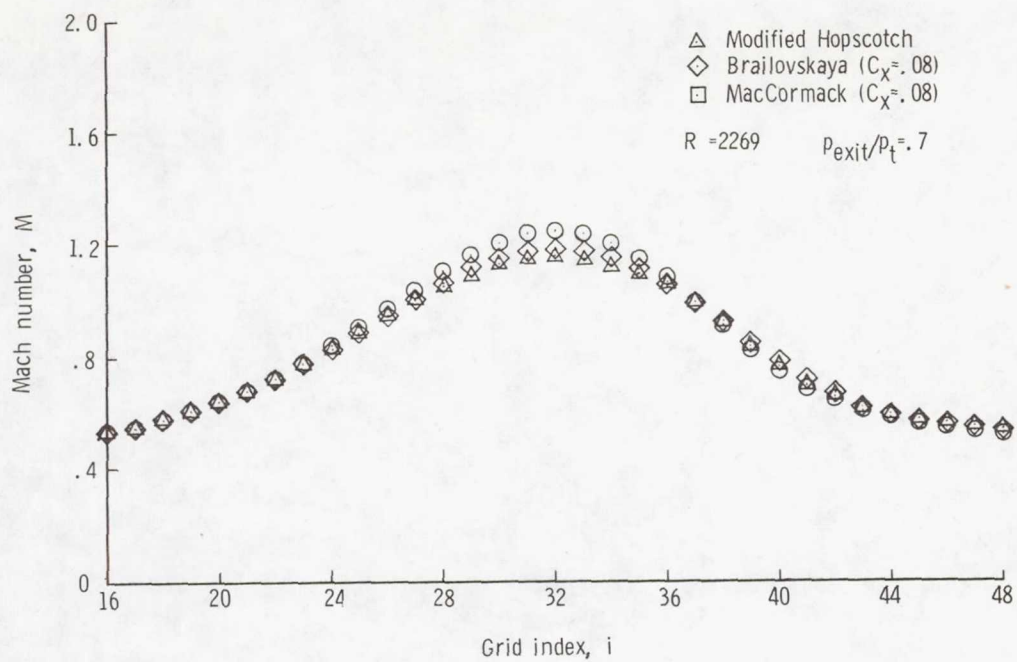
Figure 6.- Mach number distribution (case 4).
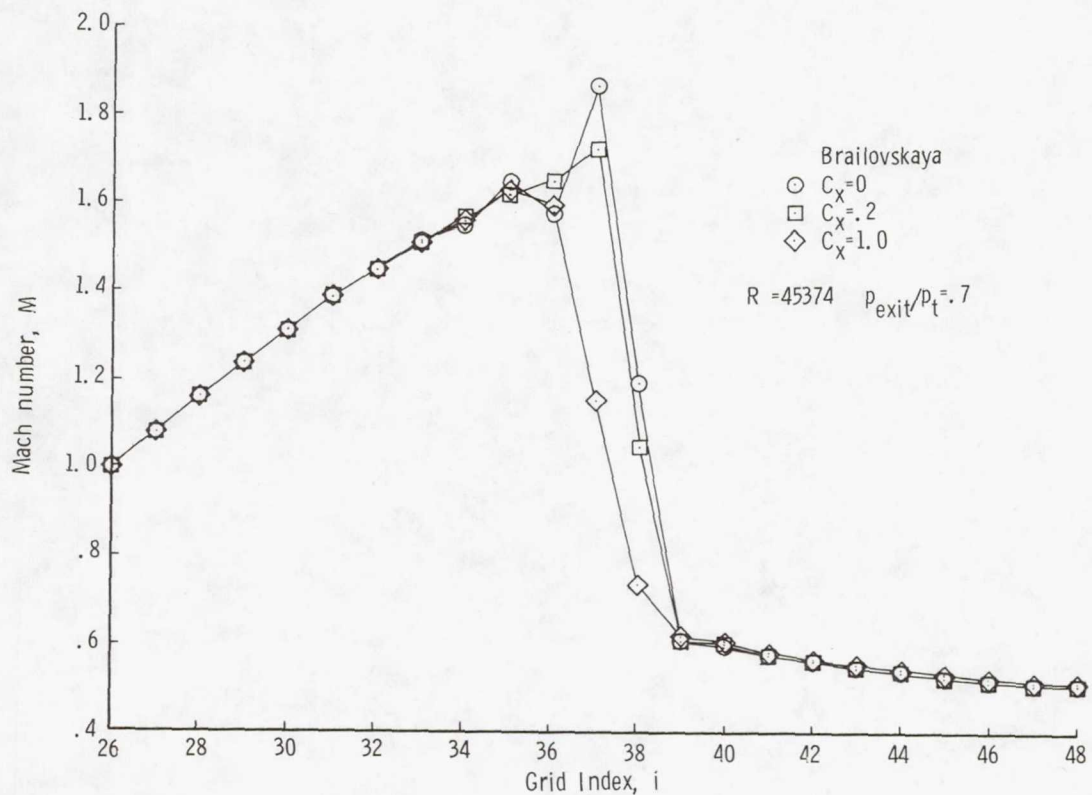
Figure 7.- Effect of artificial smoothing.

Page intentionally left blank

CALCULATION OF A SEPARATED TURBULENT

BOUNDARY LAYER

Barrett Baldwin
Ames Research Center

Ching Mao Hung
DCW Industries and Ames Research Center

SUMMARY

The properties of a Navier-Stokes solution of a shock-separated turbulent flow over a flat wall are investigated. Refinements of an algebraic relaxation turbulence model previously shown to be of value for the simulation of separated flows are presented. A simplified analysis applicable near an adiabatic wall is developed and used to help verify the accuracy of the numerical solution. Features of the time-dependent response of a turbulent boundary layer to shock impingement are presented.

INTRODUCTION

Computers now available are capable of practical calculations of complex flow fields, including separated turbulent boundary layers. However, as discussed in reference 1, development of adequate turbulence models is a pacing item that impedes progress toward that goal. Recent improvements in numerical methods, such as those described in reference 2, have made it feasible to test a variety of modifications of existing turbulence models (see, e.g., references 3-5 and the more comprehensive reference lists therein). For engineering purposes, it would be practical to use simplified models calibrated from experiments conducted at nearby flow conditions. The shortage of experimental information on separated flows prevents calibration with precision at this time. Nevertheless, it seems worthwhile to proceed with the development of computer codes for complex flows based on simplified turbulence models that can be adjusted to accommodate the existing experiments. With presently available information, it may be possible to accomplish this for high Reynolds number flows at Mach numbers up to 3 using the boundary-layer approximation for viscous and Reynolds stress terms in the layers near solid surfaces. More complicated procedures can be incorporated when they are justified or can be used to aid in the calibration of the simplified models.

In reference 5, it was shown that an inner layer algebraic eddy viscosity model used by Clauser (ref. 6) provides better agreement with two separated flow experiments than more conventional models. In this paper, the properties of a Navier-Stokes solution of a shock-separated flow based on a variation of that

model are investigated. A simplified analysis applicable near an adiabatic
wall is presented. Favorable comparisons of results from this analysis with
the Navier-Stokes solution show that the boundary-layer approximation is valid
near the wall for this case and that the Navier-Stokes solution is accurate.
As an example of the type of information that can result from such numerical
solutions, features of the time-dependent response of a boundary layer to
impingement of a shock wave are presented.

SYMBOLS

A	constant (eq. (22))
B	constant (eq. (23))
B_{F3}	constant in turbulence model (eq. (6))
C	constant (eq. (17))
C_p	specific heat at constant pressure
$f_1(y+)$	universal function (eq. (18))
$f_2(y+)$	universal function (eq. (19))
k	Karman constant (0.4)
K	Clauser constant (0.016)
p	pressure, $N/m^2 (lb/ft^2)$
P_{RT}	turbulent Prandtl number (0.9)
S_1, S_2	constants in Sutherland viscosity law (eq. (20))
T	temperature, K (°R)
u	velocity in x-direction, m/sec (ft/sec)
$u_{\tau 2}$	friction velocity (eq. (4)), m/sec (ft/sec)
$u_{\tau 3}$	friction velocity (eq. (5)), m/sec (ft/sec)
V	constant in Van Driest damping factor (eq. (8))
V_F	Van Driest damping factor (eq. (8))
x,y	Cartesian coordinates, m (ft)
y^+	law of the wall variable (eq. (9))

δ boundary-layer thickness, m (ft)

δ^* kinematic displacement thickness (eq. (10)), m (ft)

λ relaxation parameter (eq. (5))

μ molecular coefficient of viscosity, kg/m-sec (slugs/ft-sec)

μ_t turbulent eddy viscosity coefficient (eqs. (1),(2)) kg/m-sec (slugs/ft-sec)

ρ gas density, kg/m^3 $(slugs/ft^3)$

τ shear stress (eq. (11)), N/m^2 (lb/ft^2)

Subscripts:

0   initial profile at station ahead of interaction

2   value of y at which $u_{\tau 2}$ is evaluated (eqs. (3),(4))

3   value of y at which $u_{\tau 3eq}$ is evaluated (eq. (6))

i   position of inviscid shock impingement on wall

max   maximum velocity in profile

w   value at wall

METHOD

Numerical Method for Navier-Stokes Solutions

The basic numerical method used in this investigation is described in reference 7. Recently, MacCormack has improved the method such that the calculations require an order of magnitude less computation time than formerly (see ref. 2). The compressible Navier-Stokes equations to be solved are also listed in reference 7.

Experiment Used for Comparison

The experimental flow field (ref. 8) is depicted in figure 1. A shock wave generated by a plate set at 13° to the free stream impinges on the boundary layer on the upper wind tunnel wall. A separation bubble containing reversed flow forms and extends upstream of the inviscid shock impingement point. A pattern containing induced and reflected shocks forms. The free-stream Mach number is 3 and the Reynolds number based on initial boundary-layer thickness ahead of the interaction is 10^6.

Turbulence Model

The two-layer algebraic eddy viscosity model used in the present calculations is defined by the following equations:

$$\left(\mu_t\right)_{inner} = \left\{ \begin{array}{ll} \rho_2 \dfrac{\mu}{\mu_2} kyu_{\tau 3} V_F^2 & , \quad (y \lessgtr y_2) \\[12pt] \rho kyu_{\tau 3} V_F^2 & , \quad (y > y_2) \end{array} \right\} ; \quad k = 0.4 \tag{1}$$

$$\left(\mu_t\right)_{outer} = K\rho u_{max} \delta^* \quad , \quad K = 0.0168 \tag{2}$$

where ρ_2 and μ_2 are evaluated at $y = y_2$ with y_2 determined from the relations

$$\widetilde{y}_2^+ = \left(\frac{\rho u_{\tau 2} y}{\mu}\right)_{y=y_2} = 100 \tag{3}$$

$$u_{\tau 2} = \left(ky \frac{\partial u}{\partial y}\right)_{y=y_2} \tag{4}$$

The quantity $u_{\tau 3}$ is determined from the relaxation formula

$$\frac{du_{\tau 3}}{dx} = \frac{u_{\tau 3eq} - u_{\tau 3}}{\lambda \delta_0} \quad , \quad \lambda = 5 \tag{5}$$

where

$$u_{\tau 3eq} = B_{F3} \left(ky \frac{\partial u}{\partial y}\right)_{y=y_3} \quad , \quad B_{F3} = 1.18 \tag{6}$$

with y_3 determined from the relation

$$\widetilde{y}_3^+ = \left(\frac{\rho ky \frac{\partial u}{\partial y} y}{\mu}\right)_{y=y_3} = 2000 \tag{7}$$

The quantity V_F is the Van Driest damping factor

$$V_F = 1 - \exp(-y^+/V) \quad , \quad V = 18 \tag{8}$$

where

$$y^+ = \frac{\rho_2 u_{\tau 3} y}{\mu_2} \tag{9}$$

1486

The transition from the inner to the outer formula takes place at the minimum value of y at which $(\mu_t)_{inner} = (\mu_t)_{outer}$. The kinematic displacement thickness δ^* is given by

$$\delta^* = \int_0^\delta \left(1 - \frac{u}{u_{max}}\right) dy \tag{10}$$

The foregoing model differs from that developed in reference 5 in several respects. Replacement of ρ with $\rho_2 \mu / \mu_2$ at $y < y_2$ in equation (1) has the effect of removing the dependence of μ_t / μ on variations of temperature and density in the viscous sublayer. Although future experimental data may show such a dependence, it seems preferable at this time to make μ_t / μ dependent on y^+ alone, and thus to maintain a close correspondence with incompressible flows. Additionally, the factor B_{F_3} in equation (6) allows a close correspondence of the present inner layer Clauser model with more conventional models for flows with zero pressure gradient. Finally, use of y^+ as defined in equation (9) in the Van Driest damping factor instead of the definition used in reference 5 requires rescaling of V to $V = 18$.

Simplified Analysis Applicable Near an Adiabatic Wall

The following approximate relationships, obtained from the compressible Navier-Stokes equations, are useful for checking the adequacy of the mesh used for the numerical solution. They may also be useful for deducing values of parameters in the turbulence model from experimental data obtained from separated and attached boundary-layer flows with pressure gradients. Upon neglecting the convection and inertia terms, the steady-state x-momentum and energy equations can be approximated by

$$\tau = (\mu + \mu_t) \frac{du}{dy} = \tau_2 + (y - y_2) \frac{dp}{dx} \tag{11}$$

$$\frac{C_p T}{P_{RT}} + \frac{1}{2} u^2 = \frac{C_p T_2}{P_{RT}} + \frac{1}{2} u_2^2 \quad \text{(adiabatic wall)} \tag{12}$$

Replacement of the y-momentum equation with $\partial p / \partial y = 0$ and use of the equation of state for a perfect gas yields

$$\frac{\rho}{\rho_2} = \frac{T_2}{T} \tag{13}$$

With the definition

$$du^+ = \begin{cases} \dfrac{\mu}{\mu_2} \, du/C & , & (y \leq y_2) \\[2ex] \dfrac{\rho}{\rho_2} \, du/C & , & (y > y_2) \end{cases} \tag{14}$$

and substitution of the foregoing inner-layer eddy viscosity model into equation (11), the following expression for u^+ can be derived:

$$u^+ = (1 - p^+) f_1(y^+) + \frac{p^+}{y_2^+} f_2(y^+)$$ (15)

where

$$p^+ = y_2 \frac{dp/dx}{\tau_2} = 1 - \frac{\tau_w}{\tau_2}$$ (16)

$$C = u_{\tau 2} \left[\frac{1}{ky_2^+} + V_F^2(y_2^+) \right] \approx u_{\tau 2}$$ (17)

$$f_1(y^+) = \int_0^{y^+} \frac{dy^+}{1 + ky^+ V_F^2(y^+)} \approx 5.5 + \frac{1}{k} \ln(y^+)$$ (18)

$$f_2(y^+) = \int_0^{y^+} \frac{y^+ dy^+}{1 + ky^+ V_F^2(y^+)} \approx \frac{1}{k} y^+$$ (19)

The approximations for f_1 and f_2 on the right apply at $y^+ \gtrsim 60$ where $V_F \approx 1$.

To obtain the relation between u^+ and u, we use the Sutherland viscosity law in the form

$$\mu(T) = \frac{S_1 T^{3/2}}{S_2 + T}$$ (20)

Linearization of the Sutherland relation and substitution of equations (12) and (13) into (14) leads to

$$u^+ = \begin{cases} \dfrac{\mu_w}{\mu_2} \left(1 - \dfrac{1}{3} AB^2 u^2\right) \dfrac{u}{C} & (u \lesssim u_2) \\[4mm] u_2^+ + \dfrac{BC_p T_2}{C\, P_{RT}} \ln \left[\dfrac{(1 + Bu)(1 - Bu_2)}{(1 - Bu)(1 + Bu_2)} \right] & (u > u_2) \end{cases}$$ (21)

where

$$A = \frac{2 + 3S_2/T_w}{1 + S_2/T_w}$$ (22)

$$B = \left(\frac{2C_p T_2}{P_{RT}} + u_2^2 \right)^{-1/2}$$ (23)

A time-dependent solution of the compressible Navier-Stokes equations based on the foregoing eddy viscosity model has been carried out. The initial flow field is uniform in the x-direction with a boundary-layer profile corresponding to an upstream station in the experiment of reference 8. At the lower boundary of the computational field, boundary conditions are imposed corresponding to the shock wave in the experiment (see fig. 1). During the calculation, the shock wave grows toward the upper nozzle wall. Eventually, a steady state is reached corresponding to the conditions at which experimental measurements were made. As an illustration of the type of information that can result from such calculations, features of the time-dependent response of the boundary layer to growth of the incident, induced, and reflected shock pattern will be presented. However, the simplified analysis in the preceding section will first be used to check the adequacy of the computational mesh.

The steady-state Navier-Stokes solution was used to compute dimensionless profiles of u^+ versus y^+ according to equations (9) and (21). Three such profiles are contained in figure 2. The circles represent the Navier-Stokes solution and are at the computational mesh points. The dashed lines are obtained from the simplified analysis (eq. 15)), using values of p^+ and y_2^+ evaluated from the Navier-Stokes solution according to equations (3), (4), (9) and (16). The upper two profiles are at stations aft of reattachment where relatively small pressure gradients are present. The bottom profile is in the region of constant pressure ahead of the separated region, which extends from $-2.6 \lesssim (x - x_i/\delta_0) \lesssim 0.5$. The close correspondence between the approximate and numerical solutions leads to two conclusions: (1) Use of the boundary-layer approximation with additional neglect of convection and inertia terms is a valid approximation near the wall for small pressure gradients; and (2) the computational mesh used for the Navier-Stokes solution provides adequate resolution. However, are the same conclusions valid at stations where strong pressure gradients exist?

Profiles near separation and in the middle of the reversed flow bubble are shown in figure 3. Again the Navier-Stokes solution is represented by symbols and the simplified boundary-layer approximation by dashed lines. Near separation, the approximate results are invalid for values of y^+ greater than about 300 because of neglect of the convection and inertia terms. In the middle of the separation (lower curve), the simplified analysis retains validity to large values of y^+. The resolution of the Navier-Stokes solution is again shown to be adequate. Profiles near reattachment are shown in figure 4. The two solutions agree closely over a large range of y^+ in this region.

With confidence in the resolution of the Navier-Stokes solution established, it is of interest to observe the time-dependent response of the boundary layer to shock impingement. Figure 5 contains plots of wall pressure distribution at a series of time intervals after the start of the calculation. Shortly after the shock reaches the boundary layer and a reflected shock has formed, the wall pressure rise is steep and extends about one boundary-layer thickness upstream of the inviscid shock impingement point, which occurs at 0 on the

abscissa scale. During succeeding time intervals, the pressure gradient decreases and the pressure rise moves upstream. Eventually, a steady state is reached in which the initial pressure rise occurs about three boundary-layer thicknesses ahead of the inviscid shock impingement point. The plot at the top includes the corresponding experimental steady-state pressure distribution from reference 8 for comparison.

Figure 6 contains plots of the skin-friction distributions after the same series of time intervals. In the plot at the top, the calculations are in close agreement with a Preston tube measurement of the initial skin-friction coefficient C_f and oil-flow observations of separation and reattachment points (ref. 8). Skin-friction measurements were not made at other stations in this experiment.

REFERENCES

1. Chapman, D. R.; Mark, H.; and Pirtle, M. W.: Computers vs Wind Tunnels for Aerodynamic Flow Simulation. Astronautics and Aeronautics, vol. 13, no. 4, April 1975, pp. 22-30.

2. MacCormack, R. W.: A Rapid Solver for Hyperbolic Systems of Equations. Paper presented at 5th International Conference on Numerical Methods in Fluid Dynamics, The Netherlands, June 28 to July 3, 1976.

3. Hung, C. M. and MacCormack, R. W.: Numerical Simulation of Supersonic and Hypersonic Turbulent Compression Corner Flows Using Relaxation Models. AIAA Paper 76 — presented at AIAA 9th Fluid Dynamics Conference in San Diego, July 14-16, 1976.

4. Horstman, C. C.: A Turbulence Model for Nonequilibrium Adverse Pressure Gradient Flows. AIAA Paper 76-412, presented at AIAA 9th Fluid and Plasma Dynamics Conference in San Diego, July 14-16, 1976.

5. Baldwin, B. S. and MacCormack, R. W.: Modifications of the Law of the Wall and Algebraic Turbulence Modeling for Separated Boundary Layers. AIAA Paper 76-350, presented at AIAA 9th Fluid and Plasma Dynamics Conference in San Diego, July 14-16, 1976.

6. Clauser, F.: On Turbulent Flow Near a Wall. Jour. Aero. Sci., vol. 23, no. 11, 1956, pp. 1007-1011.

7. MacCormack, R. W. and Baldwin, B. S.: A Numerical Method for Solving the Navier-Stokes Equations with Application to Shock-Boundary Layer Interactions. AIAA Paper 76-1, presented at AIAA 13th Aerospace Sciences Meeting in Pasadena, Jan. 20-22, 1975.

8. Reda, D. C. and Murphy, J. D.: Shock Wave Turbulent Boundary Layer Interaction in Rectangular Channels, Part II: The Influence of Sidewall Boundary Layers on Incipient Separation and Scale of Interaction. AIAA Paper 73-234 presented at AIAA 11th Aerospace Sciences Meeting in Washington, D. C., Jan. 10-12, 1973.
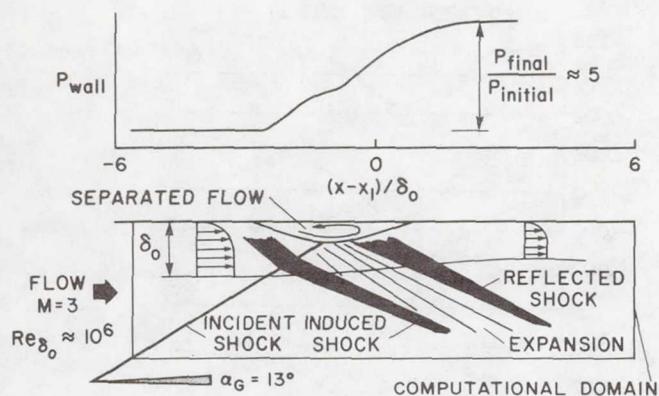
Figure 1.- Experimental flow field.
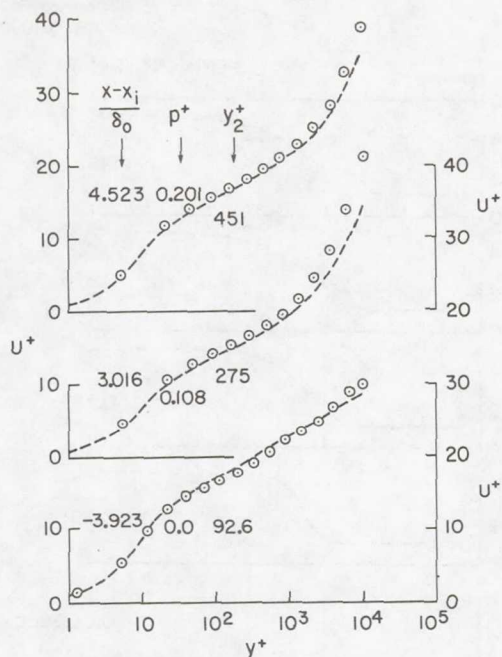
Figure 2.- Attached velocity profiles.
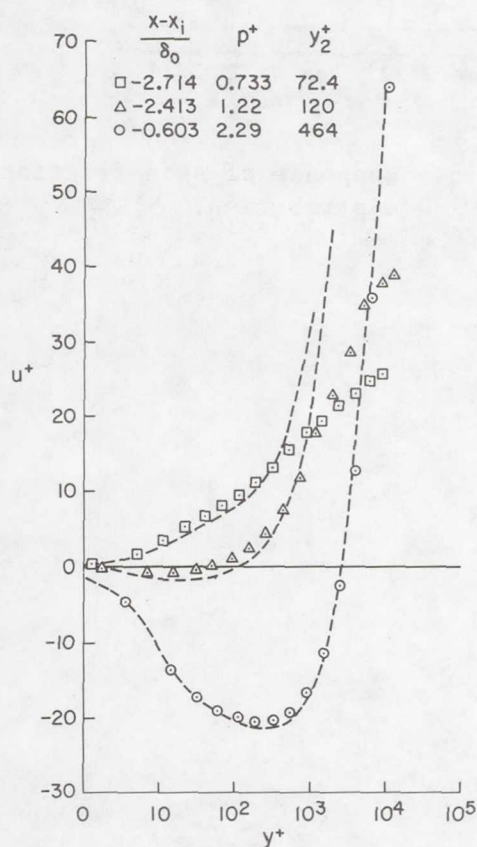
Figure 3.- Velocity profiles near separation.
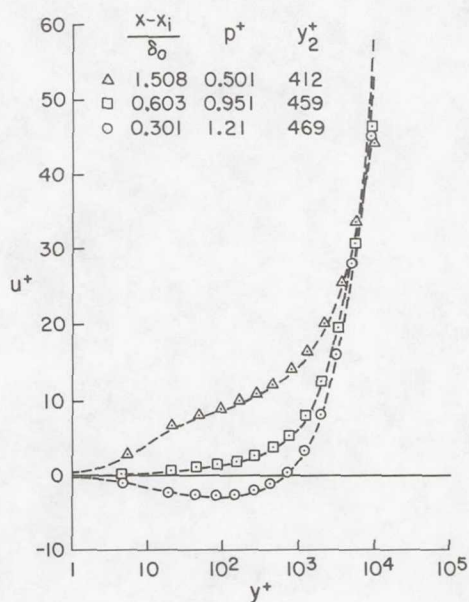
Figure 4.- Velocity profiles near reattachment.
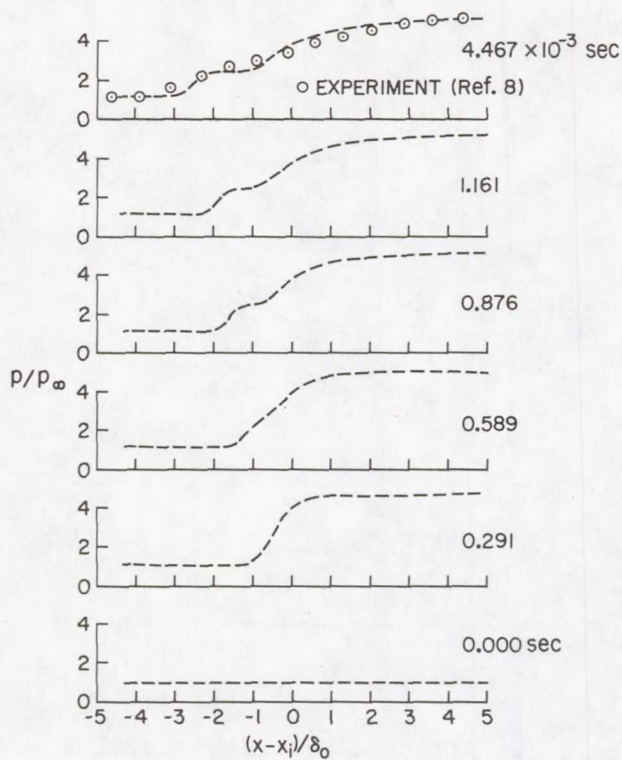
Figure 5.- Response of wall-pressure
distribution.
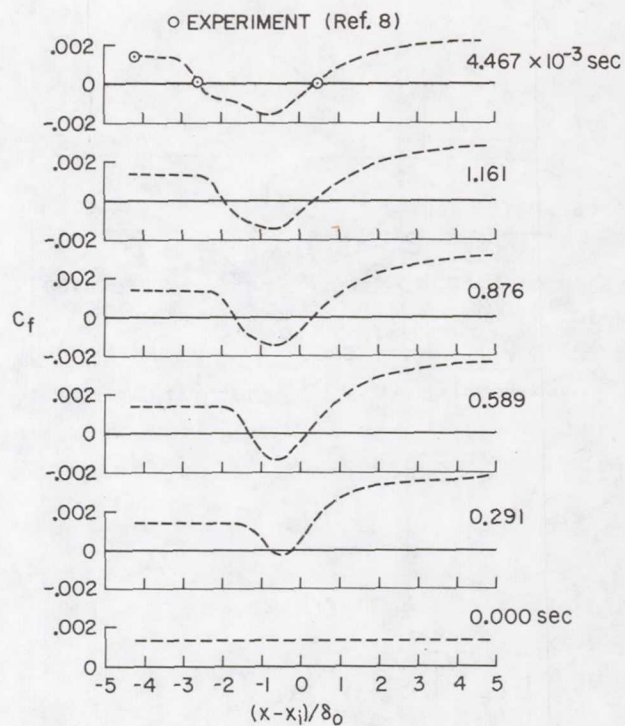
Figure 6.- Response of skin-friction
distribution.

THE LIFT FORCE ON A DROP IN UNBOUNDED

PLANE POISEUILLE FLOW

Philip R. Wohl
Old Dominion University

SUMMARY

The lift force on a deformable liquid sphere moving in steady, plane Poiseuille-Stokes flow and subjected to an external body force is calculated. The results are obtained by seeking a solution to Stokes' equations for the motion of the liquids inside and outside the slightly perturbed sphere surface, as expansions valid for small values of the ratio of the Weber number to the Reynolds number. When the ratio of the drop and external fluid viscosities is small, the lift exerted on a neutrally buoyant drop is found to be approximately one-tenth of the magnitude of the force reported by Wohl and Rubinow (ref. 1) acting on the same drop in unbounded Poiseuille flow in a tube. The resultant trajectory of the drop is calculated and displayed as a function of the external body force.

INTRODUCTION

Understanding the dynamics of a single particle and suspensions of particles in slow viscous flow is of fundamental importance in many branches of science and technology, such as air pollution, raindrop formation, fluidization in the chemical process industry, blood flow, the flow of fiber suspensions in paper making, et al. (refs. 2, 3).

The migration of a single spherical particle across the streamlines of a nonuniform creeping flow cannot be explained on the basis of Stokes' equations, even in the presence of bounding walls; i.e., a sphere experiences no transverse force at zero Reynolds number. A transverse force does exist theoretically if inertial forces are taken into account (refs. 4, 5, 6). However, the situation is different for flexible particles. Experimental observations (ref. 7) reveal that at low Reynolds numbers, even when a rigid sphere experiences a negligible transverse force, neutrally buoyant deforming drops (and

flexible solid particles) migrate rapidly across streamlines. This suggests
that the lift force which produces migration arises from the interaction be-
tween the particle deformation and the surrounding flow field, rather than from
an inertial effect.

Chaffey et al.(ref. 8) considered the problem of a deformable liquid sphere
in Couette-Stokes flow (linear shear). Assuming the drop to be 'close' to the
plane wall bounding the flow, they found that the effect on the deformed drop
was to produce a force tending to push the drop away from the wall. This force
has two failings when used alone as a basis for explaining the migration of drops
in plane Poiseuille flow. First, it neglects the force due to the interaction
of the parabolic profile with the resultant deformation of the drop. Secondly,
it cannot be expected to be valid when the drop is not close to the wall. In
fact, Karnis & Mason (ref. 9) have shown experimentally that the migration rates
calculated by Chaffey et al. are significantly larger than those which are ob-
served. The experimental observations were recorded at a considerable distance
from the walls relative to the particle size.

In this paper, the hydrodynamic force arising out of the interaction between
the incident plane parabolic flow and the sphere deformation is calculated. The
interaction between the drop and the boundary walls is neglected. The analysis
herein follows that of reference 1 wherein the case of Poiseuille flow in a
tube is considered (see also refs. 10, 11, 12).

FORMULATION

The drop surface is defined by
$$r = 1 + f(\theta, \phi), \tag{1}$$
where (r, θ, ϕ) are spherical polar coordinates with pole fixed at the center of
the undistorted drop and the axis $\theta = 0$ along the direction of the undisturbed
velocity $\vec{U}$. We denote the velocity of the fluid exterior to this surface by
$\vec{v}$ and the pressure by p. All external lengths, velocities and stresses have been
non-dimensionalized by a , U_0 and $\mu U_0 a^{-1}$, respectively, where a is the
radius of the undeformed drop, U_0 is a reference velocity to be specified later,
and μ is the viscosity of the fluid outside the drop. Quantities character-
izing the interior of the drop are distinguished with a prime. It is assumed
that $\{\vec{v},p\}$ and $\{\vec{v}',p'\}$ satisfy the Stokes' equations and conditions:

$$\Delta \vec{v} - \nabla p = 0, \quad \nabla \cdot \vec{v} = 0, \quad \vec{v} = \vec{U} \text{ at } r = \infty, \left. \right\} \tag{2}$$
$$\Delta \vec{v}' - \nabla p' = 0, \quad \nabla \cdot \vec{v}' = 0, \quad \vec{v}' \text{ bounded,}$$

$$v_n = v_n' = 0, \quad \vec{v}_t = \vec{v}'_t, \quad \vec{\tau}_t = \alpha \vec{\tau}'_t \text{ at } r = 1 + f(\theta, \phi), \tag{3}$$

$$\varepsilon \tau_n = \varepsilon \alpha \, \tau_n' + R_1^{-1} + R_2^{-1} \text{ at } r = 1 + f(\theta, \phi), \tag{4}$$

where v_n represents the normal velocity component, $\vec{v}_t$ the tangential velocity vector, $\vec{\tau}_t$ the tangential stress vector, τ_n the magnitude of the normal stress; $\alpha = \mu'/\mu$; R_1 and R_2 are the two principal radii of curvature of the drop surface; and the dimensionless parameter $\varepsilon = \mu U_0 T^{-1}$, where T is the constant surface tension associated with the interface between the two viscous media. The pressure p' includes a body force K per unit volume which is assumed to act on the drop in the positive-z direction. Equation (4) is Laplace's formula for the equilibrium between the normal stress across the surface and the tension and curvature of the surface.

We seek the solution of equations (2) - (4) as expansions valid for small values of ε which, upon neglecting terms of $O(\varepsilon)$, are of the form

$$\vec{v} = \vec{v}_0 + \varepsilon \vec{v}_1, \quad p = p_0 + \varepsilon p_1, \left. \right\}$$
$$\vec{v}' = \vec{v}_0' + \varepsilon \vec{v}_1', \quad p' = \varepsilon^{-1} p'_{-1} + p_0' + \varepsilon p_1', \right\} \tag{5}$$
$$f = \varepsilon f_1 .$$

The solution in general will depend on the parameter α. We shall see (eq. (6)) that the term $\varepsilon^{-1} p'_{-1}$, which gives the internal pressure of the drop in its spherical shape when $\vec{U} = 0$, is needed in order to satisfy condition (4). The deformation f is assumed to be $O(\varepsilon)$ so that the drop is spherical when $\vec{U} = 0$. Upon inserting equations (5) into equations (2) and equating coefficients of each power of ε in each equation, we find that $\{\vec{v}_i, p_i, \vec{v}_i', p_i'\}$ for $i = 0, 1$ satisfy the Stokes' equations, $\nabla p'_{-1} = 0$, $\vec{v}_0 = \vec{U}$ at $r = \infty$, and $\vec{v}_1 = 0$ at $r = \infty$.

The boundary conditions (3) - (4) must be examined carefully in order to determine the contributions at the various orders of ε. It can be shown (ref. 1) that the normal and tangential components of the velocity and stress vectors can be expressed, through a small rotation, in terms of spherical coordinate components. This small rotation is defined with the aid of two Eulerian angles,

which are related to the deformation of the drop. A Taylor expansion about
r = 1 of the quantities in equations (3) - (4) is then used to transform to an
equivalent set of boundary conditions evaluated on the undeformed sphere surface.
Finally, taking account of equations (5) yields:

$O(\varepsilon^0)$,

$$p'_{-1} = 2/\alpha, \tag{6}$$

$$\left.\begin{array}{l} v_{0r} = v'_{0r} = 0, \ v_{0\theta} = v'_{0\theta}, \ v_{0\phi} = v'_{0\phi}, \\ \tau_{0r\theta} = \alpha\tau'_{0r\theta}, \ \tau_{0r\phi} = \alpha\tau'_{0r\phi}, \end{array}\right\} \text{ at } r = 1 \tag{7}$$

$O(\varepsilon)$,

$$v_{1r} + f_1 \frac{\partial v_{0r}}{\partial r} = [\text{primes}] = \frac{\partial f_1}{\partial \theta} v_{0\theta} + \text{cosec}\theta \frac{\partial f_1}{\partial \phi} v_{0\phi},$$

$$v_{1\theta} + f_1 (\partial v_{0\theta}/\partial r) = [\text{primes}],$$

$$v_{1\phi} + f_1 (\partial v_{0\phi}/\partial r) = [\text{primes}], \qquad\qquad \text{at } r = 1$$

$$\tag{8}$$

$$\tau_{1r\theta} + f_1 \frac{\partial \tau_{0r\theta}}{\partial r} + \frac{\partial f_1}{\partial \theta}(\tau_{0rr} - \tau_{0\theta\theta}) - \text{cosec}\theta \frac{\partial f_1}{\partial \phi}\tau_{0\theta\phi} = \alpha [\text{primes}],$$

$$\tau_{1r\phi} + f_1 \frac{\partial \tau_{0r\phi}}{\partial r} - \frac{\partial f_1}{\partial \theta}\tau_{0\theta\phi} + \text{cosec}\theta \frac{\partial f_1}{\partial \phi}(\tau_{0rr} - \tau_{0\phi\phi})$$
$$= \alpha [\text{primes}]$$

$$\tau_{0rr} = \alpha\tau'_{0rr} - (2 + \text{cosec}\theta \frac{\partial}{\partial \theta}(\sin\theta \frac{\partial}{\partial \theta}) + \text{cosec}^2\theta \frac{\partial^2}{\partial \phi^2}) f_1 \quad \text{at } r = 1. \tag{9}$$

Equations (7) involve only the $O(\varepsilon^0)$ terms of the expansion, and equation (9)
gives the deformation f_1 in terms of the quantities determined from the $O(\varepsilon^0)$
solution. The function f_1 is determined as a particular solution of equation (9)
subject to the auxiliary conditions that the volume of the drop remains constant,
and that the centroid of the drop is chosen to coincide with the origin of the
coordinate system.

PLANE PARABOLIC FLOW

We now consider U to be a plane parabolic flow represented by

$$U = \beta + \delta x + \gamma x^2, \tag{10}$$

with respect to a coordinate system fixed at the centroid of the drop, where
β, δ and γ are constants. In order to relate this to plane Poiseuille flow, let
the drop be located at an orthogonal distance X = b measured from the mid-plane
between two parallel walls, one stationary, with the positive X-axis pointing

in the direction of the other wall moving in the positive-z direction with velo-city U_w. Suppose that the drop is moving with dimensionless velocity $c = dZ/dt$, with respect to a coordinate system fixed in the stationary wall, and in the same direction as the Poiseuille flow field. Then the velocity of the flow with respect to a coordinate system fixed at the centroid of the drop is

$$\left. \begin{array}{c} U = 1 - (\frac{X}{b_0})^2 + \frac{U_w}{2U_0} (1 + \frac{X}{b_0}) - c \\ X = b + ax. \end{array} \right\} \tag{11}$$

where

Here the reference velocity $U_0 = -b_0^2 G/2\mu$ where b_0 is one-half the distance between the walls bounding the flow, and $G \neq 0$ is the constant applied pressure gradient. By comparing equation (10) with equation (11) it follows that

$$\left. \begin{array}{c} \beta \equiv 1 - (\frac{b}{b_0})^2 + \frac{U_w}{2U_0} (1 + \frac{b}{b_0}) - c, \\ \delta \equiv \frac{aU_w}{2U_0 b_0} - \frac{2ab}{b_0^2} , \ \gamma \equiv -(a/b_0)^2. \end{array} \right\} \tag{12}$$

Since the $O(\varepsilon^0)$ velocity field satisfies the boundary condition $\vec{v}_0 \rightarrow U\vec{k}$ as $r \rightarrow \infty$, where $\vec{k}$ is the unit vector in the z direction, it follows from the linearity of Stokes' equations that the $O(\varepsilon^0)$ solution is easily obtained as the sum of the known flows past a liquid sphere in uniform stream, linear shear and plane quadratic shear. From these solutions the $O(\varepsilon^0)$ hydrodynamic force $\vec{F}_0$ on the drop is calculated to be

$$\vec{F}_0 = 6\pi\mu a \ U_0 \left[\frac{\alpha + \frac{2}{3}}{\alpha + 1} \ \beta \ + \ \frac{1}{3} \frac{\alpha}{\alpha + 1} \ \gamma \right] \ \vec{k}. \tag{13}$$

This is the drag force acting on the undeformed drop. The value of β (or equivalently the velocity c of the drop via eq. (12))is determined so that the body force $\frac{4}{3}\pi a^3 K\vec{k}$ balances $\vec{F}_0$, viz.

$$\beta = - \frac{\alpha}{3\alpha + 2} \ \gamma - \frac{2}{3} \ k \ (\frac{\alpha + 1}{3\alpha + 2}), \tag{14}$$

where k is the non-dimensional body force given by $k = K a^2 / \mu'U_0$.

The deformation f_1 is found from equation (9) to be

$$f_1 = f_{11} + f_{12},$$

$$f_{11} = \frac{19}{24}\,\delta\,\frac{\alpha+\frac{16}{19}}{\alpha+1}\,\cos\emptyset\,P_2^1\,(\cos\theta),$$

$$f_{12} = \frac{-11}{40}\,\gamma\,\frac{\alpha+\frac{10}{11}}{\alpha+1}\,[P_3^0(\cos\theta) - \frac{1}{6}\,\cos 2\emptyset\,P_3^2\,(\cos\theta)],$$

(15)

where P_2^1, P_3^0 and P_3^2 are associated Legendre polynomials. It is seen that the deformation is independent of the body force.

To determine the $O(\varepsilon)$ fields $\{\vec{v}_1, p_1, \vec{v}_1', p_1'\}$ we must solve Stokes' equations subject to the interface boundary conditions (8) at $r = 1$, in addition to having $\vec{v}_1$ vanish at infinity. It is found that the drop does not experience any hydrodynamic force owing to incident linear shear (δx) and quadratic shear (γx^2), considered independently. However, their combination gives rise to an additional $O(\varepsilon)$ flow needed to satisfy additional interaction terms in the boundary conditions (8). It is this interaction field which produces a transverse force on the drop. In particular, define the interaction contributions w_{1r} and $\sigma_{1r\theta}$ by

$$v_{1r} = v_{1r}^{(1)} + v_{1r}^{(2)} + w_{1r},\quad \tau_{1r\theta} = \tau_{1r\theta}^{(1)} + \tau_{1r\theta}^{(2)} + \sigma_{1r\theta},$$

(16)

where $v_{1r}^{(1)}$ and $v_{1r}^{(2)}$ represent the linear shear and quadratic shear flows, considered independently. There are no contributions arising from the uniform flow (β) in equations (16) because to $O(\varepsilon)$ uniform flow produces no deformation of the drop (eqs. (15)). Substituting equations (16) and analogous expressions for the other $O(\varepsilon)$ velocity and stress components into conditions (8) together with the deformations (15), we find that the interaction field must satisfy, at $r = 1$:

$$w_{1r} + \frac{\partial}{\partial r}\,(f_1\,v_{0r}^{(0)} + f_{12}\,v_{0r}^{(1)} + f_{11}\,v_{0r}^{(2)}) = [\text{primes}]$$

$$= \frac{\partial f_1}{\partial\theta}\,v_{0\theta}^{(0)} + \frac{\partial f_{12}}{\partial\theta}\,v_{0\theta}^{(1)} + \frac{\partial f_{11}}{\partial\theta}\,v_{0\theta}^{(2)}$$

$$+ \operatorname{cosec}\theta\,(\frac{\partial f_{11}}{\partial\emptyset}\,v_{0\emptyset}^{(2)} + \frac{\partial f_{12}}{\partial\emptyset}\,v_{0\emptyset}^{(1)}),$$

(17a)

$$w_{1\theta} + \frac{\partial}{\partial r}\,(f_1 v_{0\theta}^{(0)} + f_{12}\,v_{0\theta}^{(1)} + f_{11}\,v_{0\theta}^{(2)}) = [\text{primes}],$$

$$w_{1\emptyset} + \frac{\partial}{\partial r}\,(f_{11}\,v_{0\emptyset}^{(2)} + f_{12}\,v_{0\emptyset}^{(1)}) = [\text{primes}],$$

$$\sigma_{1r\theta} + \frac{\partial}{\partial r}\left(f_1\,\tau_{0r\theta}^{(0)} + f_{12}\,\tau_{0r\theta}^{(1)} + f_{11}\,\tau_{0r\theta}^{(2)}\right) - \frac{\partial f_1}{\partial\theta}\,\tau_{0\theta\theta}^{(0)}$$

$$+ \frac{\partial f_{12}}{\partial\theta}\left(\tau_{0rr}^{(1)} - \tau_{0\theta\theta}^{(1)}\right) + \frac{\partial f_{11}}{\partial\theta}\left(\tau_{0rr}^{(2)} - \tau_{0\theta\theta}^{(2)}\right)$$

$$- \csc\theta\,\frac{\partial f_{11}}{\partial\phi}\,\tau_{0\theta\phi}^{(2)} + \frac{\partial f_{12}}{\partial\phi}\,\tau_{0\theta\phi}^{(1)} = \alpha\,[\text{primes}]$$

$$\sigma_{1r\phi} + \frac{\partial}{\partial r}\left(f_{11}\,\tau_{0r\phi}^{(2)} + f_{12}\,\tau_{0r\phi}^{(1)}\right) - \frac{\partial f_{11}}{\partial\theta}\,\tau_{0\theta\phi}^{(2)} - \frac{\partial f_{12}}{\partial\theta}\,\tau_{0\theta\phi}^{(1)}$$

$$+ \operatorname{cosec}\theta\,\frac{\partial f_{11}}{\partial\phi}\left(\tau_{0rr}^{(2)} - \tau_{0\phi\phi}^{(2)}\right) + \frac{\partial f_{12}}{\partial\phi}\left(\tau_{0rr}^{(1)} - \tau_{0\phi\phi}^{(1)}\right)$$

$$= \alpha\,[\text{primes}]. \qquad\qquad (17b)$$

The quantity $v_{0r}^{(i)}$ in equations (17) denotes the $O(\epsilon^0)$ radial velocity component corresponding to a uniform stream, linear shear flow and quadratic shear flow for $i = 0$, 1, and 2, respectively, and similarly for the other velocity and stress components.

THE LIFT FORCE AND TRAJECTORY

The $O(\epsilon)$ interaction field can now be found by first inserting the known deformations and $O(\epsilon^0)$ fields into boundary conditions (17). The solid spherical harmonics and their coefficients in Lamb's general solution (ref. 13, p. 595) to Stokes' equations for a sphere are then chosen so that conditions (17) are satisfied. However, the perturbation to the $O(\epsilon^0)$ force experienced by the drop after deformation depends only upon one solid spherical harmonic of order -2 in Lamb's general solution (ref. 14). This $O(\epsilon)$ force can be expressed by

$$\vec{F}_1 = -4\pi\mu\epsilon U_0 a\,\nabla(r^3 P_{-2}),$$

where

$$P_{-2} = A_{-2}^1\,r^{-2}\,P_1^1(\cos\theta)\cos\phi \qquad (18)$$

in the case of a parabolic flow represented by equation (10). Upon substituting equation (14) into the computed value of the coefficient A_{-2}^1, we obtain the result

$$\vec{F}_1 = \frac{19}{20}\,\pi\mu\epsilon U_0\,a\,\delta\,\gamma\,\sum_{n=0}^{2} F_{1n}\,\vec{i}, \qquad (19)$$

where

$$F_{10} = \left(\frac{\alpha}{2} + \frac{\alpha+1}{3}\frac{k}{\gamma}\right) \left(\frac{1}{\alpha+1}\right)^3 \left(\frac{1}{\alpha+\frac{2}{3}}\right) \left(\alpha + \frac{16}{19}\right) \left(\alpha^2 - \frac{11}{3}\alpha + 6\right),$$

$$F_{11} = -\left(\frac{1}{\alpha+1}\right)^3 \left(\alpha + \frac{16}{19}\right) \left(\frac{1}{\alpha+4}\right) \left(\frac{43}{64}\alpha^3 - \frac{3119}{504}\alpha^2 - \frac{4233}{224}\alpha + \frac{321}{56}\right),$$

$$F_{12} = -\left(\frac{1}{\alpha+1}\right)^3 \left(\alpha + \frac{10}{11}\right) \left(\frac{108867}{148960}\alpha^2 - \frac{153439}{223440}\alpha + \frac{28237}{15960}\right). \tag{20}$$

The direction of the force $\vec{F}_1$ is orthogonal to the direction of the undisturbed flow at infinity. We note that the factor γ appearing in equation (19) causes the contributions made by the coefficients F_{11} and F_{12} to vanish when the quadratic shear portion of the incident parabolic flow is set equal to zero, whereas the body force contribution appearing in the coefficient F_{10} remains finite and proportional to the body force parameter k. In this case $\vec{F}_1$ represents the transverse force exerted on a drop when the incident flow consists of a uniform stream plus a linear shear flow. It is observed from the detailed calculation which has been performed that the contributions made by the coefficients F_{11} and F_{12} to $\vec{F}_1$ arise, respectively, from interactions between (a) the $O(\epsilon^0)$ quadratic shear flow and the linear shear deformation f_{11}, and (b) the $O(\epsilon^0)$ linear shear flow and the quadratic shear deformation f_{12}. It is seen that the interaction between $O(\epsilon^0)$ uniform stream and f_{12} does not contribute to the $O(\epsilon)$ force.

The sign of the force $\vec{F}_1$ can be determined by inspection of equation (19) after inserting the value of b, given by equation (22). The coefficients (20) and their sum are plotted against α in figure 1 for a neutrally buoyant drop, when k is zero. For small α, the sum $F_{10} + F_{11} + F_{12}$ is negative. In this case the migration of the drop is always towards the point of zero velocity gradient, viz. $X = U_w b_0/4U_0$. It is observed from equations (20) that, in general, the direction of migration depends only on the parameters k/γ and α and not upon radial position (other than which side of the point where $dU/dX = 0$ the drop is).

We shall now calculate the trajectory of the drop. Its lateral velocity $d\vec{b}/dt$ is determined by equating the Hadamard & Rybczynski drag force for a liquid sphere to $\vec{F}_1$. Thus,

$$\frac{db}{dt} = \epsilon \left(\frac{a}{b_0}\right)^2 \left(\frac{aU_w}{4U_0 b_0} - \frac{ab}{b_0^2}\right) F,$$

$$F = -\frac{19}{60} \left(\frac{\alpha+1}{\alpha+\frac{2}{3}}\right) \sum_{n=0}^{2} F_{1n}. \tag{21}$$

Integration of equation (21) yields

$$b = \frac{U_w b_0}{4U_0} + (b_1 - \frac{U_w b_0}{4U_0})\, e^{-t/\tau} ,$$

$$\tau = b_0^4 / \varepsilon U_0 a^3 F,$$

$$(22)$$

where b_1 is the initial position of the drop. The trajectory of the drop is obtained by dividing db/dt, given by equation (21) into $dZ/dt = c$, given by equation (14). Upon integration we obtain

$$\frac{Z}{b_0} = \frac{-1}{\varepsilon (a/b_0)^3 F}\left[(1 + \frac{2}{3}\frac{\alpha+1}{3\alpha+2} k - \frac{\alpha}{3\alpha+2}\frac{a^2}{b_0^2} + \frac{U_w}{2U_0} + \frac{U_w^2}{16U_0^2})\, \ln\left(\frac{\frac{b}{b_0} - \frac{U_w}{4U_0}}{\frac{b_1}{b_0} - \frac{U_w}{4U_0}}\right)\right.$$

$$\left. - \frac{1}{2}\left[(\frac{b}{b_0})^2 - (\frac{b_1}{b_0})^2\right] + \frac{U_w}{4U_0}(\frac{b}{b_0} - \frac{b_1}{b_0})\right].$$

$$(23)$$

The ratio U_w/U_0 may be either positive or negative depending on the sign of the applied pressure gradient. In undisturbed flow some layers of the fluid will move in a direction opposite to U_w when U_0 is sufficiently negative. The critical pressure gradient occurs when $dU/dX = 0$ at $X = -b_0$, i.e., when $U_w/U_0 = -4$. Theoretical curves based on equation (23) are shown in figure 2(a) for $U_w = 0$, $U_0 > 0$ and in figure 2(b) for $U_w/U_0 = -4$, for the parameter values $\alpha = 0$, $\varepsilon = 0.01$, $a/b_0 = 0.1$ and $b_1/b_0 = 0.5$, and for various values of the body force parameter k. These trajectories show that the drop may move inwards or outwards. The direction of migration as $t \to \infty$ for the various values of k can be determined by examination of equations (21) and (14).

Figure 2(a) (wherein $U_w = 0$) shows that the drop moves in the positive-z direction and approaches the axis midway between the walls ($b = 0$) asymptotically for $k > -0.011$ (to three decimal places). When $k = -0.011$, the drop travels along the line $b = b_1$ in the positive-z direction. For $-2.25 < k < -0.011$, the drop migrates radially outwards, initially in the positive-z direction. When $k < -2.25$, the trajectories are always in the negative-z direction and radially outwards. When the above trajectories are compared with those of a drop in Poiseuille flow in a tube, depicted in Figure 7 of Wohl and Rubinow (ref. 1), it is observed that there is negligible difference except in the case $|k| \ll 1$. This observation is to be expected because when $\alpha = 0$ and $a/b_0 = 0.1$, it is found that $F = 1.337 + 120k$ (to three decimal places) from equations (21) and

(20). The value of F for circular Poiseuille flow is 10.075+ 120k (to three decimal places). The body force parameter k dominates both expressions unless $|k| \ll 1$. Figure 2(b) (wherein $U_w/U_0 = -4$) displays the drop moving in the positive-z direction and approaching the stationary wall ($b = -b_0$) asymptotically for k < -0.011. For -0.011 < k < 6.75, the trajectories are always in the positive-z direction and radially outwards. When k > 6.75 the drop migrates radially outwards, initially in the negative-z direction.

SCOPE OF THE ANALYSIS

The incident parabolic flow is considered to be unbounded in the sense that the secondary effect of the wall on the perturbed flow produced by the drop is neglected, i.e., interaction between the drop and the boundary walls is neglected. Also, the results herein are not applicable unless the effects of $O(\epsilon)$ and (nonlinear) inertial effects can be neglected.

REFERENCES

1. Wohl, P. R. & Rubinow, S. I.: 1974 J. Fluid Mech. 62, 185.

2. Happel, J. & Brenner, H.: 1965 Low Reynolds Number Hydrodynamics. Prentice-Hall.

3. Goldsmith, H. L. & Skalak, R.: 1975 Ann. Rev. Fluid Mech. 7, 213.

4. Rubinow, S. I. & Keller, J. B.: 1961 J. Fluid Mech. 11, 447.

5. Saffman, P. G.: 1965 J. Fluid Mech. 22, 385.

6. Cox, R. G. & Brenner, H.: 1968 Chem. Enging. Sci. 23, 147.

7. Goldsmith, H. L. & Mason, S. G.: 1962 J. Colloid Sci. 17, 448.

8. Chaffey, C. E.; Brenner, H.; & Mason, S. G.: 1965 Rheol. Acta 4, 64; correction 1967, 6, 100.

9. Karnis, A. & Mason, S. G.: 1967 J. Colloid Sci. 24, 164.

10. Cox, R. G.: 1969 J. Fluid Mech. 37, 601.

11. Haber, S. & Hetsroni, G.: 1971 J. Fluid Mech. 49, 257.

12. Hetsroni, G.; Haber, S.; Brenner, H.; & Greenstein, T.: 1972 Progr. in Heat & Mass Transfer, Vol. 6, Pergamon (Hetsroni, G., ed.), 591.

13. Lamb, H.: 1945 Hydrodynamics, 6th edn. Dover.

14. Brenner, H.: 1964 Chem. Engng. Sci. 19, 519.
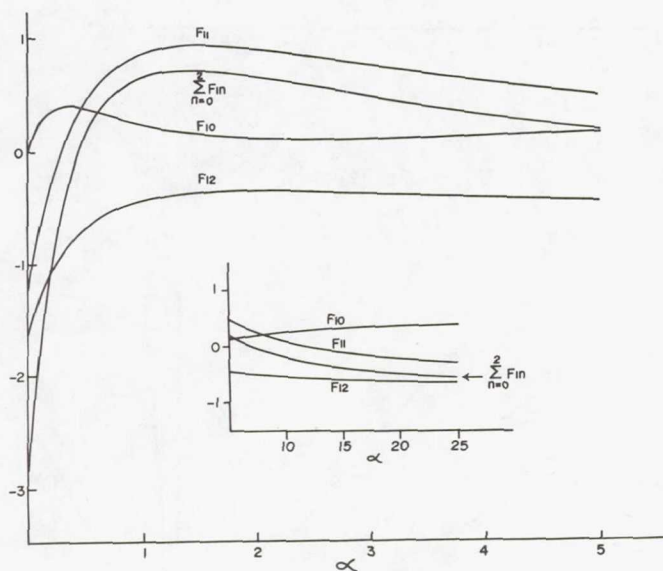
Figure 1.- Contributions to the force $\vec{F}_1$ defined by equations
(20) with the body force parameter $k = 0$, as a function of
the viscosity ratio α.
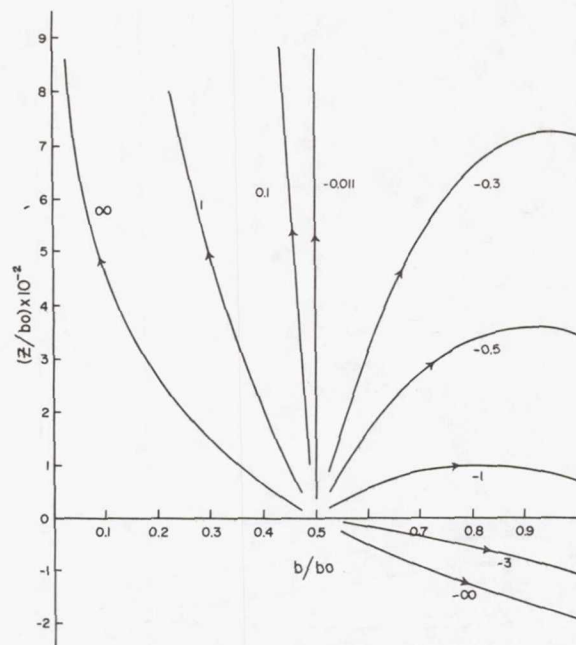
(a) $U_w = 0$; $U_0 > 0$.
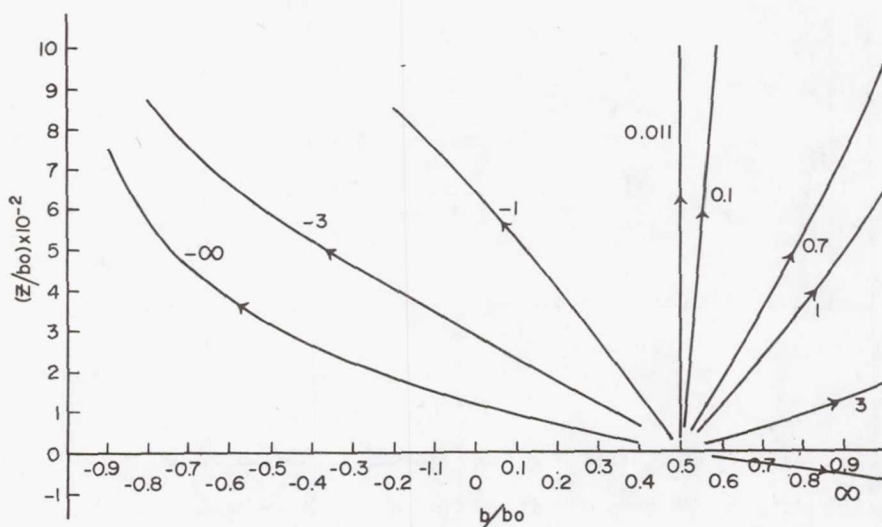
(b) $U_w/U_0 = -4$.

Figure 2.- Trajectories of a drop in plane Poiseuille flow and subject to a body force, according to equation (23). It is assumed that $\alpha = 0$, $\varepsilon = 0.01$, $a/b_0 = 0.1$, and $b_1/b_0 = 0.5$. The labels denote various values of the body force parameter $k = Ka^2/\mu'U_0$. The line $b = 0$ is located midway between the two walls bounding the flow. The arrowheads indicate the direction of migration.

Stability of Flow of a Thermoviscoelastic Fluid Between Rotating Coaxial Circular Cylinders

Nabil N. Ghandour and M.N.L. Narasimhan
Department of Mathematics, Oregon State University

Abstract

The stability problem of thermoviscoelastic fluid flow between rotating coaxial cylinders is investigated using non-linear thermoviscoelastic constitutive equations due to Eringen and Koh (ref. 1). In the course of the investigation, the solution set for the steady state Couette flow problem is first found. The velocity field is found to be indentical with that of the classical viscous case and the case of the viscoelastic fluid, but the temperature and pressure fields are found to be different. By imposing some physically reasonable mechanical and geometrical restrictions on the flow, and by a suitable mathematical analysis, the problem is reduced to a characteristic value problem. The resulting problem is solved in this paper and stability criteria are obtained in terms of critical Taylor numbers. In general, it is found that thermoviscoelastic fluids are more stable than classical viscous fluids and viscoinelastic fluids under similar conditions.

Introduction

Although stability problems of a wide variety of classical viscous flows have been exhaustively investigated to date, significant qualitative and quantitative analytical studies concerning varieties of non-Newtonian fluid flow stability problems are still lacking. Since non-Newtonian fluids such as high polymer solutions, paints, colloidal suspensions, etc., occur very commonly in many laboratory experiments concerned with technological and biophysical studies, it is of great importance to investigate the stability of flows of such fluids. Among these stability problems of non-Newtonian fluids which have been investigated are those of a viscoinelastic fluid in a Couette flow in the presence of a circular magnetic field by Narasimhan (ref. 2) and that of a pseudoplastic material in a Couette flow by Graebel (ref. 3). In the present investigation we study the stability of Couette flow of a thermoviscoelastic fluid based on the constitutive equations of Eringen and Koh (ref. 1).

Mathematical Analysis

In the course of the analysis, the steady state solution
is first obtained for the Couette flow of a thermoviscoelastic
fluid. Then by superposing axisymmetric, time-dependent small
disturbances on the basic steady flow and linearizing with
respect to these small disturbances, the problem is reduced to a
characteristic value problem. The requirement that nontrivial
solutions exist for this problem leads to a characteristic equa-
tion between the parameters of the problem, namely $(T, q, a,
\alpha_i, N_i, M_j, G)$, where T is the Taylor number, q, represents
the disturbance temperature field, a represents the wave
number of the disturbance, α_i represent the material coeffi-
cients, N_i, M_j and G represent geometric parameters and
thermoviscoelastic properties of the fluid. The resulting
characteristic value problem consists in finding those sets of
values for these parameters which represent the solution of the
system at marginal stability, i.e., determining the mode of un-
stable motion which will appear at the onset of instability.
This would give a sequence of values of T for different values
of a, the lowest values of which would be of interest in ob-
taining marginal stability because the mode described by this
value would appear before the others. Thus the characteristic
value problem becomes one of finding this minimum lowest posi-
tive, real value of T for various values of a. The stability
criterion is then determined in terms of these critical Taylor
numbers by using the principle of exchange of stabilities and by
employing the orthogonal development technique of Chandrasekhar
(ref. 4).

Conclusions and Remarks

The numerical results obtained are compared with the
existing stability investigations. We find that thermovisco-
elastic fluids in a Couette flow are more stable than classical
viscous fluids like Bingham plastics and unlike viscoinelastic
fluids which have been found to be less stable than viscous
fluids. This behavior of the fluid in our case is essentially
due to the viscoelastic nature of the fluid under thermal as well
as rotational effects.

References

1. A.C.Eringen and S.L. Koh, On the foundations of nonlinear thermoviscoelasticity, Int. J. Engng. Sci. $\underline{1}$, pp 199-229. 1963.

2. M.N.L. Narasimhan, Stability of flow of a non-Newtonian liquid between two rotating cylinders in the presence of a circular magnetic field, Proc. Fourth Int. Congress on Rheology, Brown University, Providence, R.I., pp 345-363, 1963.

3. W.P. Graebel, The hydrodynamic stability of a Bingham fluid in Couette flow, Proc. of IUTAM Symposium on Second Order effects in elasticity, plasticity and fluid dynamics, Haifa, Israel, pp 636-649, 1962.

4. S. Chandrasekhar, "Hydrodynamic and Hydromagnetic Stability", Pergamon Press, Oxford, England, 1961.

Page intentionally left blank

STABILITY OF A VISCOUS FLUID IN A RECTANGULAR CAVITY

IN THE PRESENCE OF A MAGNETIC FIELD

C. Y. Liang and Y. Y. Hung
Oakland University

SUMMARY

The stability of an electrically conducting fluid subjected to two
dimensional disturbance was investigated. The physical system consists of two
parallel infinite vertical plates which are thermally insulated. Applied
normal to the plates is an external magnetic field of constant strength. The
fluid is heated from below so that a steady temperature gradient is maintained
in the fluid. The governing equations were derived by perturbation technique,
and solutions were obtained by a modified Galerkin method. It was found that
the presence of the magnetic field increases the stability of the physical
system, and instability can occur in the form of neutral or oscillatory
instability.

INTRODUCTION

The Bérnard problem of stability of a viscous, stationary fluid heated
from below has been a subject of many investigations (ref. 1). It is found
that when the temperature gradient exceeds a critical value, instability sets
in as stationary cellular convection. For the case of an electrically con-
ducting fluid in the presence of a magnetic field, however, the physical
phenomenon becomes more complicated. The motion of the fluid crossing the
magnetic field causes electrical currents to be generated, and the current
carrying fluid elements traversing the magnetic field gives rise to an
additional body force (the Lorentz force) which tends to retard the fluid
motion. Consequently, the stability of the system is greatly increased.
Furthermore, Chandrasekhar (ref. 1) proved that depending on the relationship
between the electric resistivity and the thermal diffusivity of the fluid,
instability can manifest itself in the form of stationary or oscillatory
motion.

Exact solution of instability due to small two dimensional disturbance of
a viscous fluid bounded by two parallel vertical planes was obtained by Yih
(ref. 2). The bounding planes are thermally insulated, and an upward tempera-
ture gradient is applied to the fluid. Yih showed that for disturbances

periodic in the vertical direction, the most unstable modes are associated with the wave number zero. It is also shown that instabilities due to anti-symmetric disturbances with respect to a median vertical plane are more easily excited than those due to symmetric disturbances of the same wave number.

In this investigation, it is proposed to extend Yih's finding by incorporating the effect of a magnetic field applied normal to the bounding walls. The governing equations were simplified by using Boussinesq approximation. The onset of neutral as well as oscillatory instabilities was studied.

SYMBOLS

d distance between the vertical planes

g acceleration due to gravity

H_o intensity of applied magnetic field of constant strength

h perturbation quantity of magnetic intensity

n wave number

P pressure

Pr_1 Prandtl number, ν/κ

Pr_2 magnetic Prandtl number, ν/η

Pr_2' parameter defined as η/κ

Q electromagnetic number, $(\mu H^2 d^2)/(4\pi\rho\nu\eta)$

Q' parameter defined as $(\mu H^2 d^2)/(4\pi\rho\kappa^2)$

R Rayleigh number, $(g\alpha\beta d^4)/(\kappa\nu)$

u,w perturbation velocity quantity in x and z direction

x,z space co-ordinates

α coefficient denoting change of fluid density per degree rise in temperature

β temperature gradients in fluid

η electric resistivity

θ fluid temperature

κ thermal diffusivity

μ magnetic permeability

ν kinematic viscosity

ρ density

ω_c critical wave speed

$\delta\bar{\omega}$ parameter defined as $(\delta P/\rho) + (\mu H_o h_x)/(4\pi\rho)$

∇^2 Laplace operator, $\dfrac{\partial^2}{\partial x^2} + \dfrac{\partial^2}{\partial z^2}$

Superscript:
*   dimensionless

Subscripts:
x,z   x and z component, respectively
c   critical

FORMULATION

The physical system under study consists of two infinite and thermally insulated vertical planes placed at a distance d apart. Applied normal to the bounding planes is an external magnetic field of constant strength H_o. The electrically conducting fluid is heated from below so that a steady temperature gradient is maintained in the fluid. Figure 1 shows the schematic diagram of the physical system and the Cartesian co-ordinate adopted for this study.

A detailed development of the governing differential equations and the perturbation equations are presented in chapters 2 and 4 in reference 1. For the present problem, the perturbation equations are given below:

Continuity equation

$$\frac{\partial u}{\partial x} + \frac{\partial w}{\partial z} = 0 \tag{1}$$

Momentum equation

$$\frac{\partial u}{\partial t} = -\frac{\partial}{\partial x}(\delta\bar{\omega}) + \nu\nabla^2 u + \frac{\mu H_o}{4\pi\rho}\frac{\partial h_x}{\partial x} \tag{2}$$

$$\frac{\partial w}{\partial t} = -\frac{\partial}{\partial z}(\delta\overline{\omega}) + g\alpha\theta + \nu\nabla^2 w + \frac{\mu H_o}{4\pi\rho}\frac{\partial h_z}{\partial x} \tag{3}$$

Energy equation

$$\frac{\partial\theta}{\partial t} = \beta w + \kappa\nabla^2\theta \tag{4}$$

Equations for E-M field

$$\frac{\partial h_x}{\partial x} + \frac{\partial h_z}{\partial z} = 0 \tag{5}$$

$$\frac{\partial h_x}{\partial t} = H_o\frac{\partial u}{\partial x} + \eta\nabla^2 h_x \tag{6}$$

$$\frac{\partial h_z}{\partial t} = H_o\frac{\partial w}{\partial x} + \eta\nabla^2 h_z \tag{7}$$

The physical variables used in the above equations are defined in the SYMBOLS. In order to reduce the above equation to dimensionless form, the following dimensionless quantities are introduced:

$$u^* = \frac{ud}{\kappa}, \quad w^* = \frac{wd}{\kappa}, \quad x^* = \frac{x}{d},$$

$$z^* = \frac{z}{d}, \quad h_x^* = \frac{h_x}{H_o}, \quad h_z^* = \frac{h_z}{H_o},$$

$$\theta^* = \frac{\theta}{\beta d}, \quad t^* = \frac{\kappa t}{d^2}, \quad \delta\overline{\omega}^* = \frac{d^2}{\kappa^2}\delta\overline{\omega}$$

By employing these dimensionless quantities, eqs. (1) to (7) can be expressed in non-dimension form as in the following:

$$\frac{\partial u^*}{\partial x^*} + \frac{\partial w^*}{\partial z^*} = 0 \tag{8}$$

$$\frac{\partial u^*}{\partial t^*} = -\frac{\partial}{\partial x^*}(\delta\overline{\omega}^*) + Pr_1\nabla^{*2}u^* + Q'\frac{\partial h_x^*}{\partial x^*} \tag{9}$$

$$\frac{\partial w^*}{\partial t^*} = -\frac{\partial}{\partial z^*}(\delta\overline{\omega}^*) + Pr_1 R\,\theta^* + Pr_1\nabla^{*2}w + Q'\frac{\partial h_z^*}{\partial x^*} \tag{10}$$

$$\frac{\partial\theta^*}{\partial t^*} = w^* + \nabla^{*2}\theta^* \tag{11}$$

$$\frac{\partial h_x^*}{\partial x^*} + \frac{\partial h_z^*}{\partial z^*} = 0 \tag{12}$$

$$\frac{\partial h_x^*}{\partial t^*} = \frac{\partial u^*}{\partial x^*} + Pr_2' \nabla^{*2} h_x^* \tag{13}$$

$$\frac{\partial h_z^*}{\partial t^*} = \frac{\partial w^*}{\partial x^*} + Pr_2' \nabla^{*2} h_z^* \tag{14}$$

Elimination of $\partial\bar{\omega}^*$ from eqs. (9) and (10) yields

$$[\frac{\partial}{\partial t^*} - Pr_1 \nabla^{*2}](\frac{\partial u^*}{\partial z^*} - \frac{\partial w^*}{\partial x^*}) = Pr_1 R \frac{\partial\theta^*}{\partial x^*}$$

$$+ Q' \frac{\partial}{\partial x^*} [\frac{\partial h_x^*}{\partial z^*} - \frac{\partial h_z^*}{\partial x^*}] \tag{15}$$

The system of equations can be simplified by introducing the following stream functions ψ and ϕ which satisfy eqs. (8) and (12) automatically,

$$u^* = -\frac{\partial\psi}{\partial z^*} , \ w^* = \frac{\partial\psi}{\partial x^*}$$

$$h_x^* = -\frac{\partial\phi}{\partial z^*}, \ h_z^* = \frac{\partial\phi}{\partial x^*} \tag{16}$$

Substituting eq. (16) into eqs. (15), (11) and (14), the governing eqs. become

$$[\frac{\partial}{\partial t^*} - Pr_1\nabla^{*2}] \nabla^{*2}\psi = Pr_1 R \frac{\partial\theta^*}{\partial x^*} + Q' \frac{\partial}{\partial x^*} (\nabla^{*2}\phi) \tag{17}$$

$$[\frac{\partial}{\partial t^*} - \nabla^{*2}] \theta^* = \frac{\partial\psi}{\partial x^*} \tag{18}$$

$$[\frac{\partial}{\partial t^*} - Pr_2'\nabla^{*2}] \frac{\partial\phi}{\partial x^*} = \frac{\partial^2\psi}{\partial x^{*2}} \tag{19}$$

Eqs. (17), (18), and (19) are subjected to the boundary conditions

at $\quad x^* = \pm\frac{1}{2}, \ \psi = D\psi = D\theta^* = \phi = 0$ \hfill (20)

SOLUTION

Solutions were sought by using Galerkin method modified by Finlayson (ref. 3). Assuming disturbances of the following form

$$\psi = A(t) \ \psi(x) \ e^{inz} \tag{21}$$

$$\theta^* = B(t) \ \Theta(x) \ e^{inz} \tag{22}$$

$$\phi = C(t) \ \Phi(t) \ e^{inz} \tag{23}$$

In selecting an appropriate trial function for Ψ, a disturbance symmetrical with respect to the medium plane was chosen as

$$\Psi_i = \frac{\text{Cosh } \lambda_i X^*}{\text{Cosh } (\lambda_i/2)} - \frac{\text{Cos } \lambda_i X^*}{\text{Cos } (\lambda_i/2)} \tag{24}$$

where the characteristic values λ_i are given by

$$\tanh \ (\lambda_i/2) + \tan \ (\lambda_i/2) = 0 \tag{25}$$

The assumed function for Θ and s are

$$\Theta = \sin \alpha_i x^* \ , \ s = \sin \beta_i x^* \tag{26}$$

where $\alpha_i = (2j-1) \ \pi$, $\beta_i = 2j\pi$ and $j = 1,2,3$, etc.

Substituting the trial functions given by eqs. (24) and (26) into the governing eqs. (17), (18) and (19), and after diagonalization, the governing differential equations are reduced to

$$[(C_j/C_i'' - \eta^2 (C_j/C_i)] \ \frac{dA}{dt} = Pr_1 [(C_j/C_i^{iv}) - 2\eta^2 (C_j/C_i'')$$

$$+ \ \eta^4 (C_j/C_i)] \ A + Pr_1 R\alpha_i (C_j/Cos\alpha_i X^*)B +$$

$$Q' \ [-\beta_i(\beta_i^2 + \eta^2)(C_j/Cos\beta_i x^*)]C \tag{27}$$

$$(\sin\alpha_j/\sin\alpha_i) \ \frac{dB}{dt} = (\sin\alpha_i/C_i')A + [-(\alpha^2 + \eta^2)(\sin\alpha_j/\sin\alpha_i)]B \tag{28}$$

$$(\sin\beta_j/\sin\beta_i) \ \frac{dC}{dt} = (\sin\beta_j/C_i')A + Pr_2'[(\beta_i^2 + \eta^2)(\sin\beta_j/\sin\beta_i)]C \tag{29}$$

Where the inner products are defined in the following manner

$$(C_j/C_i'') = \int_{-\frac{1}{2}}^{\frac{1}{2}} C_j D^2 C_i dx^* \tag{30}$$

The method for determining the stability criteria for eqs. (28), (29) and (30) is presented in reference 3.

DISCUSSION OF RESULTS

Numerical results were obtained by using a digital computer. The critical Rayleigh number was obtained for different combinations of the Prandtl number

Pr_1, the electromagnetic Prandtl number Pr_2, the electromagnetic number Q and wave number n. The results were presented in graphical form from figures 2 to 5.

For the case when Q = 0, the present problem was reduced to the Yih's problem. Examination of the results presented in Table 1 shows that the critical Rayleigh number converges rapidly to Yih's exact solution with the second approximation, thus confirming the validity of the results.

Table 1: COMPARISON OF R_c FOR Q = 0

	n	0	1	2	4
R_c	Yih's soln.	500.8	592.0	856.0	2952
	1st approx.	514.6	597.1	885.5	3100
	2nd approx.	501.0	578.8	857.0	2927

For the case of neutral stability, the critical Rayleigh number is only a function of the wave number n and Q which is a measure of the strength of the applied magnetic field (see figs. 2 and 3). The Prandtl numbers Pr_1 and Pr_2 have no effect on the stability of the system. This is expected since for the case of neutral stability, the terms involving the time derivative in the governing equations (eqs. 28 to 30) are dropped, and Pr_1 and Pr_2 would be cancelled from the resulting equations. Similar situations arise in the Bérnard problem.

For the present physical system, overstability can occur. Figure 4 shows the variation of R_c as a function of Q, Pr_1 and Pr_2. The results show that an increase in either Pr_1 or Pr_2 tend to decrease R_e. This finding is in agreement with the results obtained for Bérnard Problem (Chapter 4, ref. 1).

With the trial functions used in this study, the convergence of the numerical results are fairly satisfactory. This is especially so in the case of neutral stability; an average discrepancy of about 5% was observed between the first and second approximation. For the case of overstability, greater deviation is observed. A difference of 25% was observed between the first and second approximations. Higher order approximation would be needed to obtain more accurate results.

CONCLUDING REMARKS

The following conclusions can be drawn from this study:

1. The presence of a magnetic field increases the stability.

2.   In the presence of a magnetic field, instability can occur in the form of neutral or oscillatory instability. When oscillatory instability occurs, the effect of Pr_1 and Pr_2 becomes important. An increase in either one or both parameters tend to render the system less stable.

3.   The most unstable modes are associated with the wave number zero.

REFERENCES

1.   Chandrasekhar, S.: Hydrodynamic and Hydromagnetic Stability. Oxford Press, 1968.

2.   Yih, C. S.: Thermal Instability of Viscous Fluid. Quart. Appl. Math., Vol. 17, pp. 25-42, 1959.

3.   Finlayson, B. A.: The Galerkin Method Applied to Convective Instability Problems. J. of Fluid Mechanics, Vol. 33, Part 1, pp. 201-208, 1968.
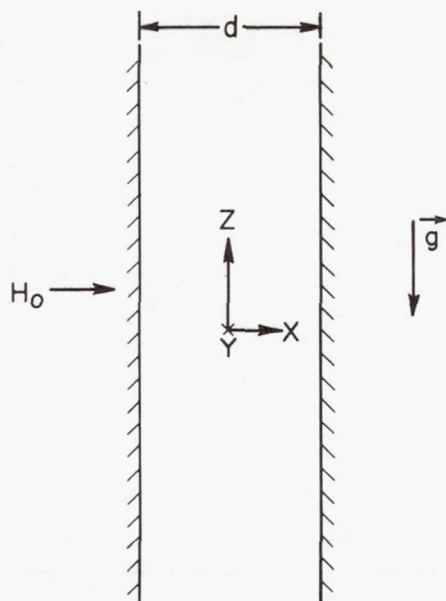
Figure 1.- Schematic diagram of physical system.
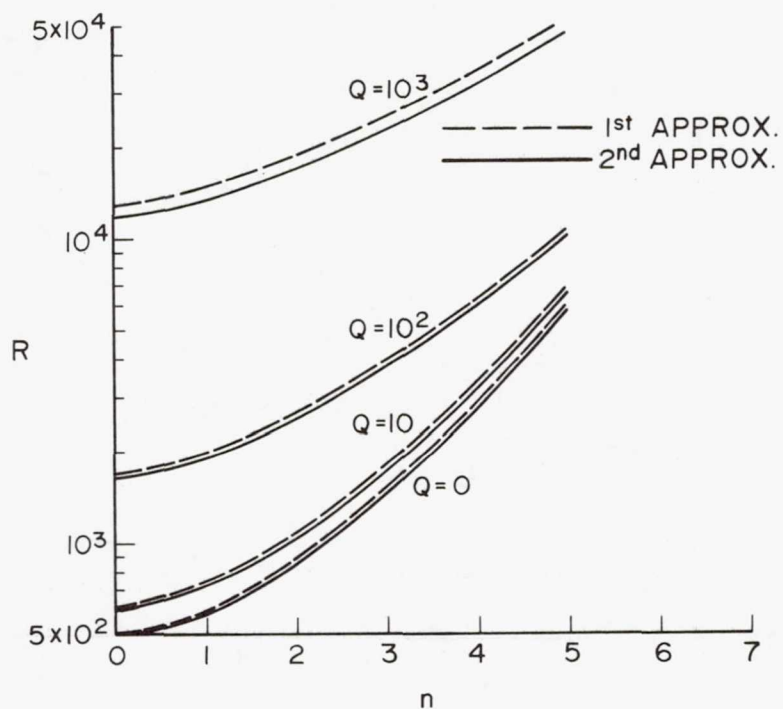
Figure 2.- Variation of R as a function of n and Q for onset of neutral stability.
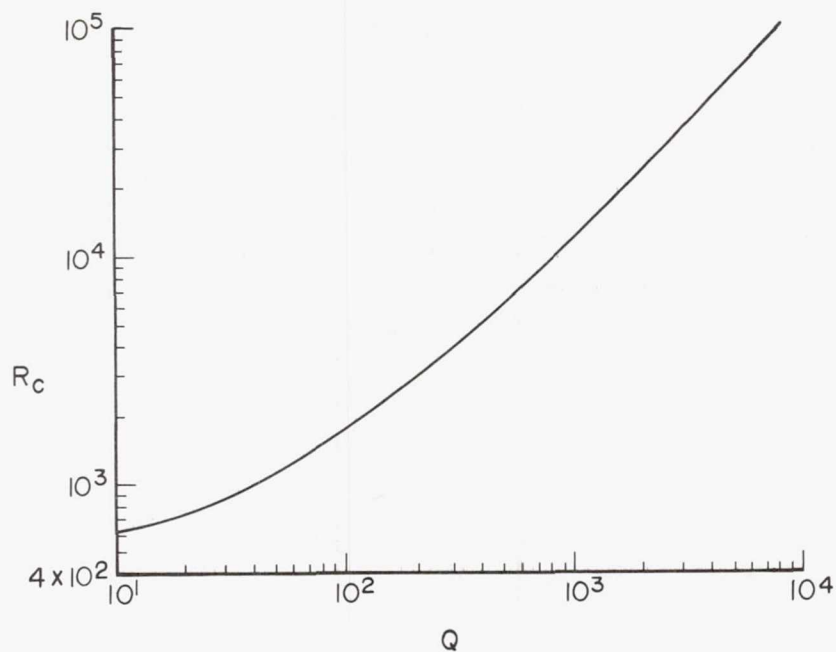
Figure 3.- Variation of R_c as a function of Q for onset of neutral stability ($Q = 0$).
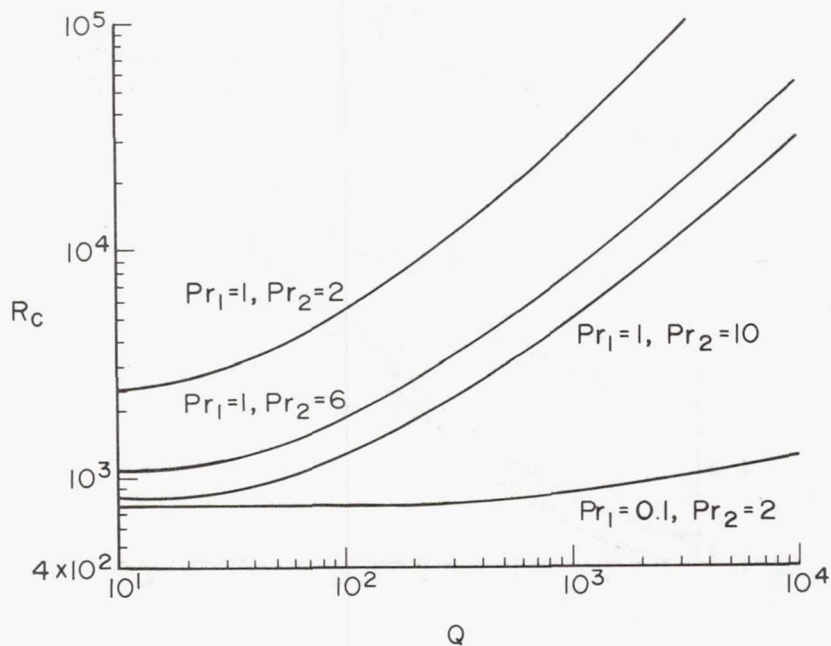
Figure 4.- Variation of R_c as a function of Q, Pr_1 and Pr_2 for onset of overstability.
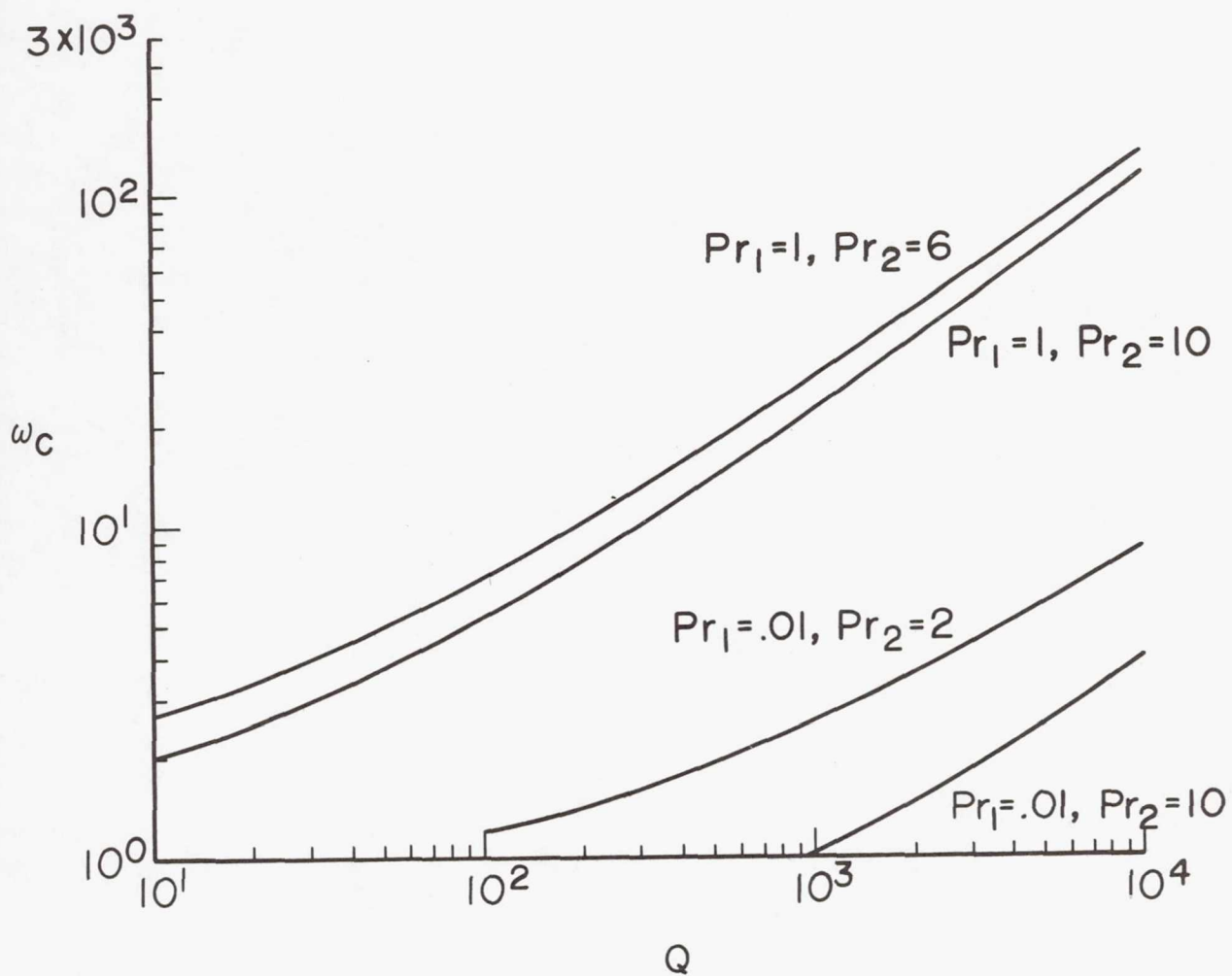
Figure 5.- Variation of critical wave speed ω_c for onset of overstability.

Page intentionally left blank

ADVANCED TRANSONIC AERODYNAMIC TECHNOLOGY

Richard T. Whitcomb
Langley Research Center

SUMMARY

The primary discussion is of NASA supercritical airfoils and their applications to wings for various types of aircraft. The various wings discussed have been designed for a subsonic jet transport with increased speed, a variable sweep fighter with greater transonic maneuverability, a high subsonic speed STOL jet transport with improved low speed characteristics, and a subsonic jet transport with substantially improved aerodynamic efficiency. Results of wind tunnel and flight demonstration investigations are described. Also discussed are refinements of the transonic area rule concept and methods for reducing the aerodynamic interference between engine nacelles and wings at high subsonic speeds.

INTRODUCTION

It is generally recognized that the transonic speed range is that in which the flow about an aerodynamic configuration is an interacting mixture of subsonic and supersonic fields. The Mach number for the onset of such conditions is called the critical Mach number, thus transonic flow at subsonic freestream Mach numbers is called supercritical flow. Most high performance aircraft operate at least part time at supercritical or transonic conditions. Therefore, this speed regime is of great practical interest. Further, because of the mixture of subsonic and supersonic flow fields both the theoretical and experimental research in this area is extremely complex. Because of the practical interest and the complexity, extensive theoretical and experimental research is being conducted in this area. This research has led to a number of significant advances in recent years. The theoretical work in this area is covered by other papers of this conference. In this paper some of the experimental research will be described. Because of the prescribed brevity of the paper only that work with which the author has been directly involved will be discussed. Even this discussion is, of necessity, very superficial.

SYMBOLS

c airfoil chord

c_d section drag coefficient

C_D airplane drag coefficient

C_L airplane lift coefficient

C_p pressure coefficient

c_n section normal-force coefficient

M Mach number

t airfoil maximum thickness

NASA SUPERCRITICAL AIRFOILS

Description

The well-known flow problem for conventional airfoils at high subsonic
speeds is illustrated at the top of figure 1. A local region of supersonic or
supercritical flow develops above the upper surface of a lifting airfoil which
terminates in a strong shock wave. The wave itself causes some increase in
drag, but usually the principal effect is separation of the boundary layer with
a significant increase in drag, stability problems, and buffet. For the NASA
supercritical airfoils, as shown at the bottom of figure 1, the curvature of
the middle region of the upper surface is substantially reduced with a resulting
decrease in the strength and extent of the shock wave. The drag associated with
the wave is reduced and, more importantly, the onset of separation is substan-
tially delayed. The lift lost by reducing the curvature of the upper surface
is regained by substantial camber of the rear portion of the airfoils.

The airfoils also incorporate other features which are important to the
total effectiveness of the new shape. The middle region of the lower surface
is designed to maintain subcritical flow for all operating conditions of the
airfoils, because the pressure rise associated with a shock wave superimposed
on the pressure rise caused by the cusp would cause separation of the lower-
surface boundary layer. To minimize the surface curvatures and thus the induced
velocities on the middle regions of both the upper and lower surfaces, the
leading edge is made substantially larger than for previous airfoils. It is
more than twice that for a 6-series airfoil of the same thickness-to-chord ratio.

The rear portion of the upper surface is designed to produce a constant or
decreasing pressure behind the shock wave for the design condition. This
feature stabilizes the boundary layer behind the shock before it enters the
subsonic pressure recovery. In particular, it substantially delays the final
detachment of the boundary-layer bubble present under the strong shock for high-
lift conditions. Results to be presented later will define this effect
more explicitly. The pressure distribution on the aft portion of the lower
surface is designed by the Stratford criteria to obtain the largest increase in
lift by the cusp without incurring boundary-layer separation in the cusp. This
involves a rapid initial increase in pressure followed by a more gradual

increase. At the trailing edge the slope of the lower surface is made approximately equal to that of the upper surface to reduce to a minimum the required pressure recovery at the upper-surface trailing edge.

At Mach numbers or lift coefficients less than the design conditions, the shock wave is farther forward with an increase in velocity aft of the shock to a second velocity peak in the vicinity of the three-quarter chord. This peak must be carefully controlled to prevent the development of a second shock with associated separation on the extreme rearward portion of the airfoils. At Mach numbers higher than the design value, the shock wave moves rearward and becomes stronger. Also, the pressure plateau disappears. As a result, the boundary layer usually separates aft of the shock. A more complete description of the aerodynamic flow on the NASA supercritical airfoils at and off the design condition is presented in reference 1.

Two-Dimensional Results

A comparison of the drag variation with Mach number at a normal-force coefficient of 0.7 for a 10-percent thick conventional airfoil (NACA 64A-410) and two 10-percent thick versions of the NASA supercritical airfoils is shown in figure 2. The early supercritical airfoil for which results are shown is similar to that used for all applications up to 1973. The abrupt drag rise for this airfoil is more than 0.1 Mach number later than that for the 6-series airfoil. This early supercritical airfoil experienced a drag creep at Mach numbers below the abrupt drag rise. This drag is associated with relatively weak shock waves above the upper surface at these speeds.

Much of the recent work at Langley has been devoted to the elimination of this undesirable drag creep, and the solid curve of figure 2 shows an example of the results of these efforts. Refinements to the airfoils were involved primarily with changes which resulted in a more favorable flow over the forward region of the upper surface and the elimination of the region of flow over-expansion near the three-quarter chord location on the upper surface. A slight loss in force-break or drag-divergence Mach number is noted (about 0.01) as a result of slightly increased wave losses at the higher Mach numbers, but this compromise is felt to be of little consequence relative to the gains achieved in eliminating drag creep. It should be noted that, unlike the early work, the shaping changes used in the design of the recent airfoils were guided in part by the use of the recently developed analytical program of reference 2 to achieve desired pressure distributions for the various cases.

In figure 3 the Mach number for the onset of severe separation, that is, for buffet or abrupt drag rise, is plotted against normal-force coefficient for the same airfoils as in the previous figure. The results indicate that not only does the supercritical airfoil delay drag rise at near cruise lift coefficients but it also substantially increases both the Mach number and lift coefficient at the characteristic high-lift corner of the curve. This effect, which results primarily from the stabilization of the bubble under the shock wave as discussed earlier, is particularly important for improving maneuverability.

Recent airplane designs incorporate airfoils with somewhat higher drag rise Mach numbers than for the NACA 6-series shown here. However, it has been difficult to acquire two-dimensional data for such airfoils. Results obtained with a C-5A airplane model in the Langley Research Center 8-foot tunnel indicate that one of these new shapes, the Pearcey peaky airfoil, delays the drag-rise Mach number 0.02 or 0.03 compared with the NACA 6-series airfoils but at a loss in the maximum lift.

The aft loading (fig. 1) associated with the new shape results, of course, in more negative pitching moments.

Supercritical technology can also be used to substantially increase the thickness ratios of an airfoil without an associated reduction in the Mach number for separation onset. Obviously, the increased thickness allows a weight reduction or an increase in aspect ratio and provides added volume for fuel or other required equipment in the wing. Figure 4 shows a 17-percent thick airfoil designed by W. E. Palmer of the Columbus Division of the Rockwell International Corporation. A more detailed description of this airfoil is presented in reference 3.

APPLICATIONS OF SUPERCRITICAL AIRFOILS

Three-Dimensional Wing Considerations

Explicit theoretical methods for designing three-dimensional swept-wing configurations for supercritical flight conditions are not as fully developed as those for two-dimensional configurations. However, some rational qualitative approaches have been developed which will be discussed briefly.

For wings of reasonably high aspect ratio, the airfoil sections of the midsemispan and outboard regions can be the same as those of the two-dimensional airfoils. For the supercritical wing developed for the F-8 flight demonstration to be described later and shown in figure 5 such an agreement holds even for sections on the outboard part of the nontrapezoidal region of the wing. The section near the wing-fuselage juncture is substantially different in detail from the two-dimensional section. However, even here some aft camber provided the most satisfactory results.

Substantial wing twist is usually required for the best overall performance of supercritical swept wings, as for previous swept wings intended for high-speed flight. Experiments at the Langley Research Center and in industry have indicated that for both previous and supercritical swept wings a twist significantly greater than that which theoretically provides an elliptical load distribution provides the best overall design. This large amount of twist substantially reduces or eliminates the trim penalty associated with the greater negative pitching moment for the supercritical airfoil for a sweptback wing.

The planform as shown in figure 5 is an important part of obtaining a high drag-rise Mach number as well as a practical structure for a swept wing. The

rearward extension of the root section allows for the attachment of landing gear in a transport application of such a wing. The glove extending forward is an attempt to provide the same drag-rise Mach number for the root sections as for the outboard regions of the wing. Experiments and theory have indicated that at supercritical speeds the isobars on any sweptback wing move rearward near the root sooner and more rapidly than outboard, with a resulting premature drag rise for this region. The forward root extension turns the isobars forward for subcritical conditions, so that at supercritical design conditions the sweeps of the isobars of the inboard region more nearly match those of the outboard region. The wing shown in figure 5 is described in more detail in reference 4.

Flight Demonstration Program

Because of the drastically different nature of the flow over the supercritical airfoils there was considerable concern as to how the new shape would operate in actual flight. Therefore, the several U. S. government agencies responsible for the development of aircraft, that is NASA, the Air Force, and the Navy, undertook a coordinated, three-part flight demonstration program. The program was to evaluate the application of the new airfoils to a high speed, long-range transport wing configuration, a thick wing, and a variable-sweep fighter wing. In each case existing military aircraft were used as test beds. However, in none of the cases was it intended the test wing would be applied to production versions of these aircraft.

The transport wing configuration was flown on a Navy F-8 fighter (fig. 6). The wing was designed for cruise at very close to the speed of sound ($M \approx 0.98$). This program was sponsored by NASA. The wing structure was designed and fabricated by Los Angeles Division of the Rockwell International Company and the flight tests were conducted at the NASA Dryden Flight Research Center. Results from this program are presented in reference 3.

The thick wing was flown on a Navy T-2C trainer. A comparison of aircraft with and without the thick section is shown in figure 7. This program was sponsored by the Navy and NASA. The configuration and structural design, fabrication, and flight tests were conducted by the Columbus Division of the Rockwell International Company. Results from this program are presented in reference 3.

The variable sweep fighter wing was flown on an Air Force F-111 (fig. 8). The wing was designed to achieve substantially improved maneuverability at high subsonic speed and a higher cruise speed. This program, called TACT, was sponsored by the Air Force and NASA. The wing structure was designed and fabricated by the Fort Worth Division of the General Dynamics Company and the flight tests were conducted at the NASA Dryden Flight Research Center. The initial wind tunnel results of this program are presented in reference 5.

The results from all three flight programs verified the wind tunnel results. The performance gains predicted were achieved and no off design problems were encountered.

Recent Applications

The first U. S. pre-production prototype airplane configurations to incorporate NASA supercritical airfoils are the Air Force advance medium STOL transport (AMST) configurations designed by the McDonnell Douglas Company (YC-15) and the Boeing Company (YC-14). The Douglas configuration is shown in figure 9. The advantage of this airfoil in delaying the onset of the adverse supercritical flow effects has been exploited in these aircraft by eliminating wing sweep. This change allows higher useable lift coefficient for landing and take off with a resulting improvement in the performance for these conditions.

In the initial effort of applying NASA supercritical airfoils to transport aircraft it was assumed that the airfoil should be exploited through an increase in the speed, since this had been the traditional area of advance for such aircraft. The work on the wing demonstrated on the F-8 took this direction. With the recent dramatic increase in the price of fuel the airlines are now more interested in fuel economy rather than speed. Therefore, the more recent research effort at the Langley Research Center has been directed toward using these airfoils to achieve high lift-to-drag ratios. This research is summarized on figure 10. As has already been mentioned the airfoils allow an increased thickness-to-chord ratio for a given drag rise Mach number. This allows a greater span with the same structural weight which, of course, results in lower induced drag. With the higher span the design lift coefficient must be increased. Also, as for the AMST configurations described previously, the use of this airfoil allows a reduction of wing sweep with a resulting improvement of the landing and take off characteristics. In this case the improvement is exploited by a reduction in wing area and thus weight. One of the models used in this investigation is shown in figure 10. The wind tunnel results indicate that for a given wing weight the lift-to-drag ratio can be increased by 18 percent at the cruise Mach numbers of current transports.

AREA RULE REFINEMENTS

The area rule, developed in the 1950's, is a concept which relates the shock wave drag of airplane configurations at transonic and supersonic speeds to the longitudinal development of the cross-sectional area of the total configuration. On the basis of this concept the minimum wave drag for an airplane configuration at supersonic speeds is achieved when the longitudinal development of cross-sectional area is the same as that for a body of revolution with minimum supersonic wave drag. The application of this concept usually results in an indented fuselage. This idea has been exploited primarily in military aircraft. Most present subsonic commercial transport aircraft do not fly at sufficiently high speeds to justify the use of this concept. However, the application of the NASA supercritical airfoil allows speeds of such transports to be such that the area rule can be applied to advantage. Following the wind tunnel development of the transport supercritical wing demonstrated on the F-8 considerable wind tunnel research was carried out on a transport configuration incorporating not only this wing but also fuselage modification based on the area rule. The configuration was intended for efficient cruise flight near

the speed of sound ($M \approx 0.98$). The results of this research are presented in reference 6. During this research several improvements of the area rule concept were developed.

First, a body of revolution with an increased drag rise Mach number was developed using the same approach as that for the NASA supercritical airfoils. This body was intended to provide the basis for the optimum longitudinal development of cross-sectional area for an airplane intended for flight just below the speed of sound rather than supersonic speeds. The streamwise distribution of cross-sectional area for this body of revolution is shown in figure 11. This distribution is substantially different than that for a body with minimum wave drag at supersonic speeds. It has a nose with substantial bluntness. Also, the curvature of the distribution near the maximum area is substantially less than for the minimum supersonic wave drag body of the same fineness ratio.

The area rule is essentially a linear theory concept for zero lift. During the research on the near sonic transport configuration it was found that to achieve the most satisfactory drag characteristics at lifting conditions the fuselage shape had to be modified from that defined by the simple application of the area rule as previously described to account for the non-linearity of the flow at such conditions. For lifting conditions at near sonic speeds there is a substantial local region of supercritical flow above the wing surface which results in local expansions of the stream tube areas. In the basic considerations of the area rule concept this expansion is equivalent to an increase in the physical thickness of the wing. To compensate for this effect the fuselage indentation required to eliminate the far field effects of the wing must be increased. The corrections in cross-sectional areas required for the transport investigated are shown at the bottom of figure 11 and are designated B. The distribution used to design the total configuration is the optimum zero lift distribution described earlier with the correction area B subtracted. The fuselage indentation based on this corrected area distribution resulted in a significant (.02) delay in the drag rise Mach number compared with that for the indentation based on the zero lift distribution.

The drag rise characteristics for the transport configuration incorporating both the supercritical wing and a fuselage shape based on the refined area rule is shown as a solid line in figure 12. The cruise Mach number is approximately 18 percent higher than that for the current wide body transports. Following the wind tunnel development of this configuration three aircraft companies under contract to NASA designed possible transport configurations based on such an arrangement. One of the designs is shown in figure 13.

WING AND ENGINE NACELLE INTERFERENCE

The initial designs of most high performance aircraft configurations with externally mounted engines have resulted in an adverse aerodynamic interference between the flows around the wing, engine nacelles, and pylons at transonic speeds. This interference results from the super-position of the induced

flows of the several components. Considerable research has been conducted to reduce these adverse interferences to acceptable levels.

An extreme example of such interference was encountered during a recent wind tunnel investigation of the application of a supercritical wing to an executive or business jet. The configuration is shown in figure 14. The forward portion of the rear mounted engine extends well forward over the upper surface of the wing. Because of the curvatures of the various components a converging and then diverging channel was present between the components. As a result a high supersonic local Mach number developed in this region at the intended cruise Mach number. Wind tunnel research has indicated that the most straight forward method for greatly reducing such interference is to move the engine nacelle rearward. However, because of a balance problem for this airplane the engine could not be moved rearward. For this configuration the shapes of the upper surface of the wing and the pylons were drastically modified to provide an approximately uniform cross-sectional area channel between the components.

Results of the modifications are shown in figure 15. The configuration without the engines added is shown by the short dash line. With the initial configuration of the nacelles and pylons the drag at the intended cruise Mach number of 0.80 was increased by approximately 0.0040. The configuration was completely unacceptable. With the reshaping of the wing and pylons the drag increment is approximately 0.0010 at the cruise condition, which is about as low as can be achieved with the severe practical constraints imposed on the arrangement.

For engines mounted forward under the wing, as for many jet transports, similar interference problems can be present. They also can be greatly reduced by reshaping the configuration.

CONCLUDING REMARKS

Application of NASA supercritical airfoils can provide substantial improvements in the speed, efficiency, maneuverability, and landing and take off characteristics of aircraft intended to operate at transonic speeds. Further, refinements in the area rule concept can be used to achieve efficient cruise at very close to the speed of sound ($M \approx 0.98$). Also the proper shaping of the wing and pylon can greatly reduce the adverse aerodynamic interference which can be present between the wing engine pylon arrangement at transonic speeds.

REFERENCES

1. Whitcomb, Richard T.: Review of NASA Supercritical Airfoils. ICAS Paper No. 74-10, Presented at The Ninth Congress of the International Council of the Aeronautical Sciences, Haifa, Israel, August 1974.

2. Bauer, Frances; Garabedian, Paul; Korn, David; and Jameson, Antony: Super-critical Wing Sections II. Springer-Verlag, 1975.

3. Supercritical Wing Technology. A Progress Report on Flight Evaluations. NASA SP-301, February 1972.

4. Bartlett, Dennis W.; and Re, Richard J.: Wind-Tunnel Investigation of Basic Aerodynamic Characteristics of a Supercritical-Wing Research Airplane Configuration. NASA TM X-2470, February 1972.

5. Ayers, Theodore G.: A Wind-Tunnel Investigation of the Application of the NASA Integral Supercritical Airfoil to a Variable-Wing-Sweep Fighter Airplane. NASA TM X-2759, October 1972.

6. Langhans, R. A.; and Flechner, S. G.: Wind-Tunnel Investigation at Mach Numbers From 0.25 to 1.01 of a Transport Configuration Designed to Cruise at Near-Sonic Speeds. NASA TM X-2622, August 1972.

FLOW FIELDS

CONVENTIONAL
AIRFOIL
M = 0.7

SUPERSONIC
FLOW

STRONG
SHOCK
WAVE

SEPARATED
BOUNDARY
LAYER

PRESSURE DISTRIBUTIONS

UPPER
SURFACE

c_p,
SONIC

c_p

LOWER SURFACE

SUPERCRITICAL
AIRFOIL
M = 0.8

WEAK
SHOCK
WAVE
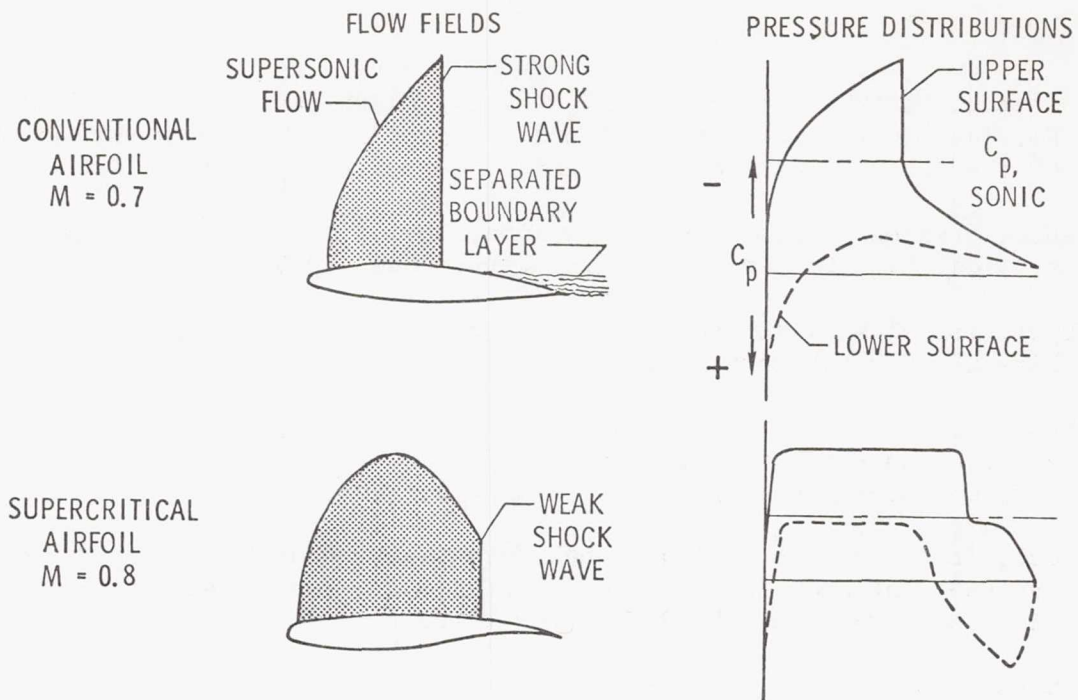
Figure 1.- Supercritical phenomena.

CONVENTIONAL

EARLY
SUPERCRITICAL

c_d

REFINED
SUPERCRITICAL

MACH NUMBER, M
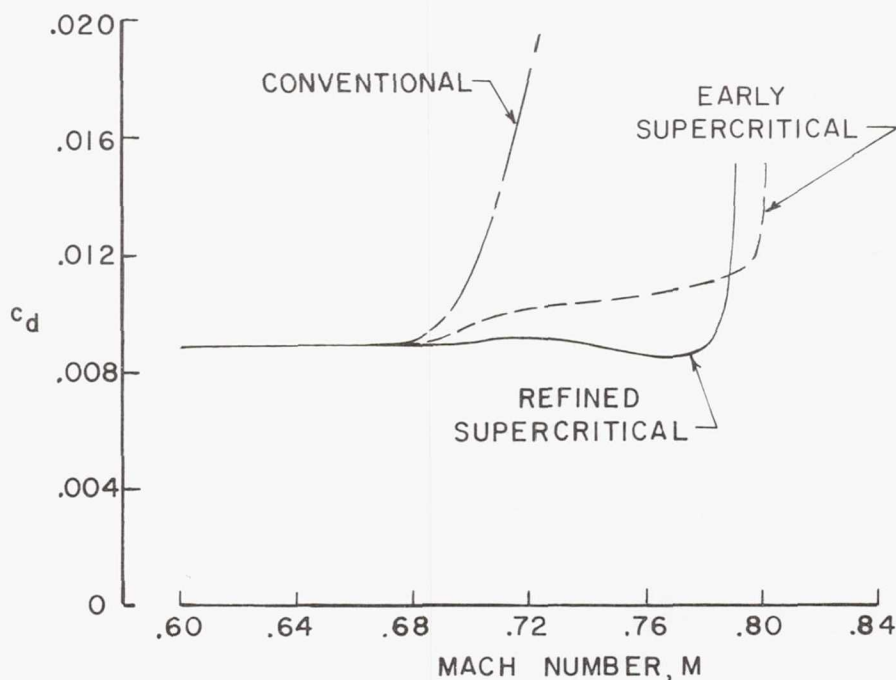
Figure 2.- Drag-rise characteristics for various airfoils.
$c_n = 0.7$; t/c = 0.10.
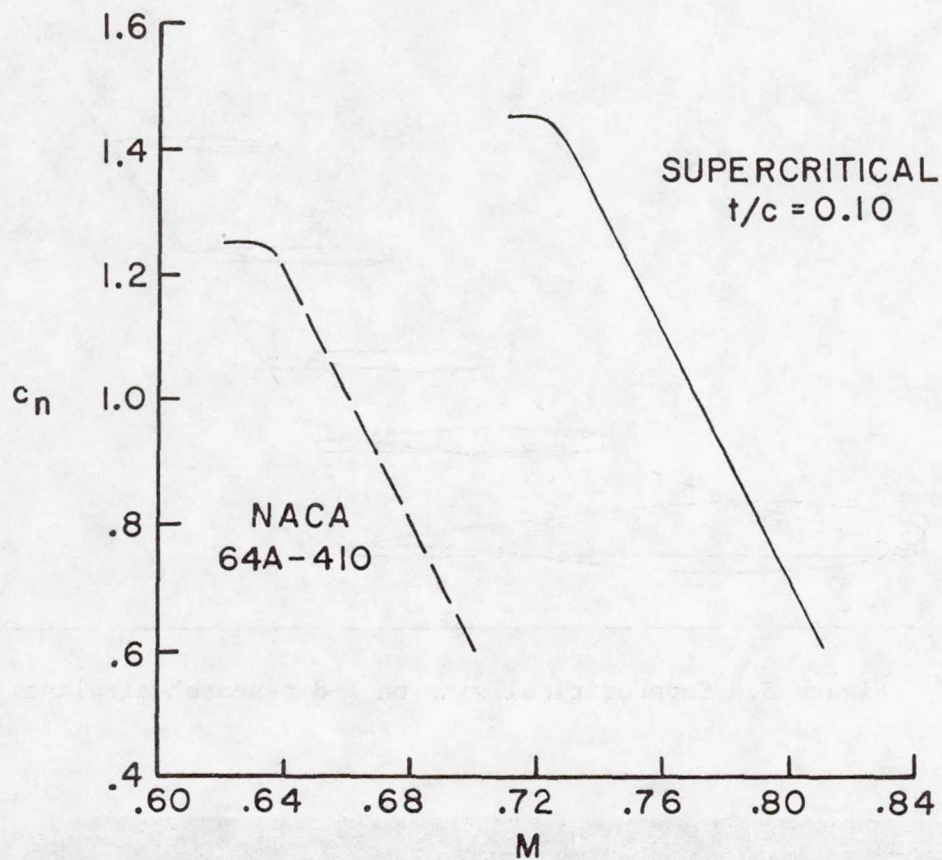
Figure 3.- Onset of drag rise.
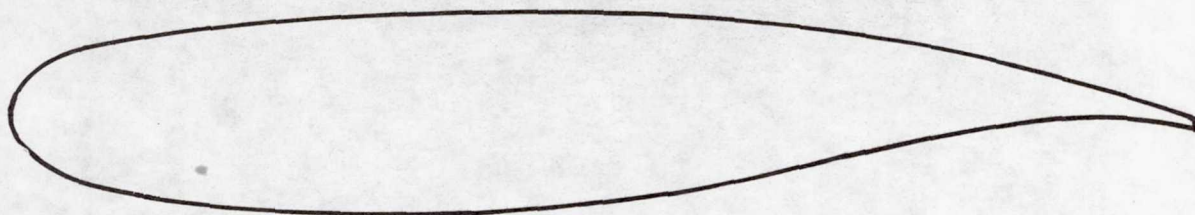
Figure 4.- Thick supercritical airfoil (Palmer of Columbus Division
of Rockwell International).
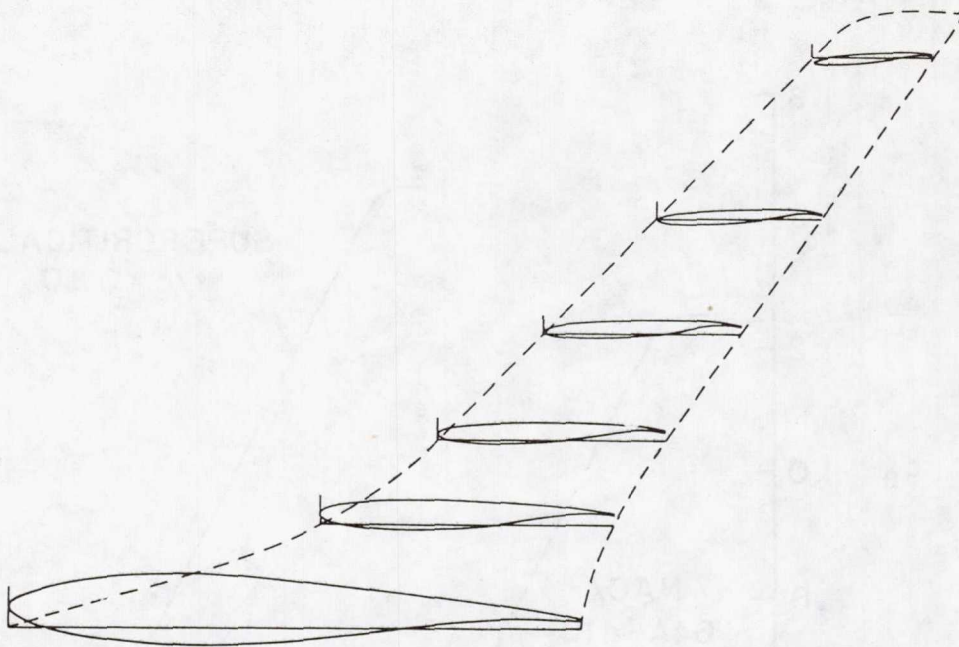
Figure 5.- Supercritical wing on F-8 research airplane.
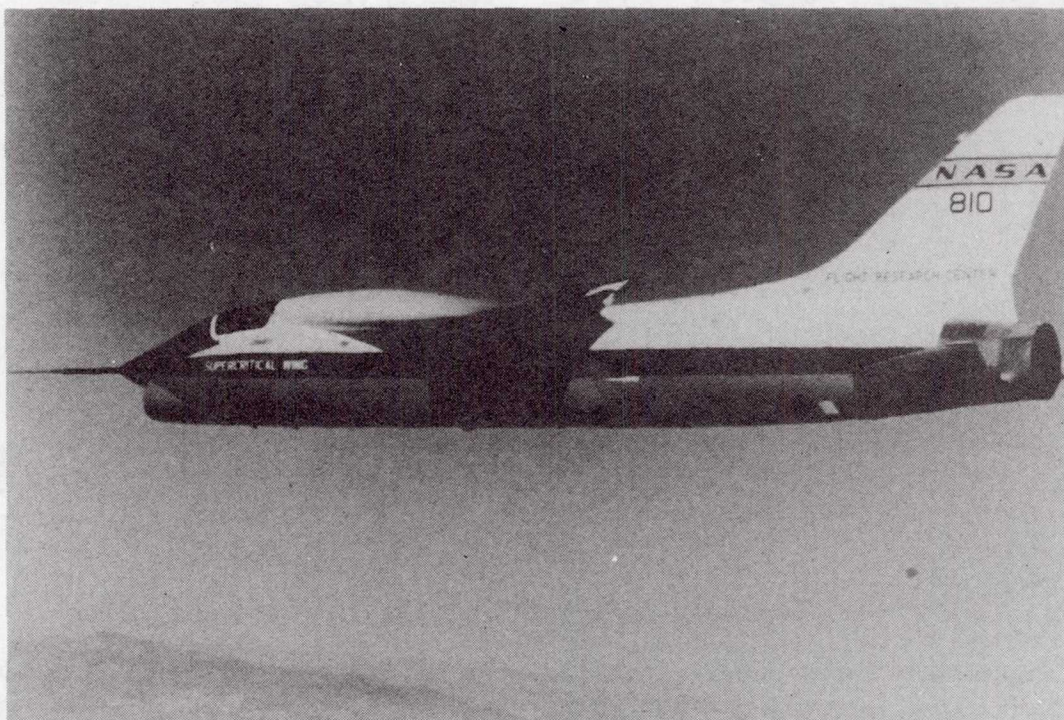
Figure 6.- U.S. Navy F-8 with transport type supercritical wing.
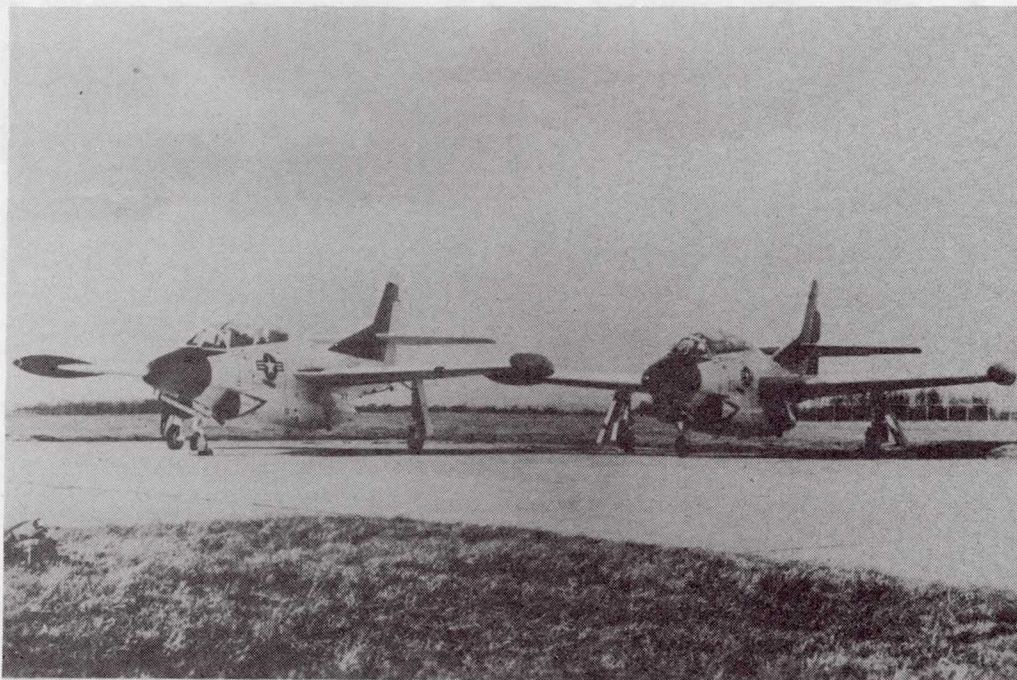
Figure 7.- Comparison of U.S. Navy T-2C airplane with and without thick supercritical airfoil.

Figure 8.- U.S. Air Force F-111 with supercritical wing (TACT).

Figure 9.- McDonnell-Douglas YC-15 with supercritical wing.
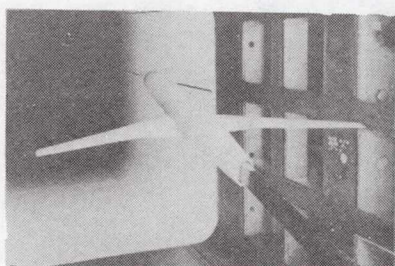
SUPERCRITICAL WING EMBODIES :

INCREASED THICKNESS-TO-CHORD RATIO
GREATER SPAN
HIGHER DESIGN LIFT COEFFICIENT
REDUCED SWEEPBACK
REDUCED AREA

18 % - INCREASE IN AERODYNAMIC EFFICIENCY

INSTEAD OF

15 % - INCREASE IN SPEED

PRESENT TRANSPORTS

LIFT / DRAG

MACH NUMBER
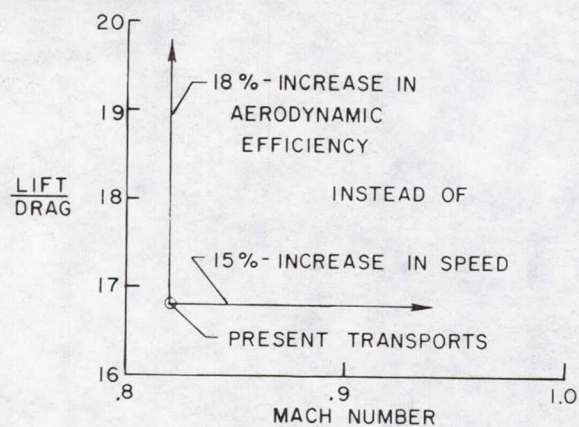
Figure 10.- Supercritical wing for increased lift-to-drag ratio.
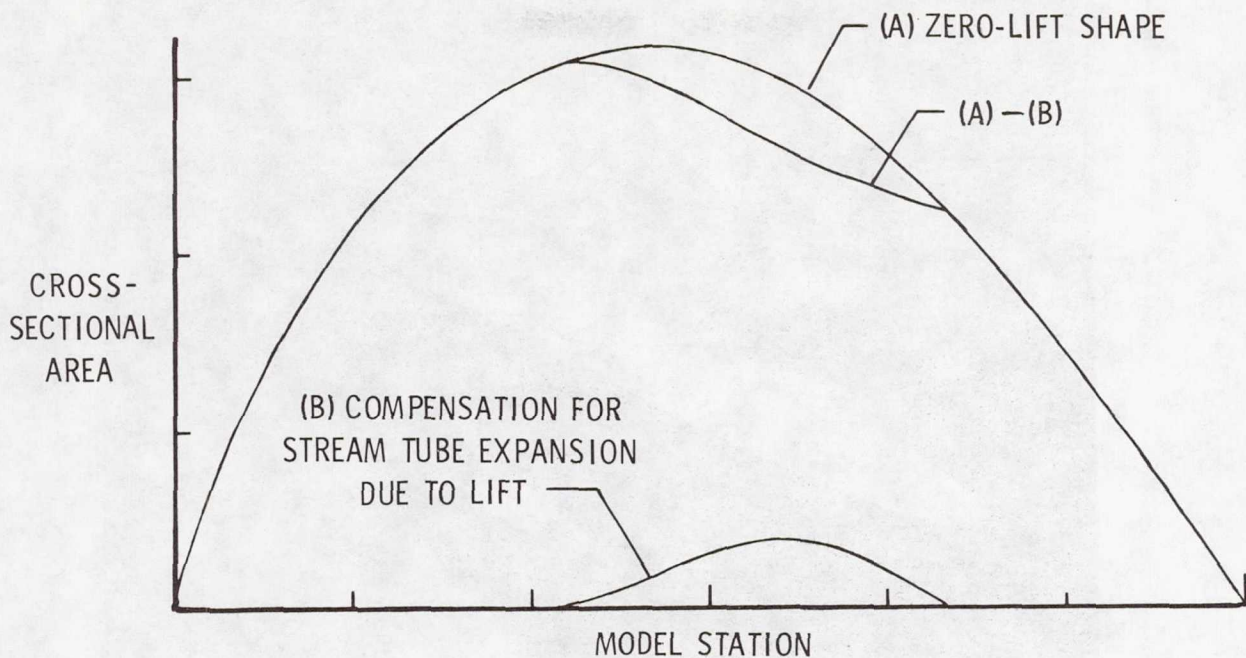
Figure 11.- Second order area-rule considerations.
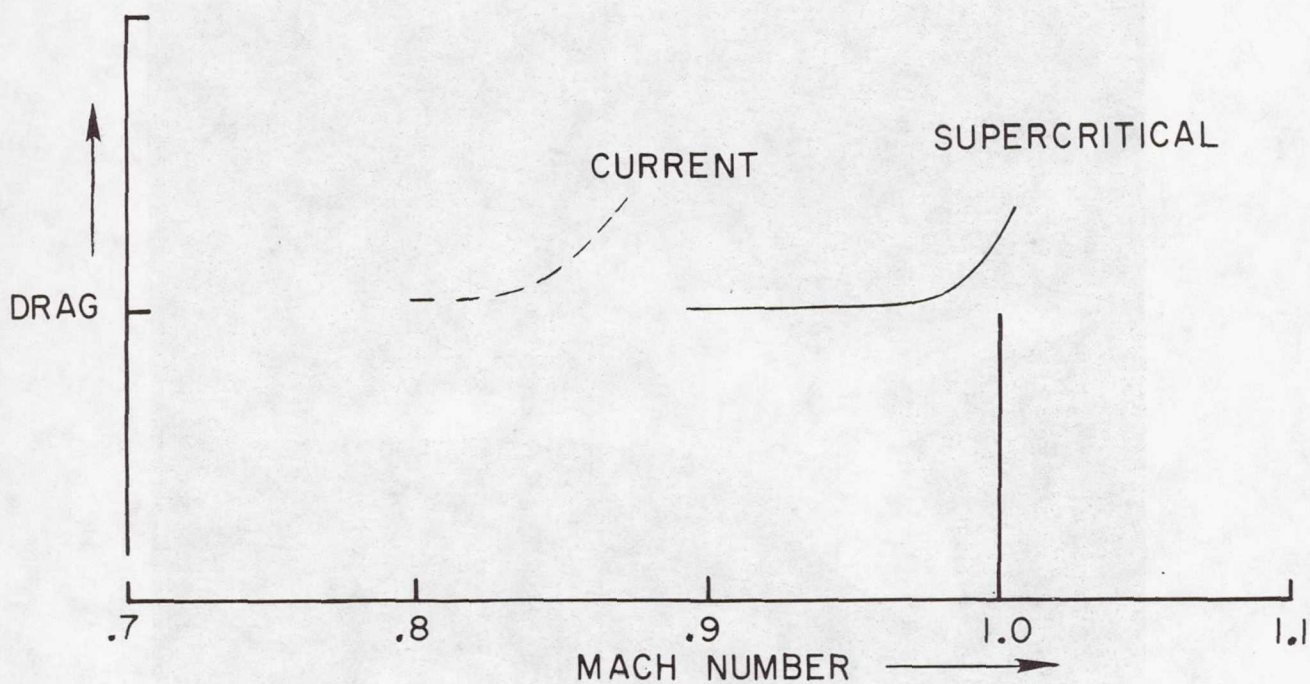
Figure 12.- Drag rise for jet transports (cruise lift).

Figure 13.- Artist's concept of a near-sonic transport incorporating a supercritical wing.
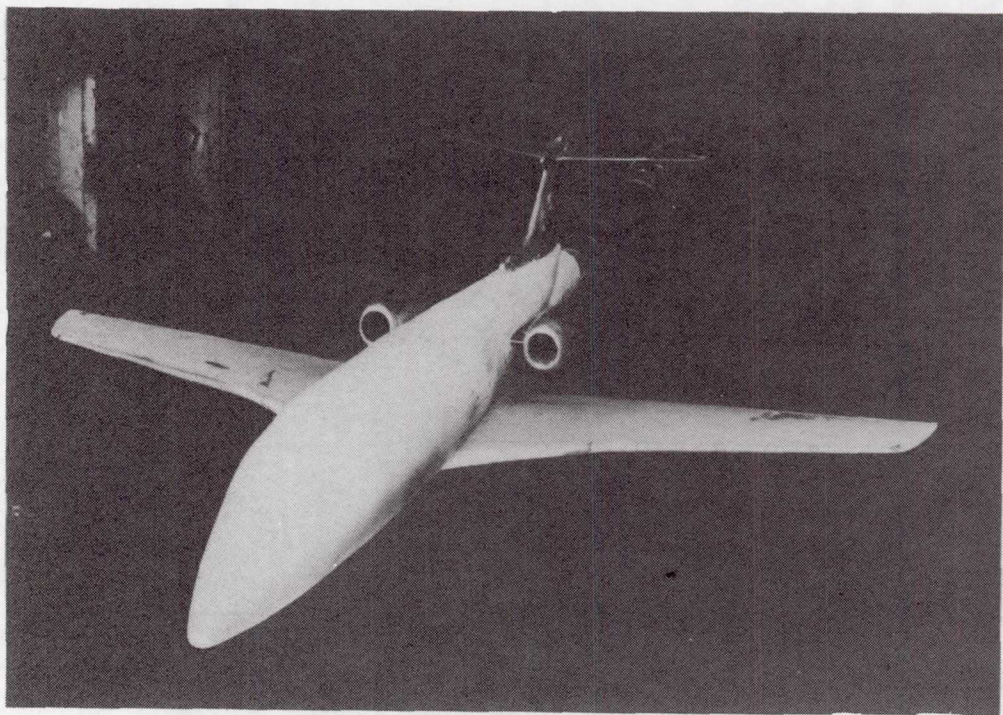
Figure 14.- Model of business jet with supercritical wing.
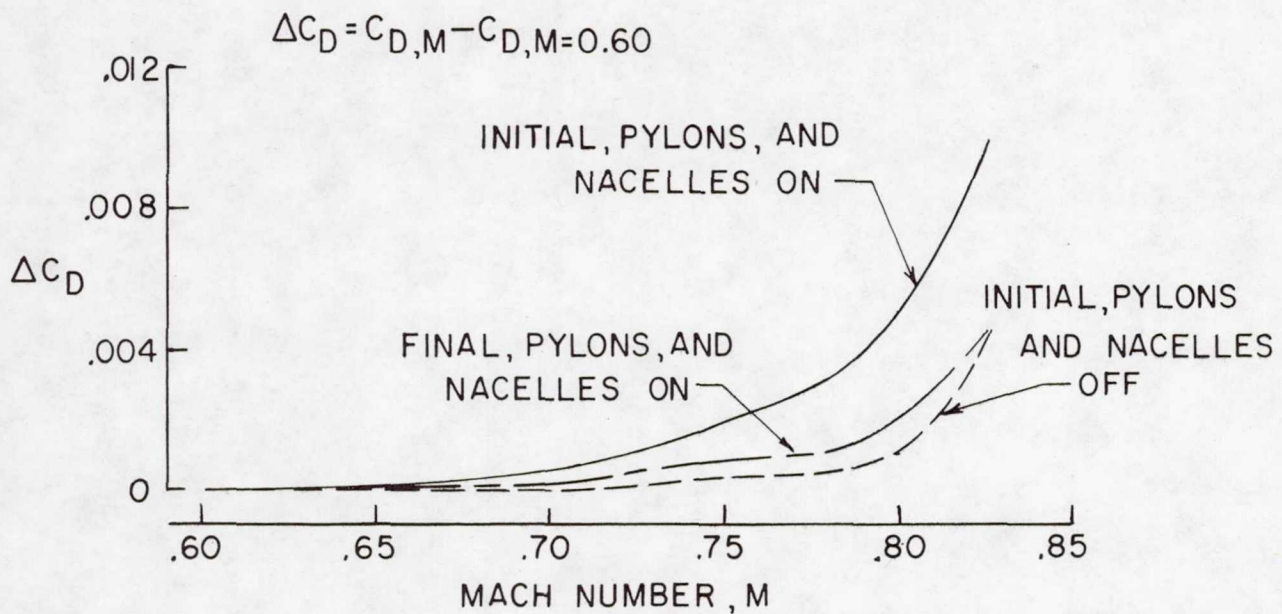
Figure 15.- Effects of wing-root and pylon modifications. Executive-type aircraft; $C_L = 0.25$.

Page intentionally left blank

DESIGN CONSIDERATIONS FOR LAMINAR-FLOW-CONTROL AIRCRAFT*

R. F. Sturgeon and J. A. Bennett
Lockheed-Georgia Company

SUMMARY

A study was conducted to investigate major design considerations involved in the application of laminar flow control to the wings and empennage of long-range subsonic transport aircraft compatible with initial operation in 1985. For commercial transports with a design mission range of 10,186 km (5500 n mi) and a payload of 200 passengers, parametric configuration analyses were conducted to evaluate the effect of aircraft performance, operational, and geometric parameters on fuel efficiency. Study results indicate that major design goals for aircraft optimization include maximization of aspect ratio and wing loading and minimization of wing sweep consistent with wing volume and airport performance requirements.

INTRODUCTION

The recognition of potential long-term shortages of petroleum-based fuel, evidenced by increasing costs and limited availability since 1973, has emphasized the need for improving the efficiency of long-range transport aircraft. This requirement forms a common theme in the recent literature devoted to the analysis of future transport aircraft systems (ref. 1-5). All of these analyses recognize the contribution of aerodynamic drag reduction to aircraft efficiency and that, of the variety of drag reduction concepts which have been subjected to critical analysis, laminar flow control offers the greatest improvement.

This paper summarizes the initial phase of studies conducted to evaluate the technical and economic feasibility of applying laminar flow control to long-range subsonic transport aircraft (ref. 6). The primary objective of the investigations reported herein is the evaluation of the impact of both configuration and mission performance parameters on the fuel efficiency of laminar-flow-control aircraft.

SYMBOLS AND ABBREVIATIONS

Values are given in both SI and U. S. Customary Units. The measurements and calculations were made in U. S. Customary Units.

AR	aspect ratio	S	area, m^2 (ft^2)
BPR	engine bypass ratio	SLS	sea level standard
DOC	direct operating cost, $\cent$/skm ($\cent$/ssm)	W/S	aircraft wing loading, kg/m^2 (lb/ft^2)

1539

H	cruise altitude, m (ft)	η	ratio of required to available
LFC	laminar flow control		thrust at cruise
M	Mach number	Λ	wing sweep angle, rad (deg)

PROCEDURES

Assumptions and Criteria

All analyses conducted as a part of this study are consistent with the guidelines and requirements outlined below.

(1) Basic Study Mission

o   Design Payload   —   23,769 kg (52,400 lb), consisting of 200 passengers and 4536 kg (10,000 lb) of belly cargo.

o   Design Range   —   10,186 km (5500 n mi)

o   FAR Field Length (SLS)   —   3353 m (11,000 ft)

(2) Aircraft Life Cycle

o   The life cycle of the aircraft evaluated in this study assumes initial passenger operation in 1985. The assumed technology level for all aircraft elements is compatible with this operational date.

o   All aircraft evaluated are compatible with the Air Traffic Control Systems and the general operating environment envisioned for the post-1985 time period.

(3) Design Criteria

o   The aircraft studied satisfy the requirements for type certification in the transport category under Federal Aviation Regulations - Part 25, and are capable of operating under pertinent FAA rules.

o   All aircraft satisfy the noise requirements of Federal Aviation Regulations — Part 36 minus 10 EPNdB.

(4) Configuration Constraints

o   This study is directed toward a practical commercial transport aircraft for initial operation in 1985. Therefore, only conventional aircraft configurations are evaluated. Variations which maximize the effectiveness of laminar flow control, such as flying wings or aircraft with aspect ratios sufficiently high to require external struts, are not considered.

o   The configurations of this study recognize the preference of commercial airlines for low-wing passenger aircraft.

o   The configurations of this study are limited to the fuel volume available in the wing, with wing center-section fuel volume employed as required.

Baseline Aircraft Configuration

Figure 1 illustrates the conventional wide-body fuselage configuration, sized for the required passenger and cargo payload with associated accommodations, used for all parametric analyses. The parametric configurations use five LFC suction units with two pylon-mounted units per wing semi-span and one tail-mounted unit. This LFC suction unit arrangement was selected to minimize ducting requirements within the wing and ensure adequate volume for fuel and ducting over the wide range of wing geometries considered. Subsequent analyses indicated the desirability of utilizing two fuselage-mounted LFC suction units for aircraft configurations compatible with this arrangement. A non-structural LFC surface configuration is assumed, with a weight of 7.323 kg/m^2 (1.5 lb/ft^2) above that of the basic wing structure. Suction requirements for the parametric studies are consistent with those outlined in reference 7. Laminar areas of the wings and empennage for parametric aircraft are illustrated by figure 1. In a later phase of the study, it was determined that the chordwise extent of laminarization shown in this figure is very near that which provides minimum total fuel consumption.

Parametric Variations

The procedure used in the selection of configuration parameters is illustrated by figure 2. As outlined in this figure, an initial matrix of LFC aircraft was exercised in the Generalized Aircraft Sizing Program with fuselage geometry, main propulsion engine characteristics, and the chordwise extent of laminarization held constant. These initial parametric investigations considered both three and four aft fuselage-mounted primary propulsion engines. An engine bypass ratio of 7.50 and a cruise power ratio of 0.80 were used. For fixed values of these parameters, the influence of the variables shown in table 1 was evaluated by allowing aircraft size to vary as required to perform the specified mission. All combinations of the variables listed in table 1 were considered, resulting in the evaluation of a matrix of 768 aircraft configurations.

TABLE 1. CONFIGURATION MATRIX

M	0.70	0.75	0.775	0.80
H, m, (ft)	10,973 (36,000)	12,192 (40,000)	13,411 (44,000)	
Λ , rad (deg)	0	0.175 (10)	0.349 (20)	0.524 (30)
W/S, kg/m^2 (lb/ft^2)	391 (80)	488 (100)	586 (120)	683 (140)
AR	8	10	12	14

In general, the parametric configurations defined by the first phase of the analysis do not precisely satisfy takeoff distance and second-segment climb gradient requirements. For parametric configurations which minimize fuel consumption, as determined from the configuration matrix, engine number and location, cruise power ratio, and bypass ratio were varied to define point-design configurations compatible with takeoff distance and second-segment climb requirements. The final configuration parameters were selected from these point-design configurations on the basis of fuel efficiency and compatibility with projected airline traffic.

LOWER
SURFACE
$(x/c)_L = 0.75$

$(x/c)_L = 0.75$

UPPER
SURFACE
$(x/c)_L = 0.72$

$(x/c)_L = 0.75$
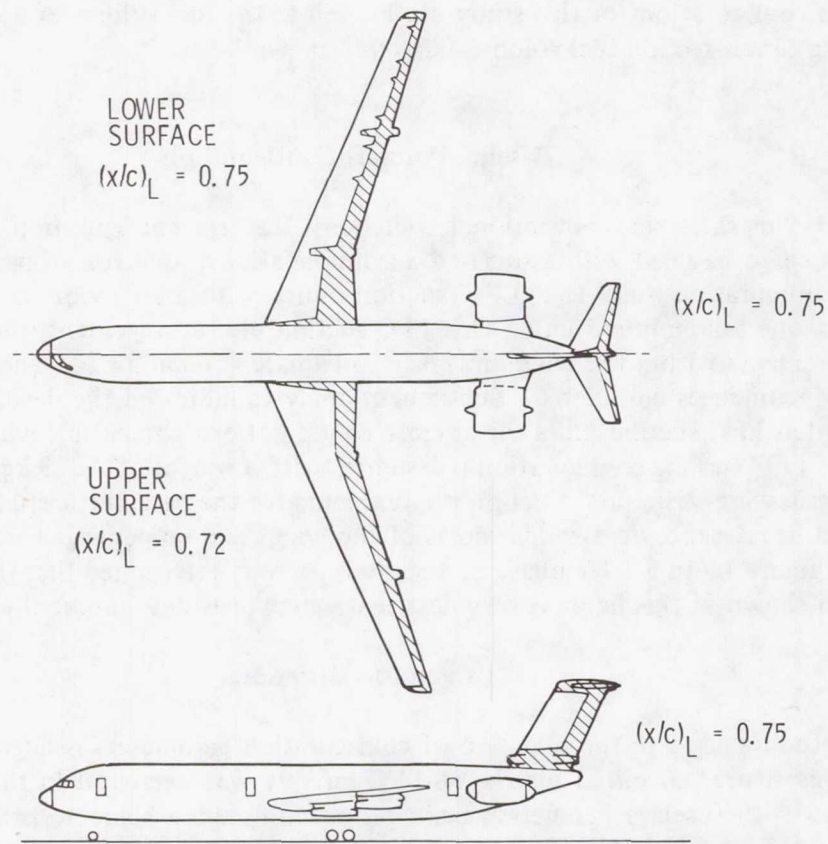
FIGURE 1. BASELINE CONFIGURATION FOR PARAMETRIC ANALYSES

CONFIGURATION
MATRIX

CONSTANTS

o FUSELAGE GEOMETRY
o ENGINE NUMBER / LOCATION
o BYPASS RATIO
o CRUISE POWER RATIO
o EXTENT OF LAMINARIZATION

VARIABLES

o CRUISE MACH NUMBER
o CRUISE ALTITUDE
o WING SWEEP
o WING LOADING
o ASPECT RATIO

PARAMETRIC
CONFIGURATION
VARIATIONS

o ENGINE NUMBER/
LOCATION
o BYPASS RATIO
o CRUISE POWER
RATIO

SELECTED
CONFIGURATION
PARAMETERS

FIGURE 2. PARAMETER SELECTION PROCEDURE

RESULTS AND DISCUSSION

Wing Geometry and Cruise Parameters

Figures 3 and 4 illustrate representative results of the parametric study. For a cruise altitude of 10,973 m (36,000 ft), these figures show the effect of variations in wing loading, aspect ratio, and cruise Mach number on block fuel for wing sweep angles of 0 and 0.524 rad (30 deg). These data show that minimum block fuel is realized for a cruise Mach number of 0.75. For all cruise speeds, fuel consumption is minimized by configurations with unswept wings, high wing loading, and high aspect ratio.

Of particular significance in the selection of LFC configuration parameters is the fuel volume limit, shown as a dashed line in figures 3 and 4. The combination of a relatively small payload, a long mission range, and the wing volume required for ducting and distribution of LFC suction air, places a severe constraint on the selection of wing parameters. In these figures, only the values of wing loading and aspect ratio which lie above the fuel volume limit line represent aircraft configurations with adequate fuel volume to satisfy the design mission requirements.

Figure 5 summarizes the block fuel requirements of M = 0.75 and M = 0.80 LFC configurations as a function of wing sweep angle for an aspect ratio of 14. All of the configurations represented by the curves of this figure have the minimum fuel volume required for the design mission and thus represent the optimum LFC configurations compatible with practical design constraints. It is significant, and not unexpected, that cruise at M = 0.75 results in a lower block fuel requirement than cruise at M = 0.80 for all wing sweep angles. The minimum block fuel for M = 0.75 aircraft is realized by an unswept wing, while a wing sweep of about 0.384 rad (22 deg) minimizes block fuel for M = 0.80 aircraft.

The influence of cruise M and wing sweep on block fuel and DOC is shown in figure 6 for configurations with a wing loading of 537 kg/m^2 (110 lb/ft^2) and an aspect ratio of 14. It will be observed that fuel consumption is minimized by selecting a cruise M of 0.75 or less, but that minimum DOC occurs for a cruise M of about 0.78.

Figures 7 and 8 illustrate the effect of cruise altitude and cruise M on block fuel and DOC for configurations with the same wing loading and aspect ratio for wing sweep angles of 0 and 0.349 rad (20 deg). For either wing sweep, minimum block fuel is obtained at the lowest altitude considered at a cruise M of 0.75 or less. Minimum DOC is also realized by cruising at the lowest altitude, but optimum cruise M is from 0.75 to 0.79, depending on altitude and wing sweep.

Engine Parameters

The parametric configurations defined in the configuration matrix were based on a constant cruise power ratio of 0.80, and do not recognize a field length constraint. For a representative configuration geometry, bypass ratio and cruise power ratio variations were conducted as required to satisfy the specified FAR field length requirement of 3353 m (11,000 ft). In conducting these variations, it was determined that a cruise altitude of 11,582 m (38,000 ft) allowed a better match of cruise and takeoff thrust requirements than cruise at 10,973 m (36,000 ft).

H, m(ft) = 10,973 (36,000)
BPR   = 7.50
η   = 0.80
— — — INTERNAL FUEL
VOLUME LIMIT
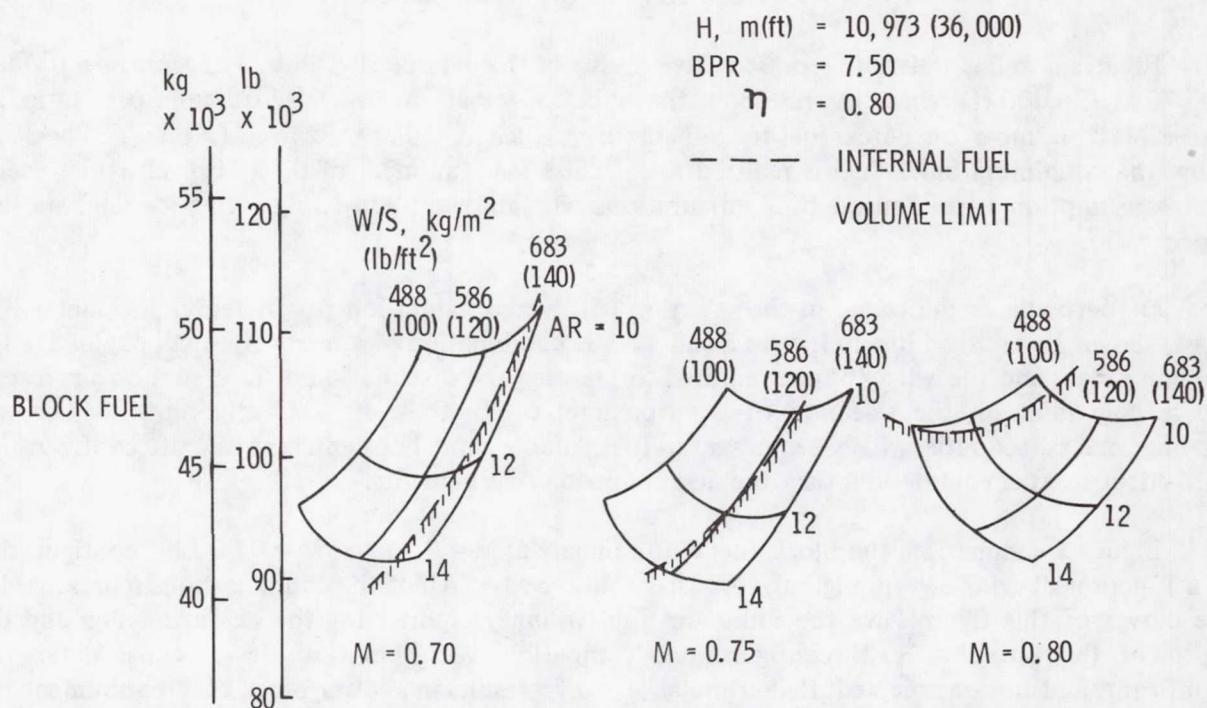
FIGURE 3.   BLOCK FUEL VS. WING LOADING AND ASPECT RATIO, Λ = 0

H, m(ft) = 10.973 (36,000)
BPR   = 7.50
η   = 0.80
— — — INTERNAL FUEL
VOLUME LIMIT
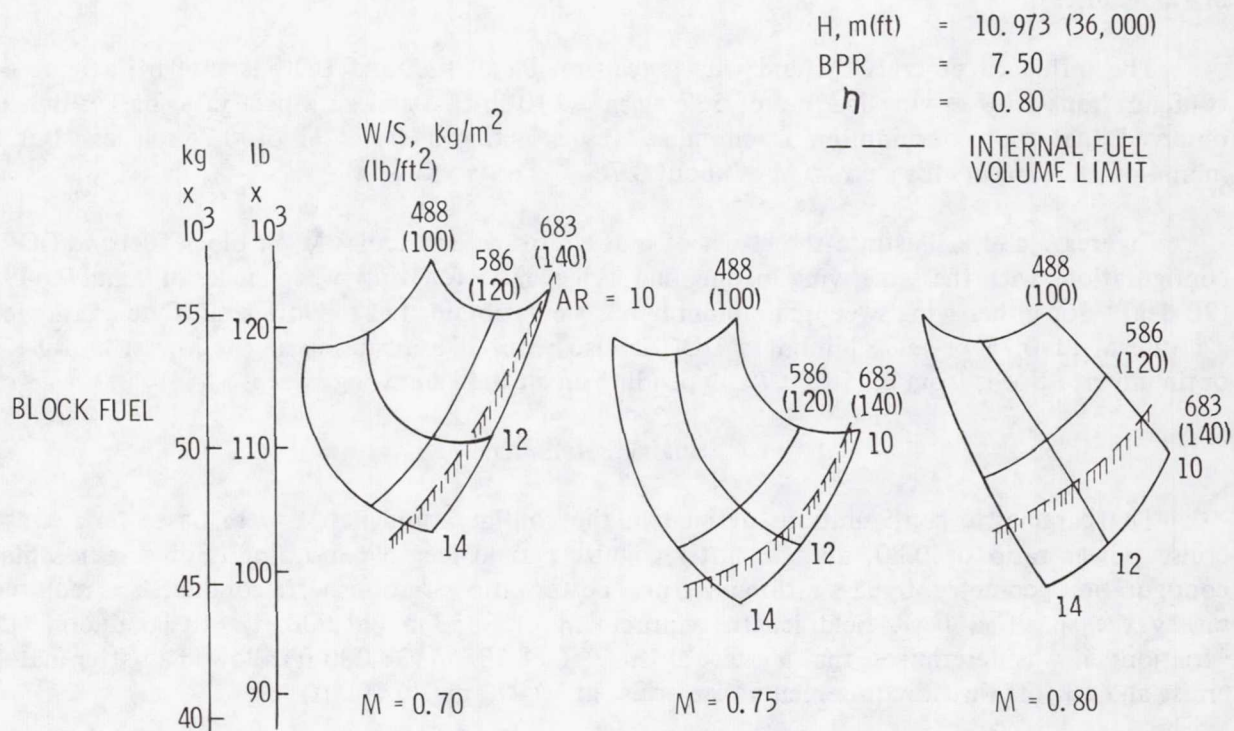
FIGURE 4.   BLOCK FUEL VS. WING LOADING AND ASPECT RATIO, Λ = 0.524 RAD (30 DEG)

1544

H, m(ft)   = 10, 973 (36, 000)
AR   = 14
BPR   = 7. 50
η = 0. 80

kg
x 10³

lb
x 10³

BLOCK FUEL
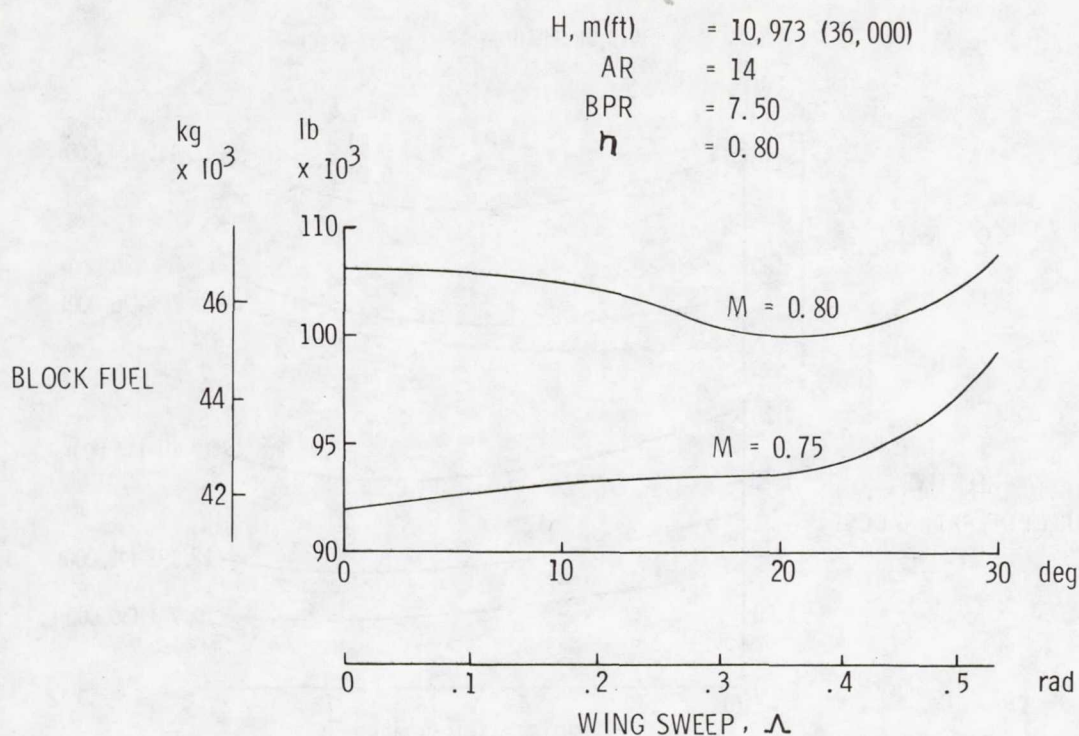
WING SWEEP , Λ

FIGURE 5.   BLOCK FUEL VS. WING SWEEP

H, m(ft)   = 10, 973 (36, 000)
W/S, kg/m²(lb/ft²) = 537 (110)
AR   = 14
BPR   = 7. 50
η = 0. 80

Λ , rad (deg)

kg
x 10³

lb
x 10³

BLOCK FUEL

RELATIVE
DIRECT OPERATING COST
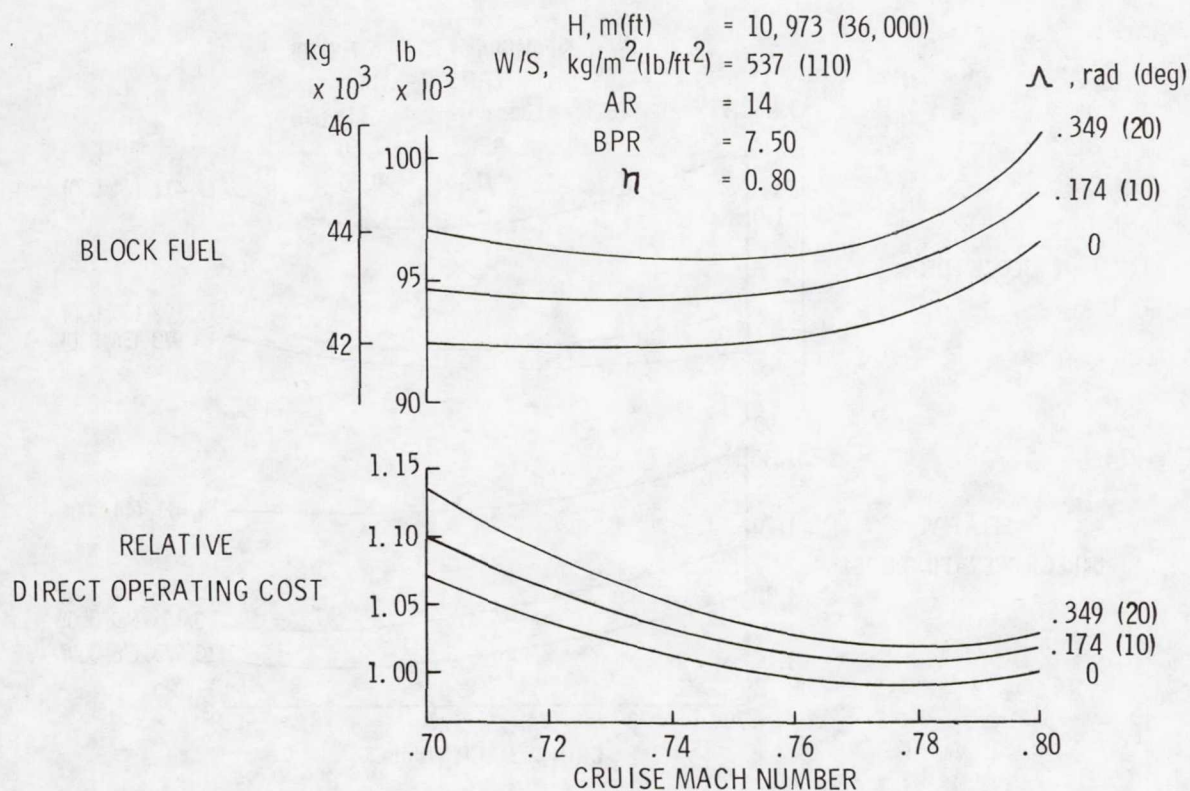
CRUISE MACH NUMBER

FIGURE 6.   EFFECT OF WING SWEEP AND CRUISE MACH NUMBER ON BLOCK FUEL AND RELATIVE DOC
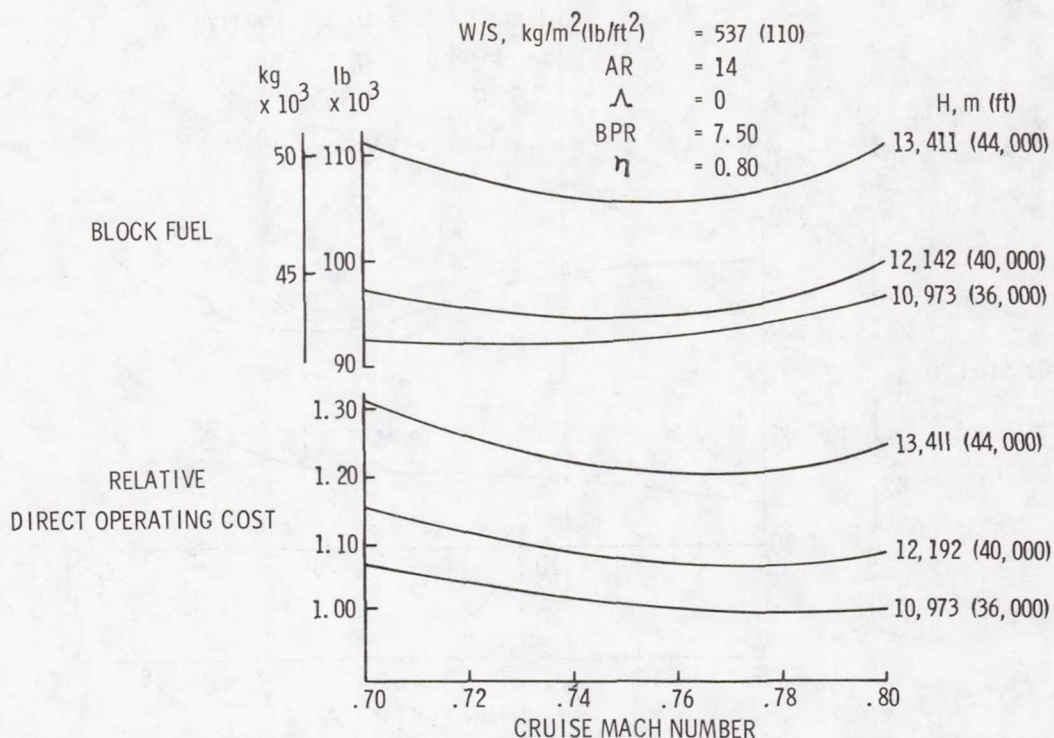
FIGURE 7. EFFECT OF CRUISE ALTITUDE AND CRUISE MACH NUMBER ON BLOCK FUEL AND RELATIVE DOC,
$\Lambda = 0$
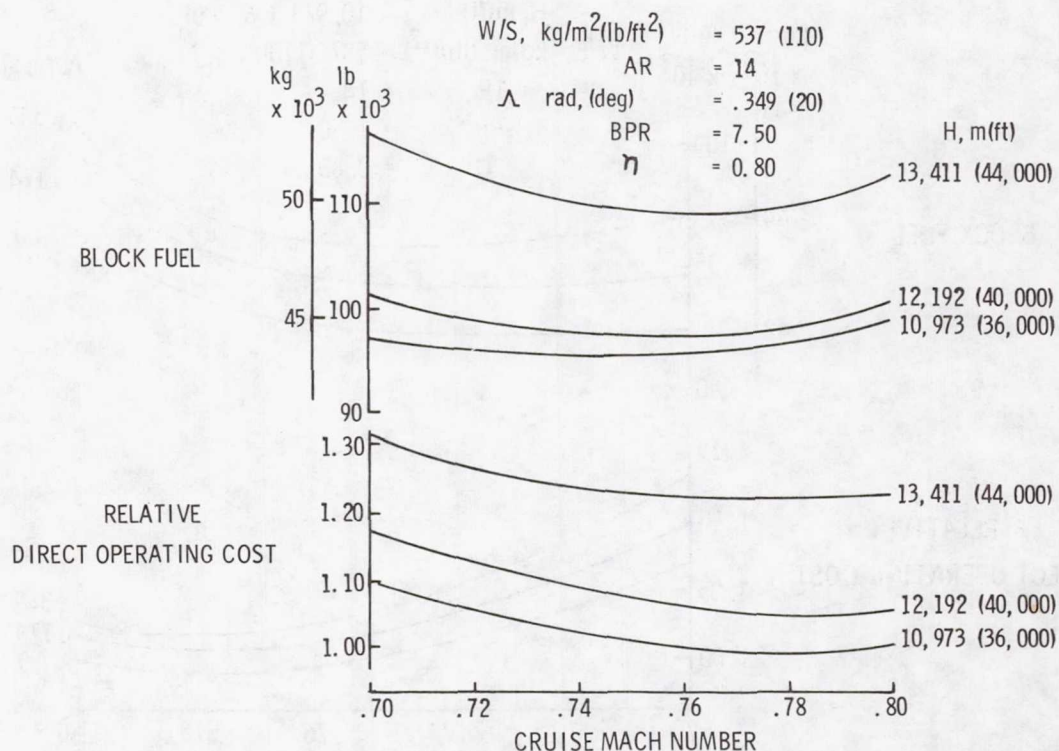
FIGURE 8. EFFECT OF CRUISE ALTITUDE AND CRUISE MACH NUMBER ON BLOCK FUEL AND DOC,
$\Lambda = 0.349$ RAD (20 DEG)

$$M = 0.75$$
$$H, m (ft) = 11,582 (38,000)$$
$$W/S, kg/m^2 = 537 (110)$$
$$\Lambda = 0$$
$$\eta = 0.80$$
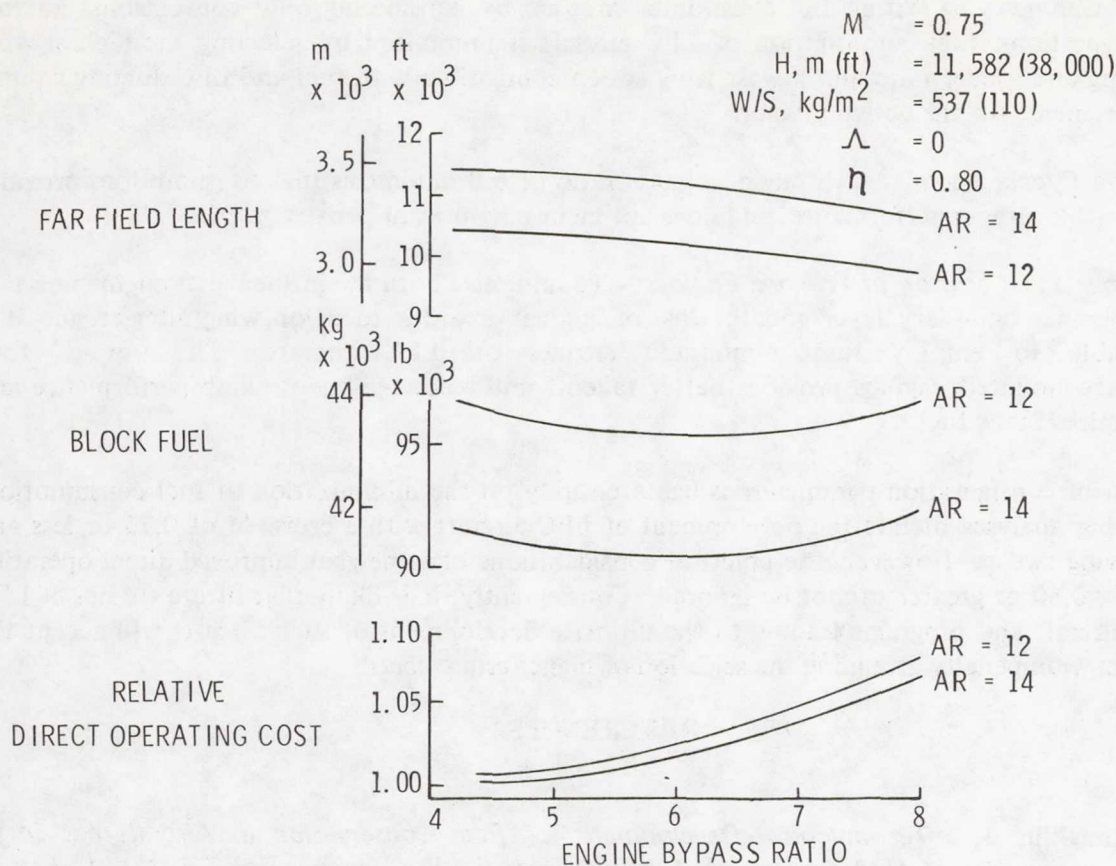
FIGURE 9. ENGINE BYPASS RATIO VARIATIONS

The variation of FAR field length, block fuel, and DOC with aspect ratio and engine bypass ratio is shown in figure 9 for M= 0.75 aircraft with fixed wing sweep and wing loading. Configurations with the lower aspect ratio demonstrate better takeoff performance, but block fuel and DOC are minimized by the high-aspect-ratio configurations. Fuel consumption is minimized by selecting a bypass ratio of about 6.0. This value also represents a reasonable compromise relative to takeoff performance and DOC.

CONCLUSIONS

The following summarizes the design considerations implied by the data generated in the parametric analysis of LFC transport aircraft for the specified mission:

(1) *Cruise Mach number* — Fuel consumption of LFC aircraft is minimized by selecting a cruise M of 0.75 or less. On the basis of DOC, the optimum cruise M is between 0.76 and 0.79, depending on aircraft configuration.

(2) *Cruise Altitude* — Both fuel consumption and DOC are minimized for LFC aircraft by selecting the lowest cruise altitude above 10,670 m (35,000 ft) which permits a reasonable match of cruise and takeoff thrust requirements.

1547

(3) *Wing Geometry* – Within the constraints imposed by considering only conventional aircraft configurations, fuel consumption of LFC aircraft is minimized by selecting the highest wing loading and aspect ratio and lowest wing sweep compatible with fuel and LFC ducting volume requirements for the design mission.

(4) *Engine Bypass Ratio* – An engine bypass ratio of 6.0 minimizes fuel consumption, provides reasonable airport performance, and does not incur a significant penalty in DOC.

(5) *Number and Location of Primary Engines* – To minimize both the influence of engine noise on the laminar boundary layer and the loss of laminar area due to pylon/wing interference, it is desirable to employ fuselage-mounted engines on LFC aircraft. The use of four fuselage-mounted engines provides better takeoff and second-segment climb performance and minimizes block fuel.

If selection of configuration parameters is based entirely on the minimization of fuel consumption, the preceding analyses dictate the development of LFC aircraft with a cruise M of 0.75 or less and near-zero wing sweep. However, the practical considerations of somewhat improved direct operating costs at M = 0.80 or greater cannot be ignored. Consequently, it is likely that future studies of LFC transport aircraft and programs leading to the ultimate development of such aircraft will accept the fuel consumption penalty attending the selection of higher cruise speeds.

REFERENCES

1. McLaughlin, J.: *Technological Development for Fuel Conservation in Aircraft and in the Prospective Use of Hydrogen as an Aviation Fuel.* SAWE Journal, Vol. 34, No. 1, January 1975.

2. Clay, C. W. and Sigalla, A.: *The Shape of the Future Long-Haul Transport Airplane.* AIAA Paper 75-305, February 1975.

3. Black, R. E. and Stern, J. A. *Advanced Subsonic Transports – A Challenge for the 1990's.* AIAA Paper 75-304, February 1975.

4. Nagel, A. L., Alford, W. J., and Duggan, J. F.: *Future Long-Range Transports; Prospects for Improved Fuel Efficiency.* NASA TM-X-72659, February 1975.

5. Shevell, R. S.: *Technology, Efficiency, and Future Transport Aircraft.* Astronautics and Aeronautics, September 1975.

6. Sturgeon, R. F., Bennett, J. A., Etchberger, F. R., Ferrill, R. S., and Meade, L. E.: *Study of the Application of Advanced Technologies to Laminar-Flow Control Systems for Subsonic Transports.* NASA CR-133949 and NASA CR-144975, prepared by the Lockheed-Georgia Company under Contract NAS 1-13694, May 1976.

7. Staff, LFC Engineering Section: *Laminar Flow Control Demonstration Program Final Report, LFC Design Data.* NOR-61-141, Northrop Corporation, Norair Division, April 1964.

ON THE STATUS OF V/STOL FLIGHT

Barnes W. McCormick
Department of Aerospace Engineering
The Pennsylvania State University

SUMMARY

Basic principles relating to the accomplishment of V/STOL flight are
reviewed as they pertain to current prototype developments. Particular
consideration is given to the jet flap, flow augmentation and circulation
control separately and in combination. To be discussed will be such
configurations as the augmentor wing, upper-surface blown flaps, externally
blown flaps and the circulation-controlled rotor.

INTRODUCTION

The development of an airplane with vertical or short take off and landing
capability, (V/STOL), and yet competitive with conventional airplanes in cruise,
has been an elusive target over the last twenty years. Except for the Hawker-
Siddeley Harrier and a few small STOL's none of the many experimental proto-
types have gone into production. This includes such configurations as the
compound helicopter, tilt-wing, deflected-slipstream, direct lift, tail sitter,
tilting ducted propellers and the fan-in-wing.

At the present time there are six developments, three VTOL's and three
STOL's, which appear to hold some promise. These are:
1. The tilt rotor; the Bell XV-15
2. Augmented VTOL; the Rockwell XFV-12A
3. Circulation control; the X-wing concept
4. Upper-surface blowing; the Boeing AMST YC-14
5. Externally blown flaps; the McDonnell-Douglas AMST YC-15
6. Augmentor wing; modified DeHaviland Buffalo

There are also other V/STOL configurations currently being proposed or investi-
gated, such as the lift/cruise fan research and technology aircraft,
undoubtedly worthy of discussion but this present paper will be limited
primarily to a consideration of the above six configurations.

SYMBOLS

A throat area of thrust augmentor (Fig. 1), m^2

A_E exit area of thrust augmentor (Fig. 1), m^2

A_j primary nozzle area of thrust augmentor (Fig. 1), m^2

C_L wing lift coefficient

$C_{L_{max}}$ maximum value of the wing lift coefficient

C_μ jet momentum coefficient (ratio of jet momentum flux per unit surface area to free stream dynamic pressure)

m   mass flow, kg/s

P   power, W

T   thrust, N

w   induced velocity, m/s

α ratio of A_j to A

β ratio of A_E to A

ϕ thrust augmentation ratio; ratio of total thrust of augmentor to thrust of primary nozzle

C_l rolling moment coefficient

C_{l_α} $\dfrac{\partial C_l}{\partial \alpha}$

δ_f flap deflection

δ_a aileron deflection

VTOL

In the design of a VTOL aircraft the division between hovering and cruising flight in the mission profile plays a dominant role in determining the aircraft's configuration. This statement is easily understood from basic momentum principles. A static lift system having a mass flow rate of m and producing a thrust of T will, on the average, accelerate the flow to a final velocity of w where m, T and w, in consistent units, are related by,

$$T = mw \tag{1}$$

the power, P, delivered to the mass flow, by the lift system will equal the flux of kinetic energy in the ultimate wake; hence,

$$P = \frac{1}{2} mw^2 \tag{2}$$

Thus, combining (1) and (2), the power, thrust and average induced velocity in the ultimate wake are related by:

$$\frac{T}{P} = \frac{2}{w} \tag{3}$$

The above is actually an ideal upper limit on the thrust to power ratio. Because of other power losses in the system, T/P must always be less than the value predicted by Equation (3). Nevertheless, (3) provides a relative basis for comparing static thrust systems and suggests, for the same thrust, that the

fuel flow rate will vary directly with the induced velocity. Typically w induced by a helicopter is approximately 12 m/s (40 fps); 70 m/s (230 fps) for propellers; 180 m/s (590 fps) for lift fans and 300 m/s (980 fps) for lift jets. Thus direct lift jet systems, on the one extreme, will burn fuel at a rate approximately 30 times that of the helicopter at the other end of the w spectrum. On the other hand the weight of a direct lift jet system will generally be less than that of a system with a low w (such as a helicopter with its large blades, hub, transmissions, etc.) so that weight can be traded for fuel.

One means of reducing the induced velocity in the ultimate wake is by the use of augmentation. As shown schematically in Figure 1, the primary jet is introduced into the throat of a surrounding nozzle, either along the centerline or along the walls of the nozzle. Viscous shear and turbulent mixing along the boundary of the primary jet entrains a secondary flow through the nozzle. This secondary flow mixes with the primary jet to produce an augmented mass and momentum flux issuing from the nozzle which can be appreciably greater than that of the primary nozzle.

The performance of an augmentor can be improved by diffusing the mixed flow as shown in Figure 1. The theoretical maximum performance of such an augmentor is shown in Figure 2 as taken from Reference 1. Here the ratio, ϕ, of the total thrust to the thrust of the primary jet is presented as a function of β for various values of α where; α is the ratio of primary nozzle area, A_j, to throat area, A and β is the ratio of nozzle exit area, A_E, to throat area. These curves neglect any losses and assume complete mixing of the primary and secondary flows resulting in a uniform flow at the diffusor exit.

The theoretical performance shown in Figure 2 is difficult to achieve in practice. First the primary flow suffers losses in total head as it is directed to the primary nozzle, and secondly, complete mixing of the two flows with a uniform discharge from the diffuser exit is never achieved.

For the last 5 or 6 years, experimental and analytical studies have been performed by personnel at the Aerospace Research Laboratories (Refs. 2-5) on means of achieving more complete mixing in augmentors. These efforts have led to the development of the so-called hypermixing nozzle. In this nozzle the exit plane is segmented so as to produce adjacent jets exiting in slightly different directions. Streamwise vortices then form between the jets which enhance the mixing between the primary flow and the secondary flow. Using these nozzles, augmentation ratios as high as approximately 2.0 have been achieved for β values of approximately 2.0 with ejectors half the length of earlier models. Some of these results are also shown in Figure 2 taken from Reference 5 .

An aircraft currently under development which utilizes thrust augmentation is the Rockwell XFV-12A. Scheduled for first flight in September 1976, this aircraft appears to be a typical high-performance jet aircraft but with a canard configuration. However both the canard and main wing are flapped to open as shown in Figure 3. Engine exhaust is diverted by means of a plug nozzle-sleeve valve combination and ducted to slots along the entrance walls of the diffuser formed by the flaps. The exhaust also exits in the middle of the

diffuser entrance from a third smaller flap segment as shown. The outer jets are issued tangential to the diffuser walls in the direction of the diffuser centerline and are then turned to the vertical direction by the Coanda effect.

According to Reference 6, the installed engine thrust-to-weight ratio for the XFV-12A is estimated to be 0.72 with a net augmented thrust-to-weight ratio of 1.12 resulting in an augmentation ratio, ϕ, of 1.55. On the average, the exit velocity of the augmented flow is estimated at approximately 130 m/s, (427 fps), considerably higher than that for a helicopter but appreciably less than direct lift jet systems.

The above ϕ value may be somewhat optimistic. Recent results reported in Reference 7 show that a ϕ of 1.5 has been achieved to date out of ground effect for the main wing with a value of 1.3 reported for the canard surface. Since most of the weight is borne by the main wing, the combined ϕ is close to producing the net thrust-to-weight ratio of 1.05 called for in the Navy specification.

A definite plus for this configuration is its **probable** STOL performance. An appreciable portion of the main wing is ahead of the augmented flaps so that in forward flight the wing behaves as a jet-flapped wing with characteristics similar to the externally blown flap (EBF), the augmentor wing, and the upper-surface blown (USB) flap discussed in the next section. According to **Reference** 6, allowing the XFV-12A to operate as a STOL with only a 100 m takeoff roll increases the payload by 22241 N (5000 lbs).

Equipped with a better understanding of rotor-blade airframe dynamics and advanced material technology, the U.S. Army and NASA have revived the tilting rotor concept with the Bell XV-15 pictured in Figure 4. In hover this airplane enjoys the benefits of a disc loading not much higher than the helicopter. In forward flight it avoids the retreating blade stall or advancing blade compressibility limitations of the helicopter and is designed to cruise at a speed of approximately 185 m/s (360 kts).

This VTOL is powered by two uprated Lycoming T-53 engines, each with a contingency rating of 1342 kW (1800 SHP). The design maximum VTOL takeoff weight is 57826 N (13000 lbs). With two rotors each having a diameter of 7.62 m (25.0 ft), the disc loading is 634 N/m^2 (13.2 psf). Thus at standard sea level the downwash velocity w will be approximately 16.06 m/s (52.7 fps).

The X-wing at this point in time is only a proposed configuration. As shown in Figure 5 it is a stopped rotor configuration; however, the rotor is unique in its application of an elliptical airfoil section employing circulation control. As shown in Figure 6, by blowing tangentially from the upper surface of an ellipse near its trailing edge (Ref. 8), much higher lift coefficients are obtained than with a jet-flapped airfoil at the same momentum coefficient, C_μ. In addition to the high lift coefficients, circulation control achieves lift to drag ratios (including blowing power) for 20% or thicker sections comparable to those obtained by a 12% conventional airfoil. Thus, without sacrificing aerodynamic efficiency, one may be able to meet the structural requirements of the X-wing by using thicker sections.

At the present time a circulation controlled rotor (CCR) is being built for the U.S. Navy by the Kaman Corporation. This rotor will be flight tested on a modified H-2. Cyclic control will be achieved by means of a cyclic throttling of the blowing air to each blade. It should also be noted that a similar type of section has already been flown on a fixed-wing aircraft designed, built and tested by the Department of Aerospace Engineering at the West Virginia University (Ref. 9).

The WVU Technology Demonstrator STOL aircraft is a modified BD-4 incorporating drooped ailerons and a circulation-controlled, circular trailing edge flap over approximately 60% of the wing span. In cruise the circular trailing edge is designed so that it swings forward and retracts into the wing to form a conventional sharp trailing edge as pictured in Figure 7. Another unique feature of this system is also shown in the figure. Instead of blowing directly over the cylindrical trailing edge, the blowing is augmented as shown. This scheme not only provides increased blowing momentum for the circulation control but accomplishes suction boundary layer control as well at the flap hinge.

Finally, in the area of VTOL, it should be noted that several promising prototypes are being developed in the helicopter field. These include the Boeing-Vertol and Sikorsky entries in the Utility Tactical Transport (UTTAS) competition; the Bell and Hughes entries in the Advanced Attack Helicopter (AAH) competition; several commercial developments; and the Sikorsky Advancing Blade Concept (ABC). Innovations in the rotary wing field include fly-by-wire, extensive use of bonded honeycomb and advanced composite structures, elastomeric bearings, hingeless rotor and advanced airfoil technology. By careful attention to weight, aerodynamic cleanliness, and mechanical simplicity, the helicopter is rapidly improving its operating efficiency with operational cruising speeds in excess of 150 kts.

STOL

The concept of the jet flap has been known since the 1930's (Ref. 10). A theoretical solution to this device was first presented by Spence in 1956 (Ref. 11). The essence of Spence's solution together with some other aspects of the jet flap can be found in Reference 1. Essentially a thin sheet of high-momentum air issues from the trailing edge of an airfoil at some angle to the free stream and is turned in the direction of the free stream. In turning, its momentum is redirected so that a pressure difference is sustained across the jet sheet. The effect approximates the addition of a physical flap to the airfoil with both C_l and C_{l_α} being significantly increased. All three STOL prototypes mentioned earlier employ high-lift systems which approximate the jet flap. These systems, pictured in Figure 8, are referred to as the augmentor wing, upper-surface blowing (USB) and the externally blown flap (EBF).

The augmentor wing is a combination of flow augmentation with the jet flap. This scheme is currently being test flown on a modified DeHaviland Buffalo under a joint Army-NASA program at the Ames Research Center. Here high pressure air exits from a choked nozzle into a throat formed between two flap

surfaces. The augmented flow is then diffused slightly and exits at some angle to the main stream to produce the effect of a jet flap.

In the USB configuration exhaust from the jet engine is spread laterally over the upper surface near the trailing edge of the airfoil and is turned by the flap system leaving the wing again in a manner similar to the jet flap. The USB high lift system is being incorporated into the Boeing YC-14 Advanced medium STOL transport (AMST) which is expected to be flown shortly.

EBF is employed on the McDonnell-Douglas entry for the AMST competition, the YC-15. Here the engines are mounted close to the underneath surface of the wing so that the jet exhaust passes through the flap system again spreading somewhat and producing an effect comparable to that of the jet flap.

Aerodynamically, it is difficult to make a choice between the augmentor wing, USB and EBF systems. Figure 9 (from Ref. 12) presents $C_{L_{max}}$ as a function of C_μ for the augmentor wing. Figure 10 (from Ref. 13) presents trim drag polars for both the USB and EBF configurations. Obviously all three systems are capable of producing C_L values much higher than those attainable without power. Also, for a given C_μ value it appears as if the performance of the three are about equal. The choice of one system over the other will probably depend upon such factors as mechanical complexity, weight, engine-out performance, noise, and cost.

The YC-14, which is yet to fly, is described in References 14 and 15. Figure 11 depicts this AMST which has a wing area of 163.7 m^2 (1762 sq. ft.), a gross weight of approximately 751,745 N (169,000 lbs.) and powered by two GE CF 6-50D engines with an installed thrust of 214,848 N (48,300 lbs.). This airplane is designed to operate routinely in and out of 600 m (2000 ft.) fields with a 120,100 N (27,000 lbs.) payload. Its approach speed is approximately 43.8 m/s (85 kts) while the takeoff speed is 50.0 m/s (97 kts). On landing the trim lift coefficient is approximately 3.60 for a C_μ of 0.78. The airplane has several unique features worthy of note. The USB flaps operate independently to provide thrust vector control. The lift system is further enhanced by leading edge blowing of the Krueger flaps through a series of closely-spaced holes. Being landing limited, the leading edge BLC allowed a reduction in wing area for the STOL mission. According to the specifications both AMST's, with one engine inoperative must have a 0.3 g maneuver margin at constant speed and a 20% speed margin from stall in one g flight. In order to obtain good performance from the engine nozzles which blow the flaps, a door is included on the outboard side of each nozzle. For takeoff the door is opened for maximum thrust but closed in the cruise mode. It is also interesting to note that turning is enhanced in the engine exhaust by the use of vortex generators which extend into the flow when the flaps are lowered but retract in the cruise configuration.

Both the YC-14 and YC-15 employ advanced technology airfoils and are thus able to cruise at M = 0.7 or higher with relatively thick, unswept wings. They are thus approximately 40% faster than current tactical transports.

The YC-15, pictured in Figure 12, is currently being flight tested and according to Reference 16 is performing up to expectations. In addition to this reference, a description of the aircraft can be found in Reference 17.

For the STOL mission this aircraft has a weight of 676,100 N (152,000 lbs.) comprised of an empty weight of 458,160 N (103,000 lbs.), a payload of 120,100 N (27,000 lbs.) with the remainder being the fuel required for the mission. The aircraft is powered by four Pratt and Whitney JT8D-17 engines rated at 71,170 N (16,000 lbs.) per engine. Its wing area is 162 m^2 (1740 sq. ft.) with an aspect ratio of 7.0. Direct lift control is provided through the use of spoilers. Control is accomplished through a fly-by-wire system which has stability and control augmentation.

CONCLUDING REMARKS

As the result of wind tunnel and laboratory investigations performed in recent years, improved thrust augmentors and blown flap systems have been developed. Because of these efforts, several new V/STOL prototype airplanes have been designed which hold promise of becoming operational.

REFERENCES

1. McCormick, B. W.: Aerodynamics of V/STOL Flight. Academic Press, New York, London, 1967.

2. Fancher, R. B.: Low-Area Ratio, Thrust-Augmenting Ejectors, J. of Aircraft, vol. 9, no. 3, March 1972.

3. Quinn, B.: Compact Ejector Thrust Augmentation. J. of Aircraft, vol. 10, no. 8, August 1973.

4. Bevilaqua, P. M.: Evaluation of Hypermixing for Thrust Augmenting Ejectors. J. of Aircraft, vol. 11, no. 6, June 1974.

5. Bevilaqua, P. M.: Analytical Description of Hypermixing and Test of an Improved Nozzle. J. of Aircraft, vol. 13, no. 1, January 1976.

6. Robinson, C. A.: XFV-12 May Spur Navy VTOL Family. Aviation Week and Space Technology, April 16, 1973.

7. Anonymous: XFV-12A Prototype Components Tested. Aviation Week and Space Technology, April 26, 1976.

8. Williams, R. M.: Application of Circulation Control Rotor Technology to a Stopped Rotor Aircraft Design. First European Rotorcraft and Powered Lift Aircraft Forum, U. of Southampton, England, September 1975.

9. Loth, J. L., Fanucci, J. B., and Roberts, S. C.: Flight Performance of a Circulation Controlled STOL. AIAA Paper no. 74-994, 6th Aircraft Design, Flight Test and Operations Meeting, Los Angeles, California, August 1974.

10. Schubauer, G. B.: Jet Propulsion with Special Reference to Thrust Augmentation. NACA TN 442, January 1933.

11. Spence, D. A.: The Lift of a Thin Jet-Flapped Wing. Proc. Roy. Soc., A238, 1956.

12. Koenig, D. G., Corsiglia, V. R. and Morelli, J. P.: Aerodynamic Characteristics of a Large-Scale Model with an Unswept Wing and Augmented Jet Flap. NASA TN D-4610, March 1968.

13. Phelps, A. E. and Smith, C. C.: Wind-Tunnel Investigation of an Upper Surface Blown Jet-Flap Powered-Lift Configuration. NASA TN D-7399, December 1973.

14. Wimpress, John K.: Upper Surface Blowing Technology as Applied to the YC-14 Airplane. SAE Paper 730916, National Aerospace Engineering and Manufacturing Meeting, Los Angeles, California, October 1973.

15. May, F. W. and Bean, G. E.: Aerodynamic Design of the Boeing YC-14 Advanced Medium STOL Transport (AMST). AIAA Paper no. 75-1015, AIAA 1975 Aircraft Systems and Technology Meeting, Los Angeles, California, August 1975.

16. Lewis, K. W.: YC-15 Flight Test Program Report. Proc. of 19th Symposium, Soc. of Experimental Test Pilots, Tech. Review, vol. 12, no. 4, Beverly Hills, California, September 1975.

17. Heald, E. R.: External Blowing Flap Technology on the USAF McDonnell Douglas YC-15 (AMST) Program. SAE Paper 730915, National Aerospace Engineering and Manufacturing Meeting, Los Angeles, California, October 1973.
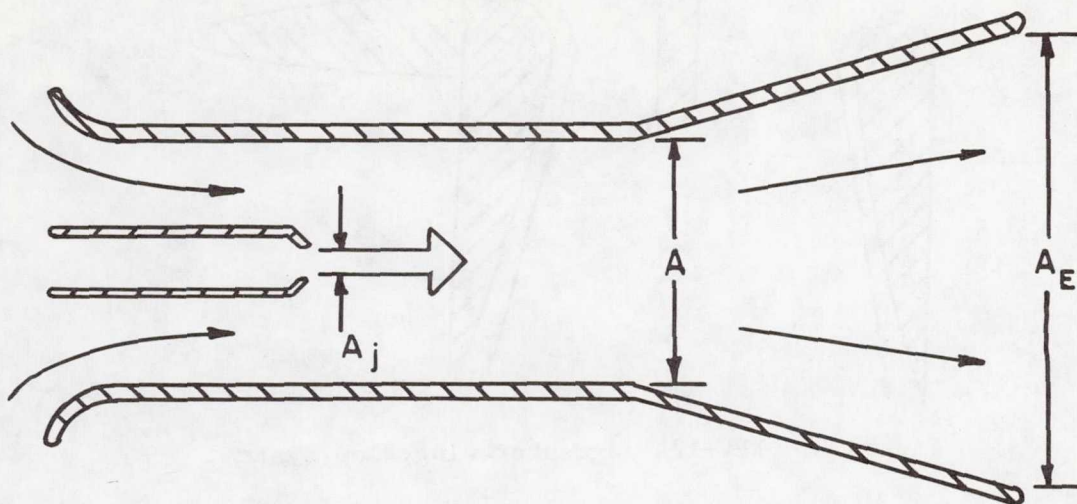
Figure 1.- Thrust-augmenting nozzle-diffuser combination.
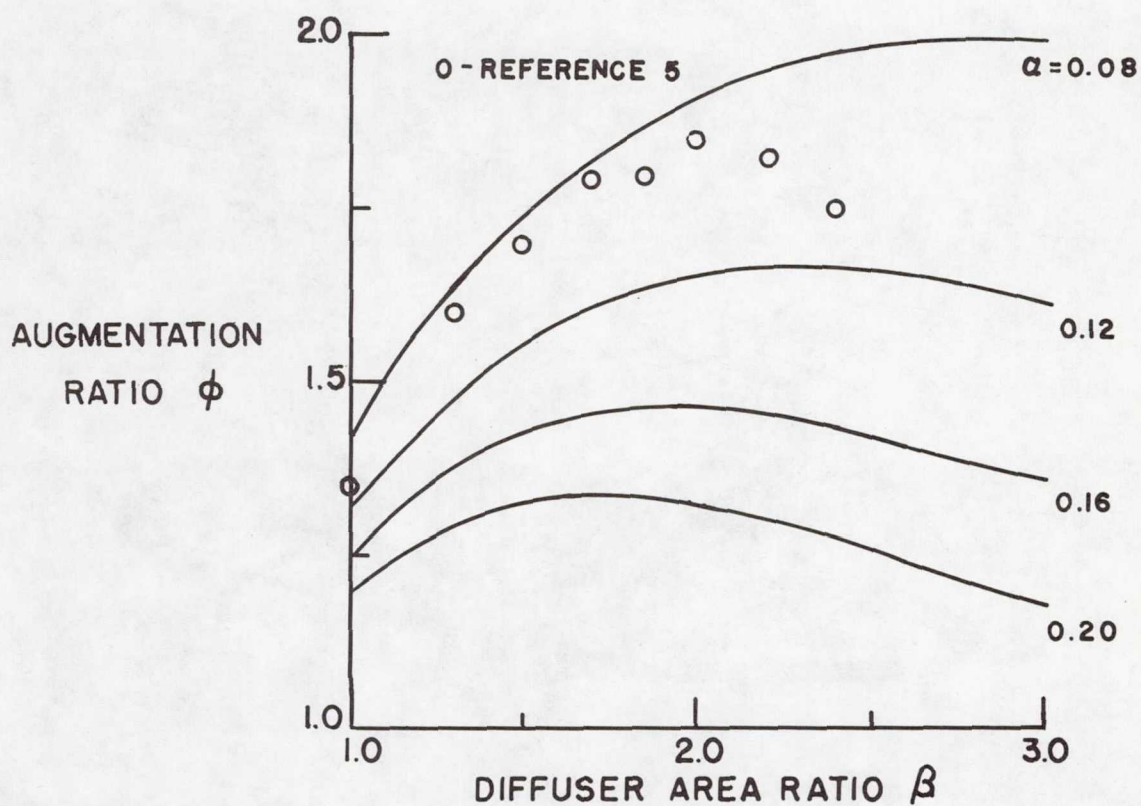
Figure 2.- Theoretical performance of a thrust augmentor
including some experimental results.
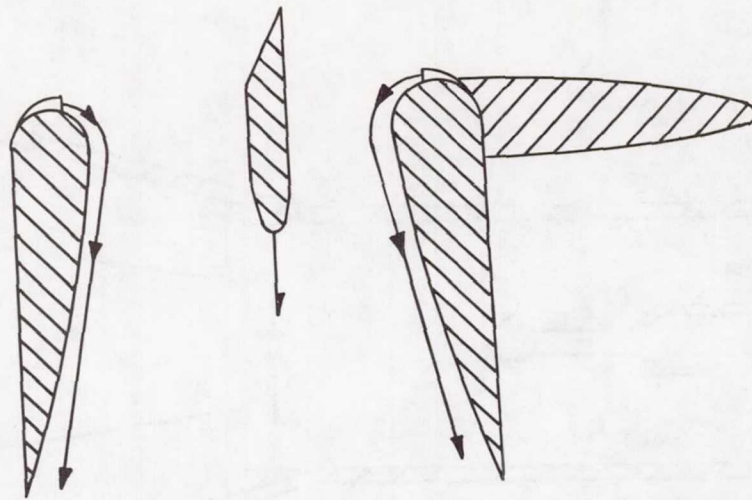
Figure 3.- XFV-12A augmentor wing-flap system.

BELL HELICOPTER 300083
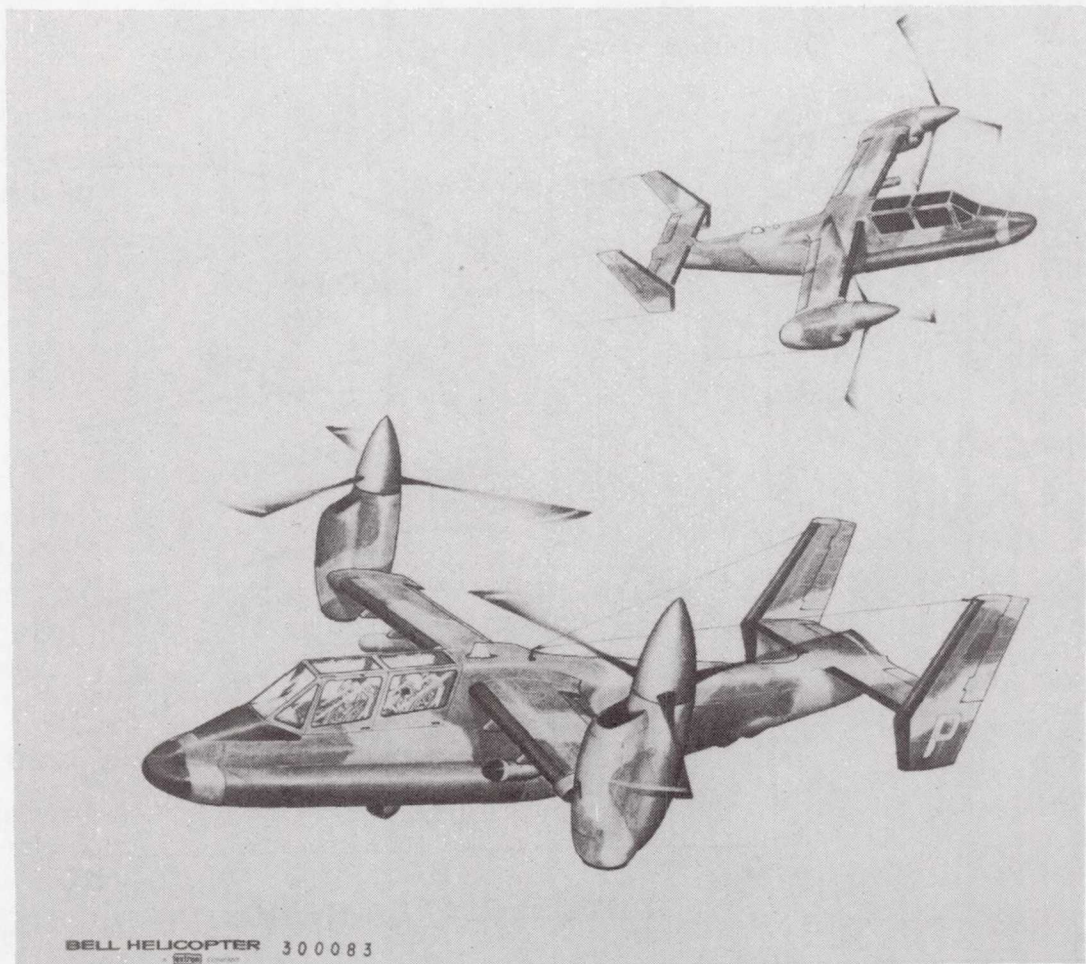
Figure 4.- Bell XV-15 tilt-rotor VTOL airplane.
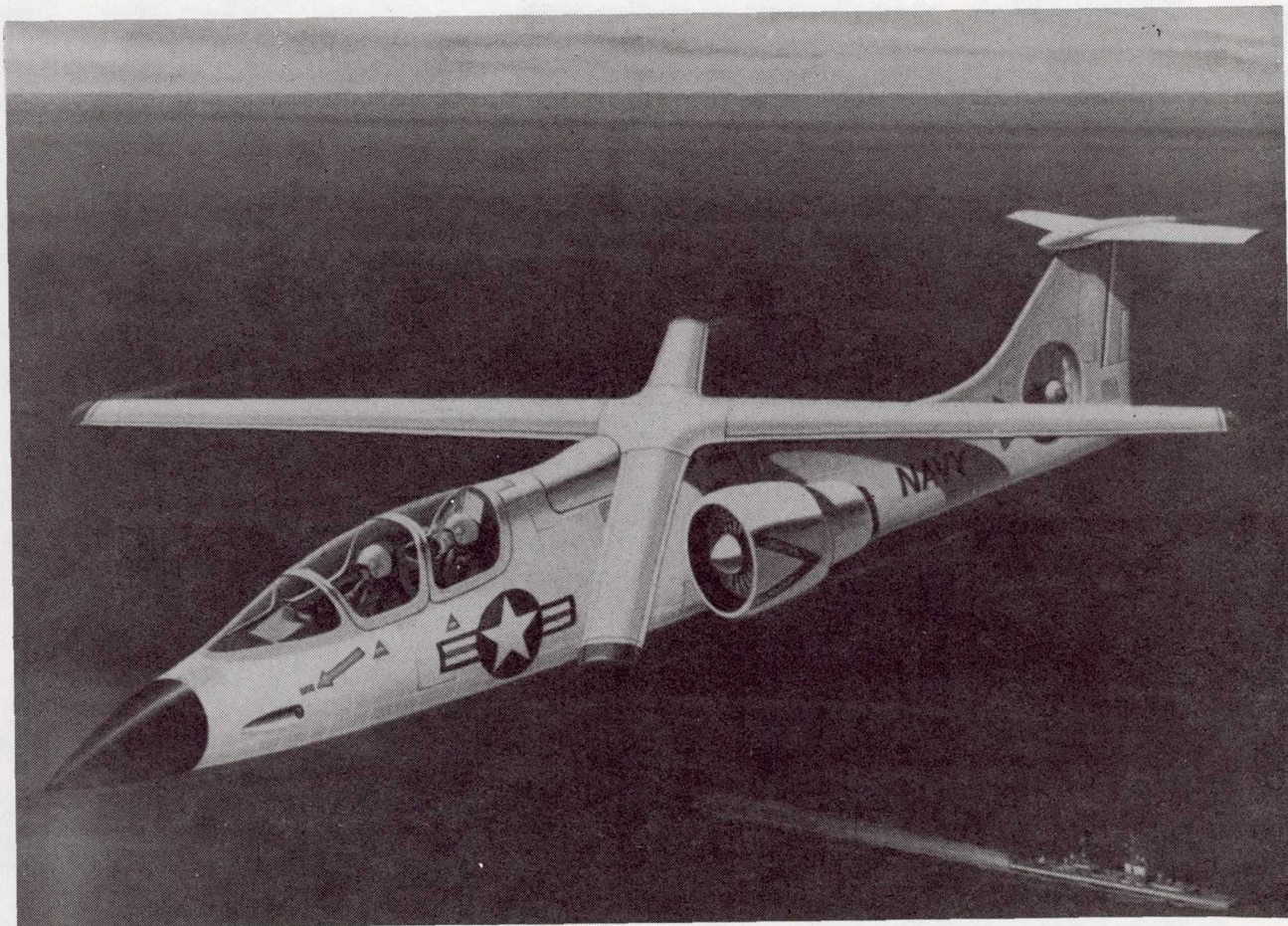
Figure 5.- Proposed X-wing VTOL configuration.
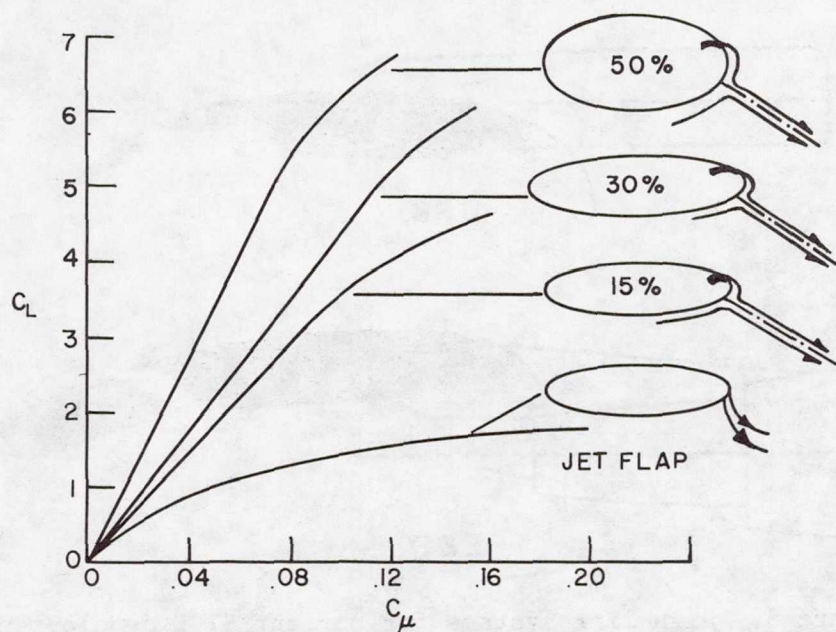
Figure 6.- Lift performance of elliptic airfoil sections with circulation control.

EJECTOR

HIGH PRESSURE DUCT
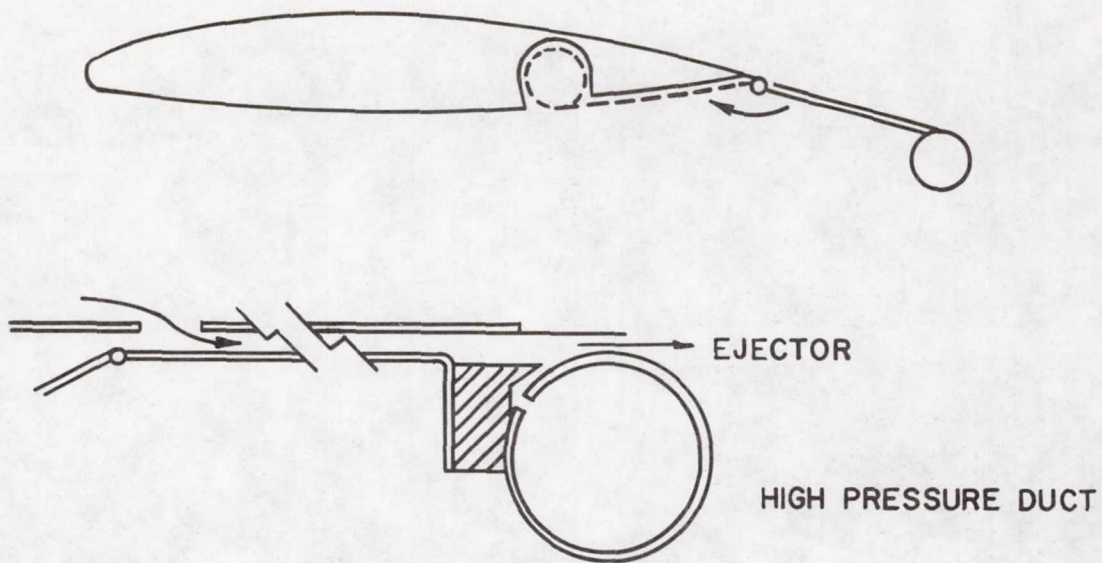
Figure 7.- Flap system for West Virginia University's technology demonstrator aircraft.

AUGMENTOR WING

USB

EBF
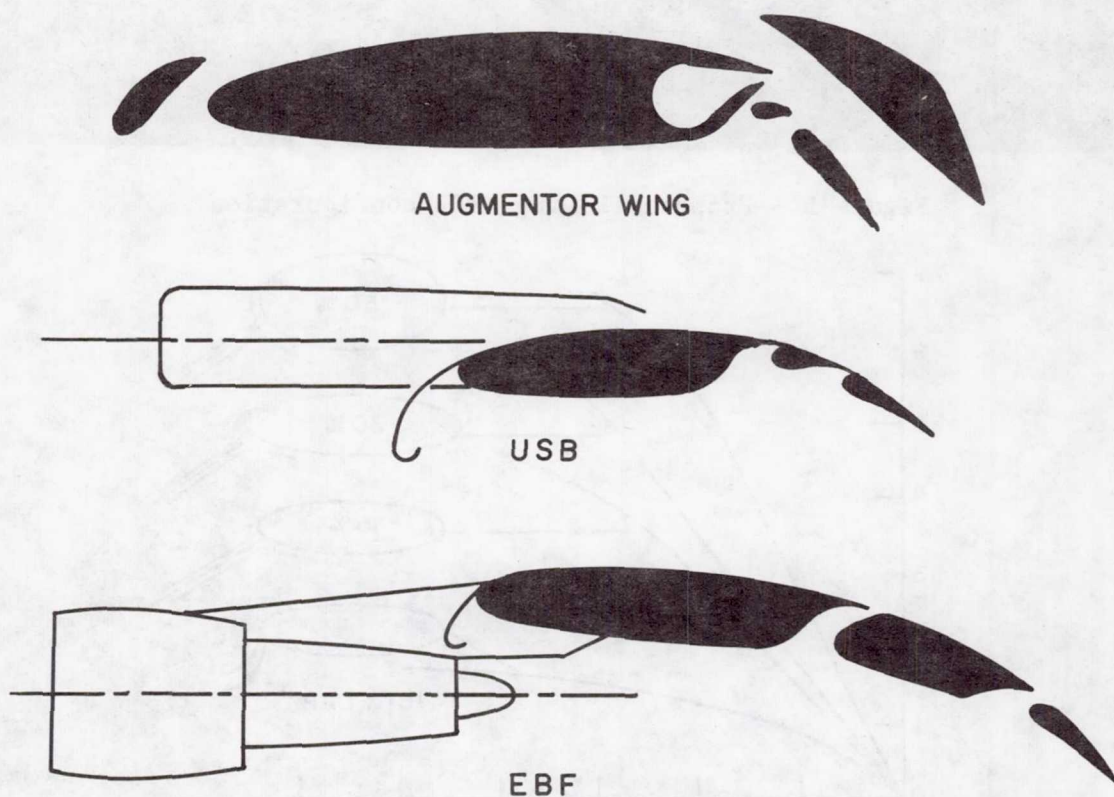
Figure 8.- High-lift systems for current STOL developments.

8

7

6

$C_{L_{max}}$ 4

3

	δ_f	δ_a	BLC
○	30°	0°	OFF
□	45°	45°	OFF
◇	60°	45°	OFF
△	70°	45°	OFF
▷	70°	45°	ON
⌐	100°	45°	ON

0

0.0   0.4   0.8   1.2   1.6   2.0

C_μ
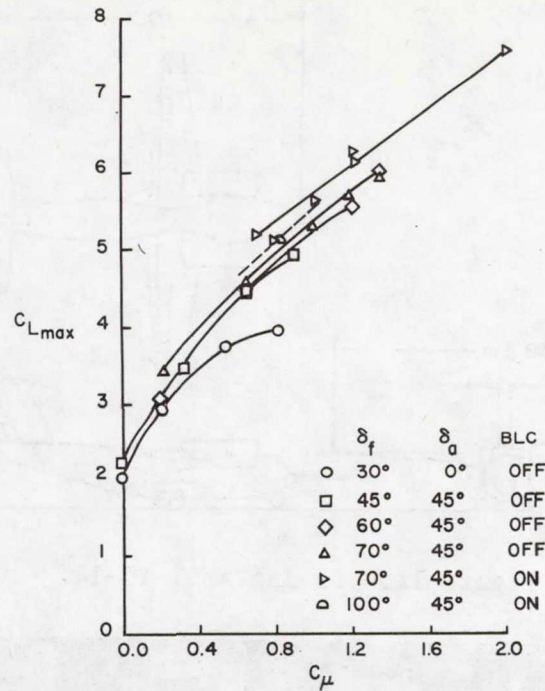
Figure 9.- Lift characteristics of an augmentor wing.

12

10

USB SEMISPAN MODEL
C_μ =4.24
δ_f =60,50,30°

USB
C_μ =4.32
δ_f =35°

EBF FULL-SPAN
MODEL
C_μ = 4.0
δ_f =55°

C_L

USB
C_μ =4.32
δ_f =55°

EBF FULL-SPAN MODEL
C_μ =4.0
δ_f =35°

0

-2   -1   0   1   2   3

C_D
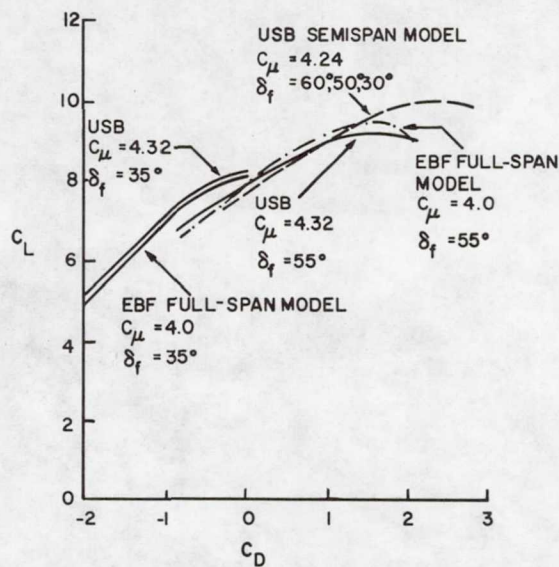
Figure 10.- Trim drag polars for the EBF and USB
high-lift configurations.
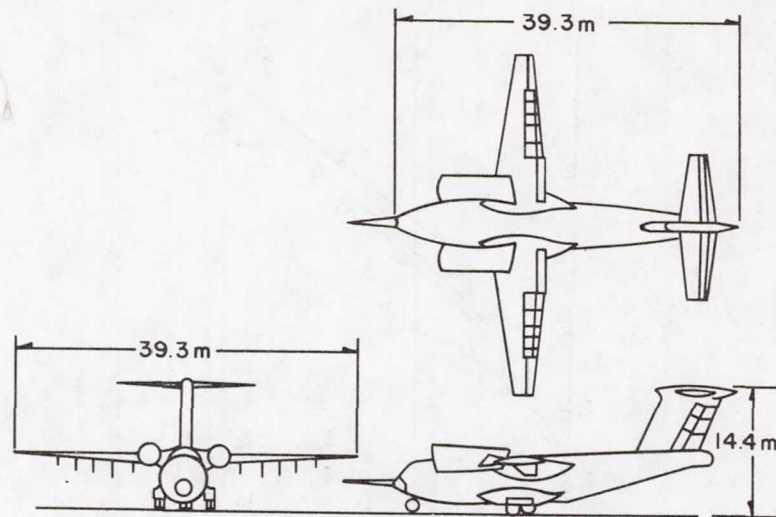
Figure 11.- Boeing AMST YC-14.

Figure 12.- McDonnell Douglas YC-15 advanced medium STOL transport.

DEVELOPMENT OF THE YC-14

Theodore C. Nark Jr.
Boeing Aerospace Company

ABSTRACT

The objective of the AMST program was to develop a prototype of a low cost replacement for the C-130. The basic goals were straight forward.

o   400 n. mi. radius
o   27,000 lb payload
o   2000 ft field length
o   2600 n. mi. ferry range
o   Low unit production cost

The combination of low unit cost and STOL capability constituted a real design challenge. The resulting YC-14 configuration embodies design elements that reflect both constraints. The interplay between design to cost and design for STOL will be examined and the compromises will be explained. The technical issues which drive the definition of a STOL configuration will be identified and a description of the YC-14 solution will be shown. The manner in which the YC-14 configuration was impacted by the trade-offs between an upper surface blown STOL design and a high speed cruise design will be demonstrated. The predicted flight characteristics will be shown and when possible, compared with flight test data.

Page intentionally left blank

THE CRYOGENIC WIND TUNNEL

Robert A. Kilgore
NASA Langley Research Center

SUMMARY

Based on theoretical studies and experience with a low-speed cryogenic tunnel and with the Langley 1/3-meter transonic cryogenic tunnel, the cryogenic wind-tunnel concept has been shown to offer many advantages with respect to the attainment of full-scale Reynolds number at reasonable levels of dynamic pressure in a ground-based facility. The unique modes of operation available in a pressurized cryogenic tunnel make possible for the first time the separation of Mach number, Reynolds number, and aeroelastic effects. By reducing the drive-power requirements to a level where a conventional fan-drive system may be used, the cryogenic concept makes possible a tunnel with high productivity and run times sufficiently long to allow for all types of tests at reduced capital costs and, for equal amounts of testing, reduced total energy consumption in comparison with other tunnel concepts.

1. INTRODUCTION

Present interest in the development of transports and maneuvering aircraft to operate efficiently in the transonic range has resulted in a review of the problem of flow simulation in transonic wind tunnels. Among the more serious problems is that related to inadequate test Reynolds number. It is this problem and an attractive solution to the problem that is the subject of this paper.

The need for increased testing capability in terms of Reynolds number has been well documented. (See, for example, refs. 1 and 2.)

At a given Mach number, the Reynolds number may be increased by using a heavy gas rather than air as the test gas, by increasing the size of the tunnel and model, by increasing the operating pressure of the tunnel, and by reducing the test temperature. The method chosen to increase Reynolds number will, in general, also affect dynamic pressure, mass flow rate, and the energy consumption of the tunnel for a given amount of testing.

The use of a heavy gas is a well-known method of achieving high Reynolds number. Freon-12 is one of the most suitable of the heavy gases for use in a wind tunnel (ref. 3). However, the differences in the ratio of specific heats become important when compressibility effects become significant, thus making Freon-12 a questionable transonic test gas (ref. 4).

An obvious way to increase Reynolds number is to increase the model size. In order to avoid increasing the wall interference effects, however, there must be a commensurate increase in tunnel size. Design studies for tunnels large enough to give full-scale Reynolds number at normal temperatures and moderate

pressures show that they would be very large, and therefore very costly, and would make heavy demands on power (ref. 5). An alternate solution is to restrict the tunnel and model sizes and increase the operating pressure. This method is feasible, of course, but the aerodynamic forces on the model, balance, and support system are greatly increased at the operating pressures that are required to achieve the desired Reynolds number in a tunnel of moderate size. From a power standpoint, a high-pressure tunnel is preferable to a large, moderate-pressure tunnel. However, for the required increase in Reynolds number, the power requirements are still undesirably large.

Operating a tunnel at cryogenic temperatures, first proposed by Smelt (ref. 6) in 1945, offers an attractive means of increasing Reynolds number while avoiding many of the practical problems associated with testing at high Reynolds numbers in conventional pressure tunnels. Personnel of the NASA Langley Research Center have been studying the application of the cryogenic concept to high Reynolds number transonic tunnels since the autumn of 1971. The results of a theoretical investigation aimed at extending the analysis of Smelt and the results of an experimental program using a low-speed wind tunnel have been reported in references 7 and 8. In order to provide information required for the planning of a large high Reynolds number transonic cryogenic tunnel, as described in reference 9, a relatively small pressurized transonic cryogenic tunnel was built and placed into operation in 1973. As a result of the successful operation of the pilot transonic tunnel, it was classified by NASA in late 1974 as a research facility, re-named the Langley 1/3-meter transonic cryogenic tunnel, and is now being used for aerodynamic research as well as cryogenic wind-tunnel technology studies.

In addition to reviewing the cryogenic wind-tunnel concept, this paper presents some details of the design and operation of the Langley 1/3-meter transonic cryogenic tunnel and describes some of the research done in the tunnel related to validation of the cryogenic wind-tunnel concept. Also presented are the future plans for the 1/3-meter tunnel.

A new fan-driven high Reynolds number transonic cryogenic tunnel is being planned for the United States. This tunnel, to be known as the National Transonic Facility, will take full advantage of the cryogenic concept to provide an order of magnitude increase in Reynolds number capability over existing tunnels. Details of this new facility will be given in a subsequent paper by D. Baals.

2. SYMBOLS

a   Speed of sound

c   Chord of two-dimensional airfoil

$\bar{c}$ Mean geometric chord

C_D Drag coefficient, $\dfrac{Drag}{qS}$

C_L Lift coefficient, $\dfrac{\text{Lift}}{qS}$

C_m Pitching-moment coefficient, $\dfrac{\text{Pitching moment}}{qS\bar{c}}$

C_p Pressure coefficient, $\dfrac{p - p_\infty}{q_\infty}$

ℓ Linear dimension of model

M Mach number

p Pressure

q Dynamic pressure, $1/2\ \rho V^2$

R Reynolds number, $\rho V \ell / \mu$

S Reference wing area

T Temperature

V Velocity

x Linear dimension

α Angle of incidence

μ Viscosity

ρ Density

Subscripts:

max   Maximum

min   Minimum

t   Stagnation conditions

∞   Free stream

3.   THE CRYOGENIC CONCEPT

The use of low temperatures in wind tunnels was first proposed as a means of reducing tunnel drive-power requirements at constant values of test Mach number, Reynolds number, and stagnation pressure. Reynolds number, which, of course, is the ratio of the inertia force to the viscous force, is given by

$$R = \frac{\text{Inertia force}}{\text{Viscous force}} = \frac{\rho V^2 \ell^2}{\mu V \ell}$$

which reduces to the well-known equation

$$R = \frac{\rho V \ell}{\mu} = \frac{\rho Ma \ell}{\mu}$$

As the temperature is decreased, the density ρ increases and the viscosity μ decreases. As can be seen from the above equations, both of these changes result in increased Reynolds number. With decreasing temperature, the speed of sound a decreases. For a given Mach number, this reduction in the speed of sound results in a reduced velocity V which, while offsetting to some extent the Reynolds number increase due to the changes in ρ and μ, provides advantages with respect to dynamic pressure, drive power, and energy consumption.

It is informative to examine the underlying mechanism through which changes in pressure and temperature influence Reynolds number. To the first order μ and a are not functions of pressure while ρ is directly proportional to pressure. Thus, increasing pressure produces an increase in Reynolds number by increasing the inertia force with a commensurate increase in model, balance, and sting loads. Also, to the first order, $\rho \propto T^{-1}$, $V \propto T^{0.5}$, and $\mu \propto T^{0.9}$. Thus, decreasing temperature leaves the inertia force unchanged at a given Mach number due to the compensating effects of ρ and V^2. The increase in Reynolds number with decreasing temperature is thus due strictly to the large reduction in the viscous force term as a result of the changes in μ and V with temperature.

The effect of a reduction in temperature on the gas properties, test conditions, and drive power are illustrated in figure 1. For comparison purposes, a stagnation temperature of 322 K (+120° F) for normal ambient temperature tunnels is assumed as a datum. It can be seen that an increase in Reynolds number by more than a factor of 6 is obtained with no increase in dynamic pressure and with a large reduction in the required drive power. To obtain such an increase in Reynolds number without increasing either the tunnel size or the operating pressure while actually reducing the drive power is extremely attractive and makes the cryogenic approach to a high Reynolds number transonic tunnel much more desirable than previous approaches.

3.1   The Advantages of a Cryogenic Tunnel

3.1.1 Reduced Dynamic Pressure and Drive Power

For a selected tunnel size and Reynolds number the previously described effects of cryogenic operation are manifested in large reductions in the required tunnel stagnation pressure and, therefore, in large reductions in both the dynamic pressure and the drive power. These reductions are illustrated in figure 2, where both dynamic pressure and drive power are shown as functions of

stagnation temperature for a constant chord Reynolds number[*] of 50 x 10^6 at $M_\infty = 1.0$ for a tunnel having a 2.5- by 2.5-m test section. As the tunnel operating temperature is reduced, the large reductions in both dynamic pressure and drive power are clearly evident and provide the desired relief from the extremely high values that would be required for a pressure tunnel operating at normal temperatures. Some of the specific advantages resulting from the reduction in dynamic pressure include reduced model and balance stresses, with the resulting increased test lift coefficient capability, reduced sting size for a given lift which reduces sting interference and permits more realistic aft fuselage modeling, and an increased stress margin for aeroelastic matching.

The large reduction in drive power makes a fan-driven tunnel practical even at this high Reynolds number. The resulting efficiency and increased run time provide important advantages relative to intermittent tunnels, such as increased productivity, improved dynamic testing capability, and reduced operating costs and total energy consumption for equal amounts of testing.

An additional advantage of a fan-driven tunnel is realized by having run times sufficient to insure the avoidance of problems caused by heat transfer between the model and the stream. In tunnels where the flow is generated by expansion waves, spurious scale effects due to heat transfer can only be avoided by cooling the model to the expected recovery temperature (ref. 3). Such problems are avoided in a continuous-flow tunnel where the model is never far from thermal equilibrium with the stream. In general, no additional testing time is required to allow the model to achieve thermal equilibrium since the flow initiation process is gradual and test conditions are not changed abruptly in a fan-driven tunnel.

The advantages of the cryogenic concept with respect to reduced dynamic pressure and reduced drive power are shown in figure 2 for constant Reynolds number and constant test-section size. For a constant tunnel size, both the shell costs, which may account for as much as two-thirds of the total cost of a wind tunnel, and the costs of the drive system for the tunnel vary nearly linearly with the maximum stagnation pressure of the tunnel. Therefore, for conditions of constant Reynolds number and tunnel size, the reduction in the stagnation pressure which is needed to achieve the desired Reynolds number at cryogenic temperatures results in a reduction in capital costs even when the higher costs of the structural materials which are suitable for use at cryogenic temperatures is taken into account.

If the attainment of increased Reynolds number is accomplished by increasing stagnation pressure, for many configurations a pressure limit is reached beyond which the loads on the model will preclude testing at the desired lift coefficient. With this in mind, an alternate approach to the design of a high Reynolds tunnel is to establish the maximum usable pressure and allow tunnel size to decrease with design temperature in order to attain the desired Reynolds

---

[*]For consistency throughout this paper, Reynolds number is based on a wing chord equal to 0.1 times the square root of the test-section area; for wings of small aspect ratio the actual values may be two or three times the value given.

number. Under these conditions, there is a very strong impact of the cryogenic concept on capital cost due to the large reduction in tunnel size required for the attainment of a given Reynolds number.

At a constant pressure, the cost of the tunnel shell varies approximately with the cube of the tunnel size, whereas the cost of the drive system varies approximately with the square of the tunnel size. Thus, a reduction in tunnel size by a factor of 5 or 6, which, as can be inferred from figure 1, may be realized by operating at cryogenic temperatures, represents a substantial savings in capital costs over the much larger ambient-temperature tunnel which would be required to achieve the desired Reynolds number at the same stagnation pressure.

3.1.2 Reduced Peak Power Demand and Total Energy Consumption

Because of the high peak power demands of large ambient-temperature transonic tunnels, the tunnel designer has, up until now, been forced to abandon the conventional continuous-flow tunnel and adopt some form of intermittent tunnel using energy storage techniques. However, since a fan is the most efficient method of driving a tunnel, the reduction in peak power demand obtained by going to conventional energy storage techniques is realized only by accepting an increase in total energy consumption. By reducing the drive power requirements to a level where a fan drive again becomes practical even for large tunnels, the cryogenic concept makes available not only the many technical advantages of the conventional continuous-flow tunnel but, at the same time, results in significant reductions in the total energy consumed during a test for a given Reynolds number and stagnation pressure (ref. 9). This reduction in total-energy requirement which results from cryogenic operation is especially significant in this age when the conservation of energy is assuming increasing importance.

3.1.3 Unique Operating Envelopes

In addition to the advantages of reduced dynamic pressures and reduced drive-power and energy requirements, the cryogenic wind-tunnel concept offers the aerodynamic researcher some unique and extremely useful operating envelopes. For a given model orientation, any aerodynamic coefficient is a function of, among other things, Mach number M, Reynolds number R, and the aeroelastic distortion of the model, which is, in turn, a function of the dynamic pressure q. A cryogenic tunnel with the independent control of Mach number, temperature, and pressure has the unique capability to determine independently the effect of Mach number, Reynolds number, and aeroelastic distortion on the aerodynamic characteristics of the model.

To illustrate the manner in which this is accomplished, a constant Mach number operating envelope is presented for a cryogenic transonic pressure tunnel having a 2.5- by 2.5-m test section. The main purpose of presenting the envelope is to illustrate the unique testing capability available in a cryogenic tunnel. However, the size of the tunnel and the ranges of temperature, pressure, and Mach number have been selected to represent the anticipated characteristics of the proposed National Transonic Facility.

The constant Mach number operating envelope showing the range of dynamic pressure and Reynolds number available for sonic testing is presented in figure 3. The envelope is bounded by the maximum temperature boundary (taken in this example to be 340 K), the minimum temperature boundary (chosen to avoid saturation at free-stream conditions), the maximum pressure boundary (8.8 atm), and the minimum pressure boundary (0.5 atm). With such an operating capability, it is possible, for example, to determine at a constant Mach number the true effect of Reynolds number on the aerodynamic characteristics of the model without having the results influenced by changing model shape due to changing dynamic pressure, as is the case in a conventional pressure tunnel. (There will be a slight variation of the modulus of elasticity E of most model materials with temperature. To correct for this variation in E, the dynamic pressure q may be varied by varying total pressure so that the ratio q/E remains constant over the Reynolds number range.) This ability to make pure Reynolds number studies is of particular importance, for example, in research on the effects of the interaction between the shock and the boundary layer. As indicated on the envelope, pure aeroelastic studies may be made under conditions of constant Reynolds number. In addition, combinations of R and q can be established to represent accurately the variations in flight of aeroelastic deformation and changes in Reynolds number with altitude. Similar envelopes are, of course, available for other Mach numbers. In addition to the constant Mach number operating envelope, two other types of envelopes are available in a pressure tunnel capable of cryogenic operation. These are the constant Reynolds number envelope and the constant dynamic pressure envelope. These envelopes have been described elsewhere (ref. 8) and will not be discussed further in this paper. From the aerodynamic research point of view, the most attractive feature of the cryogenic tunnel is the ability to isolate and study independently the effects of Reynolds number, Mach number, and aeroelasticity. The ability to isolate these effects is extremely desirable, since both aeroelasticity and Reynolds number can produce profound effects on critical aerodynamic phenomena, such as shock boundary-layer interactions.

3.2   Real-Gas Studies

In the cryogenic tunnel concepts developed at Langley, the test gas is nitrogen rather than air. Since 1972, an extensive study has been made by researchers at Langley to evaluate any possible adverse real-gas effects on aerodynamic data taken at cryogenic temperatures. The studies have been divided into two parts. The first part has looked at the effect of thermal and caloric imperfections on the isentropic expansion and normal-shock flow properties for the real gas, nitrogen, as compared to an ideal diatomic gas. These studies have shown that for pressures up to 5 atmospheres or so the behavior of nitrogen at cryogenic temperatures can be considered to be the same for all practical purposes as the behavior of an ideal gas. Portions of this part of the real-gas studies have been reported in reference 10 and will not be discussed further in this paper.

The second part of the real-gas studies has been concerned with determining the minimum usable stagnation temperature. When testing at cryogenic temperatures, it is highly desirable to take maximum possible advantage of reduced temperature in order to increase test Reynolds number. As can be seen from

figure 4, the changes in Reynolds number per degree Kelvin change in stagnation temperature approaches 2% at the lower temperatures. An additional incentive to operate at lower temperatures is the reduction in fan-drive power and an attendant reduction in the amount of liquid nitrogen required for cooling.

Early theoretical studies of the minimum operating temperature were based on the assumption that condensation of the stream must be avoided under the most adverse flow conditions existing in the test section. Condensation is most likely to begin in the high local Mach number region over the model being tested where the pressure of the gas is at a minimum. Under the assumption that the gas is in static equilibrium at this low pressure, it can be shown that lique-faction of the stream will begin when the temperature associated with the low-pressure region just matches the saturated vapor temperature. Thus, under the assumption that condensation must be avoided, there exists for a given stagna-tion pressure and temperature a maximum local Mach number which must not be exceeded.

As noted in reference 7, the assumptions made for the early look at mini-mum operating temperature were recognized as overly conservative. Based on theoretical considerations as well as on experimental results (see refs. 11 and 12) it is apparent that temperatures considerably lower than those based on maximum local Mach number considerations can, under certain circumstances, be used and still avoid any effects of condensation on the data.

4. THE LANGLEY 1/3-METER TRANSONIC CRYOGENIC TUNNEL

Following the successful completion of the low-speed tunnel work described in references 7 and 8, it was decided to construct a relatively small continuous-flow fan-driven transonic pressure tunnel in order to extend the design and operational experience to the pressure and speed range contemplated for a large high Reynolds number facility. The purposes envisioned for the pilot transonic cryogenic tunnel were to demonstrate in compressible flow that the results obtained when Reynolds number is increased by reducing temperature are equiva-lent to those obtained when Reynolds number is increased by increasing pressure, to determine experimentally any limitations imposed by liquefaction, to verify engineering concepts with a realistic tunnel configuration, and to provide addi-tional operational experience. Design of the transonic tunnel began in December 1972 and initial operation began in September 1973.

4.1   Description of the Tunnel

The tunnel is a single-return fan-driven tunnel with a slotted, octagonal test section measuring 34 cm from flat to flat. A sketch of the tunnel circuit is shown in figure 5. The fan is driven by a 2.2-MW variable-frequency motor which is capable of operating the tunnel at Mach numbers from about 0.05 to about 1.3 at stagnation pressures from slightly greater than 1 atm to 5 atm over a stagnation temperature range from about 77 K to 350 K. As was the case with the low-speed tunnel described in references 7 and 8, the wide range of operating temperatures is obtained by spraying liquid nitrogen (LN_2) directly

into the tunnel circuit to cool the structure and the gas stream and to remove the heat of compression added to the stream by the drive fan.

Although the test-section width is only 34 cm, the combination of a pressure of 5 atm and cryogenic capability provides a chord Reynolds number of over 10×10^6 at $M_\infty = 1$, which is equivalent to an ambient tunnel having a test section greater than 7 m by 7 m. The range of operating temperature and pressure also provides the opportunity of investigating independently the effects of temperature and pressure over almost a five-to-one range of Reynolds number. A more detailed description of the Langley 1/3-meter transonic cryogenic tunnel and its ancillary equipment can be found in reference 13.

4.2   Experimental Results From the Langley 1/3-Meter Transonic Cryogenic Tunnel

Two types of experimental data are being obtained from the transonic cryogenic tunnel. The first type relates to the operation and performance of the tunnel itself. The data for the most part consist of the usual tunnel calibration information but with particular emphasis being placed on identifying any problems related either to the method of cooling or to the wide range of operating temperature.

The major conclusions with respect to operation and performance to be made after almost 600 hours of running at cryogenic temperatures are as follows:

1.   Purging, cooldown, and warmup times are acceptable and can be predicted with good accuracy.
2.   Liquid nitrogen requirements for cooldown and running can be predicted with good accuracy.
3.   Cooling with liquid nitrogen is practical at the power levels required for transonic testing. Test temperature is easily controlled and good temperature distribution obtained by using a simple nitrogen injection system.
4.   Test-section flow quality is good over the entire range of operating conditions.

The experimental data on which these conclusions are based as well as other information related to the operational and performance characteristics of the Langley 1/3-meter transonic cryogenic tunnel have been reported in references 13, 14, and 15 and will not be discussed further in this paper.

In addition to the experimental results related to the operational and performance aspects of the cryogenic tunnel, there have been a series of aerodynamic experiments primarily aimed at determining the validity and practicality of the cryogenic concept in compressible flow. In the following sections will be presented some of the results of these validation experiments.

4.2.1 Two-Dimensional Airfoil Tests

Based on the real-gas studies of reference 10, there is little doubt that airfoil pressure distributions measured for given values of Reynolds number and Mach number should be the same at cryogenic and ambient temperature conditions. However, in order to provide experimental verification of this equivalence, the

pressure distribution on a two-dimensional airfoil has been measured in the Langley 1/3-meter transonic cryogenic tunnel at ambient and cryogenic temperatures under conditions of constant Reynolds number and Mach number.

A modified NACA 0012-64 airfoil having a 13.72-cm chord was used for the two-dimensional airfoil pressure tests. The airfoil spanned the octagonal test section and was fastened to the walls in such a way that incidence could be varied. An airfoil somewhat larger than would normally be tested in this size tunnel was selected in order to allow for more accurate model construction, a reasonable number of pressure orifices, and higher chord Reynolds number. The fact that the relatively high ratio of chord to tunnel height might result in wall-induced interference was of no particular concern since the tests were being made only to determine whether the airfoil pressure distribution was modified in any way by real-gas effects associated with testing at cryogenic temperatures. The pressure distribution data should therefore be looked at from the point of view of agreement or lack of agreement between data obtained at ambient and cryogenic conditions and the results used only as an indication of the validity of the cryogenic concept. The conditions selected to insure a valid and critical cryogenic evaluation were:

1. Ambient and cryogenic temperature tests were made in the same tunnel on the same model at the same Mach number and Reynolds number.
2. The airfoil was tested with free transition to allow any possible temperature effect on boundary-layer development.
3. The symmetrical airfoil was tested at zero incidence to eliminate any shape or incidence change due to the dynamic-pressure differences between the ambient and cryogenic temperature conditions.
4. Free-stream Mach number exceeded the Mach number normal to the leading edge of typical near-sonic transport designs.

A comparison of the pressure distribution for ambient and cryogenic temperature tests at free-stream Mach numbers of 0.75 and 0.85 are shown in figure 6. For this comparison, the same chord Reynolds number was obtained at each temperature and constant Mach number by an appropriate adjustment of pressure with temperature. As can be seen, there is excellent agreement at both Mach numbers between the pressure distributions obtained at ambient and cryogenic conditions. This is considered to be a valid check in view of the large variation in the gas properties over this large temperature and pressure range. In addition, this agreement is particularly significant with regard to setting tunnel conditions when one considers, for example, the large variation of the speed of sound with temperature and the sensitivity of the airfoil pressure distribution to changes in Mach number.

The distribution at $M_\infty = 0.85$ is of perhaps greater significance since the pressure distribution shows the flow to be supersonic over a large portion of the airfoil, reaching a local Mach number of about 1.22 just ahead of the strong recompression shock. This type of flow, typical of supercritical flows, should be extremely sensitive to any anomalous behavior of the test gas due to operation at cryogenic temperatures. The almost perfect agreement in the pressure distributions provides experimental confirmation that nitrogen at cryogenic temperatures behaves like a perfect gas and is therefore a valid transonic test gas as predicted by the real-gas studies.

4.2.2 Three-Dimensional Model Tests

Three-dimensional model tests have been made in the transonic cryogenic tunnel on a delta-wing model with a sharp leading edge, an aspect ratio of 1.07, and a sweep of 75°. The overall length of the model was 20 cm and the maximum span was 10.4 cm.

The purpose of the three-dimensional model tests were (1) to investigate any possible effects of testing at cryogenic temperatures on the aerodynamic characteristics of a configuration having flow characterized by a separation-induced leading-edge vortex, and (2) to obtain experience at cryogenic temperatures with an electrically heated internal strain-gage balance and the accompanying sting, supporting strut, and angle-of-attack measuring device. (Similar tests with satisfactory results had been made previously in the low-speed cryogenic tunnel at Langley with a water-heated balance and the results reported in reference 8.)

The results show that flows with leading-edge vortex effects are duplicated properly at cryogenic temperatures.

An example of the results which have been obtained on the delta-wing model and reported in reference 16 are presented in figure 7 which shows the variation of pitching-moment, drag, and lift-force coefficients with angle of attack at both ambient and cryogenic temperatures for a Mach number of 0.8. The circular symbols indicate experimental results obtained at a stagnation pressure of 4.6 atm and at a stagnation temperature of about 301 K. The square symbols are data taken at a stagnation pressure of 1.2 atm and at a stagnation temperature of 114 K. The Reynolds number, based on mean geometric chord, was 8.5×10^6 for both sets of data. As can be seen, there is good agreement between the experimental results obtained at ambient and cryogenic temperatures.

The three-dimensional model results provide additional evidence that cryogenic nitrogen is a valid test gas even under conditions of separated and reattached (vortex) flow. In addition, there has been no indication of any major problem areas associated with obtaining angle-of-attack or strain-gage balance measurements at cryogenic temperatures.

5. FUTURE PLANS

In addition to being used to verify the validity of the cryogenic wind-tunnel concept and providing more than 600 hours of experience in the operation of a fan-driven cryogenic tunnel, the 1/3-meter tunnel is being used for aerodynamic research in several areas where either the very high unit Reynolds number ($R/m \approx 3 \times 10^8$ at $M_\infty = 1$) or the 25 to 1 range of Reynolds number is required. Some of the future plans for this unique facility are shown in the sketch presented in figure 8 and described in the following sections.

5.1   Two-Dimensional Test Section

Because of the renewed interest in airfoil research and the sensitivity of many of the advanced airfoils to Reynolds number, a two-dimensional test-section leg has been constructed and is being installed in the Langley transonic cryogenic tunnel. The floor and ceiling of the 20- by 60-cm test section are slotted and there is provision for sidewall suction near the model as well as removal of the sidewall boundary layer just ahead of the model.

Pressure orifices on the model and a wake survey device will be used to provide the test data. In addition, a schlieren system is provided to allow for visual observation of the flow field. This new test-section leg will provide a unique facility for fundamental fluid-dynamics research and airfoil development at test Reynolds numbers of up to 50 million on a two-dimensional airfoil having a 15-cm chord.

5.2   Self-Streamlining Two-Dimensional Test Section

A two-dimensional self-streamlining flexible-wall test-section leg is being designed for the 1/3-meter tunnel based on the work by Goodyer and coworkers at the University of Southampton. (See refs. 17 and 18.) Initially, the test section will be used for testing in flows where the Mach number at the walls never exceeds unity. By permitting increased chord length, the flexible-wall test section will allow testing under interference-free conditions at chord Reynolds numbers approaching 100 million.

5.3   Magnetic Suspension and Balance System

The reduction in model loads made possible by the cryogenic wind-tunnel concept and the reduction in the size of the coils used in a magnetic suspension and balance system made possible by superconductor technology makes the combination of these two concepts an attractive means of providing high Reynolds number test capability free from support interference. In such a facility, it will be possible to test free of support interference effects as well as to determine the magnitude of such effects by direct comparison with data obtained by using conventional model support systems. The demonstrated ease and rapidity with which the orientation of the model may be changed with the magnetic suspension system while keeping the model in the center of the test section will facilitate the rapid acquisition of the aerodynamic data which is a desirable feature of any high Reynolds number tunnel. In addition, the retrieval of the model from the test section of a cryogenic tunnel for model configuration changes would be a simple operation with a magnetic-suspension and balance system.

Because of the many advantages offered by a magnetic-suspension and balance system, NASA has supported for several years both in-house and sponsored research in this area. Significant accomplishments resulting from NASA sponsored research include the development of an electromagnetic position sensor at the Aerophysics Laboratory of the Massachusetts Institute of Technology

(ref. 19) and the development of an all-superconductor magnetic-suspension and balance system for aerodynamic testing at the Research Laboratories for the Engineering Sciences at the University of Virginia (ref. 20).

Additional studies are being made at both Langley and the University of Virginia with the aim of building a six-component superconducting magnetic suspension and balance system to be used in conjunction with an interchangeable test-section leg for the Langley 1/3-meter transonic cryogenic tunnel (ref. 21). Current plans are for the test section of this leg to be octagonal in cross section and to measure approximately 0.45 m from flat to flat. The combination of 5 atmospheres operating pressure and cryogenic temperatures will result in test Reynolds numbers of about 15 million.

6.   CONCLUDING REMARKS

Based on theoretical studies and experience with a low-speed cryogenic tunnel and with the Langley 1/3-meter transonic cryogenic tunnel, the cryogenic concept has been shown to offer many advantages with respect to the attainment of full-scale Reynolds number at reasonable levels of dynamic pressure in a ground-based facility. The unique modes of operation which are available only in a pressurized cryogenic tunnel make possible for the first time the separation of Mach number, Reynolds number, and aeroelastic effects. By reducing the drive-power requirements to a level where a conventional fan-drive system may be used, the cryogenic concept makes possible a tunnel with high productivity and run times sufficiently long to allow for all types of tests at reduced capital costs, and for equal amounts of testing, reduced total energy consumption in comparison with other tunnel concepts.

7. REFERENCES

1. Heppe, Richard R.; O'Laughlin, B. D.; and Celniker, Leo: New Aeronautical Facilities — We Need Them Now. Astronaut. & Aeronaut., Vol. 6, No. 3, Mar. 1968, pp. 42-54.

2. Hills, R.: The Need for a Large Transonic Wind Tunnel in Europe: A Summary of the Report of an AGARD Working Group (LaWs). AIAA Paper No. 74-630, July 1974.

3. Pozniak, O. M.: Investigation Into the Use of Freon 12 as a Working Medium in a High-Speed Wind Tunnel. Note No. 72, Coll. Aeronaut., Cranfield (Engl.), Nov. 1957.

4. Treon, Stuart L.; Hofstetter, William R.; and Abbott, Frank T., Jr.: On the Use of Freon-12 for Increasing Reynolds Number in Wind-Tunnel Testing of Three-Dimensional Aircraft Models at Subcritical and Supercritical Mach Numbers. Facilities and Techniques for Aerodynamic Testing at Transonic Speeds and High Reynolds Number, AGARD CP No. 83, Aug. 1971, pp. 27-1 — 27-8.

5. Baals, Donald D.; and Stokes, George M.: A Facility Concept for High Reynolds Number Testing at Transonic Speeds. Facilities and Techniques for Aerodynamic Testing at Transonic Speeds and High Reynolds Number, AGARD CP No. 83, Aug. 1971, pp. 28-1 — 28-12.

6. Smelt, R.: Power Economy in High-Speed Wind Tunnels by Choice of Working Fluid and Temperature. Rep. No. Aero. 2081, Brit. R.A.E., Aug. 1945.

7. Goodyer, Michael J.; and Kilgore, Robert A.: The High Reynolds Number Cryogenic Wind Tunnel. AIAA Paper No. 72-995, Sept. 1972.

8. Kilgore, Robert A.; Goodyer, Michael J.; Adcock, Jerry B.; and Davenport, Edwin E.: The Cryogenic Wind-Tunnel Concept for High Reynolds Number Testing. NASA TN D-7762, 1974.

9. Polhamus, E. C.; Kilgore, R. A.; Adcock, J. B.; and Ray, E. J.: The Langley Cryogenic High Reynolds Number Wind-Tunnel Program. Astronaut. and Aeronaut., Vol. 12, No. 10, Oct. 1974, pp. 30-40.

10. Adcock, Jerry B.; Kilgore, Robert A.; and Ray, Edward J.: Cryogenic Nitrogen as a Transonic Wind-Tunnel Test Gas. AIAA Paper No. 75-143, Jan. 1975.

11. Hall, Robert M.: Preliminary Study of the Minimum Temperatures for Valid Testing in a Cryogenic Wind Tunnel. NASA TM X-72700, 1975.

12. Hall, Robert M.: Further Study of the Minimum Temperatures for Valid Testing in a Cryogenic Wind Tunnel. NASA TM X-72924, 1976.

13. Kilgore, Robert A.: Design Features and Operational Characteristics of the Langley Pilot Transonic Cryogenic Tunnel. NASA TM X-72012, 1974.

14. Kilgore, Robert A.; Adcock, Jerry B.; and Ray, Edward J.: Simulation of Flight Test Conditions in the Langley Pilot Transonic Cryogenic Tunnel. NASA TN D-7811, 1974.

15. Ray, Edward J.; Kilgore, Robert A.; and Adcock, Jerry B.: Analysis of Validation Tests of the Langley Pilot Transonic Cryogenic Tunnel. NASA TN D-7828, 1975.

16. Kilgore, Robert A.; and Davenport, Edwin E.: Static Force Tests of a Sharp Leading-Edge Delta-Wing Model at Ambient and Cryogenic Temperatures With a Description of the Apparatus Employed. NASA TM X-73901, June 1976.

17. Goodyer, M. J.: A Low-Speed Self-Streamlining Wind Tunnel. Paper 13 of AGARD CP-174, Proceedings of the AGARD Conference on Wind Tunnel Design and Testing Techniques, London, U.K., 6-8 Oct. 1975.

18. Judd, M.; Wolf, S. W. D.; and Goodyer, M. J.: Analytical Work in Support of the Design and Operation of Two-Dimensional Self-Streamlining Test Sections. NASA CR-145019, 1976.

19. Stephens, Timothy: Design, Construction, and Evaluation of a Magnetic Suspension and Balance System for Wind Tunnels. NASA CR-66903, 1969.

20. Humphris, R. R., et al.: Performance Characteristics of the U. Va. Super-conducting Wind Tunnel Balance. Paper presented at the 1974 Applied Superconductivity Conference.

21. Zapata, Ricardo N.: Magnetic Suspension Techniques for Large-Scale Aero-dynamic Testing. Paper 39 of AGARD CP-174, Proceedings of the AGARD Conference on Wind Tunnel Design and Testing Techniques, London, U.K., 6-8 Oct. 1975.

GAS PROPERTIES

TEST CONDITIONS AND DRIVE POWER

VALUES RELATIVE TO 322 K

REYNOLDS NUMBER

DYNAMIC PRESSURE

POWER

STAGNATION TEMPERATURE, K

ρ

a

μ
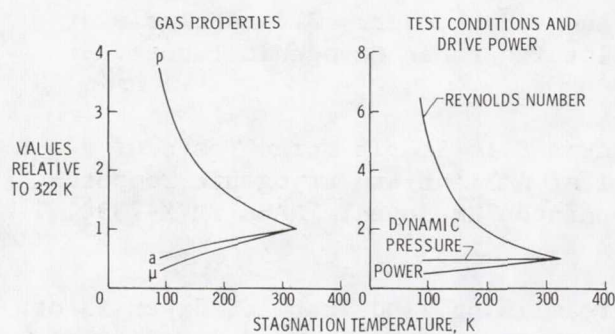
Figure 1. Effect of temperature reduction on the gas properties, test conditions, and drive power. $M_\infty = 1.0$; constant stagnation pressure and tunnel size.

$M_\infty = 1.0$, 2.5- BY 2.5- m TEST SECTION

$T_{t, max} = 340K$ $P_{t, max} = 8.8 \, atm$

DYNAMIC PRESSURE, q, kN/m^2

$T_{t, min}$

PURE REYNOLDS NUMBER STUDIES

PURE AEROELASTIC STUDIES

$P_{t, min} = 0.5 \, atm$
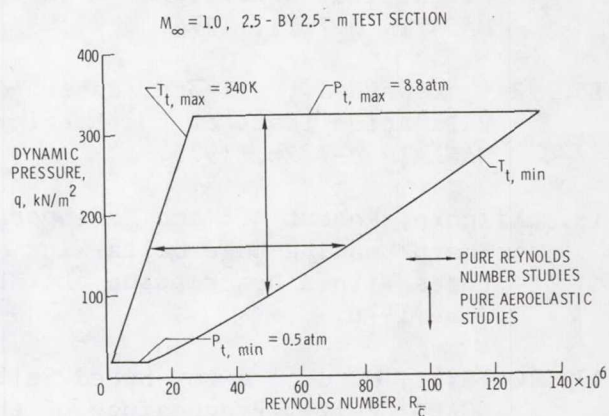
REYNOLDS NUMBER, $R_{\bar{c}}$

Figure 3. Constant Mach number operating envelope for cryogenic nitrogen tunnel.

$M_\infty = 1.0$, $R_{\bar{c}} = 50 \times 10^6$,   2.5- BY 2.5- m TEST SECTION

DYNAMIC PRESSURE, q, kN/m^2

DYNAMIC PRESSURE

DRIVE POWER, MW

DRIVE POWER

STAGNATION TEMPERATURE, K
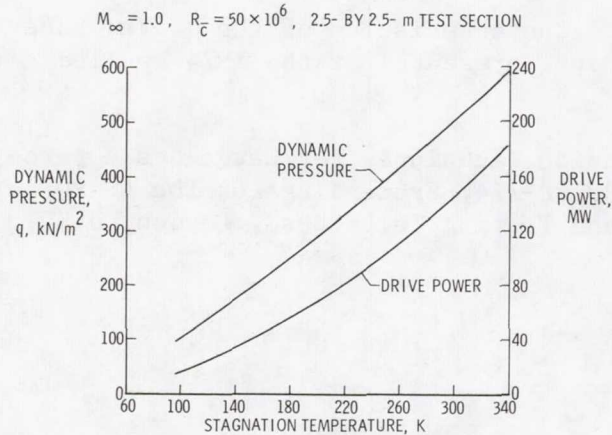
Figure 2. Effect of temperature reduction on dynamic pressure and drive power.

PERCENT CHANGE OF REYNOLDS NUMBER PER 1^{0}K CHANGE OF T_t

STAGNATION TEMPERATURE, T_t , K
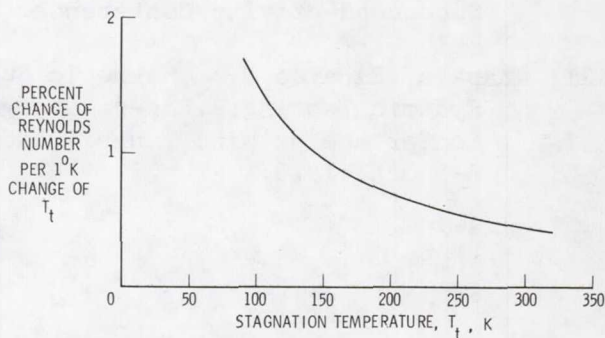
Figure 4. Change in Reynolds number per 1° change in stagnation temperature.
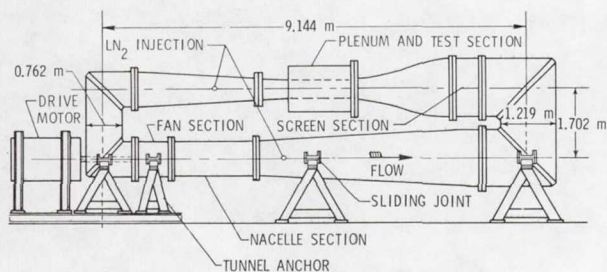
Figure 5. Layout of Langley
1/3-meter transonic
cryogenic tunnel.
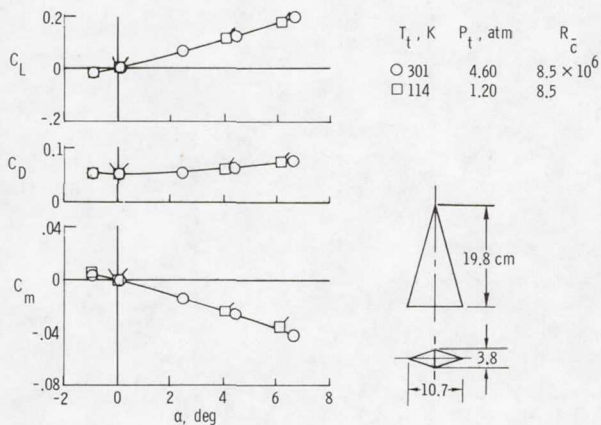
Figure 7. Static aerodynamic charac-
teristics of a delta-wing model at
ambient and cryogenic temperatures
as a function of angle of attack.
$M_\infty = 0.80$; $R_{\bar{c}} = 8.5 \times 10^6$.
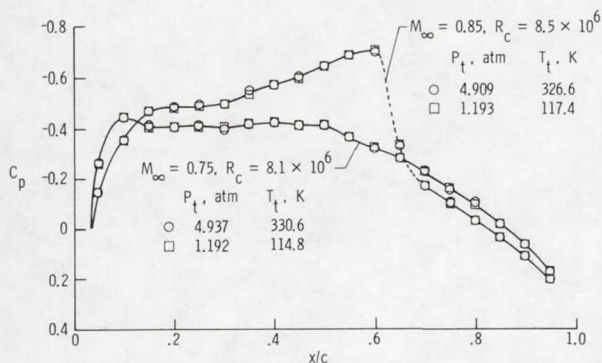
Figure 6. Comparison of the pressure
distributions for a symmetrical
two-dimensional airfoil obtained
at ambient and cryogenic conditions.
$\alpha = 0°$.
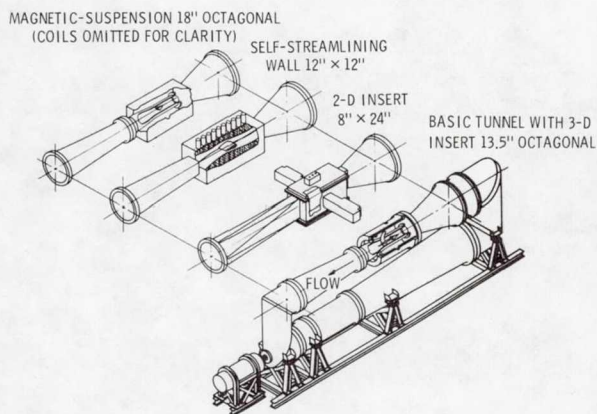
Figure 8. Interchangeable test sec-
tions of the Langley 1/3-meter
transonic cryogenic tunnel.

Page intentionally left blank

DESIGN CONSIDERATIONS OF THE NATIONAL

TRANSONIC FACILITY

Donald D. Baals
Joint Institute for Advancement of Flight Sciences
The George Washington University

SUMMARY

The current inability of existing wind tunnels to provide aerodynamic test data at transonic speeds and flight Reynolds numbers is an area of great technical concern. The proposed National Transonic Facility (NTF) is a high Reynolds number transonic wind tunnel designed to meet the research and development needs of NASA, DOD, industry, and the scientific community. The proposed facility will employ the cryogenic approach to achieve high transonic Reynolds numbers at acceptable model loads and tunnel power. By using temperature as a test variable, there is provided a unique capability to separate scale effects from model aeroelastic effects. The performance envelope of NTF is shown to provide a ten-fold increase in transonic Reynolds number capability ($R \approx 500 \times 10^6$/meter at $M=1$ in a 2.5 meter test section) compared to currently available facilities.

SYMBOLS

Values are given in both SI and U. S. Customary Units (latter in parentheses).

A	Cross-sectional area
$\bar{c}$	Wing mean chord
°F	Degrees Farenheit
hp	Horsepower
K	Kelvin
kW	Kilowatt
ℓ	Length
M	Mach number
p	Pressure

q	Dynamic pressure, $1/2\ \rho V^2$
R	Reynolds number $= \dfrac{\rho V \ell}{\mu}$
T	Temperature
V	Velocity
ρ	Density
μ	Viscosity

Notations and Subscripts:

bar	10^5 Newtons/m^2 (0.987 atmospheres)
L	Local
psf	Pounds per square foot
psia	Pounds per square inch absolute
t	Total
TS	Test section
∞	Free stream

INTRODUCTION

The historical aeronautical leadership of the United States in the development of high-speed aircraft - commercial as well as military - has been largely due to the excellent facilities used in the conduct of aeronautical research and development. In spite of this hallmark, during the last ten years it has become clearly apparent that better facilities are needed to simulate the complex aerodynamic phenomena occurring at speeds near the speed of sound. This urgent need for a new research and development facility has been recognized at all levels of NASA and DOD, by the U. S. aerospace industry, and by the scientific community. The sense of urgency has been increased by the current national thrust toward energy conservative aircraft and the importance of maintaining military preparedness in a world of turmoil.

HIGH REYNOLDS NUMBER FACILITY NEED

Transonic flows are found to embrace almost every aspect of flight — for aircraft (fig. 1) as well as space vehicles. The performance of the slowest of aircraft — the helicopter — is constrained by rotor "compressibility effects"

1584

on efficiency and noise, while commercial transports cruise at the "drag-rise" Mach number where shock waves first form on the wing. Modern military aircraft fight at altitude and penetrate on-the-deck at transonic speeds. The supersonic transport experiences its minimum thrust margin for acceleration near Mach 1. For space vehicles, the maximum dynamic pressure and buffeting occur during acceleration through the transonic speed regime, while critical transonic stability and control problems are encountered during reentry.

The area of great technical concern is the inability of existing wind tunnels to provide accurate design information for civil and military aircraft which must operate in the transonic flight regime near the speed of sound. The major transonic test deficiency has been Reynolds number simulation of full-scale flight. This deficiency has been dramatized during the past decade by unexpected problems in flight which have often required expensive redesign.

The wing is the most critical element. An appreciation of the complex nature of transonic flows can be gained from figure 2 where low Reynolds number flow over an airfoil is made visible by special methods (Schlieren system). Flow is from left to right. The subsonic flow ahead of the airfoil accelerates to supersonic speeds over the upper surface. At the base of the shock, the thin "boundary layer" of air adjacent to the surface thickens and separates from the airfoil creating a broad wake of fluctuating flow. These flow characteristics result in changes in lift and pitching moment, and increased drag and buffeting compared to the high Reynolds number flows characteristic of flight.

The shock wave pattern in the main field of flow is governed by the test Mach number — defined as the ratio of free-stream velocity to the speed of sound. The boundary-layer flow adjacent to the surface, however, is governed by a different parameter — "Reynolds number." If one tests a model at "full-scale" Reynolds number, the boundary layer characteristics will be similar, and the skin-friction drag will be the same as in flight. There are many wind tunnels in use that can test models at flight Mach numbers, however, there are none which can provide the transonic Reynolds number simulation of full-scale flight. In fact, the capability of present aircraft to fly near the speed of sound at low altitudes and the increased size of transport aircraft are such that the best transonic test facilities only provide about one-tenth of the required Reynolds number. The complex nature of the flow in the transonic region makes it impossible to analyze the performance or to extrapolate accurately from scale model tests obtained with current Reynolds number capability.

The transonic Reynolds number phenomenon of concern was first evidenced in flight tests of the USAF C-141 cargo aircraft about a decade ago (fig. 3). Correlation of the wing pressure coefficient measurements between wind tunnel and flight at high subsonic speeds demonstrated a significant difference in the chordwise location of the wing shock. Subsequent research at Langley (ref. 1) showed these results to be a Reynolds number phenomenon associated with the small scale of the wind-tunnel tests. At low test Reynolds numbers, the shock position is forward on the airfoil with a resultant increase in the separated region behind the shock and attendant increase in drag. As the test Reynolds number is increased, however, the shock wave moves rearward and the region of separated flow and attendant drag is reduced. Modifications to the C-141 were required to accommodate the air loads associated with flight conditions, and to

this day all C-141 aircraft carry approximately a one-percent payload penalty in added structural weight for the fix.

As transonic aircraft continue to grow in size, they place even greater demands on the wind tunnel. The problems that have been evidenced in today's transport development programs will become even more critical as the gap between wind tunnel and flight Reynolds number continues to widen as shown in figure 4. Current wind tunnels provide full-scale test capability for "DC-3" type aircraft only. As the speed and size of aircraft have increased, currently available facilities provide only about one-tenth full-scale cruise conditions for projected aircraft.

The lack of high Reynolds number experimental facilities has greatly slowed the progress of basic transonic research. Since basic research is the cornerstone upon which future advances are founded, a critical facility lack can seriously jeopardize aeronautical progress. The future of aeronautics will be based on the knowledge of the researcher and the quality of his facilities. Progress may come one small step at a time. But a one-percent improvement in ten different areas results in a 10-percent gain — which is significant by any standard. And occasionally these step advances in the hands of an enlightened scientist will coalesce into a technical breakthrough which can revolutionize the whole field of aeronautics. The "area-rule" concept for the design of transonic/supersonic aircraft and the "supercritical airfoil" developed within the U. S. merit such a classification. It is toward future advances such as these that a new high Reynolds number transonic facility is aimed.

EVOLUTION OF THE NATIONAL TRANSONIC FACILITY

During the past several years, there has emerged a clear national and international consensus of the priority need for a large, high Reynolds number transonic wind tunnel (ref. 2-4). It was recognized early that because of the projected very large construction costs, this must necessarily become a government sponsored facility. Many approaches to high Reynolds number have been explored and developed both in the United States and in Europe (ref. 5). A chronology of activities in the field of development of high Reynolds number ground-test facilities in the United States is presented in figure 5.

An important influence on the facility development program was the significant technology advance in a wind-tunnel concept employing cryogenic nitrogen to provide increased Reynolds numbers with modest drive horsepower and reduced model loads (ref. 6 and 7). The potential of low temperature operation to achieve high Reynolds numbers had been considered previously by Smelt of the Royal Aircraft Establishment in 1945 (ref. 8), but the concept was not pursued until an effort was initiated at the Langley Research Center in 1971.

From the Langley experimental efforts, details were worked out for a high Reynolds number transonic tunnel using extremely cold nitrogen to cool the flow and provide increased Reynolds numbers with reasonable drive power requirements and model loads. Figure 6 illustrates the effects of decreasing tunnel temperature on the tunnel test conditions. It will be noted that as the temperature

is decreased from a nominal value of 322 K (120°F) characteristic of conventional water-cooled tunnels, the Reynolds number of the flow increases approximately five-fold as the temperature approaches 89 K (-300°F). Further, this is accomplished with approximately a 50-percent reduction in drive power. This represents a ten-fold decrease in installed drive power compared to a conventional wind tunnel (322 K; 120°F) of the same size operating at the same Mach number and pressurized to provide the same test Reynolds number. This major reduction in installed drive power requirements makes possible the location of a continuous flow, high Reynolds number transonic tunnel at an existing research center having modest power resources.

Also noted in figure 6 is the fact that the increase in Reynolds number through a reduction in test temperature is accomplished without an increase in dynamic pressure which influences model loads. This is a significant benefit of cryogenic operation, for the range of high Reynolds number testing can be greatly expanded before encountering limiting structural loads on the model or excessive model distortion. The cryogenic tunnel concept provides the unique experimental capability of changing test Reynolds number without an attendant change in model loads (and therefore model shape). This is considered by many experimenters as a technical breakthrough in its own right.

Langley accelerated its cryogenic tunnel effort and extended the theoretical studies of "real gas" effects, developed a practical means for obtaining low temperatures, and constructed and operated two pilot cryogenic tunnels. The pilot facilities in a series of critical experiments validated the cryogenic concept for aerodynamic testing, demonstrated the attainment of uniform temperatures in the settling chamber, and provided useful experience relative to the operating problems of liquid nitrogen injection, research instrumentation, and cryogenic shell design (ref. 9 to 11).

NASA and USAF both developed firm plans for transonic facilities during 1973 and 1974. The Air Force had obtained Congressional approval in the FY 75 budget for an intermittent operation High Reynolds Number Tunnel (HIRT), and NASA had planned for a fan-driven cryogenic transonic research tunnel (TRT) to be included in the FY 76 budget. Both the NASA and USAF tunnel projects encountered the abrupt escalation of construction costs in 1974, causing the USAF to defer construction of HIRT and NASA to withhold TRT from its FY 76 budget request. DOD and NASA officials then agreed to undertake an additional joint study under cognizance of the Aeronautics and Astronautics Coordinating Board (AACB) to seek a common solution to transonic wind-tunnel needs. Accordingly, a special AACB Aeronautical Facilities Subpanel of NASA/DOD representatives was organized in November of 1974 to initiate this study.

The Subpanel in May of 1975 recommended that a single, continuous-flow facility employing the cryogenic concept should be built at the earliest possible date to serve the combined needs of both NASA and DOD (ref. 12). Recommendations for NTF performance characteristics were agreed upon (fig. 7). The Subpanel further recommended that the facility be located at the NASA Langley Research Center and be known as the National Transonic Facility (NTF). A memorandum of agreement accepting the AACB Subpanel recommendations was signed by NASA and DOD (June 2, 1975). It was emphasized in the Subpanel report that the NTF was to be a national facility with approximately 40 percent of the

occupancy projected for DOD work, 40 percent for NASA, 15 percent for proprietary aerospace industry work, and 5 percent for other government agencies and the scientific community. The Aeronautics Panel of the AACB would be charged with oversight responsibility.

The basic performance characteristics of the NTF follow the specific recommendations of the AACB Aeronautical Facilities Subpanel as summarized previously in figure 7.

DESCRIPTION OF THE NATIONAL TRANSONIC FACILITY

General Arrangement

The National Transonic Facility will be a conventional wind tunnel in appearance (fig. 8) and is described in detail in reference 13. The NTF will be a closed-circuit, fan-driven pressure tunnel capable of operating at pressures up to 9 bars (130 psia). It will have a slotted test section of 2.5 by 2.5 meters in cross section. The existing 4-Foot Supersonic Pressure Tunnel (4' SPT) drive motors and their drive control system will be utilized. The 4' SPT will be deactivated and the NTF constructed on its site. In addition to the existing drive motors which are rated at 52,220 kW (70,000 hp) for 10 minutes, an additional 44,760 kW (60,000 hp) motor will be added in line to provide the power required to drive the tunnel at maximum pressure and a test Mach number of 1.0.

The most unconventional feature of the NTF will be at its cryogenic operation. The tunnel will operate at temperatures from 353 K (175°F) down to 89 K (-300°F). Liquid nitrogen will be expanded into the circuit for the initial cool down and to absorb the heat rise associated with the gas compression by the fan. Pressure control will be provided through the controlled venting of the gaseous nitrogen through a large vent stack to assure mixing with air and eliminate any hazards which might result if cold gaseous nitrogen were allowed to accumulate at ground level. The current baseline design of the tunnel incorporates an internal insulation system which will be discussed in more detail subsequently.

Aerodynamic Circuit

As mentioned previously, the NTF will have a slotted test section 2.5 meters (8.2 ft.) square (fig. 9). To assure high-quality flow, a contraction from the stilling chamber to the test section of 15 to 1 in area is employed. Three anti-turbulence screens are located at the beginning of the contraction. A "quick" diffuser accommodates the large channel area increase to the stilling chamber and screens. This diffuser requires a flow resistance with accompanying pressure loss to assure the absence of flow separation. This loss was accepted as a trade-off against a large increase in cost of the pressure shell for a more efficient diffuser.

Test Section

The test section for the NTF (fig. 10) is designed similar to that of the existing Langley 8-Foot Transonic Pressure Tunnel which is known to be efficient and have good quality flow. The length of the slotted region is three test-section heights. The top and bottom walls, which are adjustable in divergence angle to compensate for boundary-layer growth, have six longitudinal slots in each wall. The side walls are fixed with two longitudinal slots in each wall. The design will allow the slot open width and edge shape to be easily modified. Adjustable and remotely controlled reentry flaps are provided at the downstream end of each slot. The position of these flaps during tunnel operation will be adjusted to control Mach number gradients through the test section and to minimize power consumption.

Complete models will be sting supported from a circular arc strut affording a total model pitch angle range of 24°. The sting will have a roll mechanism capable of rolling the model through 270°. Model pitch rate is controllable in either a continuous or pitch/pause mode at rates from 0° to 4° per second. Provisions for accommodating wall-mounted half-span models will be made for cases where larger model sizes are required.

Test Section Isolation System

Although the cryogenic approach using LN_2 has been shown to require the least capital investment and to be the most energy conservative approach to high Reynolds number testing, the cost per data point for high Reynolds number tests will be considerably higher than for current low Reynolds number data. Consequently, every step possible is being taken to conserve nitrogen, which is the largest single contributor to operating costs. One of the provisions made to conserve nitrogen is test-section isolation doors (fig. 11) which will be capable of isolating the test section such that the pressure can be reduced to atmospheric without venting the entire circuit. The test-section side walls can be lowered to insert work access tunnels from both sides which capture the test model and seal around the model sting to provide a "shirt-sleeve" environment for model change.

Drive System

The cryogenic concept requires that the drive system be capable of producing a constant compression ratio over a large temperature range. This requirement has a major impact on the design of the drive system in view of the direct relationship between fan performance and the stagnation temperature of the gas entering the fan. The desired performance in the NTF is obtained by using a single-stage fan with variable inlet guide vanes and fixed outlet stators in combination with a main drive system incorporating a two-speed gear box.

The electric motors in the drive are coupled through the gear box in a unique arrangement. The two existing motors are wound rotor induction motors and have a Kramer drive control system which accurately controls their rpm to within 1/4%. These motors are capable of 52,220 kW (70,000 hp) for 10 minutes

at 840 rpm (fig. 12). A reduction gear reduces the maximum fan speed to 600 rpm. To maximize the horsepower available, liquid rheostats are added to provide constant torque at rpm values down to 60% of the maximum speed. A low-speed gear is available which will permit a shift in rpm and allow full Kramer horsepower also to be available at 360 rpm. This rpm will be used largely for the cryogenic operation and the maximum pressure which are combined to produce the maximum Reynolds number. The horsepower required to drive the tunnel at M=1.0 for the maximum Reynolds number condition is more than is available from the existing motors, therefore an in-line 44,760 kW (60,000 hp) synchronous motor has been added to meet this need. The existing motors will be used to bring the synchronous motor up to speed. A maximum fan shaft power of 93,250 kW (125,000 hp) is available at a fan speed of 360 rpm. Under this condition, Mach number control is achieved by moving the position of the inlet guide vanes. The guide vanes are capable of controlling Mach numbers over a range between M=0.4 and M=1.2 with an acceptable level of efficiency.

Internal Insulation

The NTF will employ in its design an internal insulation to minimize the temperature excursions of the large pressure shell. In doing so, it (1) greatly reduces the liquid nitrogen required to approach steady-state operating conditions, (2) it minimizes the thermal stress in the pressure shell, thereby alleviating thermal fatigue and enhancing the service life of the pressure shell, and (3) it affords the opportunity to combine thermal insulation and acoustic attenuation functions into a system which could reduce the noise in the tunnel circuit. The baseline design of the insulation system (fig. 13) employs about 6 inches of fiberous insulation contained with close-woven glass cloth and covered with a corrugated flow liner which is supported by "tee" rings welded to the pressure shell and insulated from the liner. The "tee" rings are about 1.22m (4 ft.) apart. The liner is corrugated to absorb the circumferential thermal strain. Slip joints are provided for the longitudinal movement. Filler blocks are used under the corrugation to block flow from one insulation segment to the next. Considerations of insulation flammability, service life, and thermal performance under a high pressure and flowing cryogenic environment are the subject of an extensive verification test program.

NTF PERFORMANCE

Reynolds Number Test Capability

With the drive system described previously, the NTF performance at a selected Mach number can be presented as shown in figure 14. The operating map for Mach 1 shows the variation of chord Reynolds number as a function of stagnation pressure for various values of constant temperature. Similar plots can be made for other Mach numbers. The boundaries of the operating envelope are defined on the left by the maximum tunnel operating temperature (353°K; 175°F) and the compression ratio limit of the fan-drive system; on the upper left corner by the available drive power limit (93,250 kW; 125,000 hp); across the top by the maximum operating pressure (9 bar; 130 psia); and on the right by the

nitrogen condensation boundary (heavy dashed line). The latter boundary represents a limiting value of pressure and temperature where condensation of gaseous nitrogen will occur at a local Mach number of 1.4. Within the lower dark shaded region, the NTF can be operated with the variable-speed induction motors only in the high gear ratio. For pressures above the shaded region, the low gear ratio is required and the drive is operated at synchronous speed (360 rpm).

Inspection of figure 14 illustrates the unique test capability of a cryogenic tunnel. The dynamic pressure $(1/2\rho V^2)$ is independent of temperature and is a function only of stagnation pressure and Mach number. Thus for a given test Mach number, the dynamic pressure can be held constant while the temperature is varied to provide a controlled variation in Reynolds number. Such a test capability permits isolation of pure Reynolds number effects from aerodynamic loading changes which arise from unwanted model distortion under changing dynamic pressure. Conventional wind tunnels, which tend to operate at essentially constant temperature, follow along a single temperature line requiring a change in pressure to produce a change in Reynolds number. This unique capability of cryogenic tunnels opens a new dimension in wind-tunnel testing and may well become the single most important capability of this facility concept. It should also be noted that pure model aeroelastic effects can be evaluated by holding Reynolds number constant while the pressure is varied (moving vertically on the plot).

Maximum Performance Envelope

The maximum test Reynolds number usually occurs where the nitrogen condensation boundary intersects the shell pressure limit. The maximum Reynolds number is plotted as a function of Mach number in figure 15. This overall maximum tunnel Reynolds number capability is bounded by the shell operating pressure limit for Mach numbers up to 1.0. Between M=1.0 and 1.2, the performance is limited by the maximum horsepower available. Above M=1.2 the fan maximum compression ratio limits the performance. Note that the goal of a Reynolds number of 120×10^6 for M=1.0 is achieved. At the bottom of figure 15 is an overall envelope of the Reynolds number capability of wind tunnels in the United States. The NTF will be capable of increasing ground-test Reynolds number by about one order of magnitude over currently existing facilities.

Model Loads

A critical design problem of NTF is associated with the large model loads encountered in the operation of the facility at maximum performance conditions. The model stress is related to the level of test dynamic pressure $(1/2\rho V^2)$, which is a function of stagnation pressure and Mach number but independent of temperature. In figure 15, lines of constant dynamic pressure are superimposed on the overall performance map of the tunnel. Most current large transonic wind tunnels operate at dynamic pressure levels up to about 0.5 bar (approx. 1000 psf). There are a few tunnels which have dynamic pressure capability up to about 1 bar (approx. 2000 psf). The NTF will have a maximum dynamic pressure capability of 3.3 bar (approx. 7000 psf). Although the NTF, by virtue of employing the cryogenic approach, will have a much lower ratio of dynamic

pressure to Reynolds number as compared to the other approaches to high Reynolds number testing, it can still produce model loads up to three times those experienced in existing wind tunnels. Technology appears to be in hand to accommodate these loads. However, force measuring balances, sting deflections, and model deformation will tend to take on more importance as the NTF is utilized to its maximum Reynolds number capability.

Productivity

The NTF is being designed to satisfy a national need for high Reynolds number test capability at transonic speeds. Moreover, as a national facility it must accommodate the projected workload of NASA, the DOD, the aero industry and the scientific community. As a consequence of this, as well as the need to conserve energy, the NTF is being designed to produce data at a relatively high rate. Typical existing wind tunnels produce data at about 26,000 specific sets of test conditions in a year, where a set of test conditions is defined by a combination of Mach number, Reynolds number, angle of attack, angle of yaw, and so forth. The NTF is targeted to produce measurements at the rate of 104,000 sets of test conditions per year, or four times the conventional rate. To achieve this goal, the tunnel control and data acquisition system is highly automated. Computer control is used extensively to insure optimum procedures and safety in the tunnel operation. A modern data acquisition system will be provided with "quick look" data capability to minimize retesting due to improper measurements.

Full-Scale Flight Simulation

The test Reynolds number capability of NTF in meeting projected requirements of advanced aircraft is summarized in figure 16 for civil aircraft. It will be noted that for large subsonic transports of the B-747 category, the NTF will attain full-scale test conditions for the cruise point (solid circle) as well as for the high-speed, "max. q" load condition. The high Reynolds number peak at M=0.5 cannot be met by the design NTF performance envelope. This is not considered a significant deficiency, however, for the Reynolds number effects for fully subsonic flows at low angles of attack are usually small and predictable at high Reynolds number levels. For the advanced "span loader" transport ($\bar{c}$=16.8m; 55 ft.) in the one million kg (2.2 million lbs.) category, the NTF can attain full-scale test conditions for the cruise point. The high-speed "max. q" load condition, however, can only be met by use of a side-wall mounted, semispan model. This is an accepted test procedure for high aspect-ratio configurations.

For the large supersonic transport (341,000 kg; 750,000 lbs.), full-scale test conditions can be attained for the subsonic cruise point (M=0.95) and for the major portion of the transonic climb and let-down corridor. The high Reynolds number peaks in the M=0.5 range can largely be met in NTF by the use of larger-size models permitted for purely subsonic testing. For the space shuttle type configurations, the NTF will attain full-scale test conditions for all subsonic/transonic flight conditions.

NTF OPERATING PLAN AND SCHEDULE

Although the NTF is being designed and constructed by NASA and is en-
visioned to be operated by NASA, it is, in fact, a national aeronautical re-
source. As such, it will be managed in a manner which will effectively serve
the aeronautical research and aircraft development needs of the government,
industry, and scientific organizations. The facility will be staffed to the
level required to support the needs of the varied users. Current organization-
al plans provide for NTF oversight responsibility to be assigned to the NASA-
DOD Aeronautics and Astronautics Coordinating Board (AACB).

The final design of the NTF is underway. Funding is programmed for
initial appropriation in the FY 1977 budget. Construction is scheduled to
begin in October 1976 and to be complete at the end of 1980. Checkout and
calibration is to be completed in July 1981, at which point the facility should
be ready for use as a research and development tool. The total project budget
is 65 million dollars including contingency and escalation.

CONCLUDING REMARKS

Plans are underway to provide this nation with a new high Reynolds number
transonic wind tunnel designated the National Transonic Facility. This facili-
ty is designed to satisfy the combined testing requirements of NASA, DOD, the
aeronautical industry, and the scientific community. Gaseous nitrogen at cryo-
genic temperatures will be used as the test medium to provide high Reynolds
numbers at transonic speeds. The NTF will provide a ten-fold increase in
transonic Reynolds number test capability as compared to existing U. S. facili-
ties and will permit testing current and projected aircraft at or very near
full-scale flight conditions. A unique research capability inherent in the
cryogenic approach provides for valid separation of the effects of model aero-
elasticity, Reynolds number, and Mach number on aircraft configuration perfor-
mance. The NTF will be located at the NASA Langley Research Center and is pro-
jected to be operational in 1981.

REFERENCES

1. Loving, Donald L.: Wind Tunnel-Flight Correlation of Shock-Induced Separated Flow. NASA TN D-3580, 1966.

2. Heppe, R. O.; O'Laughlin, B. D., and Celniker, L.: New Aeronautical Facilities - We Need Them Now. Astronautics and Aeronautics, vol. 6, no. 2, March 1968, pp. 42-54.

3. Large Wind-Tunnel Working Group: The Need for Large Wind Tunnels in Europe. AGARD-AR-60, December 1972.

4. Whitfield, J. D.: Ground Testing and Simulation - An Overview. Part I. Astronautics and Aeronautics, vol. 12, no. 6, June 1974, pp. 54-55.

5. Baals, Donald D. and Stokes, George M.: A Facility Concept for High Reynolds Number Testing at Transonic Speeds. Facilities and Techniques for Aerodynamic Testing at Transonic Speeds and High Reynolds Number. AGARD CP no. 83, August 1971, pp. 28-1 to 28-12.

6. Goodyer, M. J. and Kilgore, R. A.: High Reynolds Number Cryogenic Wind Tunnel. Paper No. 72-995, presented at the AIAA Seventh Aeronautics Testing Conference, Palo Alto, CA, September 3-5, 1972, AIAA Journal, vol. 11, no. 5, May 1973, pp. 613-619.

7. Kilgore, R. A.; Goodyer, M. J.; Adcock, J. B.; and Davenport, E. E.: The Cryogenic Wind-Tunnel Concept for High Reynolds Number Testing. NASA TN D-7762, November 1974.

8. Smelt, R.: Power Economy in High-Speed Wind Tunnels by Choice of Working Fluid and Temperature. Report Aero. 2081, Royal Aircraft Establishment, Farnborough, England, August 1945.

9. Polhamus, E. C.; Kilgore, R. A.; Adcock, J. B.; and Ray, E. J.: The Langley Cryogenic High Reynolds Number Wind-Tunnel Program. Astronautics and Aeronautics, vol. 12, no. 10, October 1974.

10. Adcock, J. B.; Kilgore, R. A.; and Ray, E. J.: Cryogenic Nitrogen as a Transonic Wind-Tunnel Test Gas. AIAA Paper No. 75-143, 1975.

11. Hall, Robert M.: Further Study of the Minimum Temperatures for Valid Testing in a Cryogenic Wind Tunnel. NASA TM X-72924, 1976.

12. National Transonic Facility. Report of the National Aeronautical Facilities Subpanel to the Aeronautics Panel, AACB, May 1975.

13. McKinney, Linwood W.; Howell, Robert H.: The Characteristics of the Planned National Transonic Facility. Presented at the AIAA Ninth Aerodynamic Testing Conference, Arlington, TX, June 7-9, 1976.
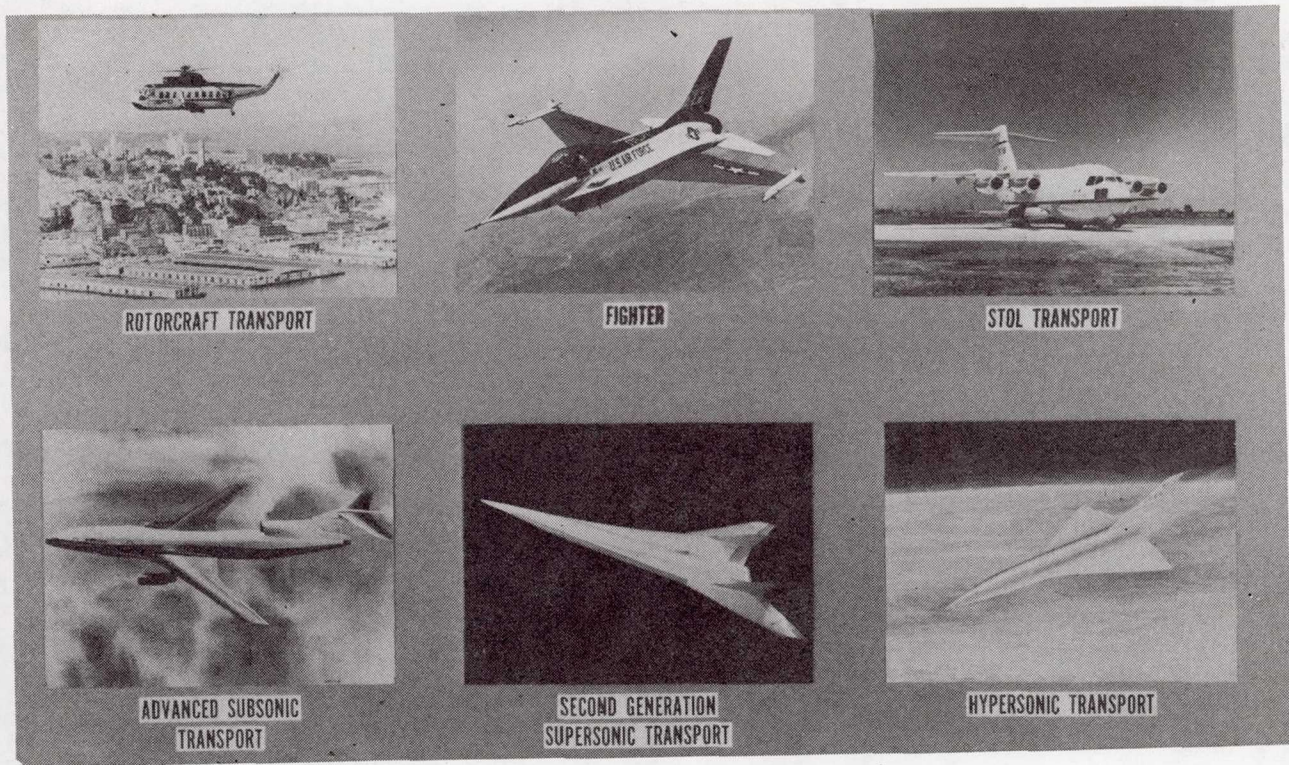
Figure 1.- Transonic flows affect all aircraft.
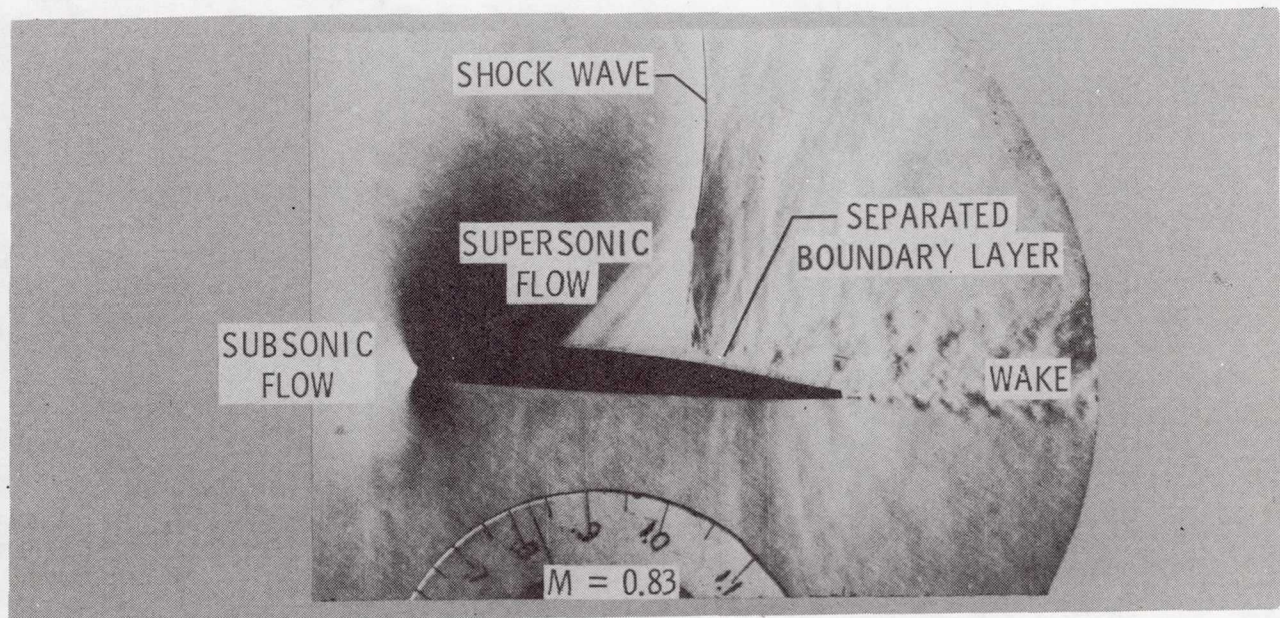
Figure 2.- Schlieren photograph of complex transonic flow over 2-D airfoil.
M = 0.83.

FLIGHT
HIGH REYNOLDS NUMBER

SHOCK

LOCAL PRESSURE
COEFFICIENT

WIND TUNNEL
LOW REYNOLDS NUMBER

SHOCK

CHORDWISE LOCATION, PERCENT
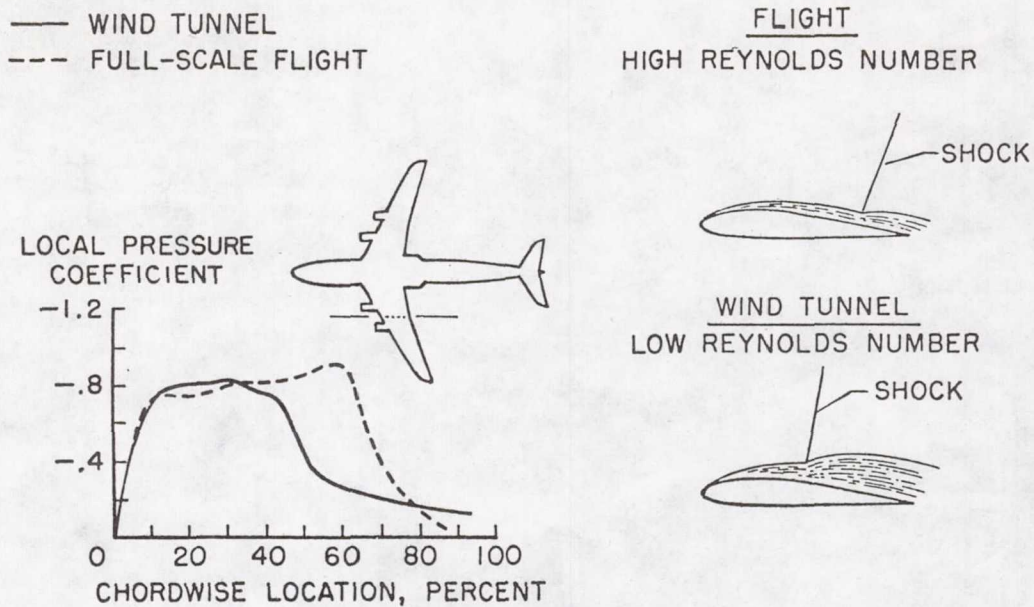
Figure 3.- Effects of shock induced flow separation over wing of
transport aircraft. M = 0.85.

CHORD
REYNOLDS
NUMBER
AT
CRUISE

● PAST
■ FUTURE

C-XX

C-X

C-5   747
C-141   707

ELECTRA

DC-3   DC-6

EXISTING WIND TUNNELS

MACH NUMBER
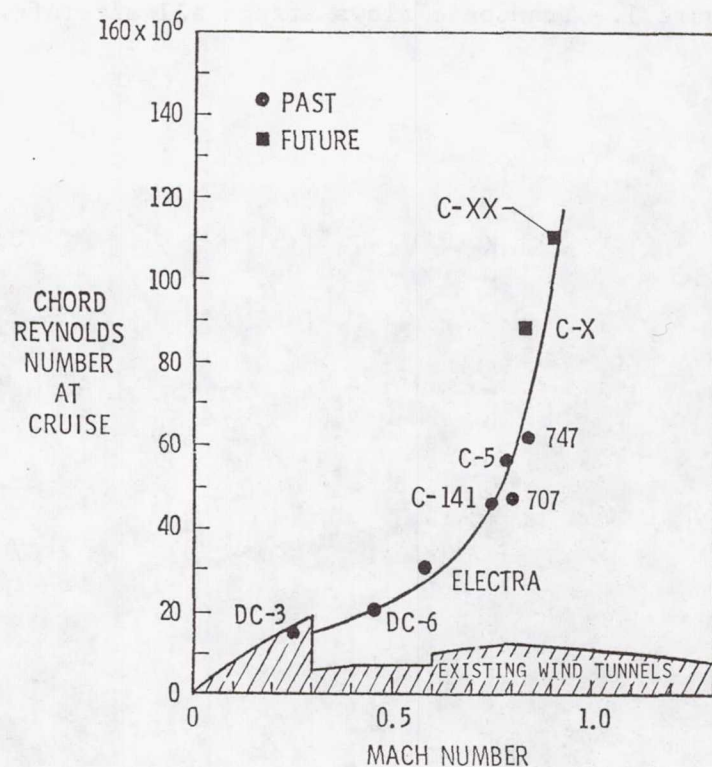
Figure 4.- Illustration of the growing facility gap in test
Reynolds number capability.

DATE	FACILITY	STATUS
1967	8 X 10 FT. LUDWIEG TUBE (HIRT)	PROPOSAL
1969	.078 SCALE HIRT	PILOT MODEL
1969	32-INCH LUDWIEG TUBE	OPERATIONAL AT MSFC (32"DIA.)
1970	HYDRAULIC DRIVE TUNNEL	A/E STUDY (6 X 6 METER)
1971	BLOWDOWN TUNNEL	600 & 3000 PSI TANK FARM
1972	INJECTOR TUNNEL	600 & 3000 PSI PILOT TUNNEL
1972/73	CRYOGENIC TUNNEL	LOW SPEED MODEL PILOT TRANSONIC MODEL
1974	HIRT	PRELIMINARY ENGINEERING REPORT
1974	TRANSONIC RESEARCH TUNNEL	PRELIMINARY ENGINEERING REPORT

Figure 5.- Chronology of high Reynolds number facility concepts and pilot tunnel development within the United States.

GAS PROPERTIES

TEST CONDITIONS AND DRIVE POWER

VALUES RELATIVE TO 322K
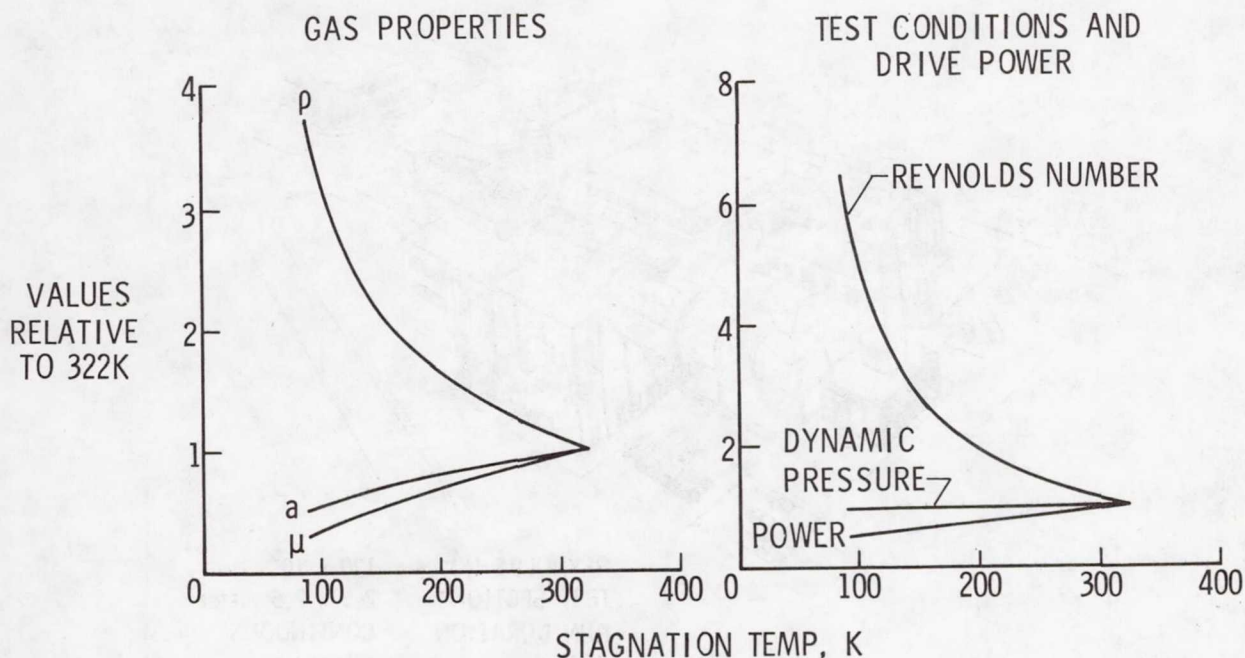
STAGNATION TEMP, K

Figure 6.- Effect of temperature reduction on test conditions and drive power. $M_\infty = 1$; constant stagnation pressure.

1597

- A SINGLE TRANSONIC TEST FACILITY IDENTIFIED AS THE NATIONAL TRANSONIC FACILITY (NTF)

- CRYOGENIC CONCEPT

- NTF HAVE THE FOLLOWING LEADING CHARACTERISTICS:

TEST SECTION SIZE	2.5 METERS SQUARE
DESIGN PRESSURE	130 PSIA OR $\approx$ 9 BAR
DESIGN MACH NUMBER RANGE	0.2 - 1.2
STREAM FLUID	NITROGEN
PRODUCTIVITY/EFFICIENCY	8,000 POLARS/YR
REYNOLDS NUMBER[1]	120×10^6 (M = 1)

- NTF BE LOCATED AT LANGLEY RESEARCH CENTER

[1]BASED ON $\bar{c}$ = 0.25 METER (0.82 FEET)

Figure 7.- Summary of AACB Subpanel recommendations relative to NTF.

REYNOLDS NO.	120×10^6
TEST SECTION	2.5 x 2.5 meter
RUN DURATION	CONTINUOUS
COST	$65 Mil
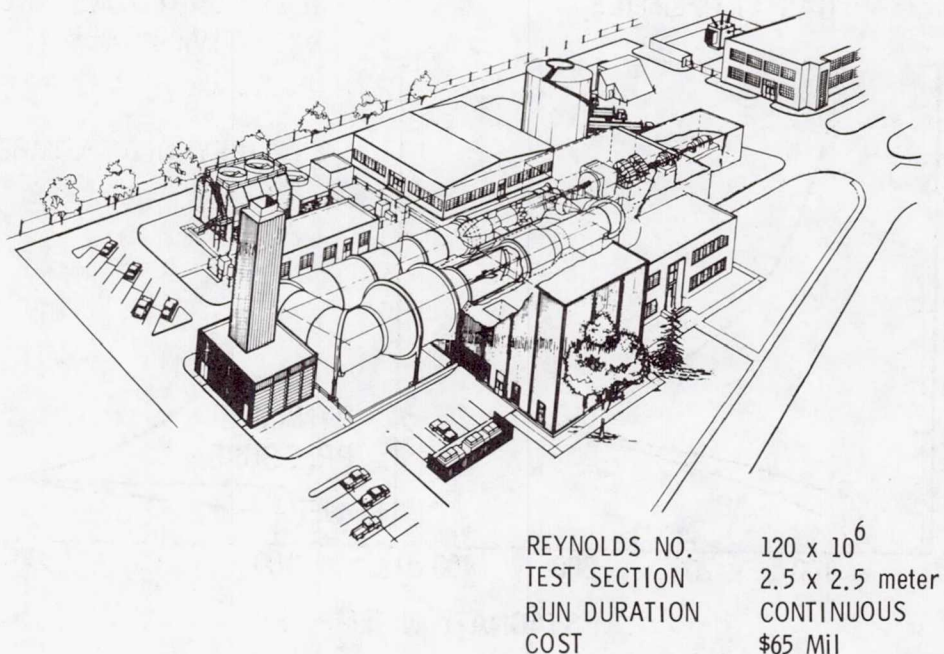
Figure 8.- The planned National Transonic Facility.
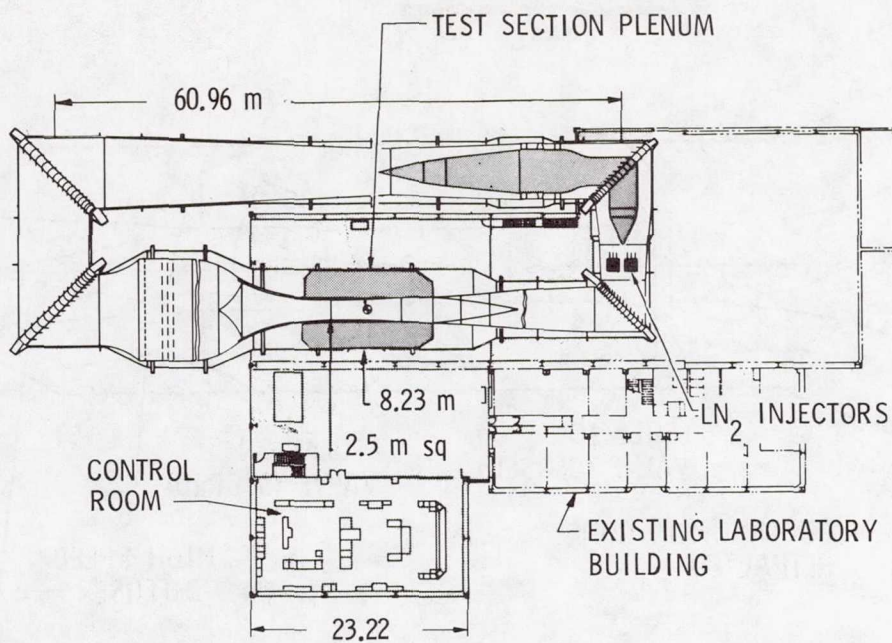
Figure 9.- Plan view of the facility.
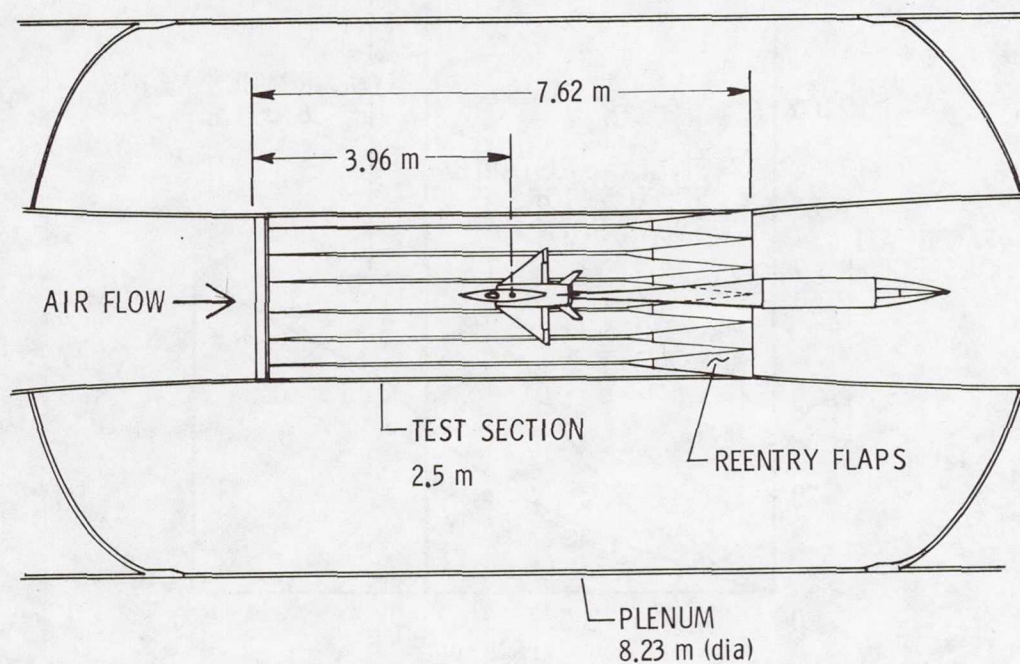
Figure 10.- Baseline slotted wall and model support system.
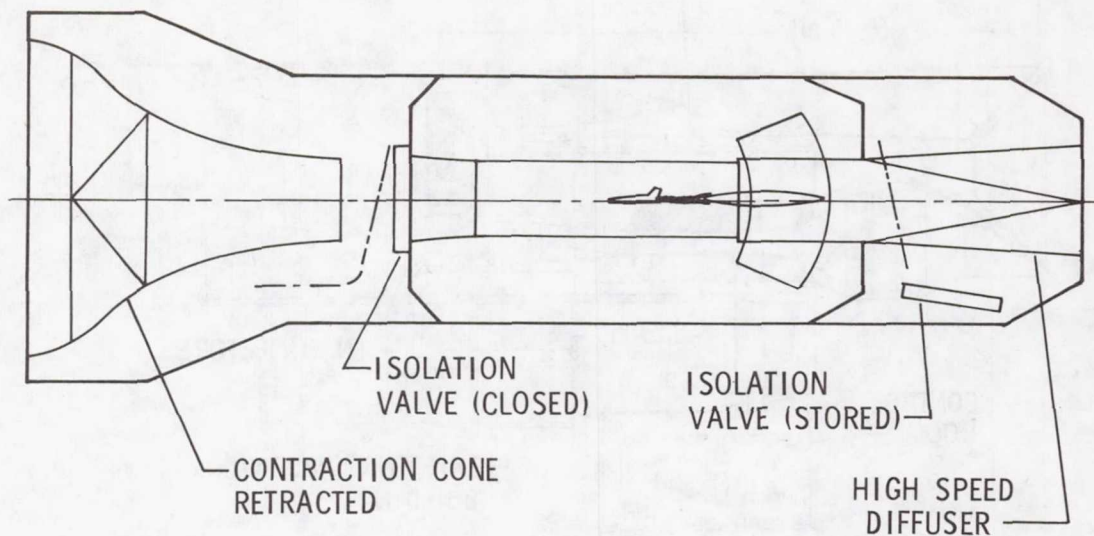
Figure 11.- Test section isolation system.
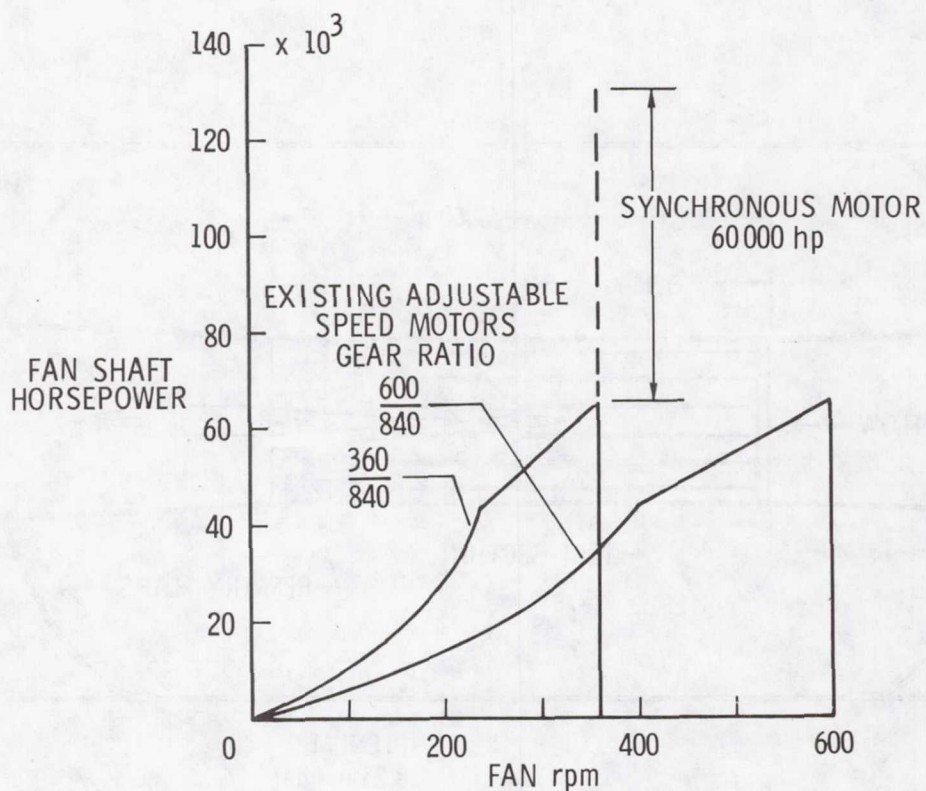
Figure 12.- Available fan drive power (10-minute rating).

CORRUGATED ALUMINUM LINER

THERMAL ISOLATOR

FIBROUS INSULATION

(END VIEW)

9% NICKEL STEEL SHELL
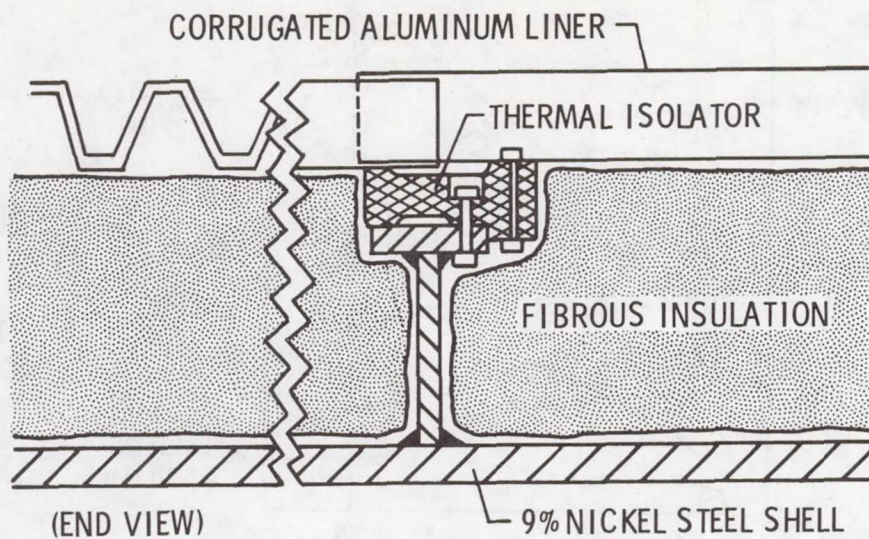
Figure 13.- Internal insulation and liner concept.
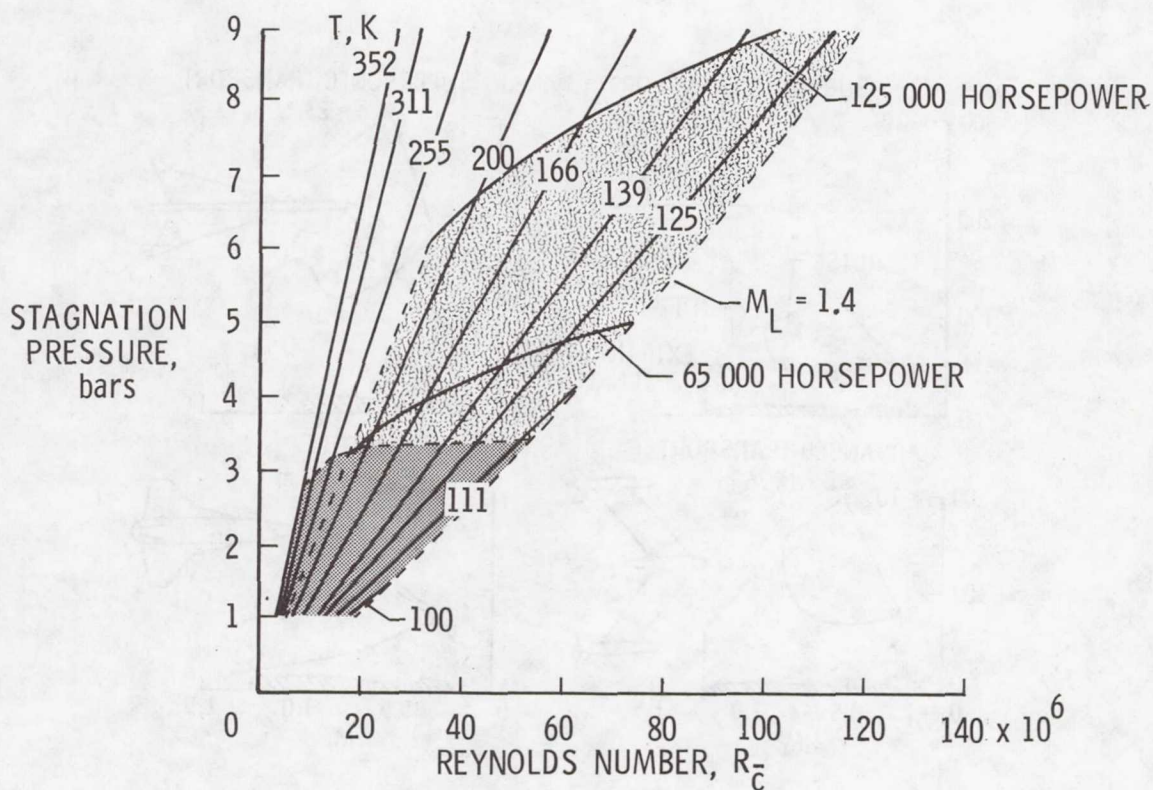
Figure 14.- NTF operating envelope at M_∞ = 1.   ($\bar{c}$ = 0.25 m).
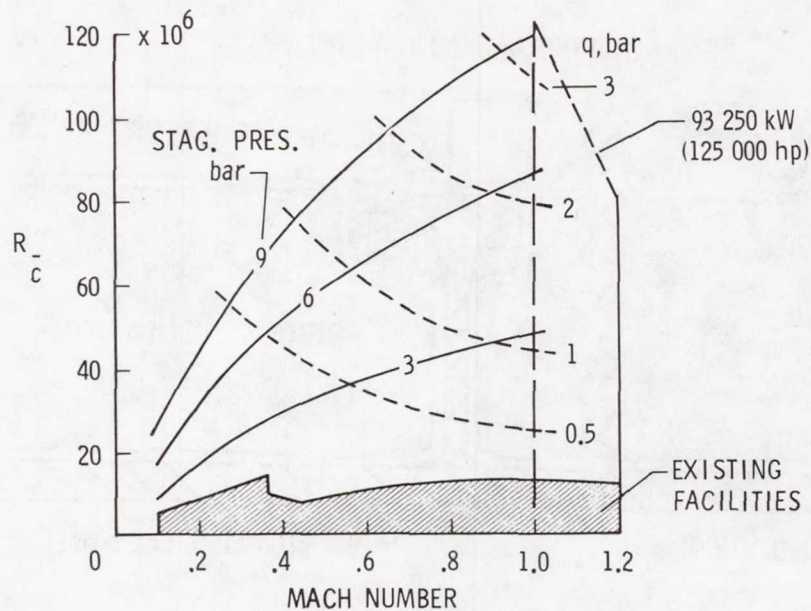
Figure 15.- Maximum Reynolds number operating envelope.
($\bar{c}$ = 0.25 m).
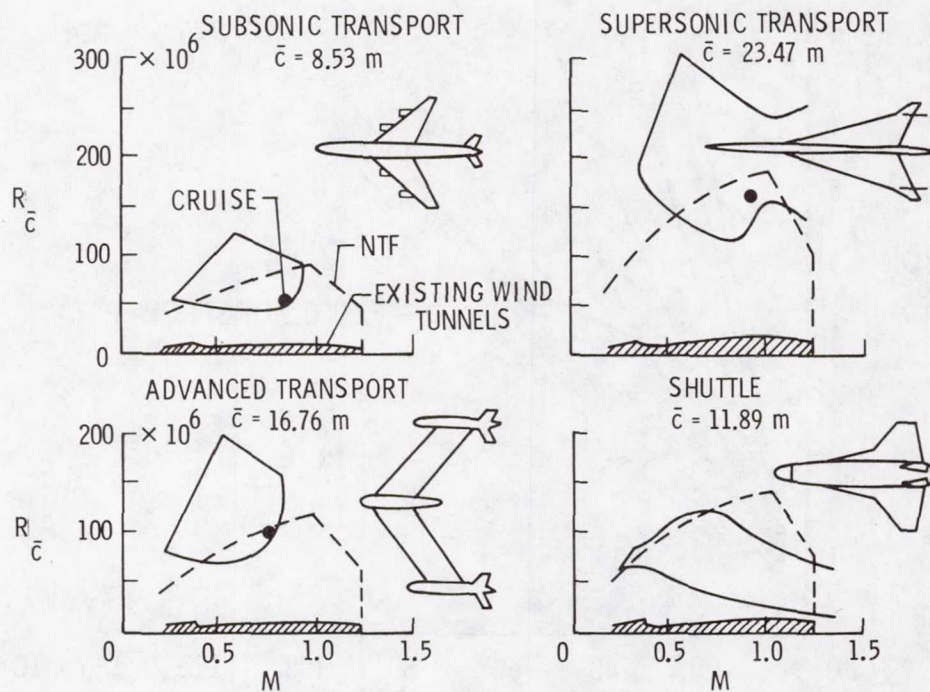
Figure 16.- Comparison of typical flight Reynolds number requirements
with NTF capability for various civil aircraft.

AERODYNAMIC MEASUREMENT TECHNIQUES

USING LASERS

William W. Hunter, Jr.
NASA Langley Research Center

SUMMARY

Laser characteristics of intensity, monochromatic, spatial coherence, and temporal coherence have served to advance the development of laser-based diagnostic techniques for aerodynamic related research. Considering two broad categories of visualization and optical measurements, three techniques have received significant attention. These are holography, laser velocimetry, and Raman scattering. Examples of the quantitative laser velocimeter and Raman scattering measurements of velocity, temperature, and density indicates the potential of these nonintrusive techniques. A continued vigorous effort in the development of laser-based diagnostic techniques is expected.

INTRODUCTION

It would be presumptuous to present this paper as a definitive survey of techniques which utilize lasers for aerodynamic research diagnostics. A fairly complete literature search of this subject field and related areas, such as fluid dynamics, reveals over 600 published references covering an approximate period of 6 years. The limited length of this paper restricts the scope and could not possibly cover all aspects presented in such a volume of references.

Therefore, the purpose of this paper is to briefly note various diagnostic techniques using lasers which have been used for or are suitable for application to aerodynamic related research. Examples of important diagnostic techniques, laser velocimetry and Raman scattering, will be given. Also near term future developments related to these examples will be noted.

IMPORTANT LASER CHARACTERISTICS

Light Amplification by Stimulated Emission of Radiation or LASER devices have properties that provide a significant opportunity to improve or develop new diagnostic techniques for aerodynamic testing. One of the most noted properties is the ability to achieve high-intensity radiation levels. It is common to think of achieving laser radiation power levels in terms of watts with continuous wave systems and peak powers in megawatts with very short (nanoseconds) pulsed systems.

The high power property alone is not sufficient to describe the uniqueness of the laser. Lasers are monochromatic sources of radiation. That is, the laser is capable of containing its energy in several or even one narrow band of radiation. The monochromatic property coupled with the power levels routinely achieved is essential to diagnostic techniques that depend on radiation scattering and absorption processes.

Spatial and temporal coherence are important laser properties. For example, application of lasers to interferometry relieves the problem of having to closely match relative path differences to obtain good fringe contrast because of its temporal or long coherence length. The laser is also a large aperture point source because of its spatial coherence, or uniform phase front, property thereby achieving greater radiation levels than could be achieved with conventional interferometer point sources.

Properties of intensity, monochromatic, spatial coherence, and temporal coherence plus reliable and ready availability of practical laser systems with a wide range of operating frequencies have made the laser an important research tool as well as an object of research interest. The laser has provided a needed stimulus to the research and development of flow-field diagnostic techniques in the areas of fluid dynamics and aerodynamics.

DIAGNOSTIC TECHNIQUES USING LASERS

For convenience of this discussion, the diagnostic techniques that utilize lasers are divided into two broad groups. The first group consists of those techniques of visualization which provide qualitative and, in some cases, quantitative information. Second grouping is optical measurement techniques which are nonintrusive or probeless methods which provide quantitative information.

Included in the visualization grouping are a variety of photography, shadowgraph, holography, and Schlieren techniques. Holography has been the major benefactor of the development of laser sources.

The advantage of a laser source for direct photography is gained from the combination of intense short pulse and monochromatic radiation burst. Combined, these properties permit stop action photography of tests in which narrow band optical filters can be used to filter out unwanted background or object radiation. Such test conditions are often found in ballistic range and shock tube tests of hypersonic aerodynamic models (refs. 1 and 2).

The techniques which depend on refractive index gradients, shadowgraph and Schlieren, benefit chiefly from the same laser properties as photography. Some differences in the normal physical set-up are required because of the use of a source that produces parallel, monochromatic and coherent light. These differences are discussed in reference 3.

As noted previously, the holography technique has been a major benefactor of laser devices. This occurred because of the basic need for the laser coherence properties. Fundamentally, the holographic process is a recording

of wavefront information including amplitude and phase. Phase information is obtained through interferometric techniques. Holography is an attractive process since it can record three-dimensional spatial information on film and this information can be retrieved at a later time at the experimenter's leisure. Holography has been used in aerodynamic testing for visualization, to ascertain particle content in a flow field, to study particle interaction with model-generated shock waves, and for obtaining quantitative density information on flow fields about aerodynamic models (refs. 4 and 5).

Laser optical measurement techniques for aerodynamic testing have received considerable attention in laboratories involved in aerodynamic and related research. The reason for this interest in optical measurement techniques is several fold. First, remote optical techniques do not disturb the local flow field such as occurs with intrusive probe techniques. Second, most optical techniques determine basic individual gas parameters, e.g., number density, temperature, velocity and specie concentration, as opposed to probe measurements which are usually dependent on more than one basic parameter.

Many of the optical techniques depend on absorption, fluorescence or some type of scattering process; Rayliegh, Raman, Mie, etc. Of all of the optical techniques, most attention at this time is being directed toward the laser anemometer technique (refs. 6 and 7) which can provide velocity vector flow field measurements about aerodynamic models or any other general flow field of interest. This technique is dependent on Mie scattering from small particulates imbedded in the flow field. The ultimate limitation of this measurement process is the fidelity of the particle motion with respect to the local flow field. Analytical and experimental work has been performed (refs. 8 and 9) and it is generally accepted that in many flow fields of interest significant experimental information can be obtained before particle motion fidelity becomes a significant limiting factor.

Another optical technique receiving significant interest is the Raman scattering process (refs. 10, 11, and 12). The process provides local point measurements of the species concentration and temperature. This technique has found considerable interest in the study of engine combustion processes and engine exhaust characteristics. Also, Raman scattering has a place in aerodynamic testing, especially those found in supersonic and high enthalpy facilities.

As can be seen from the limited discussion and references cited above, a number of laser visualization and optical techniques have been investigated and used as aerodynamic testing diagnostic techniques. All of this activity has been stimulated by the development of laser devices as practical and reliable tools and the need for new and improved aerodynamic research diagnostic techniques.

EXAMPLES OF DIAGNOSTIC TECHNIQUES
USING LASERS

Numerous examples of the laser diagnostics techniques previously discussed can be found in any number of journals, conferences, and special symposiums reports. For purposes of illustration, several examples of the laser velocimeter and Raman scattering techniques are included in this discussion. These two diagnostic techniques were chosen because they are representative of the state of the art and indicate the quantitative data that can be obtained.

Recently, the velocity flow field above a stalled model wing was surveyed with a laser velocimeter. These tests were conducted in the Langley 7- by 10-foot high-speed wind tunnel by Mr. J. F. Meyers, NASA Langley Research Center, and Dr. W. H. Young, U.S. Army Air Mobility R&D Lab., Langley Research Center. The tests were conducted with a NACA 0012 airfoil at a 0.49 Mach number. Before describing the results of these tests, it is worthwhile to note the fundamental simplicity of the technique. This is best shown by the basic equation

$$V_i = f_D \left(\frac{\lambda}{2 \sin \theta/2} \right) \tag{1}$$

where the bracketed term describes the fringe spacing formed by crossing two laser beams of wavelength, λ, at an angle, θ. The quantities λ and θ are determined by the experimental system. As a particle crosses the fringes, scattered (Mie) radiation is detected by a photodetector and with suitable electronic processing equipment the detected signal frequency, f_D, or Doppler frequency, is measured and the resultant velocity component, V_i, is determined through equation (1).

The system used in these tests measured two velocity components u and v. Figure 1 shows the wing installation and the laser beams in the tunnel test section. In these tests velocities were measured at 178 points in the plane of the wing center span. Data are collected in histogram form and consisted typically of 200 to 1000 individual measurements or Mie scattering events. A composite of the measure flow field velocity vectors is shown in figure 1 and represents a quantitative flow field pattern above the wing. A typical set of histograms for a number of points along a normal to the wing is shown in figure 2. From these histograms the mean values are calculated.

The laser velocimeter velocity measurement capability is complemented by the measurements of density and temperature by the Raman scattering process. The inelastic light-scattering Raman process and its potential as a flow diagnostic technique has been noted by a number of authors (refs. 10, 11, and 12).

Basically, frequency shift of the scattered radiation is dependent on the scattering molecular rotational and vibrational energy states and the intensity of the scattered radiation is dependent on the population density of these states. That is the intensity and intensity variations in the scattered radiation spectrum can be directly related to the gas molecular density

and temperature. The static temperature can be determined by ratioing the intensities of two pure rotational Raman transitions. The relationship for temperature, T, is given by

$$T = A/\ln(R/B)$$

where A and B are constants which are determined by the specified transitions used and R is the intensity ratio. Selection of the transitions used in the ratio, R, is determined by the constituents in the gas mixture and the temperature range of interest.

The example chosen to illustrate the Raman diagnostic techniques is a series of measurements conducted in a Mach 5 free jet test facility (ref. 13). A schematic of the test set-up is shown in figure 3, and the results of several density and temperature measurements are shown in figure 4. These tests were conducted in an air flow field about a flat plate set at various angles of attack, α. Temperature measurements were made by ratioing (6,4) anti-Stokes to the (1,3) Stokes rotational transitions of nitrogen. Density measurements were also obtained by intensity measurements of the (6,4) transition. Density measurements require prior calibration to account for instrumentation factors whereas the temperature measurements based on the ratio procedure do not.

The preceding examples illustrate the types of laser optical measurement techniques that are being used in most of the major laboratories involved in aerodynamic research and development. The near term future also offers several very interesting variants of the laser velocimeter and Raman methods.

A logical step is to combine the laser velocimeter and Raman techniques to achieve essentially simultaneous point velocity, temperature, and density measurements in the flow field about a model. Several experiments have been conducted, references 14 and 15, which demonstrate the feasibility of this approach. Such a system will significantly add to a research facility capability. The near term future also promises much more compact laser-optic systems. Development of reliable laser diodes which deliver 5 milliwatts in the continuous wave mode and 10 watts peak power in the pulse mode (≈ 50 nanoseconds) have been obtained. Potential application of the laser diode for aerodynamic testing is illustrated in figure 5. That is, where there are very confined regions or regions too close to surfaces which may not be accessible to external laser velocimeter systems, then a compact laser diode velocimeter package may be used.

CONCLUDING REMARKS

Development of laser devices whose unique radiation properties of high intensity, monochromatic, spatial coherence, and temporal coherence has provided significant impetus to the advancement of diagnostic techniques for use in aerodynamic testing. Of all the techniques using lasers, two have received

significant attention and effort in the past 6 or 7 years. These are the holography and the laser velocimeter methods. Certainly the ability to visualize the local flow field about a model, such as can be obtained with holography, always provides the aerodynamicist significant insight into the interaction of model and the field. But quantitative information is necessary for the full understanding of the model-field interaction. The laser velocimeter provides quantitative velocity information and, as was illustrated, can provide a quantitative flow field pattern. This pattern provides a form of visualization in terms of velocity field characteristics rather than in terms of density field characteristics as provided by holography.

Laser Raman scattering would probably rank after laser velocimetry and holography in term of attention and effort in the past 6 or 7 years. The physics of this technique is well understood and its potential as a flow field diagnostic technique is being exploited. The ability to obtain simultaneous velocity, density, and temperature at a point when combined with velocimeter technique makes this an extremely useful diagnostic technique.

A continued and increasing use of remote nonintrusive laser-based measurement techniques for aerodynamic research diagnostics is expected. This expectation is based on the apparent advantages of the techniques demonstrated and continued development and improvement of laser devices

REFERENCES

1. Hendrix, R. E.; and Dugger, P. H.: Instrumentation for an Aeroballistic Range Ablation Test Facility. International Congress on Instrumentation in Aerospace Simulation Facilities 1973 Record, 1973, pp. 45-50.

2. Barber, J. P.; and Taylor, H. R.: High Speed Laser Photographic Techniques for Hypersonic Erosion Studies. International Congress on Instrumentation in Aerospace Simulation Facilities 1975 Record, 1975, pp. 100-107.

3. Oppenheim, A. K.; Urtiew, P. A.; and Weinberg, F. J.: On the Use of Laser Light Sources in Schlieren-Interferometer Systems. Proceedings of the Royal Society, Series A, Vol. 291, April 5, 1966, pp. 279-290.

4. Matulka, R. D.: Application of Laser Optics to Aeronautical Engineering. AGARD-AG-195, North Atlantic Treaty Organization, Advisory Group for Aerospace Research and Development, December 1974, pp. 12/1-12/23.

5. Hannah, B. W.; and Havener, A. G.: Application of Automated Holographic Interferometry. International Congress on Instrumentation in Aerospace Simulation Facilities 1975 Record, 1975, pp. 237-246.

6. Yeh, Y.; and Cummins, H. Z.: Localized Fluid Flow Measurements with an He-Ne Laser Spectrometer. Applied Physics Letters, Vol. 4, No. 10, May 1964, pp. 176-178.

7. Rudd, M. J.: A New Theoretical Model for the Laser Dopplermeter.
   Journal of Scientific Instruments, Journal of Physics E, Series 2,
   Vol. 2, 1969, pp. 55-59.

8. Yanta, W. J.: Measurements of Aerosol Size Distributions with a Laser
   Doppler Velocimeter (LDV). American Institute of Aeronautics and
   Astronautics Paper 73-705, 1973.

9. Walsh, M. J.: Influence of Particle Drag Coefficient on Particle Motion
   in High Speed Flow with Typical Laser Velocimeter Application.
   NASA TN D-8120, 1976.

10. Widhopf, G.; and Lederman, S.: Specie Concentration Measurements Utiliz-
    ing the Raman Scattering of a Laser Beam. American Institute of
    Aeronautics and Astronautics Journal, Vol. 9, No. 2, February 1971,
    pp. 309-316.

11. Salzman, G. A.; Mosica, W. J.; and Coney, T. A.: Determination of Gas
    Temperatures from Laser Raman Scattering. NASA TN D-6336, 1971.

12. Bandy, A. R.; Hillard, M. E.; and Emory, M. L.: Evaluation of Raman
    Scattering as a Sensor of Temperature and Molecular Density. Applied
    Spectroscopy, Vol. 27, No. 6, November/December 1973, pp. 421-424.

13. Hillard, M. E., Jr.; Morrisett, E. L.; and Emory, M. L.: Raman Scatter-
    ing Applied to Hypersonic Air Flow. American Institute of Aeronautics
    and Astronautics Journal, Vol. 12, No. 8, August 1974, pp. 1160-1162.

14. Hillard, M. E., Jr.; Hunter, W. W., Jr.; Meyers, J. F.; and Feller, W. V.:
    Simultaneous Raman and Laser Velocimeter Measurements. American
    Institute of Aeronautics and Astronautics Journal, Vol. 12, No. 10,
    October 1974, pp. 1445-1447.

15. Lederman, S.: Some Application of Laser Diagnostic to Fluid Dynamics.
    American Institute of Aeronautics and Astronautics Paper 76-21,
    AIAA, January 1976.
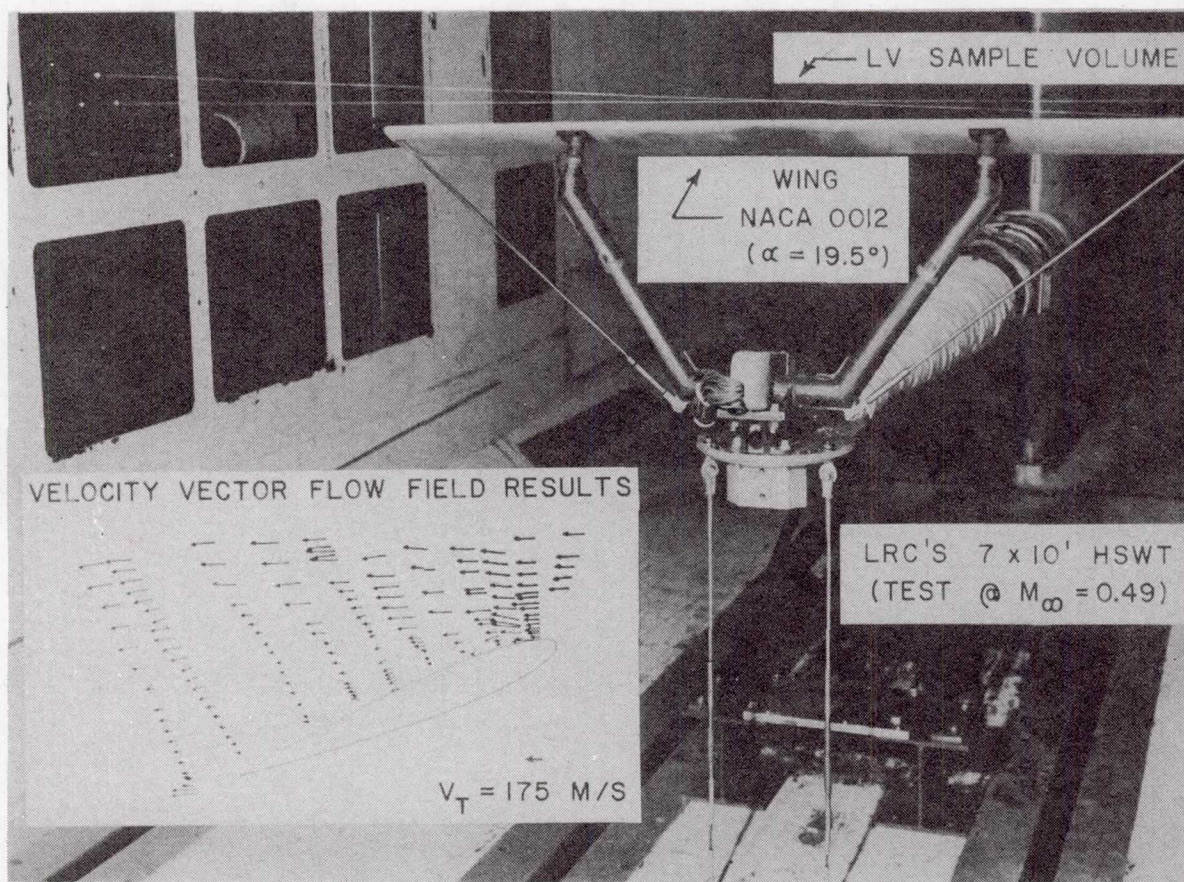
Figure 1.- Laser velocimeter survey test conditions and velocity vector
flow field results.
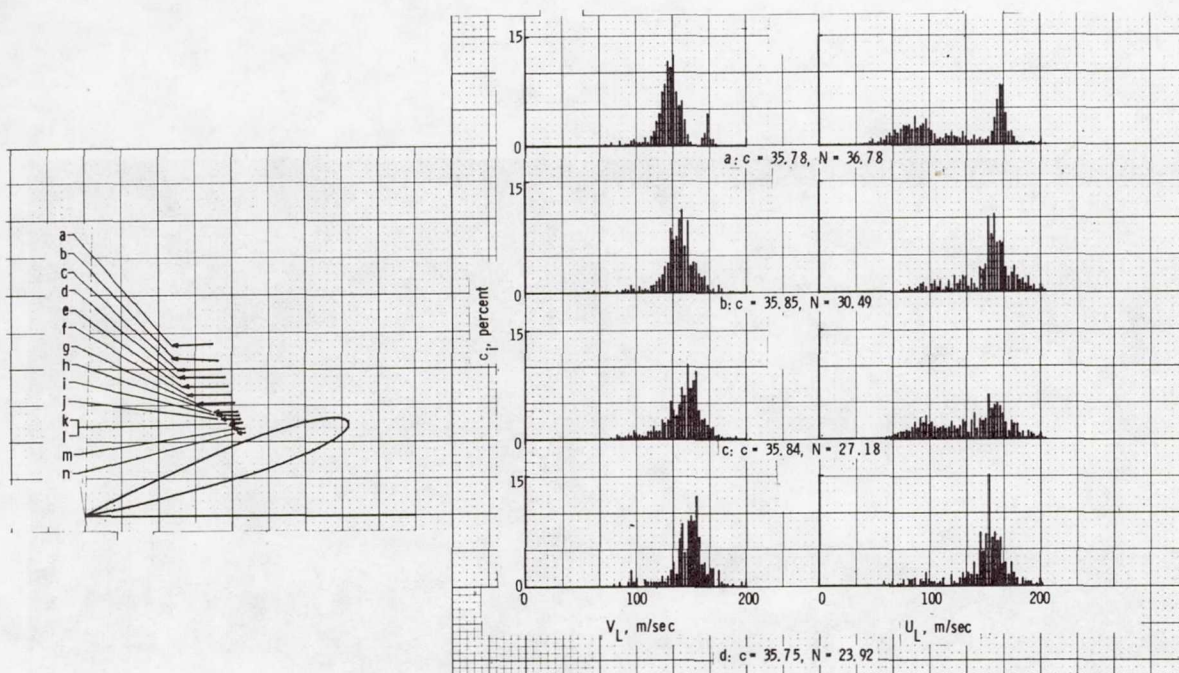
Figure 2.- Laser velocimeter histograms for indicated locations a,
b, c, and d. Left hand set for +45° and right hand set for −45°
vector components about the horizontal. Chordwise position c
and distance along normal N both in percent chord.
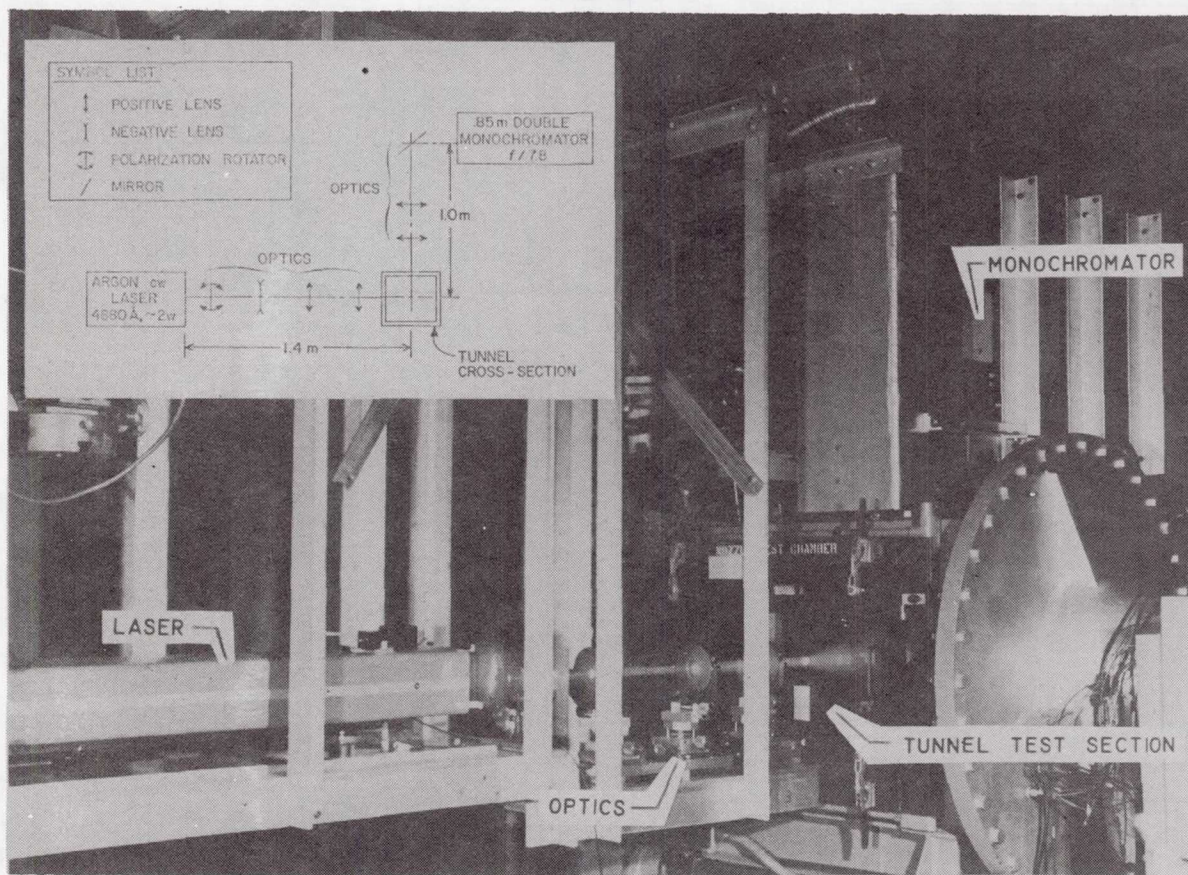
Figure 3.- Raman test set-up in Mach 5 nozzle test chamber.
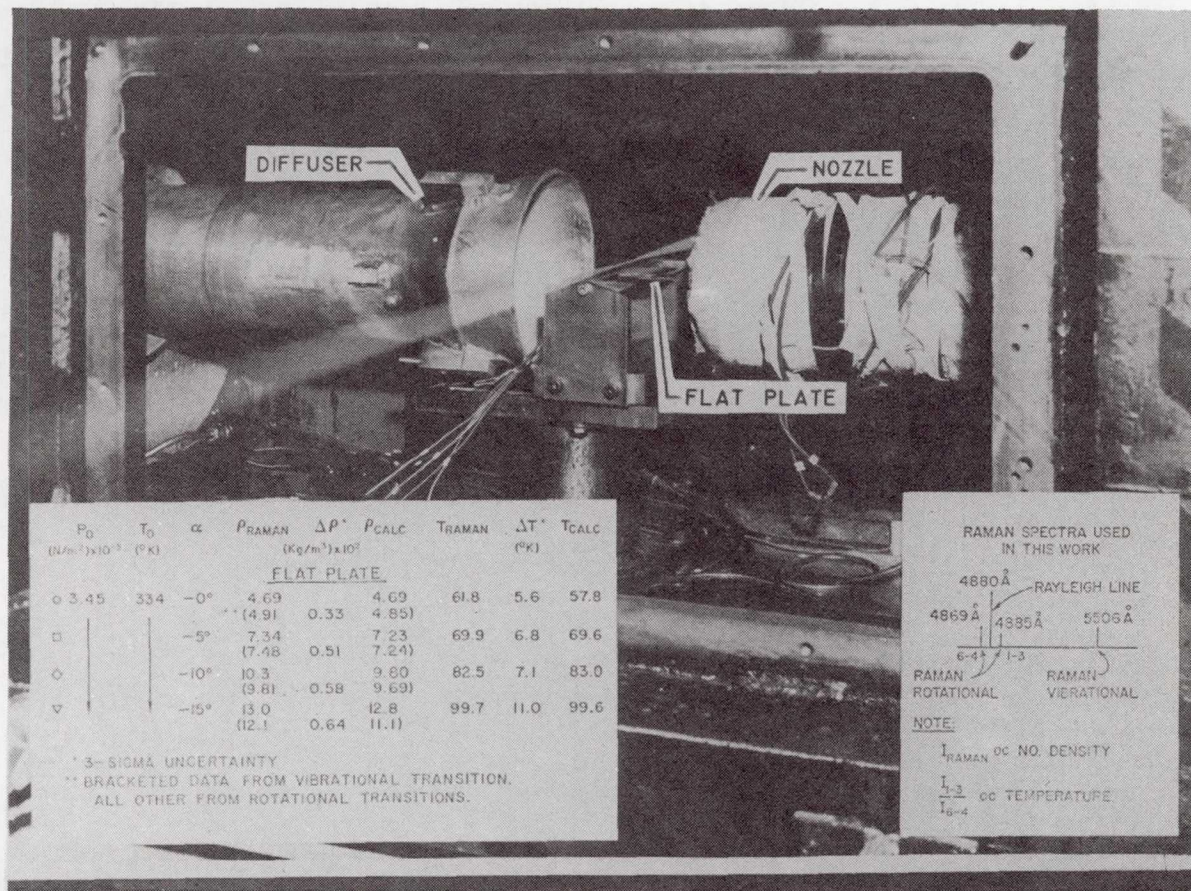
Figure 4.- Interior view of Mach 5 nozzle test chamber and comparison of calculated density ρ and temperature T values with experimental values.
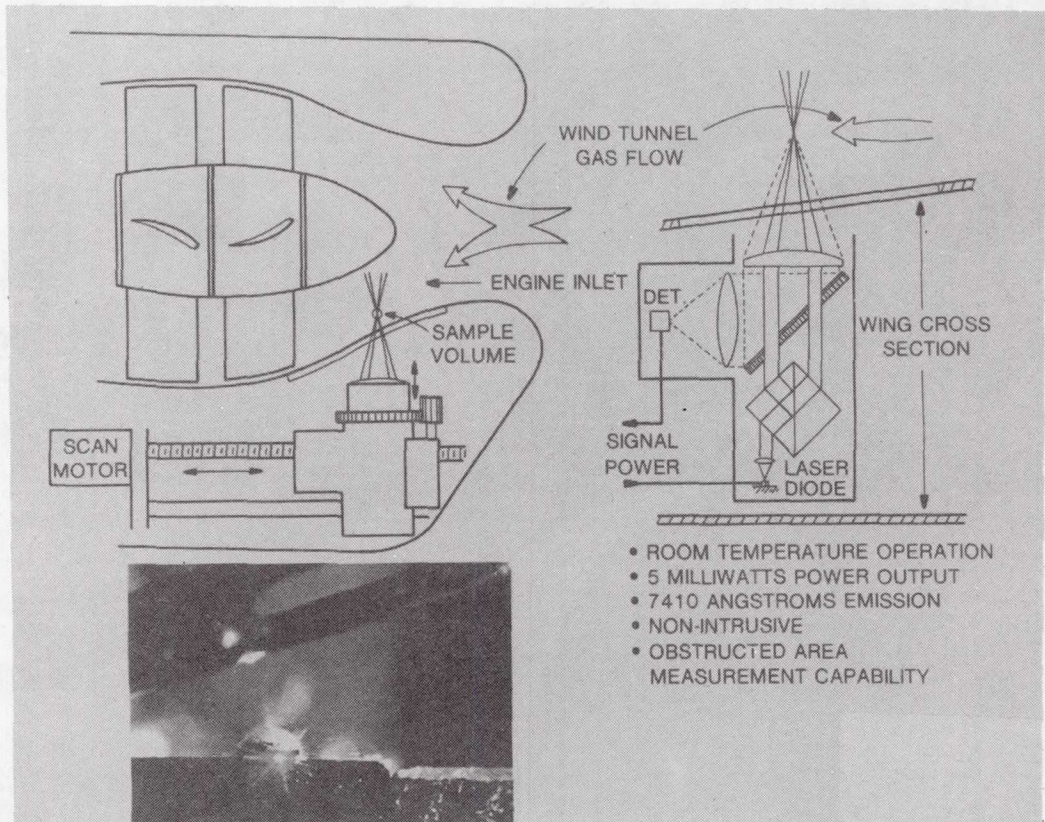
Figure 5.- Proposed applications for a laser diode velocimeter
and typical characteristics.

HYPERSONIC HEAT-TRANSFER AND TRANSITION CORRELATIONS

FOR A ROUGHENED SHUTTLE ORBITER

John J. Bertin, Dennis D. Stalmach, Ed S. Idar and Dennis B. Conley
The University of Texas at Austin

Winston D. Goodrich
Johnson Space Center

SUMMARY

The effect of roughness on the heat-transfer distributions and the transition criteria for the windward pitch plane of the Shuttle Orbiter at an angle of attack of 30° was studied using data obtained in hypersonic wind tunnels. The heat-transfer distributions and the transition locations for the roughened models were compared with the corresponding data for smooth models. The data were correlated using theoretical solutions for a nonsimilar, laminar boundary layer subject to two different flow-field models for the Orbiter.

INTRODUCTION

In order to predict the convective heat-transfer distribution for the windward surface of the Space Shuttle entry configuration, one must develop engineering correlations for the three-dimensional, compressible boundary layer. Since the aerodynamic heating rates generated by a turbulent boundary layer may be several times greater than those for a laminar boundary layer at the same flight condition, the correlations must include a transition criteria suitable for the complex flow fields. Because the windward surface of the Orbiter is composed of a large number of thermal protection tiles, the transition criteria must include the effect of the distributed roughness arising from the joints and possible tile misalignment. Thus, the transition correlation is complicated by the presence of roughness which interacts with other transition-related parameters. As discussed in reference 1, parameters, such as wall cooling, which decreases the boundary-layer thickness and delays transition on a smooth body, might actually promote transition for a given surface roughness. Morrisette (ref. 2) found that although the effective roughness Reynolds number increases significantly in the presence of a favorable pressure gradient near the centerline, much smaller roughness was required to promote transition near the shoulder of an Orbiter configuration, where again there was a favorable pressure gradient (this one associated with cross flow).

During tests in which a ring of spherical roughness elements were located in a supersonic flow past a cone, Van Driest and Blumer (ref. 3) observed variations in the relative roles played by the disturbances in the basic flow field

and those resulting from the presence of roughness elements. For some conditions, the disturbances associated with the basic flow field were predominant in establishing transition, whereas for other flows, the roughness elements dominated the transition process.

McCauley et al (ref. 4) found that the spherical roughness elements required to trip the boundary layer on sphere noses were several times larger than the boundary-layer thickness, whereas the trips required for a cone were within the boundary layer. Heat-transfer data (ref. 5) obtained in Tunnel B of the Arnold Engineering Development Center (AEDC) for a 0.04-scale Orbiter indicated that a ring of spherical trips, which were 0.079 cm. (0.031 in.) in diameter and were 0.11L from the nose, caused the transition location to move considerably upstream of the natural transition location (i.e., that for a smooth body). In the same test program (ref. 5), a simulated interface gap between two insulation materials, which was 0.102 cm. (0.040 in.) wide by 0.203 cm. (0.080 in.) deep and was located at x = 0.02L, had no measurable effect on boundary-layer transition at α = 40° and $Re_{\infty,L}$ = 8.6 x 10^6. In a series of tests using delta-wing Orbiter models (ref. 6), premature boundary-layer transition was observed on a model having simulated heat-shield panels with raised joints. Slot joints, however, did not cause premature transition of the boundary layer. The former model featured a series of transverse panels 0.635 cm. (0.250 in.) wide separated by a raised retaining strip 0.025 cm. (0.010 in.) wide by 0.0025 cm. (0.001 in.) high. The panels on the model with slotted joints were 0.635 cm. (0.250 in.) square separated by slots 0.020 cm. (0.008 in.) wide by 0.005 cm. (0.002 in.) deep. The Reynolds number ($Re_{\infty,L}$) for these tests ranged from 6.5 x 10^6 to 9.0 x 10^6 using a model 0.403 m (1.321 ft.) long.

The present paper discusses the results of an experimental investigation in which heat-transfer data were obtained on a Shuttle Orbiter model for which the first 80% of the windward surface was roughened either by a simulated vertical tile misalignment or by a grit-blasting technique. The misaligned tiles were 0.0023 cm. to 0.0025 cm. high on the 0.0175-scale Orbiter. Heat-transfer data were obtained in Tunnel B and in Tunnel F over a Mach number range from 8.0 to 12.1 and over a Reynolds number range (based on model length) from 1.17 x 10^6 to 17.63 x 10^6.

<div align="center">SYMBOLS</div>

h local heat-transfer coefficient, $\dot{q}/(T_t-T_w)$

$h_{t,ref}$ heat-transfer coefficient for the reference stagnation-point heating rate

k height of roughness element

L axial model length, 0.574 m (1.882 ft)

msf metric scale factor equal to the equivalent radius divided by L

M_e local Mach number at the edge of the boundary layer

M_∞ free-stream Mach number

r_{ref} radius of reference sphere reduced to model scale, 0.5334 cm. (0.0175 ft.)

Re_{ns} Reynolds number behind a normal shock, $\rho_{ns} u_{ns} r_{ref}/\mu_{ns}$

Re_s Reynolds number based on local flow properties integrated over the length from the stagnation point to the point of interest

$Re_{\infty,L}$ free-stream Reynolds number based on model length

Re_θ Reynolds number based on local flow properties at the edge of the boundary layer and on the momentum thickness

x axial coordinate

δ^* displacement thickness

The subscript tr designates parameters evaluated at the transition location.

EXPERIMENTAL PROGRAM

The experimental program was conducted to investigate what effect tile misalignment representative of a reasonable manufacturing tolerance has on heat-transfer and transition criteria in the plane of symmetry of the Shuttle Orbiter. Thus, a 0.0175-scale Orbiter model, which had been tested previously in a smooth surface condition in Tunnel B and in Tunnel F of the AEDC was modified. Selected tiles, slightly raised above the model surface, were precisely deposited on the windward surface using an electroless plating technique (ref. 7). Heat-transfer rates to the tile-roughened model were obtained first in Tunnel B and then in Tunnel F. However, 60% of the tiles were lost from the model during the initial runs of the Tunnel F program. After the initial runs, the remaining tiles were removed and the windward surface roughened by a grit-blasting technique.

Model. - The model used in the test programs (see the sketch of Fig. 1) was a 0.0175-scale model of the 29-0 Shuttle Orbiter. Twenty-seven coaxial surface thermocouples were used to obtain the heat-transfer-rate distribution for the windward plane of symmetry. The uncertainty for most of the heat-transfer-rate measurements was approximately 10% (refs. 8 and 9).

Tile roughness. - A herringbone pattern (symmetric about the plane of symmetry) of raised tiles covered the windward surface of the Orbiter model up to the tangent line of the chines from x = 0.02L to 0.80L. The raised tiles, which were selected randomly, represented 25% of the tiles in the area of interest as shown in the photograph of Fig. 2. The selected tiles were 0.267 cm. (0.105 in.) square and were 0.0023 cm. (0.0009 in.) to 0.0025 cm. (0.0010 in.) in height.

The vertical misalignment, thus simulated, of 0.1306 cm. (0.0514 in.) to 0.1451 cm. (0.0571 in.) full scale was considered representative of manufacturing tolerance.

Grit roughness. - The tiles remaining after the initial runs of the Tunnel F program were removed and the surface roughened over the first 80% of the windward surface using a grit-blasting technique. The average peak-to-valley distance for ten readings in a 0.25 cm. (0.10 in.) length as read from a photomicrograph was 0.0041 cm. (0.0016 in.).

Test Program. - Heat-transfer rates were obtained in Tunnel B at a free-stream Mach number of 8 over a range of Reynolds number (based on model length) from 1.89×10^6 to 7.07×10^6. The surface temperature for the Tunnel B tests varied from $0.40 \ T_t$ to $0.43 \ T_t$. For the Tunnel F tests the Mach number varied from 10.73 to 12.06 while the Reynolds number varied from 1.17×10^6 to 17.63×10^6. The surface temperature for the Tunnel F tests varied from $0.14 \ T_t$ to $0.28 \ T_t$. The data presented in the present paper were obtained at an angle of attack of 30°.

For additional details regarding the model or the test program, the reader is referred to references 8 and 9.

THEORETICAL SOLUTIONS

Theoretical solutions for a nonsimilar, laminar boundary layer were generated for the pitch plane of the Orbiter model at an angle of attack of 30° to determine the flow properties at the transition location. The theoretical solutions were computed using a modified version of the code described in reference 10. Required as input for the code are the flow conditions at the edge of the boundary layer, the radius of the "equivalent" body of revolution, and the wall-temperature distribution. The metric scale-factor describing the streamline divergence was used to represent the radius of the equivalent body of revolution in the axisymmetric analogue for a three-dimensional boundary layer. The metric coefficients were calculated using the relations described by Rakich and Mateer (ref. 11).

Two different flow-field models were used to generate the required inviscid solution for the plane of symmetry. The pressure distribution and the streamlines for the first flow model, designated "Newt, NSE", represent modified Newtonian flow. For this flow model, it was assumed that the fluid at the edge of the boundary layer was that which had passed through the normal portion of the bow shock wave and had accelerated isentropically from the stagnation point. The inviscid flow properties for the second flow-field model, designated "LFF, VarEnt", were supplied by the Lockheed Electronics Company using the code described in reference 12. This flow model accounts for the entropy variation in the shock layer which results because of the curvature of the shock wave. Thus, the entropy of the fluid at the edge of the boundary layer varied with distance from the apex. The pressure distributions and the metric

scale-factor distributions, thus calculated for a free-stream Mach number of 8 (the nominal value of the Tunnel B tests) and for $\alpha = 30°$, are presented in Figure 3 for the two flow models. Whereas the pressure distributions are similar, significant differences exist in the local entropy distribution and in the metric scale-factor distributions for the two flow models. As a result, the values for local flow properties, such as the velocity, the Mach number, and the unit Reynolds number, were much higher for the LFF, VarEnt model than for the Newt, NSE model.

EXPERIMENTAL DATA FOR AN ANGLE OF ATTACK OF 30°

The heat-transfer measurements for the tile-roughened models are compared in Figure 4 with the heat-transfer data obtained in a previous Tunnel B program (ref. 13) in which a smooth model was subjected to essentially identical flow conditions. The experimental values for the local heat-transfer coefficients have been divided by the theoretical value for the stagnation point of a 0.5334 cm. (0.0175 ft.) radius sphere as calculated using the theory of Fay and Riddell (ref. 14). For purposes of data presentation the recovery factor has been set equal to unity. For $x \leq 0.90L$, the local heat transfer coefficients for the tile-roughened model were typically between 8% to 26% greater than those for the smooth model. This was true both for the laminar and for the transitional portions of the boundary layer. The data for the thermocouple at $x = 0.20L$ were counter to this trend, but the measurements at this thermocouple are believed to be slightly low for the tile-roughened model (refer also to Fig. 5). At the downstream end of the model, i.e., $0.90L < x < 1.00L$, the local heat-transfer coefficients were approximately the same (i.e., within the uncertainty of the measurements) when the boundary layer was transitional or turbulent. There were not sufficient data for fully turbulent boundary layers at comparable flow conditions to warrant general conclusions. For the lowest Reynolds number tests, the heat transfer at the downstream end of the tile-roughened model was from 25% to 55% greater than that of the smooth model. However, since these heating rates were relatively low, the experimental uncertainty of the data was between 10% to 25% (ref. 8). The increased heating, which was significantly greater than the experimental uncertainty, may be due to roughness-induced perturbations to the relatively thick laminar boundary layer or to the slightly premature onset of transition. Since the roughness presented by the vertical misalignment of the tiles perturbed the flow sufficiently to produce weak shock waves (refer to the shadowgraphs presented in ref. 7), the increased heating evident in the data of Figure 4 is not unexpected.

Experimentally determined heat-transfer data obtained in Tunnel B for the tile-roughened model are compared in Figure 5 with the theoretical solutions for a laminar boundary layer. Despite the roughness-induced perturbations to the heat transfer, the experimental laminar values are between the theoretical values for the two flow-field models. The streamwise variation of the measurements more closely follows the theoretical distribution based on the LFF, VarEnt flow model. Thus, the data indicate that one should include the variations in entropy when developing correlations for the aerothermodynamic environment of the Shuttle. The departure of the experimental heat-transfer

measurements from the laminar correlation, which is indicated by the arrows in Figure 5, was defined as the onset of transition.

The experimentally determined heat-transfer distributions obtained in Tunnel F for the tile-roughened model are presented in Figure 6. From $0.20L \leq x < 0.55L$, the heat-transfer measurements for the two higher Reynolds-number flow conditions were as much as 30% above the corresponding values for the lowest Reynolds number. These locally high heating rates may be an indication of "incipient" transition. As will be discussed later, the transition correlation parameter (using local properties based on the LFF, VarEnt flow model) was relatively low for these two flow conditions. Thus, if these data are indeed indicative of "incipient" transition, the favorable pressure gradient inhibited the transition process and the boundary layer was laminar for $x > 0.60L$. Again, the experimentally determined laminar heat-transfer coefficients were in reasonable agreement with the theoretical values calculated using LFF, VarEnt flow model.

Experimentally determined heat-transfer distributions obtained in Tunnel F for the grit-roughened model are presented in Figure 7. For the highest Reynolds-number flow condition (i.e., $Re_{\infty,L} = 13.45 \times 10^6$), transition occurred at $x = 0.06L$. It should be noted that a strong favorable pressure gradient existed in this region (see Fig. 3a). With transition occuring so near the stagnation point, the theoretical value for the boundary-layer displacement thickness was less than the average peak-to-valley distance for the grit roughness (i.e., $\delta_{tr}^* = 0.351$ k for Newt, NSE and $\delta_{tr}^* = 0.434$ k for LFF, VarEnt). Thus, the grit may have been effective in tripping the boundary layer for the highest Reynolds-number flow. As the Reynolds number decreased, transition moved downstream and the grit-roughness elements became immersed in the boundary layer. Using the theoretical values for the LFF, VarEnt flow model, δ_{tr}^* was 0.684 k, 4.90 k, and 7.67 k when $Re_{\infty,L}$ was 9.45×10^6, 7.51×10^6, and 3.99×10^6, respectively. The heat-transfer measurements for $Re_{\infty,L} = 7.51 \times 10^6$ were slightly greater than the companion laminar measurements from $x = 0.20L$ to the assumed transition location (i.e., $x_{tr} = 0.40L$). Again, the possibility exists that the data indicate a roughness-induced incipient transition process countered by a stabilizing pressure gradient.

Although the local heating was measurably increased by the tile misalignment, the Tunnel B data of Figure 4 indicated that the transition locations were not affected by tile misalignment of the magnitude considered in the present tests. Pate (ref. 15) has found that, to a significant degree, the tripped location at supersonic speeds is dependent on the free-stream disturbances in a tunnel. He concluded that it appeared appropriate to relate roughness effects by comparing the roughened-model transition locations to the smooth-wall transition location when attempting to normalize tunnel flow effects. Therefore, the effect of roughness on the present transition locations is indicated by comparing smooth-wall data with rough-model data from the same tunnel as a function of Re_{ns}. Data obtained in Tunnel B for a smooth model (ref. 13) and for a tile-roughened model (ref. 8) are presented in Figure 8a.

Data obtained in Tunnel F for a smooth model (ref. 16) and for a grit-roughened model (ref. 9) are presented in Figure 8b. It is evident that the roughness elements of the present tests caused premature transition only for the highest Reynolds-number flow conditions in Tunnel F. These were the only flow conditions for which δ_{tr}^* was less than k, the roughness height. It should also be noted that the grit-blasted roughness, which promoted transition in these runs, was greater in height than the misaligned tiles.

Values for the transition correlation parameters, $(Re_\theta/M_e)_{tr}$ and $Re_{s,tr}$, which have been calculated using the two flow-field models, are presented in Figure 9. As noted previously, even though the pressure distributions are similar, the assumed flow process (i.e., an isentropic expansion from the stagnation point or an adiabatic process subject to the entropy distribution defined by the shock shape) had a profound effect on the local flow properties. Note a single value for either transition parameter, i.e., $(Re_\theta/M_e)_{tr}$ or $Re_{s,tr}$, was not found from the correlations made using either flow model. For the Newt, NSE flow model, $(Re_\theta/M_e)_{tr}$ is approximately equal to 0.348 $(Re_{s,tr})^{0.5}$. The correlation for the parameters evaluated based on the LFF, VarEnt flow model is not as simple. The data may be considered as falling into one of three groups: (1) the roughness-promoted transition which occured in the highly favorable pressure gradient near the nose (i.e., the open symbols for $Re_{s,tr} < 400,000$), (2) the incipient transition locations for the data discussed in Figure 6 (i.e., the filled symbols), and (3) the remaining data for which the transition locations were unaffected by model roughness (i.e., the open symbols for $Re_{s,tr} > 900,000$). These data are being studied further.

CONCLUDING REMARKS

Heat-transfer data for the Shuttle Orbiter at an angle of attack of 30° have been obtained in Tunnel B and in Tunnel F. The first 80% of the windward surface of the model was roughened either by a simulated vertical tile mis-alignment or by a grit-blasting technique. Based on the data obtained in these tests, the following conclusions are made.

(1) Surface roughness of the magnitude considered did not have a significant effect on the transition location until the Reynolds number was sufficiently high to cause transition near the nose. At these high Reynolds numbers, the roughness elements became large relative to the boundary layer and became effective as tripping elements.

(2) The local heat-transfer coefficients for the tile-roughened model were measurably greater than the corresponding values for the smooth model. This was true both for the laminar and for the transitional portions of the boundary layer.

(3) Both theoretical flow models produced heat-transfer distributions which were in reasonable agreement with the magnitude of the laminar data. The

flow model which included the entropy gradients in the flow field, i.e., the "more exact" LFF, VarEnt flow model, provided a better correlation of the streamwise variation in heating. The two theoretical models produced markedly different correlations for the transition parameters. Additional study is needed to define the impact of these variations on the correlations for flight conditions.

REFERENCES

1. Braslow, A.L., "A Review of Factors Affecting Boundary-Layer Transition", NASA TND-3384, Apr. 1966.

2. Morrisette, E.L., "Roughness Induced Transition Criteria for Space Shuttle-Type Vehicles", Journal of Spacecraft and Rockets, Feb. 1976, Vol. 13, No. 2, pp. 118-120.

3. Van Driest, E.R., and Blumer, C.B., "Boundary-Layer Transition at Supersonic Speeds - Three-Dimensional Roughness Effects (Spheres)", Journal of the Aerospace Sciences, Aug. 1962, Vol. 29, No. 8, pp. 909-916.

4. McCauley, W.D., Saydah, A.R., and Bueche, J.F., "Effect of Spherical Roughness on Hypersonic Boundary-Layer Transition", AIAA Journal, Dec. 1966, Vol. 4, No. 12, pp. 2142-2148.

5. Carver, D.B., "Heat-Transfer Tests on the Rockwell International Space Shuttle Orbiter with Boundary-Layer Trips (OH-54)", AEDC-TR-76-28, May 1976.

6. Seegmiller, H.L., "Effects of Roughness on Heating and Boundary Layer Transition, Part I - Effects of Simulated Panel Joints on Boundary-Layer Transition", Space Shuttle Aerothermodynamics Technology Conference, Volume II-Heating, NASA TM X-2507, February 1972.

7. Stalmach, C.J., Jr., and Goodrich, W.D., "Aeroheating Model Advancements Featuring Electroless Metallic Plating", presented at the AIAA 9th Aerodynamic Testing Conference in Arlington, Texas, June 1976.

8. Siler, L.G., and Martindale, W.R., "Test Results from the NASA Space Shuttle Orbiter Heating Test (MH-2) Conducted in the AEDC-VKF Tunnel B", AEDC-DR-75-103, Oct. 1975.

9. Siler, L.G., "Test Results from the NASA Space Shuttle Orbiter Heating Test (MH-1) Conducted in the AEDC-VKF Tunnel F", AEDC-DR-76-13, Mar. 1976.

10. Bertin, J.J., and Byrd, O.E., Jr., "The Analysis of a Nonsimilar Boundary Layer - A Computer Code (NONSIMBL)", University of Texas at Austin, Aerospace Engineering Report 70002, Aug. 1970.

11. Rakich, J.V., and Mateer, G.G., "Calculation of Metric Coefficients for Streamline Coordinates", AIAA Journal, Nov. 1972, Vol. 10, No. 11, pp. 1538-1540.

12. Goodrich, W.D., Li, C.P., Houston, C.K., Chiu, P., and Olmedo, L., "Numerical Computations of Orbiter Flow Fields and Heating Rates", AIAA Paper 76-359, presented at the AIAA 9th Fluid and Plasma Dynamics Conference, San Diego, Cal., July 1976.

13. Martindale, W.R., and Trimmer, L.L., "Test Results from the NASA/Rockwell International Space Shuttle Test (OH4A) Conducted in the AEDC-VKF Tunnel B", AEDC-DR-74-39, May 1974.

14. Fay, J.A., and Riddell, F.R., "Theory of Stagnation Point Heat Transfer in Dissociated Air", Journal of the Aeronautical Sciences, Feb. 1958, Vol. 25, No. 2, pp. 73-85, 121.

15. Pate, S.R., "Supersonic Boundary-Layer Transition:Effects of Roughness and Freestream Disturbances", AIAA Journal, May 1971, Vol. 9, No. 5, pp. 797-803.

16. Boudreau, A.H., "Test Results from the NASA/RI Shuttle Heating Test OH-11 in the AEDC-VKF Tunnel F", AEDC-DR-74-16, Feb. 1974.
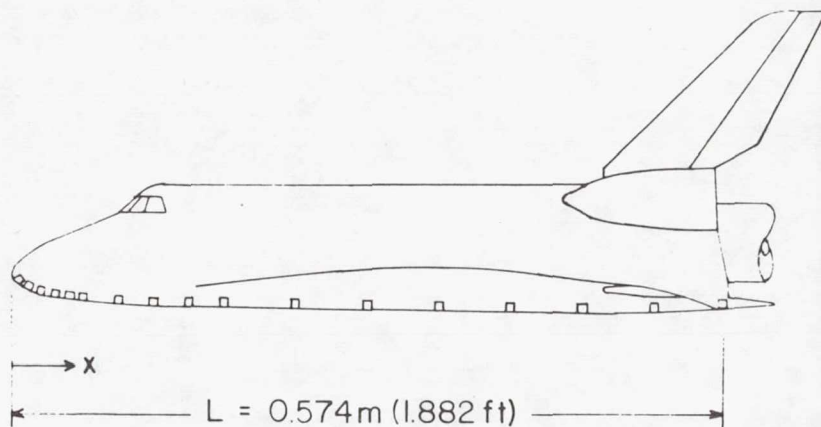
Fig. 1. - Sketch of the 0.0175-scale Orbiter model.

L = 0.574m (1.882 ft)
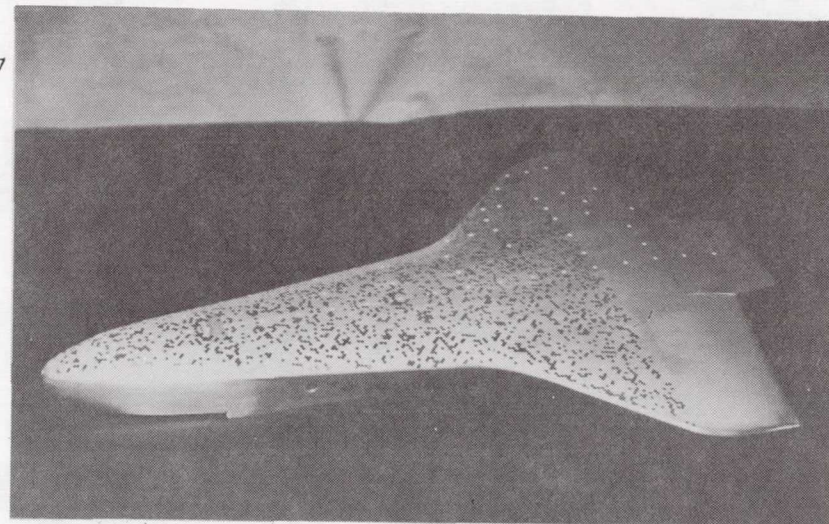
Fig. 2. - Photograph of the Orbiter model showing the vertically misaligned tiles (plated to 0.0023 cm. in height).

Fig. 3. - A comparison of the inviscid flow-field parameters for $M_\infty = 8$ flow past the Orbiter at $\alpha=30°$.

Newt, NSE
LFF, VarEnt
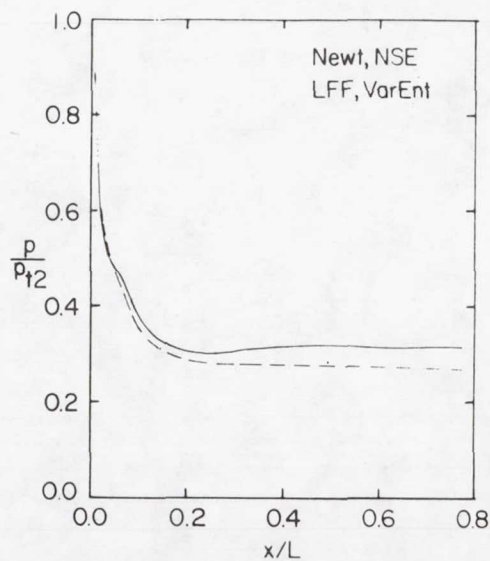
(a) Pressure distribution
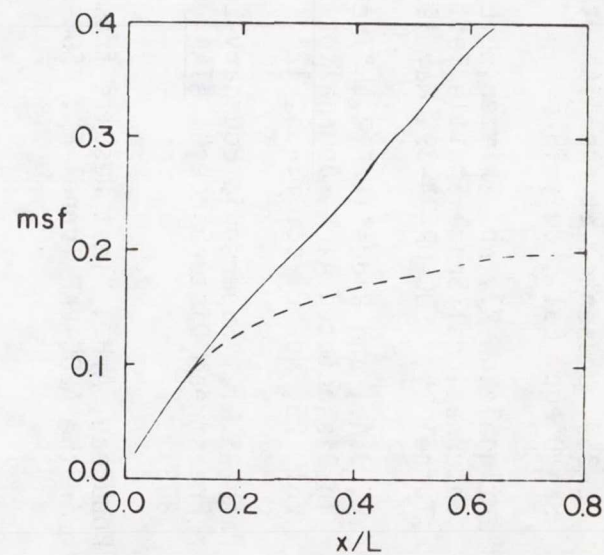
(b) Metric scale-factor distribution

Data	M_∞	$Re_{\infty,L}$	Re_{ns}
○	8.00	7.1×10^6	7200
◇	7.98	4.6×10^6	4700
○	7.94	1.9×10^6	1900

Open symbols: Tile-roughened model
Filled symbols: Smooth model

Data	M_∞	$Re_{\infty,L}$	Re_{ns}
○	8.00	7.07×10^6	7237
◇	7.99	5.63×10^6	5759
△	7.98	4.63×10^6	4733
□	7.98	3.65×10^6	3718
↑	Transition Location, x_{tr}		

Theoretical Solutions for Laminar Boundary Layer

——— LFF, VarEnt
– – – – Newt, NSE
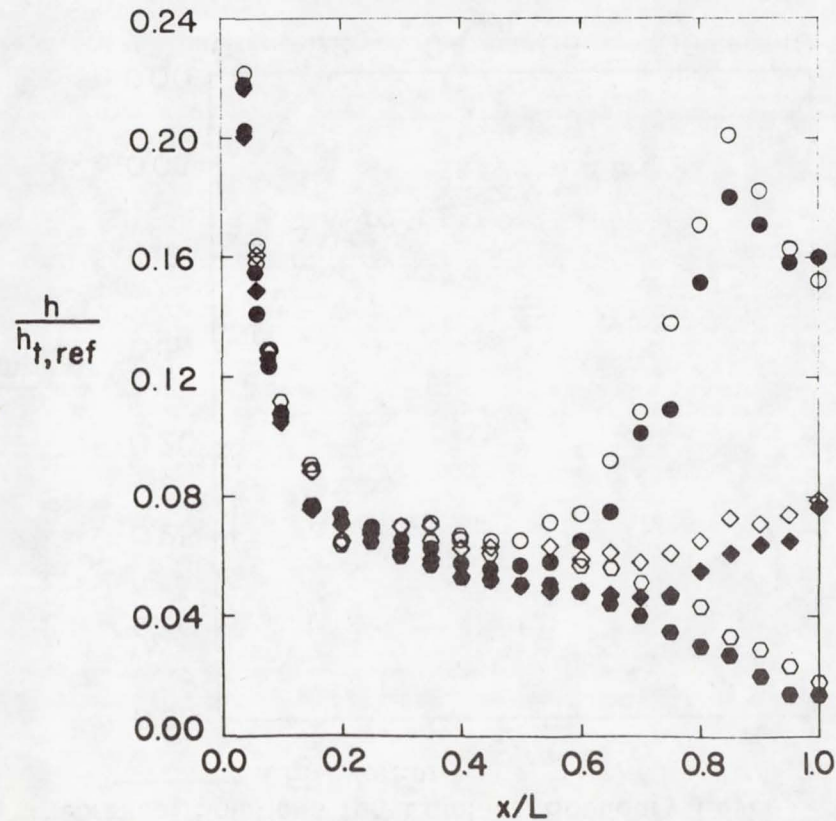
Fig. 4. - The effect of tile roughness on the heat-transfer distributions obtained in Tunnel B for $\alpha = 30°$.
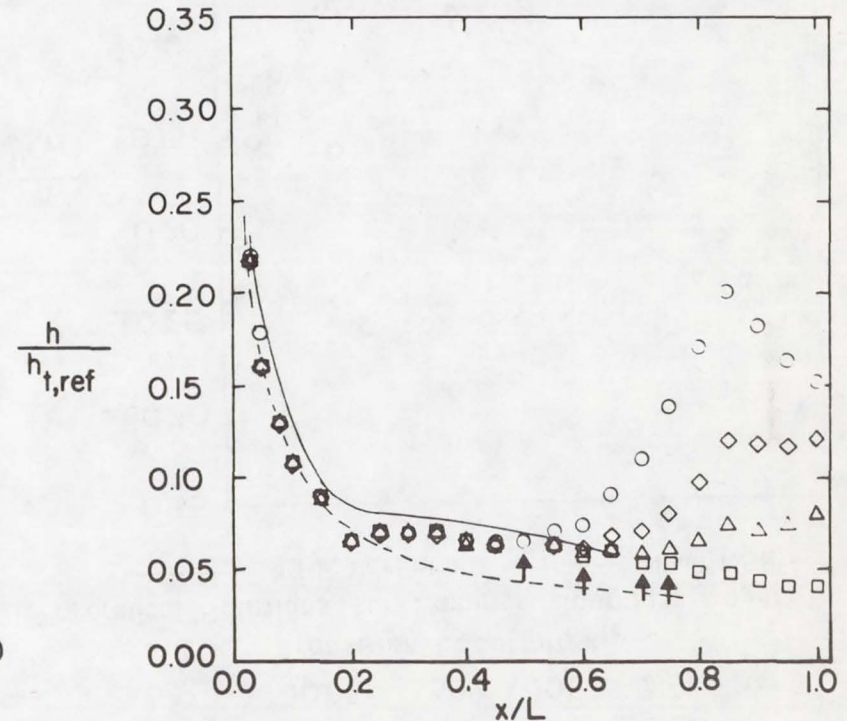
Fig. 5. - Heat-transfer distributions from the plane of symmetry of the tile-roughened model (Tunnel B) compared with theoretical laminar distributions.

Data	M_∞	$Re_{\infty,L}$	Re_{ns}
○	11.53	3.74×10^6	2673
◇	11.37	2.23×10^6	1853
△	11.79	1.43×10^6	1054

Theoretical Solutions for Laminar Boundary Layer

——— LFF, VarEnt
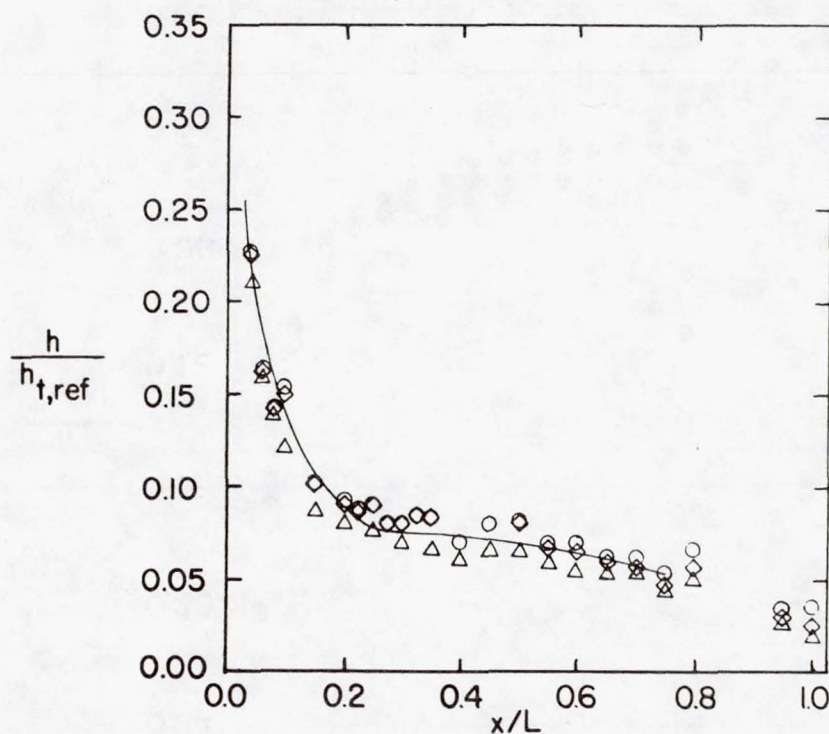
Fig. 6. - Heat-transfer distributions from the plane of symmetry of the tile-roughened model (Tunnel F) illustrating incipient transition.

Data	M_∞	$Re_{\infty,L}$	Re_{ns}
○	10.83	13.45×10^6	10240
◇	10.78	9.45×10^6	7671
△	10.82	7.51×10^6	6138
□	10.83	3.99×10^6	3181
↑	Transition Location, x_{tr}		

Theoretical Solutions for Laminar Boundary Layer

——— LFF, VarEnt   – – – – Newt, NSE
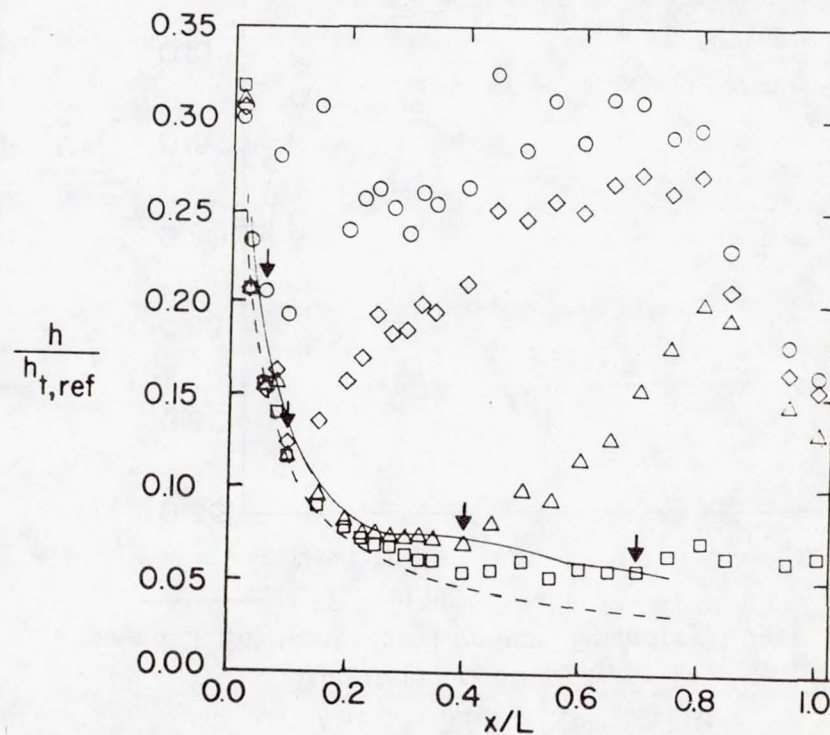
Fig. 7. - Heat-transfer distribution from the plane of symmetry of the grit-roughened model (Tunnel F) compared with theoretical laminar distributions.

Open symbols: Roughened model   Filled symbols: Smooth model

Note: Tile-roughened model

Note: Grit-roughened model

(a) Tunnel B

(b) Tunnel F
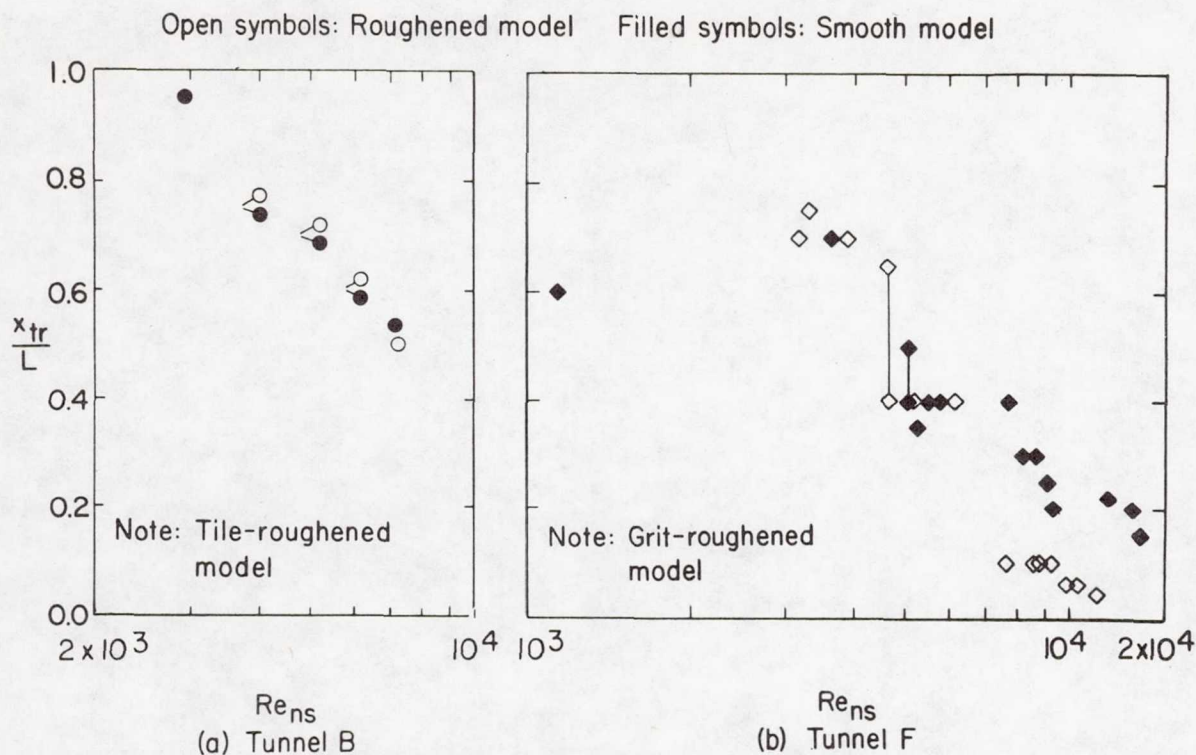
Fig. 8. - The effect of roughness on the transition locations for $\alpha = 30°$.

Flagged symbols designate data for models with tile roughness
Filled symbols designate incipient "transition" locations

○ Tunnel B data
◇ Tunnel F data

(a) Newt, NSE

(b) LFF, VarEnt
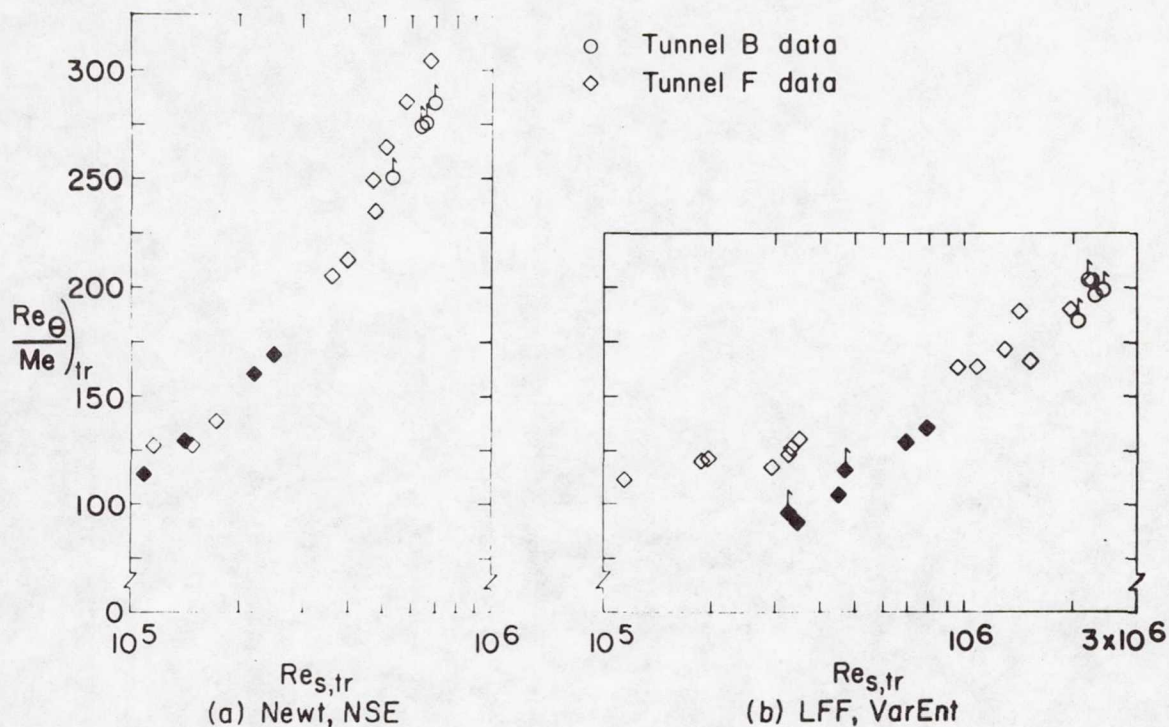
Fig. 9. - Transition correlations for the roughened Orbiter model at $\alpha = 30°$.

1627

Page intentionally left blank

HYDROGEN-FUELED SCRAMJETS:

POTENTIAL FOR DETAILED COMBUSTOR ANALYSIS

H. L. Beach, Jr.
NASA Langley Research Center

SUMMARY

Combustion research related to hypersonic scramjet (supersonic combustion ramjet) propulsion is discussed from the analytical point of view. Because the fuel is gaseous hydrogen, mixing is single-phase and the chemical kinetics are well-known; therefore, the potential for analysis is good relative to hydrocarbon-fueled engines. Recent progress in applying two- and three-dimensional analytical techniques to mixing and reacting flows indicates cause for optimism, and identifies several areas for continuing effort.

INTRODUCTION

Research in hypersonics, while lying dormant for the last 8 to 10 years throughout much of the R&D community, has been proceeding at a quite viable pace at NASA Langley. There have been technology advancements in a number of areas, including propulsion. The realities that have driven the new concepts for hypersonic engines are the need for hydrogen fuel (for performance and cooling), the need for supersonic combustion (to reduce internal pressure, gas dissociation, and heat flux), and the necessity to very closely integrate the propulsion system with the aircraft. For example, at Mach 10 almost all of the airflow between the underside of the vehicle and its bow shock must be utilized in the propulsion cycle, and this implies an inlet capture shaped much like the vehicle undersurface as shown in figure 1. By dividing this area into smaller units, the propulsion system becomes a set of modules whose size and shape are appropriate for test in a ground facility. With this arrangement, the entire vehicle undersurface is an integral part of the engine; the forebody precompresses the flow coming into the inlet, and the afterbody serves a major function of the nozzle. Installation losses, which are extremely severe for pod-type engines, can easily be minimized by shaping of the lower surface or cowl.

Complete descriptions of engine module design philosophy, performance, and status are discussed in references 1 to 3. Summarizing briefly with the aid of figure 1, the module is highly three-dimensional, has a rectangular capture area and employs fixed geometry. The inlet process is completed by the side-walls and three struts which are swept to the oncoming flow and span the vertical dimension of the module. The sweep, coupled with a cutback cowl, causes spillage which allows starting of the inlet at low flight Mach numbers. In addition to being part of the inlet, the struts are the fuel injectors.

Multiple fuel injection planes provided by the struts make the combustor shorter; this, combined with a diverging combustor area, gives good performance with lower internal pressure and cooling requirements than a constant-area combustor with wall injection.

The combustor flow field can be regarded, at least for high Mach number flight, as mixing controlled. Advantage is taken of the differences between the mixing characteristics of parallel and perpendicular fuel injection to control the heat release over a wide speed range. Understanding and predicting mixing in the presence of turbulence and reaction are prime areas for research because they are real keys to effective engine operation. Other influences which must be addressed include streamwise and transverse pressure gradient, shock and expansion waves, injection disturbances, external (such as acoustic) disturbances, and three-dimensional interactions. While these make a formidable list for a potential combustor analyst, there are several inherent advantages which lead to optimism. First, the combustor geometry is relatively simple downstream of the struts (plane walls, no flame holders). Second, the hydrogen fuel is injected as a gas, and the flow is single-phase. Third, hydrogen-air combustion kinetics are very well-known compared to conventional hydrocarbon fuels.

The purpose of this paper is to discuss areas of research directed toward combustor analysis and design currently being pursued in and out of house in the Langley hypersonic propulsion program. (See reference 4 for a discussion of earlier work).

SYMBOLS

D_j injector diameter

P_T pitot pressure

R radial distance measured from flow centerline

T static temperature

U streamwise velocity

X streamwise direction

Y, Z transverse directions defined in figure 6

α_i species mass fraction

ν_i species mole fraction

Subscripts:

c centerline

o at $x = 0$

COMBUSTOR ANALYSIS DEVELOPMENT

Combustion-related research in hypersonic propulsion is divided into the general areas of basic research, which covers fundamental problems relevant to any combustor concept, and combustor development. Both areas have experimental and theoretical aspects. Due to facility requirements, most experimental work has been done in-house, while many analytical developments have been accomplished out of house.

Basic Research

Significant effort has been devoted to the analysis of simple-geometry, parabolic, turbulent, mixing/reacting flows. (Descriptions of various approaches by a number of researchers can be found in references 5 and 6). The approach currently being employed in scramjet work at Langley (ref. 7) utilizes boundary-layer-type equations with two differential equations for turbulent kinetic energy and dissipation of turbulent kinetic energy leading to the turbulent viscosity. Fuel and oxidizer concentration fluctuations which allow the modeling of turbulence effects on reaction are also computed. The turbulent reaction model being used for very high-temperature flows is a modification of that described in reference 8. and is based on the rate at which the concentration fluctuations dissipate (eddy breakup) rather than molecular processes (chemical kinetics). However, this model will not be adequate in lower temperature flows or regions of flows where kinetics effects may be competing equally with turbulence effects, and studies are continuing to develop an appropriate model including both. At any rate, it is clear that the reaction model can be extremely important in describing the details of a reacting flow. For example, the degree of reaction is coupled directly to the local temperature, indirectly to the pressure, and through both of these (and composition) to the density. Not only will errors arise in these variables from an inadequate reaction model, but also in more qualitative parameters such as the "spread" of the mixing zone.

Two alternate approaches are now being investigated which could have substantial impact on the future character of both turbulence and reaction models. The first solves differential equations for the second-order turbulence correlations (second-order closure, ref. 9). This technique is powerful but quite complex and requires the solution of up to thirty partial differential equations. For this reason, its applicability may be restricted to simple geometry. The second approach employs statistical theory to develop distribution functions from which any flow field quantities of interest can be derived (ref. 10). Here again, practical considerations may limit the applicability. Because temperature, velocity, specie concentration and temperature fluctuations are computed in both approaches, however, the potential exists for detailed study and improved understanding of turbulence-mixing-reaction interactions.

Since shocks, expansions, and transverse pressure gradients are inevitable in a supersonic combustion ramjet, the ability to account for them is essential. A combined hyperbolic-parabolic technique has been developed (viscous characteristics, ref. 11) and applied (ref. 12) with some success to an underexpanded hydrogen diffusion flame. This technique computes the shocks explicitly rather

than smearing them. Whether shocks must be explicitly handled in the combustor is not clear at this time, but it is apparent that any characteristics method will need very sophisticated coupling with other techniques when there are adjacent or imbedded regions of subsonic flow.

Other pertinent areas of basic combustion research, such as the use of acoustical disturbances to alter mixing rates and investigation of large-scale turbulence, are in the planning stage. Development of models to describe such flows awaits the generation of appropriate experimental data.

Component Analysis

Combustor component flow fields generally exhibit most of the characteristics studied in basic research; in addition, they are three-dimensional. The goal is therefore to build three-dimensional computation tools that incorporate all of the salient features possible. A beginning in this area has been accomplished with the development of finite-difference (ref. 13) and finite-element (ref. 14) computer codes. These are parabolic codes currently being evaluated by comparisons with pertinent mixing and reacting data. At this time, both have the capability for two-equation turbulence modeling with equilibrium chemistry. Features to be added will depend on the basic research identification of the key issues.

TYPICAL RESULTS

A serious problem in the evaluation of turbulent reacting flow analysis is the lack of appropriate experimental data with which to compare. Nearly always the real unknowns in the analysis are the turbulence quantities, and these are the most difficult to measure. For now, in turbulent flames of interest in supersonic combustion ramjets, the only reliable in-stream measurements are time-averaged pitot and static pressure and gas composition. The potential for time and spatially resolved temperature and species measurement exists through laser-Raman scattering techniques, but their practical application is still some time off. Comparisons are therefore possible only with mean quantities, and the value of a particular turbulence or reaction model must be inferred from the mean flow.

To add to the data base for analysis evaluation, a coaxial, axisymmetric, experimental program was conducted in the Langley combustion test stand. A description of the apparatus is given in reference 12; it consists of a Mach 2 test gas nozzle with an exit diameter of 6.57 cm, and a centerline mounted, 0.95 cm diameter, Mach 2 hydrogen injector. The high-temperature test gas was obtained by burning hydrogen in air and replenishing the volumetric oxygen content; it therefore contained significant water vapor. Test gas total temperature was approximately 2400 K, and injector hydrogen total temperature was 460 K. Measurements consisted of radial pitot pressure profiles at five axial locations and gas samples at four locations.

Centerline data for hydrogen and water mass fractions and pitot pressure are shown in figure 2 along with the theory of reference 7. Initial conditions

for the calculation were derived from measured nozzle-exit profiles; initial turbulence quantities were generated by iterative short-step calculations which allowed the turbulent kinetic energy and dissipation profiles to develop. The composition comparisons are reasonably good, and appear to improve with increasing downstream distance. Pitot pressures do not compare as well; this is very likely due to the assumption in the analysis of uniform static pressure. Computation of pitot pressure is accomplished by use of local Mach number, specific heat ratio, static pressure and the Rayleigh pitot formula; sensitivity to the level of static pressure is therefore large, and even a very weak shock can cause considerable error (particularly on the centerline in axisymmetric flow). Computed composition profiles at the 26.7 diameter station are compared with experimental data in figure 3. Note that the theoretical profile shapes look reasonable, and the reaction model predicts an overlap of hydrogen and oxygen profiles such as that found in the data. However, the curves are displaced radially. It is believed that the displacement is due to a combination of pressure effects and reaction model effects; both of these cause density inaccuracies that distort the computed profiles.

Better agreement with experiment is found in the application of the same theory to the data of reference 15 (figs. 4 and 5). Here again hydrogen is injected coaxially into an airflow, but in this case the flow is very low-speed. Centerline comparisons are quite good, and radially, the degree to which the theory overpredicts the spread of the mixing zone is less than in supersonic flow (fig. 3). It should be noted, however, that the supersonic case covers only the near field where initial conditions, injector geometry, and associated shock and expansion waves may have significant effects on the actual flow that are not accounted for in the theoretical calculation. The collective supersonic and subsonic results indicate that promising progress is definitely being made in analyzing turbulent reacting flows, but also emphasize the need for the ongoing work particularly in the treatment of reaction and pressure gradient.

The lack of appropriate experimental data for fundamental theoretical evaluation is even worse for three-dimensional flows. While a multitude of combustor data for a wide variety of geometries and applications are available, the detailed measurements are typically at the combustor exit. Defining initial conditions for a computation is sketchy at best due to the scarcity of measurements in the complex near-injector flow. To help alleviate this problem in the evaluation of three-dimensional combustor analyses, a cold-flow, strut-injection, constant-area, helium-air mixing experiment was conducted. Helium was used in place of hydrogen as a safety measure for cold-flow data acquisition. A schematic of the apparatus is shown in figure 6 (see reference 16 for details). The air nozzle is Mach 2.7, and the strut leading edge has a 6° half-angle. Helium injection took place from five equally spaced fuel injectors dividing the flow region at the strut into nearly square mixing regions. Four of the injectors are 10° conical nozzles (Mach 3.6); the other injector is actually two sonic jets directed toward each other.

Extensive pressure and composition measurements to provide initial conditions for analysis were taken at the 10.2 cm station. Detailed information was again obtained at the duct exit, and computations compared with these data. Figure 7 shows typical comparisons of velocity, temperature, and helium concentration in three vertical lines at the duct exit. The theoretical curves represent

the theory of reference 13, with the same type of two-equation turbulence model used in the 2-D theory. Agreement between data and theory is quite encouraging for all three variables. It should be noted that advantage was taken in the computation of symmetry planes along the center of the duct ($Y = Z = 0$) and between jets. Detailed handling of the complete duct in a single computer run is not practical at this time due to computer storage and to run-time constraints. However, the 150 K storage and 250 second run time for the figure 7 computations (on a CDC 6600) are also very encouraging.

Since the quantity of numerical information produced in a typical three-dimensional calculation is enormous, qualitative evaluation of each run is desirable with the aid of contour plots similar to those shown in figure 8. The decay of the central helium jet in figure 6 is depicted in this figure as computed by the finite-element theory of reference 14. Information such as profile spreading, boundary condition checks, and discretization checks can readily be determined from such plots. For example, the continuing sharp peak on the center-line in figure 8 indicates a need for additional elements inside the helium jet.

Application of the three-dimensional codes to hydrogen-air reacting flow in the same apparatus is currently underway. Also, modeling of the very near field is proceeding in order that the upstream data station (currently the initial computation station) can be represented satisfactorily from known conditons at the strut itself. Both semi-empirical global analysis and detailed elliptic analysis are being pursued. Pending successful achievement of these developments, coupled with turbulence and reaction models formulated from basic research, reasonably detailed analysis of scramjet combustors should be possible.

CONCLUDING REMARKS

Scramjet combustor analysis is progressing both in the turbulent mixing/reaction areas and in the handling of more complex geometries. Recent results have shown very promising agreement between theory and data, and research to further develop the various techniques is continuing. It should be emphasized that computations are generally only as good as their initial conditions, and models of the very near field must be improved if the state of the art is to progress beyond analysis to design. With persistent effort, however, the outlook is good for reasonably detailed prediction of scramjet combustor flow fields within the foreseeable future.

REFERENCES

1. Anderson, G. Y.: Hypersonic Propulsion. Paper XV, NASA SP-381, May 1975.

2. Henry, J. R.; and Beach, H. L.: Hypersonic Airbreathing Propulsion. Paper No. 8, NASA SP-292, Nov. 1971.

3. Henry, J. R.; and Anderson, G. Y.: Design Considerations for the Airframe-Integrated Scramjet. NASA TM X-2895, 1973.

4. Evans, J. S.; and Anderson, G. Y.: Supersonic Mixing and Combustion in Parallel Injection Flow Fields. Presented at AGARD Propulsion and Energetics Panel Meeting (Liege, Belgium), Apr. 1974.

5. Free Turbulent Shear Flows. NASA SP-321, 1973.

6. Murthy, S. N. B., ed: Turbulent Mixing in Nonreactive and Reactive Flows. Plenum Press, 1975.

7. Spalding, D. B.; Launder, B. E.; Morse, A. P.; and Maples, G.: Combustion of Hydrogen-Air Jets in Local Chemical Equilibrium. NASA CR-2407, 1974.

8. Lilley, D. G.: Turbulent Swirling Flame Prediction. AIAA Paper 73-651, July 1973.

9. Donaldson, C. DuP.: On the Modeling of the Scalar Correlations Necessary to Construct a Second-Order Closure Description of Turbulent Reacting Flows. Turbulent Mixing in Nonreactive and Reactive Flows, S. N. B. Murthy, ed, Plenum Press, 1975, pp. 131-162.

10. Chung, P. M.: A Kinetic Theory Approach to Turbulent Chemically Reacting Flows. TR E75-1, College of Engineering, University of Illinois at Chicago Circle, 1975.

11. Dash, S.; and Del Guidice, P.: Analysis of Supersonic Combustion Flow Fields with Embedded Subsonic Regions. (ATL TR 169, Advanced Technology Laboratories; NASA Contract NAS1-10948), NASA CR-112223, 1972.

12. Jenkins, R. V.: Mixing and Combustion of an Underexpanded H_2 Jet in Supersonic Flow. AIAA Paper 76-610, July 1976.

13. Dyer, D. F.; Maples, G.; and Spalding, D. B.: Combustion of Hydrogen Injected into a Supersonic Airstream (A Guide to the HISS Computer Program). NASA CR-2655, 1976.

14. Zelazny, S. W.; Baker, A. J.; and Rushmore, W. L.: Modeling of Three-Dimensional Mixing and Reacting Ducted Flows. NASA CR-2661, 1976.

15. Kent, J. H.; and Bilger, R. W.: Turbulent Diffusion Flames. Fourteenth Symposium (International) on Combustion, The Combustion Institute, pp. 615-625, 1973. (Primary Source - Kent, J. H.; and Bilger, R. W.: Measurements in Turbulent Jet Diffusion Flames. T.N. F-41, University of Sydney, 1972).

16. McClinton, C. R.: Evaluation of Scramjet Combustor Performance Using Cold Nonreactive Mixing Tests. AIAA Paper 76-47, Jan. 1976.
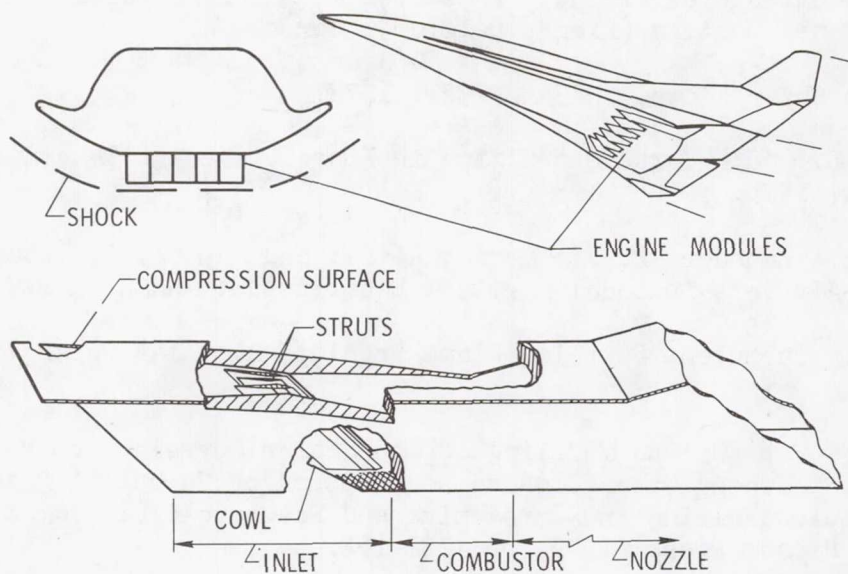
Figure 1.- Scramjet module concept. Fixed geometry from speeds of Mach 3 to 10.
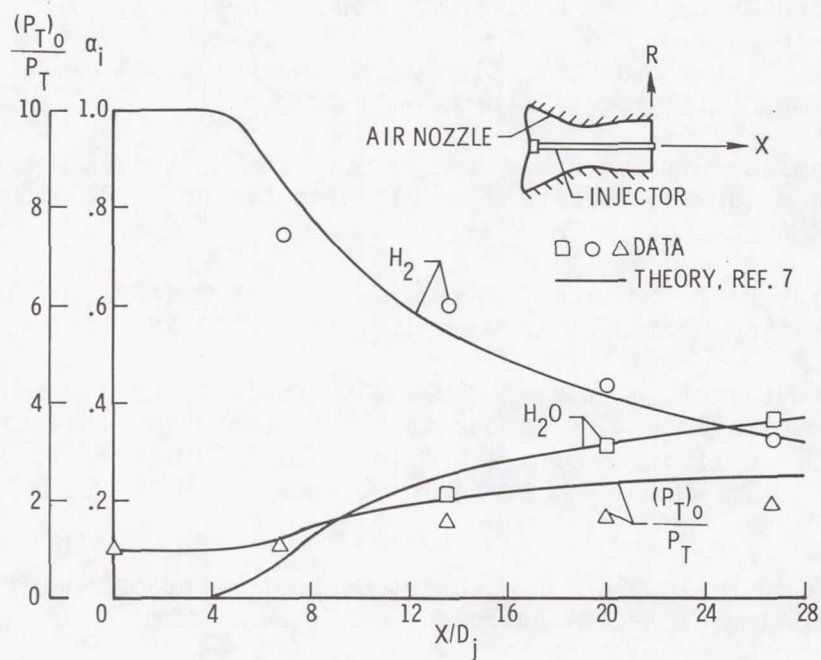
Figure 2.- Comparison of measured and computed centerline properties in supersonic flow.
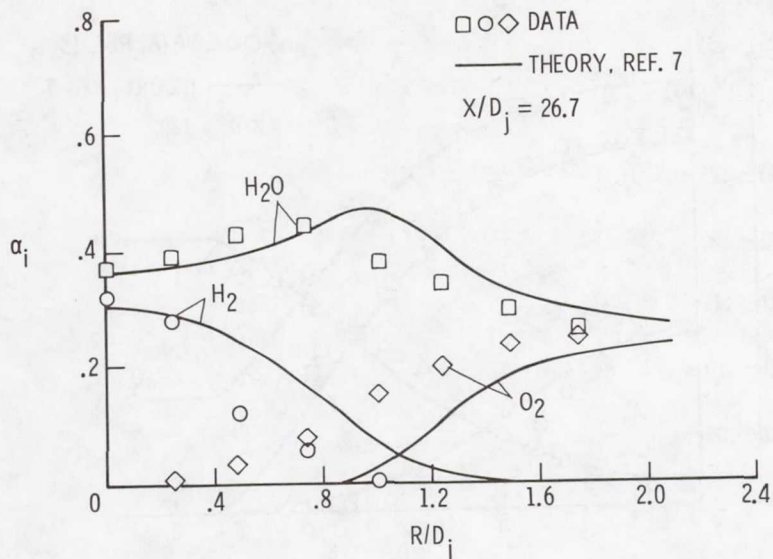
Figure 3.- Comparison of measured and computed radial properties in supersonic reacting flow.
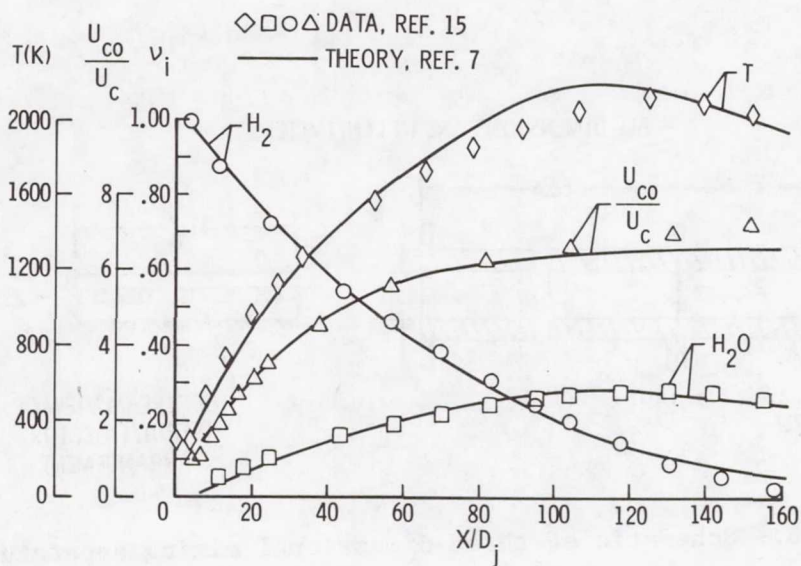
Figure 4.- Comparison of measured and computed centerline properties in subsonic reacting flow.
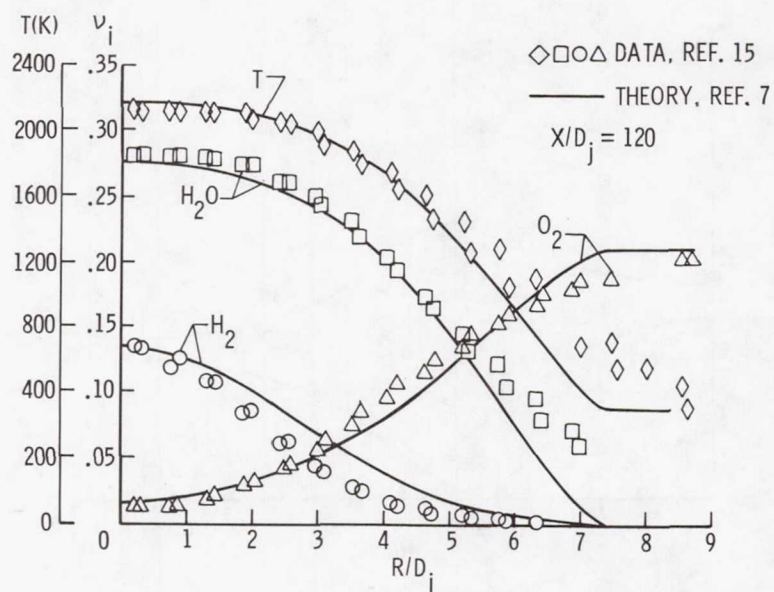
Figure 5.- Comparison of measured and computed radial properties in subsonic reacting flow.
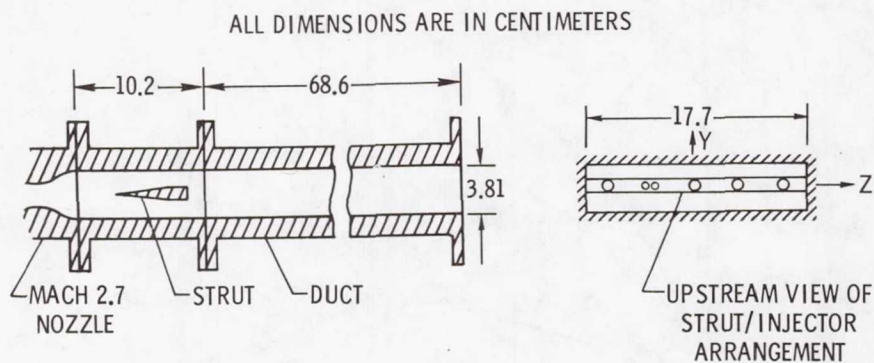
Figure 6.- Schematic of three-dimensional mixing apparatus.
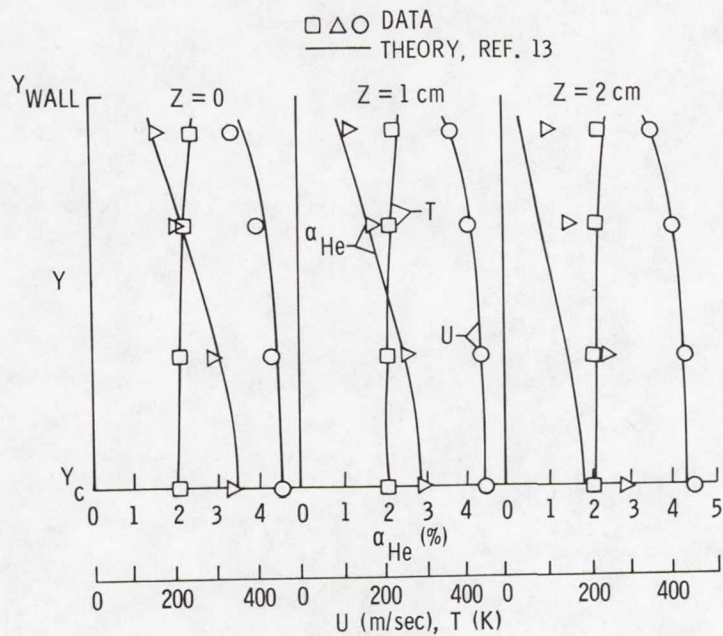
Figure 7.- Typical data-theory comparison at duct exit.
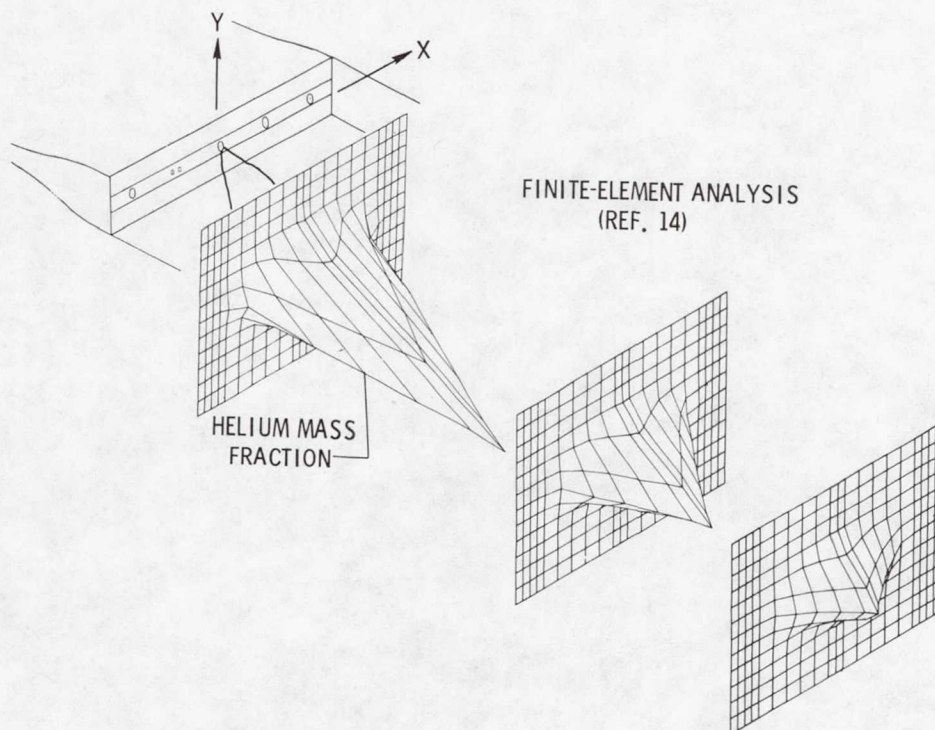
Figure 8.- Decay of central helium jet with downstream distance.

1639

Page intentionally left blank

THREE-DIMENSIONAL FINITE ELEMENT ANALYSIS OF ACOUSTIC INSTABILITY

OF SOLID PROPELLANT ROCKET MOTORS*

Robert M. Hackett and Radwan S. Juruf
Vanderbilt University

SUMMARY

A three-dimensional finite element solution of the acoustic vibration prob-
lem in a solid propellant rocket motor is presented. The solution yields the
natural circular frequencies of vibration and the corresponding acoustic pres-
sure mode shapes, considering the coupled response of the propellant grain to
the acoustic oscillations occurring in the motor cavity. The near incompressi-
bility of the solid propellant is taken into account in the formulation. A
relatively simple example problem is solved in order to illustrate the applica-
bility of the analysis and the developed computer code.

INTRODUCTION

Present solid propellant rocket combustion instability state-of-the-art
technology employs a linear analysis for predicting unsteady motions in the com-
bustion chamber of the rocket based on the hypothesis that the influences of
combustion and flow can be represented as perturbations of an acoustic problem
in a closed chamber. In order to perform an accurate combustion instability
analysis, one must have adequate knowledge of the natural circular frequency
and corresponding pressure mode shape for the different modes of acoustic oscil-
lation occurring in the motor cavity in the absence of combustion and flow.

The cavities in functional rocket motors generally have complex shapes
that may include a number of symmetrically located slots (or fins) cut into the
propellant, the purpose of which is to increase the area of the burning surface
(fig. 1). During the past several years, the need for experimental acoustic
modeling of such irregular cavity geometries has been greatly reduced through
the use of finite element modeling techniques (ref. 1). In the finite element
method, a continuum is modeled as an assemblage of elements, connected at dis-
crete locations (nodes). Natural frequencies and mode shapes are then obtained
from an eigensolution of the resulting equations of equilibrium of the modeled
dynamic system. Applications of the finite element method to more generalized
acoustic analysis problems are found in references 2 and 3.

The presence of the solid propellant grain can significantly shift the
acoustic system frequency from that of the gas phase alone, a portion of the
acoustic energy being dissipated by the deformable solid material. This effect
can be one of the more significant sinks for acoustic energy in both large and
small rocket motors, the amount of damping depending on the grain geometry, pro-
pellant mechanical properties, and the acoustic mode shape and frequency. It

is thus important to have the capability of finite element modeling of both the acoustic cavity and the propellant grain structure and, therefore, of a combination and coupling of fluid and solid elements. Analyses of coupled plate-acoustic systems are found in references 4 and 5, and a three-dimensional finite element coupled acousto-mechanical analysis is formulated in reference 6.

In the case at hand, the problem involves the coupling of the irrotational motions of an inviscid compressible fluid with the deformations of an incompressible (viscoelastic) solid material enclosing the fluid. Since the propellant grain is only accurately modeled as a nearly incompressible material, the well-known minimum potential energy finite element formulation, based upon Navier's equations of equilibrium and the Ritz procedure, is invalid. Formulations for cases of incompressible and nearly incompressible materials are found in references 7, 8, 9, 10, and 11. The solid finite element formulation utilized in this development is a linear displacement-linear mean pressure tetrahedron (ref. 10), similar to the Herrmann variational formulation (ref. 7) which employs a linear displacement function and a constant mean pressure function.

The eigensolution technique employed in the developed program is that of condensation, which is discussed in reference 12. The technique utilizes the master and slave degree-of-freedom (d.o.f.) concept. In this application, the fluid pressure d.o.f. are designated master and the solid displacement and mean pressure d.o.f. are designated slave.

SYMBOLS

Values are given in both SI and U.S. Customary Units. The calculations were made in U.S. Customary Units.

a,b,c,d	exponential factors
B	bulk modulus
[D]	degree-of-freedom to strain transformation matrix
[$\overline{E}$]	constitutive coefficient matrix
[f]	fluid element potential energy coefficient matrix
[F]	fluid system potential energy coefficient matrix
G	shear modulus
H	mean pressure parameter
[I]	identity matrix
[k]	solid element stiffness matrix
[K]	solid system stiffness matrix
L	natural or volume tetrahedral coordinate
[m]	solid element consistent mass matrix
[M]	solid system consistent mass matrix
p	pressure
P	point (defined in fig. 2)
S	surface area
[t]	fluid element kinetic energy coefficient matrix
[T]	fluid system kinetic energy coefficient matrix
u,v,w	displacement components
[U]	acoustic-solid coupling matrix
V	element volume
x,y,z	rectangular Cartesian coordinates
β	direction cosine
{Δ}	displacement vector
ε	strain

ν	Poisson's ratio
$[\Phi]$	transformation matrix defined by equation (14)
ρ	mass density
ω	natural circular frequency

Subscripts:

C	coupled		
i,j,ℓ,m	element node identifiers	e	element
p,q	number of degrees-of-freedom	T	transpose (of a matrix)
r,s	node identifiers (eq.(4))		
S	solid		

Superscripts:

EQUATIONS OF EQUILIBRIUM

Acoustic Cavity

In applying the finite element method, the region of concern is divided into a number of subregions, or elements. Applications of the method in modeling the behavior of a fluid continuum involve several pecularities not encountered in the usual structural applications. In the discretization of a fluid continuum, the finite elements represent spatial rather than material subregions of the continuum; i.e., instead of representing finite elements of the fluid material, the elements represent subregions in the space through which the fluid moves (Eulerian description of motion). Values of pressure at the nodal points of the element represent the pressures at the nodes rather than of the nodes (ref. 13).

For a three-dimensional region, a volume element is associated with a number of nodal points which define its shape. Within each fluid tetrahedral element the variation of the pressure p is prescribed by the values associated with the four element nodes through the expression:

$$p(x,y,z) = \lfloor L \rfloor \{p\}^e = \lfloor L_i \ L_j \ L_\ell \ L_m \rfloor \begin{Bmatrix} p_i \\ p_j \\ p_\ell \\ p_m \end{Bmatrix} \tag{1}$$

where the natural or volume coordinates $L_i, L_j, L_\ell,$ and L_m are defined mathematically by

$$\begin{Bmatrix} L_i \\ L_j \\ L_\ell \\ L_m \end{Bmatrix} = \begin{bmatrix} 1 & 1 & 1 & 1 \\ x_i & x_j & x_\ell & x_m \\ y_i & y_j & y_\ell & y_m \\ z_i & z_j & z_\ell & z_m \end{bmatrix}^{-1} \begin{Bmatrix} 1 \\ x \\ y \\ z \end{Bmatrix} \tag{2}$$

and physically by figure 1.

The matrix form of the homogeneous acoustic wave equations for the discretized fluid continuum is given by

$$([F] - \omega^2[T])\{p\} = \{0\} \tag{3}$$

where F is the coefficient matrix derived from a consideration of the potential energy of a fluid element, and T is the coefficient matrix derived from a consideration of the kinetic energy of the fluid element. The natural circular frequency of the discretely modeled fluid continuum is designated as ω.

The matrix F is developed through a superpositioning of the individual symmetric 4x4 element matrices, f, with restraint of the appropriate d.o.f. A typical term of the f matrix is (ref. 14):

$$f_{rs}^e = \frac{1}{\rho}\left(\frac{\partial L_r}{\partial_x}\frac{\partial L_s}{\partial_x} + \frac{\partial L_r}{\partial_y}\frac{\partial L_s}{\partial_y} + \frac{\partial L_r}{\partial_z}\frac{\partial L_s}{\partial_z}\right)V \tag{4}$$

where r and s take the values i,j,ℓ,m cyclically. The fluid mass density and the volume of the tetrahedron are designated ρ and V, respectively.

The matrix T is likewise developed through the superpositioning of the individual symmetric 4x4 element matrices, t, with restraint of the same appropriate d.o.f. The t matrix has the form (ref. 14):

$$[t] = \frac{1}{B}\int \begin{bmatrix} L_i^2 & L_iL_j & L_iL_\ell & L_iL_m \\ & L_j^2 & L_jL_\ell & L_jL_m \\ & & L_\ell^2 & L_\ell L_m \\ \text{sym} & & & L_m^2 \end{bmatrix} dxdydz \tag{5}$$

where B is the bulk modulus of the fluid. A useful integration formula for evaluating the terms in the t matrix is:

$$\int L_i^a L_j^b L_\ell^c L_m^d \ dxdydz = \frac{a!b!c!d!}{(a+b+c+d+3)!}6V \tag{6}$$

Solid Propellant

Within each solid tetrahedral element, the variation of displacement is prescribed by the displacement of each element node through the expression:

$$\begin{Bmatrix} u(x,y,z) \\ v(x,y,z) \\ w(x,y,z) \end{Bmatrix} = [L]\{\Delta\}^e = [L_iI \quad L_jI \quad L_\ell I \quad L_mI] \begin{Bmatrix} \Delta_i \\ \Delta_j \\ \Delta_\ell \\ \Delta_m \end{Bmatrix} \tag{7}$$

where I is the 3x3 identity matrix and where

$$\lfloor \Delta_i \rfloor = \lfloor u_i \quad v_i \quad w_i \rfloor, \text{ etc.} \tag{8}$$

The u,v,w terms are the displacement components in the x,y,z directions, respectively.

The matrix form of the homogeneous equations of motion for the discretized solid continuum is given by

$$\left(\begin{bmatrix} K \end{bmatrix} - \omega_S^2 \begin{bmatrix} M & 0 \\ \hline 0 & 0 \end{bmatrix} \right) \left\{ \frac{\Delta}{H} \right\} = \{0\} \tag{9}$$

where K is the stiffness matrix and M is the mass matrix. The term ω_S is the natural circular frequency of vibration of the solid system. The linear variation of the mean pressure parameter

$$H(x,y,z) = \frac{1}{1-2\nu} (\varepsilon_{xx} + \varepsilon_{yy} + \varepsilon_{zz}) \tag{10}$$

is prescribed in the same manner as were the pressure (in the acoustic cavity) and the displacement function, i.e.,

$$H(x,y,z) = \lfloor L \rfloor \{H\}^e = \lfloor L_i \quad L_j \quad L_\ell \quad L_m \rfloor \left\{ \begin{array}{c} H_i \\ H_j \\ H_\ell \\ H_m \end{array} \right\} \tag{11}$$

The terms ε_{xx}, ε_{yy}, and ε_{zz} are the normal strain components and ν is Poisson's ratio.

The matrix K is developed through a superpositioning of the individual symmetric 16x16 element stiffness matrices, k, with restraint of the appropriate d.o.f. The form of the matrix k is given by (ref. 10):

$$[k] = \begin{bmatrix} D^T & 0 \\ \hline 0 & I \end{bmatrix} \int [\Phi]^T [\bar{E}][\Phi] \, dxdydz \begin{bmatrix} D & 0 \\ \hline 0 & I \end{bmatrix} \tag{12}$$

where I is the 4x4 identity matrix and where

$$[D] = \begin{bmatrix}
\frac{\partial L_i}{\partial x} & \frac{\partial L_j}{\partial x} & \frac{\partial L_\ell}{\partial x} & \frac{\partial L_m}{\partial x} & 0 & 0 & 0 & 0 & 0 & 0 & 0 & 0 \\[4pt]
0 & 0 & 0 & 0 & \frac{\partial L_i}{\partial y} & \frac{\partial L_j}{\partial y} & \frac{\partial L_\ell}{\partial y} & \frac{\partial L_m}{\partial y} & 0 & 0 & 0 & 0 \\[4pt]
0 & 0 & 0 & 0 & 0 & 0 & 0 & 0 & \frac{\partial L_i}{\partial z} & \frac{\partial L_j}{\partial z} & \frac{\partial L_\ell}{\partial z} & \frac{\partial L_m}{\partial z} \\[4pt]
\frac{\partial L_i}{\partial y} & \frac{\partial L_j}{\partial y} & \frac{\partial L_\ell}{\partial y} & \frac{\partial L_m}{\partial y} & \frac{\partial L_i}{\partial x} & \frac{\partial L_j}{\partial x} & \frac{\partial L_\ell}{\partial x} & \frac{\partial L_m}{\partial x} & 0 & 0 & 0 & 0 \\[4pt]
0 & 0 & 0 & 0 & \frac{\partial L_i}{\partial z} & \frac{\partial L_j}{\partial z} & \frac{\partial L_\ell}{\partial z} & \frac{\partial L_m}{\partial z} & \frac{\partial L_i}{\partial y} & \frac{\partial L_j}{\partial y} & \frac{\partial L_\ell}{\partial y} & \frac{\partial L_m}{\partial y} \\[4pt]
\frac{\partial L_i}{\partial z} & \frac{\partial L_j}{\partial z} & \frac{\partial L_\ell}{\partial z} & \frac{\partial L_m}{\partial z} & 0 & 0 & 0 & 0 & \frac{\partial L_i}{\partial x} & \frac{\partial L_j}{\partial x} & \frac{\partial L_\ell}{\partial x} & \frac{\partial L_m}{\partial x}
\end{bmatrix} \quad (13)$$

$$[\Phi] = \begin{bmatrix}
1 & 0 & 0 & 0 & 0 & 0 & 0 & 0 & 0 & 0 \\
0 & 1 & 0 & 0 & 0 & 0 & 0 & 0 & 0 & 0 \\
0 & 0 & 1 & 0 & 0 & 0 & 0 & 0 & 0 & 0 \\
0 & 0 & 0 & 1 & 0 & 0 & 0 & 0 & 0 & 0 \\
0 & 0 & 0 & 0 & 1 & 0 & 0 & 0 & 0 & 0 \\
0 & 0 & 0 & 0 & 0 & 1 & 0 & 0 & 0 & 0 \\
0 & 0 & 0 & 0 & 0 & 0 & L_i & L_j & L_\ell & L_m
\end{bmatrix} \quad (14)$$

and

$$[\bar{E}] = 2G \begin{bmatrix}
1 & 0 & 0 & 0 & 0 & 0 & \nu \\
0 & 1 & 0 & 0 & 0 & 0 & \nu \\
0 & 0 & 1 & 0 & 0 & 0 & \nu \\
0 & 0 & 0 & \frac{1}{2} & 0 & 0 & 0 \\
0 & 0 & 0 & 0 & \frac{1}{2} & 0 & 0 \\
0 & 0 & 0 & 0 & 0 & \frac{1}{2} & 0 \\
\nu & \nu & \nu & 0 & 0 & 0 & -\nu(1-2\nu)
\end{bmatrix} \quad (15)$$

where G is the shear modulus of the material. The ordering of rows and columns in the k matrix corresponds to

$$\begin{bmatrix} u_i & u_j & u_\ell & u_m & v_i & v_j & v_\ell & v_m & w_i & w_j & w_\ell & w_m & H_i & H_j & H_\ell & H_m \end{bmatrix}$$

The matrix M is developed through the superpositioning of the individual symmetric 12x12 element mass matrices, m, with restraint of the same appropriate d.o.f. The consistent mass matrix, derived in references 15 and 16, is used in the formulation and is defined by:

$$[m] = \rho_S [L]^T [L] \, dxdydz \tag{16}$$

where ρ_S is the mass density of the solid propellant grain and where

$$[L] = [L_i I \quad L_j I \quad L_\ell I \quad L_m I] \tag{17}$$

Acoustic-Solid Coupling

The formulation of the coupled acoustic-solid equations through equilibrium considerations is found in references 5 and 6. Reference 5 deals with the transient response of a coupled system while, in reference 6 the eigenvalue problem is formulated. The matrix form of the homogeneous equations of equilibrium for the discretized coupled system is given by

$$\left(\begin{bmatrix} F & | & 0 \\ \hline -U^T & | & K \end{bmatrix} - \omega_C^2 \begin{bmatrix} T & | & U \\ \hline 0 & | & \begin{matrix} M|0 \\ \hline 0|0 \end{matrix} \end{bmatrix} \right) \begin{Bmatrix} P \\ \hline \Delta \\ \hline H \end{Bmatrix} = \{0\} \tag{18}$$

where ω_C is the natural circular frequency of the coupled system.

The matrix U of equation (18) has dimensions pxq, where p is the number of pressure d.o.f. and q is the number of displacement and mean pressure parameter d.o.f. The components of the U matrix are projections of the cavity-propellant interface area associated with each surface nodal point, the surface area distribution being physically defined in figure 3. The portion of the U matrix associated with the i,j,ℓ triangular surface area of a boundary tetrahedron is given by

$$\begin{bmatrix} \beta_{ix}S_i & 0 & 0 & | \beta_{iy}S_i & 0 & 0 & | \beta_{iz}S_i & 0 & 0 & | 0 & 0 & 0 \\ 0 & \beta_{jx}S_j & 0 & | 0 & \beta_{jy}S_j & 0 & | 0 & \beta_{jz}S_j & 0 & | 0 & 0 & 0 \\ 0 & 0 & \beta_{\ell x}S_\ell & | 0 & 0 & \beta_{\ell y}S_\ell & | 0 & 0 & \beta_{\ell z}S_\ell & | 0 & 0 & 0 \end{bmatrix}$$

where $\beta_{ix}, \dots, \beta_{\ell z}$ are the direction cosines and S_i, S_j and S_ℓ are the contributing (to a node) surface areas.

SOLUTION

Solution of the system mathematically modeled by equation (18) is facilitated by the use of condensation (ref. 12). In applying the technique to this problem, the pressure d.o.f. are designated _master_ and the displacement and mean pressure parameter d.o.f. are designated _slave_.

Example Application

The developed program is applied to the solution of the simple acoustic-solid system shown in figure 4. The plane defined by nodes 5678 is the acoustic-solid interface. The pressure is set equal to zero at nodes 1,2,3, and 4. Thus, for the corresponding solution, $p = 4$ and $q = 32$.

The properties of the cavity gas used are: a mass density ρ of 1.225 kg/m^3 (1.146 x 10^{-7} lb-sec^2/in^4) and a bulk modulus B of 1.42 x 10^5 Pa (20.59 lb/in^2). The properties of the solid propellant grain used are: a shear modulus G of 4.41 x 10^7 Pa (6400 lb/in^2), a Poisson's ratio ν of 0.5 and a mass density ρ_S of 1.770 x 10^3 kg/m^3 (1.656 x 10^{-4} lb-sec^2/in^4).

The solution for the coupled system yielded frequencies of 488 Hz, 1008 Hz, 1193 Hz, and 1804 Hz, compared to respectively corresponding values of 3670 Hz, 6934 Hz, 10,358 Hz, and 12,368 Hz obtained for the fluid system alone.

CONCLUDING REMARKS

It has been demonstrated through the use of a simple example that the developed computer code can be used to predict the effect of solid propellant grain structure on the natural frequency associated with the acoustic vibrations occurring in the rocket motor cavity. It can be concluded that the effect of certain suppression devices such as resonance rods can be predicted in the same manner.

REFERENCES

1. Final Report on the Investigation of Pressure Oscillations During Firing of the Minuteman II Stage III Motor. MTO-1124-34, Hercules Inc., Jan. 1971.

2. Craggs, A.: The Use of Simple Three-Dimensional Acoustic Finite Elements for Determining the Natural Modes and Frequencies of Complex Shaped Enclosures. J. Sound Vib., vol. 23, no. 3, 1972, pp. 331-339.

3. Shuku, T.; Ishihara, K.: The Analysis of the Acoustic Field in Irregularly Shaped Rooms by the Finite Element Method. J. Sound Vib., vol. 29, no. 1, 1973, pp. 67-76.

4. Pretlove, A.J.; Craggs, A.: A Simple Approach to Coupled Panel-Cavity Vibrations, J. Sound Vib., vol. 11, no. 2, 1970, pp. 207-215.

5. Craggs, A.: The Transient Response of a Coupled Plate-Acoustic System Using Plate and Acoustic Finite Elements. J. Sound Vib., vol. 15, no. 4, 1971, pp. 509-528.

6. Hackett, R. M.: Three-Dimensional Acoustic Analysis of Solid Rocket Motor Cavities. Tech. Rep. RK-76-7, U.S. Army Missile Command, Nov. 1975.

7. Herrmann, L. R.: Elasticity Equations for Incompressible and Nearly Incompressible Materials by a Variational Theorem. J. American Inst. Aero. Astro., vol. 3, no. 10, Oct. 1965, pp. 1896-1900.

8. Taylor, R. L.; Pister, K.; Herrmann, L. R.: On a Variational Theorem for Incompressible and Nearly Incompressible Orthotropic Elasticity. Int. J. Solids Struct., vol. 4, 1968, pp. 875-883.

9. Key, S. W.: A Variational Principle for Incompressible and Nearly Incompressible Anisotropic Elasticity. Int. J. Solids Struct., vol. 5, 1969, pp. 951-964.

10. Hughes, T. J. R.; Allik, H.: Finite Elements for Compressible and Incompressible Continua. Proc. Symp. Appl. Finite Element Meth. Civil Eng., Vanderbilt Univ., Nov. 1969, pp. 27-62.

11. Hwang, C. T.; Ho, M. K.; Wilson, N. E.: Finite Element Analysis of Soil Deformations. Proc. Symp. Appl. Finite Element Meth. Civil Eng., Vanderbilt Univ., Nov. 1969, pp. 729-746.

12. Cook, R. D.: Concepts and Applications of Finite Element Analysis, John Wiley & Sons, Inc., 1974.

13. Oden, J. T.; Somogyi, D.: Finite Element Applications in Fluid Dynamics. Proc. American Soc. Civil Eng., vol. 95, no. EM 3, June 1969, pp. 821-826.

14. Arlett, P. L.; Bahrani, A. K.; Zienkiewicz, O. C.: Application of Finite Elements to the Solution of Helmholtz's Equation. Proc. Inst. Elect. Eng., vol. 115, no. 12, Dec. 1968, pp. 1762-1766.

15. Archer, J. S.: Consistent Mass Matrix for Distributed Mass Systems. J.Struct. Div. American Soc. Civil Eng., vol. 89, no. ST4, Aug. 1963, pp. 161-178.

16. Archer, J. S.: Consistent Matrix Formulations for Structural Analysis Using Finite Element Techniques. J. American Inst. Aero. Astro., vol. 3, no. 10, Oct. 1965, pp. 1910-1918.
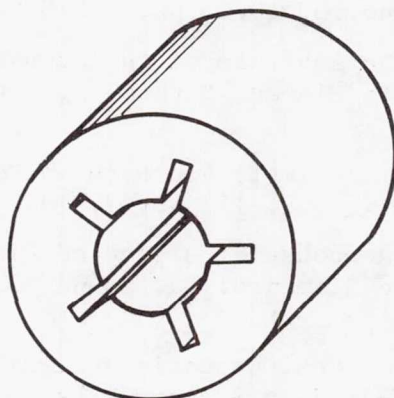
Figure 1.- Solid propellant configuration.

$$L_I = \frac{V_i}{V} \text{ , etc.}$$
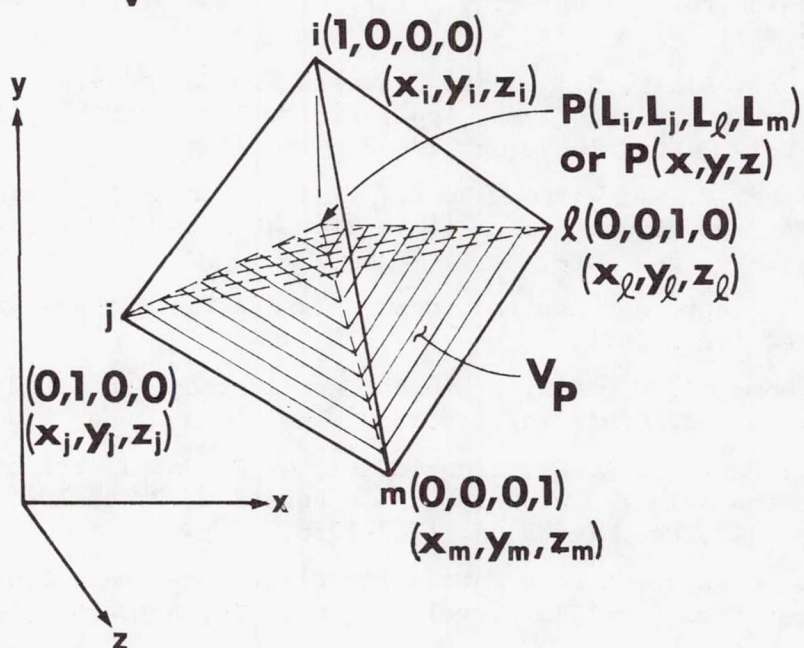
Figure 2.- Tetrahedral element (natural and global coordinates).
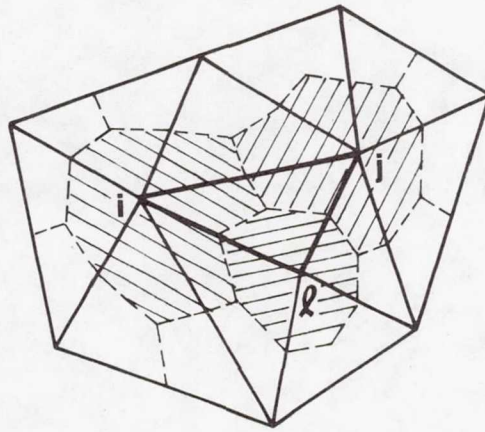
Figure 3.- Surface areas associated with
interfacial nodal points.
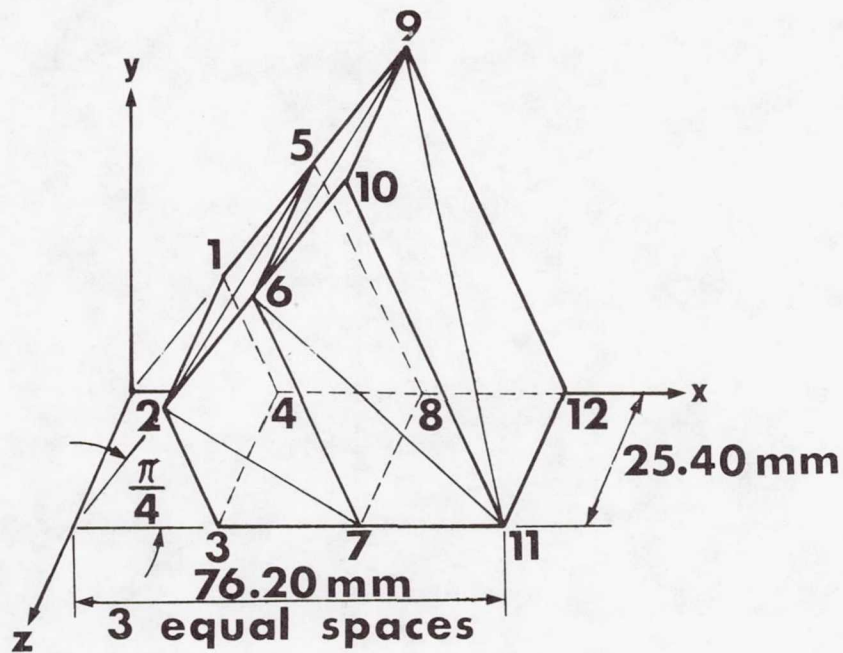
Figure 4.- Acoustic-solid system.

Page intentionally left blank

ACOUSTIC DISTURBANCES PRODUCED BY AN

UNSTEADY SPHERICAL DIFFUSION FLAME

Maurice L. Rasmussen
University of Oklahoma

SUMMARY

The disturbances produced by a moving spherical diffusion flame are investigated within the framework of a linearized theory. After the flame position and species concentrations are determined, the problem of determining the associated density, pressure, temperature, and velocity fields is delineated. Explicit results for certain limiting situations are discussed.

INTRODUCTION

This paper deals with the acoustic disturbances produced by an unsteady spherical diffusion flame. The basic problem is envisaged as follows. Inside an initial sphere of radius r_0, a mixture of oxidant (or fuel) and product gases exists, and outside the sphere a mixture of fuel (or oxidant) and product gases exists, as depicted in Figure 1. At an initial instant the spherical surface that separates the two initial mixtures disappears, and the subsequent combustion and acoustic disturbances are to be determined. We assume that the combustion of the initially unmixed oxidant and fuel species is confined to a spherical Burke-Schumann flame surface.

This problem is associated with the theory of particle and liquid-droplet combustion at high pressures, such as treated by Spalding (Ref. 1) and Rosner (Ref. 2). An applicable situation occurs when bubbles of oxidant (or fuel) are injected into a medium of fuel (or oxidant). The bubbles burst, or are ignited, and the subsequent disturbance field is to be determined. This investigation also pertains to the general study of unsteady diffusion flames and to the broad subject of spherical explosions.

Most investigations of diffusion flames have dealt with steady flows, starting with the original work of Burke and Schumann (Ref. 3). A number of such problems are described in texts and review articles (Refs. 4 and 5). In particular, detailed mathematical expositions for steady linearized flows have been developed by Clarke (Refs. 6 and 7); the present work is something akin to this framework of analysis. Unsteady diffusion flames have not been as thoroughly treated. Clarke and Stegen (Ref. 8) considered unsteady perturbations on a two-dimensional flame sheet. Rasmussen (Refs. 9 and 10) developed a linearized theory for the one-dimensional motion induced by a diffusion flame. In this paper the related problem of a spherical diffusion flame is treated.

Whereas the general form of the problem is nonlinear, the limiting acoustic approximation is of some interest. The explicit analytic results obtained within the linearized theory contain the embryonic behavior of the more complicated nonlinear problem. The linearized results, besides having their own intrinsic value, can be used to estimate the magnitude of convective terms and deviations from constant-property approximations. The gas dynamic interactions of the pressure, temperature, and velocity fields can be examined coherently within a linearized framework.

FORMULATION OF THE PROBLEM

Preliminary Remarks

We consider the basic combustion process that involves a mixture of oxidant (X), fuel (F), and product (P) species governed by the reaction equation

$$\chi\ X + f\ F \underset{t_r}{\overset{t_f}{\rightleftarrows}} g\ P \tag{1}$$

where χ, f, and g are the stoichiometric coefficients. The corresponding molecular weights for the species are denoted by W_X, W_F, and W_P. The forward and reverse reaction times are denoted by t_f and t_r. The essence of combustion is that $t_f \rightarrow 0$ and $t_r \rightarrow \infty$. In this sense, the reaction associated with (1) moves only to the right, and this is the limiting situation considered here. This simple reaction model has been utilized previously (Refs. 5-10). In this limit a uniform oxidant-product mixture exists inside the initial spherical diaphragm, of radius $\bar{r}_0$, and a uniform fuel-product mixture outside (or vice versa).

In the framework of a linearized theory, we begin with a basic uniform medium composed of entirely the product species at pressure, density, and temperature conditions denoted by p_0, ρ_0, and T_0. Inside the initial sphere we suppose that the pressure and temperature are perturbed such that $p = p_0(1+\Delta_p)$ and $T = T_0(1+\Delta_T)$. The corresponding oxidant and fuel mass fractions inside the initial sphere are denoted by $C_X = \Delta_X$ and $C_F = 0$. Outside the initial sphere the pressure and temperature are unperturbed, but the mass fractions are given by $C_X = 0$ and $C_F = \Delta_F$ (see Fig. 1). At a given instant, t = 0, the diaphragm disappears. We assume that the ambient temperature and density, T_0 and ρ_0, are sufficient to initiate combustion spontaneously. Combustion of the oxidant and fuel occurs at an interface, and a diffusion flame is established. In the limit $t_f \rightarrow 0$, the diffusion flame collapses to a discontinuity surface, and all the reactions occur entirely on this surface. On either side of the surface there are no reactions, but binary diffusion takes place.

The limiting situation $t_f \rightarrow 0$ produces a singular perturbation problem. The outer problem corresponds to the flame envisaged as the discontinuity surface. The inner problem deals with the structure of the flame and is obtained by matching with the outer problem. This procedure has been established previously for steady-flow problems (Refs. 5-7) and for one-dimensional unsteady flow problems (Refs. 9 and 10). Here we restrict ourselves to the lowest-order outer problem, with the flame treated as a discontinuity surface.

Basic Equations

When the mass fractions C_X and C_F are small, the pressure and thermal diffusion coefficients are small and are represented by nonlinear contributions. Consequently, since binary diffusion prevails on either side of the flame sheet, the diffusion-flux vectors are represented by Fick's law. As is usual in these problems, we assume the binary-diffusion coefficients are equal: $D_{XP} = D_{FP} = D$. We also assume that the components of the mixtures behave as thermally perfect gases. We now introduce dimensionless pressure, density, and temperature perturbations p', ρ', T' defined by

$$p = p_o(1+p') \quad , \quad \rho = \rho_o(1+\rho') \quad , \quad T = T_o(1+T') \tag{2}$$

We have correspondingly for the mass fractions and velocity:

$$C_X = C_X' \quad , \quad C_F = C_F' \quad , \quad C_P = 1 - C_X' - C_F' \tag{3}$$

$$\vec{v} = \vec{V}/a_{f_o} \quad , \quad a_{f_o}^2 = \gamma\, p_o/\rho_o \tag{4}$$

where a_{f_o} is the frozen speed of sound of the ambient medium and γ is the ratio of specific heats of the product species in the ambient medium. We represent the dimensionless space and time variables by

$$\vec{r} = a_{f_o}\, \vec{\bar{r}}/\widetilde{\nu}_o \quad , \quad \tau \equiv a_{f_o}^2\, t/\widetilde{\nu}_o \tag{5}$$

where $\widetilde{\nu}_o \equiv (2\mu_o + \lambda_o)/\rho_o$, and μ_o and λ_o are the first and second coefficients of viscosity. Since the problem of interest is spherically symmetric we introduce a velocity potential, $\vec{v} = \nabla\varphi$, where $\nabla \equiv \partial/\partial r$ (the barred space variables are dimensional). The characteristic Prandtl and Schmidt numbers are defined as

$$P_r \equiv \rho_o \widetilde{\nu}_o c_{p_o}/k_o \quad , \quad S_c \equiv \widetilde{\nu}_o/D_o \tag{6}$$

where c_{p_o} is the constant-pressure specific heat of the product species and k_o is the thermal conductivity, the subscript naught denoting the ambient state. With the above definitions, the linearized equations for mass, momentum, species, energy, and thermal equation of state become

$$\frac{\partial \rho}{\partial \tau} + \nabla^2\varphi = 0 \quad , \quad p = \gamma\left[\nabla^2\varphi - \frac{\partial\varphi}{\partial\tau}\right] \tag{7a,b}$$

$$D_S C_X = -S_c\, \chi\, W_X R \quad , \quad D_S C_F = -S_c\, f W_F R \tag{8a,b}$$

$$D_P T = \frac{\gamma-1}{\gamma}\, P_r \frac{\partial p}{\partial \tau} + P_r Q\, R \quad , \quad p = \rho + T + \alpha_X C_X + \alpha_F C_F \tag{9a,b}$$

The primes denoting the perturbation variables have been omitted. In the above we have the operators D_P and D_S, the parameters of α_X and α_F, and the dimensionless heat of reaction Q defined as

$$D_P \equiv P_r \frac{\partial}{\partial t} - \nabla^2 \quad , \quad D_S \equiv S_c \frac{\partial}{\partial \tau} - \nabla^2 \tag{10}$$

$$\alpha_X \equiv \frac{R_X}{R_P} - 1 \quad , \quad \alpha_F \equiv \frac{R_F}{R_P} - 1 \tag{11}$$

$$Q \equiv \left[\chi \, W_X (h_{X_O} - h_{P_O}) + f W_F (h_{F_O} - h_{P_O}) \right] / c_{P_O} T_O \tag{12}$$

where R_X, R_F and R_P are the specific gas constants. The symbol R denotes the dimensionless reaction rate. For the flame discontinuity sheet, R is given by

$$R = S(\tau) \, \delta(Z_n) \tag{13}$$

where $S(\tau)$ is the flame strength and $\delta(Z_n)$ is the Dirac delta function with Z_n the coordinate measured normal from the flame sheet. Derivations of these equations can be found in references 6, 9 and 10, and also in references 11 and 12 when there are no chemical reactions.

Continuity Conditions

All the physical flow variables are continuous at the flame sheet. Integration of equations (8a,b) and (9a) across the flame sheet shows that the following normal derivatives are discontinuous across the flame sheet:

$$\left[\frac{\partial}{\partial n} \left(\frac{C_X}{\chi W_X S_C} \right) \right]_-^+ = \left[\frac{\partial}{\partial n} \left(\frac{C_F}{f W_F S_C} \right) \right]_-^+ = - \left[\frac{\partial}{\partial n} \left(\frac{T}{Q P_r} \right) \right]_-^+ = S(\tau) \tag{14}$$

where the bracket rotation denotes the jump in value across the discontinuity. These jump conditions suggest that the following new variables be defined that do have continuous normal derivatives across the flame:

$$c^* \equiv C_F - \Psi \frac{\Delta_F}{\Delta_X} C_X \quad , \qquad T^* \equiv T + \frac{P_r Q}{S_C \chi W_F} C_X \tag{15a,b}$$

where

$$\Psi \equiv \frac{f W_F \Delta_X}{\chi W_X C_F} \tag{16}$$

is the stoichiometric fuel-oxidant ratio. With the new variables c^* and T^*, the reaction rate can be eliminated from the set of equations. Equations (8a,b) can be combined and equation (9a) can be recast to read

$$D_S c^* = 0 \quad , \qquad D_P T^* = \frac{\gamma - 1}{\gamma} P_r \frac{\partial p}{\partial \tau} + \frac{P_r Q (P_r - S_c)}{S_C \chi W_X} \frac{\partial C_X}{\partial \tau} \tag{17a,b}$$

The linearized state equation (9b) becomes

$$p = \rho + T^* \llcorner \alpha_F c^* - E \, C_X \quad \text{where} \quad E \equiv \frac{P_r Q}{S_c \chi W_X} - \alpha_X - \alpha_F \Psi \frac{\Delta_F}{\Delta_X} \tag{18a,b}$$

Equation (17a) is uncoupled from the other equations and can be solved separately, yielding C_X and C_F as well as the flame position. A single equation for the velocity potential can then be found by eliminating T^* in equation (17b) by means of equation (18) and then utilizing equations (7a,b) to eliminate p and ρ. We obtain

$$L(\varphi) = (S_c - P_r) \left[\alpha_F \, c^*_{\tau\tau} + \frac{P_r Q}{S_c \chi W_X} C_{X_{\tau\tau}} \right] + E \, D_P \, C_{X_\tau} \tag{19}$$

where

$$L(\varphi) \equiv \gamma \, \nabla^4 \varphi_\tau + \nabla^2 \left[\nabla^2 \varphi - (\gamma + P_r) \varphi_{\tau\tau} \right] + P_r \left[\varphi_{\tau\tau} - \nabla^2 \varphi \right]_\tau \tag{20}$$

Equation (17a) for C* can be solved separately. The initial conditions are $C*(r > r_0, 0) = \Delta_F$ and $C*(r < r_0) = -\psi\Delta_F$. Further, C* is finite at the origin and infinity, and both C* and C_r^* are continuous at $r=r_0$. The result is (Ref. 2):

$$\frac{C^*}{\Delta_F} = -\Psi + \frac{\Psi+1}{2}\left[\text{erfc}\left(\frac{1-r_*}{\sqrt{4\tau_*}}\right) + \text{erfc}\left(\frac{1+r_*}{\sqrt{4\tau_*}}\right)\right.$$

$$\left. + \frac{2}{r_*}\sqrt{\frac{\tau_*}{\pi}}\left\{e^{-(1-r_*)^2/4\tau_*} - e^{-(1+r_*)^2/4\tau_*}\right\}\right] \tag{21}$$

where $\quad r_* \equiv r/r_0$ and $\tau_* \equiv \tau/(r_0^2 S_c)$. $\hfill$ (22), (23)

The flame position $r = r_s(\tau)$ is determined from the condition $C^*(r_s, \tau) = 0$ but $r_s(\tau)$ cannot be obtained explicitly. For small τ_*, however, we obtain

$$r_{s*}(\tau_*) = 1 + 2 A\tau_*^{\frac{1}{2}} - 2\tau_* + 2A\tau_*^{3/2} - (4 + \frac{8}{3}A^2)\tau_*^2 + 0(\tau_*^{5/2}) \tag{24}$$

where $\quad\quad\quad\quad \text{erf}(A) \equiv (\Psi-1)/(\Psi+1)$. $\hfill$ (25)

The position of the flame with time is a function of the initial conditions through the parameter Ψ, defined by (16). When $\Psi=1$, the initial conditions are stoichiometric, and the flame travels inward toward the origin, linearly with τ when τ is small. When $\Psi > 1$ the initial conditions are oxidant-rich and the flame initially moves outward from the origin and then subsequently toward the origin. The case of fuel-rich initial conditions corresponds to $\Psi < 1$, and the flame moves only toward the origin, the position varying like $\tau^{\frac{1}{2}}$ when τ is small. This behavior is contrary to the one-dimensional (Refs. 9 and 10) problem in which the flame remains stationary under stoichiometric initial conditions and moves either to the right or left depending on whether Ψ is greater than or less than unity. Figure 2 shows the position of the flame as a function of τ_* for $\Psi = 1/2$, 1, and 2. When $\Psi=1$, for instance, the flame reaches the origin and becomes extinguished when $\tau_* \cong 0.21$.

The spherical diffusion flame travels ultimately inward. Because the species outside the sphere is of infinite extent and the species inside the sphere is of finite extent, the species inside the sphere tends to be consumed. Consequently, the flame eventually will move inward in order to add a relative diffusion rate for the vanishing inside species and thus maintain stoichiometric combustion at the flame. When the flame reaches the origin, the species originally inside the sphere has been completely consumed and the flame becomes extinguished.

The mass fractions are determined from the function C^*. For $r < r_s$, we have $C_X/\Delta_X = -C^*/(\Psi\Delta_F)$ and $C_F=0$. For $r > r_s$, we have $C_X=0$ and $C_F=C^*$. These profiles are plotted in Figure 3 for $\Psi=1$ and $\tau_* < 0.21$. When the flame becomes extinguished at the origin, the species inside the original sphere has been completely consumed, in this case the oxidant. For times greater than the extinguish-time, the species outside the original sphere proceeds to establish a uniform state. The return to a uniform state is shown in Figure 4.

Laplace-Transform Analysis

With C^* and C_x known, equation (19) constitutes a fifth order non-homogeneous equation for φ. Because the position of the flame varies with time, the problem is difficult to solve. A great simplification occurs when we set $P_r=S_c$ and $E=0$. For most gases setting $P_r=S_c$ is a good approximation. The approximation $E=0$ is valid when ratios of specific heats of all the species are the same. These approximations correspond to the Shvab-Zeldovich approximation (Ref. 4). With these approximations, the problem is very similar to the binary diffusion problem of Reference 12, without pressure diffusion, and we proceed in similar fashion.

If $\overline{\varphi}(r,s)$ denotes the Laplace transform with respect to time of $\varphi(r,\tau)$, the solution of the transform of $L(\varphi) = 0$ is

$$r\,\overline{\varphi}(r < r_o, s) = -\frac{r\Delta_p}{\gamma s^2} + A_1 \sinh \lambda_1 r + A_2 \sinh \lambda_2 r \tag{26a}$$

$$r\,\overline{\varphi}(r > r_o, s) = B_1 \exp(-\lambda_1 r) + B_2 \exp(-\lambda_2 r) \tag{26b}$$

where A_1, A_2, B_1 and B_2 are arbitrary constants of integration, and

$$\lambda_{1,2} \equiv \left[\frac{(\gamma+P_r)s^2 + P_r s \pm s \sqrt{\left[(\gamma-P_r)s + P_r\right]^2 + 4(P_r-1)P_r s}}{2(1+\gamma s)} \right]^{\frac{1}{2}} \tag{27}$$

where the plus sign holds for λ_1 and the negative sign for λ_2. The Laplace transforms of the pressure and density are found from (7a,b):

$$\overline{p}(r,s) = \gamma \left[(r\overline{\varphi})_{rr} - s\, r\, \overline{\varphi} \right]/r \tag{28}$$

$$\overline{\rho}(r < r_o, s) = -(\Delta_\rho/s) - (r\overline{\varphi})_{rr}/(rs) \tag{29a}$$

$$\overline{\rho}(r > r_o, s) = -(\alpha_F \Delta_F)/s - (r\overline{\varphi})_{rr}/(rs) \tag{29b}$$

The reduced temperature, T^*, is determined by means of equation (18). The velocity is determined by $v = \varphi_r$.

The constants A_1, A_2, B_1, and B_2 are determined by requiring that $\overline{\rho}$, $\overline{p}$, $\overline{v}$, and $\overline{T}_r^*$ be continuous at $r=r_o$. We find that

$$A_1 = (1+\lambda_1 r_o)e^{-\lambda_1 r_o} \Lambda_1/\lambda_1 \quad , \quad A_2 = -(1+\lambda_2 r_o)e^{-\lambda_2 r_o} \Lambda_2/\lambda_2 \tag{30a,b}$$

$$B_1 = (\sinh \lambda_1 r_o - \lambda_1 r_o \cosh \lambda_1 r_o)\Lambda_1/\lambda_1 \tag{31a}$$

$$B_2 = -(\sinh \lambda_2 r_o - \lambda_2 r_o \cosh \lambda_1 r_o) \Lambda_2/\lambda_2 \tag{31b}$$

where

$$\Lambda_1 \equiv \left[(\Delta_\rho + \alpha_F \Delta_F)(\lambda_2^2 - s)/s + \Delta_p \lambda_2^2/(\gamma s^2) \right]/(\lambda_2^2 - \lambda_1^2) \tag{32a}$$

$$\Lambda_2 \equiv \left[(\Delta_\rho + \alpha_F \Delta_F)(\lambda_1^2 - s)/s + \Delta_p \lambda_1^2/(\gamma s^2) \right]/(\lambda_2^2 - \lambda_1^2) \tag{32b}$$

$$\Delta_p = \Delta_\rho + \Delta_T + \alpha_X \Delta_X \tag{33}$$

The inversion of the transformed variables now remains.

Constant-Pressure Solution

When $P_r = S_c = 1$ we have the simplified results $\lambda_1 = \sqrt{s}$ and $\lambda_2 = s/\sqrt{1+\gamma s}$. Further when $\Delta p = 0$, the factor Λ_2 vanishes (hence $A_2 = B_2 = 0$), and the pressure perturbation is identically zero, $p(r,\tau) = 0$. The remaining solution is entirely diffusive:

$$v(r,\tau) = \frac{\Delta_\rho + \alpha_F \Delta_F}{2r^2 \sqrt{\pi \tau}} \left[(rr_o - 2\tau)e^{-(r-r_o)^2/4\tau} + (rr_o + 2\tau)e^{-(r+r_o)^2/4\tau} \right] \tag{34}$$

$$\rho(r,\tau) = \Delta_\rho - (\Delta_\rho + \alpha_F \Delta_F)\left[\psi + (C^*/\Delta_F) \right]/(1 + \psi) \tag{35}$$

$$T^*(r,\tau) = \Delta_{T^*}\left[1 - (C^*/\Delta_F) \right]/(1+\psi) \tag{36}$$

where C^*/Δ_F is given by equation (21), and $\Delta_{T^*} \equiv \Delta_T + (Q\Delta_X/\chi W_X)$. Wave behavior does not occur in this special case.

The temperature at the flame sheet is determined from expression (36) by setting $C^* = C_X = 0$. We obtain

$$\Delta T_f \equiv T^*(r_s,\tau) = \left[\Delta_T + (Q\Delta_X/\chi W_X) \right]/(1 + \psi) \tag{37}$$

The increment ΔT_f is the adiabatic flame temperature. It does not vary with time. The temperature is found from equation (15b) to be

$$T(r \le r_s,\tau) = \Delta T_f + (\Delta T_f - \Delta_T) C^*/(\psi \Delta_F) \tag{38a}$$

$$T(r \ge r_s,\tau) = \Delta T_f \left[1 - (C^*/\Delta_F) \right] \tag{38b}$$

This temperature distribution is shown in Figure 5 for $\psi = 1$ and $\Delta_T = 0$.

Large-Time Behavior

An asymptotic approximation can be obtained for large times, and the results for density, pressure, velocity and T* are similar to those obtained in References 11 and 12. The major difference from these results occurs in the temperature distribution (as contrasted with the reduced temperature T*). When $\Delta_p \ne 0$, a gasdynamic expansion wave travels inward from the initial sphere, r_o, cooling the gas. This wave reflects from the origin and travels outward. The result after this reflected wave passes the position of the initial sphere is a reduction in temperature by an amount $(\gamma - 1)\Delta_p/\gamma$. This temperature residual is subsequently eliminated by thermal diffusion (Ref. 11). Thus for times long after the reflected wave passes the initial sphere, the net effect is to change the initial temperature increment such that

$$\Delta_T \rightarrow \Delta_T - (\gamma - 1)\Delta_p/\gamma \tag{39}$$

For large Reynolds numbers ($r_o \gg 1$), the wave processes are much faster than the diffusion processes, and under these circumstances formulas (36-38) hold

for the temperature long after the reflected wave passes the initial sphere, with the modification (39) noted. When $P_r \neq 1$, the time is also modified such that $\tau \rightarrow \tau/P_r$ in the function $C*$.

When $\Delta_p = 0$, but $P_r \neq 1$, there is a weak pressure wave generated that is proportial to (P_r-1) (Refs. 10 and 13). This wave does not affect the temperature distribution near the flame since Δ_T is left unaltered.

CONCLUDING REMARKS

The present analysis demonstrates the main features associated with unsteady spherical diffusion flames. It would be useful to continue the analysis without the approximations $P_r = Sc$ and $E = 0$. For the one-dimensional problem (Ref. 10) there are weak waves generated by the combustion at a stationary diffusion flame that are proportional to E. It would be interesting to investigate these waves for a moving spherical diffusion flame. The inner problem associated with the structure of the flame is also worthy of further attention.

REFERENCES

1. Spalding, D.B.: Theory of Particle Combustion of High Pressures. ARS Journal, Vol. 29, 1959, pp. 828-834.

2. Rosner, D.E.: On Liquid Droplet Combustion at High Pressures. AIAA Journal, Vol. 5, No. 1, 1967, pp. 163-166.

3. Burke, S.P. and Schumann, T.E.W.: Diffusion Flames. Ind. Engr. Chemistry, Vol. 20, 1928, pp. 998-1004.

4. Williams, F.A.: Combustion Theory, Addision-Wesley, London, 1965, Chap. 3.

5. Williams, F.A.: Theory of Combustion in Laminar Flows. Annual Review of Fluid Mechanics, Annual Reviews, Inc., Palo Alto, Calif., Vol. 3, 1971, pp. 171-188.

6. Clarke, J.F.: The Laminar Diffusion Flame in Oseen Flow: The Stoichiometric Burke-Schumann Flame and Frozen Flow. Proc. Roy. Soc., A296, 1967, pp. 519-545.

7. Clarke, J.F.: The Laminar Diffusion Flame Behind a Blunt Body: A Constant Pressure Oseen Flow Model. J. Inst. Maths. Applics., Vol. 3, 1967, pp. 347-361.

8. Clarke, J.F. and Stegen, G.R.: Some Unsteady Motions of a Diffusion-Flame Sheet. J. Fluid Mechanics, Vol. 24, Part 2, 1968, pp. 343-358.

9. Rasmussen, M.L.: Diffusion Flames Associated with Weak Explosions. Aero Note 2-74, Cranfield Institute of Technology, Aerodynamics Division, Cranfield, Bedford, England, 1974.

10. Rasmussen, M.L.: Acoustic Motion Induced by a Diffusion Flame. AIAA

Paper No. 75-525, AIAA 2nd Aero-Acoustics Conference, Hampton, Va., March 24-26, 1975. To appear Vol. 1 of "Jet, Combustion and Engine Core Noise" of AIAA Progress Series in Astronautics and Aeronautics.

11. Rasmussen, M.L. and Lake, J.G.: Viscous and Heat-Conduction Effects in Weak Spherical Explosions. Developments in Mechanics, Vol. 7, Proceedings of the 13th Midwestern Mechanics Conference, Univ. of Pittsburgh Engr. Dept., 1973, pp. 217-230.

12. Rasmussen, M.L. and Frair, K.L.: Diffusion Effects on Weak Spherical Disturbances in Binary Mixtures. Developments in Theoretical and Applied Mechanics, Vol. 8, Proceedings of 8th Southeastern Conference on Theoretical and Applied Mechanics, VPI and SU, Blacksburg, Va., 1976, pp. 589-601.

13. Frair, K.L.: An Investigation of Weak Spherical Explosions. Ph.D. Dissertation, University of Oklahoma, Norman, Oklahoma, 1974.

$$\overline{r} < \overline{r}_o, \ t < 0$$

$$C_X = \Delta_X$$
$$C_F = 0$$
$$p' = \Delta_p$$
$$T' = \Delta_T$$

$$\overline{r}_o$$
$$\overline{r}$$

$$\overline{r} > \overline{r}_o, \ t < 0$$

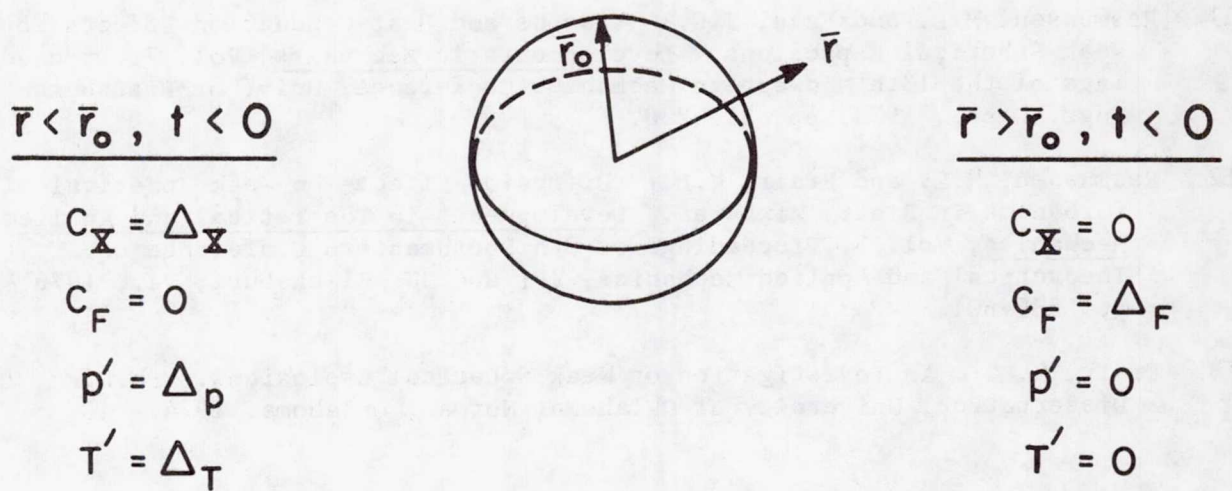$$C_X = 0$$
$$C_F = \Delta_F$$
$$p' = 0$$
$$T' = 0$$
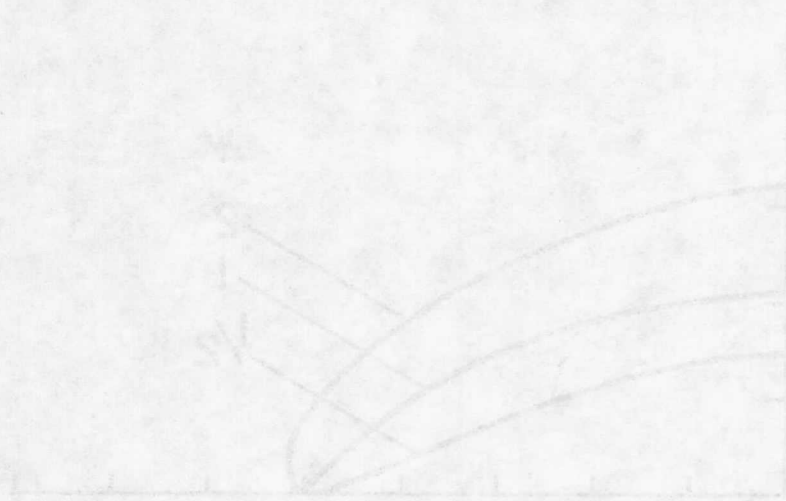
Figure 1.- Initial conditions and spherical configuration.
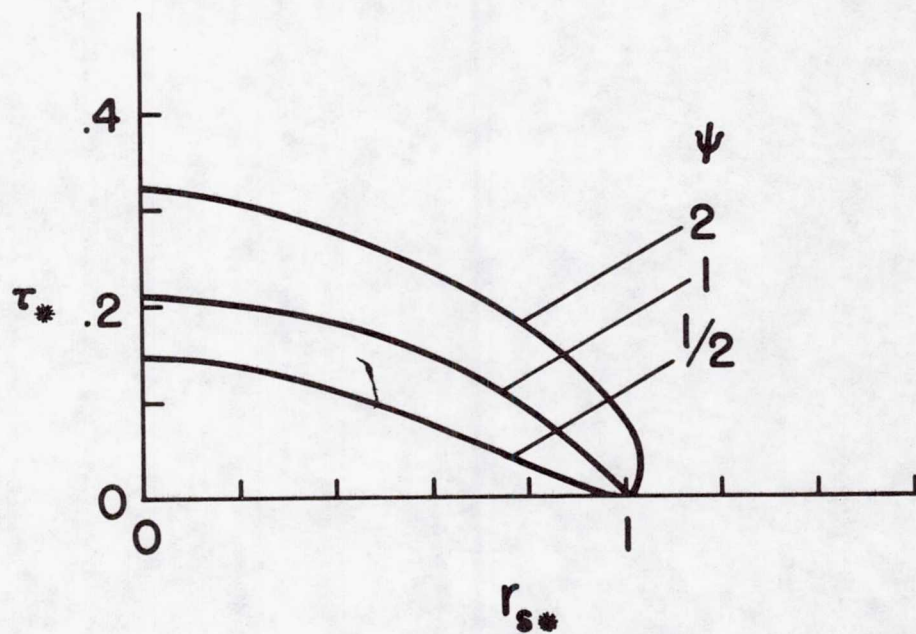

Figure 2.- Flame position as a function of time.
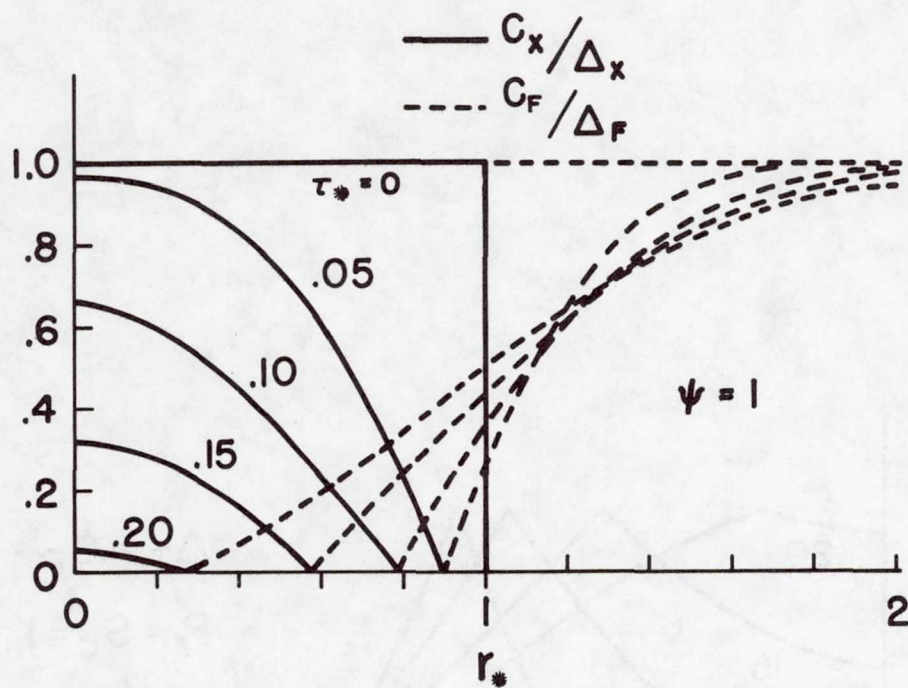
Figure 3.- Oxidant and fuel concentrations before flame extinguishment.
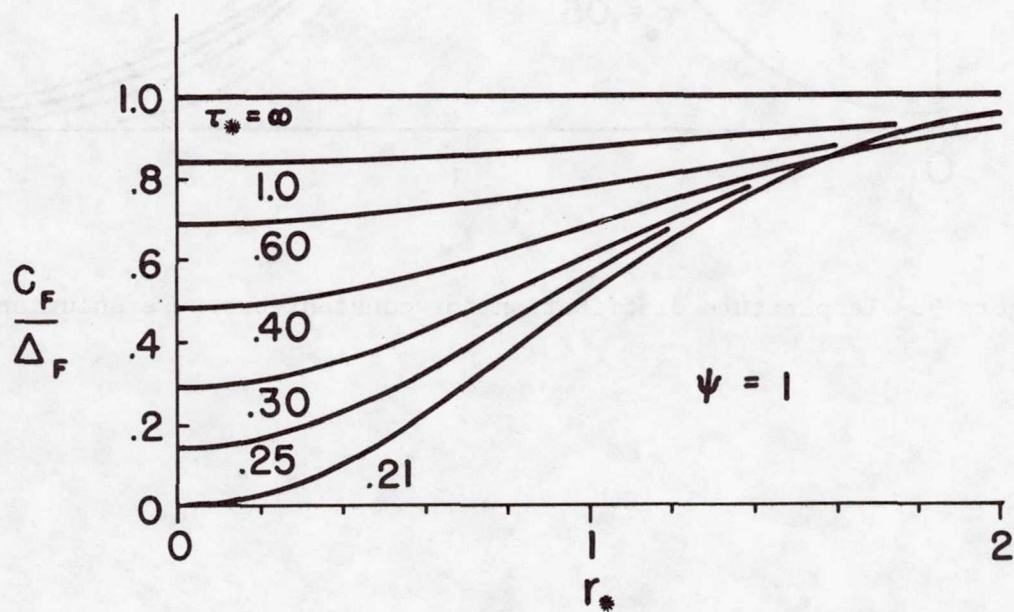
Figure 4.- Fuel concentration after flame extinguishment.
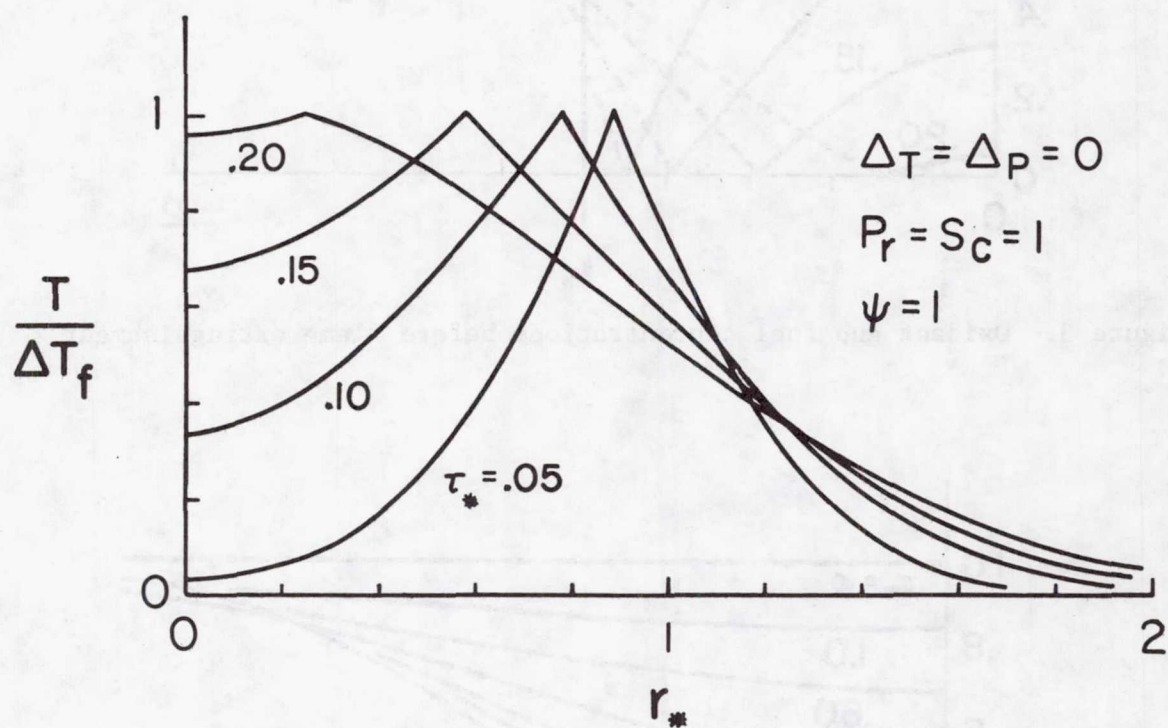
Figure 5.- Temperature distribution for constant-pressure solution.

FLOW FIELD FOR AN UNDEREXPANDED, SUPERSONIC NOZZLE

EXHAUSTING INTO AN EXPANSIVE LAUNCH TUBE

Robert R. Morris and John J. Bertin
The University of Texas at Austin

James L. Batson
U.S. Army Missile Command

SUMMARY

Static-pressure distributions along the launcher wall and pitot-pressure measurements from the annular region between the rocket and the launcher have been made as an underexpanded supersonic nozzle exhausted into an expansive launch tube. The flow remained supersonic along the entire length of the launcher for all nozzle locations studied.

INTRODUCTION

A variety of military rockets are launched from launch tubes (called non-tipoff launch tubes) having a constrictive change in cross section which allows the rocket to be constrained initially after ignition, while momentum is gained. During the time when the rocket exhausts directly into the small-diameter, aft-tube, the flow downstream of the nozzle exit is entirely supersonic and inter-secting, weak shock waves occur. The weak shock wave which results when the exhaust flow impinges on the wall produces a streamwise increase in the pres-sure. Although some of the fluid in the shear layer cannot overcome the adverse pressure gradient due to the weak, impingement shock and is turned upstream into the annular region between the rocket and the launcher, i.e., becomes blow-by flow, the mass-flow rate of the blow-by flow is negligible. The resultant flow field is that for an underexpanded, supersonic jet exhausting into a constant-area tube having an inside diameter which is slightly larger than the nozzle exit (ref. 1).

Since the rocket has gained sufficient momentum by the time the nozzle-exit plane clears the aft tube, the rocket flies free of constraints in the forward tube. However, as the exhaust flow encounters the constrictive change in area, a considerable fraction of the exhaust flow may be turned upstream. The mass-flow rate of the blow-by flow depends on the characteristics of the flow impingement (and, therefore, on the Mach number and the pressure in the nozzle-exit plane, on γ of the exhaust gas, on the nozzle-half angle, and on the ratio forward-tube radius:nozzle-exit radius), on the distance from the nozzle-exit plane to the constriction, and on the constrictive geometry (i.e., the step geometry and the ratio aft-tube radius:forward-tube radius).

Significant blow-by flow was observed during a flight-test program (ref. 2) in which rockets were launched from non-tipoff launch tubes, for which the ratio $A_{aft}:A_{for}$ was 0.595. Because of the complexity of the flow in the launcher, additional data were needed to construct a realistic flow model. The necessary data were obtained in a test program (ref. 3) in the Rocket Exhaust Effects Facility at the University of Texas at Austin in which an underexpanded jet of unheated air was exhausted from a stationary nozzle into a constrictive launch tube. These cold-gas tests clearly showed that the exhaust flow was choked by the constriction so that the impingement shock was a normal shock wave. As a result, a significant fraction of the exhaust flow (approximately 14%) could not overcome the large adverse pressure gradient associated with the strong impingement shock.

Negligible blow-by flow was observed during a flight-test program (ref. 4) in which rockets were launched from a non-tipoff launch tube for which the ratio $A_{aft}:A_{for}$ was 0.717. However, in the supplementary cold-gas tests, the exhaust flow choked and significant blow-by flow was measured once the nozzle-exit plane had gone 15 r_{ne}, or more, into the forward tube of a launcher for which $A_{aft}:A_{for}$ was 0.735. The discrepancy between the flight-test data and the cold-gas data was attributed (ref. 5) to differences in the growth characteristics of the boundary layer for the two tests, in the nozzle half-angle, and in the geometry of the constriction.

The flow fields which result when the underexpanded, supersonic nozzle exhausts into a constrictive launch tube are qualitatively similar to the flows which are generated in second-throat ejector-diffuser systems (ref. 6). However, the generation of significant blow-by flow prohibits close correlations between the launcher flow fields and the ejector-diffuser flows.

Since the creation of possible unbalanced forces on the rocket by exhaust gases which are turned upstream as blow-by flow are of special concern, it is desirable to eliminate blow-by flow completely. Therefore, a series of tests were conducted in which unheated air was exhausted through an underexpanded, supersonic nozzle into an expansive launch tube. For this launch tube, the ratio $A_{aft}:A_{for}$ was 1.680. The pressure distributions along the launcher wall and the blow-by flow rates which were recorded when the nozzle exit plane was located from 0.00 r_{ne} to 5.86 r_{ne} into the small-diameter forward tube are discussed in the present paper.

SYMBOLS

p   static wall pressure

p_{atm} atmospheric pressure

p_p pitot pressure

p_{t1} reservoir stagnation pressure

r_{ne} nozzle-exit radius

x axial coordinate relative to the change in cross section

x_{ne} axial location of the nozzle-exit plane

TEST PROGRAM

Static wall-pressure distributions and pitot pressures were measured as the underexpanded, supersonic jet exhausted into the expansive launcher.

Rocket Exhaust Effects Facility. - Unheated air, for which γ was 1.4, exhausted from a convergent:divergent nozzle. The throat radius was 0.95 cm. (0.38 in.), the nozzle-exit radius was 1.44 cm. (0.565 in.), and the half angle of the conical nozzle was 10°. Data were obtained for reservoir stagnation pressures from 1.66 x 10^6 N/m^2 (240 psia) to 6.90 x 10^6 N/m^2 (1000 psia). Thus, assuming isentropic flow in the nozzle, the theoretical value of the static pressure in the nozzle-exit plane for the lower reservoir pressure was only slightly greater than the atmospheric value.

The instrumented, variable-area launch tube could be moved axially to vary the location of the nozzle-exit plane relative to the constriction and, thereby, to simulate (in a quasi-steady manner) the flow fields which result when the rocket accelerates through the launcher. The assumption that the exhaust flow for the dynamic rocket launching was quasi-steady was based on the fact that the velocity of the exhaust gas was more than twenty times the velocity of the rocket as it left the launcher. As illustrated by the sketch of Fig. 1, the overall length of the launcher was approximately 84.6 cm. (33.3 in.). The large-diameter, aft tube, which was approximately 38.6 cm. (15.2 in.) long, was 4.45 cm. (1.75 in.) in diameter. The forward tube, which was approximately 46.0 cm. (18.1 in.), was 3.43 cm. (1.35 in.) in diameter. The change in cross section was accomplished by a rectangular step, which served as the origin for the dimensionless axial coordinate system. Thus, as indicated in Fig. 1, a negative value of the dimensionless, axial coordinate corresponds to a location in the small-diameter, forward tube of the launcher.

RESULTS AND DISCUSSION

A pitot probe was located in the annular region between the "rocket" nozzle and the launch tube at the forward end of the launcher (i.e., the left end of the launcher in Fig. 1) to record the possible existence of blow-by. The pitot pressure measured when the nozzle-exit plane was at the step (i.e., x_{ne} = 0.0 r_{ne}) is presented in Fig. 2 as a function of the reservoir stagnation pressure. Over the entire range of stagnation pressure tested, the experimentally determined pitot pressure was less than the atmospheric pressure. Thus,

the nozzle:expansive-launcher configuration acted as an ejector system and there was no blow-by flow. The increasing pitot pressure indicates that the entrained flow rate decreased as the reservoir stagnation pressure increased. As the reservoir stagnation pressure increased, the pressure in the nozzle-exit plane increased in direct proportion. As a result, the exhaust flow expanded through a greater angle as it left the nozzle and, therefore, had to be turned through a greater angle by the wall, increasing the pressure downstream of the impingement shock wave and reducing the entrained mass-flow rate.

The static wall-pressure distribution near the impingement of the exhaust flow is presented in Fig. 3 for x_{ne} = 0.0 r_{ne}. A schlieren photograph of the flow exhausting into the atmosphere (which has been trimmed where the launcher wall would be) is included to illustrate the flow mechanisms which produce the pressure distribution. Shock waves which intersect at the nozzle axis indicate that the acceleration of the flow in the conical divergent section was not an isentropic process. However, measurements of the transverse pitot-pressure distributions indicate that these intersecting shock waves were relatively weak. (See ref. 7 for a discussion of the origin of these shocks.) The inter- cepting shock wave and the viscous shear layer at the jet boundary are evident farther from the axis. The oblique shock wave generated as the flow impinged on the wall produced a sudden increase in the static-wall pressure. Downstream of the impingement shock, the streamwise pressure decrease, due to the acceler- ation of the flow, was terminated abruptly as the shock generated within the nozzle and the intercepting shock wave intersected at the wall. These imping- ing shock waves produced a slight increase in pressure.

However, as indicated in the pressure distributions presented in Fig. 4, the flow remained supersonic throughout the launcher. This remained true as the nozzle was moved farther into the small-diameter, forward tube (refer to Fig. 1 for the nozzle exit positions for which pressures are presented in Fig. 4). Since the ratio of the radius of the forward tube to the radius of the nozzle-exit plane (r_{ne}) was only 1.195, the angle between the flow at the jet boundary and the wall was relatively large when the underexpanded nozzle exhausted into the forward tube. Thus, the impingement shock wave was stronger for the nozzle-exit locations of Figs. 4b and 4c. However, the supersonic flow downstream of the impingement shock accelerated through the change in area. As a result, there was no blow-by flow for any of the nozzle-exit positions.

CONCLUDING REMARKS

The static pressure distributions along the launcher wall and the pitot- pressure measurements from the annular region between the rocket and the launcher indicate that no blow-by occurred when the underexpanded, supersonic nozzle exhausted into an expansive launch tube. This was true for all values of the reservoir stagnation pressure and of the nozzle exit location.

REFERENCES

1. Fabri, J., and Siestrunck, R.: "Supersonic Air Ejectors", Advances in Applied Mechanics, Vol. V, Academic Press, Inc., New York, 1958, pp. 1-34.

2. Bertin, J.J., and Batson, J.L.: "Experimentally Determined Rocket-Exhaust Flowfield in a Constrictive Tube Launcher", Journal of Spacecraft and Rockets, Dec. 1975, Vol. 12, No. 12, pp. 711-717.

3. Bertin, J.J., Morris, R.R., Garms, G.M., Motal, M.R., and Faria, H.T.: "Experimental Study of an Underexpanded, Supersonic Nozzle Exhausting Into A Constrictive Launch Tube", Aerospace Engineering Report 75001, June 1975, The University of Texas at Austin.

4. Bertin, J.J., and Galanski, S.R.: "The Analysis of Launch Tube Flow-Field for Arrow Firings", Aerospace Engineering Report 75004, May 1975, The University of Texas at Austin.

5. Bertin, J.J., and Batson, J.L.: "Comparison of Cold-Gas Simulations and Rocket-Launch Data for Constrictive Launchers", submitted for possible publication in the Journal of Spacecraft and Rockets.

6. German, R.C., Bauer, R.C., and Panesci, J.H.: "Methods for Determining the Performance of Ejector-Diffuser Systems", Journal of Spacecraft and Rockets, Feb. 1966, Vol. 3, No. 2, pp. 193-200.

7. Back, L.H., and Cuffel, R.F.: "Detection of Oblique Shocks in a Conical Nozzle with a Circular-Arc Throat", AIAA Journal, Dec. 1966, Vol. 4, No. 12, pp. 2219-2221.
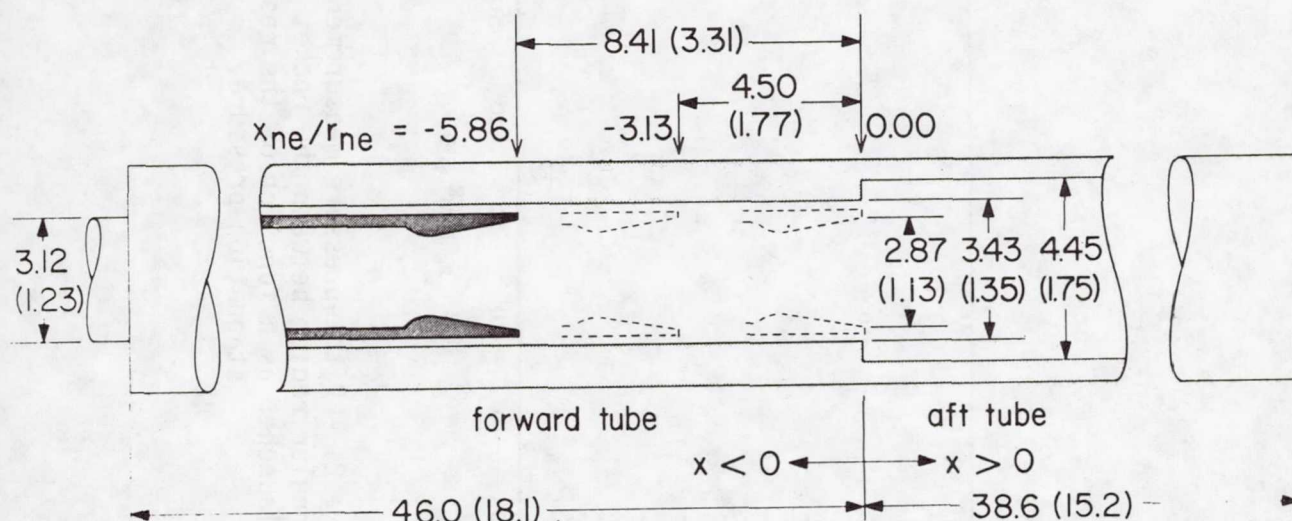
Figure 1. - Sketch of supersonic "rocket" nozzle in the expansive launch tube.
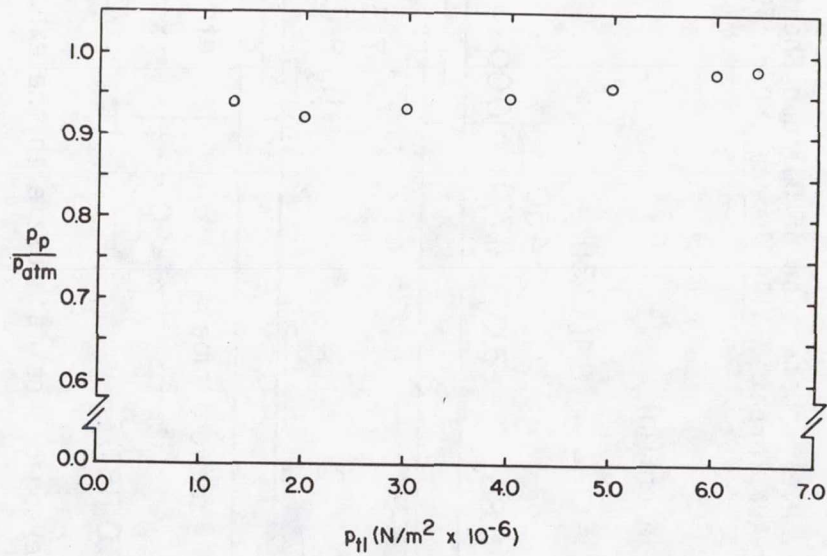
Figure 2. - Pitot-pressure measurements from the annular region between the rocket and the launcher as a function of the reservoir stagnation pressure.
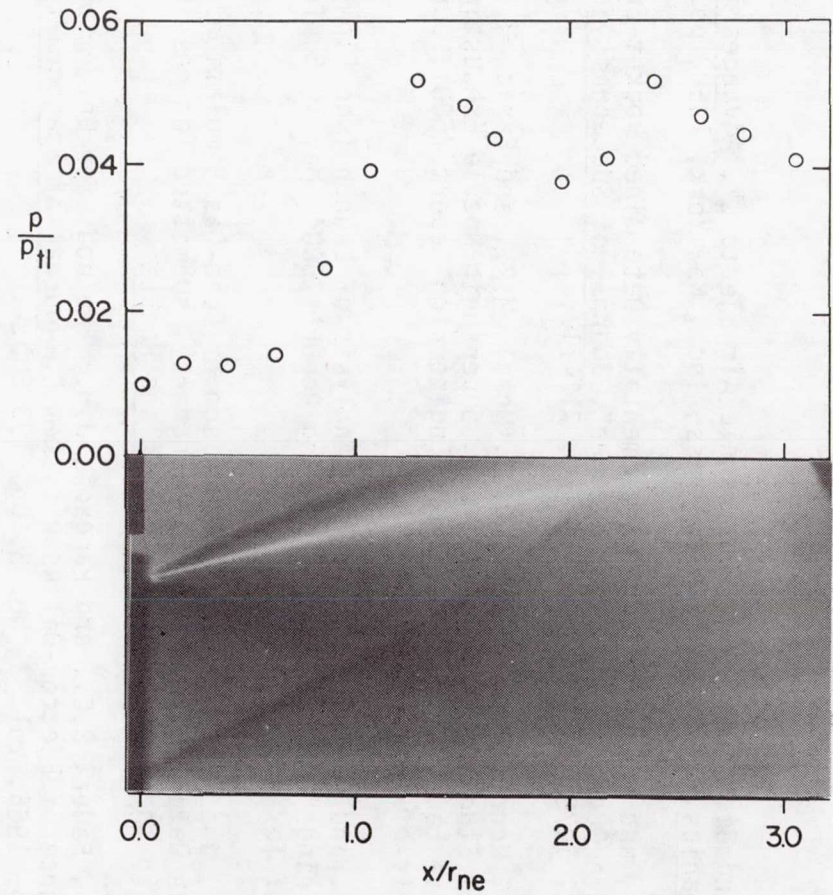
Figure 3. - Static-wall-pressure distribution near the impingement of the exhaust flow.

$$p_{t1} \approx 6.4 \times 10^6 \ N/m^2,$$
$$x_{ne} = 0.0 \ r_{ne}.$$
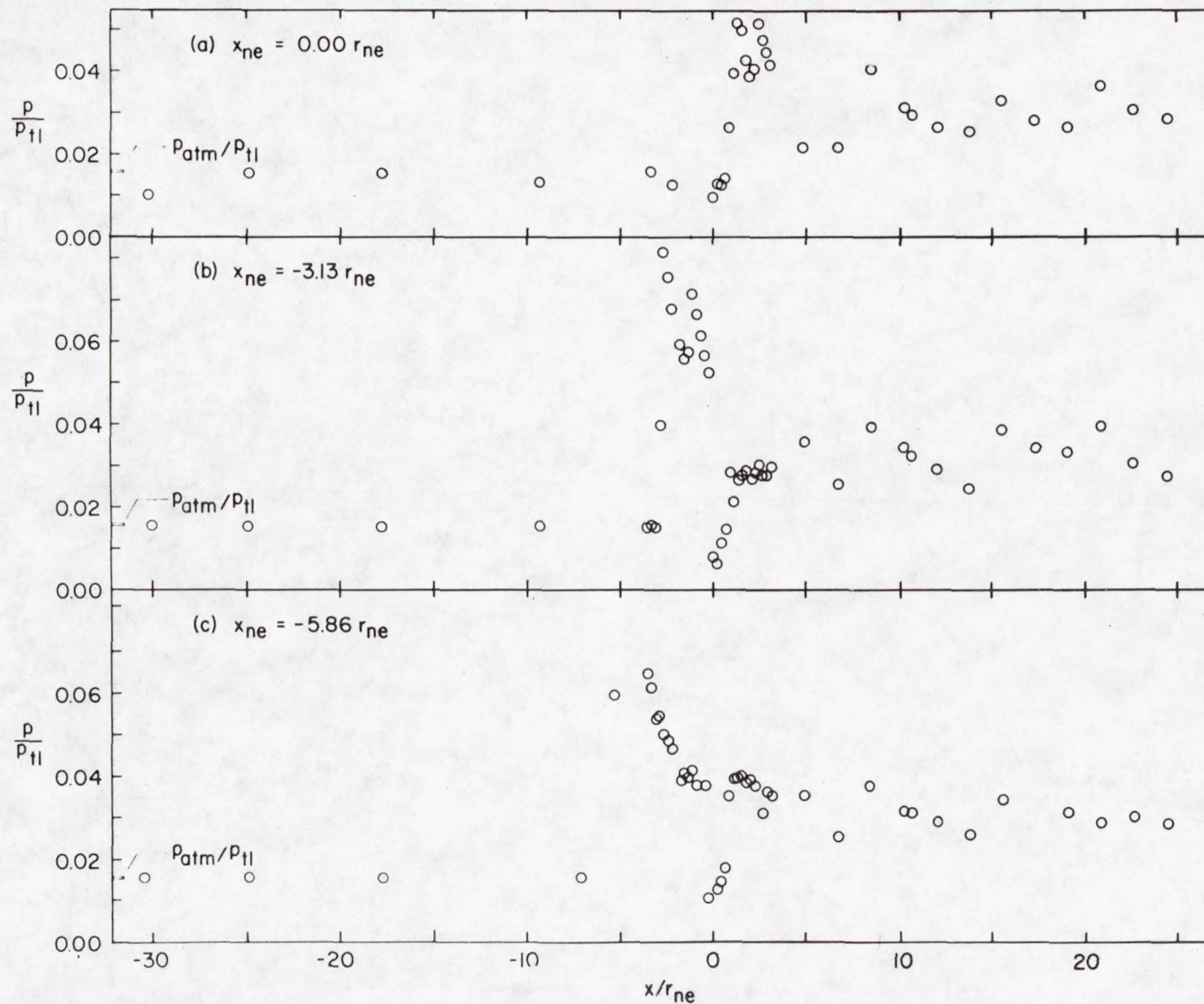
Figure 4. - The static wall-pressure distributions for the entire expansive launch tube for three nozzle-exit locations. $p_{t1} \approx 6.4 \times 10^6$ N/m^2.

Page intentionally left blank

EFFECTS OF PERIODIC UNSTEADINESS
OF A ROCKET ENGINE PLUME ON
THE PLUME-INDUCED SEPARATION
SHOCK WAVE[*]

Julian O. Doughty
The University of Alabama, Tuscaloosa

SUMMARY

A wind-tunnel investigation was conducted to study the flow field in which separation is caused by an expanding plume, with emphasis on effects associated with periodic unsteadiness in the plume. The separation shock was photographed with high-speed motion pictures, from which mean shock position and excursion data are reported. Pressure fluctuations were measured beneath the separation shock and statistics of the results are reported. A response of the separation shock to plume periodic unsteadiness was identified, and the magnitude of a corresponding transfer function was defined and is reported.

INTRODUCTION

A rocket booster vehicle will typically have a significantly under-expanded engine exhaust in the latter duration of its burn. The exhaust then plumes to a large diameter and alters the vehicle flow field considerably. Significantly, the plume is usually large at the altitude where the vehicle encounters maximum dynamic pressure.

When a large plume is generated by a vehicle in supersonic flight, it causes separation of the vehicle boundary layer well forward of the plume itself, and a separation shock wave radiates from a position near the separation point. The flow field is illustrated in figure 1. An inherent unsteadiness exists for this flow field as is often experienced in rigid surface compression corner flow at large Reynolds numbers. (For example, see references 1,2,3, and 4.) Separation shock excursions of several meters were reported by Jones from in-flight observations of a Saturn V vehicle (ref. 5). One would expect rather severe surface pressure fluctuations to accompany such shock motion.

Since large liquid fuel rocket engines exhibit a periodic unsteadiness, the question of that influence on the separation shock excursions and the resulting surface pressures becomes one of importance. This paper

presents some results of a wind-tunnel simulation of plume-induced flow separation with and without periodic plume unsteadiness.

SYMBOLS

Values are given in SI Units. The measurements and calculations were made in U.S. Customary Units.

F	plume forcing, atm^2
f	frequency, Hz
G	power spectral density, atm^2-sec
$\lvert H(f) \rvert$	transfer function magnitude
q	test-section dynamic pressure, atm
R	response to periodic plume unsteadiness, atm^2
U	test-section freestream velocity, m/sec
x	shock position, cm (figure 1)
$\bar{x}$	mean shock position, cm
δ	boundary-layer thickness, cm
θ	shock angle, deg (figure 1)
σ	standard deviation, cm

MODEL AND TEST FACILITIES

Model Description

The basic configuration of the model used in this study is a cone-cylinder body which uses secondary air flow to produce a plume near the aft end. (See figure 2.) The model is wall-mounted with its axis of symmetry located at the wind-tunnel wall boundary-layer displacement thickness as calculated by the method of Maxwell and Jacocks (ref. 6). This mounting arrangement was selected to provide access for the secondary plume flow and to minimize the distance from the generation of the plume unsteadiness (plume pulsing) and the plume itself. (The significance of minimizing this distance will be discussed later.)

Stainless steel fins are used to isolate the plume to a sector. The

upper fin surfaces extend into the plume nozzle and settling chamber so that
all model geometry in the sector between the fins is that of a body of revo-
lution. Therefore, flow in the sector between the fins simulates true axi-
symmetric flow except for the boundary layer on the fin surfaces, and the
distance from the fin leading edge to the separation shock is kept small to
minimize the boundary-layer effect. The leading edge of the fin is sharp,
beveled away from the flow sector. A dihedral angle, limited by line-of-
sight requirements across the top of the model, is set into the fins to re-
move them from the tunnel wall boundary layer. Oil flow studies, pressure
measurements on the upper model surface, and Schlieren studies were con-
ducted to assure that axisymmetric flow had been realized. All indications
were positive except for some flow angularity in a small region at the fin-
cylinder intersection. A lightly knurled band is located just behind the
cone-cylinder intersection to promote a turbulent boundary layer.

Plume Generation

The plume is generated by secondary flow directed through the tunnel
wall into a settling chamber in the core of the plume (figure 3). Flow from
the settling chamber issues through the nozzle which is formed by two conical
surfaces sharing a common vertex. Therefore, the nozzle flow is approximately
spherical source flow, and it has an isentropic exit Mach number of 2.94.
The solid core in the plume center not only provides space for a settling
chamber and instrumentation, but also greatly reduces the secondary mass flow
required while still generating the required forward plume surface for the
study. Without the plume core the secondary mass flow requirements would
have presented severe problems in terms of the physical size of the supply
ports.

Plume Pulsing

Pulsing or periodic unsteadiness was induced in the plume stagnation
pressure by a periodic partial relief of the plume supply air. This was
accomplished by periodically diverting a part of the plume supply air to the
atmosphere. The apparatus for doing this was a variable-speed rotating disk
with evenly spaced holes on a circumference which aligned with a teflon
orifice which was teed off the plume air supply. Pulse frequency was con-
trolled by the disk rotational speed and the pulse magnitude was controlled
by the orifice size. The arrangement is shown in figure 3.

The pressure signal, measured in the plume settling chamber, generated
by the pulsing apparatus was that of a periodic component superimposed on a
larger steady component. The periodic part was approximately a sine wave,
especially for cases in which the orifice size was about the same as the disk
holes. The wave was somewhat like a "flattened sine wave" for tests in which
the orifice was considerable smaller than the disk holes.

The time required for a pulse to travel from the orifice to the plume
settling chamber places an upper limit on the frequency for which a good
pressure signal can be generated. In this experiment the distance from the
orifice to the settling chamber was approximately 10 cm, and wave distortion

was evident at frequencies above 500 or 600 Hz. At 1000 Hz the distortion was severe. A periodic wave was produced but with a greatly reduced amplitude and an appearance more like a rectified sine wave. It was assumed that individual pulses were interfering with each other. Data reported here are for frequencies well below the distortion range.

Instrumentation

Surface pressure fluctuations at the separation shock were measured by a flush-mounted strain-gage-type transducer with a diameter of 2 mm and a natural frequency above 100 kHz. The static pressure level was eliminated by feeding the signal from a surface orifice, located laterally adjacent to the transducer, through a 3 m length of tubing to the reverse side of the transducer diaphragm. The length of tubing filtered the fluctuations and provided a time-average reference so that the transducer sensed only the fluctuations. This technique was suggested by Mr. L. Muhlstein, Jr. of Ames Research Center, who was also kind enough to supply filtering data.

Plume pressure fluctuations were measured by a crystal-type transducer located in the plume settling chamber. All fluctuating pressure data were stored on magnetic tape for subsequent reduction.

Separation shock geometric data were taken from high-speed Schlieren motion pictures taken at 800 frames per second with an exposure of 0.002 seconds. Measurements were then made by single frame projection of the resulting film onto a grid.

Boundary-layer thickness was measured by using two parallel stagnation probes mounted on a micrometer locater. The edge of the boundary layer was identified as the position, nearest the body, for which the pressures balanced.

Wind Tunnel

The wind tunnel used in this project was a blowdown supersonic tunnel with a 16-by 16-cm test section, located at The University of Alabama, Tuscaloosa. A major part of the data collection and reduction was done by Messers J. D. Dagen and F. L. Smith.

Test Conditions

All data reported are for the following freestream conditions:

Mach no. = 2.9

airspeed = 607 m/sec

stagnation temperature = 288 to 294 K

static pressure = 0.151 atm

stagnation pressure = 4.76 atm

dynamic pressure = 0.878 atm

Reynolds no. = 4.9×10^7 per meter.

The plume stagnation pressure was nominally 33 atm. That value located the mean position of the separation shock on the surface pressure transducer and generated a characteristic signal which could readily be identified on an oscilloscope.

RESULTS

Separation Shock Excursion

Observation and measurements from the high-speed motion pictures showed that the separation shock was in constant motion, regardless of whether or not there was plume pulsing. As it moved, it maintained essentially a constant shock angle with the freestream. In these tests, the shock angle was 28 degrees and mean shock location, $\bar{x}$, was 5.87 cm. In this context, shock location and separation length are taken to be the same (see figure 1). Histograms of shock excursion for a steady plume and for four different pulsing frequencies are shown in figure 4. Each histogram represents 4,000 measured positions. The root-mean-square level of plume pressure pulses for these data is 4.3 percent of the plume stagnation pressure.

There are no distinctions among the histograms which could not be attributed to experimental error and the finite data sample. The magnitude of plume pulsing used was sufficient to produce obvious distinctions in the surface pressure power spectra associated with the separation shock excursions (to be discussed later). Therefore, if any effect exists of plume unsteadiness on the shock excursion histogram, it is rather subtle.

The motion pictures of shock travel were viewed at several different frame speeds. It was not possible to distinguish the effect of plume pulsing in this manner. In all instances the impression from viewing movement of the shock was that it jumps from one position of momentary stability to another in an apparently random manner.

Fluctuating Pressure Power Spectra

One of the most obvious effects of periodic plume unsteadiness appears on the power spectrum of the surface pressure beneath the separation shock. A spike, located at the pulsing frequency, is generated in the spectrum, (see figures 5 and 6). Figure 5 shows the pressure signals as taken directly from a one-third octave filtering system, and figure 6 shows power spectra of the

same data normalized as suggested by Coe* (ref. 1). The spike is produced
by 80 Hz plume pulsing at an RMS level of 3.76 percent of the plume stag-
nation pressure. The broadband level of the basic spectrum (unpulsed) is
166.6 dB and that of the spectrum associated with 80 Hz pulsing is 166.9 dB.

Comparing the spectra and noting that the broadband (integrated)
levels are the same leads to the conclusion that the spike is formed at the
expense of the balance of the spectrum. In fact, within the limits of data
scatter, this conservation of the spectrum integral, with respect to periodic
plume pulsing at various frequencies and strengths, has been observed in all
instances (over 100 tests) in the course of this project.

<div align="center">Response to Plume Pulsing</div>

For the purpose of quantitatively relating plume unsteadiness to the
pressure fluctuations at the foot of the separation shock, the plume forcing
magnitude is defined to be that area under the resulting spectrum spike which
is above the spectrum with the spike faired out. In determining the area
under the spike, each one-third-octave band produces a rectangular area
consistent with the filter process by which the spectrum is produced. This
is not withstanding the fact that it is often the practice to connect the
points with a curve to display the spectrum. The quantities identified as
"forcing" and "response" are clearly not the only ones which could have been
chosen. Since there is some arbitrariness, the "best" definitions will
likely vary according to personal preference and situation. However, it is
hoped that the definitions selected are reasonable and useful.

With the definitions stated, the response to periodic plume unsteadiness
is displayed in figure 7. Within experimental error, over the range tested,
a linear relationship exists which is independent of pulse frequency. The
results can be expressed in terms of a transfer function if it is postulated
that forcing and response are reasonably represented by a linear differential
equation. Then the magnitude of the transfer function is

$$|H(f)| = \sqrt{\frac{R(f)}{F(f)}} = 0.0169 \qquad (16\text{Hz} \le f \le 250 \text{ Hz}), \tag{1}$$

and is constant for these data.

---

*Except that Coe used δ measured just ahead of the shock, whereas in this
case δ was measured at the shock location, but in the absence of a plume
and consequently a separation shock. For these data, δ = 0.53 cm.

CONCLUDING REMARKS

Several effects associated with plume-induced flow separation have been identified. The following statements are applicable over the range of this study:

1. The separation shock exhibits an excursion about some mean location and maintains essentially constant direction as it moves. This is true with or without plume unsteadiness.

2. The probability that the separation shock is located in a given position interval at a given instant is not influenced by plume unsteadiness.

3. Periodic plume unsteadiness produces a spike on the separation shock surface pressure power spectrum. The spike strength is proportional to the plume pulsing magnitude. The proportionality is constant over a frequency range.

4. The broadband level of the separation shock surface pressure fluctuations is not affected by periodic plume unsteadiness, so that the spectrum spike is produced at the expense of the balance of the spectrum.

REFERENCES

1. Coe, C. F.: Surface-Pressure Fluctuations Associated with Aerodynamic Noise. NASA SP-207, 1969, pp. 409-424.

2. Coe, C. F. and Chye, W. J.: Pressure-Fluctuation Inputs and Response of panels Underlying Attached and Separated Supersonic Turbulent Boundary Layers. NASA TM X-62, 189, 1972.

3. Kistler, A. L.: Fluctuating Wall Pressure Under a Separated Supersonic Flow. J. Acoust. Soc. Am., Vol. 36, No. 3, 1964, p. 543.

4. Trilling, L.: Oscillating Shock Boundary-Layer Interactions. J. Aero. Sci., May 1958, pp. 301-304.

5. Jones, J. H.: Acoustic Environmental Characteristics of the Space Shuttle. Proc. Space Shuttle Technology Conf., July 1970.

6. Maxwell, H. and Jacocks, J. L.: Nondimensional Calculation of Turbulent Boundary-Layer Development in Two-Dimensional Nozzles of Supersonic Wind Tunnels. AEDC-TN-61-153, 1962.
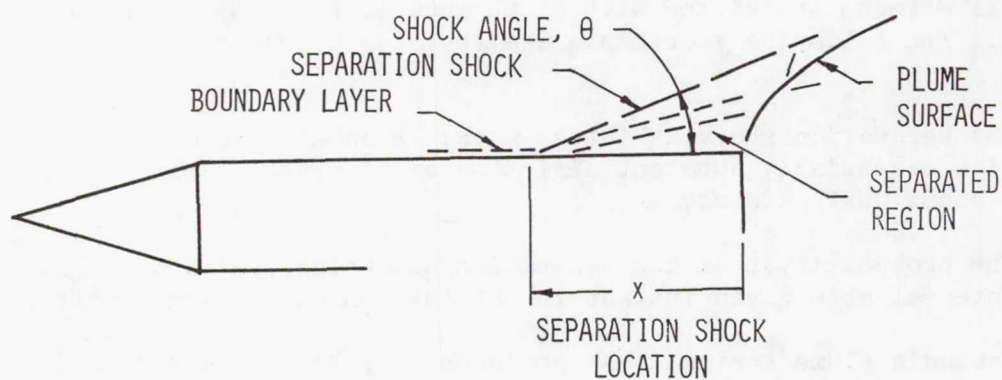
Figure 1.- Plume-induced flow separation.
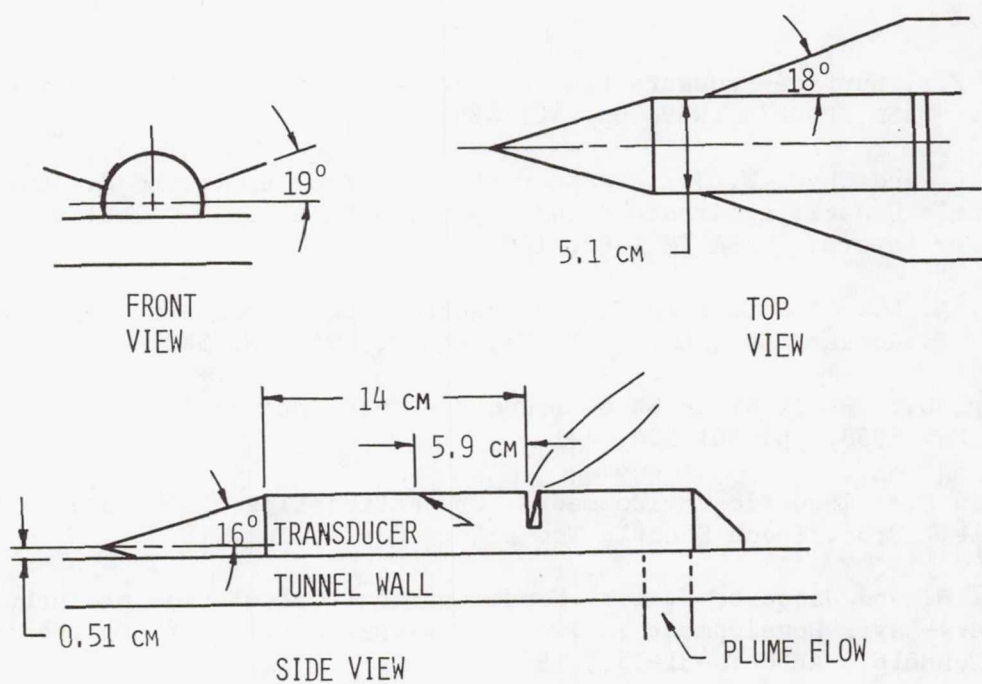
Figure 2.- The test model.
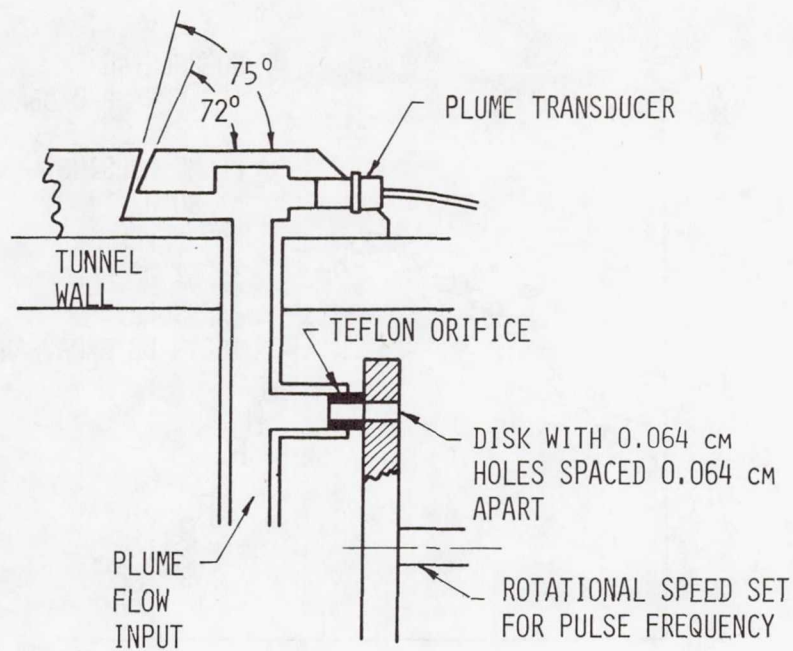
Figure 3.- Plume generation details.
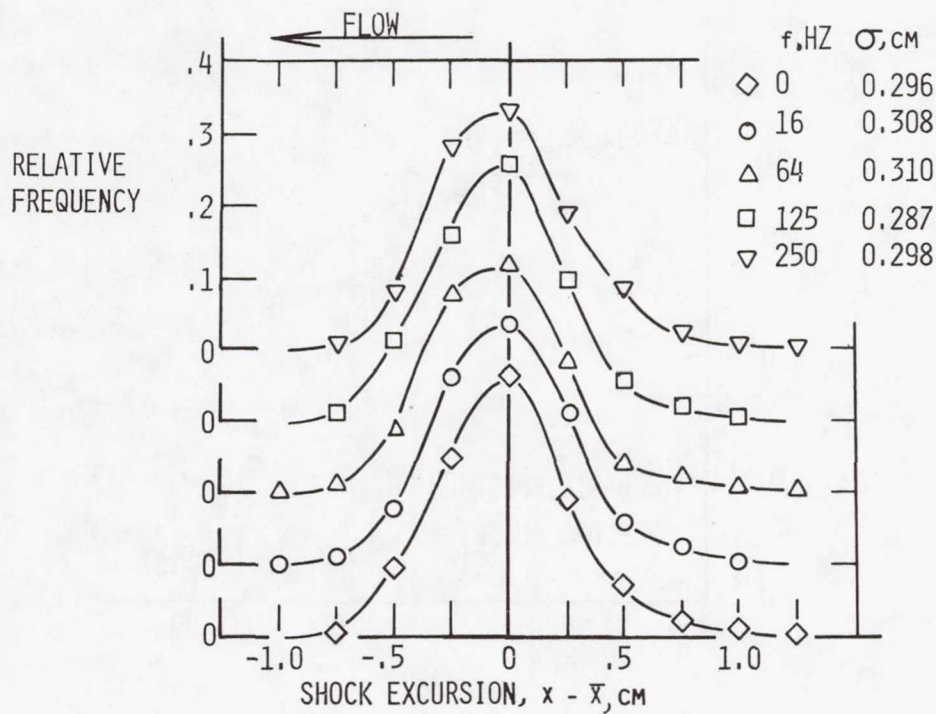
Figure 4.- Effect of plume pulse frequency on shock excursions.
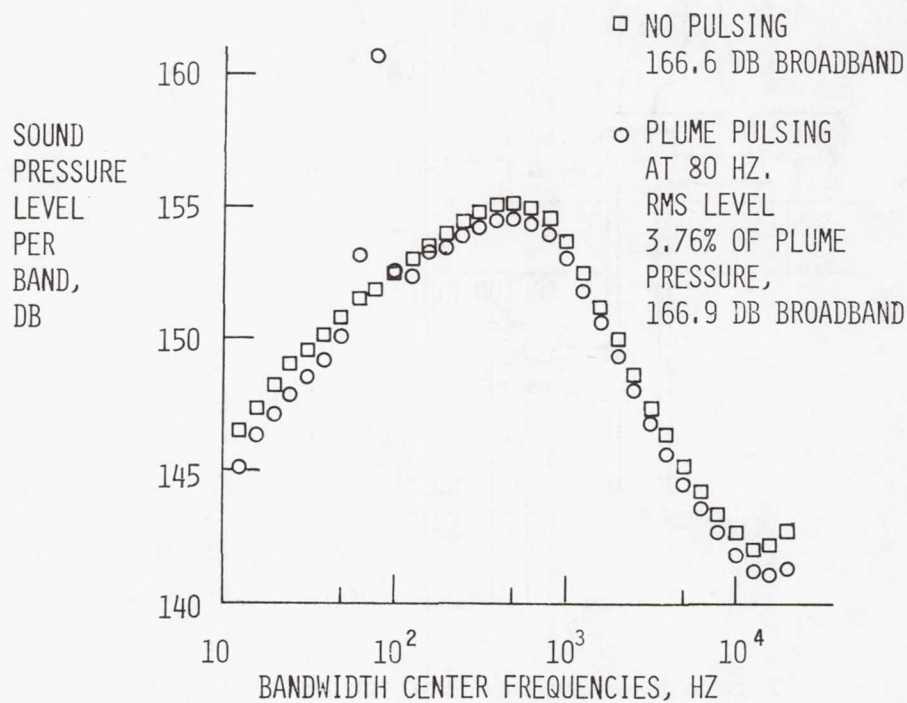
Figure 5.- Shock fluctuation pressure raw data.
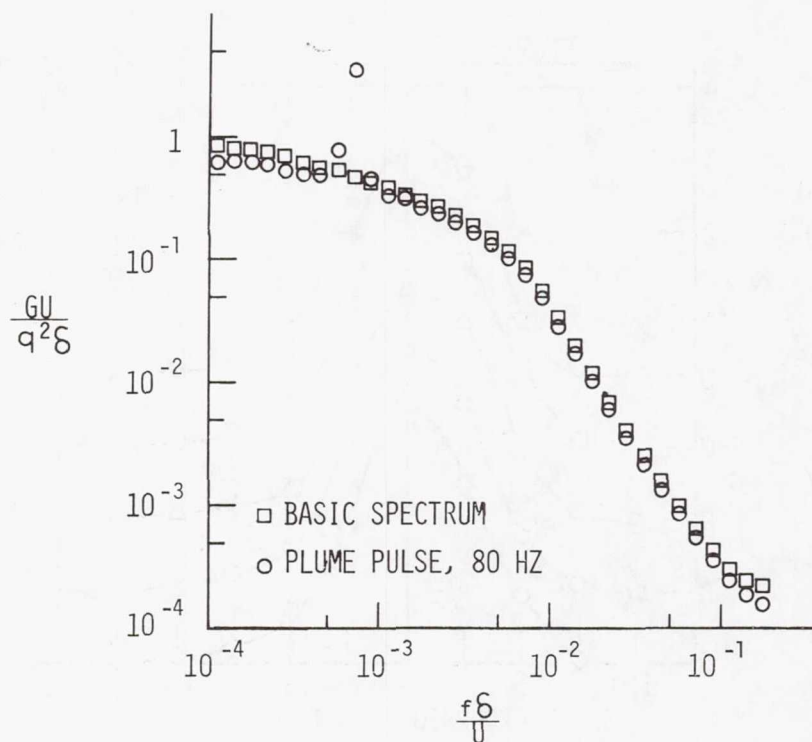
Figure 6.- Shock power spectra.
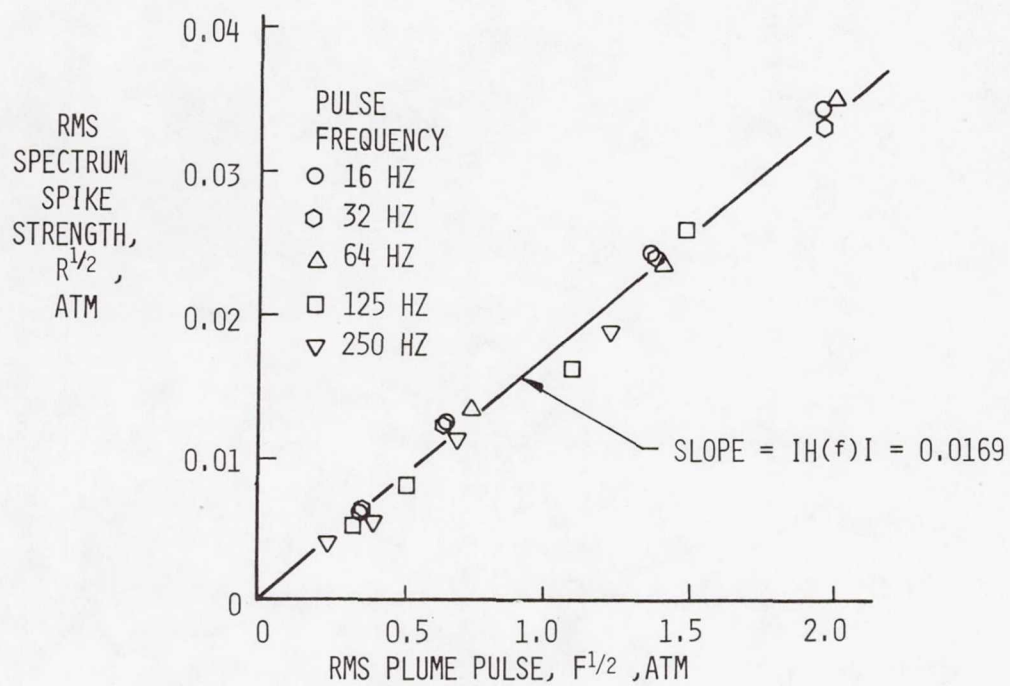
Figure 7.- Power spectra response to plume pulsing.

Page intentionally left blank

AERIAL PURSUIT/EVASION*

Henry J. Kelley
Analytical Mechanics Associates, Inc.

SUMMARY

This presentation was based upon two recent papers describing two differential gaming efforts at air-combat analysis (refs. 1 and 2). One (ref. 1) is based upon homicidal-chauffeur (Breakwell and Merz, ref. 3) and game-of-two-cars (Cocayne, ref. 4) results slightly extended to account in a limited way for excursion of the two craft out of the horizontal plane. The second employs energy models and simplified kinematics for study of turning duels. Some results obtained with these approaches and their relationship to other approaches, such as simulation, were discussed.

The game of two cars is a chase in a horizontal plane between a pursuer having a certain capture radius and a more maneuverable evading vehicle, both constant speed. An estimate of miss, or capture radius required, is given by an analytical approximation based on the "sidestepping" maneuver of the homicidal chauffeur game and a modification to account for the effect of evader turning rate. This turns out to agree remarkably well with Cocayne's point-capture result (ref. 4).

The turning game is played in a three-space; two of the state variables being the specific energies of pursuer and evader, the third, the difference in heading angles. The analogue of point-capture (approximating the gunnery case) is angular closure with sufficient specific energy that the pursuer can follow the evader in a pull-up, so-called "loft-ceiling" match in energy state approximation. The families of trajectory pairs are fairly complex, the trajectories themselves commonly having two or three subarcs. The main features of interest in the results are the barrier surfaces that separate successful pursuit from successful evasion.

REFERENCES

1. Kelley, H.J. and Lefton, L.; "Estimation of Weapon-Radius Versus Maneuverability Trade-Off for Air-to-Air Combat," Analytical Mechanics Associates, Inc. Report No. 75-37, revised June 1976; to appear in AIAA Journal.

2. Kelley, H.J. and Lefton, L.; "Calculation of Differential-Turning Barrier Surfaces," preprint volume, Atmospheric Flight Mechanics Conference, Arlington, Texas, June 7-9, 1976; to appear in Journal of Aircraft.

3. Breakwell, J. and Merz, A.W.; "Toward a Complex Solution of the Homicidal Chauffeur Game," First International Conference on the Theory and Applications of Differential Games, University of Massachusetts, Amherst, Mass., 1969.

4. Cocayne, E.; "Plane Pursuit with Curvature Constraints," SIAM Journal on Applied Mathematics, November 1967.

DESIGN OF ACTIVE CONTROLS FOR THE NASA

F-8 DIGITAL FLY-BY-WIRE AIRPLANE

Joseph Gera
Langley Research Center

SUMMARY

This paper describes the design of a set of control laws for the NASA
F-8 digital fly-by-wire research airplane. These control laws implement
several active controls functions: maneuver load control, ride smoothing and
departure-boundary limiting. Included in the description are the criteria and
methods which were used in the design of the control laws. Results of linear
analyses and nonlinear simulation are summarized in the paper.

INTRODUCTION

The National Aeronautics and Space Administration has been conducting
research in digital fly-by-wire technology. In the initial phase of this
research program an Apollo Lunar Module computer and inertial measuring unit
were installed in an F-8C airplane. Flight tests were conducted on this
airplane at the Dryden Flight Research Center with the mechanical control links
removed for the very first flight. These tests demonstrated the feasibility of
digital fly-by-wire controls for conventional airplanes and the fact that such
systems can incorporate sufficient reliability for pilot confidence (ref. 1).
The second or current phase of the program is directed at (1) demonstrating
flight control systems using multiple redundant general-purpose digital
computers with redundant sensors and actuators and (2) flight testing of those
control laws which have become feasible only with the increased speed and
memory of current airborne digital computers.

The first set of control laws selected for flight testing has been
designed. It includes several functions which are projected for use in future
active controls applications. Some of these functions have been flight-tested
individually in the past; in the present program they are integrated into a
single, full-authority, flight-critical control system. This paper describes
the design criteria and methods used in developing the control laws. The
discussion also includes simulation experience with the control laws.

SYMBOLS

All units of measurements are as given below except where noted otherwise.

C_1, C_2	constants (eq. (1))
$C*$	response variable, g units
f_i, $i=1, \ldots n$	functions used in gain scheduling
g	gravitational acceleration, m/sec^2
h	altitude, m
K_i, $i=1, \ldots n$	gain
K_{C*}	CAS forward loop gain, deg/g
K_{XF}	symmetric aileron-to-elevator gain, deg/deg
M	Mach number
N_z	normal acceleration, g units
q	pitching velocity, rad/sec
V_{co}	'cross-over' velocity, m/sec
z	forward-difference operator (e.g., $z(q) = q_{n+1}$)
α	angle of attack, deg
α_L	envelope limit, deg
α_{TRIM}	trim angle of attack, deg
β	angle of sideslip, deg
ω_n	undamped natural frequency, rad/sec
ω_{sp}	frequency of longitudinal short period motion, rad/sec
ζ	damping ratio

ζ_{sp} damping ratio of short period motion

Abbreviations:

CAS   command augmentation system

SAS   stability augmentation system

DISCUSSION

Modeling

In any control law design one of the most important factors is the mathematical model of the controlled vehicle. The complete design cycle made use of two distinct models of the F-8 airplane. The first of these is a complete, nonlinear representation of the rigid F-8 airplane, flexibility effects, control surface actuation system and the flight environment (ref. 2). From the complete representation the linearized equations of motion were obtained by numerical differentiation after trimming the airplane at various altitudes, Mach numbers, fuel loads and load factors. The resulting set of linear equations of motion covered the entire operational envelope of the F-8 airplane including some high angle of attack conditions where the lateral-directional stability characteristics of the basic airplane required considerable improvement. Most of the aerodynamic data used in the mathematical model was already available except for the symmetric aileron effectiveness at high subsonic speeds. The latter became the subject of a short wind tunnel investigation using an existing model of the F-8C.

Control Law Design

Each of the pitch, roll and yaw axes have several pilot selectable control modes. The modes for the pitch axis are:

(a) Direct mode, which is essentially a proportional control mode between the pilot's stick and the horizontal tail.

(b) SAS mode. This mode was designed to improve the damping of the short period motion by compensated pitch rate feedback to the horizontal tail.

(c) CAS mode. This mode was designed to incorporate several active controls functions. These functions will be defined and briefly described in this section.

For further design details the reader is referred to reference 3. The modes for the lateral and directional axes are:

(a) Direct modes for the roll and yaw axes which are similar in structure to the pitch direct mode.

(b)   SAS modes for the roll and yaw axes which will be described later.

Conventional autopilot functions are also provided when the roll and yaw SAS modes and the pitch CAS mode are engaged.

Pitch CAS Mode.- This mode implements several active control functions. The term 'active control' means that the control system design is an integral part of a new airplane configuration development task. Since no aerodynamic or structural modifications have been made to the F-8 in the digital fly-by-wire program, flight testing the active control functions will not reveal the full performance benefits achievable by active controls. Instead, the flight tests will be aimed at evaluating the mutual interactions of the various active control concepts.

Figure 1 illustrates the basic CAS mode in the pitch axis augmentation system. In the basic CAS mode the shaped pilot's stick deflection controls a blend of pitching velocity and normal acceleration. The resulting signal is routed to the actuation system via the variable gain, K_{C*}. The latter is a function of dynamic pressure derived from altitude and Mach number. In order to minimize stick forces resulting from changing trim conditions, neutral speed stability is provided by an effective forward loop integration. The integration itself is accomplished by cancelling the position feedback signal of the elevator secondary actuators at low frequencies. The mechanical output of the secondary actuators is then used to drive the primary or power actuators which are connected directly to the control surfaces.

A significant feature of this control law is that it was designed through the application of linear optimal control theory at selected flight conditions. Specifically, the motion variable, C* defined as

$$C* = N_z + \frac{V_{co}}{g} q$$

was compared with the output of a linear, second-order 'command' model (ω_n = 7.4 rad/sec; ζ = .91). Minimization of a cost functional consisting of the integral of the weighted squares of the C* error, its integral, the elevator rate and elevator command resulted in a control law which is a linear combination of the assumed state variables. The control law was simplified by neglecting low-gain loop closures and effecting possible pole-zero cancellations. Additional details of the design procedure are given in reference 3.

The design specifications for the control system included the requirement of limiting the operating envelope of the airplane. Envelope limiting is important for two reasons, the first being that with envelope limiting the pilot can demand the full maneuvering capability of the airplane without

concern for departing from controllable flight. The second reason is that future active control applications will include relaxing the static stability requirements of the basic airplane: elevator commands beyond the available surface authority would result in loss of control for an airplane without envelope limiting.

The implementation of the envelope limiter is shown in figure 2; this system was integrated with the basic C* controller by the use of a switch labeled as 'max. value select.' in figure 1. The switch simply selects the more positive, i.e., the larger nosedown elevator command. It should be noted that at low frequencies the command signal from both controllers approximates elevator rate; switching on this approximate elevator rate has proved to be a satisfactory method to effect transition between the two controllers.

The design of the envelope limiting control law was also accomplished by using linear optimal control theory. In the cost functional the pitching velocity term was heavily weighted along with angle of attack, its integral, elevator rate, and elevator command. The control law obtained at selected flight conditions by using optimal control theory was simplified in a manner similar to simplification of the basic C* controller. The resulting controller is driven by angle of attack and its approximate time derivative obtained by high-passing the pitching velocity. The angle of attack is referenced to the value, α_L, the limit angle of attack. At present α_L is programed to include the effect of sideslip as

$$\alpha_L = C_1 - C_2 |\beta| \tag{1}$$

where C_1 and C_2 are constants.

Direct lift produced by symmetric aileron or flap deflections is utilized both for drag reduction in maneuvering flight and for ride smoothing in turbulence. The direct lift mode has the complementary structure illustrated in figure 3. Reduction of maneuvering drag is accomplished by scheduling steady state flap deflections with lagged pitching velocity. For ride smoothing the measured normal acceleration is fed back to the flaps via a scheduled gain and a high-pass filter. Tentative values of the scheduled gain were derived from loop gain considerations (ref. 3). The use of the high-pass filter avoids the necessity of gravity compensation of the accelerometer signal during steady climbs or descents. Pitching moment changes due to flap deflection are canceled by utilizing a cross-feed signal through the gain K_{XF} which is chosen to be the ratio of pitching moments produced by unit deflections of the elevator and of the flaps.

Roll SAS and Yaw SAS Modes.- Figure 4 illustrates the mechanization of the augmented modes for the lateral-directional axes. Although the roll SAS and yaw SAS modes are individually selectable by the pilot, this discussion treats

them collectively. The criteria for the design of this system included improved damping of the Dutch roll oscillating mode, positive directional stability and good turn coordination at all usable angles of attack. Application of the linear quadratic optimal control algorithm at selected flight conditions yielded a feedback gain matrix with a non-zero gain on every state variable to every control input. A separate algorithm, described in reference 4, was then used to drive those gains to zero which were impractical to implement while still satisfying conditions necessary to minimize the original cost function. In the resulting control mode, high-passed yaw rate provides improved Dutch roll damping with no steady state turn resistance. Turn coordination is enhanced by compensated lateral acceleration feedback and aileron-rudder interconnect. Automatic rudder trim is achieved by the feedback of integrated lateral acceleration to the rudder. The latter loop is opened whenever the rudder pedals are out of detent, thus enabling the pilot to command a steady sideslip. The scheduling of gains is done with angle of attack to ensure good performance at all maneuvering conditions.

Autopilot Functions.- Conventional autopilot functions are available to the pilot in addition to the inner loop functions described above. These functions are the following: attitude, altitude, Mach and heading hold modes; control stick steering and heading select are also provided with automatic return to the hold modes.

Digital Processing of Control Laws.- In order to be processed by a digital computer, the control laws must be expressed in the form of difference equations. When the equations of motion of the controlled system are converted to difference equations at the outset, finding the solution of the resulting discrete linear optimal control problem leads directly to control laws which are in the form of difference equations. These control laws are optimal relative to the particular sampling interval chosen at the beginning of the design. Changing the sampling interval requires a new design. If the control law design proceeds in the continuous time domain at the beginning and the resulting continuous control laws are then converted into difference equations, a new sampling interval does not usually require solving the entire optimal control problem again. For a limited range of sampling intervals all that is required is recomputing the coefficients of the linear difference equations expressing the control laws. The latter approach of obtaining difference equations is directly applicable to control laws which are designed for multi-rate sampling.

The difference equations which are programed in the F-8 flight computers were obtained by the second method. Thus it will be possible to study the effects of different sampling intervals in flight by a simple preflight change in the software executive timing routine, after the computer memory has been reloaded with the new coefficients of the difference equations. These coefficients are calculated from the continuous control laws off-line using Tustin's method (ref. 5). Initially, all inner loop control law functions are computed at 20 millisecond intervals while the autopilot functions and other less critical operations are executed at 80 millisecond intervals.

PERFORMANCE AND SIMULATION RESULTS

Control law performance in the various modes, predicted by linear analysis, was evaluated over the entire flight envelope in closed-loop simulation. Although the basic F-8 airplane has good response characteristics further improvements are expected in the augmented modes.

Longitudinal Modes

In figure 5 longitudinal response is illustrated in the DIRECT, basic CAS and CAS with the direct lift mode at one of the twenty flight conditions used in the design and analysis. Linear analysis gave the following modal characteristics for the short period motion:

	ω_{sp}, rad/sec	ζ_{sp}
DIRECT	3.2	.38
CAS	4.4	.73

Comparing the time histories in these modes in figure 5 shows that these improvements are realized in the full, non-linear simulation. The beneficial effect of the direct lift is reflected in the quickened normal acceleration response with moderately reduced over-shoot in pitch rate.

In figure 6 the role of the symmetric aileron deflection as a ride-smoothing device is shown. The gust-induced normal acceleration traces obtained in the full non-linear simulation substantiate the predictions of linear analysis.

The operation of the envelope limiter was also tested in the simulator. The time histories shown in figure 7 were obtained while the pilot was steadily increasing the load factor in a turning maneuver by applying aft stick pressure. In this particular test the value of α_L was set at a conservative 12 degrees with no contribution from the sideslip term in equation (1). It can be seen that after encountering the angle of attack limit of 12 degrees, any further aft movement of the stick has no effect on the maneuver. Reducing aft stick pressure results in the angle of attack moving smoothly away from the limiting 12 degree value.

Lateral-Directional Modes

Substantial improvements in the lateral-directional response are expected in the combined roll and yaw SAS mode. Linear analysis predicts the following improvements for the Dutch roll mode at the same flight condition (M = .8, h = 6100m) for which the longitudinal results were presented:

	ω_n, rad/sec	ζ
DIRECT	3.5	.11
SAS (roll and yaw)	3.4	.41

In figure 8 simulator results are shown following a β-gust of two degrees. In the same figure the time histories in response to a step lateral-stick input show the expected improvements in roll-induced sideslip and turn coordination. The latter result was obtained at the same altitude, but reduced airspeed (M = .4) which resulted in a moderately high trim angle of attack of 8.9 degrees.

In addition to being the subject of the linear analyses and non-linear simulations, the control law modes were integrated into a single FORTRAN-coded subroutine. The latter was called 32 times per second by the complete F-8 simulation program in a real-time operation. This allowed an early examination of the functional operation of all control modes, mode transfer logic and various initialization routines. This same program was interfaced with an F-8 cockpit and used in preliminary piloted simulations. The subject pilots rated the control law modes favorably, but only the actual flight tests will reveal the benefits of the various active control modes.

CONCLUDING REMARKS

One of the important technology areas the NASA digital fly-by-wire program addresses is the design and flight test of control laws suitable for future active control applications. This report describes a set of control laws, including design criteria and methods, which have been selected for flight tests on the F-8 digital fly-by-wire airplane. The following functions are mechanized in an integrated, full-authority, flight-critical control system:

(1) Command augmentation system for the pitch axis based on the C* response criterion, including apparent neutral speed stability.

(2) Maneuver load control and ride smoothing using direct lift generated by symmetric aileron deflection.

(3) Envelope limiting which allows the pilot full maneuvering capability without concern for departure from controllable flight regimes.

(4) Lateral-directional stability augmentation which provides good handling characteristics at all usable angles of attack.

(5) Conventional autopilot or outer loop functions such as attitude, Mach, altitude and heading hold including control stick steering in these modes.

Linear analyses and non-linear simulation results of the augmented modes predict substantial improvements in the airplane's response characteristics. Pilot comments on these modes have also been favorable, but only the actual flight tests will reveal the extent of benefits achievable by these control modes.

REFERENCES

1. Description and Flight Test Results of the NASA F-8 Digital Fly-By-Wire
   Control System. NASA TN D-7843, 1975.

2. Woolley, C. T.: A Real-Time Hybrid Simulation of a Digital Fly-By-Wire
   Aircraft. 1974 Summer Computer Simulation Conference, Houston, TX,
   July 9-11, 1974.

3. Hartmann, G. L.; Hauge, J. A.; and Hendrick, R. C.: F-8C Digital CCV
   Flight Control Laws. NASA CR-2629, Feb. 1976.

4. VanDierendonck, A. J.: Design Method for Fully Augmented Systems for
   Variable Flight Conditions. AFFDL-TR-71-162, January 1972.

5. Fryer, W. D., and Schultz, W. C.: A Survey of Methods for Digital
   Simulation of Control Systems. Cornell Aeronautical Laboratory Report
   No. XA-1681-E-1. July 1964.
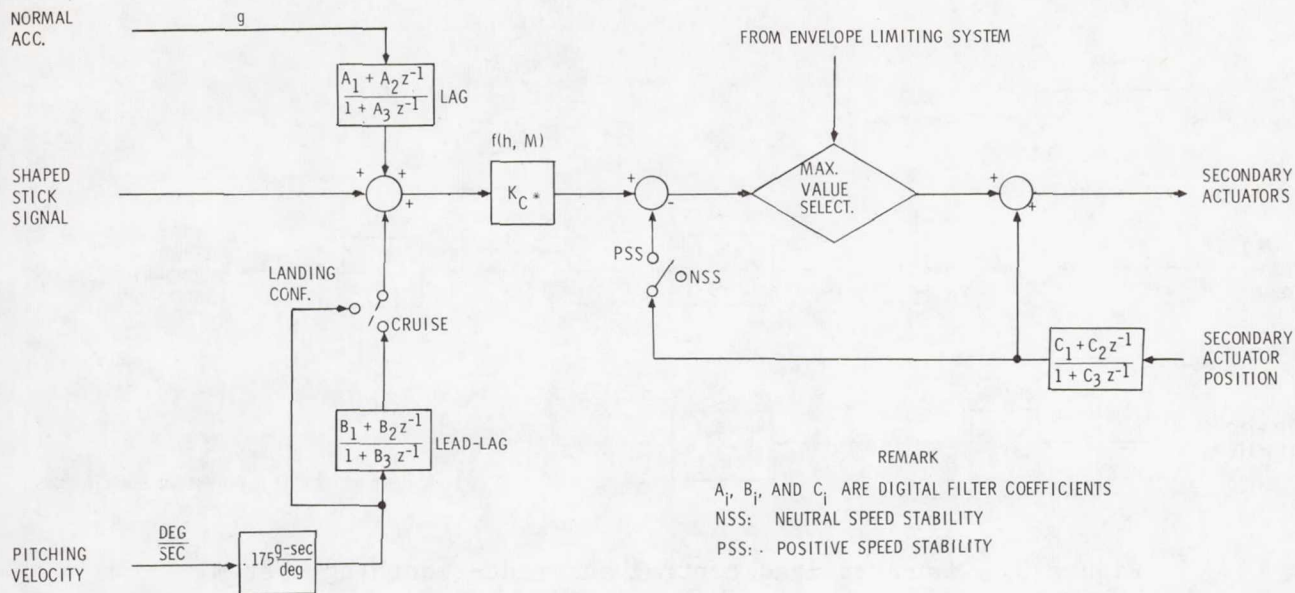
Figure 1.- Basic CAS mode (pitch axis command augmentation system).
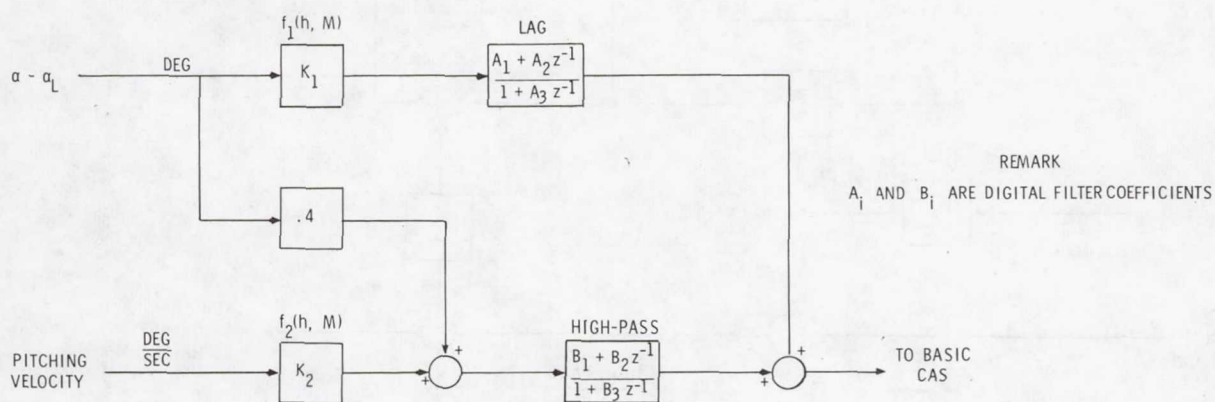
Figure 2.- Envelope limiting system.
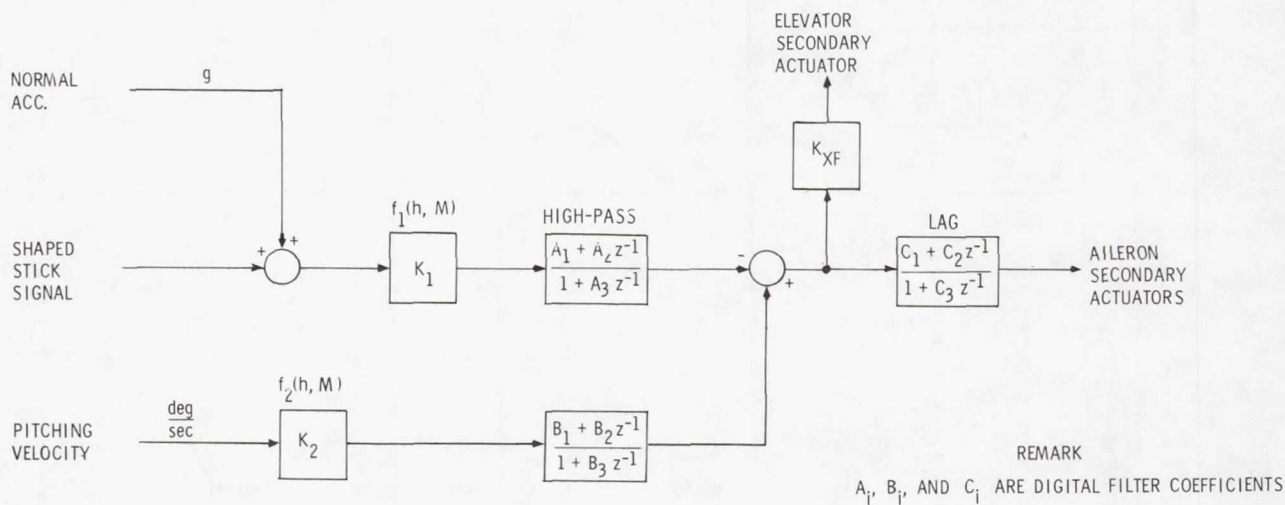
Figure 3.- Maneuver load control and ride-smoothing system.
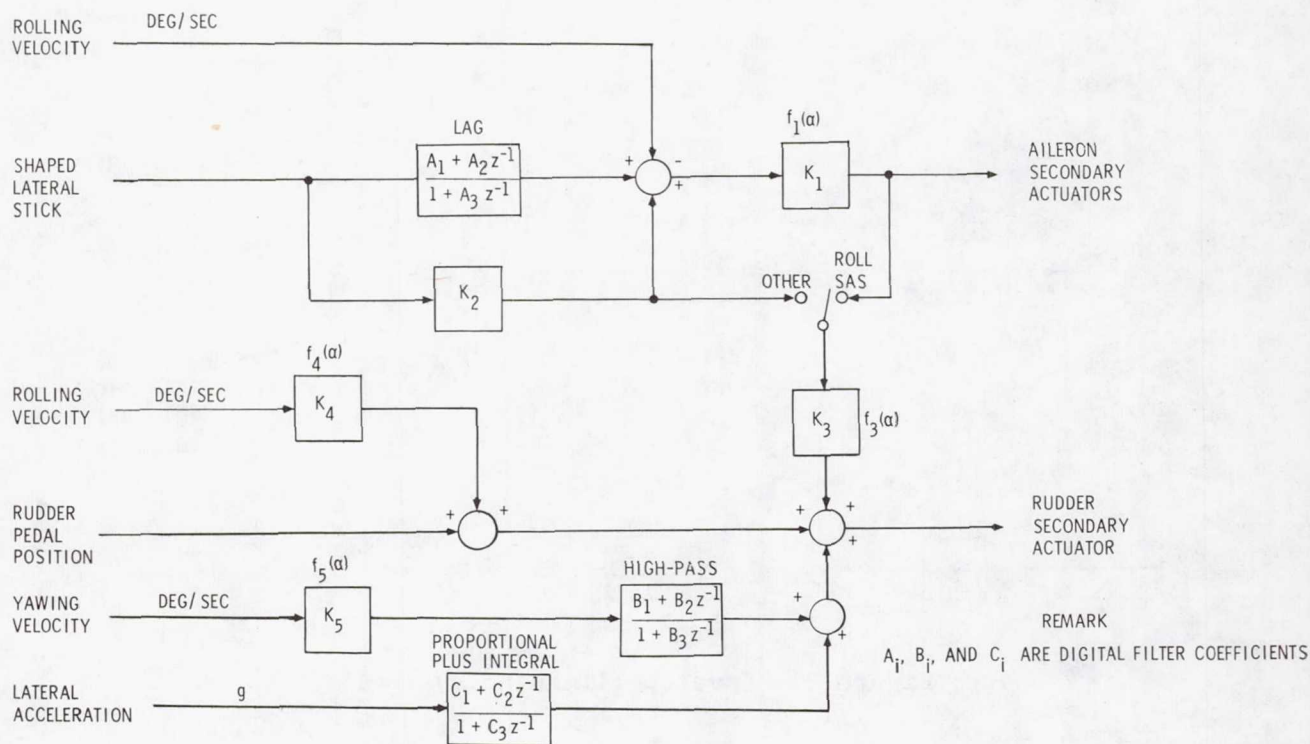
Figure 4.- Lateral-directional stability augmentation system.
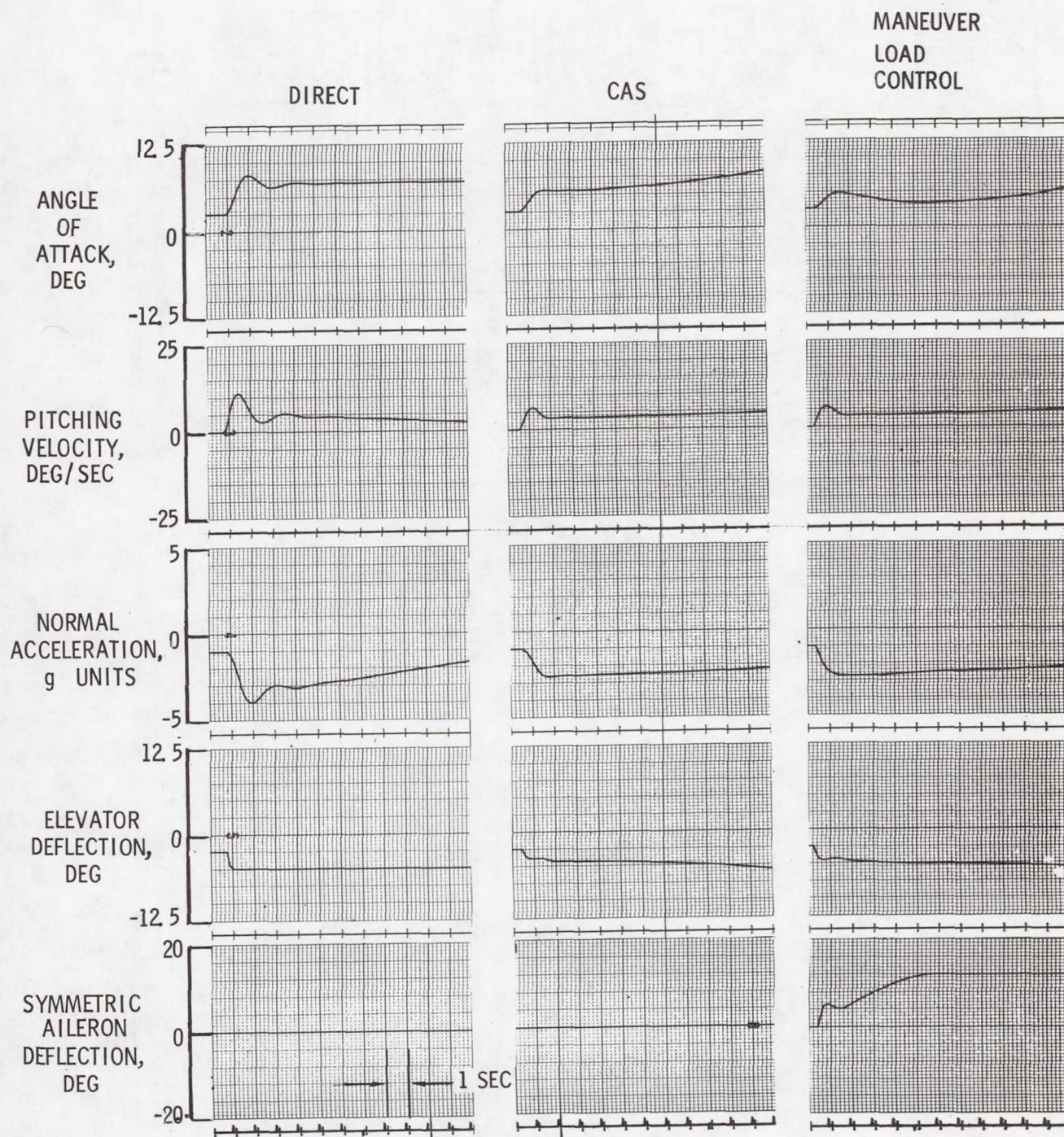
Figure 5.- Longitudinal response to a step stick input.   h = 6100 m; M = 0.8.

LINEAR ANALYSIS:

GUST INDUCED NORMAL ACCELERATION LEVELS

DIRECT
1.0^*

AUGMENTED
$.61^*$

*NORMALIZED, R.M.S. VALUES

SIMULATOR RESULT:

DIRECT

AUGMENTED

INCREMENTAL NORMAL ACCELERATION, g UNITS

SYMMETRIC AILERON POSITION, DEG

1 sec
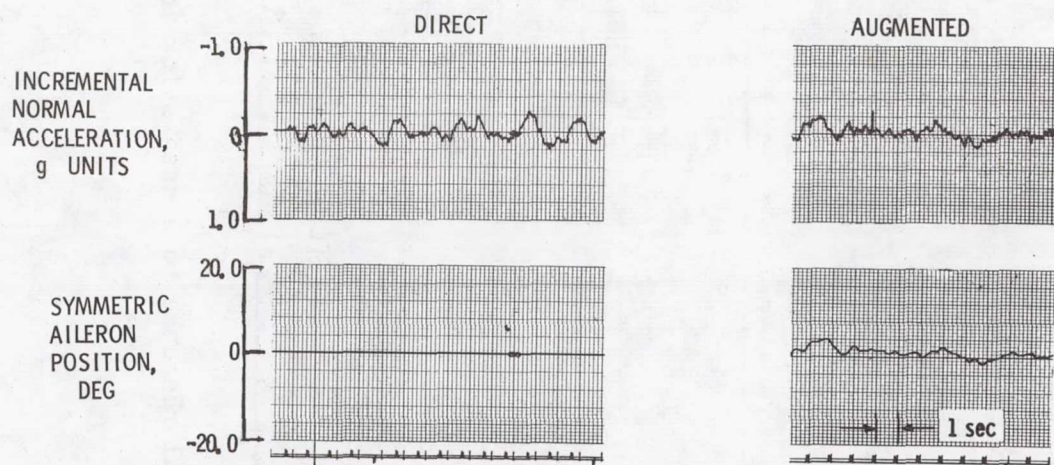
Figure 6.- Predicted performance of ride-smoothing system.

PILOT STICK DISPL., cm

1 SEC

ANGLE OF ATTACK, DEG

α_L VALUE

PITCHING VELOCITY, DEG/SEC

NORMAL ACCELERATION, g UNITS

ELEVATOR DEFLECTION, DEG

Figure 7.- Envelope limiting in non-linear simulator. α_{trim} = 3.45°; h = 6100 m; M = 0.67.
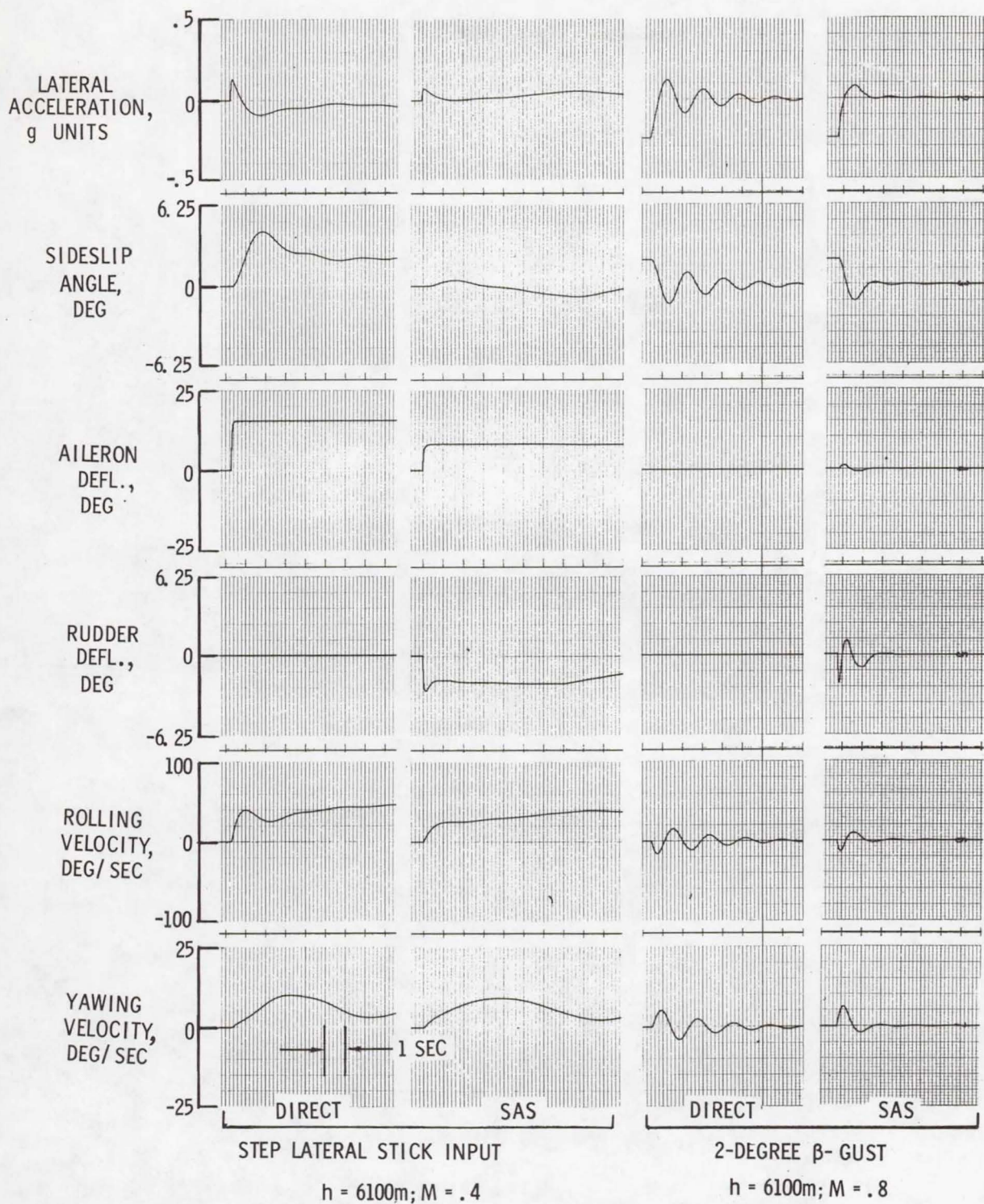
Figure 8.- Lateral-directional response.

Page intentionally left blank

PERFORMANCE ANALYSIS OF FLEXIBLE AIRCRAFT WITH ACTIVE CONTROL*

Richard B. Noll
Aerospace Systems, Inc.

Luigi Morino**
Boston University

SUMMARY

The small-perturbation equations of motion of a flexible aircraft with an active control technology (ACT) system were developed to evaluate the stability and performance of the controlled aircraft. The total aircraft system was formulated in state vector format and the system of equations was completed with fully unsteady and low-frequency aerodynamics for arbitrary, complex configurations based on a potential aerodynamic method. The ACT system equations have been incorporated in the digital computer program FCAP (Flight Control Analysis Program) which can be used for the analysis of complete aircraft configurations, including control system, with either low-frequency or fully unsteady aerodynamics. The application of classical performance analyses including frequency response, poles and zeros, mean-square response, and time response in FCAP in state vector format was discussed.

INTRODUCTION

The integrated study of the interactive effects of the flight control system in the active control of flexible aircraft has received considerable attention in recent years. In particular, Active Control Technology (ACT) is being investigated for improving ride quality, decreasing structural deformation, extending the fatigue life of the aircraft, relaxing static stability requirements, suppressing flutter, and reducing structural loads.

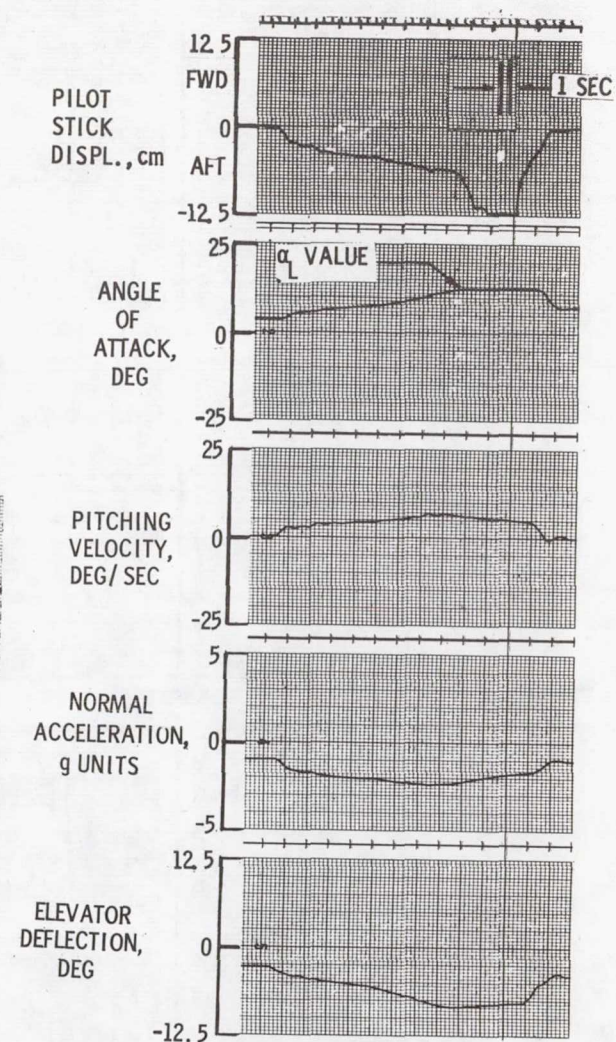A new computer program, Flight Control Analysis Program (FCAP) has been developed for NASA to analyze ACT systems (refs. 1 and 2). The program was designed in a modular fashion to incorporate aircraft dynamics, aerodynamics for complex configurations, and sensor, actuator, and control logic dynamics, as well as analysis methods for determining stability and performance of the ACT system. The formulation of the total aircraft dynamic system for FCAP was unified by casting all the equations in state space format. This paper presents the state-vector formulation of the ACT system, and discusses its application in FCAP for the performance analysis of ACT systems.

---

*This paper was derived from work conducted under NASA Contract NAS 1-13371.

**Consultant to Aerospace Systems, Inc.

SYMBOLS

A, B, C, D	state-space matrices of ACT system and subsystems
A_1	matrix defined by Equation (17)
F	matrix defined by Equation (16)
H	matrix of transfer functions
$i\omega$	imaginary part of complex frequency, s
M_R	generalized mass/inertia matrix
q	dynamic pressure
q_N	Lagrangian generalized coordinates
$R(0)$	covariance matrix of ACT system outputs
r	output vector for ACT system and subsystems
s	complex frequency
$U(0)$	covariance matrix of ACT system inputs
U_{RA}, U_{RD}, U_{RR}	generalized aerodynamic force coefficients
U_{SD}, U_{SR}, U'_{SR}	coefficient matrices of aircraft dynamics equations at sensor locations
u	input vector for ACT system and subsystems
u'_L	matrix of pilot and guidance system commands
u_R	generalized aerodynamic forces in uniform flow
u'_R	matrix of aerodynamic forces due to turbulence
$X(0)$	covariance matrix of ACT system state variables
x	state vector

Subscripts:

A	actuator
D	aircraft displacement
L	control logic
R	aircraft rate
S	sensor

1704

T   transpose

(0), (1)   coefficients of power series expansion

A tilda ($\sim$) over a symbol indicates that it is designated in the Laplace domain. A dot over a variable indicates time differentiation.

ACT ANALYSIS

The ACT system formulated in FCAP is shown in Figure 1. External disturbances to the ACT system are seen to be atmospheric turbulence and gusts contributing to the aerodynamic forces and moments, and pilot or guidance system commands introduced through the control logic. The aircraft dynamic system includes both rigid-body and flexible-body dynamics.

The analysis of ACT systems is unified by casting all system equations in either the time domain or the frequency domain, and in similar format. In state space methods, the motion of a given dynamic system is described by the following pair of matrix equations (ref. 3):

$$\left. \begin{aligned} \dot{x} &= Ax + Bu \\ r &= Cx + Du \end{aligned} \right\} \tag{1}$$

where x is the state vector, u is the input (or control) vector, r is the output vector, and A, B, C, and D are the matrix coefficients. The equations for the dynamics of the state variables, and for the outputs of the aircraft dynamics, sensors, logic, and actuators are given in the following sections. The equations are then combined with equations for aerodynamics of the aircraft, and the total system matrix equations are formulated using the compatibility relationships among the dynamic systems.

Aircraft Dynamics

The FCAP aircraft dynamics equations for N degrees of freedom (six rigid-body and (N-6) flexible-body degrees of freedom) are restricted to small perturbations which reduce the equations to linear form. This is a reasonable approximation for ACT studies (e.g., refs. 4 and 5). The aircraft equation of motion expressed in state vector form is (ref. 1):

$$M_R \dot{x}_R = A_{RR} x_R + A_{RD} x_D + u_R + u'_R \tag{2}$$

where

$$x_D = \text{state vector of the displacement variables} = \lfloor x, y, z, \Phi, \Theta, \Psi, q_7, \dots q_N \rfloor^T$$

$$x_R = \text{state vector of the rate variables} = \lfloor u, v, w, p, q, r, \dot{q}_7, \dots \dot{q}_N \rfloor^T$$

Also, M_R = generalized mass matrix, A_{RR} = Coriolis force/damping matrix, A_{RD} = stiffness/gravity-force matrix, u_R = generalized aerodynamic forces in uniform flow, and u'_R = forces due to turbulence.

The output of the aircraft dynamics at the sensor locations may be expressed linearly in terms of displacements, x_D, rates, x_R, and accelerations, $\dot{x}_R$, and, therefore, it is possible to write

$$r_D = U_{SD} x_D + U_{SR} x_R + U'_{SR} \dot{x}_R \tag{3}$$

where the coefficient matrices U_{SD}, U_{SR}, and U'_{SR} are functions of the types of sensors and their location.

Control System Dynamics

The control system is defined as consisting of sensors, control logic, and actuators for FCAP. Classically, control system dynamics are expressed in the form of a transfer function which can be redefined in the state vector form of Equation (1). In the following sections, let x_S, x_L and x_A be the state vectors for the sensors, logic, and actuators, respectively.

Sensors

The state vector equations for sensor dynamics are given by

$$\dot{x}_S = A_{SS} x_S + B_S u_S \tag{4}$$

and

$$r_S = C_S x_S + D_S u_S \tag{5}$$

where u_S is the input to the sensor system from the aircraft.

Control Logic

The state vector equations for the control logic dynamics are expressed

$$\dot{x}_L = A_{LL} x_L + B_L (u_L + u'_L) \tag{6}$$

and

$$r_L = C_L x_L + D_L (u_L + u'_L) \tag{7}$$

where u_L is the input to the control logic from the sensors, and u'_L is pilot and guidance system commands (see fig. 1).

Actuators

The equations for the dynamics of the actuators in FCAP are given by

$$\dot{x}_A = A_{AA}\, x_A + B_A\, u_A \tag{8}$$

and

$$r_A = C_A\, x_A \tag{9}$$

where u_A is the input to the actuators.

Note that a term of the type $D_A\, u_A$ is absent in Equation (9). This implies that in the transfer function of the actuators the degree of the numerator is lower than the degree of the denominator. This yields considerable advantage in expressing the low-frequency-aerodynamics closed-loop system.

Aerodynamics

The potential aerodynamic method developed in references 6 to 9 provides a unified approach for both steady and unsteady subsonic and supersonic aerodynamics around complex, three-dimensional configurations. The subsonic portion of this method is incorporated into FCAP. The aerodynamic method of reference 6 is compatible with FCAP in that the generalized aerodynamic forces are proportional to the aircraft dynamic generalized coordinates, x_D, and rates, x_R, and to actuator (i.e., control surface) deflections, r_A. In the time domain, the unsteady aerodynamic forces are expressed as

$$u_R = q(U_{RR}\, x_R + U_{RD}\, x_D + U_{RA}\, r_A) \tag{10}$$

where U_{RR}, U_{RD}, and U_{RA} are operators corresponding to frequency-dependent matrices $\tilde{U}_{RR}$, $\tilde{U}_{RD}$, and $\tilde{U}_{RA}$ usually known as aerodynamic-influence-coefficient matrices.

For system stability and performance analyses, low-frequency aerodynamics is often adequate. Therefore, in the rest of this paper only low-frequency aerodynamics is considered. In this case, the equations for the aerodynamics become linear with constant coefficients. The low-frequency aerodynamics equations are expressed in the time domain as

$$u_R = q(U_{RR}^{(0)}\, x_R + U_{RD}^{(0)}\, x_D + U_{RA}^{(0)}\, r_A)$$

$$+\; q(U_{RR}^{(1)}\, \dot{x}_R + U_{RD}^{(1)}\, \dot{x}_D + U_{RA}^{(1)}\, \dot{r}_A) \tag{11}$$

where, for example, $U_{RR}^{(0)}$ and $U_{RR}^{(1)}$ are the first two terms of the MacLaurin-Taylor series of $\tilde{U}_{RR}$. All of these coefficients are frequency-independent.

ACT System

The state vector equations for each of the ACT subsystems are given by Equations (2) to (9). Using the low-frequency aerodynamics given by Equation (11) and recognizing from Figure 1 that the input for each subsystem is the output of the previous subsystem, the ACT system can be cast in the form of Equation (1) as

$$\dot{x} = Ax + Bu \tag{12}$$

where

$$x = \lfloor x_D \; x_R \; x_S \; x_L \; x_A \rfloor^T \tag{13}$$

$$A = F^{-1} A_1 \tag{14}$$

and

$$B = F^{-1} \tag{15}$$

with

$$F = \begin{bmatrix} I & 0 & 0 & 0 & 0 \\ 0 & M_R & 0 & 0 & 0 \\ 0 & -B_S U'_{SR} & I & 0 & 0 \\ 0 & -B_L D_S U'_{SR} & 0 & I & 0 \\ 0 & -B_A D_L D_S U'_{SR} & 0 & 0 & I \end{bmatrix} + q \begin{bmatrix} 0 & 0 & 0 & 0 & 0 \\ U_{RD}^{(1)} & U_{RR}^{(1)} & 0 & 0 & U_{RA}^{(1)} C_A \\ 0 & 0 & 0 & 0 & 0 \\ 0 & 0 & 0 & 0 & 0 \\ 0 & 0 & 0 & 0 & 0 \end{bmatrix} \tag{16}$$

$$A_1 = \begin{bmatrix} A_{DD} & A_{DR} & 0 & 0 & 0 \\ A_{RD} & A_{RR} & 0 & 0 & 0 \\ B_S U_{SD} & B_S U_{SR} & A_{SS} & 0 & 0 \\ B_L D_S U_{SD} & B_L D_S U_{SR} & B_L C_S & A_{LL} & 0 \\ B_A D_L D_S U_{SD} & B_A D_L D_S U_{SR} & B_A D_L C_S & B_A C_L & A_{AA} \end{bmatrix} + q \begin{bmatrix} 0 & 0 & 0 & 0 & 0 \\ U_{RD}^{(0)} & U_{RR}^{(0)} & 0 & 0 & U_{RA}^{(0)} C_A \\ 0 & 0 & 0 & 0 & 0 \\ 0 & 0 & 0 & 0 & 0 \\ 0 & 0 & 0 & 0 & 0 \end{bmatrix} \tag{17}$$

$$u = \begin{Bmatrix} 0 \\ u'_R \\ 0 \\ B_L u'_L \\ B_A D_L u'_L \end{Bmatrix} \tag{18}$$

The input u to the ACT system depends upon the gust forces, u'_R, and the pilot and guidance system commands, u'_L.

FCAP PERFORMANCE ANALYSIS

Performance analysis routines are available in FCAP to compute frequency response, transfer function poles and zeros, mean-square response to random inputs and time response. The theoretical basis for each of these techniques is well founded in the literature; there-fore, the following discussions will emphasize the nature of the technique as applied to FCAP equations.

Frequency Response

Since the low-frequency-aerodynamics ACT system dynamics are expressed in state vector format in terms of the (constant) A, B, C, D matrices, the frequency response of the kth output to the ℓth input can be obtained (in the s-plane with zero initial conditions) from

$$(sI - A)\tilde{x} = B_\ell \tilde{u}_\ell \tag{19}$$

and

$$\tilde{r}_k = C_k \tilde{x} + D_{k\ell} \tilde{u}_\ell \tag{20}$$

Solving Equation (19) for $\tilde{x}$ and substituting into Equation (20) yields

$$\tilde{H}_{k\ell}(s) = \frac{\tilde{r}_k}{\tilde{u}_\ell} = C_k [sI - A]^{-1} B_\ell + D_{k\ell} \tag{21}$$

Classical frequency response is obtained for the special case where $s = i\omega$ by computing the amplitude and phase from Equation (21) for a range of frequencies.

Poles and Zeros

Poles and zeros are evaluated in FCAP using a different form of $\tilde{H}_{k\ell}$ than that given in Equation (21). Note that Equation (21) may be rewritten as

$$\tilde{H}_{k\ell}(s) = \frac{\tilde{r}_k}{\tilde{u}_\ell} = \mathrm{Det}\begin{bmatrix} D_{k\ell} & -C_k \\ \hline B_\ell & sI - A \end{bmatrix} \bigg/ \mathrm{Det}\begin{bmatrix} 1 & -C_k \\ \hline 0 & sI - A \end{bmatrix} \tag{22}$$

The poles of $\tilde{H}_{k\ell}$ are the zeros of the denominator, i.e., the eigenvalues of the matrix A. The zeros of $\tilde{H}_{k\ell}$ are the zeros of the numerator. The procedure to obtain them is given in references 1 and 10.

Mean-Square Response to Random Inputs

The response of a flexible aircraft to stationary random inputs may be described in the frequency domain in terms of the spectral density matrix $\bar{R}(\omega)$. The definition used for the outputs are also valid for the inputs and the state variables.

Where the inputs are represented as zero-mean white noise with constant spectral density matrix, U, the covariance matrix of the outputs $R(0)$ is given (for $D = 0$) by

$$R(0) = CX(0) \, C^T \tag{23}$$

where the covariance matrix of the state variables, $X(0)$, is determined from the linear matrix equation (ref. 11, pp. 330-332)

$$AX(0) + X(0) \, A^T + BU(0) \, B^T = 0 \tag{24}$$

Time Response

The time response of a closed-loop system with initial conditions, $x(0)$, and an arbitrary input function can be determined in FCAP using a fourth-order Runge-Kutta numerical integration algorithm. For the special case where the input for $t > 0$ has a rational Laplace transform (i.e., the input can be described as a transfer function), the solution technique described in reference 12 is used.

CONCLUDING REMARKS

The equations of motion for a flexible aircraft have been presented in matrix format and incorporated into a digital computer program FCAP. The objective in the development of FCAP was to model realistically those factors that significantly affect the stability and response of a flexible, ACT-configured vehicle. It should be noted, however, that FCAP is intended primarily for use in the analysis of the performance of an ACT system, rather than in the synthesis of the control system.

The small-perturbation equations of motion for the ACT system were obtained in state-vector format and were completed by the addition of aerodynamics of arbitrary, complex aircraft configurations. Both fully unsteady and low-frequency aerodynamic equations were presented; however, for performance analyses, low-frequency aerodynamics is usually adequate and, therefore, the ACT system equations were presented for low-frequency aerodynamics only. Program FCAP, however, allows the analysis of complete aircraft configurations, including control system, with either low-frequency or unsteady aerodynamics.

The analysis of ACT system performance in FCAP has also been presented. In particular, the application of classical frequency response, poles and zeros, mean-square response, and time response in FCAP in state-vector format has been discussed.

Program FCAP provides a computerized method of integrating multiple systems into a matrix format, and then provides the means for obtaining desired solutions through classical analysis techniques. The program is currently in the final stages of checkout and has been used to solve textbook examples of control system problems. The program thus far has proven to be simple to use and requires a minimum of input.

REFERENCES

1. Noll, R. B.; and Morino, L.: Flight Control Analysis Program (FCAP) for Arbitrary-Configuration Flexible Aircraft With Active Control; Vol. I: Theoretical Analysis. Aerospace Systems, Inc., ASI-TR-75-23, October 1975.

2. Noll, R. B.; and Morino, L.: FCAP - A New Tool for the Evaluation of Active Control Technology. AIAA Paper No. 75-1059, August 1975.

3. Schultz, D. G.; and Melsa, J. L.: State Functions and Linear Control Systems. McGraw-Hill Book Company, Inc., New York, 1967.

4. Etkin, B.: Dynamics of Flight. John Wiley and Sons, Inc., New York, 1959.

5. Ashley, H.: Engineering Analysis of Flight Vehicles. Addison-Wesley Publishing Company, Inc., Reading, MA, 1974.

6. Morino, L.: A General Theory of Unsteady Compressible Potential Aerodynamics. NASA CR-2464, December 1974.

7. Morino, L.; Chen, L. T.; and Suciu, E. O.: Steady and Oscillatory Subsonic and Supersonic Aerodynamics Around Complex Configurations. AIAA Journal, Vol. 13, no. 3, March 1975, pp. 368-374.

8. Morino, L.; and Chen, L. T.: Indicial Compressible Potential Aerodynamics Around Complex Aircraft Configurations. Published in Aerodynamic Analyses Requiring Advanced Computers, Vol. II, NASA SP-347, 1975, pp. 1067-1110.

9. Tseng, K. D.; and Morino, L.: Fully Unsteady Subsonic and Supersonic Potential Aerodynamics of Complex Aircraft Configurations for Flutter Application. Presented at AIAA/ASME/SAE 17th Structures, Structural Dynamics, and Materials Conference (King of Prussia, PA), May 5-7, 1976.

10. Konar, A. F.; et al: Digital Flight Control Systems for Tactical Fighters; Vol. I: Digital Flight Control Systems Analysis. AFFDL-TR-73-119, Vol. I, December 1973.

11. Bryson, A. E.; and Ho, Y. C.: Applied Optimal Control: Optimization, Estimation, and Control. Blaisdell Publishing Company, Waltham, MA, 1969.

12. Melsa, J. L.; and Jones, S. K.: Computer Programs for Computational Assistance in the Study of Linear Control Theory. McGraw-Hill Book Company, Inc., New York, 1973.
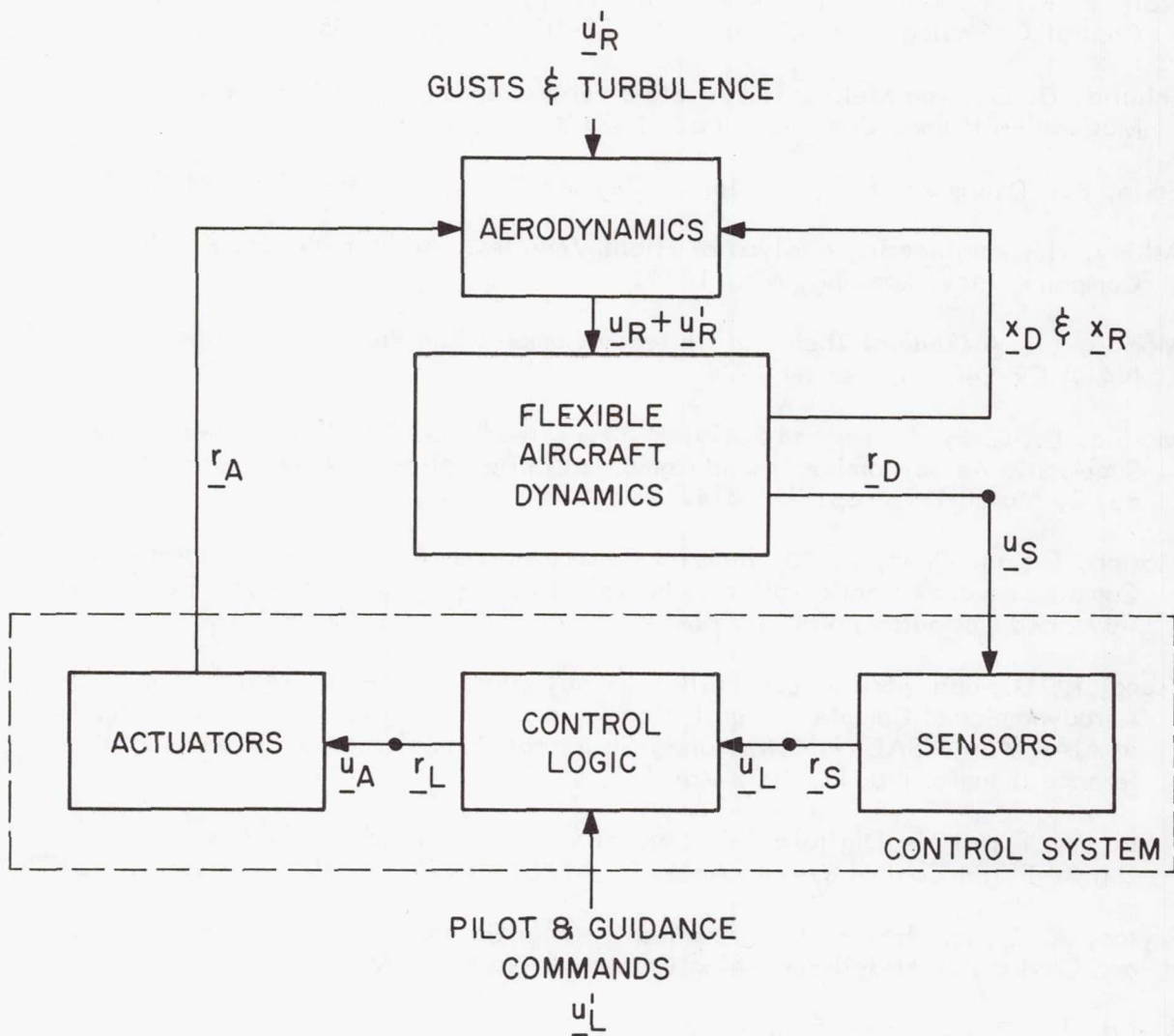
Figure 1. ACT System.

BEST-RANGE FLIGHT CONDITIONS FOR CRUISE-CLIMB

FLIGHT OF A JET AIRCRAFT

Francis J. Hale
Department of Mechanical and Aerospace Engineering
North Carolina State University

SUMMARY

The Breguet range equation is developed for cruise-climb flight of a jet aircraft to include the climb angle and is then maximized with respect to the no-wind true airspeed. The expression for the best-range airspeed is a function of the specific fuel consumption and minimum-drag airspeed and indicates that an operational airspeed equal to the fourth root of three times the minimum-drag airspeed introduces range penalties of the order of one percent.

INTRODUCTION

Although there is agreement in the literature as to the fact that a cruise-climb flight program (constant airspeed and constant lift coefficient) yields the maximum range for a given jet aircraft with a given fuel load, particularly at the longer ranges, there is no consensus as to the best-range flight conditions. Nicolai (ref. 1), for example, states that best-range occurs when the lift coefficient is equal to $(C_{DO}/2K)^{1/2}$, whereas Houghton and Brock (ref. 2) specify a lift coefficient equal to $(C_{DO}/3K)^{1/2}$. Miele (ref. 3), on the other hand, agrees with Nicolai at one point but at another implies agreement with Houghton and Brock. Perkins and Hage (ref. 4) mention the desirability of cruise-climb flight but do not identify the best-range flight conditions. Dommasch, Sherby, and Connolly (ref. 5) describe the superiority of cruise-climb flight and imply agreement with Houghton and Brock as to the best-range flight condition.

ANALYSIS

With the assumptions of quasi-steady flight, the thrust aligned with the velocity vector, and a constant flight-path angle γ that is sufficiently small so that its cosine may be assumed zero and its sine equal to the angle itself (expressed in radians), the governing equations of motion of an aircraft can be written as:

$$L = W$$
$$T = D + W\gamma \qquad (1)$$
$$\frac{dX}{dt} = V$$

1713

where T is the net installed thrust (N), L is the lift (N), W the gross weight of the aircraft (N), D the drag (N), X the range (km), and V the no-wind true airspeed (km/hr or m/s). The weight balance equation (fuel flow rate) for a jet aircraft can be expressed as:

$$\frac{dW}{dt} = - cT \tag{2}$$

where c is the thrust specific fuel consumption (N/hr/N). With the assumption of a parabolic drag polar (with the lift coefficient at minimum drag taken equal to zero) and with the flight conditions of a constant airspeed and a constant lift coefficient C_L, equations (1) and (2) can be combined and integrated to yield a cruise-climb Breguet range equation in the form:

$$X = \frac{VE}{c(1 + \gamma E)} \ln\left(\frac{1}{1 - \delta}\right) \tag{3}$$

where E is the lift-to-drag ratio (which remains constant) and δ, the cruise-fuel weight fraction, is equal to $\Delta W_f/W_1$, where ΔW_f is the cruise fuel (N) and W_1, is the weight of the aircraft at start of cruise. V is expressed in km/hr so that X is in km.

If both the lift coefficient and the airspeed are to remain constant as the weight of the aircraft decreases, the altitude must increase so as to maintain the ratio W/ρ constant, where ρ is the atmospheric density (kg/m^3). Consequently, the density ratio at the end of cruise, σ_2, can be expressed as

$$\sigma_2 = \sigma_1(1 - \delta) \tag{4}$$

By making use of the exponential approximation of the density ratio variation with altitude, the increase in altitude Δh (m) during cruise is given by

$$\Delta h = 7254 \ln\left(\frac{1}{1 - \delta}\right) \tag{5}$$

Combining equations (5) and (3) produces the following approximate expression for γ in terms of the propulsion and aerodynamic efficiencies:

$$\gamma = \frac{7.254c}{VE} \tag{6}$$

Substitution of equation (6) into equation (3) results in

$$X = \frac{VE}{c\left(1 + \frac{7.254c}{V}\right)} \ln\left(\frac{1}{1 - \delta}\right) \tag{7}$$

At this point a cruising airspeed parameter, m, is introduced by writing the cruising airspeed as

$$V = \left[\frac{2(W/S)}{\rho}\right]^{1/2}\left[\frac{mK}{C_{DO}}\right]^{1/4} = m^{1/4}\, V_{E_{max}} \tag{8}$$

where $V_{E_{max}}$ is the minimum-drag airspeed occurring at E_{max}. The lift coefficient can now be expressed as

$$C_L = \left[\frac{C_{DO}}{mK}\right]^{1/2} \tag{9}$$

where C_{DO} is the minimum-drag coefficient and K the induced drag coefficient. From equation (9) we see that Nicolai calls for an m equal to 2 for best cruise-climb range whereas Houghton and Brock think it should be 3. Miele opts for both values, although 2 is the only value he explicity states.

If V and E are expressed in terms of $V_{E_{max}}$, E_{max}, and m, equation (7) becomes

$$X = \frac{2V_{E_{max}}\, E_{max}}{c}\left[\frac{m}{(m+1)\left(m^{1/4}+\frac{7.254c}{V_{E_{max}}}\right)}\right]\ln\left(\frac{1}{1-\delta}\right) \tag{10}$$

where $V_{E_{max}}$ and E_{max} are design characteristics of the aircraft. The cruise-climb range is then maximized with respect to the airspeed by setting the first derivative of equation (10) with respect to m equal to zero (with c assumed constant). The resulting condition for the best-range airspeed is

$$m_{br}^{5/4} - 3m_{br}^{1/4} - \frac{29c}{V_{E_{max}}} = 0 \tag{11}$$

whose solution can be approximated with a high degree of accuracy by the expression

$$m_{br} = 3\left[1 + \frac{7.254c}{V_{E_{max}}}\right] \tag{12}$$

so that

$$V_{br} = m_{br}^{1/4}\, V_{E_{max}} \tag{13}$$

An expression for the associated best-range climb angle can be written as

$$\gamma_{br} = \frac{7.254c}{(VE)_{br}} = \frac{7.254c\,(m_{br}+1)}{2m_{br}^{3/4}\,(VE)_{E_{max}}} \tag{14}$$

DISCUSSION

The second term in the m_{br} expression of equation (12), $7.254c/V_{E_{max}}$, is normally small with respect to unity as can be seen in figure 1, where it is given the symbol A and represented by constant value lines for various pairings of c and $V_{E_{max}}$. As the minimum-drag airspeed increases and/or the specific fuel consumption decreases, the value of A decreases and the value of m_{br} approaches 3 as a limit so that V_{br} approaches $3^{1/4} V_{E_{max}}$. As an illustration, a $V_{E_{max}}$ of 724 km/hr (450 mph) and a c of 0.5 N/hr/N (0.5 lbf/hr/lbf) yield an A of 0.005, an m_{br} = 3.015, and a V_{br} = 954 km/hr (593 mph). If E_{max} of the aircraft is 18, then γ_{br} = 2.44 x 10^{-4} rad or +0.014 deg.

Relative ranges, normalized with respect to A = 0 (which represents the "level-flight" solution) are shown as a function of both A and m in figure 2. We see that the maximum range occurs when m = m_{br} = 3(1 + A) and that the curves are relatively flat in the vicinity of m_{br}, but drop off sharply as m is decreased below the value of 2. We also see that errors in the actual range introduced by using the level-flight solution are of the order of 1 to 1.5 percent for an m equal to 3 and of the order of 2.5 to 3.3 percent for an m of 2.

As m is increased, so also is the cruise-climb airspeed, as can be seen in figure 3, where again the relative airspeeds are normalized with respect to that for A equal to zero and m = 3. There is an upper limit to the value of m possible for a subsonic aircraft if the best-range airspeed is to remain equal to or less than the drag divergence airspeed. If equal to, m will be 3; if less than, m can be appropriately greater than 3. As a side note, if the best-range airspeed is greater than the drag divergence airspeed, then m must be less than 3 and is no longer a cruising airspeed parameter but rather a wing-loading, cruising-altitude parameter.

CONCLUSIONS

Since an aircraft operated in the cruise-climb mode will probably be characterized by an A of the order of 0.01 or less, we conclude that the use of the "level-flight" (A = 0) version of the Breguet range equation will produce range errors of less than one percent and that the "level-flight" value of m can be used operationally without the necessity of calculating a specific m for cruise-climb flight. We also conclude that the Houghton and Brock value of 3 for m_{br} is not only much closer to the actual best-range value than the other published value of 2 but also calls for a cruising airspeed that is 10 percent higher, with a corresponding decrease in the flight time.

REFERENCES

1. Nicolai, L. M.: Fundamentals of Aircraft Design. Dayton, Ohio: University of Dayton, 1975, pp. 314-316.

2. Houghton, E. L.; and Brock, A. E.: Aerodynamics for Engineering Students. London: Edward Arnold, Ltd., 1972, pp. 200-201.

3. Miele, A.: Flight Mechanics, Vol. I. Reading, Massachusetts: Addison-Wesley Publishing Company, Inc., 1962, pp. 167-168 and 170.

4. Perkins, C. D.; and Hage, R. E.: Airplane Performance Stability and Control. New York: John Wiley & Sons, Inc., 1949, p. 141.

5. Dommasch, D. O.; Sherby, S. S.; and Connolly, T. F.: Airplane Aerodynamics, Third Edition. London: Sir Isaac Pitman & Sons, Ltd., 1961, pp. 339-340.
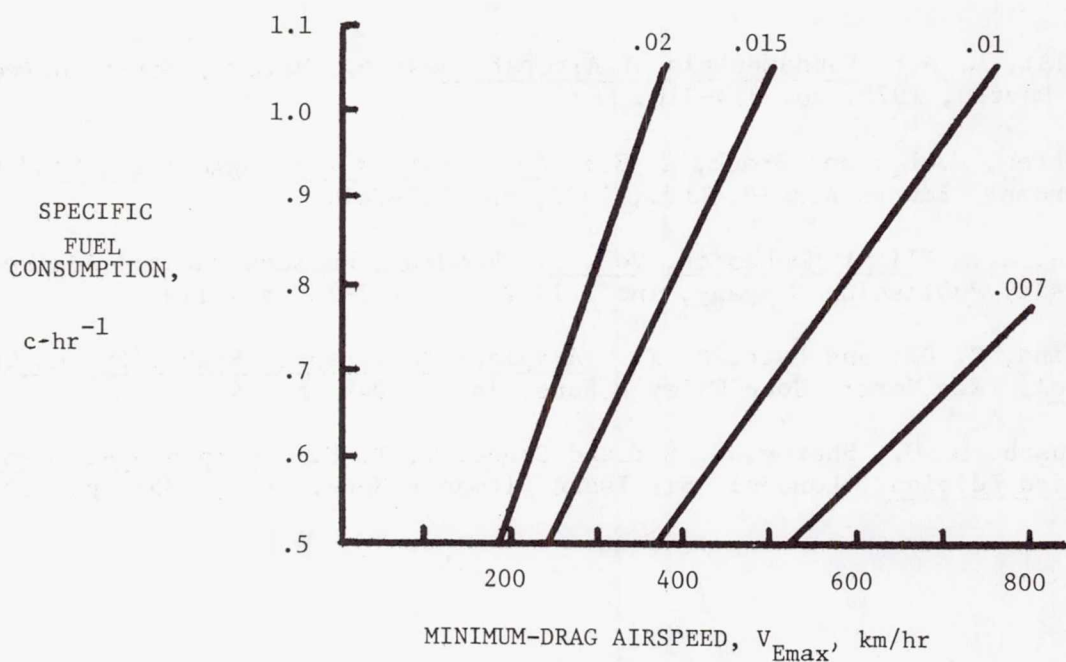
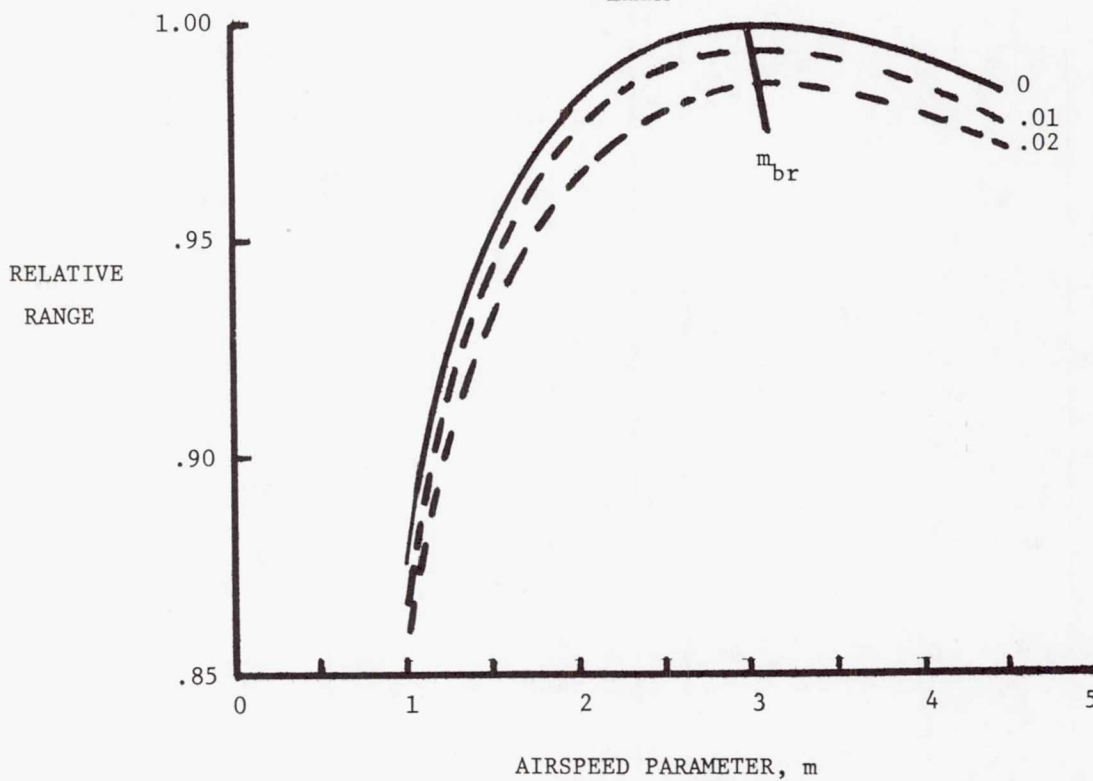Figure 1.- Constant values of a $(7.254 \ c/V_{Emax})$ for various values of c and V_{Emax}.

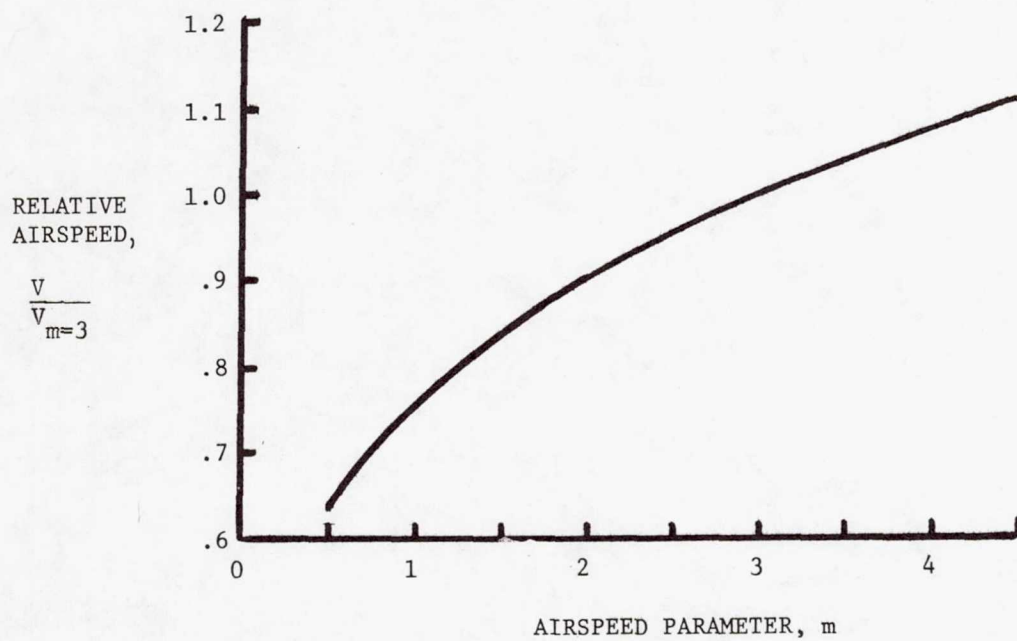Figure 2.- Relative cruise-climb range as a function of m and A.

Figure 3.- Relative airspeed as a function of the airspeed parameter m.

Page intentionally left blank

EXPERIMENT DESIGN FOR PILOT IDENTIFICATION

IN COMPENSATORY TRACKING TASKS

William R. Wells
University of Cincinnati

SUMMARY

A design criterion for input functions in laboratory tracking tasks resulting in efficient parameter estimation is formulated. The criterion is that the statistical correlations between pairs of parameters be reduced in order to minimize the problem of non-uniqueness in the extraction process. The effectiveness of the method is demonstrated for a lower order dynamic system.

INTRODUCTION

The art of human operator modeling has progressed considerably since the pioneering work of Sheridan (ref. 1), Elkind et. al. (ref. 2), and McRuer et. al. (ref. 3). Many of the accepted transfer functions for the human operator in compensatory tracking tasks are given in reference 4. The model structure for the human operator is not known as precisely for such systems as the aircraft, for example. There are large variations from one subject to another and from run to run. In most cases, the pilot model includes such physical parameters as a static gain, an effective time delay made up of transport delays, and high frequency neuromuscular lags or leads and turns which represent the low frequency characteristics of the neuromuscular system dynamics. In addition, a remnant function is generally included in the model to account for pilot anomalies and unsteady behavior. It has been pointed out by various authors (refs. 5-6) that large remnants and the quasi-predictable nature of the inputs cause difficulties in the extraction of the physical parameters in the pilot model.

Early attempts to determine the best set of parameters, in particular pilot models utilizing pilot response data, relied upon analog matching techniques (ref. 7). More recent techniques have applied Kalman filtering methods (ref. 8), maximum likelihood methods (ref. 9), or Newton-Raphson methods (ref. 9) to the system identification problem.

One of the practical difficulties in the extraction of system parameters from experimental data is the non-uniqueness in the solution for the parameter values (ref. 10). In the case of human operator dynamics, the non-uniqueness problem is amplified by the high correlations which can exist between the pilot's effective time delay and the time lags associated with the equalization characteristics discussed by McRuer et. al. (ref. 3). Normally, the time delay is either assumed known or represented by a Pade form which places it in the role of either lead or lag constants (ref. 9).

This paper addresses the task of reducing the non-uniqueness and possibly the effect of the remnant by proper design of the forcing function or disturbance used in laboratory designed tracking tasks.

MODELS

The performance of a human operator in many tracking tasks can be modeled adequately by a quasi-linear describing function. The describing function model consists of a transfer function $Y_p(s)$ and a remnant $\eta(t)$ as shown in figure 1 by the block diagram of a typical compensatory tracking task.

One of the more generalized transfer functions for the compensatory control tasks is discussed in reference 4 and is written as

$$Y_p(s) = K_p e^{-s\tau} \frac{(T_L s + 1)}{(T_I s + 1)}$$

$$x \quad \frac{(T_k s + 1)}{(T_k' s + 1)(T_{N_1} s + 1)[(\frac{s}{\omega_N})^2 + \frac{2\xi_N}{\omega_N} s + 1]} \tag{1}$$

In such a model, the parameters K_p, τ, T_L, T_I, T_k, T_k', T_{N_1}, ω_N, and ξ_N are generally poorly determined and are improved upon by using either analog matching techniques or parameter estimation methods in conjunction with pilot response data.

Depending upon the plant to be controlled, some of the parameters in equation (1) can be eliminated from consideration. For purposes of illustration of how the problem can be put into

a state space formulation for which the methods of modern estimation algorithms can be utilized, the following special case will be considered:

$$Y_c(s) = \frac{K}{s^2} \tag{2}$$

$$Y_p(s) = \frac{K_1(T_3 s+1)\, e^{-s\tau}}{(T_1 s+1)(T_2 s+1)} \tag{3}$$

In addition, it is assumed that the remnant function is the result of white noise $w_p(t)$ filtered through a second-order linear filter according to

$$\ddot{\eta}(t) + \alpha_1\, \dot{\eta}(t) + \alpha_2\, \eta(t) = w_p(t) \tag{4}$$

From the block diagram

$$T_1 T_2\, \ddot{u}(t) + (T_1 + T_2)\dot{u}(t) + u(t) = K_1[T_3\, \dot{e}(t-\tau) + e(t-\tau)] \tag{5}$$

$$\ddot{c}(t) = K\delta(t) \tag{6}$$

Equations (4)-(5) can be written in terms of the state variables

$$y(t) = (y_1, y_2, y_3, y_4, y_5, y_6)^T$$

$$= [c(t), \dot{c}(t), u(t), \frac{K_1 T_3}{T_1}\, r(t) + u(t+\tau) + T_2 \dot{u}(t+\tau),$$

$$\eta(t), \dot{\eta}(t)]^T \tag{7}$$

as

$$\dot{y}(t) = F_1\, y(t) + F_2\, y(t-\tau) + b(t) + d(t) \tag{8}$$

where

$$F_1 = \begin{bmatrix} 0 & 1 & 0 & 0 & 0 & 0 \\ 0 & 0 & K & 0 & K & 0 \\ 0 & 0 & \dfrac{1}{T_2} & 0 & 0 & 0 \\ \dfrac{K_1}{T_1} & \dfrac{K_1 T_3}{T_2} & 0 & \dfrac{1}{T_1} & 0 & 0 \\ 0 & 0 & 0 & 0 & 0 & 1 \\ 0 & 0 & 0 & 0 & -\alpha_2 & -\alpha_1 \end{bmatrix}$$ (9)

$$F_2 = \begin{bmatrix} 0 & 0 & 0 & 0 & 0 & 0 \\ 0 & 0 & 0 & 0 & 0 & 0 \\ 0 & 0 & 0 & \dfrac{1}{T_2} & 0 & 0 \\ 0 & 0 & 0 & 0 & 0 & 0 \\ 0 & 0 & 0 & 0 & 0 & 0 \\ 0 & 0 & 0 & 0 & 0 & 0 \end{bmatrix}$$ (10)

and

$$b(t) = [0,\ 0,\ 0,\ \frac{K_1}{T_1}\ r(t),\ 0,\ 0]^T$$ (11)

$$d(t) = [0,\ 0,\ 0,\ 0,\ 0,\ w_p(t)^T$$ (12)

The measurements used in the estimation procedure are generally such quantities as the plant output $c(t)$, the stick output $\delta(t)$, etc. These quantities are written as a vector

$$z(t) = h(y) + v(t) \tag{13}$$

where $v(t)$ is assumed to be a white noise process with known statistics.

DESIGN METHOD

The design of optimal inputs for non-time delay differential systems has been investigated by numerous authors. Goodwin (ref. 11) designed an input which minimized the covariance of the error estimate. Mehra (ref. 12) designed an input to maximize the sensitivity of the system output to the system parameters. The philosophy adopted in the present work is to design an input to minimize directly the correlation between certain pairs of parameters.

The problem is stated in terms of a differential-difference equation as given in equation (8) restated as

$$\dot{y}(t) = f(t, y(t), y(t-\tau), p) + u(t) + w(t) \tag{14}$$

with initial values

$$y(t) = 0, t_o - \tau \le t \le t_o$$

τ is the constant time delay and p is the unknown parameter vector. The vector $u(t)$ is to be chosen optimally based on a design criterion and $w(t)$ is the white noise process related to the remnant.

The system measurement from which p is estimated is taken as the system state vector $y(t)$. The noise in the measurement is assumed a Gaussian white noise process with zero mean and co-variance R.

In addition to the state equation expressed by equation (14) it will prove useful to introduce additional state variables defined by the elements of the sensitivity matrix $A(t)$ and the time dependent covariance matrix of the error in the estimate $C(t)$ defined respectively according to

$$\dot{A}(t) = \frac{\partial f}{\partial x(t)} A(t) + \frac{\partial f}{\partial x(t-\tau)} A(t-\tau) + \frac{\partial f}{\partial p} \tag{15}$$

$$A(t) = 0, \qquad t_o - \tau \le t \le t_o$$

and

$$\dot{C}(t) = -C(t) \, A^T(t) \, R^{-1} \, A(t) \, C(t) \qquad (16)$$

$$C(t_f) = [\int_{t_o}^{t_f} A^T(t) \, R^{-1} \, A(t) dt]^{-1} \qquad (17)$$

With these additional equations, it is possible to incorporate equations (14)-(16) into one differential equation of the form

$$F(t, \, X(t), X(t-\tau), \, \dot{X}(t), \dot{X}(t-\tau), u(t), \, w(t), \, p) = 0 \qquad (18)$$

where the augmented state vector X is defined as

$$X(t) = [x^T(t) \quad c^{(1)T}(t) \; .... \; c^{(m)T}(t) \quad A^{(1)T}(t) \; ....A^{(n)T}(t)]^T$$

and

$$c^{(1)}(t) = [C_{11}(t), \; C_{22}(t), ... \; C_{mm}(t)]^T$$

$$c^{(2)}(t) = [C_{12}(t), \; C_{23}(t), ...C_{m-1,m}(t)]^T$$
$$\cdots \cdots$$
$$c^{(m)}(t) = C_{1m}(t)$$

$$A^{(1)}(t) = [\frac{\partial x_1(t)}{\partial p_1}, \; \frac{\partial x_1(t)}{\partial p_2}, ... \; \frac{\partial x_1(t)}{\partial p_m}]^T$$

$$\cdots \cdots \cdots$$

$$A^{(n)}(t) = [\frac{\partial x_n(t)}{\partial p_1}, \; \frac{\partial x_n(t)}{\partial p_2}, \; .... \; \frac{\partial x_n(t)}{\partial p_m}]^T$$

The optimal input is designed to minimize the average value of a performance index representing a weighted sum of the squares of the correlation coefficient plus an arbitrary function in the control variable. The correlation coefficient between parameters ρ_i and ρ_j is defined as

$$\rho_{ij} = \sqrt{C_{ij}(t_f) \; / \; C_{ii}(t_f) C_{jj}(t_f)}, \qquad -1 \le \rho_{ij} \le 1$$

The performance index can then be written in conventional form as

$$J(u) = E \{ \psi(X(t_f)) + \int_{to}^{t_f} L(X(t), u(t), t) dt \} \qquad (19)$$

where the first term represents the weighted sum of the squares
of the correlation coefficients. The second term can be chosen
according to whatever physical requirement is desired between the
state and control vectors.

EXAMPLE WITH LOW ORDER DYNAMICS

As an example of the design concept, consider the scalar
system

$$\dot{x}(t) + \frac{1}{\xi} x(t-\tau) = u(t) + w(t), \quad o \leq t \leq 4 \qquad (20)$$

$$x(t) = o, \quad -\tau \leq t \leq o$$

where ξ and τ are the system parameters to be estimated and u and
w are the input and white noise funtions respectively. The in-
put or control is constrained according to

$$|u| \leq 2$$

and is assumed zero prior to time zero.

The performance index, which is the square of the correlation
coefficient between parameters ξ and τ is

$$J(u) = \frac{\int_o^4 a_1(t) a_2(t) dt)^2}{(\int_o^4 a_1^2(t) dt)(\int_o^4 a_2^2(t) dt)} \qquad (21)$$

The form of the optimal control is a bang-bang control expressed
as

$$\dot{u}(t) = 2 \operatorname{sgn} g(\hat{x}(t,\tau), t) \qquad (22)$$

where g is the switching function which can be computed from the
maximum principle. The optimal estimate of $x(t-\tau)$ denoted
$\hat{x}(t,\tau)$ has been shown by Kwakernaak (ref. 13) to be of the form

$$\hat{x}(t,\tau) = \int_o^t K^o(t,\tau,\sigma) z(\sigma) d\sigma \qquad (23)$$

where the Kernel function K^o is a function of the state equation
and noise source.

To continue, a further simplification to the deterministic
case will be made. For this case, the sensitivity matrix is the
two component row vector

$$A(t) = \left[\frac{\partial x(t)}{\partial \xi}, \quad \frac{\partial x(t)}{\partial \sigma} \right] \tag{24}$$

which satisfy the equations

$$\dot{a}_1(t) + \frac{1}{\xi} a_1(t-\tau) = -\frac{1}{\xi} \dot{x}(t) \tag{25}$$

$$\dot{a}_2(t) = \frac{1}{\xi} \dot{x}(t-\tau)$$

By use of Laplace transform techniques, the solutions to equations (20) and (25) are written as

$$x(t) = \int_0^t h(t-\sigma) u(\sigma) d\sigma \tag{26}$$

$$a_1(t) = -x(t) + \frac{1}{\xi} \int_0^t h(t-\sigma) x(\sigma) d\sigma \tag{27}$$

$$a_2(t) = h(0) x(t-\tau) + \int_0^t \dot{h}(t-\sigma x(\sigma-\tau) d\sigma \tag{28}$$

where $h(t)$ is the unit impulse response

$$h(t) = \sum^{\infty} e^{\lambda_i t} [1-\tau/\xi e^{-\lambda_i}]^{-1} \tag{29}$$

and λ_k is the kth eight value of the characteristic equation

$$\xi\lambda + e^{-\lambda\tau} = 0 \tag{30}$$

The effectiveness of the design technique for $\xi = \tau = 1/2$ is shown in figure 2. The correlation $\rho_{\xi\sigma}$ is reduced from a value of 0.60 to 0.09 by means of the design technique.

CONCLUDING REMARKS

An optimal design technique for disturbance functions used in laboratory tracking tasks has been developed. The objective is to reduce statistical correlations between various parameter pairs to effect a more efficient parameter extraction from noisy experimental data. Preliminary calculations indicate the design methods to be effective.

REFERENCES

1. Sheridan, T. B.: Time Variable Dynamics of Human Operator
    Systems. Air Force Cambridge Research Center, AFCRC-TN-60-
    169, Bedford, Mass., 1960.

2. Elkind, J. I. and Forgie, C. D.: Characteristics of the
    Human Operator in Simple Manual Control Systems. IRE Trans.
    on Automatic Control, Vol. AC-4, May 1959.

3. McRuer, D.; Graham, D.; Krendel, E.; and Reisener, W. Jr.:
    Human Pilot Dynamics in Compensatory Systems. Air Force
    Flight Dynamics Laboratory, AFFDL-TR-65-15, July 1965.

4. McRuer, D. and Jex, H.: A Review of Quasi-Linear Pilot Models.
    IEEE Transactions on Human Factors in Electronics, Vol.
    HFE8, No. 3, September 1967.

5. Mehra, R. K. and Tyler, J. S.: Modeling the Human Operator
    Under Stress Conditions Using System Identification. Pre-
    prints, 1972 Joint Automatic Control Conference, Stanford,
    Calif., August 1972.

6. Krendel, E. S. and McRuer, D. T.: A Servomechanisms Approach
    to Skill Development. J. Franklin Inst., January 1960.

7. Adams, J. J. and Bergeron, H. P.: A Synthesis of Human Res-
    ponse in Closed-Loop Tracking Tasks. NASA TN D-4842,
    October 1968.

8. Schiess, J. R.; Wells, W. R.; and Roland, V. R.: Estimation
    of Nonlinear Pilot Model Parameter Including Time Delays.
    Proceedings of the Second Symposium on Nonlinear Estimation
    Theory and its Applications, San Diego, Calif., September
    1971.

9. Kugel, D. L.: Determination of In-Flight Pilot Parameter
    Using a Newton-Raphson Minimization Technique. Proceedings
    of the 10th Annual Conference on Manual Control, Wright-
    Patterson Air Force Base, April 1974.

10. Wells, W. R. and Ramachandran, S.: Flight Test Design for
    Efficient Extraction of Aircraft Derivatives. Proceedings
    of the 3rd AIAA Atmospheric Flight Mechanics Conference,
    Arlington, Texas, June 1976.

11. Goodwin, G. C.: Input Synthesis for Minimum Covariance State
    and Parameter Estimation, Electronics Letters, Vol. 5, No.
    21, October 1969.

12.   Mehra, R. K.:   Optimal Inputs for Linear System Identifica-
      tion.   IEEE Trans. on Automatic Control, Vol. AC-19, No. 3,
      June 1974.

13.   Kwakernaak, H.:   Optimal Filtering in Linear Systems with
      Time Delays.   IEEE Trans. on Automatic Control, Vol.
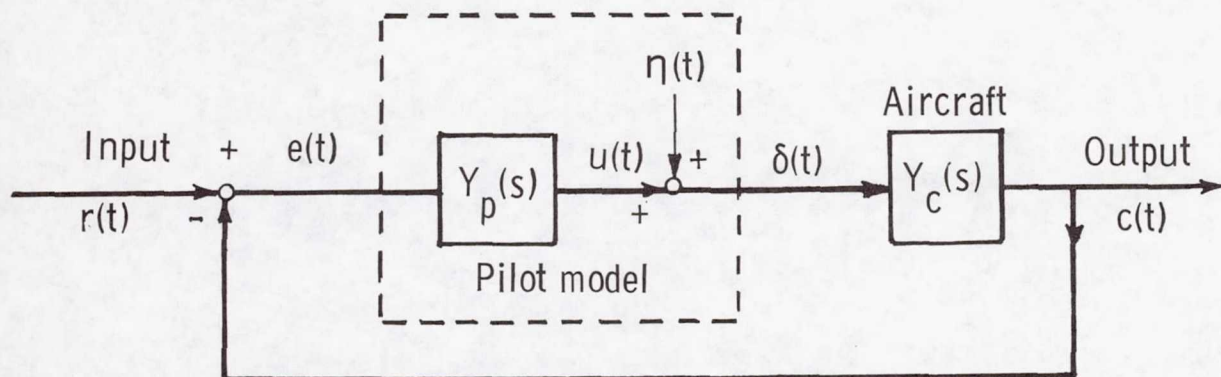   AC-12, No. 2, April 1967.

Figure 1.- Block diagram of the compensatory tracking task.
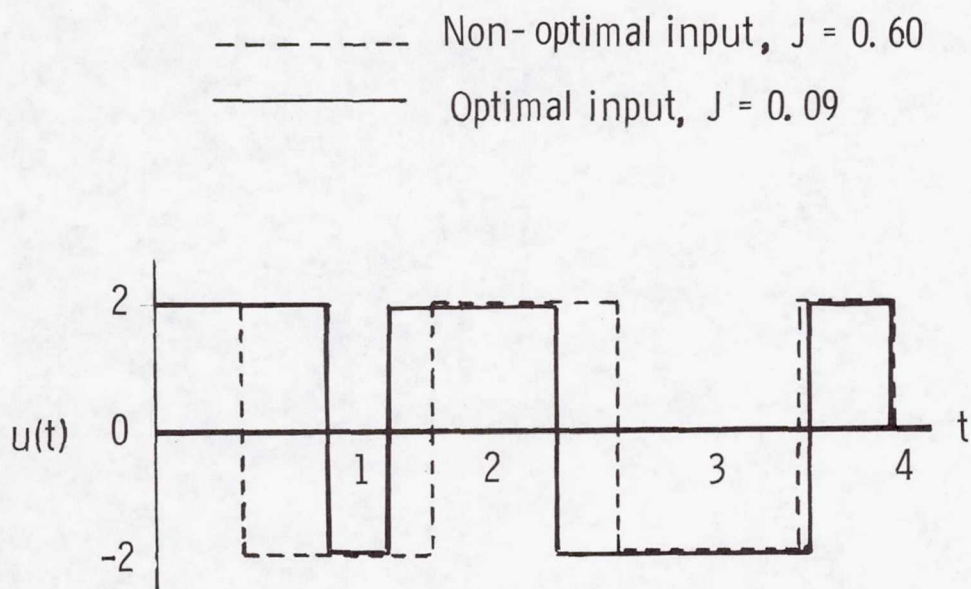

Figure 2.- Control input history.

Page intentionally left blank

RESULTS OF RECENT NASA STUDIES ON

AUTOMATIC SPIN PREVENTION FOR FIGHTER AIRCRAFT

Joseph R. Chambers and Luat T. Nguyen
NASA Langley Research Center

SUMMARY

The NASA Langley Research Center is currently engaged in a broad-based research program to eliminate or minimize inadvertent spins for advanced military aircraft. Recent piloted simulator studies and airplane flight tests have demonstrated that the automatic control systems in use on current fighters can be tailored to provide a high degree of spin resistance for some configurations without restrictions to maneuverability. Such systems result in greatly increased tactical effectiveness, safety, and pilot confidence.

INTRODUCTION

Recent experience has shown that most contemporary fighter airplanes exhibit poor stall characteristics and a strong tendency to spin. They also have poor spin characteristics, and recovery from a fully developed spin is usually difficult or impossible. As a result of these unsatisfactory stall and spin characteristics, the developed spin is currently an undesirable and potentially dangerous flight condition which should be avoided. There is, therefore, an urgent need to develop guidelines for use in the design of future military aircraft in order to minimize or eliminate spins and insure good handling qualities at high angles of attack. The National Aeronautics and Space Administration (NASA) currently has a broad research program underway to provide these guidelines. As shown in figure 1, the program includes conventional static wind-tunnel force tests, dynamic force tests, flight tests of dynamically scaled models, theoretical studies, and piloted simulator studies.

Two approaches to providing spin resistance are currently under consideration. In the first approach, the basic airframe is configured to be inherently spin resistant by virtue of good stability and control characteristics at high angles of attack. At the present time, however, the configuration-dependent nature of the problem and a lack of understanding of the major factors affecting stability and control characteristics at high angles of attack for current fighters have prevented the development of detailed design procedures for inherent spin resistance. The second more promising approach to providing spin resistance is through the use of avionics and flight control system elements in automatic spin prevention concepts. Such concepts can be highly effective in preventing inadvertent stalls and spins; however, they must be designed so as not to restrict the maneuverability and tactical effectiveness of the airplane.

1733

The present paper discusses the results of recent NASA studies on automatic spin prevention. The studies were conducted at the NASA Langley Research Center (LaRC) using piloted simulator studies.

SYMBOLS

b	wing span, m (ft)
C_ℓ	rolling-moment coefficient, $\dfrac{M_x}{qSb}$
C_{ℓ_p}	damping in roll parameter, $\dfrac{\partial C_\ell}{\partial \dfrac{pb}{2V}}$
C_{ℓ_β}	effective dihedral derivative, $\dfrac{\partial C_\ell}{\partial \beta}$, per deg
$C_{\ell_{\delta_a}}$	aileron rolling-moment derivative, $\dfrac{\partial C_\ell}{\partial \delta_a}$, per deg
C_n	yawing-moment coefficient, $\dfrac{M_z}{qSb}$
C_{n_r}	damping in yaw parameter, $\dfrac{\partial C_n}{\partial \dfrac{rb}{2V}}$
C_{n_β}	directional stability derivative, $\dfrac{\partial C_n}{\partial \beta}$, per deg
$C_{n_{\beta,dyn}}$	dynamic directional stability parameter, $C_{n_\beta} - C_{\ell_\beta} \dfrac{I_z}{I_x} \sin \alpha$, per deg
$C_{n_{\delta_a}}$	aileron yawing-moment derivative, $\dfrac{\partial C_n}{\partial \delta_a}$, per deg
I_x, I_z	moments of inertia about X- and Z-body axes, kg-m^2 (slug-ft^2)
M_x, M_z	moments about X- and Z-body axes, m-N (ft-lb)
p	rolling velocity, deg/sec
q	free-stream dynamic pressure, Pa (lb/ft^2)
r	yawing velocity, deg/sec
r_s	$\simeq r - p\alpha$, deg/sec
S	wing area, m^2 (ft^2)
$t_{1/2}$	time to half amplitude, sec

V	airspeed, m/sec (ft/sec)
α	angle of attack, deg
β	angle of sideslip, deg
δ_a	aileron deflection, deg
δ_r	rudder deflection, deg
ϕ	angle of roll, deg

AUTOMATIC SPIN PREVENTION CONCEPTS

Experience has shown that spins can generally be avoided if the proper recovery action is taken immediately after departure from controlled flight while the spin energy is low and the aerodynamic controls are effective. The problem in effecting such early recovery is that the pilot frequently is not able to take immediate corrective action because of disorientation which results from his lack of experience with spins of such aircraft, from the fact that the departure and spin entry occurred unexpectedly when he was intent on another task, and from the violent and confusing nature of the motions during spin entry for many airplanes. This situation would seem to suggest the use of an automatic system which could quickly identify the situation and take the required action. An electronic system capable of this task would have several inherent advantages over the human pilot, including (1) quicker and surer recognition of an incipient spin, (2) faster reaction time for initiation of recovery, (3) application of correct spin-recovery controls, and (4) elimination of tendencies toward spin reversal.

The idea of automatic spin-prevention, or recovery, systems is not new. Stick pushers that prevent, or discourage, stalling the airplane are, in a sense, spin-prevention systems; but they may restrict the pilot from exploiting the full potential-maneuver envelope of the airplane. The installation of more elaborate automatic spin-prevention, or recovery, systems has, until recent years, involved the addition of complete sensing, logic, and control systems at a time when such devices were not very reliable and would probably not have been maintained in proper operating condition because they were protecting against a very rare occurrence. The fact that modern tactical airplanes already incorporate most of the elements of automatic spin-prevention (or recovery) systems, together with a great increase in the reliability of avionics systems, now makes the use of these automatic systems more practical.

Several approaches to automatic spin prevention have been evaluated by NASA. The concepts studied and the area of application of each concept are graphically depicted in figure 2. Yaw rate and angle of attack are used as the primary variables identifying spin entry. For a particular airplane configuration, one can generally identify two important areas in the yaw-rate—angle-of-attack plane: the airplane maneuver envelope involving relatively low values of yaw rate and angle of attack, and the developed spin

region involving relatively high values of yaw rate and angle of attack. Three types of automatic control concepts have been evaluated: (1) automatic spin recovery, (2) automatic spin prevention, and (3) automatic departure prevention.

In the automatic-spin-recovery concept, the airplane is allowed to depart from controlled flight, experience the incipient spin, and enter the fully developed spin. Values of yaw rate and angle of attack supplied by the sensors used in the automatic control system are sampled to identify the developed spin condition and actuate the proper recovery controls. The results of a study of the effectiveness and value of such a system (ref. 1) indicated that the primary benefits of this type of concept were: rapid identification of the spin, input of proper recovery controls, and minimization or elimination of spin reversals following recovery. The concept obviously requires the airplane under consideration to have satisfactory spin-recovery characteristics. Inasmuch as most current fighter designs have poor recovery characteristics from developed spins, it would appear that systems of this type would be relatively ineffective. In fact, the concept appears to be working "the wrong end of the problem."

The automatic-spin-prevention concept indicated in figure 2 also allows the airplane to depart from controlled flight; however, recovery controls are actuated during the early stages of the incipient spin when recovery characteristics are generally good. By simultaneously sensing angle of attack and yaw rate, a control actuation boundary can be established which limits the attainable magnitudes of these variables, thereby preventing spins. An automatic-spin-prevention system concept has been studied (ref. 1) using theoretical studies and flight tests of an unpowered drop model of a current military configuration. The results of the theoretical studies showed that such a system was extremely effective in preventing developed spins, and that the exact configuration of the automatic system will depend on the stall/spin characteristics of the airplane design under consideration. The model flight tests verified the theoretical results and showed that current flight-control components could be used to implement the system.

As might be expected, the control actuation boundary for the automatic-spin-prevention concept can be designed to be in proximity to the normal flight envelope, thereby permitting only minimal excursions from controlled flight. It should be pointed out that the concept described does not infringe on the maneuverability of the airplane or restrict the tactical effectiveness of the vehicle. Rather, the system quickly senses an out-of-control condition and impending spin and applies control inputs required of the pilot in a rapid, correct manner.

The automatic-spin-prevention concept appears to be ideally suited for airplanes which are especially susceptible to inadvertent spins. In particular, configurations which exhibit a severe directional divergence and loss of control power at high angles of attack are appropriate for application of the system if no limit is desired on angle of attack attained during normal flight. Fighter configurations, however, may exhibit a divergence at an angle of attack considerably higher than those used in normal maneuvering flight. In this case, artificial angle-of-attack limiting systems may be more appropriate.

Recently, a number of fighter configurations have been developed which are dynamically stable at high angles of attack with no natural tendency to diverge in yaw. However, the designs are subject to control-induced departures from controlled flight as a result of large values of adverse yaw at high angles of attack. These vehicles are well suited for the application of automatic-departure-prevention concepts (ref. 2) which, as indicated in figure 2, operate within the normal maneuver envelope of the airplane in order to prevent natural or control-induced departures from controlled flight. It will be shown that the use of such systems does not inhibit maneuvering of the airplane at high angles of attack and actually increases the usable maneuverability as well as the pilot's confidence during strenuous maneuvers.

EVALUATION PROCEDURES

Several techniques have been developed at LaRC for the evaluation of automatic departure/spin-prevention systems. As previously mentioned, free-flight tests of dynamically scaled models and theoretical studies of flight motions have been extremely valuable in assessing the effectiveness of such systems; however, these techniques do not allow an evaluation of pilot reaction to the effects of automatic systems on maneuverability and tactical effectiveness. The Langley differential maneuvering simulator (DMS) has therefore been used to obtain such information.

The DMS is a fixed base simulator which has the capability of simultaneously simulating two airplanes as they maneuver with respect to one another. Each pilot is provided a visual display of the sky-Earth orientation with respect to his airplane; in addition, a projected image of his opponent's airplane is also provided by way of a computer-controlled television system. A sketch of the general arrangement of the DMS hardware and control console is shown in figure 3. Contained within each of two 40-ft (12.2-m) diameter projection spheres are a cockpit, an airplane image projection system, and a sky-Earth projection system. A photograph of one of the cockpits and the target visual display during a typical engagement is shown in figure 4. A cockpit and instrument display representative of current fighter aircraft equipment are used together with a fixed gunsight for tracking. A programmable, hydraulic, control-feel system provides the capability of representing realistic control-force characteristics. Some of the unique capabilities of the DMS which make it well suited for studies of automatic departure-spin prevention are: the realistic cockpit/visual presentation, the use of realistic evaluation tasks, and the ability to handle comprehensive data packages. Additional details on the DMS facility are given in reference 3.

Previous experience with the simulation of fighter stall/spin characteristics (ref. 4) has shown that visual tracking tasks which require the pilot to divert his attention from the instrument panel are necessary to provide realism in studying the possibility of unintentional loss of control and spin entry. Furthermore, earlier studies have shown that mild, well-defined maneuvers can produce misleading results inasmuch as a configuration that behaves fairly well in such mild maneuvers may be violently uncontrollable in the

complex and pressing nature of high-g, air-combat maneuvering. Finally, for purposes of evaluation in comparing the performance of several configurations, the tasks employed must be repeatable. The test procedures used in the DMS studies account for the foregoing factors and can generally be divided into two phases. The first involves nontracking tasks in which the evaluation airplane is flown through individual high-angle-of-attack maneuvers including 1-g stalls, wind-up turns, high-g roll reversals, hammerhead stalls, and coupling maneuvers. These tests allow a comprehensive examination of the airplane's overall stability and control characteristics at high angles of attack including conditions involving complex aerodynamic and inertia coupling. In addition, they indicate the types of maneuvers which are the most critical in terms of the departure susceptibility of the airplane. The second test phase involves tracking of a target airplane through a series of maneuvers representative of air combat maneuvering (ACM). In order to obtain reasonable maneuvers which, on the other hand, will force the tracking airplane into maneuvering in the critical high-angle-of-attack regime, the target airplane is programed to have the same thrust and performance characteristics as the evaluation airplane; however, the target airplane is given idealized high-angle-of-attack stability and control characteristics. The target airplane is flown by the evaluation pilot through a series of ACM tasks of varying levels of difficulty while the target's motions are recorded for playback later to drive the target as the task for the evaluation airplane. Results obtained in the first test phase are factored into the generation of these target maneuvers so that the most critical flight conditions will be encountered by the evaluation airplane during tracking. These tracking tasks generally fall into three categories: (a) steady wind-up turns for steady tracking evlauation, (b) bank-to-bank (or horizontal S) tasks with gradually increasing angle of attack up to maximum α to evaluate rapid rolls and target acquisition, and (c) complex, vigorous ACM tasks to evaluate the simulated airplane's susceptibility to high-angle-of-attack handling qualities problems during aggressive maneuvering. These tracking tasks, then, provide the complex, repeatable, pilot-attention-out-of-the-cockpit tasks which are required for realistic investigation of unintentional loss of control and spin entry.

The results of these studies using the above evaluation procedures are in the form of time-history records of airplane motions and pilot comments regarding the departure/spin susceptibility of particular configurations and the effects of automatic prevention systems on these characteristics. The objectives of such studies are: (1) to determine the controllability and departure resistance of a configuration during 1-g stalls and accelerated stalls, (2) to determine the departure susceptibility of the configuration during demanding air combat maneuvers, and (3) to identify maneuvers or flight conditions which might overpower the departure-resistant characteristics provided by the automatic control system. Some of the more significant results are reviewed in the following section.

RESULTS OF SIMULATION

At the present time, simulator studies of the application of automatic departure/spin-prevention systems have been conducted at LaRC for the F-14,

YF-16, and YF-17 airplanes. The results of the studies show that such systems can be very effective in preventing inadvertent departures from controlled flight during strenuous maneuvering. The resulting improvement in high-angle-of-attack characteristics markedly improves handling, maneuverability, and safety. As a result of these improvements, the pilot's confidence in the capability of the vehicle is greatly increased, and the configuration can be used to its full capability. All of the studies show that these automatic systems can be implemented with current flight hardware. As examples of the applications of such systems, two types of departure/spin-prevention concepts that have been studied will be discussed.

Roll-Yaw Interconnect Systems

Shown in figure 5 are typical lateral-directional control characteristics for fighter configurations with adverse yaw. The data show the variation with angle of attack of yawing moments produced by ailerons and rudder for right roll and right yaw control inputs. The yawing moments produced by ailerons at low angles of attack are favorable (nose right) for right roll control; however, the moments become adverse (nose left) at high angles of attack. Right rudder input produces a normal nose right moment, but at high angles of attack the rudder loses effectiveness because of impingement of the low energy wake from the partially stalled wing. As can be seen, the magnitudes of the adverse moments due to ailerons are much larger than the corrective moments available from the rudder. When the resulting adverse moments are coupled with low directional stability at high angles of attack, a reversal of roll response occurs wherein the airplane rolls in a direction opposite to that desired by the pilot.

Shown in figure 6 are calculated time histories which illustrate the roll reversal phenomenon. The roll response of a typical configuration is shown at an angle of attack of 25° for control inputs of rudder alone and aileron alone for right roll control. The response to the rudder input is seen to be quite normal. The airplane yaws to the right, creating nose-right sideslip. The dihedral effect then rolls the airplane to the right, as desired. In contrast to this result, input of aileron control creates adverse yaw which causes the airplane to yaw to the left, and the sideslip created is in the opposite direction, resulting in the dihedral effect opposing the rolling moment produced by the aileron. After a brief time, the airplane rolls to the left in response to the right roll control.

As would be expected, the reversed roll response to normal lateral control stick inputs presents the pilot with a coordination problem in order to avoid unintentional loss of control and spins. Most fighter pilots adapt to the situation by transitioning from lateral stick inputs for roll control at low α to rudder pedal inputs for roll control at high α. The problem becomes one of how to phase these controls in an optimum manner to obtain maximum performance, particularly during the pressure of combat.

Using the simulator at LaRC, it has been found that configurations which exhibit such characteristics are susceptible to inadvertent departures during vigorous combat maneuvers. Many proposed solutions to this problem have been

evaluated during the simulations, but the most effective has been found to be the general class of roll/yaw control-interconnect (or ARI) systems. With this scheme, the rudder is electronically linked to move with the roll control so as to counter the adverse yaw produced by that control. In addition, for situations such as that described above wherein the adverse moments due to ailerons can be much larger than the corrective moments available from the rudder, the interconnect system must also phase out the aileron deflections. In this case, pilot stick inputs drive the rudder in addition to, or instead of, the normal roll-control surfaces. Because of the wide variation of the control characteristics with angle of attack, roll/yaw control-interconnect systems are necessarily scheduled as a function of α. In addition, in some cases Mach scheduling has also been found to be necessary.

An example of interconnect scheduling is shown in figure 7. Basically, the control system was modified such that deflection of the control stick laterally produced aileron inputs at low angles of attack and rudder inputs at high angles of attack. As shown in the sketch, the ailerons for the example discussed were phased out by $\alpha = 25°$. At that point, lateral stick inputs produced only rudder inputs. In addition, the yawing moments produced by the ailerons above $\alpha = 25°$ were used to advantage in an additional stability augmentation channel which augmented directional stability.

An example of the effectiveness of the roll/yaw control-interconnect system in preventing departures is illustrated in figure 8 which shows two attempted high-g rolling reversals. With the basic control system, the pilot applied left roll control while simultaneously loading the airplane very rapidly. Initially, the airplane responded as desired; however, as α increased, an inadvertent control-induced departure to the right occurred despite the application of full left controls. When the control system was modified with the interconnect, the pilot was able to execute the task with good control throughout the maneuver (the roll was intended to be to the left in both cases). This control scheme essentially eliminated inadvertent spins in the simulator.

The net effect of the automatic interconnect scheme on roll performance is illustrated in figure 9. With the basic control system, the roll rate produced by lateral deflection of the control stick reversed near $\alpha = 20°$, and the pilot could not maneuver at higher angles of attack with only stick inputs. When the control system was modified with the interconnect, the pilot could maneuver the airplane beyond maximum lift using only stick inputs without fear or unintentional departures.

In general, the results of the simulation studies indicate that the use of a roll/yaw interconnect system can eliminate inadvertent departures on airplanes which are inherently dynamically stable at high α yet prone to control-induced departures due to adverse yaw. In addition to enhancing departure resistance, interconnect systems can also greatly improve high-α controllability characteristics such that the airplane becomes much more effective in tracking. However, it should also be mentioned that in a developed spin an interconnect system can be disadvantageous in that it does not allow the application of full recovery controls (δ_a with and δ_r against the spin). Thus, in the event of a spin, these systems should be deactivated.

Lateral-Directional Stability Augmentation

In addition to adverse yaw and lack of control effectiveness at high angles of attack, another factor that causes inadvertent departures from controlled flight is the degradation in lateral-directional stability at high angles of attack. This characteristic can be due to a loss in either static stability, C_{n_β} and C_{ℓ_β}, or damping, C_{n_r} and C_{ℓ_p}, or to a combination of the two. A solution to this problem that has been studied during the simulation investigations is the use of stability augmentation tailored for high-angle-of-attack conditions. An effective control law has been found to be $r - p\alpha$ to rudder feedback, or stability axis yaw damping. Shown in figure 10 are Dutch roll mode damping characteristics versus α in 1-g flight for an airplane with and without a stability axis yaw damper. The data show that the damper was quite effective in increasing Dutch roll stability up to 30° angle of attack; at higher α, its effectiveness decreased due to a combination of reduced rudder power and loss of static stability. In addition to augmenting damping, the use of r_s feedback also restricts the airplane to roll about its flight path which is necessary to prevent the generation of large amounts of sideslip during rolling maneuvers at high angles of attack. If the airplane is rolled about its body axis in this region, a kinematic interchange between angle of attack and sideslip occurs. The large magnitudes of sideslip thus generated, coupled with low directional stability, could result in a departure. However, if the airplane is rolled in a conical motion about its flight path, then α/β coupling does not occur, and the susceptibility to departure is decreased. The simulation results have verified that this concept does indeed enhance departure resistance in addition to providing increased damping at high angles of attack.

Degradation of lateral-directional dynamic stability at high angles of attack is most often due to loss of static directional stability and dihedral effect. Damper systems based on rate feedback, such as the stability axis yaw damper discussed above, are generally less effective in augmenting stability in this situation. Obviously, the best solution is to directly augment C_{n_β} and C_{ℓ_β} by driving the appropriate controls with a sideslip signal. Figure 11 shows data for a configuration which typifies the loss of dynamic stability at high angles of attack due to degraded C_{ℓ_β} and C_{n_β} characteristics. The loss in static stability above 25° angle of attack is reflected in a sharp drop in the parameter $C_{n_\beta,dyn}$ which indicates a possible directional divergence at $\alpha = 30°$. Also shown in figure 11 are results obtained by augmenting C_{n_β} and C_{ℓ_β} above $\alpha = 25°$. The resulting $C_{n_\beta,dyn}$ values remain large at high angles of attack indicating no instability in this region. This characteristic is confirmed in figure 12 which shows that the response of the augmented airplane to an applied rudder doublet at $\alpha = 30°$ is a well-damped, higher-frequency oscillation than that of the basic airplane. In this case, the augmentation of C_{n_β} and C_{ℓ_β} was accomplished by feeding a β signal, estimated using conventionally available measurements, to drive the ailerons above $\alpha = 25°$. Aileron deflection on the particular configuration produced very large adverse yawing moments at high angles of attack such that they

could not be used for rolling above $\alpha = 25°$. These large yawing moments, however, were used very advantageously to augment stability as shown below:

$$\text{Augmentation law: } \delta_a = K_\beta \cdot \beta, \; K_\beta > 0$$

$$C_{\ell_{\beta aug}} = C_{\ell_\beta} + K_\beta \cdot C_{\ell_{\delta_a}}$$

$$C_{n_{\beta aug}} = C_{n_\beta} + K_\beta \cdot C_{n_{\delta_a}}$$

Since $C_{\ell_{\delta_a}}$ is negative, the β feedback to the ailerons augments dihedral effect; in addition, because $C_{n_{\delta_a}}$ is positive, the feedback also augments directional stability by the increment $K_\beta \cdot C_{n_{\delta_a}}$ which is considerable since $C_{n_{\delta_a}}$ is large. Note that the simultaneous augmentation of dihedral effect and directional stability using the single control would not be possible if $C_{n_{\delta_a}}$ were not adverse. This case illustrates the important concept of using all available control moments for augmentation and control at high angles of attack, including those that are conventionally considered adverse, since these controls can often be quite powerful in the stall region.

CORRELATION WITH FLIGHT RESULTS

As indicated earlier, all the LaRC stall/spin simulations performed to date have involved actual, current, combat aircraft configurations. This situation permits correlation of the simulation results with those obtained in actual flight. In addition, qualitative validation of the simulations is obtained early in the programs by the participation of appropriate individuals to fly the simulator. These individuals include company as well as military test pilots directly involved with flight testing of the particular study configuration. Results to date have shown good qualitative correlation between simulator and flight results. The simulations have been found to be effective in predicting the general high-angle-of-attack stability and control characteristics of particular configurations; in addition, potential problems as well as benefits of various control schemes identified during the simulations have agreed well with flight results. Thus, an additional benefit of the simulation technique is that it can be used to study the effect of general control schemes, such as normal acceleration and roll-rate command, on high-α flight characteristics.

Many of the departure prevention concepts studied in the simulation programs have been implemented and are employed in current fighter aircraft. For example, LaRC studies on roll/yaw-interconnect concepts were instrumental in the development of the ARI system currently used on the F-14 airplane.

CONCLUDING REMARKS

This paper has discussed recent NASA studies on automatic spin prevention for fighter airplanes. This approach to providing spin resistance is a promising method to achieve this goal. This concept has become widely accepted by industry in the United States, and such systems have been implemented on the F-14, F-15, F-16, and F-18 designs. In order to be effective, however, the approach must be considered early in the design stages of military aircraft.

REFERENCES

1. Gilbert, William P.; and Libbey, Charles E.: Investigation of an Automatic Spin-Prevention System for Fighter Airplanes. NASA TN D-6670, 1972.

2. Gilbert, William P; Nguyen, Luat T.; and Van Gunst, Roger W.: Simulator Study of Applications of Automatic Departure- and Spin-Prevention Concepts to a Variable-Sweep Fighter Airplane. NASA TM X-2928, 1973.

3. Ashworth, B. R.; and Kahlbaum, William M., Jr.: Description and Performance of the Langley Differential Maneuvering Simulator. NASA TN D-7304, 1973.

4. Moore, Frederick L.; Anglin, Ernie L.; Adams, Mary S.; Deal, Perry L.; and Person, Lee H., Jr.: Utilization of a Fixed-Base Simulator to Study the Stall and Spin Characteristics of Fighter Airplanes. NASA TN D-6117, 1971.
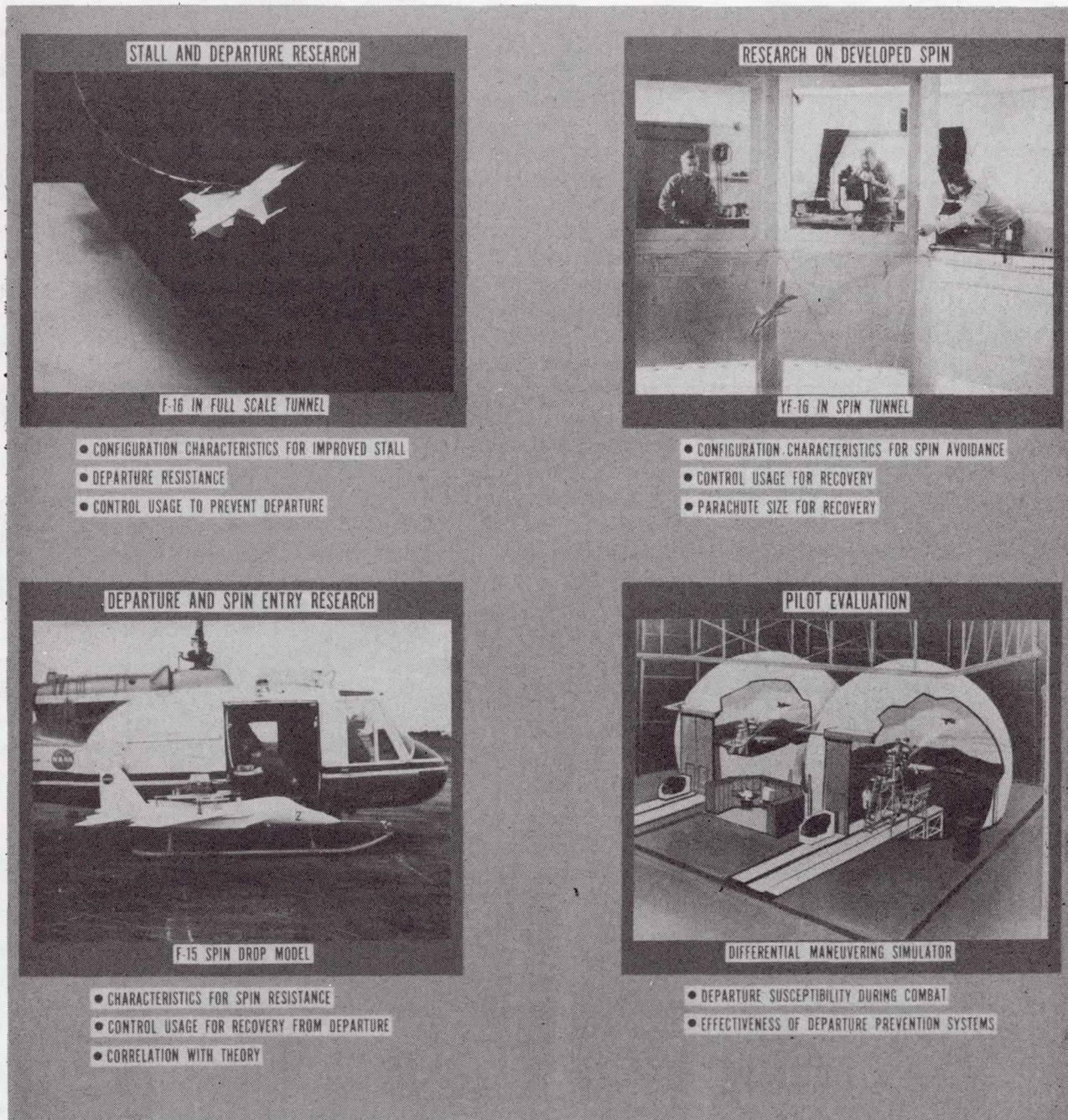
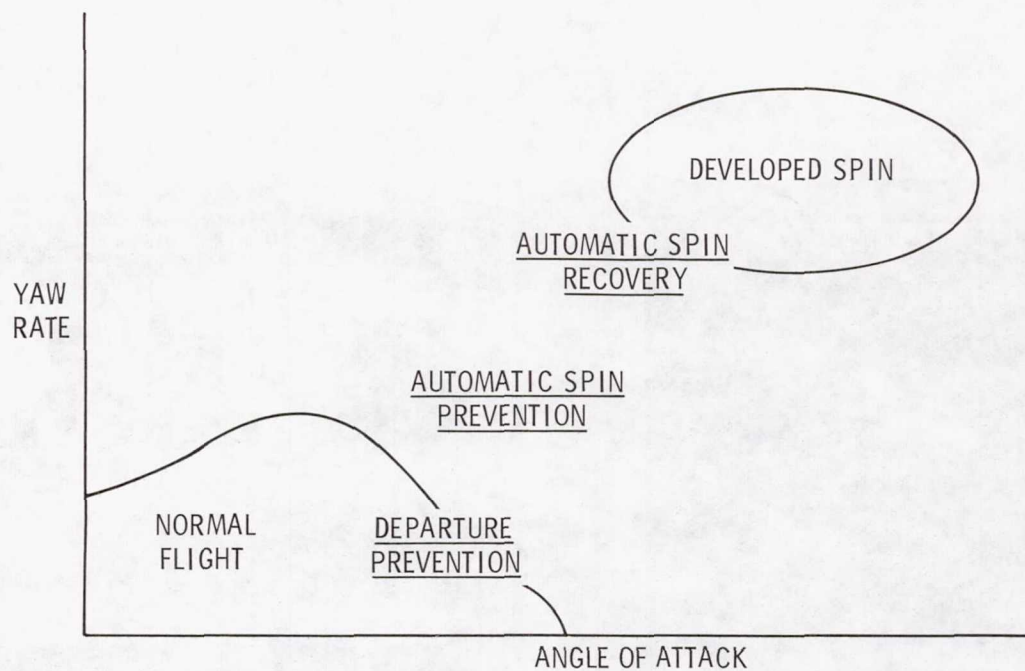Figure 1.- Scope of stall/spin research program.

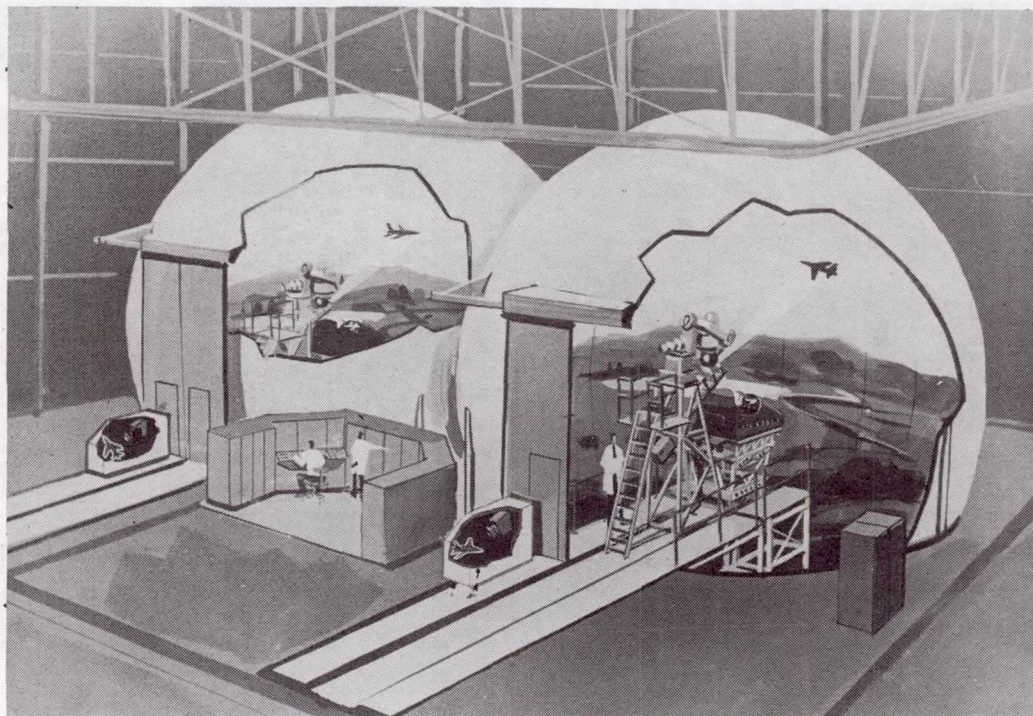Figure 2.- Automatic control concepts for departure/spin prevention.

Figure 3.- General arrangement of the Langley differential
maneuvering simulator facility.

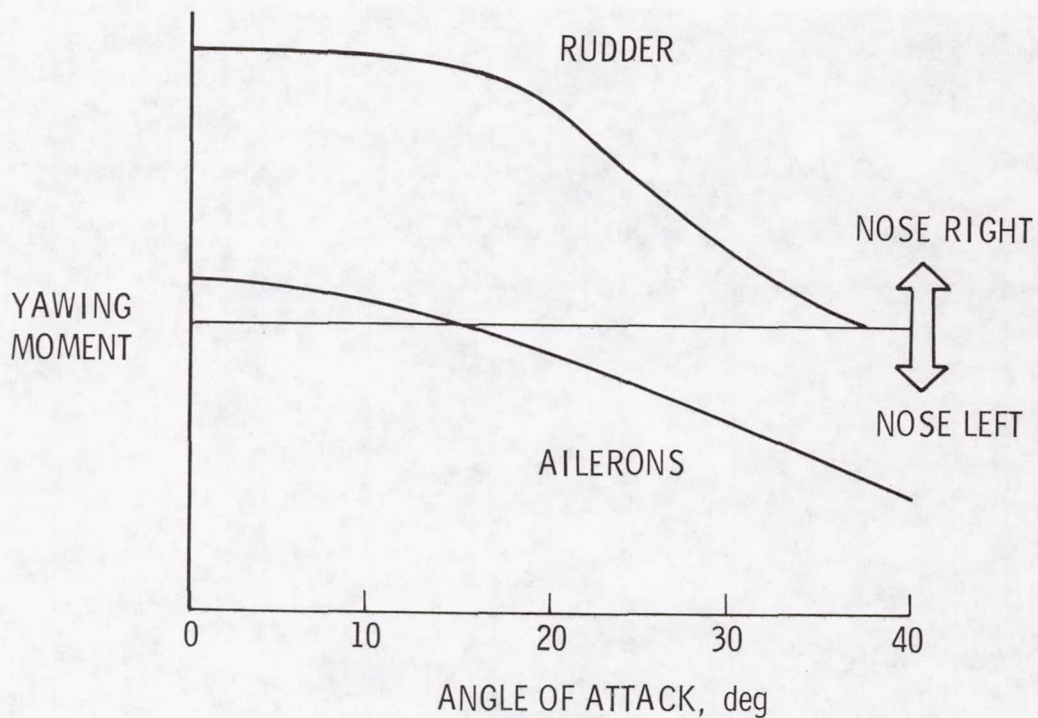Figure 4.- View of cockpit and visual display within one sphere of DMS.

Figure 5.- Yawing moments produced by lateral-directional controls.
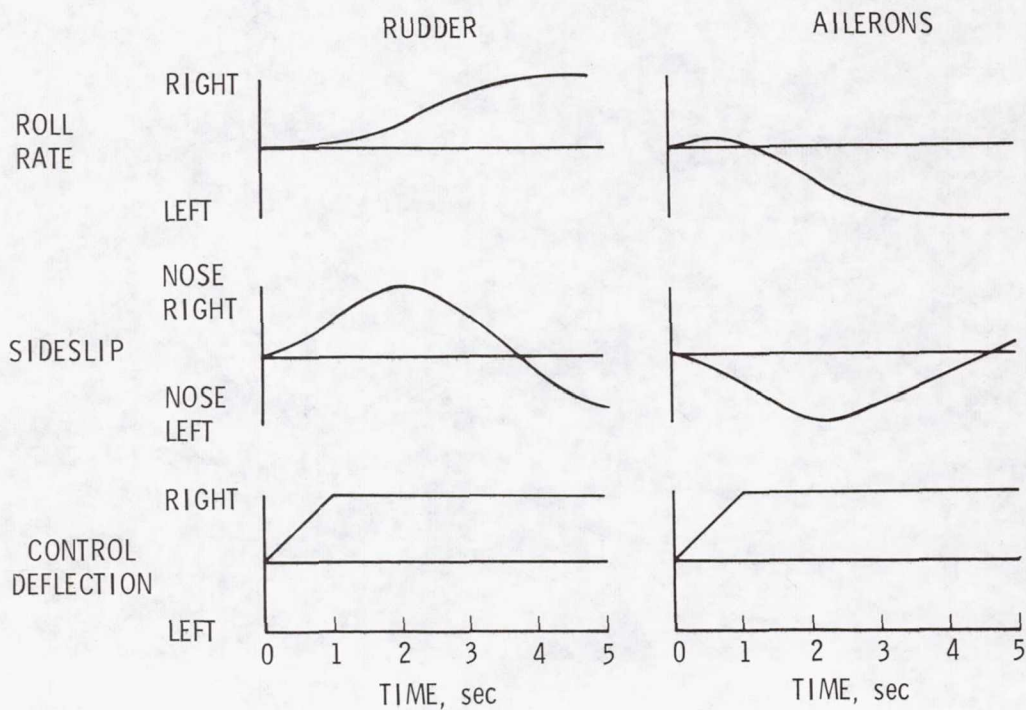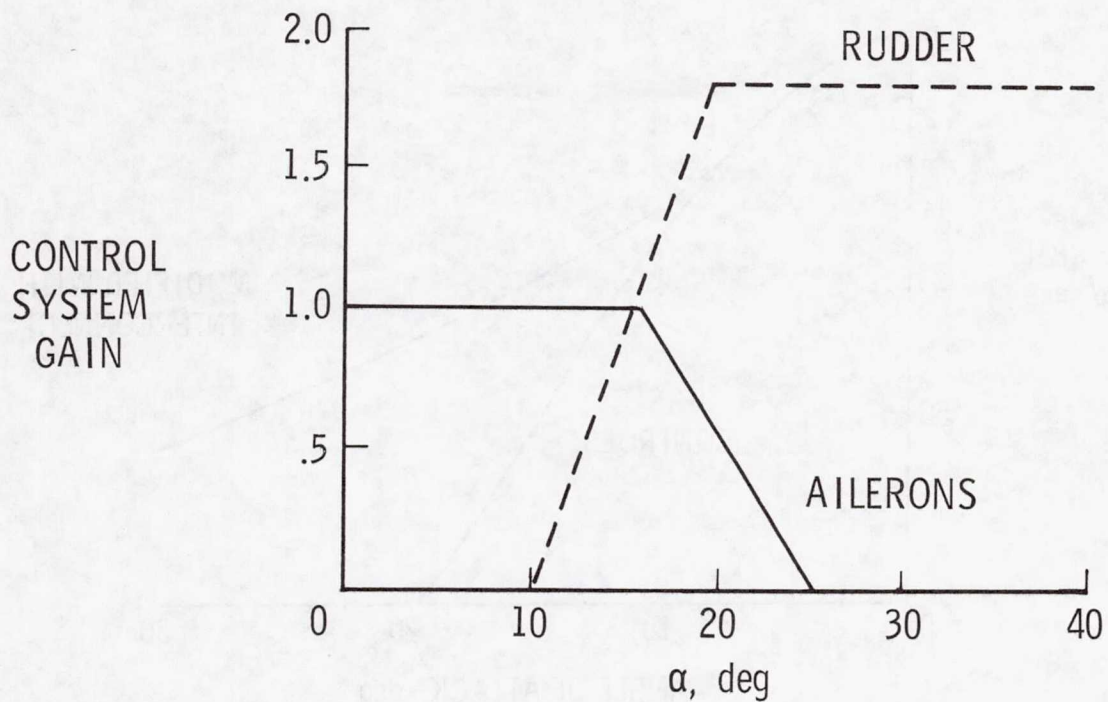

Figure 6.- Illustration of roll reversal.

Figure 7.- Stick-to-rudder interconnect concept.
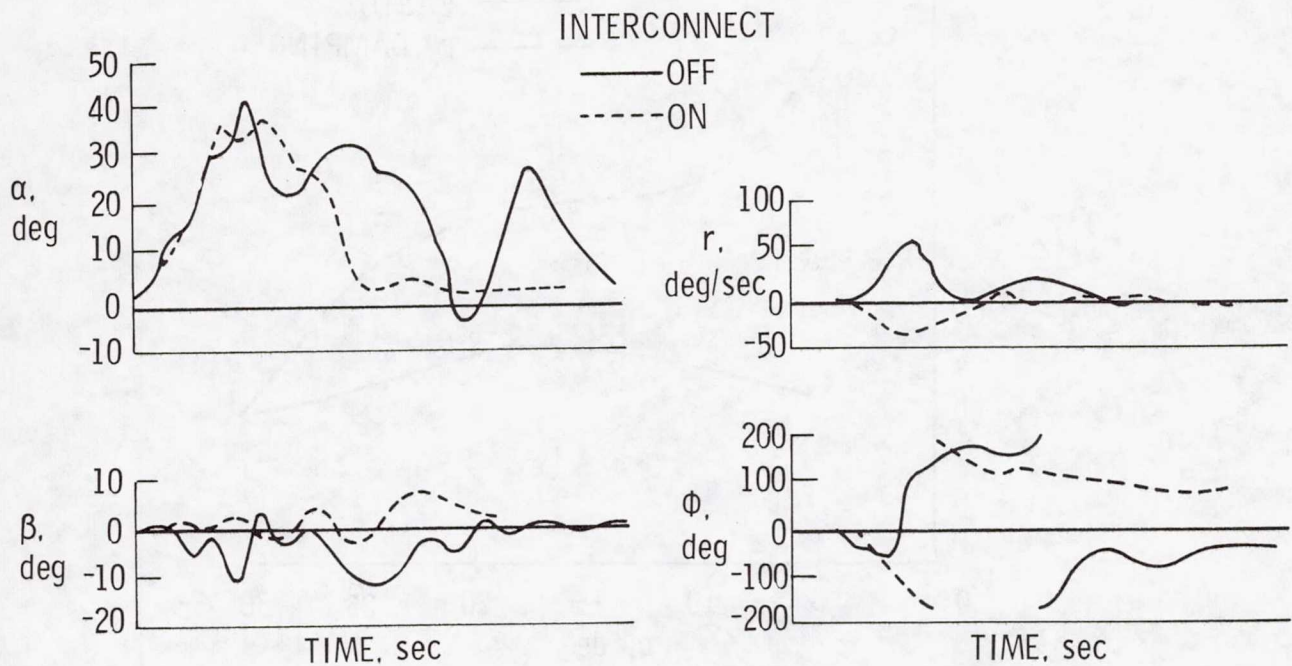

Figure 8.- Effect of roll/yaw interconnect in rolling reversal maneuver.
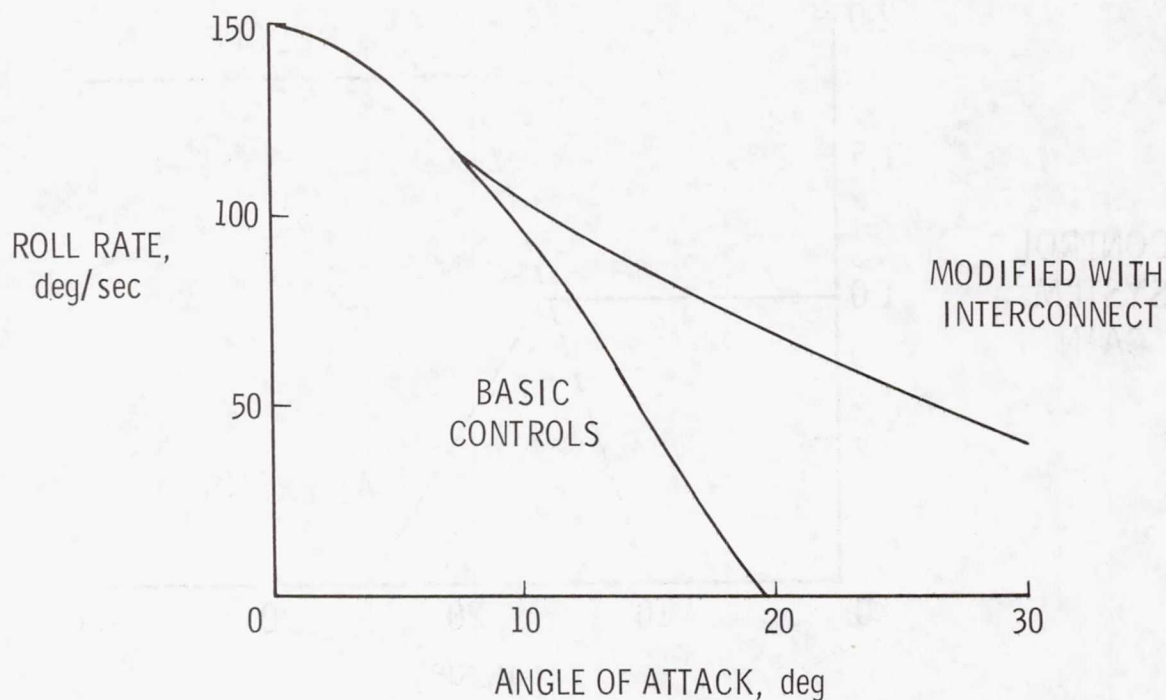
1749

Figure 9.- Effect of interconnect on roll response to lateral stick input.
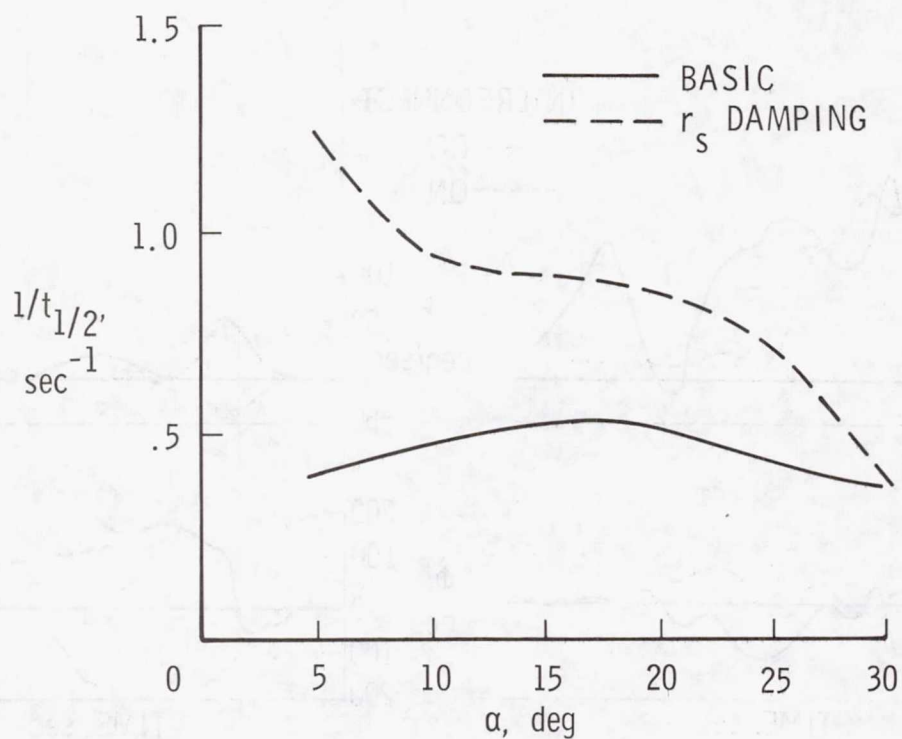

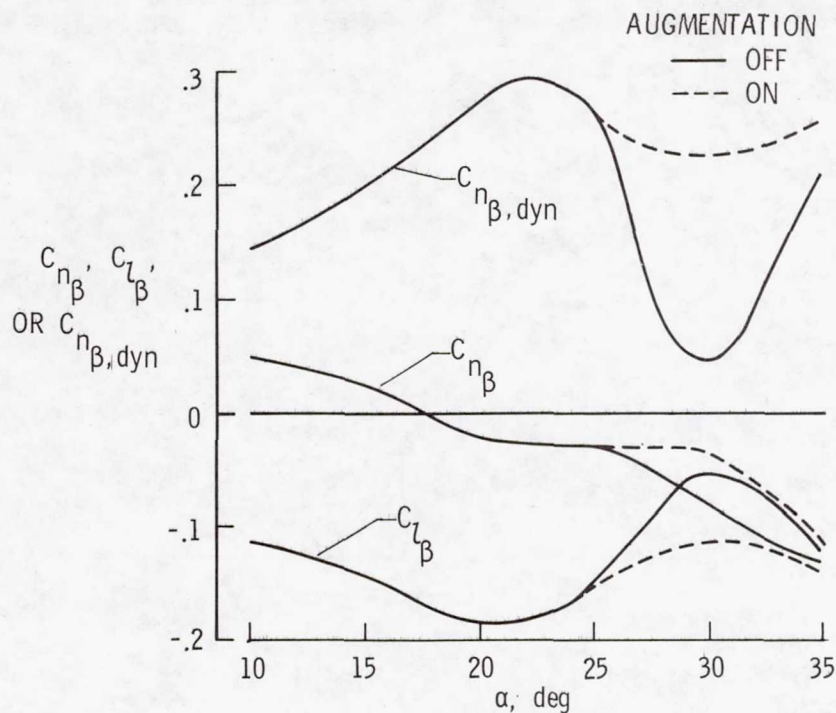Figure 10.- Effect of stability axis yaw damping
on Dutch roll mode damping.

Figure 11.- Variation of lateral-directional stability
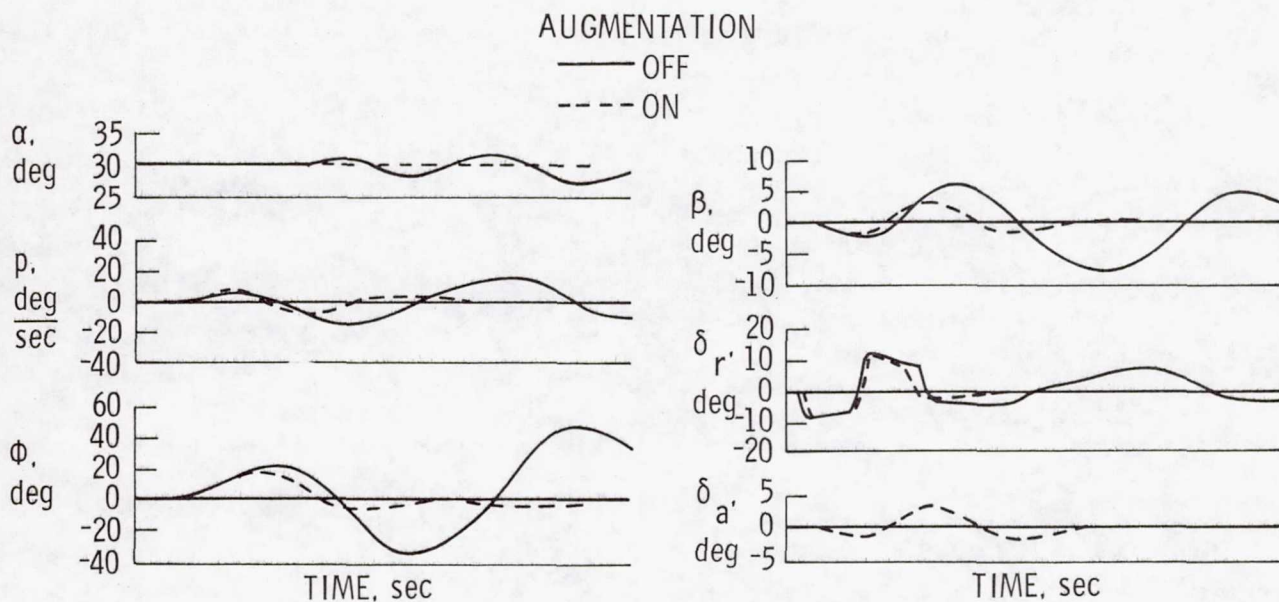characteristics with and without augmentation.

Figure 12.- Effect of augmentation on response to rudder doublet at $\alpha = 30°$.

Page intentionally left blank

HIGH ANGLE-OF-ATTACK STABILITY-AND-CONTROL ANALYSIS*

Robert F. Stengel
The Analytic Sciences Corporation

SUMMARY

Methods of linear systems analysis are applied to mathematical models of aircraft flying at high angle of attack and maneuver rate. First-order longitudinal and lateral-directional coupling is obtained by linearizing the complete nonlinear equations of motion about a generalized (quasi-steady) trim point. "Open-loop" stability boundaries are defined using the linear dynamic equations, and "pilot-in-the-loop" effects are presented. Stability augmentation structures for maneuvering flight conditions are shown to be defined readily using optimal control theory.

INTRODUCTION

High-performance aircraft are susceptible to degraded flying qualities during maneuvering flight for a number of reasons. The aircraft flies at high angle of attack, α, where aerodynamic flow fields are complex and are sensitive to small variations in flight condition. Lateral-directional modes of motion are affected by the nose-high attitude, and the desirable control moments due to aileron and rudder may be overshadowed by significant adverse effects. Large roll rates may be commanded for rapid orientation of the lift vector, and the resulting gyroscopic effects couple the longitudinal and lateral-directional modes of motion. To compound the above difficulties, the pilot must adapt his control strategies to varying aircraft dynamics and control responses at high α.

Rigorous solutions to the aircraft's equations of motion are difficult to obtain in maneuvering flight. These differential equations have coefficients which are nonlinear and time varying; hence, solutions of the general equations require direct integration, either by numerical or analog computation. The resulting time histories describe the evolution of aircraft motions for given controls, disturbances, and initial conditions, and each change in any of these quantities leads to a new time history. Consequently, the nonlinear-time-varying equations are valuable for defining specific flight paths, but their complexity can obscure the identification of the underlying mechanisms which govern aircraft response.

This paper presents new results using linear-time-invariant dynamic equations which retain much of the coupling of the nonlinear equations but which are amenable to the comprehensive techniques of linear systems analysis. The stability characteristics of two contemporary high-performance aircraft are compared at various maneuvering flight conditions. The effects of increasing angle of attack on control response are demonstrated, and a detailed mathematical model of the human pilot is applied to the prediction of flying qualities. The fully coupled linear aircraft model also forms the basis for designing stability augmentation systems that improve handling qualities and prevent departure from controlled flight.

SYMBOLS

F	fundamental matrix of linear-time-invariant system
$\underline{f}$	vector of nonlinear equations of motion
G	control effect matrix of linear-time-invariant system
I	identity matrix
K	stability augmentation gain matrix
p,q,r	body-axis angular rates (roll, pitch, yaw)
t	time
$\underline{u}$	control variable vector
u,v,w	body-axis velocities (axial, lateral, normal)
$\underline{x}$	state variable vector
x_E, y_E, z_E	translational position (forward, lateral, vertical)
$\underline{z}$	eigenvector
α	angle of attack
β	sideslip angle
λ	eigenvalue
ϕ, θ, ψ	Euler angles (roll, pitch, yaw)
$(\ )^T$	transpose of a vector
$(\dot{\ })$	derivative with respect to time
$\Delta(\ )$	perturbation quantity

EQUATIONS OF MOTION

The fundamental expression of rigid-body equations of motion contains nonlinear and time-varying terms, but simplifications can be considered in certain cases. Figure 1 illustrates the classes of models which can be considered for analyzing flight motions. If the dynamic coefficients are changing rapidly with time, in comparison with the time scale of motions, the dynamic model must be <u>time varying</u>; if the coefficients are relatively constant, a <u>time-invariant</u> model will suffice. If flight motions evidence the superposition characteristic; i.e., if doubling the input doubles the output, then <u>linear</u> models can be used; if not, the dynamic model must be <u>nonlinear</u>.

The nonlinear equations of motion can be assembled in the single "state-space" (vector) equation

$$\dot{\underline{x}} = \underline{f}(\underline{x}, \underline{u}, t) \tag{1}$$

where $\underline{x}$ is a column vector of state (or motion) variables, $\underline{u}$ is a vector of control variables, $\underline{f}$ is the vector of dynamic equations, and t is time. For rigid-body motion, $\underline{f}$ and $\underline{x}$ each have 12 elements representing the dynamic relationships and associated variables for translational and rotational kinematics and dynamics. Using conventional notation for earth-relative position, earth-body Euler angles, and body-axis rates, the state vector can be defined as

$$\underline{x}^T = \left[x_E \ y_E \ z_E \ \vdots \ \phi \ \theta \ \psi \ \vdots \ u \ v \ w \ \vdots \ p \ q \ r \right] \tag{2}$$

where $(\ )^T$ denotes the column vector transpose, i.e., a row vector. The control vector, $\underline{u}$, contains at least three elements for rotational control about all axes. Further details of the nonlinear equations of motion can be found in references 1 and 2.

Nonlinear-time-invariant models are useful if amplitude-dependent effects cannot be ignored but time variations of the coefficients are negligible. Nonlinear phenomena, such as limit cycles, subharmonic response, jump resonance, and nonlinear cross coupling may be responsible for such aircraft behavior as wing rock, porpoising (or bucking), jump response of roll rate to aileron input, and forcing of longitudinal modes by lateral oscillations during symmetric, wings-level flight (refs. 3 and 4).

The stability and control of small variations about the reference flight path can be investigated using linear dynamic models whose coefficients may vary in time as the flight condition varies. Linear-time-varying models could be required to assess aircraft stability during rapid acceleration, deceleration, or

for steep, high-speed flight paths, in which changing air density affects system dynamics (refs. 5 to 7). Reference 2 indicates that the accelerations associated with air combat maneuvering introduce time-varying coefficients in linear models; however, explicit time-varying dynamic effects were not found to be significant, and all major conclusions regarding the flight stability of the subject aircraft could be drawn from the equivalent time-invariant model.

The aircraft equations of motion can be expressed in linear form by performing a Taylor series expansion of equation (1) and retaining only first-order terms. The expansion results in

$$\dot{\underline{x}}_o + \Delta\dot{\underline{x}} = \underline{f}\left(\underline{x}_o, \underline{u}_o, t\right) + \underline{f}_{\underline{x}}\,\Delta\underline{x} + \underline{f}_{\underline{u}}\,\Delta\underline{u} \tag{3}$$

where $\underline{f}_x$ and $\underline{f}_u$ are partial derivative matrices with respect to the state and control, respectively, evaluated along the nominal flight path. The nominal flight path satisfies equation (1), and the dynamics of small perturbations from the flight path are described by

$$\Delta\dot{\underline{x}} = F\,\Delta\underline{x} + G\,\Delta\underline{u} \tag{4}$$

where $\underline{f}_x$ and $\underline{f}_u$ are denoted by F and G and may contain time-varying coefficients.

Linear-time-invariant models describe small-perturbation stability in the vicinity of a single flight condition, and can be useful for practical approximation of system dynamics, for sensitivity analyses, and for control system design. (References 8 to 11 use linear models in the examination of dynamic coupling phenomena.) As shown in figure 1, coefficients of the linear model are defined by the local slopes at a given flight condition, and the principle of superposition applies in characterizing flight motions.

The importance of linearizing about a generalized trim condition is illustrated by figure 2, which presents linear and nonlinear responses to a large rudder input. The nonlinear model's trace demonstrates significant longitudinal/lateral-directional coupling as well as large responses in sideslip, β, and roll rate, p. The model which is linearized about the initial "wings-level" flight condition does not possess this coupling, and the magnitudes of β-p oscillations are underestimated (fig. 2a). Using the generalized trim procedure[*] to define a linearization

_____

[*]This trim procedure, described in reference 1, numerically defines mean values of translational and rotational _rates_ which minimize translational and rotational _accelerations_ for given Euler angles and control settings.

point 4 sec into the maneuver introduces the missing longitudinal/
lateral-directional coupling, leading to substantially improved
modeling of the nonlinear system's oscillations (fig. 2b). The
coupled linear system's response eventually diverges from the
nonlinear response, but the fact that it stays in the proper
neighborhood for several seconds suggests the utility of the
linear-time-invariant model in defining local stability, in pro-
viding a baseline for control system design, and in analyzing
piloting effects.

MANEUVERING EFFECTS ON STABILITY

Configuration-dependent effects and common attributes of
maneuvering flight can be seen in comparisons of the stability
boundaries of two contemporary high-performance aircraft. Air-
craft A is a small, supersonic air superiority fighter (ref. 1);
aircraft B is a larger supersonic fighter with similar mission
(ref. 2).

The stability boundaries of the aircraft are defined by the
conditions at which the real parts of the eigenvalues (or roots)
of the linear-time-invariant dynamic equation (eq. (4)) change
sign. The 12 eigenvalues, λ_i ($i = 1$ to 12), of the equation are
complex numbers, each of which satisfies the following equation:

$$\det\left(\lambda_i I - F\right) = 0 \; ; \quad i = 1 \text{ to } 12 \tag{5}$$

where I is the identity matrix. Each oscillatory mode is repre-
sented by two complex-conjugate λ_i, while each convergent (or
divergent) mode is represented by one real λ_i. The λ_i describe
the time scales and stability of the normal modes of motion,
which usually partition into a longitudinal set (short period
oscillation, phugoid oscillation, and pure integrations ($\lambda_i=0$)
for range and altitude) and a lateral-directional set (Dutch
roll oscillation, roll and spiral convergences, and pure integra-
tions for crossrange and yaw angle) during "wings-level" flight.

The corresponding complex-valued eigenvectors, $\underline{z}_i$, indicate
the involvement of each motion variable in each mode, satisfying
the equation

$$\left(\lambda_i I - F\right) \underline{z}_i = 0 \; ; \quad i = 1 \text{ to } 12 \tag{6}$$

For example, in symmetric flight the two complex-conjugate eigen-
vectors associated with the short period oscillation normally
involve large pitch rate and normal velocity components (Δq and
w), small pitch angle and axial velocity components ($\Delta \theta$ and Δu),
and none of the remaining longitudinal and lateral-directional

components. Thus, the z_i are said to characterize the "shape" of each mode, while the λ_i characterize the growth or decay of the magnitude of z_i.

Several effects of maneuvering flight can be noted. Increasing mean angle of attack or pitch rate alters the time scale, stability, and shape of each mode, but it does not couple the longitudinal and lateral-directional sets, as symmetry is maintained; therefore, the number of non-zero elements in each z_i is unchanged. Introducing mean sideslip, roll rate, or yaw rate leads to full coupling, and it alters aircraft stability; hence, the number of non-zero elements in each z_i increases. It is often found that symmetric variations have greatest effect on stability (due to changes in aerodynamic flow fields), while asymmetric variations have greatest effect on mode shape (as a consequence of inertial coupling).

Figure 3 illustrates the effects of α_O and β_O on the open-loop stability boundaries of the two aircraft at an altitude of 6100 m. The different true airspeeds, V_O, used in analysis have small effect on the stability boundaries, although the differing dynamic pressures affect the natural frequencies and time constants of the normal modes. Aircraft A evidences an unstable phugoid mode at low α_O and an unstable Dutch roll mode (due to negative damping) at high α_O (fig. 3a). These results are apparently insensitive to small sideslip angles; however, there is substantial change in mode shape (not shown). Although conventional names are used, the "phugoid" mode contributes to significant roll angle motion, and the "Dutch roll" mode contains non-trivial normal velocity response. At higher sideslip angles, there are coupled, unstable oscillations and divergences, which also are found in the response of Aircraft B (fig. 3b). The latter aircraft is seen to possess unstable Dutch roll and roll-spiral oscillation bands in the vicinities of 20- and 30-deg angle of attack. Both instabilities can be traced to loss of directional restoring moments.

Fighter aircraft are capable of high roll rate, and air combat maneuvers often include such motions. For the aircraft to roll with constant aerodynamic angles, the roll rate, p_{w_O}, must occur about the wind x-axis (which is the same as the stability x-axis for constant nominal aerodynamic angles). Sideslip variations also are considered, since piloting error could easily result in non-zero β_O during a rolling maneuver. Both positive and negative p_{w_O} are considered, to account for roll "into" or "out of" the sideslip. (The senses are opposite in the first case, identical in the second.)

The stability boundaries that result from combined roll rate and sideslip are shown in figure 4, and it is interesting to note striking similarities between the boundaries of the two aircraft. These boundaries are antisymmetric about the origin (as indicated

in fig. 4b) because positive sideslip-positive roll rate has the
same effect on aircraft stability as negative sideslip-negative
roll rate. Both aircraft have stable bands near $\beta_O = 10$ deg when
p_{w_O} is large, a beneficial effect of coupling. Instability is
substantial when each aircraft is sideslipped "into" the roll.
The eigenvectors (not shown) indicate that high p_{w_O} causes the Δp
component of the short-period mode to be greater than the Δq
component.

References 1 and 2 present results regarding the stability of
symmetric pullups and a maneuver known as a "rolling reversal"
(high-g pullup, roll, inverted flight, roll-out, and pullup). Both
aircraft have lateral-directional instabilities as a result of
large positive pitch rate. Aircraft A possesses an unstable Dutch
roll mode during most of the 22-sec maneuver. Aircraft B evidences
an unstable spiral mode for much of the maneuver, with a Dutch
roll instability during the final pullup. These results predict
increased pilot workload during maneuvering flight as a consequence
of factors not normally considered in stability and control
analyses.

CONTROL RESPONSE

Control input time histories demonstrate the transient re-
sponse of Aircraft B with increasing α_O. The lateral control
input is applied for two seconds and then removed, and all re-
sponses are computed using the linear-time-invariant model.
Figure 5 shows the lateral-directional responses which result. As
angle of attack increases, both the system eigenvalues and the
control effectiveness vary. The unstable Dutch roll mode is
excited at α_O of 20 deg, and the yaw rate response is reversed.
Although the aircraft is again stable at 25 deg, the control
response is poor due to the large adverse yaw response. At 30 deg,
the lateral control input excites the unstable roll-spiral oscil-
lation, which dominates the response.

Additional results contained in reference 2 indicate that
longitudinal response to lateral control is about 50 percent of
directional response levels when α_O and β_O are each 10 deg. When
$p_{w_O} = 75$ deg/sec, the resulting Δq is one-third as large as Δr,
and $\Delta\alpha$ response is three times greater than $\Delta\beta$ response.

PILOTING EFFECTS

The effects which the pilot has on aircraft stability can
be modelled by a closed-loop system which feeds back aircraft
motions to available control surfaces. An optimal control pilot
model has been used for this purpose in references 2 and 12, and

it contains the following elements: an _estimator_, which processes the pilot's observations to provide an estimate of the aircraft state; a _controller_, which mechanizes the pilot's regulating functions and transmits the results to the neuromuscular dynamics; and a _neuromuscular model_, which represents the dynamics of the pilot's limbs.

Investigations of pilot-aircraft instability using the control-theoretic pilot model fall into two categories: those in which the pilot fails to stabilize an unstable aircraft, and those in which the pilot destabilizes a stable aircraft. In the first case, the pilot's time delay, observation noise, neuromuscular time constants, and scanning factors are important parameters. Assuming that the aircraft's linearized dynamics have one or more unstable eigenvalues, the analysis determines pilot parameters for which the optimal control model fails to exist. The second category is related to the pilot's ability to adapt to changing flight conditions. Pilot-induced oscillations (PIO) and departures can occur because a control strategy which is appropriate to one flight condition is destabilizing in another.

The control-theoretic pilot model can be used to analyze nonadapting pilot behavior in a straightforward manner. In the example considered here, the pilot model's control strategy is first determined at a low-α_O flight condition. This strategy is frozen, and the aircraft's dynamics are allowed to change. The stability of the pilot-aircraft system is determined by its eigenvalues.

Nonadapted piloting effects on pilot-aircraft stability regions can be presented in the aircraft's α_O-β_O plane. Figure 6 shows the stability regions under the assumption that the pilot is adapted to α_O = 10 deg and β_O = 0 deg. The instabilities of the longitudinal modes (phugoid and short period) are the same in both cases, since the available control is the same in both cases. Figure 6 suggests that if the pilot model does not adapt, at some point low-α_O piloting procedure combined with adverse yaw will cause an instability. In figure 6a this occurs at $\alpha_O \simeq 17$ deg, and the incorrect procedure is characterized by an unstable (closed-loop) spiral mode. When three controls are used, the instability due to incorrect procedure does not occur until $\alpha_O \simeq 26$ deg, as shown in figure 6b. These results are compatible with experimental results obtained from manned simulation and flight test of Aircraft B.

STABILITY AUGMENTATION FOR DEPARTURE PREVENTION

Flying qualities can be improved by using an automatic system to compensate for variations in aircraft dynamic characteristics. Control logic for a Departure-Prevention Stability Augmentation System (DPSAS) can be developed using optimal control theory (refs. 1 and 2). The <u>linear-optimal regulator</u> is a feedback control law of the form

$$\Delta \underline{u} = -K \Delta \underline{x} \tag{7}$$

where K is a gain matrix which scales feedback and crossfeed terms for proper stabilization and compensation of the aircraft's motion (ref. 13). K varies to maintain good flying qualities for large variations in maneuvering conditions, guaranteeing closed-loop stability and accounting for all significant longitudinal/lateral-directional coupling.

Comparisons of DPSAS closed-loop response with open-loop response of the subject aircraft are presented in figures 7 and 8. Each aircraft is performing a constant-roll-rate maneuver and is subjected to a $\Delta\beta$ initial condition of 1 deg. The roll rate leads to substantial longitudinal response for both aircraft, with Aircraft A exhibiting a lightly damped oscillation in the unaugmented condition and Aircraft B possessing a real divergence. In both cases, the DPSAS quickly damps all perturbations, using gains which are specific to the aircraft and flight condition. Linear-time-invariant dynamic models can be used to develop the necessary values of K throughout the flight envelope, and gains can be scheduled in the flight control system to minimize the probability of departure.

CONCLUSION

The analysis of aircraft flying at high angle of attack and maneuver rate can be aided by considering fully coupled linear-time-invariant dynamic models. The coupled linear equations are no more difficult to handle than uncoupled longitudinal and lateral-directional sets when "state-space" methods are used, yet they capture significant aspects of maneuvering flight which otherwise would require the solution of nonlinear equations of motion. New insights regarding open-loop stability boundaries, handling qualities, and closed-loop control can be gained by direct extension of well-established methods of linear systems analysis.

REFERENCES

1. Stengel, R.F. and Berry, P.W., "Stability and Control of Maneuvering High-Performance Aircraft," TASC TR-587-1 (to appear as a NASA Contractor Report).

2. Stengel, R.F., Taylor, J.H., Broussard, J.R., and Berry, P.W., "High Angle-of-Attack Stability and Control," TASC TR-612-1 (to appear as an ONR Contractor Report).

3. Ross, A.J., "Investigation of Nonlinear Motion Experienced on a Slender-Wing Research Aircraft," J. Aircraft, Vol. 9, No. 9, Sept 1972, pp. 625-631.

4. Schoenstadt, A.L., "Nonlinear Relay Model for Post-Stall Oscillations," J. Aircraft, Vol. 12, No. 7, July 1975, pp. 572-577.

5. Haddad, E.K., "Study of Stability of Large Maneuvers of Airplanes," NASA TN D-2447, Aug 1974.

6. Curtiss, H.C., Jr., "Dynamic Stability of V/STOL Aircraft at Low Speeds," J. Aircraft, Vol. 7, No. 1, Jan-Feb 1970, pp. 72-78.

7. Ramnath, R.V. and Sinha, P., "Dynamics of the Space Shuttle During Entry into Earth's Atmosphere," AIAA Journal, Vol. 13, No. 3, Mar 1975, pp. 337-342.

8. Phillips, W.H., "Effect of Steady Rolling on Longitudinal and Directional Stability," NACA TN-1627, June 1948.

9. Abzug, M.J., "Effects of Certain Steady Motions on Small Disturbance Airplane Dynamics," J. Aeronautical Sciences, Vol. 21, No. 11, Nov 1954, pp. 749-762.

10. Stengel, R.F., "Effect of Combined Roll Rate and Sideslip Angle on Aircraft Flight Stability," J. Aircraft, Vol. 12, No. 8, Aug 1975, pp. 683-685.

11. Johnston, D.E. and Hogge, J.R., "Nonsymmetric Flight Influence on High-Angle-of-Attack Handling and Departure," J. Aircraft, Vol. 13, No. 2, Feb 1976, pp, 111-118.

12. Broussard, J.R. and Stengel, R.F., "Stability of the Pilot-Aircraft System in Maneuvering Flight," Proceedings of the 12th Annual Conference on Manual Control, May 1976.

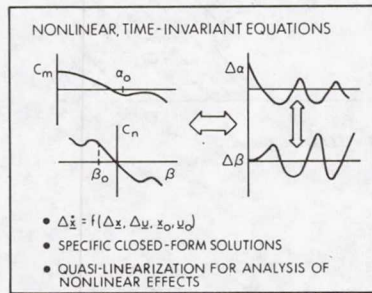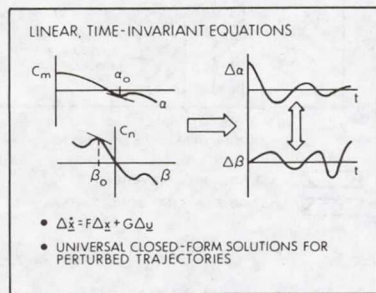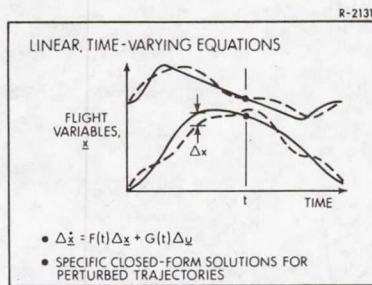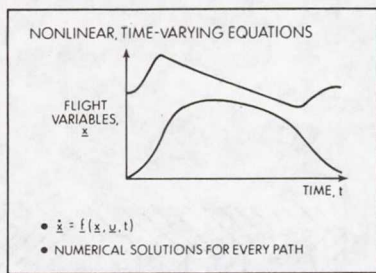13. Kwakernaak, H. and Sivan, R., Linear Optimal Control Systems, Wiley-Interscience, New York, 1972.

Figure 1.- Dynamic models for maneuvering flight.

(a) Uncoupled linearization.

(b) Coupled linearization.
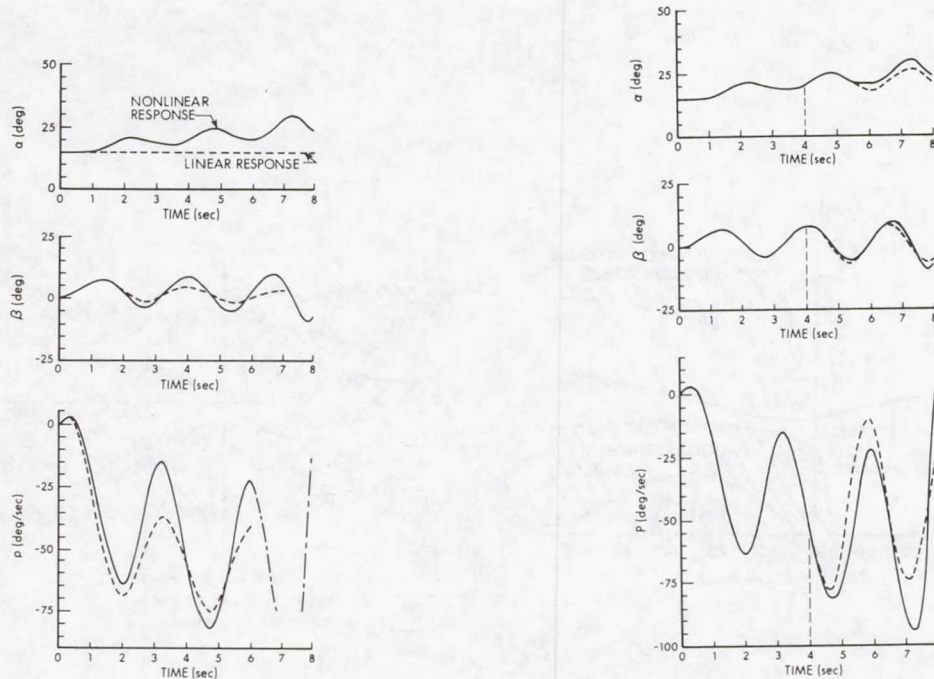
Figure 2.- Comparison of responses of nonlinear and linear models to a large rudder input. (Aircraft A).

1763
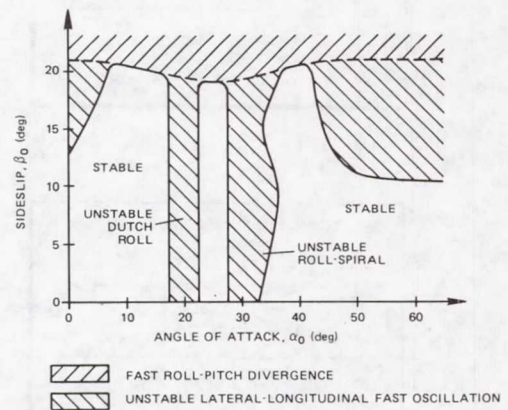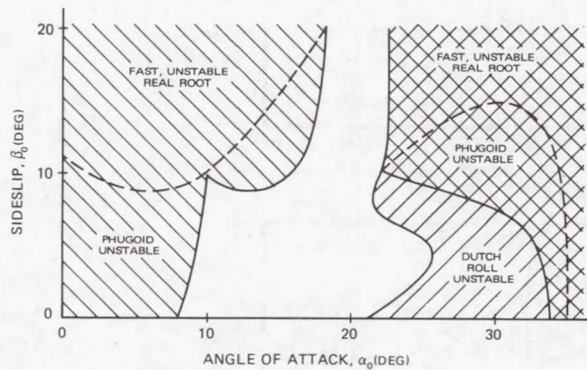
(a) Aircraft A: $V_O = 94$ m/s.   (b) Aircraft B: $V_O = 213$ m/s.

Figure 3.- Effects of mean angles of attack and sideslip on dynamic stability boundaries.
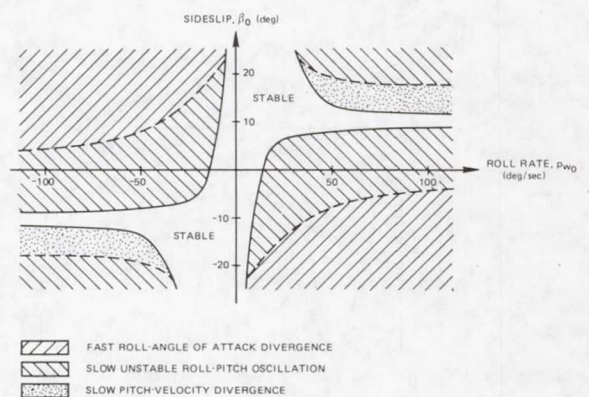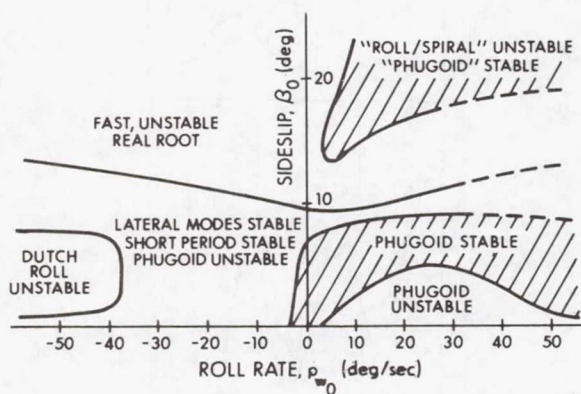
(a) Aircraft A: $V_O = 94$ m/s, $\alpha_O = 15$ deg. (b) Aircraft B: $V_O = 213$ m/s, $\alpha_O = 10$ deg.

Figure 4.- Effects of combined sideslip angle and wind-axis roll rate on dynamic stability boundaries.
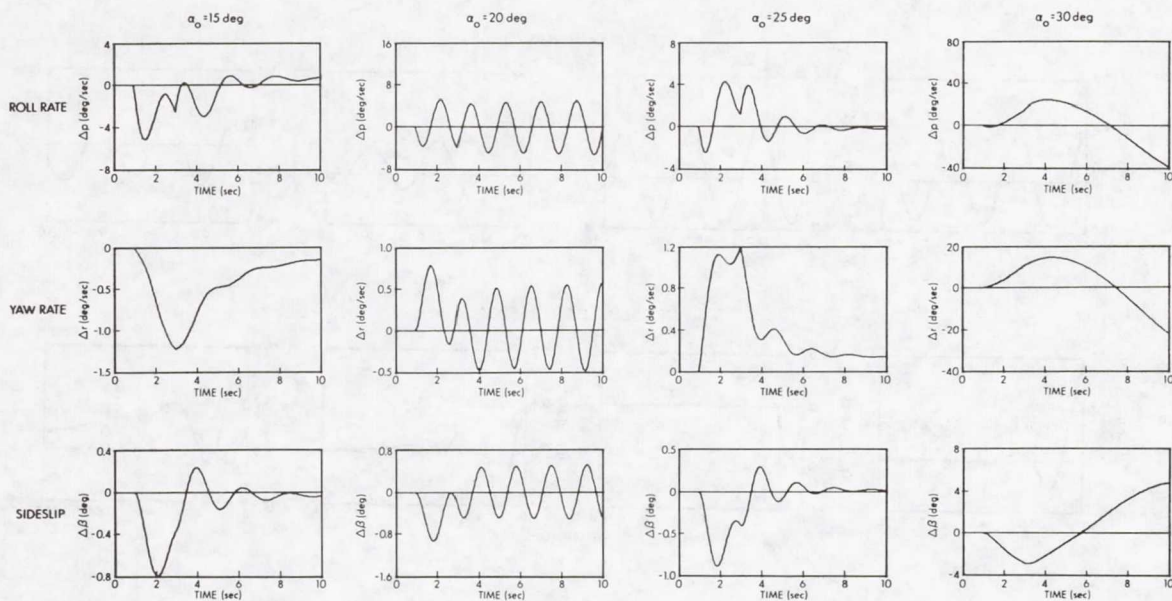
Figure 5.- Effects of increasing angle of attack on lateral control response. (Aircraft B).
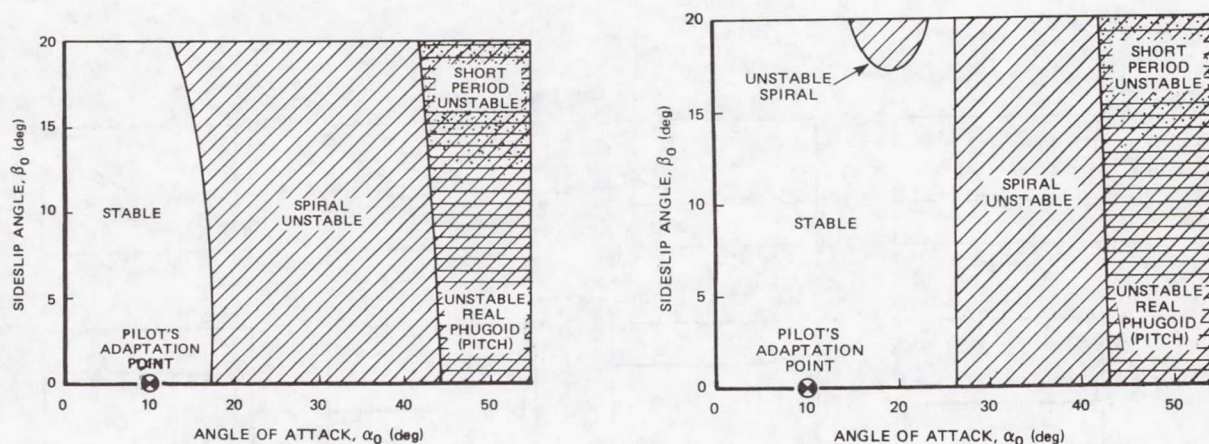
(a) Pilot uses control stick only. (b) Pilot uses control stick and rudder pedals.

Figure 6.- Stability boundaries of aircraft B with pilot control. (Pilot uses control strategies appropriate to $\alpha_0 = 10$ deg.)

R-20339
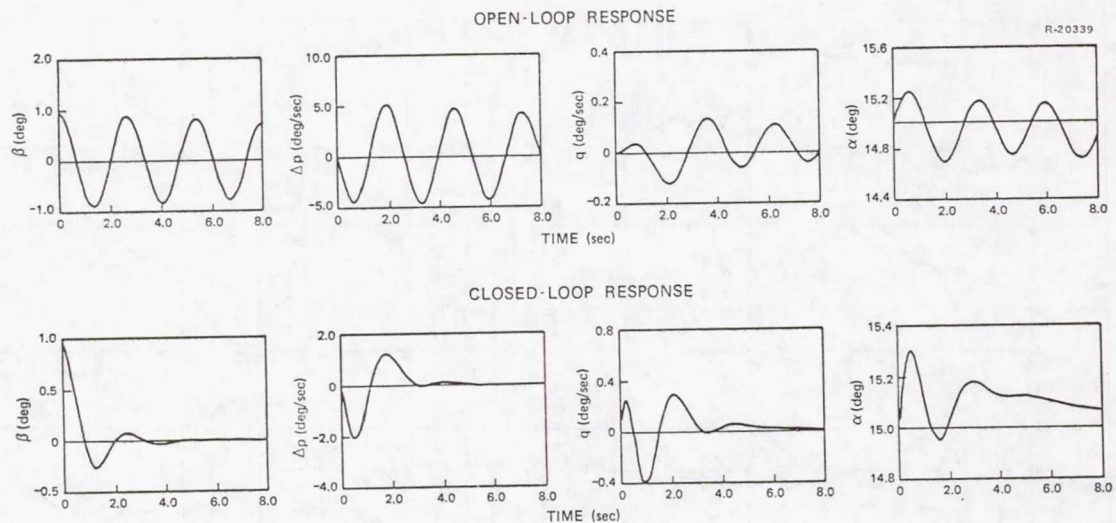
Figure 7.- Response of aircraft A to sideslip perturbation during constant-roll-rate maneuver. p_{W_O} = 39.6 deg/sec; α_O = 15°; V_O = 94 m/s.

OPEN-LOOP RESPONSE

CLOSED-LOOP RESPONSE
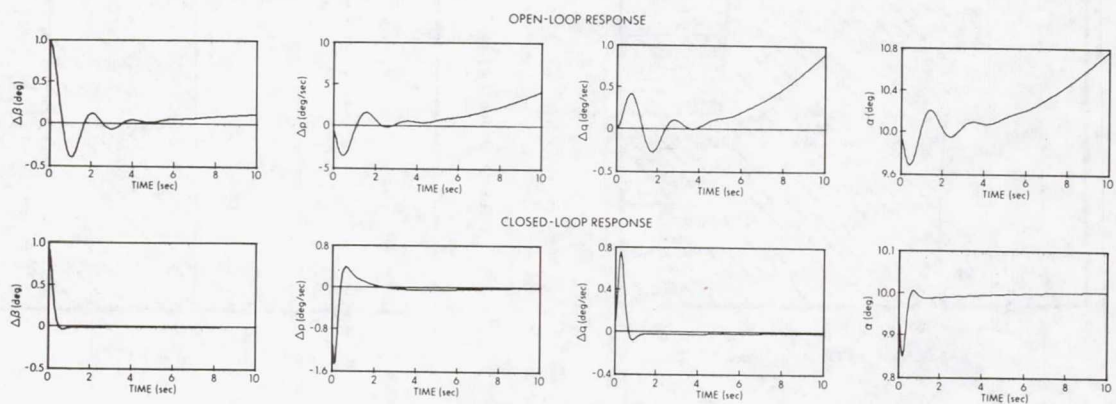
Figure 8.- Response of aircraft B to sideslip perturbation during constant-roll-rate maneuver. p_{W_O} = 75 deg/sec; α_O = 10°; V_O = 213 m/s.

TERMINAL AREA GUIDANCE ALONG CURVED PATHS - A STOCHASTIC CONTROL APPROACH*

J. E. Quaranta and R. H. Foulkes, Jr.
Youngstown State University

ABSTRACT

In this paper, stochastic control theory is applied to the problem of de-
signing a digital flight compensator for terminal guidance along a helical
flight path as a prelude to landing. The development of aircraft, wind, and
measurement models is discussed along with a control scheme consisting of feed-
back gains multiplying estimate of the aircraft and wind states obtained from
a Kalman one-step predictor. Preliminary results are presented which indicate
that the compensator performs satisfactorily in the presence of both steady
winds and gusts.

1. INTRODUCTION

During the past few decades, the number of problems associated with air-
port traffic has risen dramatically. Among the more pressing areas of concern
are high noise levels near airports, fuel conservation, and weather-induced
delays, diversions, or closures. In order to alleviate some of these problems,
NASA and the FAA have jointly initiated a long range research effort, the Term-
inal Configured Vehicle (TCV) program (ref. 1). Among the objectives of the
TCV program are increased capability for zero-visibility operation, reduced air
delays and route time, avoidance of sensitive areas, and reduced noise source
intensity. These objectives can be met, at least partially, through the devel-
opment of precise automatic control along steep, curved approach paths.

A prerequisite to such precise automatic control is the development of im-
proved ground-based navigation and guidance systems along with improved airborne
control systems. The ground based improvements in terminal area navigation and
guidance will be provided by the Microwave Landing System (MLS). The MLS will
periodically provide accurate range, elevation, and azimuth information to the
on-board control system.

The purpose of this paper is to present an application of stochastic con-
trol theory to the problem of designing an airborne control system that uses
the MLS data for terminal area guidance of a Boeing 737 along a helical flight
path as a prelude to landing. First, a system model is presented consisting of
an aircraft model, wind model, and measurement model. Next, the digital compen-
sator design is presented. Finally, a digital simulation showing the system
response using the above compensator is presented.

2. THE SYSTEM MODELS

In this chapter the aircraft, wind, and measurement models are developed.

2.1 The Aircraft Model

The notation in this section follows closely that in Etkin (ref. 2). Thus, F_I and F_E denote inertial and Earth reference frames, respectively. If $\overline{V}$ is the mass center velocity of an aircraft, $\overline{V}^I$ and $\overline{V}^E$ denote the vector quantity $\overline{V}$ measured with respect to F_I and F_E, respectively. Also $\overline{V}^E_V$ is the vector quantity $\overline{V}^E$ expressed in the vertical reference frame (F_V) coordinates.

The basic nonlinear aircraft model consists of the vector force and moment equations, a set of kinematic constraints, inertial velocity equations, and a set of actuator equations. The force equation is $\overline{f} = m\overline{a}_c$, where $\overline{f}$ is the external force and $\overline{a}_c$ is the mass center inertial acceleration. Assuming the Earth is an inertial system and is locally flat, $\overline{a}_c = \dot{\overline{V}}^E$ (the dot notation means time differentiation), so that $\overline{a}_{c_B} = \dot{\overline{V}}^E_B + \overline{\omega}^B_B \times \overline{V}^E_B$, where $\overline{\omega}^B_B = [p\ q\ r]'$ is the angular velocity of F_B and $\overline{V}^E_B$ is the mass center inertial velocity, both expressed along the body axes. The prime means transpose.

Let $\overline{W}$ denote the wind velocity. Also, let F_A be an atmosphere-fixed reference frame and $\overline{V}$ the mass center velocity with respect to F_A. Then $\overline{V}^E_B = L_{Bw}\overline{V}_w + \overline{W}_B$, where L_{Bw} transforms wind-axes components into body-axis components (ref. 2). Hence,

$$a_{\overline{c}_B} = \frac{d}{dt}(L_{Bw}\overline{V}_w + \overline{W}_B) + \overline{\omega}^B_B \times (L_{Bw}\overline{V}_w + \overline{W}_B) \tag{2.1-1}$$

The external force is $\overline{f}_B = \overline{A}_B + \overline{T}_B + m\overline{g}_B$, where $\overline{A}_B$ is the aerodynamic force, $\overline{T}_B$ is the thrust, and $m\overline{g}_B$ is the gravity force. Hence, the vector force equation is

$$\frac{d}{dt}(L_{Bw}\overline{V}_w + \overline{W}_B) + \overline{\omega}^B_B \times (L_{Bw}\overline{V}_w + \overline{W}_B) = \frac{1}{m}\overline{A}_B + \frac{1}{m}\overline{T}_B + \overline{g}_B \tag{2.1-2}$$

The vector moment equation is $\overline{G} = \dot{\overline{h}}$, where $\overline{G}$ is the external moment and $\overline{h}$ is the angular momentum. Assuming $\dot{\overline{I}} = 0$ and neglected and elastic components of $\overline{h}$, $\overline{h}_B = I\overline{\omega}^B_B$, where I denotes the body-axes moments of inertia. Thus,

$$\overline{G}_B = I\dot{\overline{\omega}}^B_B + \overline{\omega}^B_B \times I\overline{\omega}^B_B \tag{2.1-3}$$

The external moment $\overline{G}_B$ includes the effects of the gust angular velocities p_g, q_g, and r_g. These effects show up explicitly in the perturbation model.

The scalar components of (2.1-2) and (2.1-3) involve both the body-axes Euler angles ϕ, θ, and ψ (bank, pitch, and heading angles, respectively) and the body-axes rates p, q, and r. The two sets of variables are related by

$$\dot{\phi} = p + q\sin\phi\tan\theta + r\cos\phi\tan\theta$$
$$\dot{\theta} = q\cos\phi - r\sin\phi \tag{2.1-4}$$
$$\dot{\psi} = (q\sin\phi + r\cos\phi)\sec\theta$$

The Earth position is described in cylindrical coordinates with origin at the helix center at ground level. The position of the origin is assumed to be known with respect to the MLS origin. The rates of the Earth position coordinates (helix radius R, helix angle ν, and altitude h) are given by

$$\dot{R} = V\cos\gamma\cos(\psi_w - \nu) + W_x\cos\nu + W_y\sin\nu$$
$$\dot{\nu} = \frac{V}{R}\cos\gamma\sin(\psi_w - \nu) - \frac{W_x}{R}\sin\nu + \frac{W_y}{R}\cos\nu \tag{2.1-5}$$
$$\dot{h} = V\sin\gamma - W_z$$

where γ and ψ_w are wind-axes elevation and heading angles and W_x, W_y, and W_z are coordinates of $\overline{W}$ in the reference frame F_E.

The remaining equations result from modeling the thrust throttle and stabilizer actuator systems. The thrust-throttle relation is modeled as a first-order lag with a time constant of 0.5 second. Because this relation is a linearization about nominal values, the equation is given with the development of the perturbation model. In addition, throttle and stabilizer rates are commanded inputs, so that throttle and stabilizer positions are state variables.

The nonlinear aircraft model consists of the force equation (2.1-2), the moment equation (2.1-3), the kinematic constraints (2.1-4), the inertial velocity equations (2.1-5), and the actuator relations. The model can be written in usual state variable form as a single, nonlinear vector equation

$$\dot{X} = f(X, U, W, \dot{W}) \tag{2.1-6}$$

where $X = [V \; \beta \; \alpha \; p \; q \; r \; \phi \; \theta \; \psi \; R \; \nu \; h \; T \; \pi \; \delta]'$ is the total state vector, $U = [\dot{\pi} \; \dot{\delta} \; \delta_e \; \delta_r \; \delta_a \; \delta_{sp}]'$ is the commanded input vector, $W = [u_g \; v_g \; w_g \; p_g \; q_g \; r_g \; W_R \; W_T]'$ is the wind vector, and where β is the sideslip angle, α is the angle of attack, T is the thrust, π is throttle setting, δ is stabilizer, δ_e is the elevator, δ_r is the rudder, δ_a is the aileron, δ_{sp} is the spoiler, u_g, v_g, and w_g are translational gust velocities, p_g, q_g, and r_g are rotational gust velocities, and W_R and W_T are radial and tangential components of the steady wind, respectively.

The perturbation model consists of the first-order terms in a Taylor series expansion of (2.1-6) about a descending helical equilibrium. The equilibrium was determined under a zero wind condition with the aircraft flying a "truly banked" turn (ref. 2) for an airspeed of 64 m/sec (120 knots), bank angle of $15°$ and angle of elevation of $-3°$, using data for the Boeing 737 from the TCV program. The coefficients in the perturbation model were computed by evaluating the appropriate partial derivatives at the equilibrium. The coefficients of p_g, q_g, and r_g in the moment equations were computed by evaluating the partials of the aerodynamic terms in (2.1-3) with respect to p, q, and r, respectively. Finally, the thrust-throttle relation is $\delta T = -0.5 \, \delta T + 313.33 \, \delta\pi$, where the thrust is in pounds, the throttle setting in degrees, and the "δ" indicates a perturbation value. The perturbation model in usual state variable form is

$$\dot{x} = Ax + Bu + D_{01}w + D_{02}\dot{w} \tag{2.1-7}$$

where x, u, and w are the perturbation counterparts of the total vectors X, U, and W in (2.1-6).

2.2 The Wind Model

As seen in section 2.1, the wind vector in the aircraft model consists of three translational gust velocities u_g, v_g, and w_g; three rotational gust velocities p_g, q_g, and r_g; and two steady wind components W_R and W_T. The gust velocities, all of which are components along the body-axes, are modeled as having the Dryden spectra and are produced for simulation and filter design purposes by a linear system processing white noise. As an example of the linear system design, consider the gust velocity u_g, normalized by the equilibrium airspeed V_e. The power density spectrum of the normalized u_g is $\phi_u(\omega) = (2L_u\sigma_u^2/V_e^3) /(1 + (L_u\omega/V_e^2))$, where σ_u is the rms gust velocity, L_u is a turbulence scale factor, and ω is the frequency variable in rad/sec. Now, if a linear system with transfer function $H(j\omega) = 1/(1 + j\omega \, L_u/V_e)$ is subjected to a white noise

input with variance $\sigma^2 = (2L_u\sigma_u2/V_e{}^3)$, the output is a random process with the spectrum ϕ_u (ω) (ref. 3). A system with the required transfer is described in state-variable form by $\dot{x}_{w1} = (-V_e/L_u) x_{w1} + (V_e/L_u) \zeta_1$, $w_1 = x_{w1}$, where ζ_1 is a mean zero white noise process with variance $(2L_u\sigma_u2/V_e{}^3)$, x_{w1} is a state variable, and w_1 is the output having the required spectrum. The remaining gust velocities are generated in a similar manner.

As indicated in the previous section, W_R and W_T are the radial and tangential components of the steady wind, which are related to the north wind W_N and east wind W_E by the spiral angle ν:

$$W_R = W_N \cos \nu + W_E \sin \nu$$

$$\text{(2.2-1)}$$

$$W_T = W_N \sin \nu - W_E \cos \nu$$

Thus, $\dot{W}_R = - \dot{\nu} W_T$ and $\dot{W}_T = \dot{\nu} W_R$. For the simulation purposes, north and east winds are selected and W_R and W_T are computed using equations (2.2-1). For the filter design, because a constant coefficient wind model is desired and the equilibrium wind is zero, $\dot{W}_R$ and $\dot{W}_T$ are approximated by

$$\dot{W}_R = - \dot{\nu}_e W_T$$

$$\text{(2.2-2)}$$

$$\dot{W}_T = \dot{\nu}_e W_R$$

where $\dot{\nu}_e$ is the equilibrium spiral angle rate, which is constant and equal to $V_e \cos \gamma_e/R_e$.

Putting together the gust system equations and the steady wind equations (2.2-2) yields a time-invariant, linear wind model of the form $\dot{x}_w = A_w x_w + B_w\zeta$ and $w = C_w x_w$, where ζ is the white noise vector generating the gusts, x_w is the state vector of the wind model, and w is the wind vector used in the perturbation model. In order to use x_w in the perturbation model equations, $w = c_w x_w$ and $\dot{w} = C_w A_w x_w + C_w B_w \zeta$ are substituted into equation (2.1-7) to give a combined aircraft/wind model:

$$\dot{x} = Ax + Bu + D_0 x_w + D_1 \zeta$$

$$\text{(2.2-3)}$$

$$\dot{x}_w = A_w x_w + B_w \zeta$$

where $D_0 = D_{01} C_w + D_{02} C_w A_w$ and $D_1 = D_{02} C_w B_w$

2.3 The Measurement Model

Measurements available for control purposes consist of the MLS data (range, azimuth, and elevation) and a number of on-board sensor readings. The total measurement vector is $Y = [\hbar \; Az \; El \; p \; q \; r \; \phi \; \theta \; \psi \; V \; h_b \; \dot{h}_b \; \ddot{x}_B \; \ddot{y}_B \; \ddot{z}_B]'$, where $\hbar$, Az, El are the MLS data; p, q, r are angular velocities from rate gyros; ϕ, θ, ψ are bank angle, pitch, and heading from position gyros; V is an airspeed indicator reading, h_b and $\dot{h}_b$ are barometric altimeter and vertical speed indicator readings; and $\ddot{x}_B$, $\ddot{y}_B$, $\ddot{z}_B$ are body-mounted accelerometer readings.

The total measurements are computed for simulation purposes by computing the total state variables as equilibrium values plus increments and expressing the measurements in terms of the states. In order to compute the MLS data, it is assumed that the $\hbar$, Az, and El are measured with respect to a common origin and that the helix center is known with respect to that origin. If the ground coordinates of the helix center with respect the MLS origin are (x_o, y_o), then

$$r = \sqrt{(x_o + R \cos \nu)^2 + (y_o + R \sin \nu)^2 + h^2}$$

$$Az = \tan^{-1} \left[\frac{y_o + R \sin \nu}{x_o + R \cos \nu} \right]$$

$$El = \tan^{-1} \left[\frac{h}{(x_o + R \cos \nu)^2 + (y_o + R \sin \nu)^2} \right]$$

where R, ν, and h are coordinates 10, 11, and 12 of the total state vector.

The fourth through eleventh measurements are the same as total states. Also $\dot{h}_b = V_e \sin \gamma_e + \dot{x}_{12}$, where the derivative $\dot{x}_{12}$ is computed from equation 2.2-3). Finally, expressions for the accelerometer readings are obtained by writing out the scalar components of the acceleration $\overline{a}_{cB}$ from equation (2.1-1).

In the simulation, the measurements are generated using the above relations along with random noise effects. Except for the airspeed and vertical speed indicators, the noise is an additive, white, mean zero Gaussian process with standard deviation as shown in Table 1 (ref. 4 and 5). The airspeed and vertical speed indicator noises are multiplicative, where the indicated measurement is obtained by multiplying the actual measurement by a normal random variable of mean 1 and standard deviation as given in Table 1.

The incremental measurements to be used with the perturbation model are calculated by subtracting the equilibrium measurement values from the total measurements discussed above except for the first three incremental measurements. For these first three, total helix radius R, helix angle ν, and altitude h are computed from range, azimuth, and elevation using the following equations:

$$R = \sqrt{(r \cos El \cos Az - x_o)^2 + (r \cos El \sin Az - y_o)^2}$$

$$\gamma = \tan^{-1} \left[\frac{r \cos El \sin Az - y_o}{r \cos El \sin Az - x_o} \right]$$

$$h = r \sin El$$

Then the equilibrium radius, angle, and altitude are subtracted to generate the incremental measurements.

The fifteen incremental measurements are linear functions of x and x_w. Hence, the incremental measurement vector y can be written as $y = C_x + C_w X_w + v$, where v is a noise term whose coordinates are assumed to be white, mean zero Gaussian processes with standard deviations that are the same as for the total measurements except for the noise terms in y_1, y_2, y_3, y_{10}, and y_{12} (see Table 1).

3. THE CONTROL SYSTEM DESIGN

Using the aircraft, wind, and measurement models presented in the previous chapter, the total system model is

$$\dot{x}(t) = Ax(t) + Bu(t) + D_o w(t) + D_1 \zeta(t) \tag{3-1}$$

$$\dot{w}(t) = A_w w(t) + B_w \zeta(t) \tag{3-2}$$

$$y(t) + Cx(t) + C_w w(t) + v(t) \tag{3-3}$$

where x, u, w and y are the state, control, wind disturbance, and measurement vectors resp., v(t) is a white, Gaussian vector of measurement noise and $\zeta(t)$ is a white, Gaussian noise vector that drives the wind system and corrupts the air-

craft system. The matrices A, B, D_o, D_1, A_w, B_w, C and C_w are time-invariant with appropriate dimensions.

The problem of designing a feedback compensator is posed as the usual linear, stochastic regulator problem. For the regulator problem, a quadratic cost functional of the form

$$J = \frac{1}{2} E \{\int_{t_o}^{t_f} [x'(t) Qx(t) + u'(t) Ru(t)]dt\} \tag{3-4}$$

is used, where E is the expectation operator, the prime denotes the transpose, and both Q and R are positive definite, time-invariant weighting matrices. The problem can now be stated as follows. Given the linear system of equations (3-1 to 3-3), find a control u such that the cost functional J of equation (3-4) is minimized.

The first step in solving this problem is to transform the system of equations (3-1 to 3-4) into their discrete-time equivalents. This is done for several reasons. First, a digital compensator is desired since the on-board computer is digital and any control algorithm must be compatible with a digital system. Secondly, the MLS data is only provided periodically. Therefore, the measurement system is inherently a discrete-time one. Finally, a digital simulation is used to test each design. Therefore, the discrete-time equivalent difference equations make the simulation very easy to implement on a digital computer.

The equivalents are obtained by integrating the system differential equations and cost functional over each sampling period (ref. 6).

If we restrict $u(t)$ to be constant over the sampling period, the resultant discrete-time equations are

$$x_{k+1} = \phi x_k + \Gamma_2 w_k + \Gamma_1 u_k + \xi_k \tag{3-5}$$

$$w_{k+1} = \phi_w w_k + \eta_k \tag{3-6}$$

where the subscript k denotes the kth sample and $[\xi_k' \mid \eta_k']'$ is a mean zero, white noise sequence whose variance depends on the variance of the continuous noise vector $\zeta(t)$.

The discrete-time equivalent measurement equation can be obtained directly from the continuous time equation:

$$y = Cx_k + C_w w_k + v_k \tag{3-7}$$

Finally, the discrete-time equivalent of the cost functional (3-4) can be written as a sum of n integrals. The resultant expression for the cost functional becomes:

$$J = \frac{1}{2} E \{\sum_{k=o}^{n} x_{k+1}' \hat{Q} x_{k+1} + 2x_{k+1}' \hat{N} w_{k+1} + 2x_k' \hat{M} u_k + u_k' \hat{R} u_k\} \tag{3-8}$$

Note that, since the original system and cost matrices are time-invariant, so are the discrete-time system and cost matrices.

The problem can now be restated as follows. Find a control sequence u_k which minimizes the cost functional J in equation (3-8) subject to the constraints that the state equations (3-5, 6, 7) must be satisfied and that $\{u_k\}$ must explicitly depend only on the past measurements $y_k = \{y_o, y_1, \ldots, y_{k-1}\}$, where v_k is a zero-mean, Gaussian, white noise sequence independent of $[\xi_k' \mid \eta_k']'$.

The above system of equations (3-5, 6, 7, 8) can be augmented to obtain a form very similar to the discrete linear quadratic Gaussian stochastic control problem. However, if the normal method of solution is applied, an important difficulty surfaces. The total system may be unstable and uncontrollable due

to an unstable wind system. Therefore, if the augmented system is solved with an unstable wind system, the solution to the Riccati equation diverges due to the presence of unstable and uncontrollable poles. But, under certain conditions the gains will be bounded.

It can be shown (ref. 6) that the solution to the stochastic optimal control problem described previously exists and is given by:

$$u_k^* = - H_k \hat{x}_k - H_{wk} \hat{w}_k$$

$$H_k = \tilde{R}_k^{-1} G_k, \quad H_{wk} = \tilde{R}_k^{-1} G_{wk}, \quad \tilde{R}_k = \hat{R} + \Gamma_1' P_k \Gamma_1$$

$$G_k = \Gamma_1' P_k \phi + \hat{M}' \quad , \qquad G_{wk} = \Gamma_1'(P_{wk} \phi_w + P_k \Gamma_2)$$

$$P_{k-1} = \phi' P_k \phi + \hat{Q} - G_k' R_k^{-1} G_k, \quad P_n = \hat{Q}$$

$$P_{wk-1} = (\phi - \Gamma_1 \tilde{R}^{-1} G_k)'(P_{wk} \phi_w + P_k \Gamma_2) + \hat{N}, \quad P_{wn} = \hat{N}$$

where $\hat{x}_k$ and $\hat{w}_k$ are one-step predicted estimates of x_k and w_k given by:

$$\hat{x}_k = E\{x_k|y_{k-1}\} \text{ and } \hat{w}_k = E\{w_k|y_{k-1}\}$$

It should be noted that the above gain equations remain valid for any i-step predicted estimate (where i = 0 represents a filtered estimate). The one-step prediction was used here in order to account for computational delays present in the on-board computer.

Also, the equations above are of a recursive nature. Therefore, at each sampling instant a new optimal gain is calculated. To implement this would require storing all the intermediate values of each gain matrix. This, in turn would require a greater amount of storage than is normally available for small, on-board computers. For these reasons, a suboptimal design was used consisting of only the steady state gains obtained when the index on the recursive relations tends to infinity.

It should be emphasized that the optimal control for a system with disturbances consists of two parts. The first part feeds back state estimates multiplied by an optimal gain H_k. This gain is exactly the same as would have been calculated with no disturbance present. The second term feeds back the disturbance estimates multiplied by a gain H_{wk}, which depends on the disturbance.

The next step is to obtain the state and wind estimate. This is accomplished by first augmenting the discrete-time equations (3-5, 6, 7):

$$\begin{bmatrix} x_{k+1} \\ \hline w_{k+1} \end{bmatrix} = \begin{bmatrix} \phi & \Gamma_2 \\ \hline 0 & \phi_w \end{bmatrix} \begin{bmatrix} x_k \\ \hline w_k \end{bmatrix} + \begin{bmatrix} \Gamma_1 \\ \hline 0 \end{bmatrix} u_k + \begin{bmatrix} \xi_k \\ \hline \eta_k \end{bmatrix} + \chi_k$$

$$y_k = [C \mid C_w] \begin{bmatrix} w_k \\ \hline \overline{w}_k \end{bmatrix} + v_k$$

χ_k is a white noise term representing modeling error.

Given the past measurements y_k, it can be shown (ref. 7) that the one-step predicted estimates of x_{k+1} and w_{k+1} are given by the equations below:

$$\begin{bmatrix} \hat{x}_{k+1} \\ \hline \hat{w}_{k+1} \end{bmatrix} = \begin{bmatrix} \phi & \Gamma_2 \\ \hline 0 & \phi_w \end{bmatrix} \begin{bmatrix} \hat{x}_k \\ \hline \hat{w}_k \end{bmatrix} + \begin{bmatrix} \Gamma_1 \\ \hline 0 \end{bmatrix} u_k + L_k \left\{ y_k - [C \mid C_w] \begin{bmatrix} \hat{x}_k \\ \hline \hat{w}_k \end{bmatrix} \right\}$$

where $\hat{x}_o = m_o = E\{x_o\}$, $\hat{w}_o = 0$, and

$$L_k = \begin{bmatrix} \phi & \Gamma_2 \\ \hline 0 & \phi_w \end{bmatrix} \Sigma_k \; [c \mid c_w]' \; ([c \mid c_w] \; \Sigma_k \; [c \mid c_w]' + \theta_k)^{-1}$$

where $\Sigma_k = E \left\{ \begin{bmatrix} \tilde{x}_k \\ \tilde{w}_k \end{bmatrix} \begin{bmatrix} \tilde{x}_k \\ \tilde{w}_k \end{bmatrix}' \right\}$, $\begin{bmatrix} \tilde{x}_k \\ \tilde{w}_k \end{bmatrix} = \begin{bmatrix} x_k \\ w_k \end{bmatrix} - \begin{bmatrix} \hat{x}_k \\ \hat{w}_k \end{bmatrix}$ is the estimation

error, and Σ_k can be found by solving the Riccati type equation:

$$\Sigma_{k+1} = \begin{bmatrix} \phi & \Gamma_2 \\ \hline 0 & \phi_w \end{bmatrix} \left\{ \Sigma_k - \Sigma_k \; [c \mid c_w]' \; ([c \mid c_w] \; \Sigma_k \; [c \mid c_w]' + \theta_k)^{-1} [c \mid c_w] \; \Sigma_k \right\}$$

$$\begin{bmatrix} \phi & \Gamma_2 \\ \hline 0 & \phi_w \end{bmatrix}' + \Xi_k$$

where $\quad \Sigma_0 = E \left\{ \begin{bmatrix} x_0 \\ w_0 \end{bmatrix} \begin{bmatrix} x_0 \\ w_0 \end{bmatrix}' \right\}$, $\Xi_k \, \delta_{kj} = E \left\{ \begin{bmatrix} \xi_k \\ \eta_k \end{bmatrix} \begin{bmatrix} \xi_k \\ \eta_k \end{bmatrix}' \right\} + E \{\chi_k \; \chi_k'\}$

$$\theta_k \, \delta_{kj} = E \{v_k \; v_j'\}$$

and $\quad E \left\{ v_k \begin{bmatrix} \xi_j \\ \eta_j \end{bmatrix}' \right\} = E \left\{ v_k \begin{bmatrix} x_0 \\ w_0 \end{bmatrix}' \right\} = E \left\{ \begin{bmatrix} \xi_k \\ \eta_k \end{bmatrix} \begin{bmatrix} x_0 \\ w_0 \end{bmatrix}' \right\} = 0 \quad$ for all k

j = 0, 1, 2, ...

It must be noted that, as with the control equations, these equations are recursive. For the same reasons discussed previously, a suboptimal predictor was implemented using only the steady state solutions to the above equations.

Now that the optimal controls have been defined for specific cost matrices the main concern becomes testing to see if the chosen cost matrices lead to an acceptable system response or if they must be modified to achieve this goal. The digital simulation described in the next section will provide the final step of the design procedure satisfying the above testing and modification requirements.

4. SIMULATION RESULTS

The main objective considered in generating these results was to design the control system so that the aircraft position was kept close to the equilibrium in the presence of various steady wind magnitudes. Thus, the objective was to keep the helix radius, altitude, and airspeed perturbations small while allowing some of the other perturbations, such as the altitude variables, to become relatively large.

The first set of results (Table 2) shows how the control system reacts to increasing steady winds. Three simulation runs were made with steady wind velocities of 3.05 m/sec (10 ft/sec), 6.1 m/sec (20 ft/sec), and 12.2 m/sec (40 ft/sec). The rms gust velocity in all runs was 0.61 m/sec (2 ft/sec). The results in Table 2 indicate that, as the steady wind increases, the maximum deviations in the bank angle, heading angle, and helix angle also increase proportionally, while the maximum deviations in helix radius, altitude, and airspeed increase at a much smaller rate.

The results in Table 3 show the importance of the control gain matrix H_w in controlling the aircraft in the presence of winds. Two runs were made with

12.2 m/sec (40 ft/sec) winds, one with H_w used in the control scheme and one without H_w. As the results indicate, the H_w term in the control calculations has a large effect in providing satisfactory control in the presence of winds.

5. CONCLUDING REMARKS

A linear, time-invariant perturbation model of an aircraft flying a descending helix in the presence of winds was developed. An automatic control system was designed through an application of the **linear-quadratic-Gaussian** discrete-time regulator theory.

Using a performance criteria including maintaining a circular ground track of correct radius as well as maintaining proper altitude and airspeed, preliminary simulation results have shown that the control system can perform satisfactorily in the presence of steady winds without excessively large deviations in other variables, such as bank and pitch angles.

REFERENCES

1. J. P. Reeder, R. T. Taylor, and T. M. Walsh, "New Design and Operating Techniques for Improved Terminal Area Compatibility," Society of Automotive Engineers Air Transportation Meeting, Dallas, Texas, April 30 - May 2, 1974.

2. B. Etkin, Dynamics of Atmospheric Flight. New York: John Wiley & Sons, Inc., 1972.

3. A. Papoulis, Probability, Random Variables, and Stochastic Processes. New York: McGraw-Hill Book Company, 1965.

4. W. C. Hoffman, W. M. Hollister, and R. W. Simpson, "Functional Error Analysis and Modeling for ATC Systems Concepts Evaluation," Aerospace Systems, Inc., Report No. DOT-TSC-212-72-1, May, 1972.

5. W. F. Hodge and W. H. Bryant, "Monte Carlo Analysis of Inacuracies in Estimated Aircraft Parameters Caused by Unmodeled Flight Instrumentation Errors," NASA TN D-7712, Feb., 1975.

6. N. Halyo and R. H. Foulkes, "On the Quadratic Sampled-Data Regulator With Unstable Random Disturbances," Proceedings, 1974 IEEE Systems, Man, and Cybernetics Conference, Dallas, 1974.

7. J. S. Meditch, Stochastic Optimal Linear Estimation and Control. New York: McGraw-Hill Book Company, 1969.

TABLE 1. MEASUREMENT NOISE STANDARD DEVIATIONS

MEASUREMENT	NOISE STANDARD DEVIATION
Range	.305 m (1 foot)
Azimuth	0.41×10^{-3} rad
Elevation	0.61×10^{-3} rad
Helix Radius	1.52 m (5 feet)
Helix Angle	10^{-3} rad
Altitude	3.05 m (10 feet)
Rate gyros (p, q, r)	0.1 deg/sec
Bank gyro	0.5 deg
Pitch gyro	0.15 deg
Heading gyro	1. deg
Airspeed (total)	.02
Airspeed (incremental)	$.02 \, V_e$
Barometric altimeter	8.38 m (27.5 feet)
Vertical speed indicator (total)	.05
Vertical speed indicator (incremental)	$.05 \, \dot{h}_{b_e}$
Accelerometer ($\ddot{x}_B$, $\ddot{z}_B$)	4.91 cm/sec^2 (.161 ft/sec^2)
Accelerometer ($\ddot{y}_B$)	.491 cm/sec^2 (.016 ft/sec^2)

TABLE 2.   EFFECT OF STEADY WINDS

Steady Wind Magnitude, m/sec (ft/sec)	3.05 (10)	6.1 (20)	12.2 (40)
Maximum Perturbation Magnitude			
Bank angle, deg	2.0	3.1	6.7
Heading angle, deg	9.1	16.3	31.4
Helix angle, deg	5.2	9.7	19.5
Airspeed, m/sec (ft/sec)	1.7 (5.6)	1.4 (4.5)	2.0 (6.6)
Helix radius, m (ft)	5.6 (18.3)	7.3 (24.0)	11.0 (36.0)
Altitude, m (ft)	7.3 (24.0)	8.1 (26.7)	10.0 (32.8)

TABLE 3.   EFFECT OF CONTROL GAINS H_W

Maximum Perturbation Magnitude	with H_W	without H_W
Airspeed, m/sec (ft/sec)	2.1 (6.8)	3.2 (10.4)
Helix radius, m (ft)	11.3 (37.0)	81.7 (268.1)
Altitude, m (ft)	10.3 (33.8)	16.0 (52.4)

Page intentionally left blank

LIST OF PARTICIPANTS

Aberson, J. A.; 215
Adamson, T. C., Jr.; 1425
Amlicke, B. B.; 1397
Andersen, C. M.; 425
Anderson, J. M.; 215
Anderson, M. S.*
Arduini, R.; 1085
Arin, K.; 283
Atluri, S. N.; 267
Averner, M. M.; 1203

Baals, D. D.; 1583
Bahar, L. Y.; 721
Bailey, F. R.; 1311
Baker, A. J.*
Baldwin, B.; 1483
Ball, W. H. W.; 907
Ballhaus, W. F.; 1311
Barker, L. K.; 757
Barkstrom, B. R.; 1085; 1105
Barton, F.*
Basford, R. C.; 1237
Bass, H. E.; 975
Batson, J. L.; 1665
Bauer, C. L.*; 3
Baumeister, K. J.; 895
Beach, H. L., Jr.; 1629
Belytschko, T.; 385
Bennett, J. A.; 1539
Berke, L.; 365
Bernier, L.; 543
Bertin, J. J.; 1615; 1665
Bloom, A. M.; 1235
Blotter, P. T.; 339
Bobbitt, P. J.*; 1279
Borg, S.; 731
Boris, J. P.; 1281; 1291
Brandt, A.; 1359
Brito, J. D.; 1031
Brock, L. M.; 239
Brown, G. E.; 183
Browne, J. C.; 779
Buchanan, G. R.; 473
Buoncristiani, M.; 747
Burggraf, O. R.; 1437
Bushnell, D. M.*

Callegari, A. J.; 861
Callis, L. B.*
Card, M. F.; 369
Carlson, L. A.; 1387
Chambers, J. R.; 1733
Chang, C. J.; 393
Chang, W. H.; 575
Chen, E. P.; 205
Chen, T. C.; 1115
Chen, Y. M.; 227
Chow, R.; 1423
Christensen, R. M.; 157
Christiansen, V. T.; 339
Conley, D. B.; 1615
Craig, R. R., Jr.; 393
Crews, J. H., Jr.*

Davidson, K. L.; 1137
Davies, H. G.; 997
Davis, P. K.; 327
Davis, R. T.; 1451
Dawson, T. H.; 319
DeJarnette, F. R.*; 1301
Delale, F.; 291
DeVries, K. L.; 27
Dickerson, J.; 741
Dokmeci, M. C.; 481
Doughty, J. O.; 1673
Dowell, E. H.; 1057
Dugundgi, J.; 439
Durum, M. M.; 665

Edwards, E.; 543
Erdogan, F.; 291
Erickson, W. D.*
Eringen, A. C.; 1
Esterling, D. M.; 137

Fairbanks, H. V.; 61
Feng, W. W.; 417
Fenlon, F. H.; 917
Fix, G. J.; 1283
Foulkes, R. H., Jr.; 1767
Fralich, R. W.; 491
Francis, E. C.; 111
Frick, J.; 1311

---

*Session chairman

Garabedian, P. R.; 1349
Gelos, R.; 1125
Gera, J.; 1687
Ghandour, N. N.; 1505
Goble, R. L.; 1237
Goodrich, W. D.; 1615
Gupta, B. P.; 459

Hackett, R. M.; 1641
Hadden, W. J., Jr.; 1009
Hafez, M. M.; 1371
Haggard, K. V.; 1115
Hahn, H. T.; 193
Hale, A. L.; 531
Hale, F. J.; 1713
Halem, M.*
Hallquist, J. O.; 417
Hardrath, H. F.*
Hartung, R. F.; 377
Hayduk, R. J.; 595
Heckel, R. W.; 15
Hiser, H.; 1093
Hoeg, K.; 95
Holst, T. L.; 1467
Hong, C. C.; 699
Horton, T. E.; 963
Houlihan, T. M.; 1137
Huck, F. O.; 769
Hung, C. M.; 1483
Hung, Y. Y.; 1509
Hunter, W. W., Jr.; 1603
Husman, G. E.; 687
Huston, R. L.; 309

Idar, E. S.; 1615

Jensen, R. N.; 1237
Jones, C. F.; 1225
Jones, D. L.; 257
Juruf, R. S.; 1641

Kamat, M. P.; 509
Kandil, O. A.; 1321
Kaplan, M. L.; 1153
Kathiresan, K.; 267
Kelley, H. J.; 1685
Kiefer, F. W.; 339
Kilgore, R. A.; 1565
King, W. W.; 215

Kinney, W. A.; 1019
Kinsinger, R. E.; 1247
Koutsoyannis, S. P.; 851
Kraft, R. E.; 873
Krajcinovic, D.; 627
Kuhn, R. E.*

Lansing, D. L.*
Larsen, J. C.; 1105
Laufer, J.; 835
Laura, P. A. A.; 1125
Lee, S. S.; 1093
Leehey, P.; 1043
Levine, J. S.*; 1191
Liang, C. Y.; 1509
Liebowitz, H.; 257
Lin, H. C.; 449
Lin, T. H.; 67
Lin, S. R.; 67
Little, R. E.*; 51
Lo, K. H.; 157
Louthan, M. R., Jr.; 77
Luckring, J. M.; 1331
Lyon, R. H.; 1031

MacCormack, R. W.; 1285
MacElroy, R. D.; 1203
Maestrello, L.*
Maiden, D. E.; 1177
Markenscoff, X.; 301
Marshall, R. D.; 1167
Masur, E.; 501
McCormick, B. W.; 1549
McGowan, J. J.; 585
McGrath, J. E.; 37
McNitt, R. P.; 77
Meirovitch, L.; 531
Melnik, R. E.; 1423
Messiter, A. F.; 1425
Mishra, R. S.; 275
Mook, D. T.; 1321
Morris, R. R.; 1665
Mulholland, G. P.; 459
Murch, S. A.; 111
Murman, E. M.; 1371
Myers, M. K.*; 861

Nagamatsu, H. T.; 1247
Nahavandi, A. N.; 907

*Session chairman

Narasimhan, N. N. L.; 1505
Narayan, R.; 275
Nark, T. C., Jr.; 1563
Nayfeh, Adnan H.; 349
Nayfeh, Ali H.*; 821; 1321
Nguyen, L. T.; 1733
Ni, C. M.; 653
Noll, R. B.; 1703
Noor, A. K.; 425
Nuismer, R. J.; 183

Oden, J. T.; 555
Ortega, J. M.*
Orszag, S.; 1287

Padovan, J.; 409
Paine, D. A.; 1153
Park, J.; 1225
Park, S. K.; 769
Pearce, E.*
Peddieson, J., Jr.; 575; 947
Peeters, R. L.; 111
Pepe, S.; 103
Pepe, W. D.; 103
Phillips, R. L.; 791
Phoenix, S. L.; 167
Pierce, A. D.; 1009; 1019; 1071
Pinson, L. D.*
Poulose, P. K.; 257
Powell, A.; 819
Prevost, J. H.; 95

Quaranta, J. E.; 1767
Queijo, M. J.*

Raftopoulos, D. D.; 563
Rasmussen, M.; 1653
Reinhold, T. A.; 1167
Remsberg, E. E.; 1225
Reynolds, W. C.; 1289
Rice, E. J.; 883
Rochelle, S. G.; 947
Rodin, E. Y.*
Rossow, M. P.; 521
Rubin, S.*
Runyan, H. L.*

Schetz, J.*
Schmerr, L. W.; 955

Schmit, L. A., Jr.; 361
Schy, A. A.*
Scott, D. S.; 933
Sengupta, S.; 1093
Shearer, M. P.; 3
Shoosmith, J. N.*
Sih, G. C.*; 205
Simmonds, J. G.; 617
Smith, C. W.; 585
South, J. C., Jr.; 1359
Spicer, A. L.; 563
Springer, G. S.; 147
Srinivasan, M. G.; 627
Stalmach, D. D.; 1615
Stanton, E. L.; 381
Stengel, R. F.; 1753
Stern, M.*; 699
Stone, H. S.; 805
Strauss, A. M.; 103; 309
Sturgeon, R. F.; 1539
Sun, B. C.; 907
Sutterlin, M. W.; 1071
Sutton, M. A.; 327

Tauchert, T. R.; 639
Taylor, J. E.; 521
Thompson, J. F.; 1397
Tieleman, H. W.; 1167
Ting, L.; 837
Ting, T. C. T.; 85
Tsai, Y. M.; 247
Turner, R. E.; 1115

Ueng, C. E. S.; 711
Utku, S.*

Valentin, R. A.; 627
Vinson, J.*
Vondrak, R. V.; 1215

Wang, S. S.; 697
Warsi, Z. U. A.; 1397
Webb, G. R.; 747
Weinberg, N.; 1093
Wellford, L. C.; 1371
Wells, W. R.; 873; 1721
Wenzel, A.; 987
Whitcomb, R. T.; 1521
Whitesides, J. L.; 757

*Session chairman

Whitney, J.; 687
Widhopf, G. F.; 1083
Wilkins, M. L.; 227
Williams, J. C., III; 1409
Wilson, E. L.; 383
Witcofski, R. D.; 1265
Wohl, P.; 1493

Wu, E. M.*; 157
Wylie, K. F.; 963

Yuan, S. W.; 1235

Zainea, B.; 671

---

*Session chairman